Seismic Earth Pressure on Basement Walls with Cohesionless Backfill

By

Nathaniel Bryce Wagner

A dissertation submitted in partial satisfaction of the

requirements for the degree of

Doctor of Philosophy

in

Engineering – Civil and Environmental Engineering

in the

Graduate Division

of the

University of California, Berkeley

Committee in charge:

Professor Nicholas Sitar, Chair
Professor Jonathan Bray
Professor Panayiotis Papadopoulos

Spring 2016

Abstract

Seismic Earth Pressure on Basement Walls with Cohesionless Backfill

by

Nathaniel Bryce Wagner

Doctor of Philosophy in Engineering – Civil and Environmental Engineering

University of California, Berkeley

Professor Nicholas Sitar, Chair

Earth retaining structures have historically performed well under seismic loading, including cases in which the structures were designed for less intense ground motion or only considering static loading. The few reported failures are often attributable to waterfront structures retaining saturated backfill where the main factor was liquefaction. The remaining failures are rare and generally involve more complex conditions, such as sloping backfill, or poor construction or design. These observations suggest that seismic design provisions for engineered retaining structures may be too stringent, and in some cases may not be necessary. The objective of this study was to extend previous efforts to understand the seismic interaction of backfill-wall systems using experimental and numerical modeling, with an emphasis on deep, stiff basement walls in cohesionless soil and the current design methods thereof.

The experimental phase of the study consisted of a dynamic centrifuge model of a deep, stiff basement structure with a dry, level, dense sand backfill. The results obtained in the centrifuge experiment were first used to develop and calibrate a two-dimensional, finite difference model using FLAC$^{2\text{-}D}$. A non-linear, hysteretic constitutive model was used to model the cyclic behavior of the soil and linear elastic beam elements were used to model the structure. The numerical simulations captured the most important aspects of the centrifuge experiment, specifically the inertial response and dynamic soil-structure interaction. Special attention was given to the selection of model parameters, the boundary conditions, and the initialization process. The second part of the numerical modeling effort concentrated on analyzing the response of typical prototype basement structures of varying depth using the calibrated soil properties from the first phase of numerical modeling.

As would be expected, the results from the experimental and numerical analyses show that the observed seismic load increments are a function of the ground motion, wall type and the depth of embedment. The dynamic earth pressure increment distribution for deep basement structures is highly non-linear in contrast with shorter retaining structures (<6.5 m in height) for which the dynamic earth pressure increment was observed to increase linearly with depth. The point of

application of the dynamic earth pressure resultant varies between 1/3 H and 0.6 H above the base of the wall, as recommended by most current design procedures. The depth of embedment can be incorporated in traditional limit equilibrium analyses by calculating a seismic coefficient, k_{MHEA}, as the maximum of the average acceleration within the backfill over the depth of the basement structure. Results from previous centrifuge experiments and the experimental results of this study were found to be in good agreement with the seismic earth pressure coefficient, ΔK_{ae}, obtained using the Okabe (1924) pseudo-static Coulomb wedge analysis and the methodology proposed by Seed & Whitman (1970). This suggests that current design procedures overestimate seismic loads on retaining structures not necessarily through inherent conservatism in the methods, but rather due to overly conservative choice of seismic demand input.

Current design methodologies for cantilever and gravity retaining structures in highway applications utilize a similar procedure wherein the seismic coefficient is the maximum of the average acceleration in an assumed failure wedge This method utilizes a maximum value of the seismic coefficient at one instant in time and introduces bias toward the ground motion at the surface if mass-weighted over a wedge of soil that is largest near the top. For retaining structures permitted to displace, in effect allowing a failure wedge to form, the current methodology is applicable although the experimentally and analytically obtained dynamic loads are significantly lower than is predicted by the traditionally used methods. For retaining structures not permitted to translate or rotate, the proposed seismic coefficient is more rational than that computed in the current methodology wherein the peak acceleration at the surface or some fraction thereof is used. Moreover, this definition of the seismic coefficient is consistent with that recommended by Anderson et al. (2008) and Bray et al. (2010).

Evaluating static and dynamic earth pressure on retaining structures is a complex problem with a variety of competing and complementary effects to consider. In this study, a centrifuge experiment replicated the basic response of an idealized soil-basement structure system. Ultimately, further observations of performance in future seismic events and data from instrumented, full scale structures are highly desirable in order to fully validate these results. Numerical modeling offers a means to identify important aspects of the earth pressure problem. However, the results are sensitive to the input parameters, the boundary conditions, and the initialization of the process. Therefore, numerical models should be calibrated against real data when possible.

Table of Contents

List of Figures

List of Tables

Acknowledgements

I am grateful for my advisor, Professor Nicholas Sitar, for all he has done for me. He offered me a position as a research assistant in my final year as an undergraduate student, and then convinced me to embark on the journey that is a doctoral dissertation. His guidance throughout the entire process has been invaluable, and I know he will be influential in my future endeavors.

I would like to thank Professor Gabriel Candia of Universidad del Desarrollo in Santiago, Chile and Dr. Roozbeh Geraili Mikola of Jacobs Associates, who at the time I met them were doctoral students working with Professor Sitar. They were both understanding and patient with me as I learned about centrifuge testing and numerical modeling under their guidance.

I would like to thank the Geoengineering faculty at UC Berkeley: Professors Jonathan Bray, Juan Pestana, Michael Reimer and Raymond Seed. They have provided a great foundation for my future endeavors. I would like to thank the staff at the Center for Geotechnical Modeling at UC Davis: Dan Wilson, Chad Justice, Tom Kohnke, Lars Pederson and Anatoliy Ganchenko. I would like to thank the staff in the Civil & Environmental Engineering Machine Shop at UC Berkeley: Jeff Higginbotham and Matt Cataleta. This research would not have been completed without the help of all the staff at both facilities. I would also like to thank Professor Anil Chopra and Professor Panayiotis Papadopoulos for their input on my research.

I would like to thank the Geoengineering PhD students in Davis Hall during my time at Berkeley: Christine Beyzaei, Heyder Carlosama, Brian Carlton, Khaled Chowdhury, Julien Cohen-Waeber, Tonguc Deger, Estefan Garcia, Michael Gardner, Michael George, Hamed Hamedifar, Connor Hayden, Justin Hollenbeck, Katherine Jones, Robert Lanzafame, Roberto Luque, Jorge Macedos, Christopher Markham, Chukwuebuka Nweke, Nicolas Oettle, Maggie Parks, Nella Pierre-Louis, Michelle Shriro, Joseph Weber and Josh Zupan. I was fortunate to have a wonderful group of people to provide a welcoming and supportive environment.

I would like to thank my family and friends. Everyone participated in the process by asking about my work and providing emotional support when I needed it most. I would especially like to thank my parents, Jane and Craig Wagner, for supporting me and encouraging me to come to Berkeley as an undergraduate student. Without them, I would not be where I am today. Lastly, I would like to thank Gina Gavrilis. Words cannot express how much gratitude I owe her for her patience and support throughout the entire process.

Research funding was provided by a number of sources, including: NSF-NEES-CR Grant No. CMMI-0936376: “Seismic Earth Pressures on Retaining Structures”, California Geotechnical Engineering Association (CalGeo), the State of California Department of Transportation (CalTrans) Contract No. 65N2170, US Nuclear Regulatory Commission (US NRC), and Edward G. Cahill and John R. Cahill Endowed Faculty Chair Funds.

1 Introduction

1.1 Background

Coulomb (1776) developed one of the earliest analytic solutions to determine static lateral earth pressure acting on free-standing retaining structures through the introduction of a “critical slip surface” and separating the shear strength of soil into frictional and cohesive components. Almost 100 years later Rankine (1857) introduced a method to compute coefficients of active and passive pressures based on the frictional stability of a loose granular mass and assuming a general shear failure in the backfill. Currently, these two methods serve as the basis for the most commonly used methods for analyzing static earth pressure in geotechnical engineering practice.

Following the 1923 Great Kantō Earthquake in Tokyo, Japan, the first analytic solution to determine dynamic earth pressure on free-standing retaining walls was developed by Okabe (1924) and Okabe (1926) through an extension of the Coulomb (1776) solution. Mononobe & Matsuo (1929) and Mononobe & Matsuo (1932) validated the Okabe (1924) solution for cohesionless soil and short gravity walls by performing a series of pioneering shaking table experiments. This method of analysis, presently referred to as the Mononobe-Okabe (M-O) method, is widely used to determine seismic earth pressure for scenarios that are not encompassed by the original analysis framework, including non-yielding walls, deep underground structures, and cohesive soils. In this sense, it is one of the most abused analysis techniques in geotechnical engineering (Ostadan, 2005).

Many reviews and analyses have been performed to evaluate the applicability of the M-O method, including e.g. Prakash & Basavanna (1969), Seed & Whitman (1970), Nazarian & Hadjian (1979), Prakash (1981), Lew et al. (2010), and Sitar et al. (2012). However, at this juncture there is no general consensus on an appropriate seismic design method for retaining structures. Specifically, observed seismic performance of retaining structures is much better than would be predicted by the M-O method for strong ground motion, and, hence, it is a standard practice in design to use a fraction of the peak ground acceleration.

A review of the performance of retaining structures in past earthquakes by Lew et al. (2010) shows that failures of basement walls are rare, even though typically they were not designed for the level of shaking that they experienced. The failures of retaining structures that do occur are mainly observed in waterfront structures retaining saturated backfill with liquefaction being the primary factor leading to failure. Otherwise, documented failures are generally due to poor design and construction. The majority of damage reports note the lack of failure of traditional retaining structures, even under severe seismic loading. This reinforces the conclusion by Seed & Whitman (1970) that gravity retaining structures designed for an adequate factor of safety under static loading should perform well up to approximately PGA ~ 0.3 g.

Another important issue is that the height of the retaining structure is often normalized or not even considered in analytic and numerical analyses. For the majority of experimental studies, the

height of the retaining structure does not exceed approximately 6.5 m (~20 ft) in prototype scale. However, results of these studies have been extrapolated to much larger basement structures with the implicit assumption that the seismic loads increase indefinitely with the depth of the structure. Ignoring the height of the retaining structure essentially neglects the effects of incoherence in the backfill.

In this context, in most analytic methods, the effective seismic coefficient, k_h, is generally assumed to be equal to the PGA or some fraction thereof to account for allowable displacements and ductility of the wall. However, the location and time at which the PGA is measured varies from study to study. As a result, it is difficult to make direct comparisons between different experimental studies. In shaking table experiments, the PGA is usually measured at the input, i.e. the table platform; in centrifuge experiments, the PGA is measured at various locations depending on where the structure is located (on a soil foundation or attached to the base of the centrifuge).

1.2 Research Objectives & Scope of Work

This study first revisits current design recommendations and case histories to gain insight into the shortcomings of the recommendations and areas for improvement. Analytic methods are investigated to inform the development of more advanced numerical models. While the methods of analysis have become increasingly sophisticated with the advent of more powerful and specialized software, it is crucial to validate the results from such analyses with real data. With this in mind, experimental methods and results from those studies are investigated.

The experimental phase of this study consists of a centrifuge experiment on a model of a deep, stiff basement wall with a dense Nevada sand backfill and foundation. The model was subjected to a range of ground motions and a dense array of instruments was used to record the dynamic interaction between the foundation soil, the basement wall, and the backfill. The purely numerical phase of this study consisted of a series of two-dimensional, non-linear, finite difference analyses of prototype basement structures with different configurations using the FLAC$^{2\text{-}D}$ finite difference code. The results of these numerical analyses together with the experimental results provide a rational basis for a series of recommendation for the analysis and/or design of different types of soil retaining structures.

2 Literature Review

2.1 Overview of Seismic Design of Basement Walls

Building codes are guiding documents for design and construction specifications to meet a prescribed acceptable amount of risk. Generally, provisions are adopted in response to poor performance; this is especially true for seismic provisions. Changes to U.S. building codes in response to poor performance during earthquakes were published in the SEAOC Blue Book (2009). However, despite no observation of damage to basements due directly to seismic earth pressure, provisions have been introduced into building codes that impact design and costs.

2.1.1 Seismic Earth Pressure Code Provisions in the U.S.

As reported in Lew et al. (2010a), no specific requirements for seismic earth pressure applied to walls retaining earth existed in model building codes in the U.S. through 2003. The International Building Code (IBC) became the first national building code to consider seismic earth pressures on earth retaining walls in the 2006 edition.

ASCE/SEI 7-10 & 41-13

"Minimum Design Loads for Buildings and Other Structures" are published as ASCE Standard ASCE-SEI 7-10 (commonly referred to as ASCE/SEI 7-10, previously published as ASCE/SEI 7-05, and to be published as ASCE/SEI 7-16 in the future). These minimum standards serve as the primary reference for a number of other design provisions. In ASCE/SEI 7-05, earth retaining structures are designed in accordance with Section 11.8.3 which states that the geotechnical investigation report shall include "The determination of lateral pressures on basement and retaining walls due to earthquake motions."

"Seismic Evaluation and Retrofit of Existing Buildings" is published as ASCE Standard ASCE/SEI 41-13. Seismic earth pressure on a building wall is computed in Section 8.6 of ASCE/SEI 41-13, in the absence of a site-specific geotechnical investigation, as $\Delta p = 0.4 k_h \gamma_t H$, where Δp is the additional earth pressure caused by seismic shaking (assumed to be uniform along the depth of the wall), k_h is the horizontal seismic coefficient in the soil, γ_t is the total unit weight of the soil, and H is the height of the retaining wall. This pressure is added to the unfactored static active earth pressure to obtain the total earth pressure on the wall. The commentary in the Standard points out that the seismic pressure is a simplified approximation of the Mononobe-Okabe formulation (discussed later) and that the true distribution of pressure on the walls is very complex. Additionally, the seismic earth pressure computed using this method is for checking the acceptability of local wall components, and therefore should not be used to increase the total base shear on the building.

NEHRP Recommended Provisions

The "2009 NEHRP Recommended Seismic Provisions for New Buildings and Other Structures: Part 1 – Provisions" and "Part 2 – Commentary to ASCE/SEI 7-05", collectively known as the FEMA P-750 report, adopts as its primary reference ASCE/SEI 7-05. As such, identical

provisions for seismic earth pressures are included in FEMA P-750 as in ASCE/SEI 7-05. However, "Part 3 – Resource Papers (RP) on Special Topics in Seismic Design" of the FEMA P-750 report includes "Discussions of topics that historically have been difficult to adequately codify." In particular, Resource Paper 12: Evaluation of Geologic Hazards and Determination of Seismic Lateral Earth Pressures devotes nearly five pages detailing different approaches for determining seismic lateral earth pressures. Resource Paper 12 states that "damage reports for basement walls and retaining structures away from waterfronts are generally limited with only a few cases of stability failures or large permanent movements" according to Whitman (1991). A number of studies are discussed in Resource Paper 12 in detail regarding yielding walls (Okabe, 1924; Mononobe & Matsuo, 1929; Seed & Whitman, 1970) and non-yielding walls (Wood, 1973; Ostadan, 2005) with the one main finding being that "earth pressures acting on the walls of partially embedded structures (e.g., basement walls) during earthquakes are primarily governed by soil-structure interaction (SSI) and, thus, these partially embedded structures should not be treated as a non-yielding wall." Two components of SSI, kinematic and inertial, are considered and a reduction in dynamic earth pressures "may be explained if it is demonstrated that dynamic displacements induced by kinematic and inertial components are out of phase."

The "2015 NEHRP Recommended Seismic Provisions for New Buildings and Other Structures", known as the FEMA P-1050 Report, adopts ASCE 7-10 as its primary reference. However, updates regarding seismic earth pressures on basement walls were not a primary topic addressed by the Provisions Update Committee (Bonneville & Shuck, 2015).

International Building Code

The 2012 International Building Code (ICC, 2011) adopts by reference the seismic requirements of ASCE/SEI 7-10, and the 2015 IBC (ICC, 2014) does not change this practice. Therefore, the requirements for seismic design pressures mandated by ASCE 7-10 are part of IBC.

California Building Code

The California Building Code (CBC) adopts the seismic earth pressure requirements of IBC, with a slight change in language as follows from Section 1803.5.12 of the 2013 CBC (California Building Standards Commission, 2013):

> *For structures assigned to Seismic Design Category E, E or F, the geotechnical investigation required by Section 1803.5.11 shall also include all of the following as applicable:*
>
> 1. *The determination of dynamic seismic lateral earth pressures on foundation walls and retaining walls supporting more than 6 feet (1.83 m) of backfill height due to design earthquake ground motions.*

NCHRP Report 611 & FHWA-NHI-11-032

The National Cooperative Highway Research Program (NCHRP) Report 611 (Anderson et al., 2008) provides a discussion of the issues and assumptions in the limit equilibrium based analysis methods and guidance on how to assess height-dependent seismic coefficient reductions for

determining seismic earth pressure coefficients in Sections 6.1.2 and 7.5 of the report. The effects of cohesion on reducing the seismic earth pressure coefficient are discussed in Section 7.3 of the report. The Federal Highway Administration (FHWA) Report FHWA-NHI-11-032 references NCHRP Report 611 regarding the aforementioned topics.

2.1.2 Damage to Basement Walls during Earthquakes

As reported in Lew et al. (2010a), reports of damage to earth retaining structures during earthquakes are limited to cases of either poorly constructed non-engineered walls or soil-related failure causing the wall to fail. Additionally, most of the observed cases are in marine or waterfront environments.

In a report of damage from the 1971 San Fernando earthquake published by the United States Department of Commerce National Oceanic and Atmospheric Administration (Murphy, 1973), the only reported damage to building basement walls occurred at the Olive View Medical Center, Medical Treatment and Care unit. In this case, the basement wall experienced impacts from the structure that caused tension cracks on the inside (compression face) of the wall. Clough & Fragaszy (1977) studied floodway channels in the Los Angeles area and reported that no damage to retaining walls occurred until accelerations were in excess of about 0.5 g. The retaining walls for the floodway channels were not explicitly designed for seismic loading.

Following the 1989 Loma Prieta earthquake, reconnaissance efforts (Benuska, 1990; Whitman, 1991) reported no damage to basement wall structures or mechanically stabilized earth walls.

Following the 1994 Northridge earthquake, numerous studies reported no damage to basement wall structures (Stewart et al., 1994; Hall, 1995; Holmes & Somer, 1996), temporary deep excavations (Lew et al., 1995) and structures built into hillsides (Shakal et al., 1994).

The 1995 Hyogoken-Nambu earthquake near Kobe, Japan damaged some free standing retaining structures supporting embankments, but no damage to basement walls was reported. A number of subway stations were also damaged, and the Dakai station completely collapsing. It has been accepted that the Dakai station collapsed due to poor structural design and presumably liquefaction, not from dynamic earth pressure (Iida et al., 1996; Yoshida, 2009; Lew et al., 2010b).

The EERI reconnaissance report for the 1999 Kocaeli, Turkey earthquake reported no damage to building basement walls (Youd, Bardet & Bray, 2000).

Huang (2000) and Tokida et al. (2001) reported on damage to retaining structures during the 1999 Chi-Chi, Taiwan earthquake. Numerous gravity retaining walls, wrap-around type geosynthetics-reinforced soil retaining wall, and segmental retaining walls suffered damage, whereas cantilever retaining walls did not. In general, the walls that were damaged were on steep slopes and the failures often involved a combination of bearing capacity failure, overturning

failure, slope instability and direct fault offset. Damage to basement walls was not mentioned in either report.

Rathje et al. (2006) reported no damage to basement and retaining walls following the 1999 Düzce, Turkey earthquake. Gur et al. (2009) later reported on damage to half-buried basements of a four-story school building. The basement wall had windows between the top of the wall and the beams at the top of the basement, and between the exterior basement columns. Damage was concentrated in the masonry infill walls in the basement; however, the concrete retaining wall portions of the basement were undamaged. Gur et al. (2009) also reported on the 2003 Bingöl, Turkey earthquake, in which light damage was observed in basement walls of buildings that either collapsed or suffered severe structural damage.

Sitar et al. (2012) reported on the absence of significant damage to basement and retaining walls during the 2008 Wenchuan, China earthquake, the 2010 Chile earthquake and the 2011 Tōhoku earthquake in Japan. Verdugo et al. (2012) also reported in more detail on the absence of damage following the 2010 Chile earthquake. Kendal Riches (2015) reported minimal damage to retaining structures following the 2010-2011 Canterbury earthquake sequence in New Zealand.

Rollins et al. (2013) reported failures of retaining structures during the 2012 Samara, Costa Rica earthquake; however, the failures were due to poor construction, inadequate backfill drainage, or global sliding failures in soft moving ground.

Nikolaou et al. (2014) observed failure of non-engineered stone walls and walls subject to global slope stability failures during the 2014 Cephalonia, Greece earthquake. Some minor damage was observed in concrete gravity and cantilever walls; the most significant damage reported was the top half of a retaining wall toppling over due to an unreinforced cold joint at mid-height.

Rollins et al. (2014) observed moderate damage to retaining structures and some failures during the 2014 Iquique, Chile earthquake; however, the failures were not a result of excessive seismic earth pressure. Cantilever walls failed because the walls did not have footings; masonry walls failed because there was no reinforcing steel; MSE walls failed because the reinforcing strips corroded in the backfill; quay walls failed because the backfill liquefied. Some minor displacements were observed in gabion walls that were a part of bridge abutments, but no failures were observed. No damage was observed in basement walls.

Hashash et al. (2015) reported no failures and minimal damage to retaining structures during the 2015 Gorkha, Nepal earthquake.

De Pascale et al. (2015) reported no damage to retaining structures with non-liquefiable backfill during the 2015 Illapel, Chile earthquake. A gravity wall near the waterfront failed, although this was assumed to be due to the combined effects of tsunami waves, ground shaking, and possible liquefaction under the footing.

2.2 Methods for Determining Dynamic Earth Pressure

As discussed previously, building codes in the U.S. defer to recommendations from FEMA P-750 and NCHRP Report 611 to determine seismic earth pressures. Noting that static earth pressures are still determined using the theories developed by Coulomb (1776) or Rankine (1857), it is no surprise that the dynamic earth pressures are designed using procedures that are similar in theory and age. Since the first papers regarding dynamic earth pressure on walls were published (Okabe, 1924; Mononobe & Matsuo, 1929), numerous studies have been conducted using a variety of approaches. These approaches can be divided into analytical, numerical, and experimental methods, from which a methodology for rational design is sought. A vast amount of literature exists on this subject; however, this literature review summarizes only previous research of relevance to this study.

2.2.1 Analytical Methods

Analytical methods can be classified in three broad categories: limit state, elastic, and elasto-plastic methods (Veletsos & Younan, 1994a). Limit state methods are based on equilibrium of a soil wedge retained by a wall that displaces sufficiently to induce a limit or failure state in the soil. Elastic methods are based on solutions of the equilibrium equation of a linear elastic continuum, and assume small displacement of the wall. Elasto-plastic methods are also based on solutions of the equilibrium equation, however, large wall displacements of the wall and hysteretic soil behavior are considered. The limit state methods and elastic methods are oversimplifications of the earth pressure problem, resulting in conservative estimates of earth pressure unless the assumptions are satisfied. The utility of these methods is that they generally offer a quick solution that will have inherent conservatism. Elasto-plastic methods are capable of correctly modeling a true scenario accurately; however, their predictive capabilities are limited due to the more complicated formulation. Since elasto-plastic methods are generally implemented with discrete solution methods, they will be discussed in the section on numerical methods.

2.2.1.1 Limit State Methods

Limit state methods can be classified into two categories depending on the types of allowable wall movements: displacing and non-displacing scenarios (Mikola & Sitar, 2013). The preferred use of (non)-displacing over the traditional characterization as (non)-yielding is to highlight the difference between permanent deformation of the wall during a shaking event (preferred) versus exceeding allowable stresses in the structural system (not preferred). Using this definition, free-standing gravity walls and cantilever walls are considered displacing walls whereas building basement walls restrained at the top and bottom and massive gravity walls founded on rock are considered non-displacing walls.

The first limit state method for dynamic earth pressure was proposed by Okabe (1924) and Okabe (1926) in a “General Theory of Earth Pressure”, which extended the Coulomb (1776) method (modified by Mayniel, 1808 and Müller-Breslau, 1906) to include dynamic effects. The

theory was tested with shaking table experiments by Mononobe & Matsuo (1929) and Mononobe & Matsuo (1932), and the method then became known as the Mononobe-Okabe (M-O) method. The original analytic solution by Coulomb (1776) is based on the following assumptions:

- The backfill soil is dry, cohesionless, isotropic, homogeneous, and elastically undeformable with a constant internal friction angle.
- The wall is sufficiently long to cause end effects to be negligible.
- The wall yields sufficiently to mobilize the full shear strength of the backfill along potential sliding surfaces produce minimum active pressures.
- The soil satisfies the Mohr-Coulomb yield criterion and failure occurs along a planar surface that passes through the heel of the gravity wall.

The extension by Okabe (1924) includes all of the assumptions from Coulomb (1776) theory (excluding the restriction on cohesive soil, from a later study by Prakash & Saran, 1966) and includes the following additional assumption:

- Accelerations are uniform throughout the backfill and the dynamic forces are represented as equivalent forces Wk_h and Wk_v applied at the center of gravity of the soil wedge.

The forces considered in the Okabe (1924) analysis are shown in Figure 2.1a. The total seismic force acting on the wall can be expressed deterministically as $P_{ae} = 0.5\gamma H^2(1-k_v)K_{ae}$, where K_{ae} is the coefficient of seismic lateral earth pressure (Equation 2.1),

$$K_{ae} = \frac{\sin(\alpha-\phi+\theta)\cos(\alpha-\beta)\left[\cos(\beta-i)+\frac{2q}{\gamma H(1-k_v)}\cos(\beta)\right]}{\cos^2(\beta)\cos(\theta)\sin(\alpha-i)\cos(\alpha-\beta-\phi-\delta)} - \frac{2c}{\gamma H(1-k_v)}\frac{\cos(\beta-i)\cos(\phi)}{\cos(\beta)\sin(\alpha-i)\cos(\alpha-\beta-\phi-\delta)} \quad \textbf{(2.1)}$$

γ is the unit weight of the soil, H is the height of the wall, q is the surcharge, ϕ is the angle of internal friction of the soil, c is the cohesion intercept of the soil, δ is the angle of wall friction, β is the slope of the wall relative to the vertical, i is the slope of the backfill, $\theta = \tan^{-1}(k_h/(1-k_v))$, k_h is the horizontal acceleration (in g), and k_v is the vertical acceleration (in g). The coefficient K_{ae} varies with the wedge angle α and a unique failure surface is determined by solving $dK_{ae}/d\alpha = 0$. For the particular case of cohesionless backfill soil ($c = 0$) and no surcharge ($q = 0$), the seismic coefficient simplifies to the well-known M-O equation (Equation 2.2):

$$K_{ae} = \frac{\cos^2(\phi-\theta-\beta)}{\cos(\theta)\cos^2(\beta)\cos(\delta+\beta+\theta)\left(1+\sqrt{\frac{\sin(\phi+\delta)\sin(\phi-\theta-i)}{\cos(\delta+\beta+\theta)\cos(i-\beta)}}\right)^2} \quad \textbf{(2.2)}$$

Note that the Okabe (1924) analysis assumes that the earth pressure due to inertial forces is zero at the top and increases linearly with depth whereas earth pressure due to surcharge and cohesion are uniform with depth. Therefore, the point of application of the total seismic load (h_c) moves up with increasing surcharge and cohesion. The results from Mononobe & Matsuo (1932) suggest that the point of application of the total seismic load is roughly 0.622 H for a wall with rigid supports and 1/3 H or less for a wall with elastic supports, the latter of which is based on computations instead of direct measurements. Prakash & Basavanna (1969) performed a similar analysis, and determined that the dynamic earth pressure distribution is not hydrostatic, as is often assumed, and depends on ϕ, δ, and θ.

For a flat backfill ($i = 0$) and no vertical acceleration ($k_v = 0$), the coefficient K_{ae} becomes indefinite for $k_h > \tan(\phi) + 2c/\gamma H$. A similar restriction is common for other limit equilibrium solutions (Prakash & Saran, 1966; Das & Puri, 1996; Richards & Shi, 1994).

Seed & Whitman (1970) performed a parametric study of the M-O analysis to evaluate the relative importance of the various parameters for typical design values. Additionally, they proposed that the total lateral earth pressure acting on a retaining wall can be separated into static and dynamic components as Equation 2.3:

$$P_{ae} = P_a + P_{ae} = \frac{1}{2}\gamma H^2 K_a + \frac{1}{2}\gamma H^2 \Delta K_{ae} = \frac{1}{2}\gamma H^2 (K_a + \Delta K_{ae}) \qquad \textbf{(2.3)}$$

where K_a is Coulomb's coefficient of static earth pressure and $\Delta K_{ae} \approx 0.75 k_h$ is the dynamic increment for a vertical wall ($\beta = 0$), horizontal backfill slope ($i = 0$), and $\phi = 35°$. Based on shaking table experiments by Matsuo (1941), Seed & Whitman (1970) further suggested that the dynamic load increment acts at a height $0.5H$ to $0.67H$ above the base of the wall, which led to the "inverted triangle" interpretation of the dynamic earth pressure. Lastly, Seed & Whitman (1970) recommended that 80% of the PGA should be used in seismic design of retaining walls since the peak ground acceleration occurs only for an instant. The forces considered in the Seed & Whitman (1970) analysis are shown in Figure 2.1b. Note that the M-O and Seed & Whitman (1970) methods do not account for wall inertia. Richards & Elms (1979) observed that wall inertia for gravity retaining walls can be of the same order as that of the dynamic soil pressure computed by the M-O method.

In the concluding remarks, Seed & Whitman (1970) acknowledged that many walls designed only for static earth pressure conditions have performed well in seismic events. Therefore, they recommend that "walls adequately designed for static earth pressure will automatically have the capacity to withstand earthquake ground motions of substantial magnitudes and in many cases, special seismic earth pressure provisions may not be needed." In fact, Mikola & Sitar (2013) concluded that for a static factor of safety of 1.5 a retaining wall should be able to withstand an additional dynamic earth pressure resultant up to PGA = 0.3 g, and for a static factor of safety of

2.0 a retaining wall should be able to withstand an additional dynamic earth pressure resultant up to approximately PGA = 0.6 g.

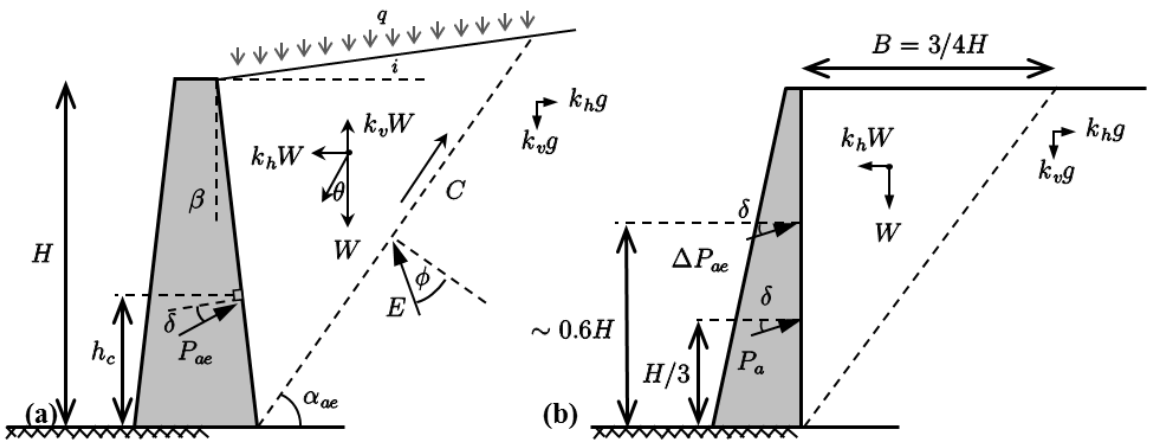

Figure 2.1: Force diagrams used in (a) Okabe (1924) and (b) Seed & Whitman (1970) (adapted from Candia & Sitar, 2013)

Whitman (1990) updated the selection of the seismic coefficient k_h to include the effects of allowable displacement more rationally by considering the wall-soil system to be analogous to a Newmark (1965) rigid sliding block analysis. The author mentions that this procedure is only applicable to gravity retaining structures. Bray et al. (2010) further updated this procedure by considering a deformable sliding mass (i.e., incoherence in the backfill) and a much larger dataset.

Mylonakis et al. (2007) developed an alternative to the M-O analysis based on the theory of discontinuous stress fields. The geometry of the problem considered is shown in Figure 2.2.

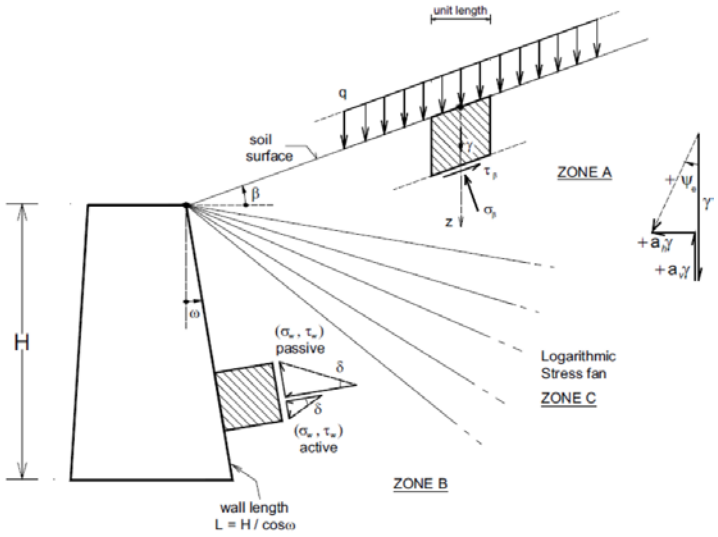

Figure 2.2: Problem geometry from Mylonakis et al. (2007) (adapted from Kloukinas et al., 2008)

The total seismic force acting on the wall can be expressed deterministically as $P_E = (1 - a_v)\left[K_{Eq} qH + 0.5 K_{E\gamma} \gamma H^2\right]$, γ is the unit weight of the soil, H is the height of the wall, q is the surcharge, and a_v is the vertical acceleration (in g). $K_{E\gamma}$ is defined in Equation 2.4, where ϕ is the angle of internal friction of the soil, δ is the angle of wall friction, ω is the slope of the wall relative to the vertical, β is the slope of the backfill, $\psi_e = \tan^{-1}(a_h/(1 - a_v))$, a_h is the horizontal acceleration (in g), $\Delta_1^* = \sin^{-1}(\sin(\beta + \psi_e)/\sin\phi)$, $\Delta_2 = \sin^{-1}(\sin\delta/\sin\phi)$, and $2\theta_E = \Delta_2 \mp (\Delta_1^* + \delta) + \beta - 2\omega - \psi_e$. K_{Eq} is defined based on $K_{E\gamma}$ as $K_{Eq} = K_{E\gamma} \cos\omega/\cos(\omega - \beta)$.

$$K_{E\gamma} = \frac{\cos(\omega - \beta)\cos(\beta + \psi_e)}{\cos\psi_e \cos\delta \cos^2\omega} \times \left[\frac{1 - \sin\phi\cos(\Delta_2 - \delta)}{1 + \sin\phi\cos[\Delta_1^* + (\beta + \psi_e)]}\right] \exp(-2\theta_E \tan\phi) \quad \textbf{(2.4)}$$

Using positive values for ϕ and δ corresponds with active conditions, and negative values correspond with passive condition. The solution is conservative compared to the results from M-O, with the conservatism increasing for high levels of horizontal seismic coefficient, smooth walls, level backfills, and high friction angles. Note that the authors mention that the solution was verified with analytical results, not experimental results.

The majority of limit state methods assume that the accelerations in the backfill are uniform, which implies that shear waves travel at infinite speed. The effects of a finite shear wave velocity in the backfill of a gravity wall founded on rock were studied by Steedman & Zeng (1990). This method is an extension of the M-O analysis considering a sinusoidal distribution of acceleration with constant amplitude in the backfill with input motion given by $\ddot{u}(t) = k_h g sin\,(\omega t)$. Steedman & Zeng (1990) concluded that the difference in phase of the backfill acceleration affects the distribution of dynamic earth pressure, but not in the total seismic load. However, this solution does not consider energy dissipation in the soil and ignores the zero shear stress boundary condition at the surface. This causes the coefficient of total earth pressure to decrease monotonically with increasing input frequency. Kloukinas et al. (2008) developed a similar solution through an extension of the approach presented by Mylonakis et al. (2007) to incorporate non-uniform acceleration in the backfill. The result was also similar, i.e., the coefficient of total earth pressure decreased monotonically with increasing input frequency.

To address these issues, Candia & Sitar (2013) developed a solution based on the dynamic response of a gravity retaining wall of height H_{wall} supporting a viscoelastic soil backfill of total depth H_{soil}. Vertically propagating shear waves are assumed to satisfy the wave equation (Schnabel, Lysmer & Seed, 1972), which can be solved analytically for sinusoidal input acceleration. Using this approach, the sinusoidal distribution of acceleration in the backfill has varying amplitude with depth, compared to a constant amplitude sinusoidal distribution for Steedman & Zeng (1990) and a uniform distribution for the M-O method. The solution accounts

for energy dissipation in the soil and satisfies the zero stress boundary condition at the surface. However, the solution predicts significant amplification of the total earth pressure resultant at the resonant frequencies of the backfill. Viscous damping reduces the total earth pressure resultant and affects the attenuation of higher frequency input motions. The effects of the frequency of the input motion and depth to bedrock were also investigated. For a wall founded on bedrock, which corresponds to $H_{wall} = H_{soil}$ in this analysis, the maximum earth pressure resultant occurs at the resonance frequency $f/f_0 = 1$, where $f_0 = V_s/4H_{wall}$. For soil deposits deeper than the height of the wall, the maximum earth pressure resultant occurs at $f/f_0 = H_{wall}/H_{soil} < 1$.

Candia, Sanhueza & Sitar (2014) further investigated the use of a wave equation analysis to study the effects of the wall height. The analysis used a non-uniform shear wave velocity profile described by $V_s(z) = V_{s0}(1 + lz)^m$ and the hyperbolic shear modulus degradation curves proposed by Darendeli (2001) to produce a more realistic soil profile. The wall height varied from 10 m to 40 m, and the results showed a decrease in the calculated dynamic earth pressure coefficient with increasing wall height for 60 acceleration records compared to the M-O method and using the peak ground acceleration at the surface as the abscissa. The authors note that the acceleration profile in the backfill became increasingly non-uniform as the wall height was increased due to considering deeper parts of the backfill in the analysis. The effect is that the inertial forces from the backfill at depth become increasingly lower than would be predicted if the acceleration profile were constant, thus the calculated dynamic earth pressure coefficient being lower for taller walls. Incorporating cohesion also caused the calculated dynamic earth pressure coefficient to decrease.

2.2.1.2 Elastic Methods

Elastic methods utilize the theory of elasticity to analyze the dynamic response of retaining structures with a linear elastic backfill modeled as a continuum and the interaction between the two modeled with appropriate boundary conditions.

Matsuo & Ōhara (1960) developed a solution for a wall on a rigid foundation with a semi-infinite elastic backfill soil subject to sinusoidal base acceleration. In this analysis, the wall was either constrained (non-displacing) or allowed to rotate about its base (displacing), the former supplying an upper bound solution to the problem. Scott (1973) expanded the idea of a simple 1-D shear beam model to evaluate the pressure acting on walls in bounded and semi-infinite backfills using Winkler springs at the soil-wall interface.

The most commonly used elastic solution is that of Wood (1973), which is generally applied for “rigid walls”. In this analysis, the soil continuum is bounded on the sides by rigid boundaries representing smooth non-displacing walls and at the base by a rigid boundary with earthquake forces modeled as a uniform body force (Figure 2.3).

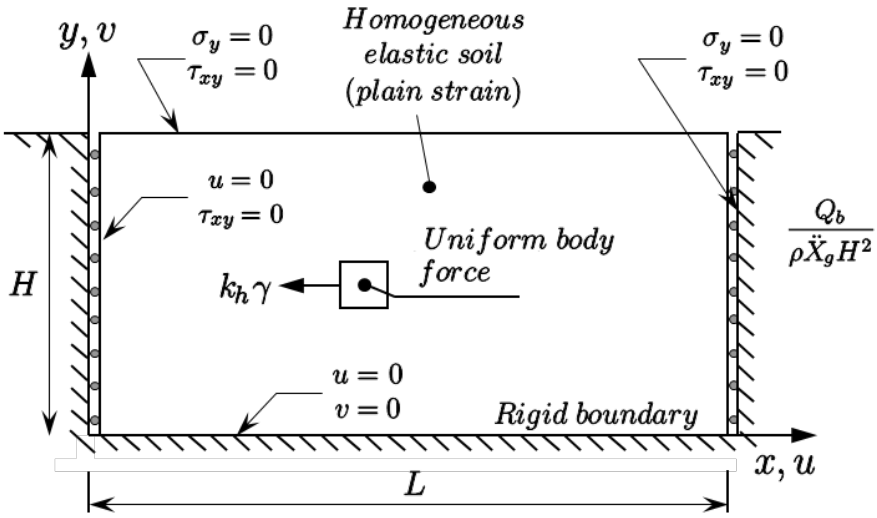

Figure 2.3: Wood (1973) model for rigid walls

The dynamic pressure resultant on the boundary wall is represented as $Q_b = Fk_h\gamma H_{wall}^2$, where F is a function of Poisson's ratio ν and the ratio of the distance between the side boundaries and the height of the wall, L/H. The value of F is approximately equal to one (Whitman, 1991), resulting in a dynamic pressure resultant approximately equal to twice that predicted by the M-O method. The point of application of the dynamic pressure resultant is taken at a height $0.55H$ to $0.60H$ above the base, similarly to Seed & Whitman (1970). Note that the results of this study are based on pseudo-static loading of the soil via body forces, and as such the effects of wave propagation in the soil are not included. Veletsos & Younan (1995) solved the same problem analytically and were able to reproduce the solution. The authors note that this solution is more applicable for tanks in nuclear facilities storing radioactive waste in cases when the waste is more appropriately modeled as deformable elastic solids rather than an incompressible liquid.

Veletsos & Younan (1994a) investigated the response of massless, rigid straight walls with a semi-infinite uniform layer of viscoelastic material subject to harmonic and earthquake excitation. The soil between the wall and the free field was modeled as a series of semi-infinite, elastically supported horizontal bars with distributed mass and horizontal linear springs. The dynamic pressure resultant is given by Equation 2.5 (updated in Veletsos & Younan, 1994b):

$$Q_b = -\frac{16\Psi_0}{\pi^3}\rho\ddot{X}_g H^2 \sum_{n=1}^{\infty} \frac{1}{(2n-1)^3} \sqrt{\frac{1+i\delta}{1-(\omega/\omega_n)^2+i\delta}}\, e^{i\omega t} \qquad \textbf{(2.5)}$$

where $\Psi_0 = \sqrt{2/(1-\nu)}$, δ is the frequency-independent soil damping factor, ω is the frequency of harmonic input, and ω_n is the nth frequency of vibration of the backfill. The solution with no vertical stress agrees with the Wood (1973) method and the earth pressure increases monotonically from zero at the base to a maximum value at the top, reinforcing the inverted

triangle interpretation implied by Seed & Whitman (1970). Veletsos & Younan (1994b) further investigated the problem by allowing a massless, rigid wall to rotate about its base through a torsional spring boundary condition (characterized by $d_\theta = GH^2/R_\theta$ where G is the elastic shear modulus of the backfill, H is the backfill height, and R_θ is the torsional spring constant), as did Wood (1973) (Figure 2.4).

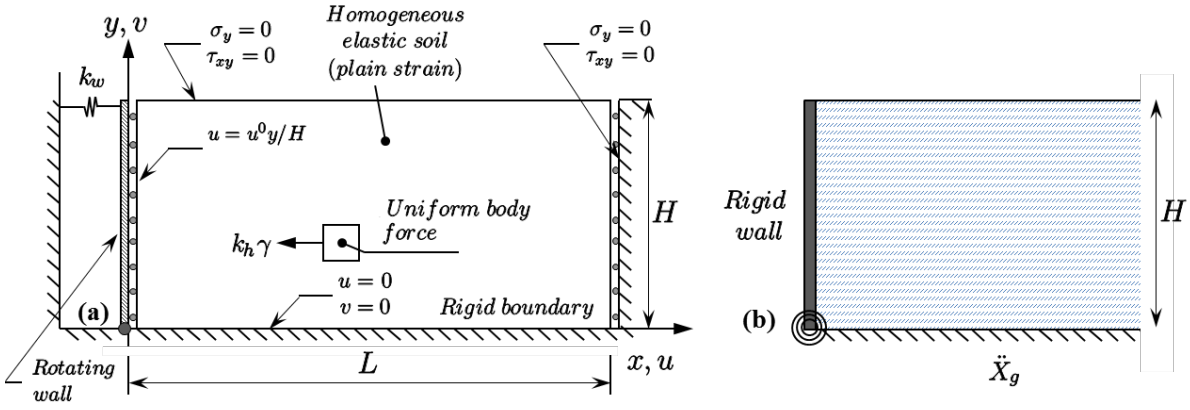

Figure 2.4: Rigid wall with rotating base (a) Wood (1973), (b) Veletsos & Younan (1994b)

Veletsos & Younan (1997) accounted for wall flexibility (characterized by $d_w = GH^3/D_w$ where $D_w = E_w t_w^3/12(1-\nu_w^2)$ is the flexural rigidity per unit length of the wall) and base flexibility and computed dynamic pressure resultants that were about half that of massless, rigid, fixed based walls (as in Wood, 1973 and Veletsos & Younan, 1994a), which agrees with the result of the M-O solution. The earth pressure distributions for Veletsos & Younan (1997) were not monotonically decreasing with depth and exhibit tensile stresses at the top of the wall for increasing flexibility of the wall or base torsional spring (Figure 2.5a, b). The total base shear on the wall and the point of application of the load decreased with increasing wall and base flexibility (Figure 2.5c, d). Veletsos & Younan (1994b) also considered a parabolic distribution of shear modulus of the backfill (Figure 2.5e). The authors noted that "for realistic wall flexibilities the total wall force or base shear is one-half or less of that obtained for a fixed-base, rigid wall". However, dynamic amplification will tend to increase the total wall force when the excitation frequency is near the fundamental frequency of the soil-wall system. The competing effects of increased system flexibility and dynamic amplification seem to cancel out near the fundamental frequency, but the effects of system flexibility dominate the response away from resonance.

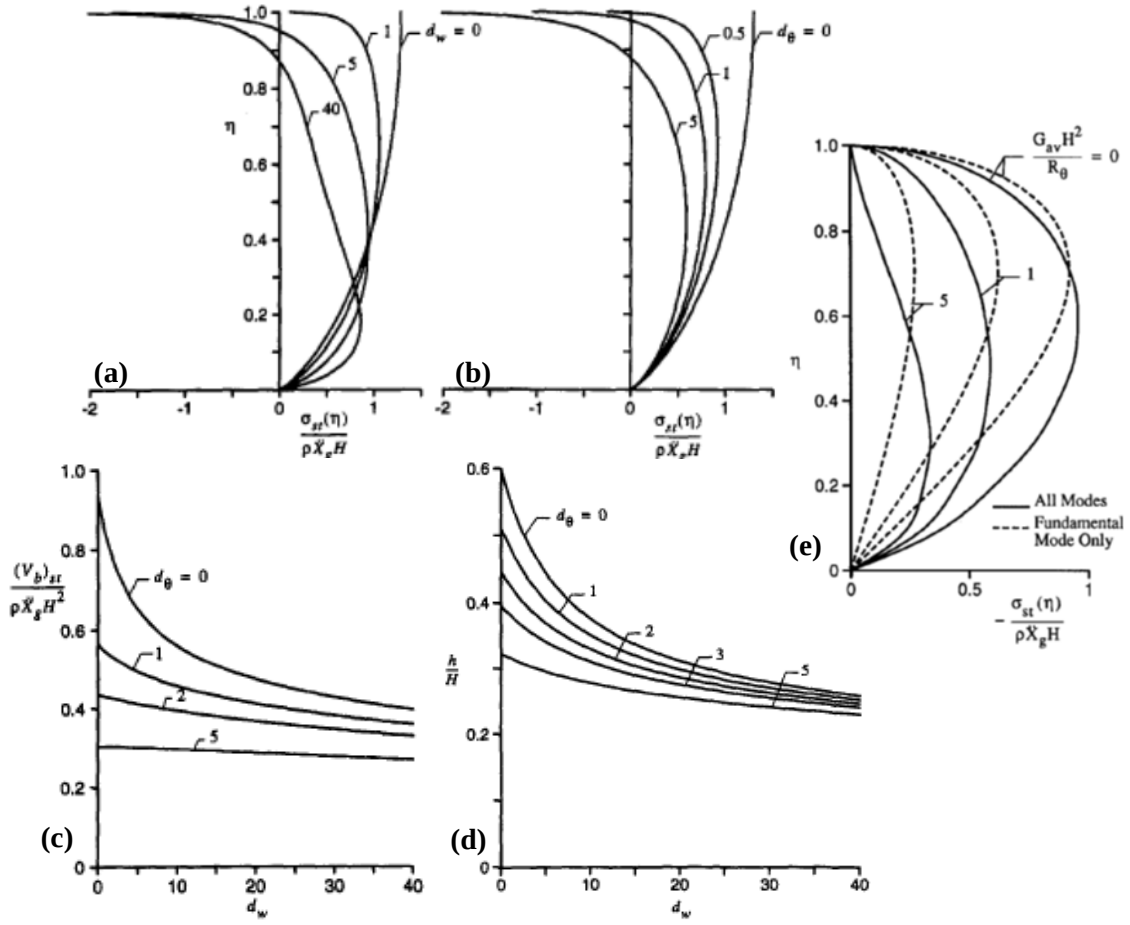

Figure 2.5: Effects on wall loading from Veletsos & Younan (1994b, 1997)
(a) effect of wall flexibility on pressure distribution, (b) effect of base flexibility on pressure distribution, (c) effect on total base shear, (d) effect on point of application on wall, (e) effect of parabolic distribution of shear modulus on pressure distribution

Note that the plots shown in Figure 2.5 are for "static" excitation, wherein the entire backfill has a uniform acceleration field corresponding to $\omega \to 0$. Veletsos & Younan (1994a) characterized the horizontal pressure distribution on a rigid, irrotational wall with uniform backfill subject to harmonic excitation as Equation 2.6:

$$\sigma_w(\eta) = -(g_1 + ig_2)\Psi_0 \rho \ddot{X}_g H \qquad \textbf{(2.6)}$$

where g_1 and g_2 are dimensionless factors that depend on η, ω and δ. The real-valued amplitude of the pressure is given by $\sqrt{g_1^2 + g_2^2}$. The heightwise variation of $\sqrt{g_1^2 + g_2^2}$ for various harmonic input frequencies characterized by ω/ω_1 is shown in Figure 2.6. Note also that the stress amplitude increases monotonically from zero at the base for $\omega/\omega_1 \lesssim 2$, indicating that the pressure distribution is dominated by the fundamental mode of vibration of the backfill. For $\omega/\omega_1 > 2$, the stress amplitude is not monotonic, indicating that higher mode contributions are not negligible for high frequency input or soft backfill material (low fundamental frequency).

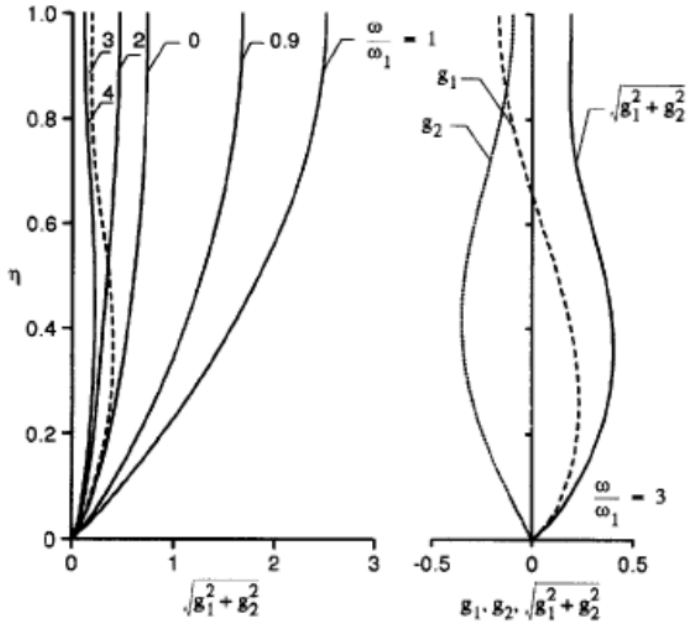

Figure 2.6: Heightwise variation of coefficients for wall pressure induced by harmonic input motion from Veletsos & Younan (1994a); $\delta = 0.1$

The dynamic pressure resultant, $|Q_b|$ (known as the real-valued amplitude of the base shear per unit length in Veletsos & Younan, 1994a), is computed by integrating $\sigma_w(\eta)$ over the height of the wall. The normalized base shear for various damping ratios (δ) is shown in Figure 2.7. Note that $|Q_b|$ is always less than $Q_b^{st} = |Q_b|_{\omega=0}$ for $\omega/\omega_1 > \sqrt{2}$ for a rigid, irrotational wall when the damping ratio is non-zero.

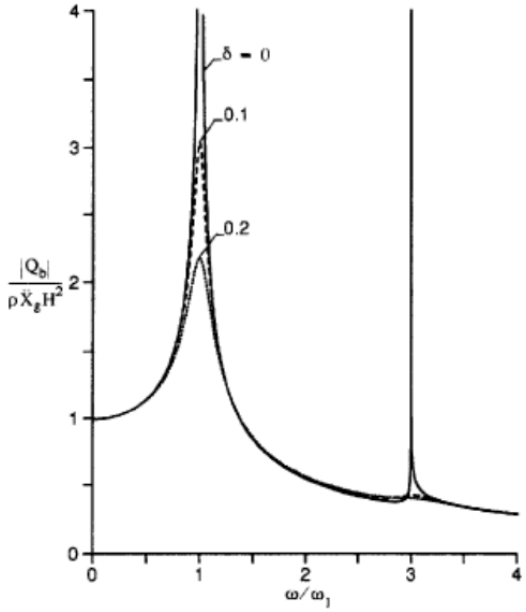

Figure 2.7: Normalized, real-valued amplitude of base shear for harmonic input motion for various soil material damping values from Veletsos & Younan (1994a)

Younan & Veletsos (2000) investigated the response of a flexible wall with a clamped support at the base and a hinge support at the top. Similar trends were observed as in previous studies; i.e., increasing flexibility of the wall decreased the magnitude of the dynamic earth pressure resultant, although the decrease was much less for the clamped-hinged wall than for a cantilever wall. Additionally, the point of application of the dynamic load increased with increasing wall flexibility when subjected to harmonic excitation. For earthquake excitation, the point of application of the dynamic load decreased slightly with increasing wall flexibility.

Richards, Huang & Fishman (1999) followed a procedure similar to that of Veletsos & Younan (1994a, 1994b, 1997) by modeling the soil as a series of springs, but included plastic deformation in the soil spring model. They concluded that the magnitude of the dynamic pressure resultant could be computed from the free field stress distribution, which was comparable to the M-O method. The distribution of pressure depends on the distribution of stiffness in the backfill as well as the deformation mode of the wall. Psarropoulos et al. (2005) validated the analytical solutions of Veletsos & Younan (1994a, 1994b, 1997) using a finite element solution and noted that elastic solutions for the case of displacing walls are not as applicable for non-displacing walls since small wall movements can induce a failure state in the soil, which contradicts the assumption of an elastic response.

Kloukinas et al. (2012) provides a simplified closed-form solution of Veletsos & Younan (1994a, 1994b, 1997) by considering a single shape function (i.e., first mode only) for the deformations in the backfill. This allowed the governing partial differential equation to be converted into an ordinary differential equation, greatly simplifying the solution at the expense of accuracy with increasing frequency of the excitation and base flexibility. This should be expected as the contributions of higher modes are more important for these cases. Most importantly, the simplified method was only compared to the case of a rigid wall with a rotationally constrained base and the effect of wall flexibility was not considered in the analysis.

More recently, Brandenberg et al. (2015) presented an analytical, linear elastic solution that includes base translation and shearing at the soil-structure interface of a U-shaped basement structure. While admitting more than one mode of deformation in the backfill, the structure was rigid and the backfill was uniform. The resulting pressure distributions increase monotonically from the base to the surface, corresponding to the results of Veletsos & Younan (1994b) for the case of a rigid wall with a rotationally constrained base undergoing “static” excitation. In the limiting case of a rigid base, their solution replicates the results of Veletsos and Younan (1994a) as would be expected.

2.2.2 Numerical Methods

Numerical methods, in particular finite elements (FE) and finite differences (FD), have been used extensively in the analysis of retaining structures. These methods have been validated with real case histories and experimental data; however, the predictive capability is debatable, especially for cases of intense dynamic loading. Clough & Duncan (1971) utilized a one-

dimensional element developed by Goodman, Taylor & Brekke (1968) to simulate the interface between a wall and retained soil for static analyses. This study sought to offer a more accurate representation of the interface, which at the time was modelled as either perfectly rough (no slip) or perfectly smooth (no shear stress). The resulting active and passive pressures were similar to limit state theory predictions, with some non-linearity depending on the mode (rotation, translation, or combined) and amount of deformation of the wall. The residual displacements were in good agreement with experimental results from Terzaghi (1934a).

Wood (1973) used finite elements to investigate the effects of soil-wall bonding and non-uniform soil stiffness on the response of non-displacing walls, and concluded that the interface did not influence the frequency response or the earth pressure distribution. Nadim & Whitman (1982) used finite elements to model a prescribed failure surface in the backfill of a gravity retaining wall, used a secant shear modulus to account for large strains and frictional slip elements for the soil-wall interface. They concluded that the ratio between predominant frequency of the earthquake and the natural frequency of the backfill was the most crucial factor in assessing the amplification of wall displacements.

Siddharthan & Magarakis (1989) used finite elements to model flexible walls retaining dry sand accounting for non-linear hysteretic behavior and increasing lateral stress and volumetric changes as a result of cyclic loading. They found that increasing relative density and wall flexibility decreased the maximum moments of the wall, and that moments computed by Seed & Whitman (1970) are conservative for flexible walls but not necessarily for stiff walls. Also, the authors advised that the foundation material of the wall should be considered in future analyses, arguing that a flexible wall rigidly attached to a rigid base would not necessarily represent founding a flexible wall on a soil foundation. Lastly, the authors noted that researchers should be cautious when using shaking table experiments to model systems with soil because the confining pressures are not equivalent to those experienced in field scale.

Wu & Finn (1999) used finite elements to model a rigid retaining wall on a rigid base with various backfill shear modulus distributions. The dynamic pressure resultant was presented as a function of the ratio of cyclic frequency of the excitation and the fundamental cyclic frequency of the soil-wall system estimated from an approximate procedure. Their results matched those of the other similar solutions (Wu, 1994; Finn et al., 1994; Wu & Finn 1996) and they concluded that the use of the Wood (1973) solution should be limited to cases where the cyclic frequency of the excitation is much less than the cyclic frequency of the soil-wall system ($\omega/\omega_{11} < 0.2$), corresponding to low frequency or long period (static) loading. Al-Homound & Whitman (1999) used finite elements to model a gravity wall founded on sand. The results were compared to those of 3-D centrifuge experiments and observed good agreement for the wall displacements of the numerical and experimental models. Green & Ebeling (2002) used finite differences to model a cantilever retaining wall retaining cohesionless backfill on a soil foundation. Their computed earth pressure coefficient values were comparable to the M-O method for low intensity ground motions ($k_h < 0.4$), but an upper bound closer to the Wood (1973) solution was suggested.

Gazetas et al. (2004) used finite elements to model L-shaped retaining walls, pre-stressed anchored pile walls, and reinforced soil walls with both linear and non-linear soil models. They observed that including realistic effects (wall flexibility, foundation soil deformability, material soil yielding, and relative movement between the soil and wall) reduced the effects of dynamic excitations on the walls.

Ostadan (2005) proposed a simplified method to predict the maximum seismic earth pressures on building walls using the concept of a single degree of freedom system in the computer program SASSI. The solution considers kinematic soil-structure interaction effects, site-specific non-linear dynamic soil properties and the characteristics of the ground motion in the computation of the seismic soil pressure. The solution assumes a rigid wall on a rigid foundation and does not include the effect of the superstructure and its inertia on seismic soil pressure. This method resulted in a range of seismic earth pressure solutions for which the M-O solution and the Wood (1973) solution represent lower and upper bounds, respectively. The five-step method to compute the seismic soil pressure following Ostadan (2005) is as follows (from FEMA P-750):

1. Perform a free-field soil column analysis and obtain the ground response motion at the depth corresponding to the base of the wall in the free-field. The response motion in terms of the acceleration response spectrum at 30 percent damping should be obtained. The free-field soil column analysis may be performed using the computer program SHAKE with input motion specified either at the ground surface or at the depth of the foundation base mat. The choice for location of the control motion should be consistent with the development of the ground motion.
2. Compute the total soil mass as $m = 0.50\rho H^2 \Psi_\nu$, where ρ is the mass density of the soil, H is the height of the wall, $\Psi_\nu = 2/[(1-\nu)(2-\nu)]^{0.5}$, and ν is Poisson's ratio.
3. Obtain the maximum lateral seismic force from the product of the total mass obtained in Step 2 and the acceleration spectral value of the free-field response at the soil column frequency obtained at the depth of the bottom of the wall obtained in Step 1. The soil column frequency is an output provided by SHAKE and computed as $f_s = V_s/4H$, where V_s is the average strain-compatible shear wave velocity of the soil column over the height of the wall.
4. Obtain the maximum lateral soil pressure at the ground surface level by dividing the lateral force obtained in Step 3 by the area under the normalized seismic pressure, $0.744H$.
5. Obtain the pressure profile by multiplying the peak pressure from Step 4 by the pressure distribution relationship given by Equation 2.7

$$p(y) = -0.0015 + 5.05y - 15.84y^2 + 28.25y^3 - 24.59y^4 + 8.14y^5 \qquad \textbf{(2.7)}$$

where y is the normalized height ratio (Y/H) measured from the bottom of the wall (ranging from 0 at the bottom of the wall to 1 at the top of the wall) and Y is the distance of the point under consideration from the bottom of the wall.

The earth pressure distribution computed using Ostadan's (2005) approach will always have the same shape corresponding to that of a rigid wall on a rigid base. As previously discussed, this was already solved analytically by Veletsos & Younan (1994a) and has been re-derived analytically for a single mode by Kloukinas et al. (2012). In fact, the pressure distribution in Equation 2.7 can be interpreted as the shape function for use the analysis by Kloukinas et al. (2012). As such, the solution by Ostadan (2005) is useful as a quick, conservative estimate of the seismic earth pressure distribution. However, the point of application of the equivalent lateral force is likely to be lower in a realistic system. Also, recall that FEMA P-750 stated "partially embedded structures should not be treated as a non-yielding wall".

Pathmanathan (2006) developed finite element models of flexible diaphragm walls, cantilever walls, and gravity walls. The walls were subjected to dynamic excitation to investigate the magnitude and distribution of dynamic earth pressure, as well as the displacements. It was concluded that the magnitude of the earth pressure resultant matched predictions by the M-O method when the levels of shaking were small. When the levels of shaking were large, the magnitude of the earth pressure resultant was lower than that predicted by the M-O method and the point of application of the dynamic increment was around $0.6H$ as proposed by Seed & Whitman (1970)

Jung & Bobet (2008) used finite elements to model the problem geometry of Veletsos & Younan (1997) and added vertical and horizontal springs to the base of the wall. This study confirmed that base rotation, wall flexibility, and horizontal translation significantly affect the magnitude and distribution of the dynamic earth pressure, whereas vertical translation has negligible effect.

Al Atik & Sitar (2010) used finite elements and Mikola & Sitar (2013) used finite differences to model displacing and non-displacing walls on a sand foundation with a sand backfill, and calibrated the models with centrifuge experiments. Also, Candia & Sitar (2013) used finite differences to model the same walls as Mikola & Sitar (2013) on a clay foundation with a clay backfill to investigate the effects of cohesion on the dynamic earth pressure. These studies concluded that a numerical model can capture essential responses of a soil-wall system provided that a constitutive model calibrated against experimental data is used for the soil model.

Gazetas et al. (2015) used finite elements to model anchored sheet-pile walls with non-linear soil models. This study concluded that pseudo-static methods are not suitable for the dynamic soil-structure interaction; Beam-on-Winkler-Foundation models are better able to capture the interaction, but cannot successfully model concentrated plastic deformation; and well established finite element codes are appropriate for providing realistic estimates of loads and displacements. However, their numerical models were not validated with a case history or a physical model.

2.2.3 Experimental Studies

Starting with the pioneering work of Mononobe & Matsuo (1929) experimental data was the basis of the development of the various methods of estimating seismic earth pressures on

retaining structures. In general physical experiments fall into three categories: (1) 1-g shaking table experiments; (2) dynamic centrifuge experiments; and (3) model scale and full scale data from instruments in the field. In general, shaking table experiments have had the model walls rigidly attached to the base of the shaking container whereas in centrifuge experiments the model walls were sometimes attached to the base and sometimes founded on soil. Both sinusoidal and earthquake excitation have been used in shaking table and centrifuge experiments. Field scale experiments and quantitative performance data as such have been very rare to date.

2.2.3.1 1-g Shaking Table Experiments

The earliest experiments to investigate seismic earth pressure on retaining walls were conducted by Mononobe & Matsuo (1929). The shaking table experiment consisted of a rigid base box mounted on rails and driven by a conical drum winch connected through a crankshaft to the base of the box (Figure 2.8). The excitation was a frequency sweep (sinusoidal with linearly varying frequency). The box was 9 ft long, 4 ft wide, and 4 ft deep. There were trap doors at the ends of the box which were spring mounted to restrict movement of the doors to rotation only; one door spanned the entire width of the box and the other only spanned half of the width of the box. Pressure gauges were mounted at the top of the doors to measure the load on the wall during the experiment. Mononobe & Matsuo (1932) used a "swing" in place of a shaking table to provide dynamic excitation during the experiment. The box was smaller than the previous work (1.30 m long, 0.43 m wide, 0.40 m deep). Also, the inertia of the wall was considered and subtracted from the measured earth pressure resultant to obtain the earth pressure only due to the action of the soil.

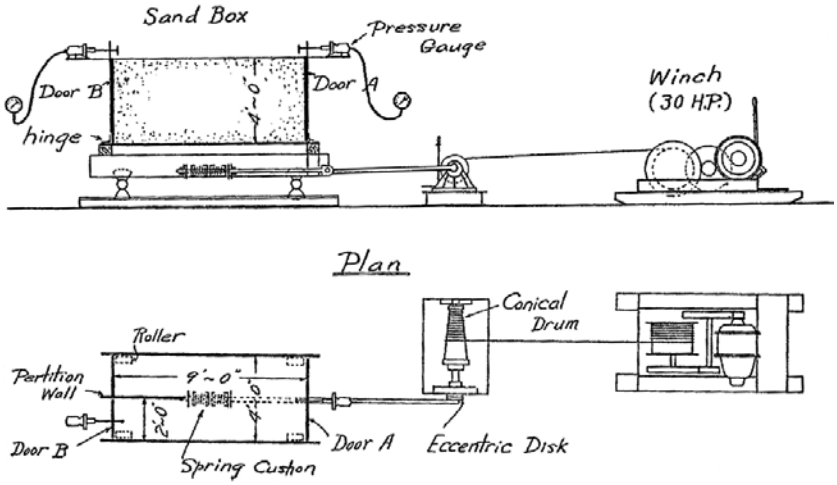

Figure 2.8: Shaking table experiment setup of Mononobe & Matsuo (1929)

Similar configurations, i.e. a rigid box subjected to sinusoidal motion were later used by Jacobsen (1939) and Matsuo (1941). The advent of hydraulically driven shaking tables provided opportunity for further experiments on small scale models by Ishi et al. (1960), Matsuo & Ōhara (1960), Ichihara & Matsuzawa (1973), Sherif et al. (1982), Fang (1983), Sherif & Fang (1984),

Matsuzawa & Sugimoto (1984), and Ishibashi & Fang (1987). Matsuzawa et al. (1985) reviewed the existing shaking table results to evaluate the hydrodynamic pressures on rigid retaining walls and proposed a design method based on the M-O method that incorporates the effects of permeability, backfill geometry and modes of wall movement. Ishibashi et al. (1994) further investigated the effects of water in the backfill following the conclusions of Matsuzawa et al. (1985). The main limitation of these experiments was that, given the frictional properties of backfill, correct scaling of soil strength and retaining structure stiffness is not trivial and there is no evidence that such scaling was attempted. Moreover, due to physical limitation of the shaking table dimensions and capacity, the model retaining structures were attached directly to the base of the model box, i.e. in effect founding the model structures directly on rock. Again the excitation was sinusoidal only, as quality earthquake records were not available at the time.

More recently, shaking table experiments by Watanabe et al. (2003), Wilson (2009), Watanabe et al. (2011), and Mock & Cheng (2011) included earthquake excitation. Watanabe et al. (2003) and Watanabe et al. (2011) developed a three part gravity wall consisting of two outer sections and a central section of plates attached to load cells to interpret the earth pressure distribution along the entire depth of the wall. The backfill was sand and the foundation soil was either sand or a thin layer of gravel (to force sliding failure before overturning failure). The inertia loads from the plates were explicitly measured and accounted for in the analysis of the load cell data when computing the dynamic earth pressure resultant. Based on the results of the experiments, an analysis procedure was proposed wherein a critical yield acceleration was computed for stability (either sliding or overturning) using a pseudo-static analysis. This yield acceleration was then used as an input for the M-O equation to calculate a maximum total seismic load. Higher total seismic loads due to higher accelerations would be “capped” at this maximum value, essentially prescribing design loads based on the stability of the wall instead of the input motion characteristics.

Wilson (2009) studied retaining walls with a slightly cohesive silty sand backfill and both at-rest and passive initial conditions. This experiment was conducted at the NEES Large High-Performance Outdoor Shake Table at the Englekirk Structural Engineering Center at UC San Diego. The model consisted of a heavily reinforced concrete wall 2.13 m tall and 0.2 m thick resting on a 0.47 m box with 0.45 m extending above a 2.15 m compacted backfill (Figure 2.9). Gaps along the sides and base of the wall were filled with soft foam to prevent soil spillage and to prevent shear resistance at the wall-container contact. Four hydraulic jacks are used to produce the correct initial displacements to induce at-rest or passive conditions, and just behind those are load cells used to measure the total dynamic load on the walls.

For at-rest initial conditions and accelerations up to approximately 0.66 g the dynamic earth pressure resultant was essentially zero and most of the load was due to the inertia of the wall. For higher accelerations (near 1.0 g), the dynamic earth pressure resultant was much larger. It was concluded that the low dynamic earth pressure resultant at low levels of shaking was due to high backfill stiffness and cohesion, the short height of the wall, the ability of the wall to translate and

rotate away from the backfill, and the deformation compatibility of the soil-wall interface. For passive initial conditions and accelerations up to approximately 0.66 g, the dynamic earth pressure resultant increased the total load about 5% of the peak static passive pressure, and for higher accelerations the total load was increased about 30%.

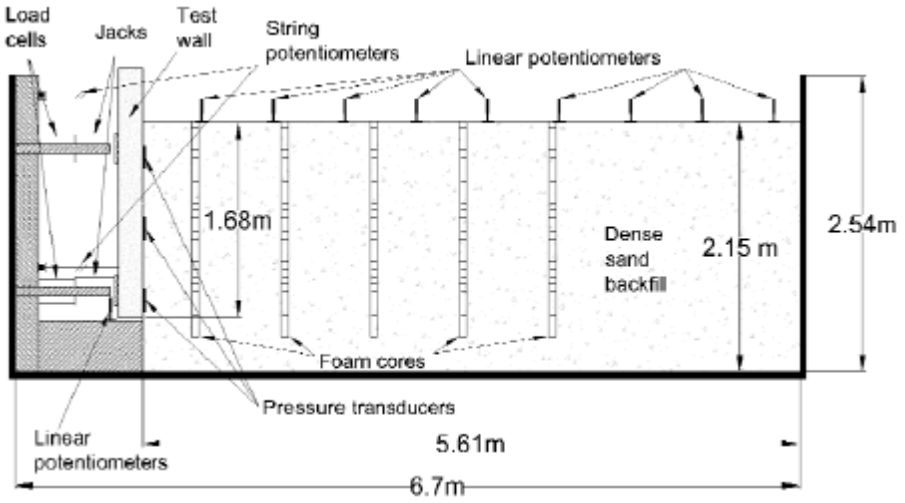

Figure 2.9: Shaking table experiment setup of Wilson (2009)

Mock & Cheng (2011) studied retaining walls with and without sound walls on a large shaking table with a silty sand backfill with minimal cohesion. This experiment was conducted at the NEES Large High-Performance Outdoor Shake Table at the Englekirk Structural Engineering Center at UC San Diego. The model without the sound wall consisted of a reinforced concrete cantilever T-wall 1.83 m tall with a 0.38 m thick base resting on a 1.07 m soil foundation (Figure 2.10).

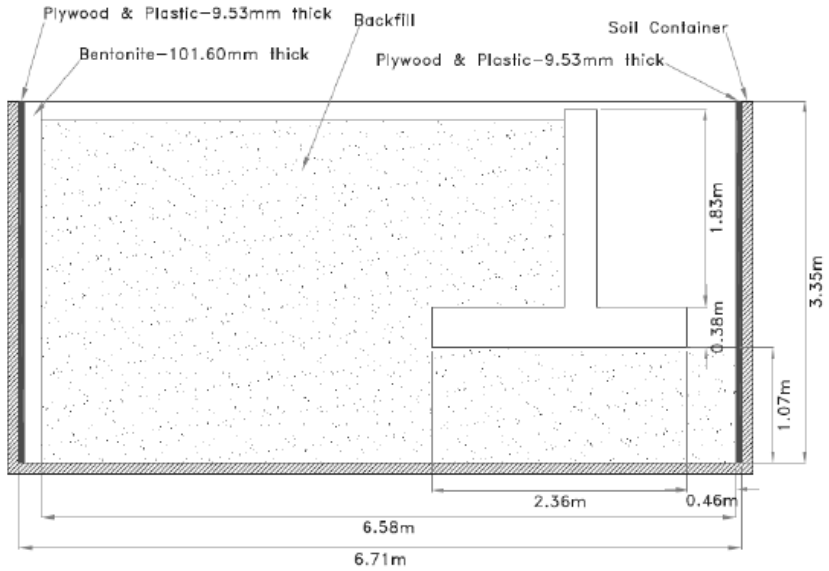

Figure 2.10: Shaking table experiment setup of Mock & Cheng (2011)

The model with the sound wall had the same configuration except for the addition of a 1.83 m tall concrete masonry block wall on top of the retaining wall. The masonry blocks were stacked with mortar then filled with grout the following day. Rebar extended from the retaining wall through the holes in the masonry blocks where the grout was placed. Plywood was placed along the inner surface of the container to prevent soil leakage and to create a rigid test container. Plastic sheeting was applied over the plywood to reduce the friction between the soil and the plywood. To prevent reflected stress waves from the back of the container, a bentonite layer enclosed in latex sheeting was installed. The boundary conditions in the experiments included a bentonite layer to reduce the effects of reflected stress waves at the back of the soil container; this proved to be inadequate as large deformations were observed in the backfill throughout the experiment. Joint seals were used to fill the gaps between the sides of the wall and the container. For the tests without sound walls, the dynamic earth pressure resultant agreed with M-O predictions and the height of the point of application was at approximately $H/3$. The observed effect of the sound wall is an increase in the dynamic pressure in the top 60-70% of the wall and increasing the point of application of the dynamic earth pressure resultant to approximately $H/2$. It was noted that the sequence of the input excitations was such that the intensity increased as the testing progressed. This caused damage to accumulate throughout the experiment, which potentially could affect the validity of the tests results.

It should be noted that the experimental work of Wilson (2009) and Mok and Cheng (2011) involved a significant effort and, in that context, was not trivial. However, neither effort attempted to provide a rationale for the scale of the models used in the experiments in the context of model scaling relationships and neither were the soil properties considered in that light. Thus, as already mentioned, an important limitation of shaking table experiments performed at 1-g, regardless of the size of the wall model are the challenging scaling issues. Similarly, ground motions have been generally applied directly from field records with the same frequency content and amplitude. Moreover, since the strength and stiffness of soil are a function of the confining stress, the soil tends to behave as a rigid plastic mass at low confining stress and the results cannot be scaled to prototype dimensions (Ortiz et al., 1983). The effects of a short wall height were addressed in the conclusions of Wilson (2009), which essentially reiterates the issues with low confining stress. Finally, boundary effects are also a major issue, since there is usually insufficient distance between the model structure and the container boundary (often rigid) to represent free field conditions, as mentioned in Mock & Cheng (2011). Nevertheless, these limitations have not stopped developers of analytical solutions from extrapolating the observed behavior to well above its applicable range and generally concluding that the original M-O solution is incorrect. This should not be a surprising outcome, since all the models suffered from the same limitations.

2.2.3.2 Dynamic Centrifuge Experiments

Centrifuge model experiments hold a significant advantage over 1-g shaking table experiments in that the stresses in the soil can be correctly scaled, the model can be a significant distance from

the boundaries, more or less in the free field, the structure can be underlain by a soil deposit, i.e. does not have to rest directly on the base of the container, and the input motions can be reasonably scaled from recorded motions. In fact, Giarlelis & Mylonakis (2011) compared the results of both shaking table and centrifuge experiments to limit state methods and the elastic solutions developed by Veletsos & Younan (1994a, 1994b, 1997). The authors determined that the discrepancy between the various methods regarding the distribution of dynamic earth pressure (and hence, the point of application of the resultant) could be explained by the wall-soil flexibility factor. For the experimental studies considered, the soil-wall systems were not characterized as "rigid" using the wall-soil flexibility factor. The authors note that the results from shaking table experiments match better with limit state solutions and the results of centrifuge experiments match better with elastic solutions. The explanation given by the authors was that the centrifuge experiments were more accurate in terms of scale.

The early centrifuge experiments were limited by the payload capacity, and as such novel methods to apply dynamic excitation were required. Ortiz (1982) tested an aluminum cantilever wall on a sand foundation in a rigid test box, and recorded maximum dynamic forces comparable to M-O predictions that acted at approximately one-third of the wall height from the base (Figure 2.11). Dynamic excitation was applied by a piston-spring mechanism capable of mimicking near-field pulse-like ground motions. Long duration, multiple cycle earthquakes could not be produced with this mechanism, and inertial effects were not explicitly considered.

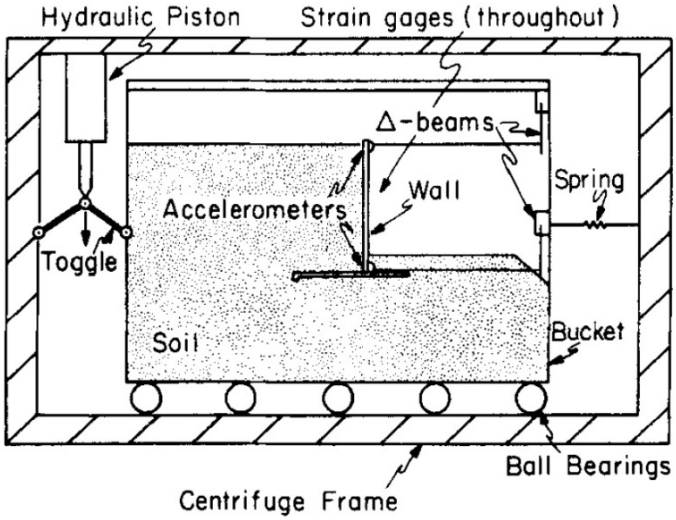

Figure 2.11: Centrifuge experiment setup of Ortiz (1982)

Bolton & Steedman (1982) and Bolton & Steedman (1984) conducted experiments on micro-concrete and aluminum cantilever walls rigidly attached to the base of the loading frame and retaining a sand backfill. Sinusoidal excitation with amplitude up to 0.22 g was applied, and the dynamic pressure resultant was observed to act at one-third of the wall height in agreement with M-O predictions. It was noted that inertial forces must be taken into account to correctly determine the dynamic earth pressure. Steedman & Zeng (1990) later reanalyzed the results of

Bolton & Steedman (1984) and concluded that the dynamic earth pressure resultant agrees with the M-O method, but the non-triangular distribution of earth pressure implies that the resultant acts above $H/3$. Additionally, they noted that amplification and phase change of ground motion should be considered since the variation in backfill acceleration contributed to the non-triangular distribution of pressure. Thus, they proposed that acceleration at the mid-height of the wall would be a more appropriate correlation parameter for the dynamic earth pressure resultant. Stadler (1996) conducted experiments on cantilever retaining walls rigidly attached to the test box retaining a sand backfill (Figure 2.12). The total (static and dynamic) earth pressure was observed to have a triangular distribution, but the dynamic component varied between triangular and rectangular. Stadler found that using a reduced acceleration coefficient (20-70%) of the original design level acceleration in the M-O equation provided good agreement with the measured forces. This recommended procedure is similar to that proposed by Watanabe et al. (2011) in that a reduced acceleration coefficient is supplied to reduce the design loads; however, the reasoning is quite different.

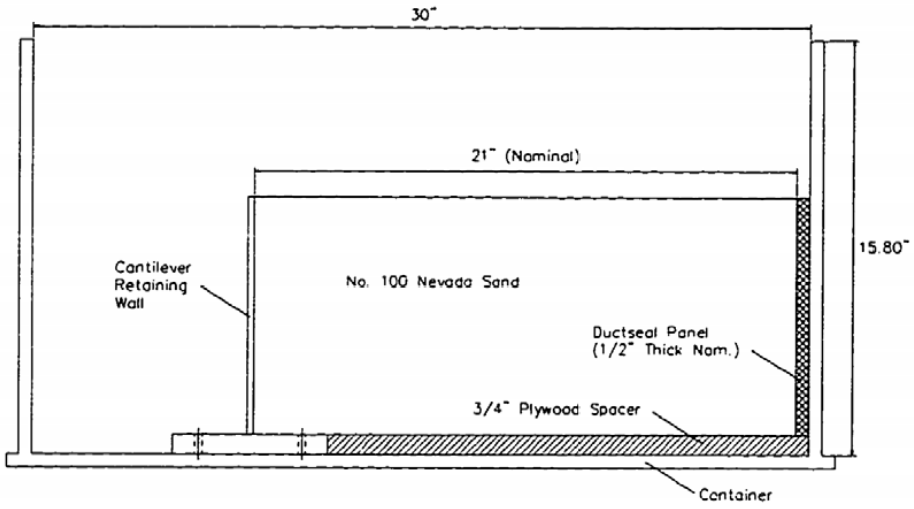

Figure 2.12: Stadler (1996) typical test configuration

Dewoolkar et al. (2001) modeled a cantilever wall rigidly attached the container and retaining liquefiable, cohesionless backfill using a metalose-water fluid to properly simulate the rate of pore pressure dissipation (Figure 2.13). Excitation was sinusoidal with varying amplitude up to approximately 0.7 g. Maximum total pressure envelopes were developed and had an approximately rectangular distribution, although the pressure distribution at discrete times was more nearly triangular. Also, they observed that the earth pressure increased considerably and the maximum measured loads exceeded M-O predictions when the backfill liquefied.

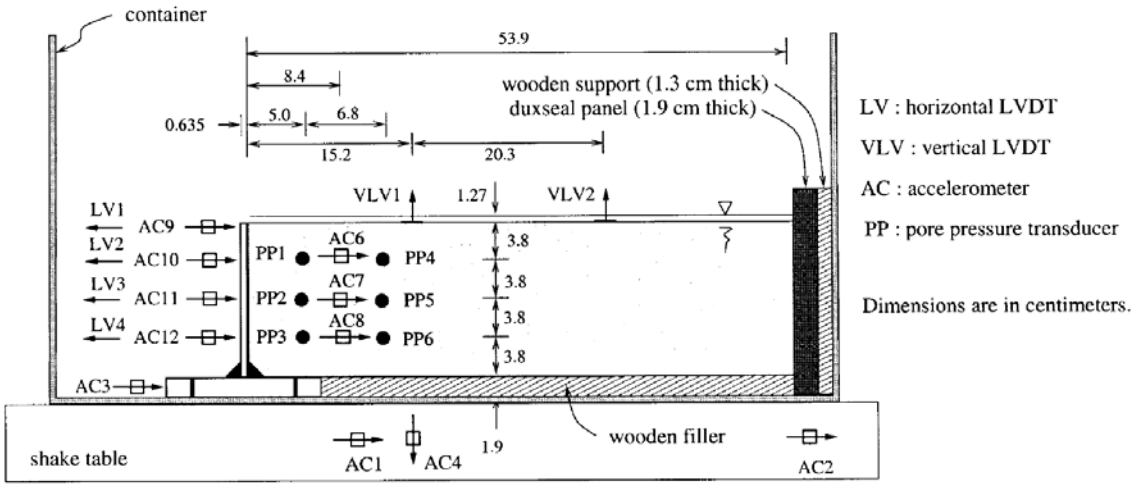

Figure 2.13: Dewoolkar et al. (2001) typical test configuration

Matsuo, Nakamura & Saito (2002) modeled a gravity wall consisting of three sections, the middle of which was outfitted with plates attached to load cells, similar to the walls used in shaking table tests by Watanabe et al. (2003) and Watanabe et al. (2011). Dynamic excitation was sinusoidal with 20 cycles and amplitude up to 0.7 g. Inertia of the wall and resisting forces from shear at the base and passive pressure on the embedded toe were removed from the dynamic earth pressure resultant acting on the back of the wall. The dynamic earth pressure resultant measured in the experiments was less than that of M-O predictions. Nakamura (2006) extended the analysis of Matsuo, Nakamura & Saito (2002) by including earthquake excitation and observed that inertia loads did not occur simultaneously with the maximum dynamic earth pressure during earthquake excitation (Figure 2.14). Also, the total earth pressure distribution was approximately rectangular during earthquake excitation whereas it was approximately triangular for sinusoidal excitation.

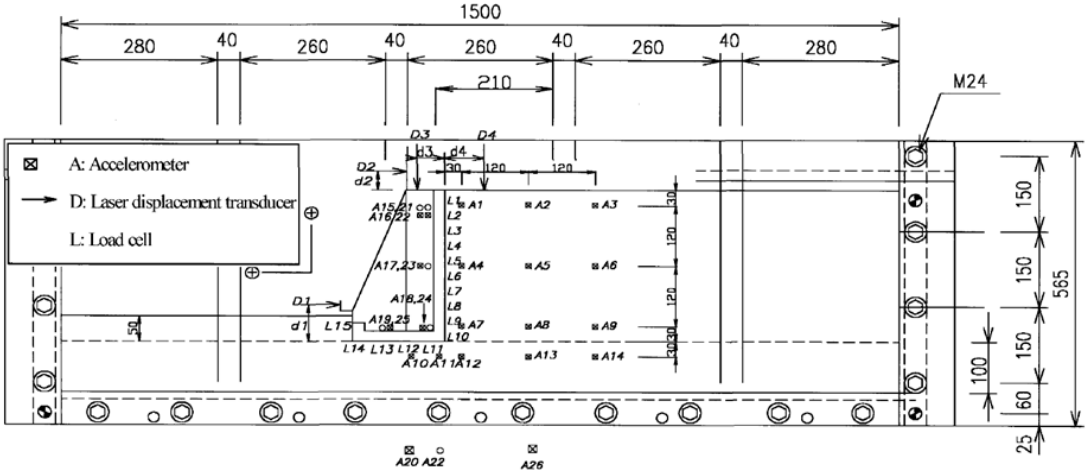

Figure 2.14: Nakamura (2006) test configuration

More recently, Al-Atik & Sitar (2010) (Figure 2.15), Mikola & Sitar (2013) (Figure 2.16 & Figure 2.17) and Candia & Sitar (2013) (Figure 2.18) performed a series of model scale centrifuge experiments on the centrifuge at the Center for Geotechnical Modeling at UC Davis. They modeled a variety of structures with different geometries and stiffness, cohesionless and cohesive backfill, and in all cases founded on soil. They concluded that the M-O method was conservative, especially for peak ground acceleration at the surface greater than 0.4 g. The observed seismic earth pressure distribution increased approximately linearly with depth, and recommended that the resultant from the Seed & Whitman (1970) method applied at 0.33H is a reasonable upper bound to the total seismic earth pressure increment.

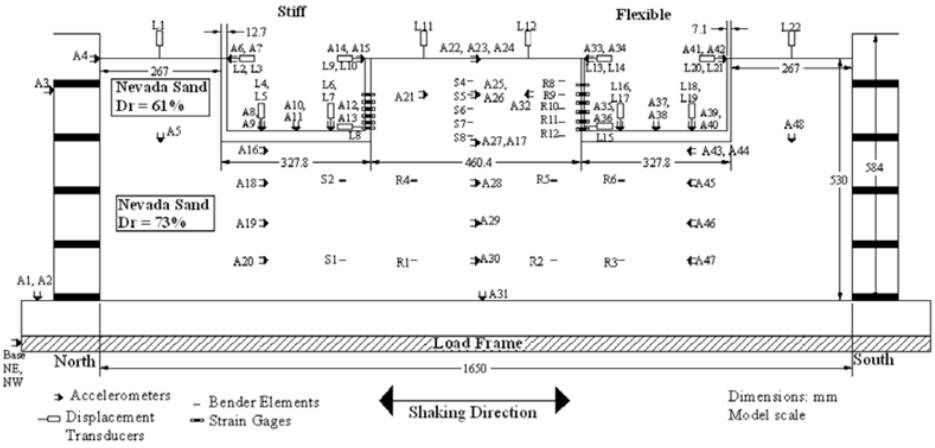

Figure 2.15: Al-Atik & Sitar (2008) test configuration

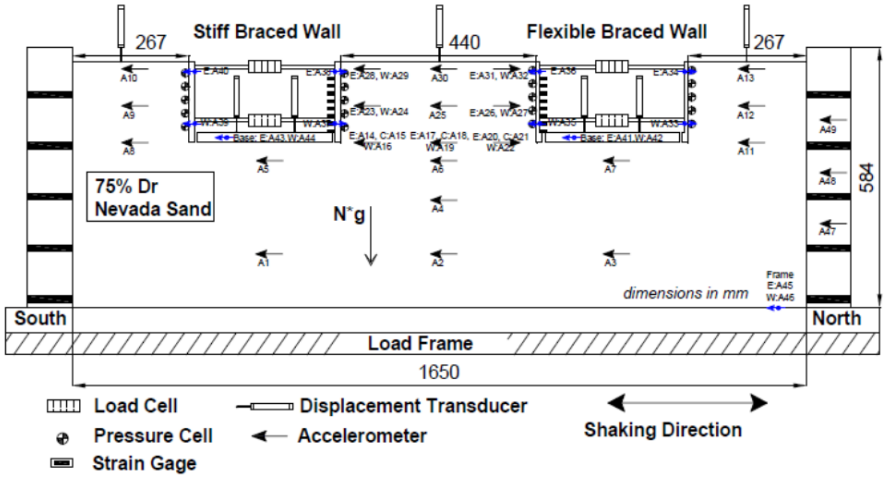

Figure 2.16: Mikola & Sitar (2013) ROOZ01 test configuration

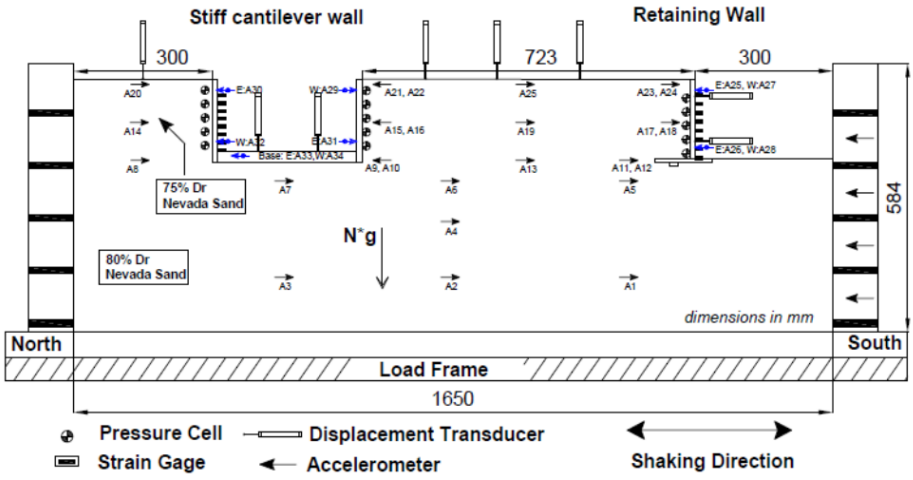

Figure 2.17: Mikola & Sitar (2013) ROOZ02 test configuration

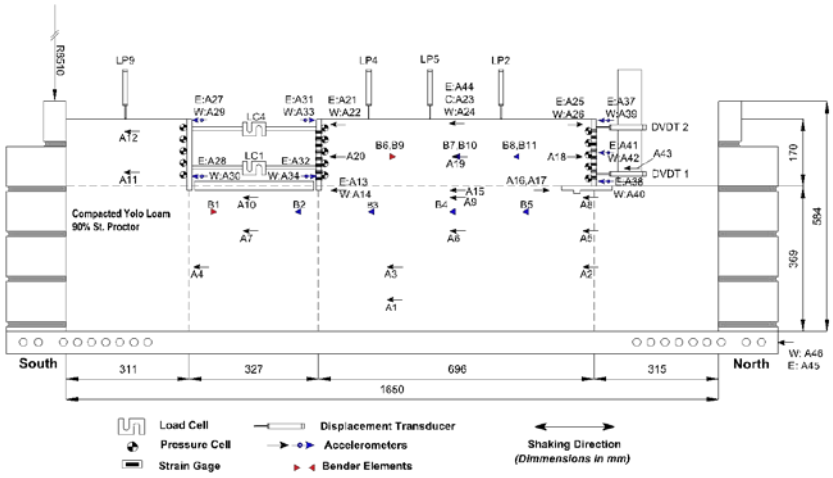

Figure 2.18: Candia & Sitar (2013) GC01 test configuration

Hushmand et al. (2014) performed centrifuge experiments on an empty water reservoir structure embedded in a sand backfill with a sand foundation (Figure 2.19a). The dynamic earth pressure computed in the pressure sensors on the wall suggests a parabolic distribution with depth (Figure 2.19b). The structures were designed to simulate a non-displacing prototype structure restrained at the base and the roof level. Note that the backfill material was medium dense (D_R = 60%) and the walls of the structure were thin relative to the height. Based on the reported acceleration response spectra, it is likely that the structure underwent some racking deformations and this additional flexibility in the system explains the lower observed pressure magnitude in comparison to the Wood (1973) solution for a rigid wall. The pressure distribution is quite similar to that obtained by Veletsos & Younan (1994b) when considering rotational flexibility and a non-uniform distribution of shear modulus with depth. Zhai et al. (2013) performed Class A predictions in FLAC of the centrifuge experiment conducted by Hushmand et al. (2014).

While the dynamic pressure distributions were not exactly the same, the magnitude of the resultant was approximately equivalent.

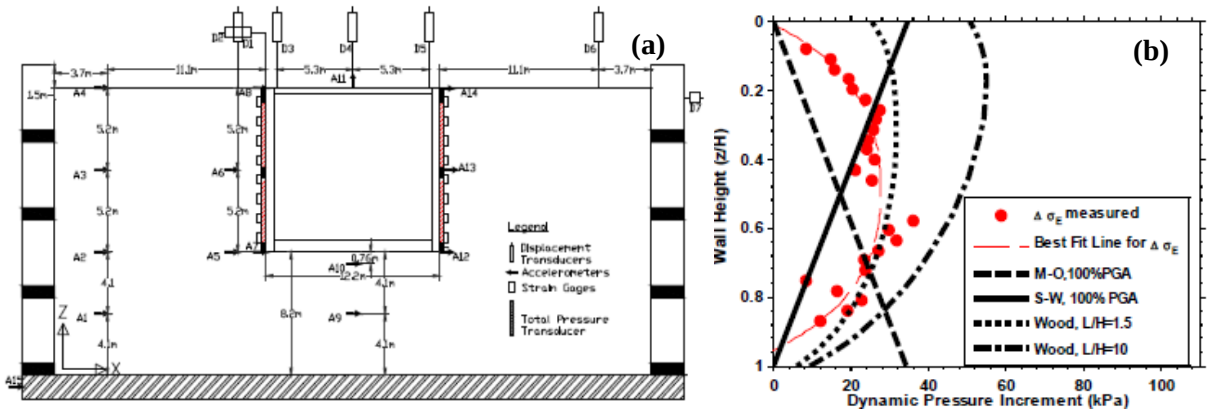

Figure 2.19: Hushmand et al. (2014) (a) test configuration (b) observed dynamic pressure profile

2.2.3.3 Field-Scale Experiment

A ¼ scale model of a nuclear power plant in Lotung, Taiwan was prepared in a joint effort by the Electric Power Research Institute (EPRI) and the Taiwan Power Company (TPC) (Chang et al. 1990, 1991). The model is a 10.52 m diameter, 15.24 m tall concrete cylinder embedded 4.57 m into the ground with triaxial accelerometers on the structure and steam generator. The walls are 0.31 m thick, the foundation is 0.91 m thick, and the roof is 1.07 m thick. Five pressure transducers are located on the shell of the structure to measure horizontal earth pressure. Many earthquakes have been recorded at this site, but the peak accelerations have been low (only up to 0.26 g). The dynamic earth pressure was interpreted using a polynomial fit to the data points along the depth of the wall. The interpreted dynamic earth pressure resultant was comparable to that of M-O method.

However, the authors noted that the observed response of this structure with low embedment would not necessarily scale to structures with deeper embedment. The model structure was thin compared to its height, which likely introduced a rocking mode during shaking which is unlikely to be observed if the structure were of the correct width. The rocking mode seems to have contributed to the interpreted earth pressure distribution wherein the dynamic earth pressure increased from the bottom of the structure to the ground surface. Also, the structure in this experiment was circular and therefore the results would not necessarily be applicable to flat basement walls; this is overlooked in the study.

2.3 Concluding Remarks

This literature review focuses on past efforts to characterize seismic earth pressure using analytic, numerical, and experimental methods. The near limitless combinations of backfill conditions and wall geometries are difficult to codify and as such a unified approach has been elusive thus far.

Analytic solutions for a rigid wall on a rigid foundation provide an upper bound for a situation that is not physically possible. Flexibility of the wall, rotational and translational compliance at the base of the wall and material damping all serve to decrease both the dynamic earth pressure and the point of application of the resultant. The relative frequency of the excitation compared to the fundamental frequency of the backfill will also influence the distribution and magnitude of the pressure. Numerical analyses have been shown to replicate the findings, and they also show that including plasticity and allowing permanent deformation can further decrease the demands on the wall. Numerous experiments have provided case histories for a variety of wall and backfill configurations. However, while 1-g shaking table experiments were useful for initiating interest in scaled experiments extrapolating the results to field-scale conditions is not readily feasible. Centrifuge experiments correctly account for scale effects, and as such they provide more realistic case studies for calibrating analytic solutions and numerical analyses. The combination of analytic solutions, numerical analyses, and centrifuge experiments is therefore invaluable to understanding the problem of seismic earth pressure.

3 Centrifuge Experiment: Development & Execution

In previous experiments, the model configurations consisted of multiple basement structures in a single test (Al Atik & Sitar, 2010; Mikola & Sitar, 2013; Candia & Sitar, 2013) or sloping ground (Candia & Sitar, 2013) that created asymmetric load distribution in the centrifuge container. In addition, analysis of data from these tests suggested that there was some boundary interaction with the model structures. The asymmetric load distribution in centrifuge container created moment imbalance that led to rocking and vertical excitation of the model. In addition, experiments with two model structures turned out to be quite challenging to interpret and model analytically.

With these issues in mind, the current experiment was designed to be simple and symmetric to reduce induced vertical excitation of the model. The instrumentation was planned to allow for maximal redundancy in the likely event of instrument malfunction. The prototype structure was approximately twice as tall (43 ft in prototype scale) as in previous experiment to investigate the effects of increased embedment.

3.1 Rationale for Centrifuge Modeling

The principle behind centrifuge modeling is that the stress state of the soil controls the response. Therefore, a 1/*N*g-scale model can be constructed and subjected to an *N*g-gravity field with the resulting stresses and strains corresponding to a prototype scale test. This is shown schematically in Figure 3.1 below. The scaling laws for centrifuge tests and 1-g tests are shown in Table 3.1. In brief, some of the advantages of centrifuge modeling are (Kutter, 1995; Dobry & Liu, 1994):

- Stress field is such that the stresses at a point in the model are “identical” to the corresponding point in the prototype;
- The test are cost effective and “repeatable” relative to full scale testing;
- Input ground motions can have a wide range of frequency contents and magnitudes;
- Models can be densely instrumented providing rich data sets;
- Constitutive relationships in numerical models can be directly validated; and
- Predictive capabilities of numerical models can be directly evaluated.

Nevertheless, there are still modeling errors and boundary effects that cannot be completely eliminated (Hausler, 2002; Al-Atik & Sitar, 2010; Mikola & Sitar, 2013; Candia & Sitar, 2013). Specifically, the stress distribution is not perfectly linear due to increasing radius of rotation with depth of the model, which creates a linearly increasing g-level with depth. The effect is less pronounced as the radius of rotation increases, i.e. the centrifuge arm is longer. As in a 1-g shaking table the model container bottom is a rigid boundary, although its effect is somewhat mitigated by a layer of soil between it and the model structure. Similarly, while the lateral boundaries can be designed to be energy absorbing, the response is not perfect and some boundary effects do remain. Finally, unbalanced, asymmetric model in direction of shaking may

induce a “rocking” or “sloshing” mode that can create high vertical accelerations during the experiment.

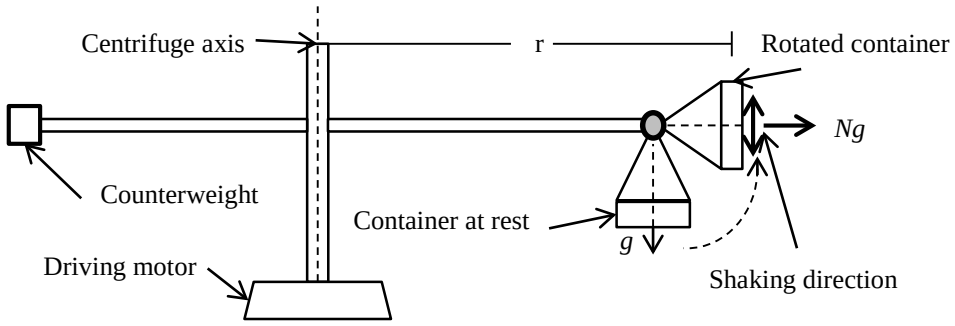

Figure 3.1: Schematic view of geotechnical centrifuge

Table 3.1: Scaling factors for geotechnical physical modeling

Parameter	1-g Shaking Table	Centrifuge
Length	$1/N$	$1/N$
Mass Density	1	1
Acceleration, Gravity	1	N
Dynamic Time	$1/N^{0.5}$	$1/N$
Dynamic Frequency	$N^{0.5}$	N
Velocity	$1/N^{0.5}$	1
Stress	$1/N$	1
Strain	1	1
Mass	$1/N^3$	$1/N^3$
Force	$1/N^3$	$1/N^2$
Moment	$1/N^4$	$1/N^3$

3.2 NW01 Model

3.2.1 Overall Model Layout

The centrifuge model experiment was performed at the NEES Center for Geotechnical Modeling (CGM) at UC Davis. The model was constructed in a flexible shear beam container FSB2 available at the CGM (http://nees.ucdavis.edu).

The model representing a basement structure was constructed at 1/36 scale and tested with a centrifuge acceleration of 36 g. It consisted of a 13.3 m deep basement structure with 0.9 m thick, 2.7 m wide strip footings founded on 5.5 m of dry medium dense sand, with all dimensions in prototype scale. The structure had cross bracing composed of short, threaded steel rods and was instrumented with load cells to measure the loads transmitted to the walls. Stiffener plates were added to the wall at the cross bracing connections to reduce racking deformation. The walls and stiffener plates were 0.5 inch thick T6061 aluminum plates and the footings were 3x1 inch

T6061 aluminum flat bar. There were a total of 89 instruments used in the experiment to measure the response of the model, including accelerometers, load cells, displacement transducers, and pressure sensors. The properties of the structure in model and prototype scale are shown in Table 3.2. The approximate location of the sensors and model layout are shown in Figure 3.2 and Figure 3.3. Detailed illustrations of the basement structure and the locations of the sensors on the basement structure are shown in Figure 3.4 and Figure 3.5, respectively. The connection details for the basement structure are shown in Figure 3.6.

Table 3.2: NW01 structure properties in model and prototype scale

Rigid Basement Properties	Units	Model	Prototype	Prototype per unit width	
Plane Strain Width	d (m)	7.76 E-01	2.79 E+01	1.00 E+00	(m/m)
Aluminum Wall					
Unit Mass	ρ (kg/m^3)	2.84 E+03	2.84 E+03	2.84 E+00	(Mg/m^3)
Cross Section	A (m^2)	1.24 E-02	1.61 E+01	5.75 E-01	(m^2/m)
Second Moment of Area	I (m^4)	4.94 E-07	8.29 E-01	2.97 E-02	(m^4/m)
Cross Bracing					
Unit Mass	ρ (kg/m^3)	3.34 E+04	3.34 E+04	3.34 E+01	(Mg/m^3)
Cross Section	A (m^2)	2.05 E-04	2.66 E-01	9.53 E-03	(m^2/m)
Second Moment of Area	I (m^4)	1.53 E-08	2.56 E-02	9.17 E-04	(m^4/m)
Footing					
Unit Mass	ρ (kg/m^3)	2.72 E+03	2.72 E+03	2.72 E+00	(Mg/m^3)
Cross Section	A (m^2)	1.97 E-02	2.55 E+01	9.14 E-01	(m^2/m)
Second Moment of Area	I (m^4)	1.07 E-06	1.80 E+00	6.43 E-02	(m^4/m)

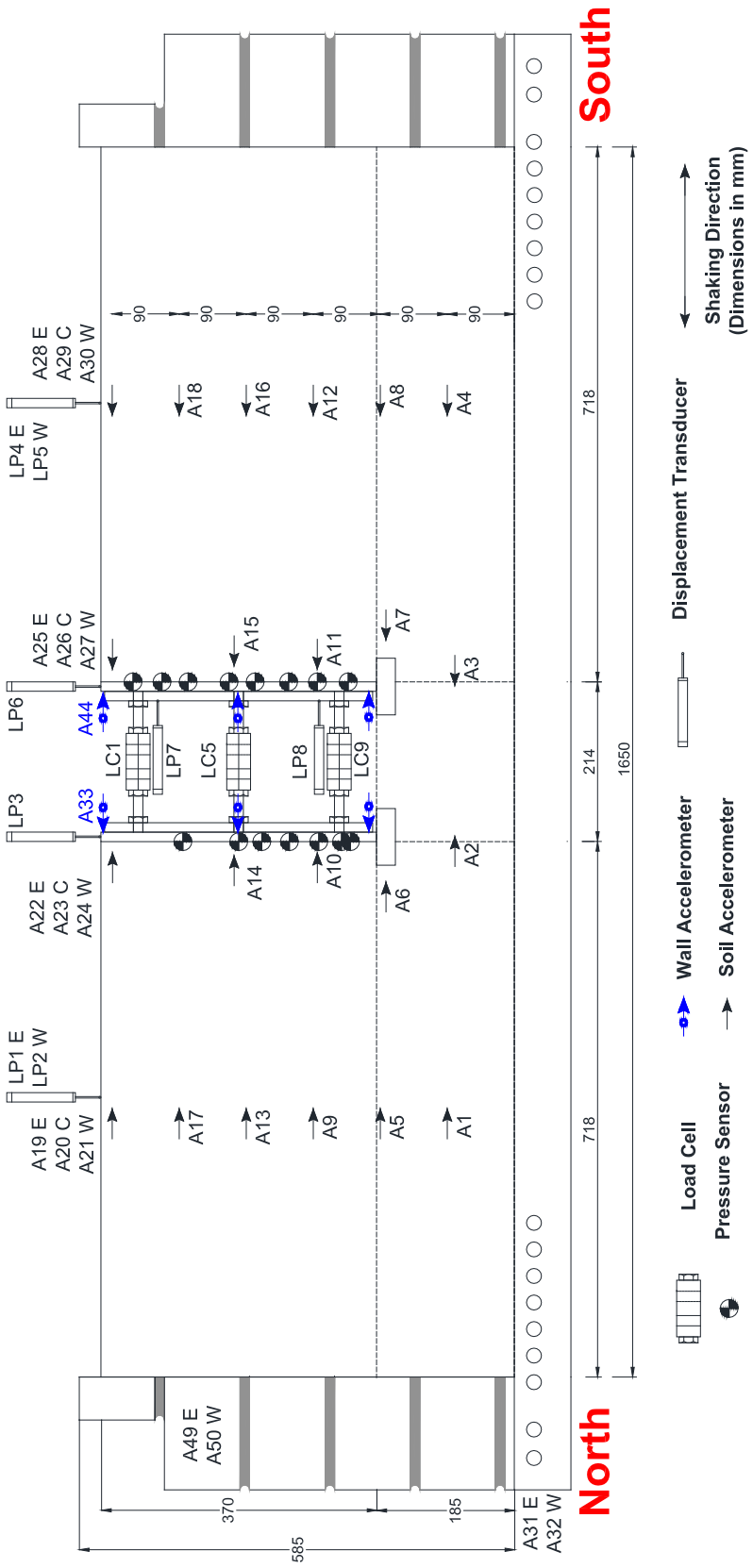

Figure 3.2: Profile of model NW01 (dimensions in mm)

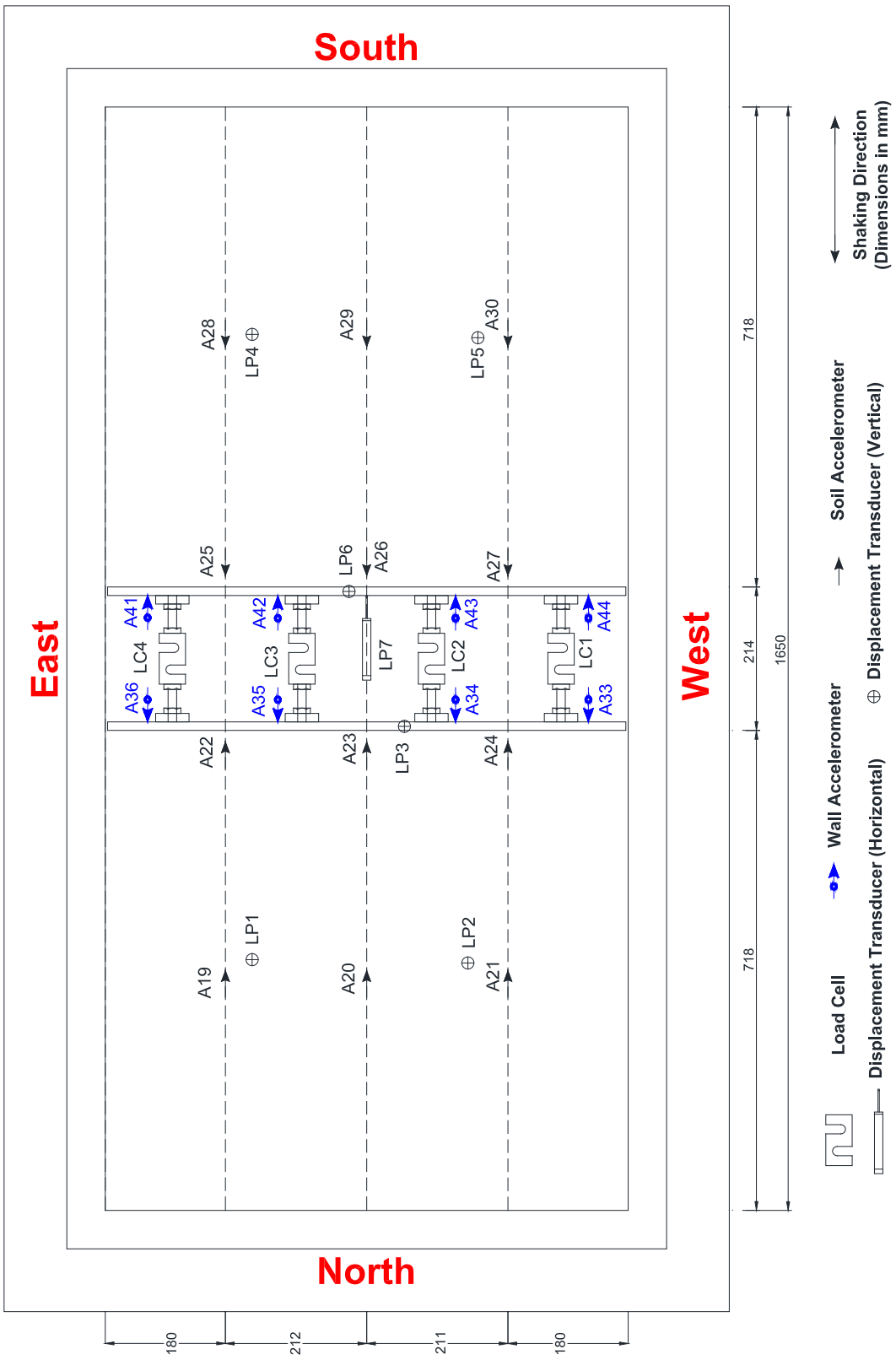

Figure 3.3: Plan view of model NW01 (dimensions in mm)

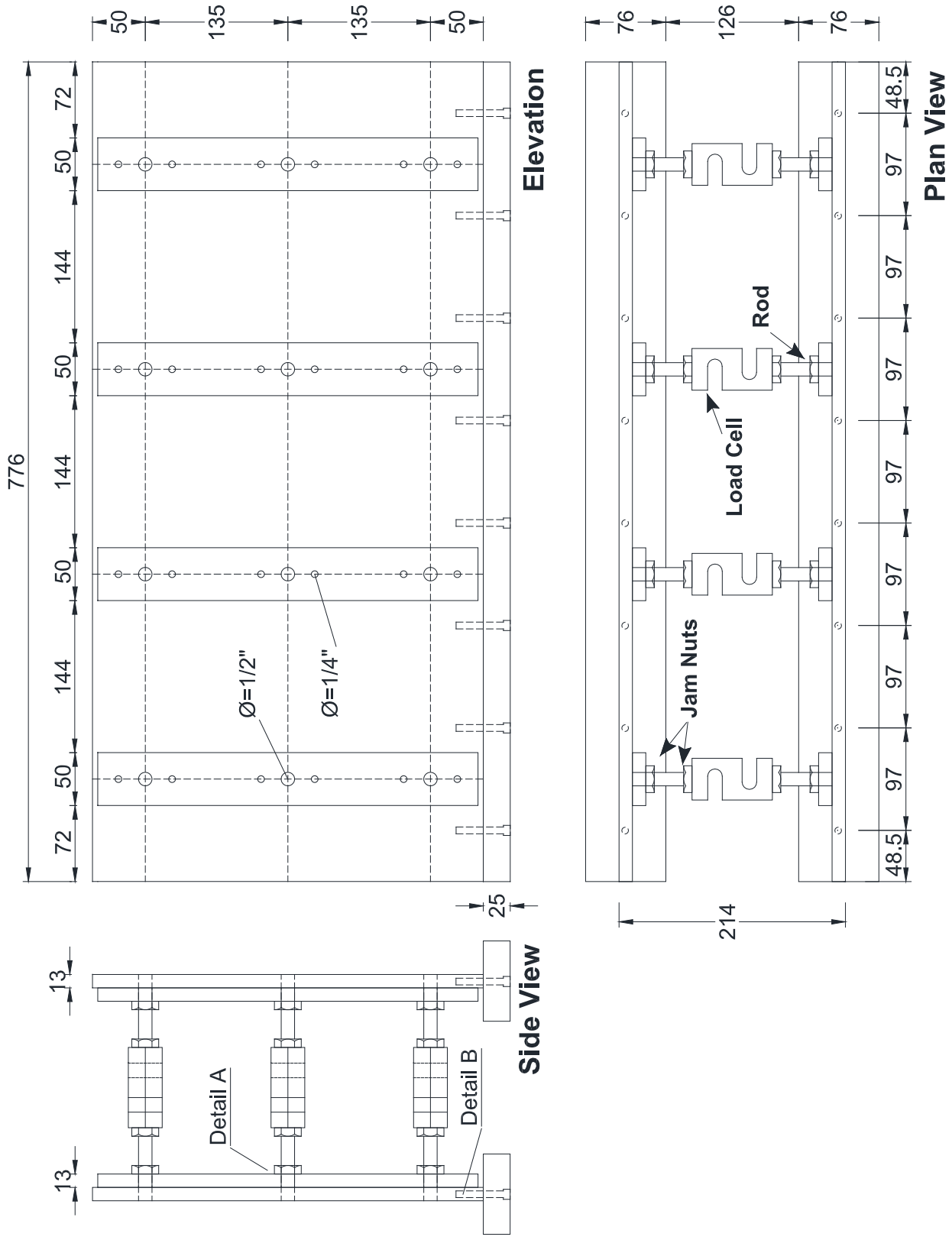

Figure 3.4: Deep basement model (dimensions in mm)

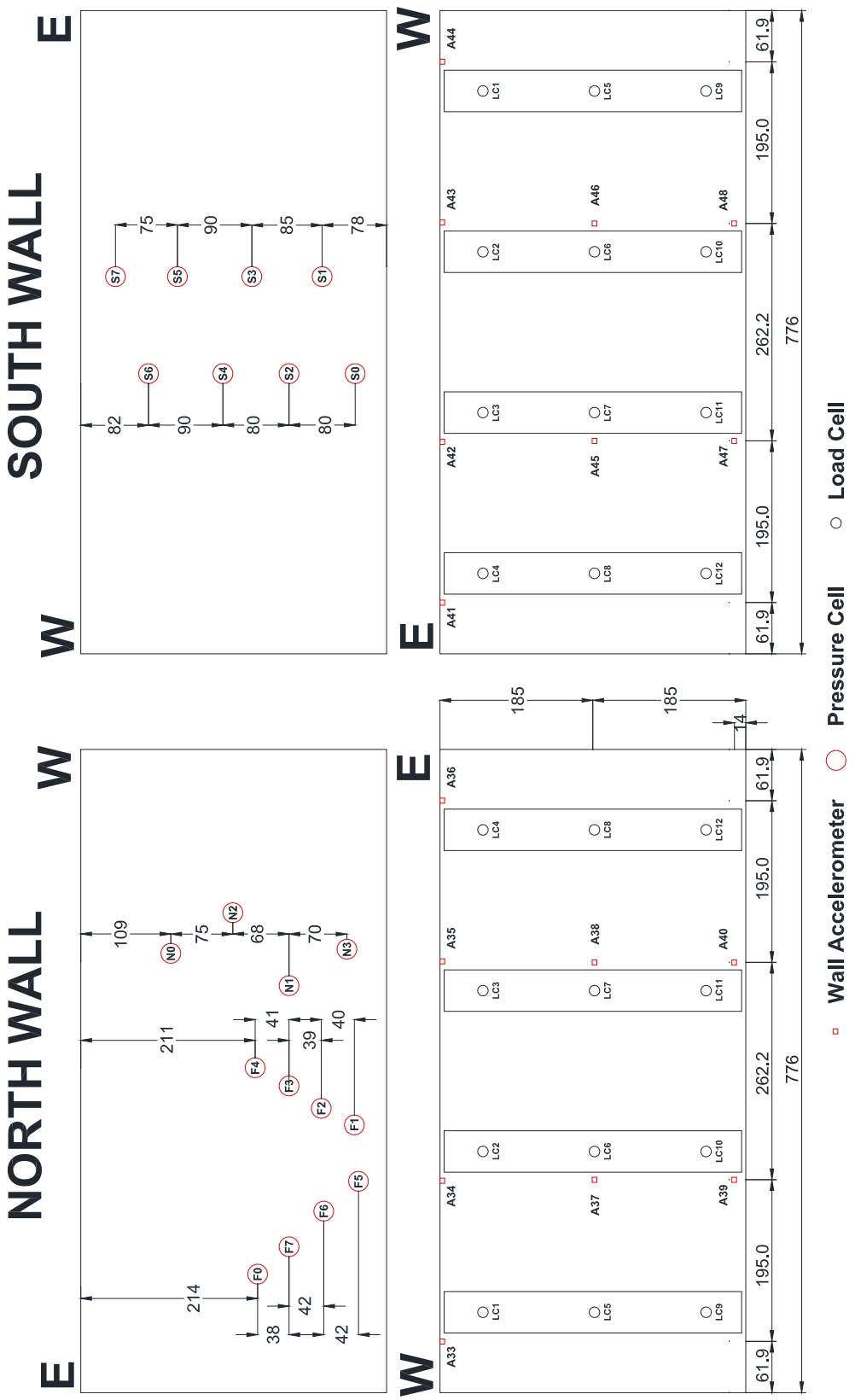

Figure 3.5: Location of sensors on basement walls (dimensions in mm)

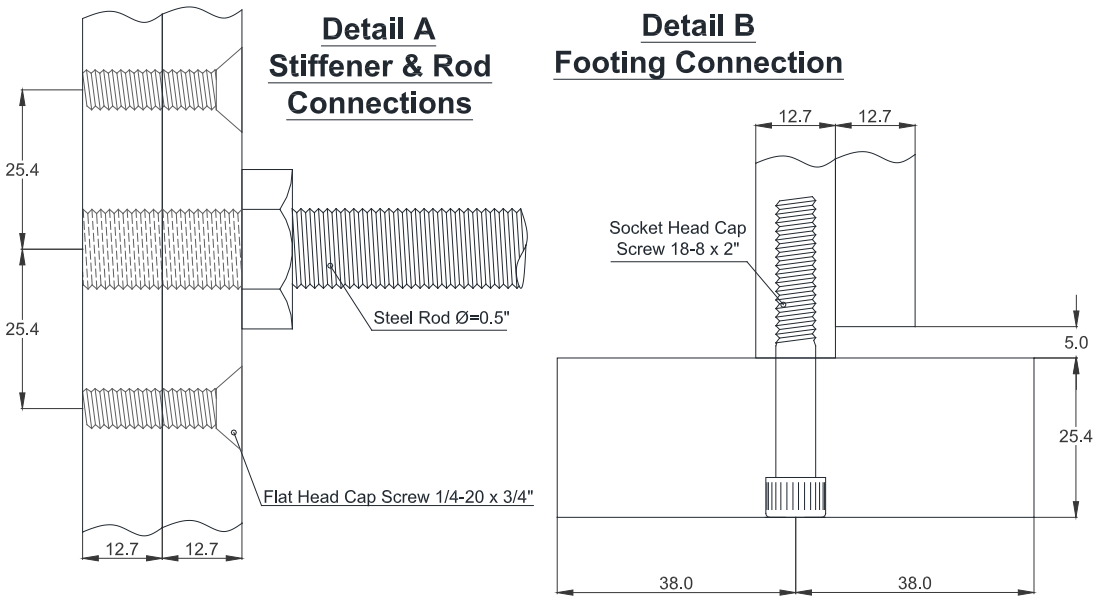

Figure 3.6: Connection details for stiffener plates & footings

3.2.2 Soil Characterization

The soil used in the model was dry Nevada Sand. The mechanical properties vary for each batch that is delivered to the CGM at UC Davis. Table 3.3 summarizes the properties of the latest batch used in this experiment as well as the historical data from various experiments. The variation in the results is attributed to the differences between the batches delivered to the CGM. For this study, the results obtained by Cooper Lab (2012) were used, namely that the minimum and maximum dry densities are 13.72 and 17.04 kN/m^3, respectively.

Table 3.3: Nevada sand properties

Source	G_s	e_{min}	e_{max}	γ_d, min (kN/m^3)	γ_d, max (kN/m^3)
Arulmoli et al. (1991)	2.67	0.51	0.887	13.87	17.33
Balakrishnan (1997)	-	0.55	0.84	14.21	16.92
Woodward Clyde (1997)	-	-	-	13.97	16.75
Kammerer et al. (2000)	2.67	0.533	0.887	13.87	17.09
UC Davis – Seiji Kano (2007)	2.65	0.486	0.793	14.50	17.49
Cooper Lab (2007)	-	0.52	0.78	14.57	17.05
Cooper Lab (2008)	2.65	0.510	0.748	14.86	17.20
Cooper Lab (2012)	2.66	0.53	0.90	13.72	17.04

3.2.3 Sensors

A variety of sensors were used to measure the response of the model during the experiment. The types of sensors are detailed below and in Table 3.4.

- **Accelerometers**: used to measure accelerations in the soil, retaining structure, and the top and bottom rings of the model; sensitivity information was provided by the manufacturer
- **Load Cells**: used to measure the axial loads in the struts connecting the north and south walls of the structure, secured with jam nuts; sensitivity information was provided by the manufacturer
- **Displacement Transducers**: used to measure settlement of the backfill and the structure, and to measure the lateral displacement of the structure with Linear Potentiometers (LP); all sensitivity information was obtained through previous calibration records using a standardized LVDT
- **Pressure Sensors**: used to measure (qualitatively) the lateral earth pressure distribution on the structure; eight Tactilus sensors were applied to the south wall, and four Tactilus and eight Tekscan sensors were applied to the north wall; since the pressure sensors were only used to obtain the distribution and not the magnitude of the earth pressure, the calibration was set to be 1psi per volt.

Table 3.4: Instruments used and manufacturer's specifications

Instrument	Manufacturer / Model	Range	Frequency Limits	Natural Frequency
Accelerometers	PCB Piezotronics 352MC68	$\pm$ 50 *g*	0.3 – 12000 Hz	$\geq$ 35000 Hz
	PCB Piezotronics 352M54	$\pm$ 100 *g*	0.3 – 13000 Hz	$\geq$ 40000 Hz
Load Cells	Interface SSM-AJ-500	$\pm$ 500 lbf	$\leq$ 2000 Hz	2150 Hz
Displacement Transducers	BEI Duncan 602R2KL.35	0 – 3 in	N/A	N/A
	BEI Duncan 601R1KL.7	$\pm$ 0.5 in	N/A	N/A
Pressure Sensors	Tactilus Free Form	0 – 15 psi	0 – 100 Hz	N/A
	Tekscan Flexiforce A201	0 – 100 lbf	N/A	N/A

3.2.4 Model Construction

The components of the wall were designed to match the desired stiffness of the structure. The walls were connected together using threaded steel rods with load cells providing a connection in the middle. Pressure sensors and accelerometers were attached to the outer and inner surfaces of the wall, respectively. Once the wall was assembled, the dry pluviation was used to place the backfill to achieve approximately 75% relative density with the Nevada Sand. The structure was

placed into the container at its predetermined depth, and the gaps between the structure and the inside of the container were filled with silicon grease to prevent sand from passing through. Additional accelerometers were placed in the backfill during the pluviation process. An aluminum frame was designed to fit over the container so that displacement transducers could be used to measure settlement during the tests. Once the model was constructed, it was loaded onto the centrifuge arm and the instruments were checked in the DAQ system by striking the container externally with a rubber mallet. The centrifuge was then balanced and spinning commenced to approximately 62-63 rpm to create 36 g acceleration at 8.5 m from the centrifuge spindle. The various stages of construction are shown in Figure 3.7.

Figure 3.7: Model construction
(a) wall construction, (b) pluviation calibration, (c) placing sand,
(d) placing structure, (e) fitting aluminum frame, (f) model on arm

3.3 Input Ground Motions

The NW01 model was subjected to two preliminary Kobe Takatori 090 earthquake ground motions to increase the density of the backfill sand from a relative density of approximately 80% to 90%. Then seven earthquake ground motions and two sine wave "sweeps" were applied during the experiment. The original earthquake ground motions that were used in the experiment are: 1989 Loma Prieta UCSC 090, 1989 Loma Prieta WVC 270, 1995 Kobe Takatori 090, 1999 Kocaeli Yarimca 060, and 1999 Kocaeli Yarimca 330. All earthquake ground motions were scaled and filtered to accommodate the limitations of the shaking table on the centrifuge (Al Atik & Sitar, 2010). The sine wave sweeps were also scaled accordingly. The response spectra from the original records are compared with the spectra recorded for each centrifuge input motion (as recorded by the accelerometer attached to the base of the container) in Figure 3.8. The recorded time histories for each of the ground motions are shown in Figure 3.9, and those for the sine wave sweeps are shown in Figure 3.10.

Seismic parameters for the input ground motions recorded during the experiment, excluding the preliminary Kobe earthquakes and the sine sweeps, are shown in Table 3.5. For each input ground motion, excluding the two sine wave sweeps and the two preliminary Kobe ground motions, the parameters are Peak Ground Acceleration (PGA), Peak Ground Velocity (PGV), Peak Ground Displacement (PGD), Arias Intensity (I_a), Significant Duration of the acceleration record ($D_{a,5-95}$), Mean Period (T_m), Predominant Period (T_p), and the spectral centroid of the input velocity (f_c). The Significant Duration is the time interval in which 90% of the seismic energy is dissipated, and is defined as $D_{a,5-95} = t(0.95I_a) - t(0.05I_a)$ (Trifunac & Brady, 1975). The Mean Period is used to characterize the frequency content of the acceleration history, and is defined as $T_m = \Sigma c_i^2 f_i^{-1} / \Sigma c_i^2$, where the c_i are the Fourier amplitude of the acceleration and the f_i are the discrete frequencies between 0.25-20 Hz (Rathje et al., 1998). The Predominant Period is also used to characterize the frequency content and is defined as $T_p = T(S_a^{max})$, where S_a is the 5% damped acceleration response spectrum. The spectral centroid of the input velocity is used to define the parameters for Rayleigh damping, and is defined as $f_c = \Sigma s_i^2 f_i / \Sigma s_i^2$, where the s_i are the Fourier amplitude of the velocity (see e.g. Massar et al. 2011).

Table 3.5: Seismic parameters of input ground motions recorded in NW01

Ground Motion	PGA (g)	PGV (cm/s)	PGD (cm)	I_a (cm/s)	$D_{a,5-95}$ (s)	T_m (s)	T_p (s)	f_c (Hz)
1) Kocaeli YPT060	0.23	11.5	1.6	25.0	6.6	0.54	0.24	1.38
2) Kocaeli YPT330	0.27	14.1	2.0	32.4	6.8	0.60	0.23	1.25
3) Loma Prieta SC – 1	0.43	27.6	4.5	110	11.0	0.59	0.35	1.06
4) Loma Prieta WVC270 - 1	0.21	17.5	2.2	25.2	5.1	0.62	0.24	1.12
5) Kobe TAK090 - 3	0.70	39.7	6.7	431	6.3	0.55	0.19	1.15
6) Loma Prieta SC – 2	0.44	26.6	4.3	110	10.8	0.58	0.35	1.09
7) Loma Prieta WVC270 - 2	0.22	17.6	2.1	27.5	5.0	0.59	0.25	1.17

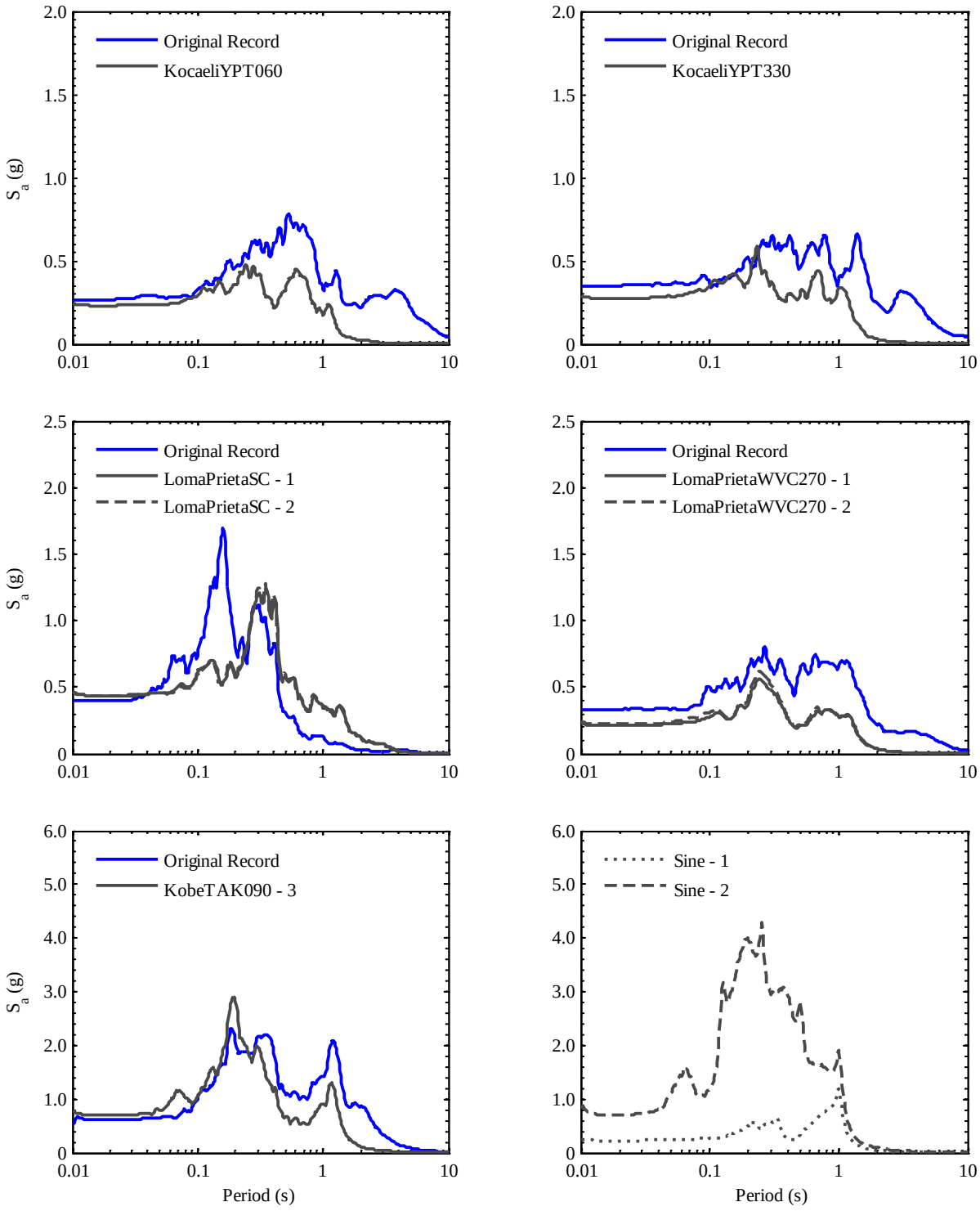

Figure 3.8: Response spectra (ξ=5%) from original record and input base acceleration

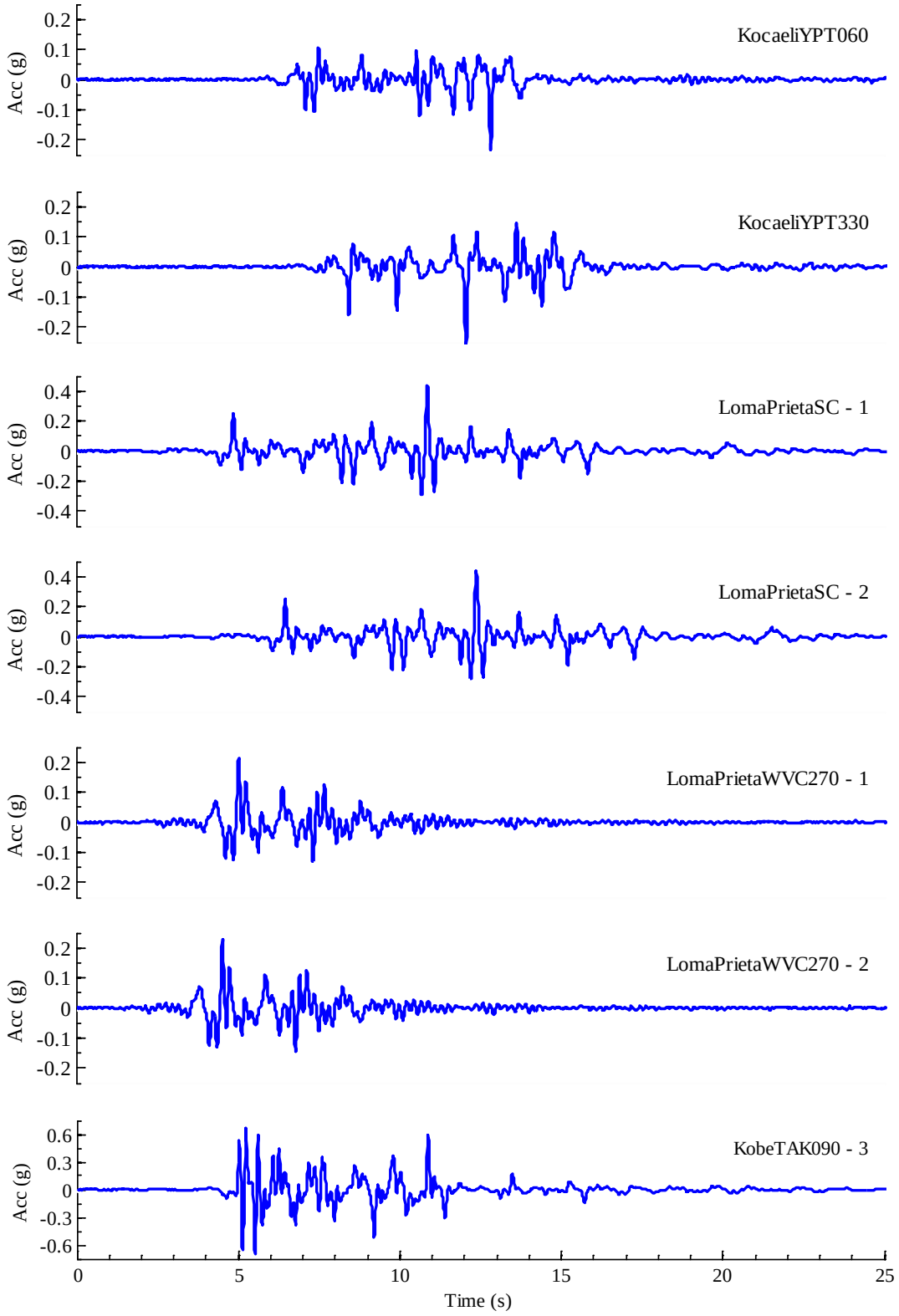

Figure 3.9: Acceleration time histories of input earthquake ground motions

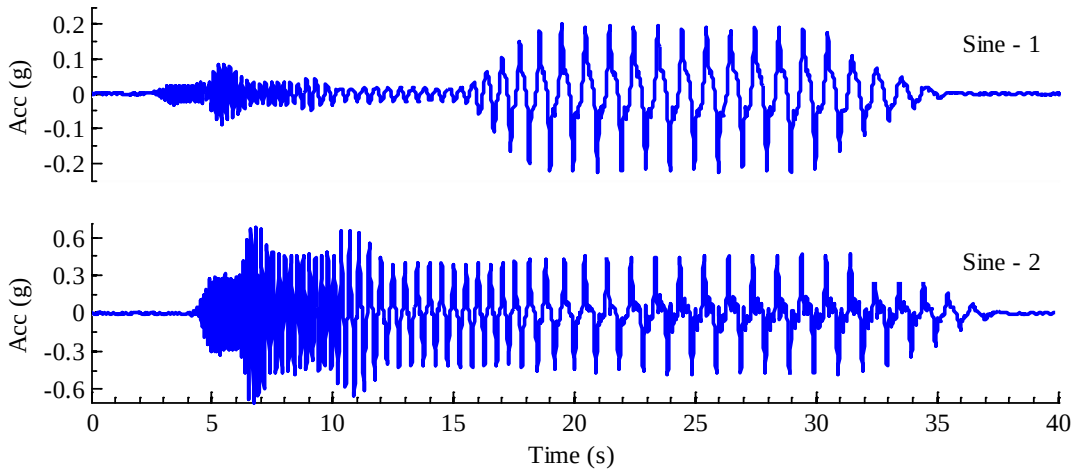

Figure 3.10: Acceleration time histories of input sine wave ground motions

3.4 Data Processing Methods

The recorded data was processed using MATLAB scripts developed by Candia & Sitar (2013) to maintain uniformity with the previous analyses. As in the previous experimental analysis, the data from each sensor was converted to engineering units and scaled to match the prototype. Filtering was applied to remove random noise.

- **Acceleration & displacement**: All accelerations and displacements were defined as positive towards the south end of the container and vertical deformation was defined as positive downward. Accelerations in the soil and structure were measured at the locations described in Figure 3.2, Figure 3.3, and Figure 3.5. A fifth order band pass Butterworth filter with cutoff frequencies f_{ch} = 0.25 Hz and f_{cl} = 15 Hz was applied to remove permanent offsets and high frequency noise. Displacement histories were evaluated using frequency domain integration of accelerometers instead of direct observation with the displacement transducers due to accuracy (Candia & Sitar 2013).

- **Inertial loads on retaining structure**: The inertial loads were determined as $\Delta P_{in} = -m\int_0^H \ddot{u}\,(t,z)dz$, where m is the mass of the wall per unit height and $\ddot{u}(t,z)$ is the acceleration distribution. The acceleration distribution is written as the product of quadratic shape functions $\mathbf{N} = [N_{top} \quad N_{mid} \quad N_{bot}]$ and the wall acceleration vector $\ddot{\mathbf{u}} = [\ddot{u}_{top} \quad \ddot{u}_{mid} \quad \ddot{u}_{bot}]^T$, with each component corresponding to the mean of each row of accelerometers on the walls. Thus, the inertial forces at each moment in time can be expressed as Equation 3.1:

$$\Delta P_{in} \approx -m\int_0^H \mathbf{N}\ddot{\mathbf{u}}dz = -m\int_0^H \left[2\frac{z^2}{H^2} - \frac{z}{H} \quad -4\frac{z^2}{H^2} + 4\frac{z}{H} \quad 2\frac{z^2}{H^2} - 3\frac{z}{H} + 1\right]\ddot{\mathbf{u}}dz$$

$$\Delta P_{in} \approx -mH\frac{\ddot{u}_{top} + 4\ddot{u}_{mid} + \ddot{u}_{bot}}{6} \qquad \textbf{(3.1)}$$

Using these shape functions implies that the distribution of inertial lateral stresses $\Delta q_{in} = -m\text{Nü}$ is nonzero at the top, as in Candia & Sitar (2013). Therefore, the above equation will only be used to estimate the magnitude and not the distribution of the inertial loads on the structure.

- **Seismic loads on retaining structure**: The total basement compression was computed by summing the load measured by the load cells as $P_{tot} = \sum P_i$. The data was scaled to prototype dimensions and filtered to remove frequencies above 15 Hz using a fifth order Butterworth filter. The soil loads were determined by adding and subtracting the inertial load of the north and south walls, respectively, as $P_{ae} = P_{tot} \pm \Delta P_{in}$, and using d'Alembert's principle applied to the free body diagram in Figure 3.11. Additionally, the soil loads can be written in incremental form as $\Delta P_{ae} = \Delta P_{tot} \pm \Delta P_{in}$ by removing the static component of the total load. The static component is computed in the same manner as in Candia & Sitar (2013); first, a fifth order low pass Butterworth filter with corner frequency f_{cl} = 0.25 Hz is used on the total load history. Then, a cumulative sum of the squared absolute value of the resulting record is computed and normalized by the last value (this operation is similar to an Arias intensity calculation). Lastly, the static component is computed by multiplying the normalized cumulative sum record by the difference in load at the beginning and end of the original total load record and adding the load at the beginning of the total load record. The effect is a monotonically increasing (or decreasing, if the final total load is less than initial load) record that approximates the static component. The accelerations of each wall are essentially the same at each height, so the total load is simply the differential soil-induced load on the walls based on this equilibrium analysis. Therefore, no inertial load is captured in the load cell recordings.

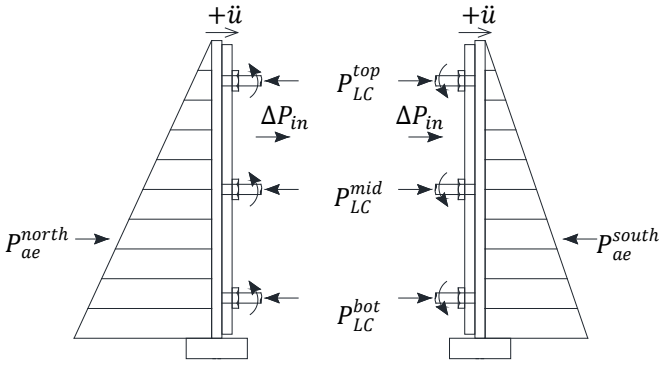

Figure 3.11: Free body diagram of retaining structure
sign convention for positive acceleration and loads indicated by arrows

- **Surface settlement & permanent offsets**: Vertical soil deformations at the beginning and end of every earthquake were recorded with four displacement transducers in the free field and two displacement transducers on the top of the structure. The density of the backfill sand was estimated using this data, which did not change much after applying the two preliminary

Kobe recordings. Lateral wall deformations were recorded with two displacement transducers mounted to an aluminum rack attached to the model container. A 0.25 Hz filter was applied to retain only the static component for all displacement transducers.

3.5 Experimental Problems & Errors

The main issue with the experiment was the poor performance of the pressure sensors. The Tactilus pressure sensors exhibited a sharp stress drop at the onset of ground motion followed by a slow build-up as the ground motion subsided. Also, the voltage output increased as the experiment continued, even between ground motions. Both of these behaviors are consistent with what was observed in the experiments conducted by Mikola & Sitar (2013) and Candia & Sitar (2013). Therefore, the Tactilus pressure sensors were use only to qualitatively estimate the distribution of the earth pressure with depth, but not the magnitude.

The Flexiforce pressure sensors did not perform as expected either. The voltage output was extremely noisy for all Flexiforce sensors, and filtering did not produce meaningful insight. A typical voltage output for one of the Flexiforce pressure sensors and for one of the Tactilus pressure sensors on the south wall of the structure are shown in Figure 3.12. For this reason, the data for the Flexiforce sensors was not considered in the analysis of the experiment. Additionally, there was a cave-in during the experiment on the northeast side of the structure on the same section as the Flexiforce sensors (Figure 3.13), which would have affected the measured earth pressure distribution. However, a careful review of the data showed that the loads from the load cells on the side with the cave-in were not significantly different from the load cells on the opposite side and, therefore, the cave-in did not affect the overall results.

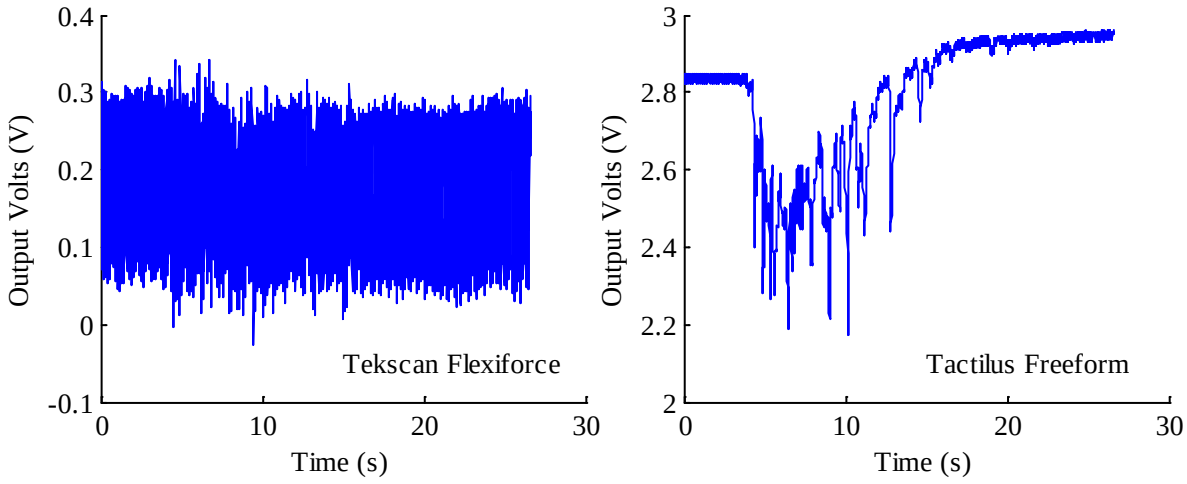

Figure 3.12: Behavior of pressure sensors F5 and S1 during Kobe TAK 090-3

(a) 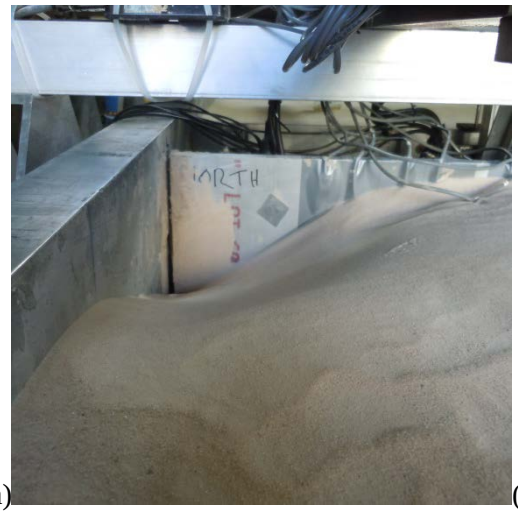 (b) 

Figure 3.13: Cave in at northeast corner of structure

The two sine wave sweeps did not function as planned in the original design of the experiment. The sine waves were supposed to have the same acceleration amplitude for the four sections of the input motion to compare the frequency response of the soil-basement system. Since the input files for the centrifuge at UC Davis accept displacement values, the desired input acceleration time history was numerically integrated twice to a obtain a displacement time history file. When the sine wave motion was applied during the experiment the recorded input acceleration did not match what was expected, and instead each section of the acceleration time history had different amplitude as shown in Figure 3.10. Therefore, the results of the two sine wave sweeps were not included in further data processing.

A summary of the other minor errors and corrections are listed below:

- Accelerometer A5 failed during the first Kobe earthquake and was substituted with that of accelerometer A8 for all of the events;
- Accelerometers A14 and A16 reached their maximum output voltage during the first and third Kobe earthquakes and the second sine sweep, and also the second Kobe earthquake for accelerometer 16. The data was substituted with accelerometer A15 and A13, respectively;
- Accelerometers A23 and A40 reached their maximum output voltage during the first Kobe earthquake and were substituted by the average recording of accelerometers A22 and A24, and the recording of accelerometer A39, respectively;
- Accelerometer A29 reached its maximum output voltage during the first two Kobe earthquakes and the second sine sweep. The data was substituted with accelerometer A30;
- Accelerometer A31 (east input accelerometer) detached during spin-up, so the data was ignored; and
- South Tactilus Pressure Sensor S4 became disconnected from its wire during pluviation and therefore no data was recorded at that location.

4 Centrifuge Experiment: Results

4.1 Acceleration Response in Soil & Structure

As, already described, the backfill and the structure were densely instrumented with accelerometers in order to evaluate accelerations throughout the backfill and within the structure itself. One way to evaluate the extent the centrifuge model response mimics prototype behavior is to look at amplification of ground motion through the soil column. Figure 4.1 is a plot of the peak ground acceleration at different levels in the backfill and different elevations in the model structure. The plot shows that in the free field, the ground motion was de-amplified for input PGA > 0.3 g and amplified slightly at lower levels of input ground motion. In the structure, the ground motion was amplified at the top of the structure and de-amplified in the mid-height of the structure, whereas the response at the foundation level of the structure was approximately the same as the input ground motion. Note that the peak response at the foundation level in both the free field and the structure did not vary much from the peak input ground motion; this suggests that little attenuation occurs between the bottom and the second ring of the container. The peak responses of the structure suggests that the foundation level moves in tandem with the input ground motion; the top level of the structure experiences amplification of the ground motion; and the middle level of the structure acts as an intermediate "pivot" point between the two with de-amplification of the ground motion. This is consistent with results obtained by Candia & Sitar (2013), when considering the depth of the shallow basement structure. A plot of a portion of the response of the structure at various depths during the Kobe TAK 090-3 ground motion is shown in Figure 4.2. Note that the acceleration response at the top and foundation levels are essentially out of phase and the response at the middle level is roughly in between, which corresponds with the de-amplification at the middle level.

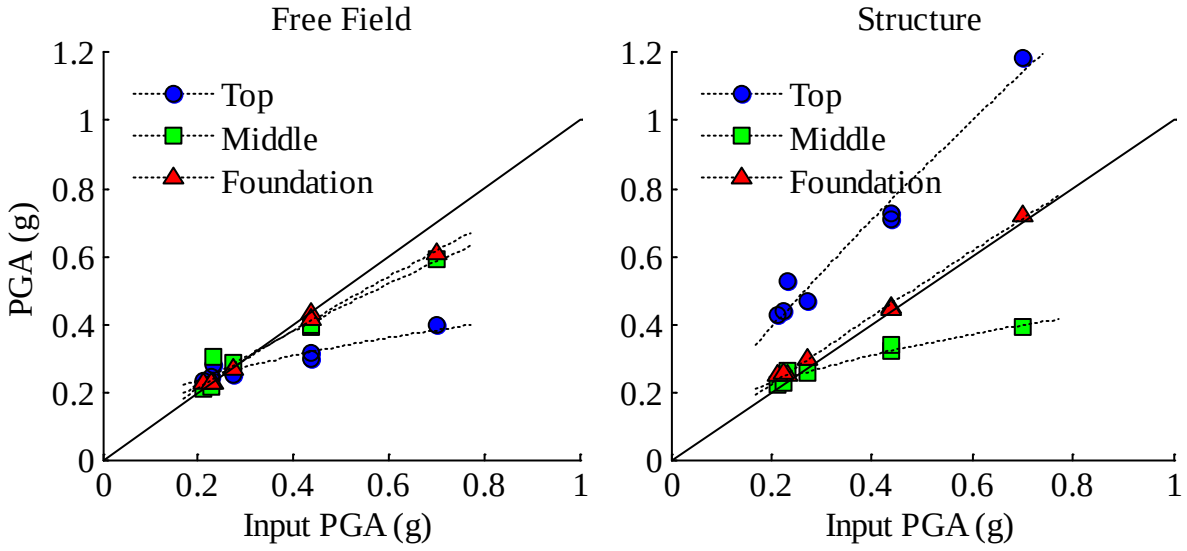

Figure 4.1: Measured ground motion amplification in free field and structure

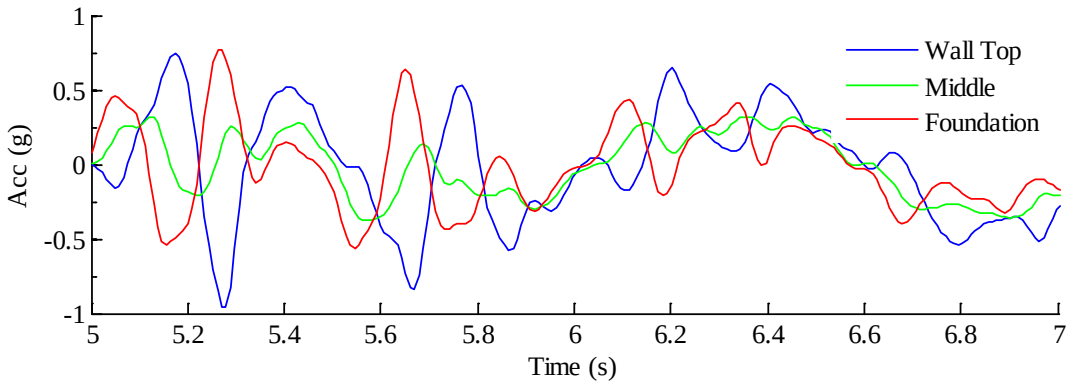

Figure 4.2: Response of basement wall at various depths during Kobe TAK 090-3

Profiles of ground acceleration and displacement relative to the base at the moment of maximum measured response in the north and south free field (PGA and PGD), are shown in Figure 4.3 for different input ground motions. In general, the accelerations and displacements increase toward the surface, primarily in the first and second modes of vibration. The two Loma Prieta SC motions had contributions from the third mode that exceeded those from the second mode. The influence of higher modes was determined using modal composition as proposed by Gazetas (1982) using three modal coordinates according to Equation 4.1:

$$u(z) \approx \psi_1 \, \bar{U}_1 + \psi_2 \, \bar{U}_2 + \psi_3 \, \bar{U}_3 \qquad \textbf{(4.1)}$$

where $\bar{U}_n = \cos(\pi z(2n-1)/2H)$ are the natural modes of a uniform soil deposit, $f_n = (2n-1)V_s/4H$ are the corresponding natural frequencies and ψ_n are the mode participation factors. The displacement mode participation factors were determined with the method of least squares and are summarized in Table 4.1 for all of the ground motions for both the north and south free field. The coefficient of determination R^2 is presented, if one, two or three modes were used. The shear wave velocity of the Nevada sand was estimated by determining the time delay of acceleration pulses between the base accelerometers and the surface level accelerometers in the free field. The computed average shear wave velocity was approximately $V_s \approx 150 \pm 15$ m/s, and it corresponds to the degraded shear modulus during shaking. Therefore, it is possible that the shear wave velocity corresponding to the maximum shear modulus would be higher. The analysis of the data shows that approximately 80% of the displacements come from the first mode ($f_1 \approx 1.9$ Hz), approximately 10-15% from the second mode ($f_2 \approx 5.6$ Hz) and less than about 5-10% from the third mode ($f_3 \approx 9.4$ Hz) and higher modes. Note that the coefficient R^2 converged towards unity for some ground motions and to lesser values for others. This is due to the variability between the response of the north and south backfills; since the accelerations and displacements are sampled from such a large volume that it is inevitable that the response will not coincide exactly with an analytical method. Also note that the third mode participation factors are all negative, implying that the third mode contribution is out of phase compared to the first and second mode contributions.

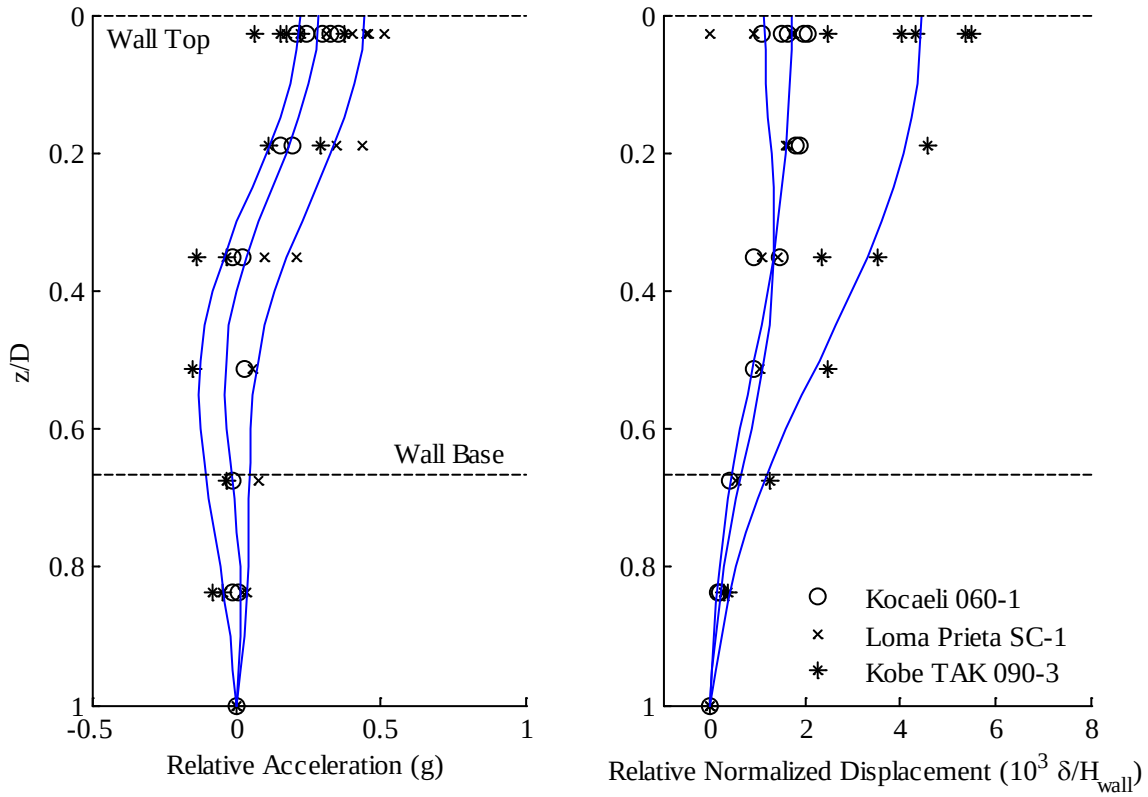

Figure 4.3: Acceleration & displacement profiles at maximum mean surface PGA and PGD

Table 4.1: Modal participation factors and coefficient of determination R^2

	Modal Participation Factors			Coefficient R^2		
Ground Motion	ψ_1(cm)	ψ_2(cm)	ψ_3(cm)	1 mode	2 modes	3 modes
1) Kocaeli YPT060	2.02	0.353	-0.084	0.943	0.961	0.962
2) Kocaeli YPT330	1.39	0.148	-0.087	0.945	0.949	0.952
3) Loma Prieta SC – 1	1.87	-0.063	-0.249	0.836	0.841	0.858
4) Loma Prieta WVC270 - 1	0.65	0.372	-0.136	0.732	0.834	0.856
5) Kobe TAK090 - 3	5.16	0.979	-0.116	0.934	0.954	0.954
6) Loma Prieta SC – 2	2.02	-0.146	-0.180	0.862	0.872	0.880
7) Loma Prieta WVC270 - 2	0.89	0.306	-0.097	0.849	0.901	0.909

Elastic response spectra with 5% damping at selected model locations are shown in Figure 4.4. The figure shows that spectral accelerations at the free surface are amplified for $T > 0.1$ to 0.2 s, except for the Kobe ground motion which attenuates accelerations for $T < 0.5$ s. The spectral accelerations on the basement wall are considerably higher for the top of the structure as compared to the base input or the free field accelerometers.

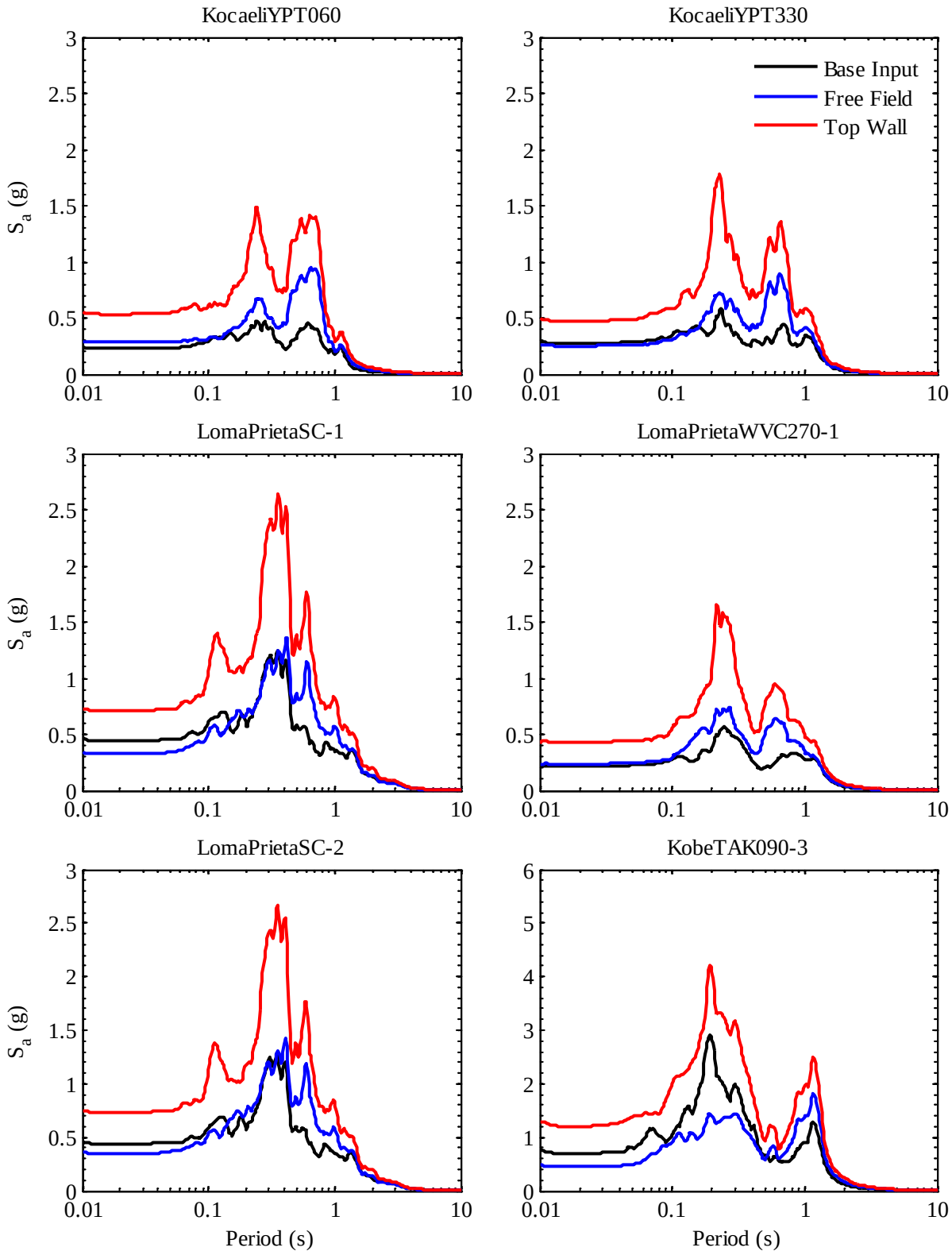

Figure 4.4: Acceleration response spectra (ζ=5%) at base, in free field, and at top of structure

4.2 Seismic Settlements & Displacements

Linear potentiometers were distributed at the free surface and at the top of the wall as shown in Figure 3.3. The first two Kobe ground motions, which served to increase the density of the backfill prior to the experiment, caused incremental surface settlements of 4.3 mm and 2.9 mm (15.2 cm and 10.6 cm in prototype scale), respectively. The basement structure settled 1.1 mm and 0.4 mm (3.9 cm and 1.4 cm in prototype scale), respectively, in response to the same ground motions. The incremental and cumulative surface and basement settlements in prototype scale are shown in Table 4.2, below, for the seven the different input motions. Note that minimal settlement occurred during each individual event, which gives confidence that the soil density remained relatively constant for each ground motion. The average unit weight of the backfill was computed as 16.62 kN/m^3.

Table 4.2: Seismically induced incremental and cumulative settlements (prototype scale)

	Surface Settlement (cm)		Basement Settlement (cm)	
Ground Motion	**Incremental**	**Cumulative**	**Incremental**	**Cumulative**
1) Kocali YPT060	0.23	0.23	0.06	0.06
2) Kocali YPT330	0.19	0.43	0.07	0.13
3) Loma Prieta SC – 1	0.50	0.92	0.14	0.27
4) Loma Prieta WVC270 - 1	0.06	0.98	0.03	0.31
5) Kobe TAK090 - 3	2.75	3.74	0.73	1.04
6) Loma Prieta SC – 2	0.95	4.68	0.15	1.20
7) Loma Prieta WVC270 - 2	0.12	4.80	0.02	1.22

To measure the permanent offsets and rotation of the structure, two spring-loaded linear potentiometers were placed horizontally near the top and bottom of the basement. The stiffness of the structure minimized racking deformations and the symmetry of the entire model prevented any significant permanent lateral displacements of the structure. The maximum incremental racking occurred during the first Loma Prieta SC event and was $\Delta\delta/\mathrm{H}$ = 0.09%; the maximum incremental rigid body displacement also occurred during the first Loma Prieta SC event and was 0.21 cm in prototype scale.

4.3 Static & Dynamic Earth Pressure

The magnitude of the static earth pressure on the basement wall was back calculated from the load cell data. The static active earth pressure distribution was estimated assuming an internal friction angle (ϕ) of 32.5° using Coulomb theory (1776) resulting in K_A = 0.30 and the static at-rest earth pressure distribution was estimated using K_0 = 0.46 for comparison with the observed static earth pressure. Figure 4.5 shows that the interpreted static earth pressure is nearly equal to the static at-rest earth pressure for the first and last earthquake shaking events, Kocaeli YPT060 and Loma Prieta WVC270-2 respectively. These results are in agreement with those observed in Mikola & Sitar (2013) for a non-displacing basement wall. The static earth pressure interpreted from the pressure sensors are included as well; although, as already noted, the pressure sensors

do not accurately reflect the magnitude of the earth pressure, but rather give a relative sense of the distribution of the load.

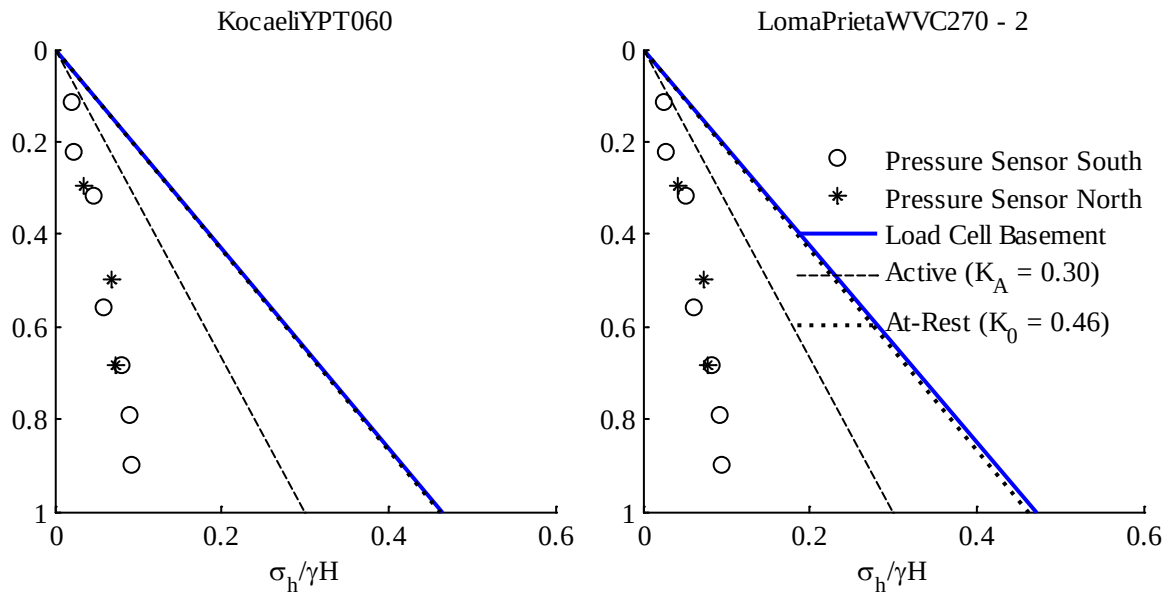

Figure 4.5: Static earth pressure in basement wall prior to ground motion (H = 13.47 m, γH ≈ 225 kN/m^2)

Therefore, the magnitude of the total seismic earth pressure on the basement was back calculated from the load cell data and the inertial loads, as described in Section 3.4. As in Candia & Sitar (2013), the results are displayed in terms of the seismic earth pressure increment Δq_{ae} using a baseline correction on the load cell data. The linear trend of increasing earth pressure with increasing depth was apparent and was similar to that observed in other experimental results in cohesionless soils (Al Atik & Sitar, 2010; Mikola & Sitar, 2013). Therefore, the distribution of the seismic earth pressure increment interpreted from the load cell data was assumed to be linear with depth and is shown in Figure 4.6 for the Kocaeli YPT060, the Kobe TAK090-3, and both Loma Prieta SC earthquakes at the time of maximum total seismic load P_{ae}. The distributions predicted by the Okabe (1924) method and the Seed & Whitman (1970) method using the PGA at the surface are included for comparison. Note that although the pressure sensor data appears to agree well with the distribution interpreted by the load cells; this is merely coincidence. Comparing the data to the static earth pressure plot in Figure 4.5, it is clear that the magnitude of the pressure sensor data is of equivalent magnitude. These results suggest that the point of application of the seismic load increment ΔP_{ae} should act at a height close to H/3 from the base of the wall, which is consistent with the previously discussed centrifuge experiment studies.

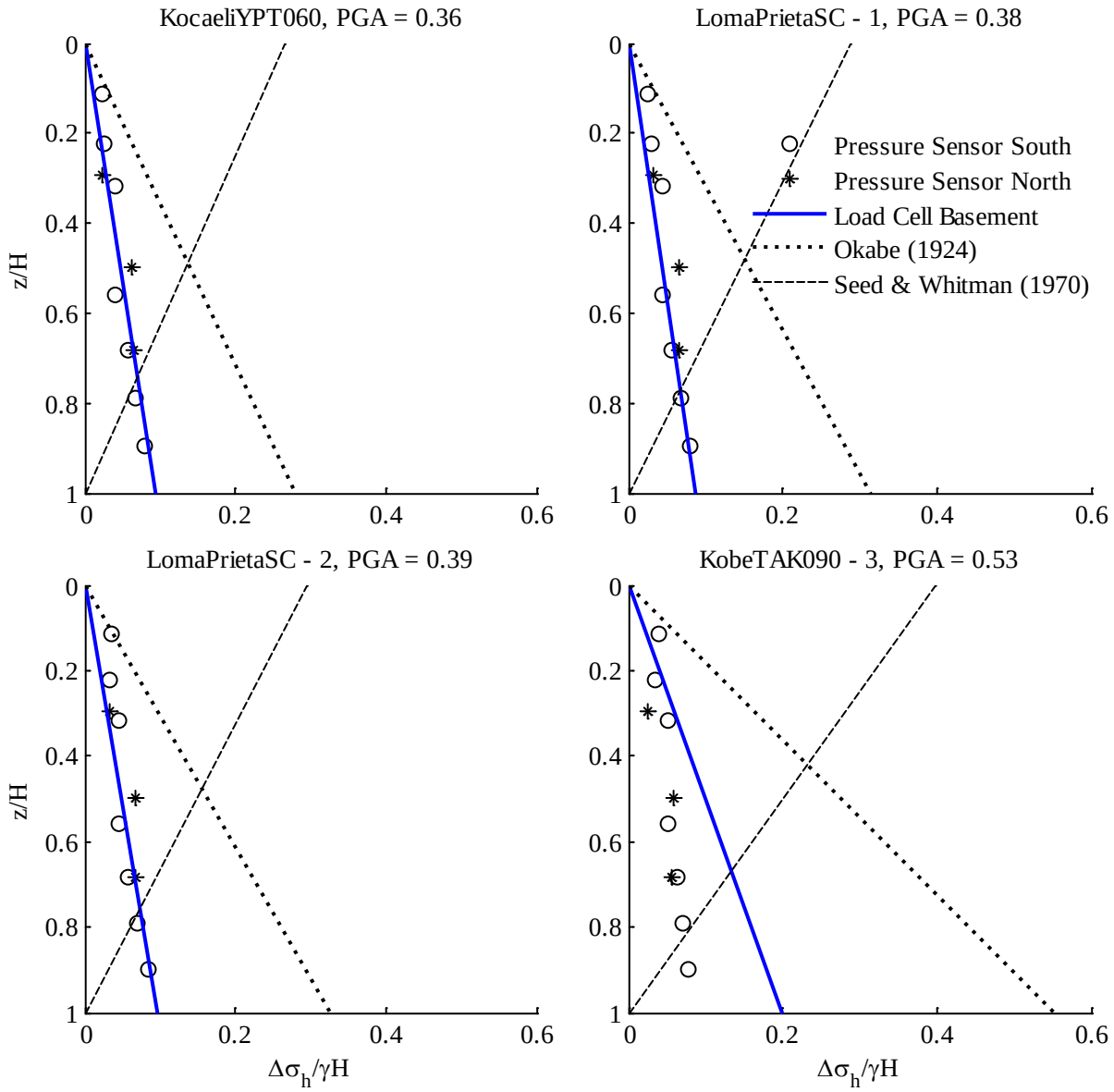

Figure 4.6: Dynamic horizontal earth pressure increment in basement wall at maximum P_{ae} (H = 13.47 m, γH ≈ 225 kN/m²)

4.4 Response of Basement Wall

The dynamic response of the basement wall is complex, since the true system to be analyzed is a composite soil-structure system with inertial and kinematic coupling. Figure 4.7 shows the seismic load increments during the Loma Prieta SC – 2 earthquake input motion. As mentioned in Section 3.4, the net incremental basement compression ΔP_{tot} corresponds to the differential soil induced load increment between the north and south walls. Based on the data in Figure 4.7a, peak incremental basement compression is preceded by a peak (either positive or negative) in the incremental inertial load; compression release then initiates as the inertial load reverses direction and the process continues. The phase difference between the basement compression peaks and

the inertial load maxima and minima is roughly 0.08 to 0.12 s; this is approximately the time delay of the acceleration pulses to travel from the bottom to the top of the basement structure based on the accelerometer data, as shown previously in Figure 4.2. Soil induced load increments on the basement structure from the north and south backfills are shown in Figure 4.7b, with positive values corresponding to active thrust of the backfill. Note that the loads are essentially out of phase; maximum load on the north wall corresponds to a minimum load on the south wall and vice versa. This is consistent with intuition and observations by Candia & Sitar (2013) for cohesive backfill materials. Similar plots and results are shown for the Kobe TAK090 – 3 earthquake input motion in Figure 4.8.

Analysis of the response of the north and south backfill shows that the accelerations measured at the same depth in backfill agree in phase and magnitude. The same can be said for the soil adjacent to the basement structure, and for the structure itself. Additionally, the acceleration of the soil adjacent to the structure at mid-height and base level agree in phase and magnitude with the acceleration of the basement structure at the same depths. However, the acceleration peaks of the soil adjacent to the structure at the surface level were consistently delayed by approximately 0.04 to 0.07 s compared to the accelerations measured at the top of the basement structure. In contrast, Candia & Sitar (2013) observed that the acceleration peaks in the structure were delayed compared to the acceleration peaks in the adjacent soil. This suggests that the relative stiffness of the structure compared to the backfill soil affects which part of the soil-structure system influences the response. In the current experiment, the shear waves apparently propagated at approximately the same velocity in the deep layers of the backfill as in the structure, but as the soil stiffness decreased due to decreasing confinement the shear waves propagated more rapidly in the structure and thus influenced the response of the surface of the backfill. Similarly, the inertial loads peaked slightly before the peak compression of the basement structure, reflecting the incoherency in the response between the structure and the backfill.

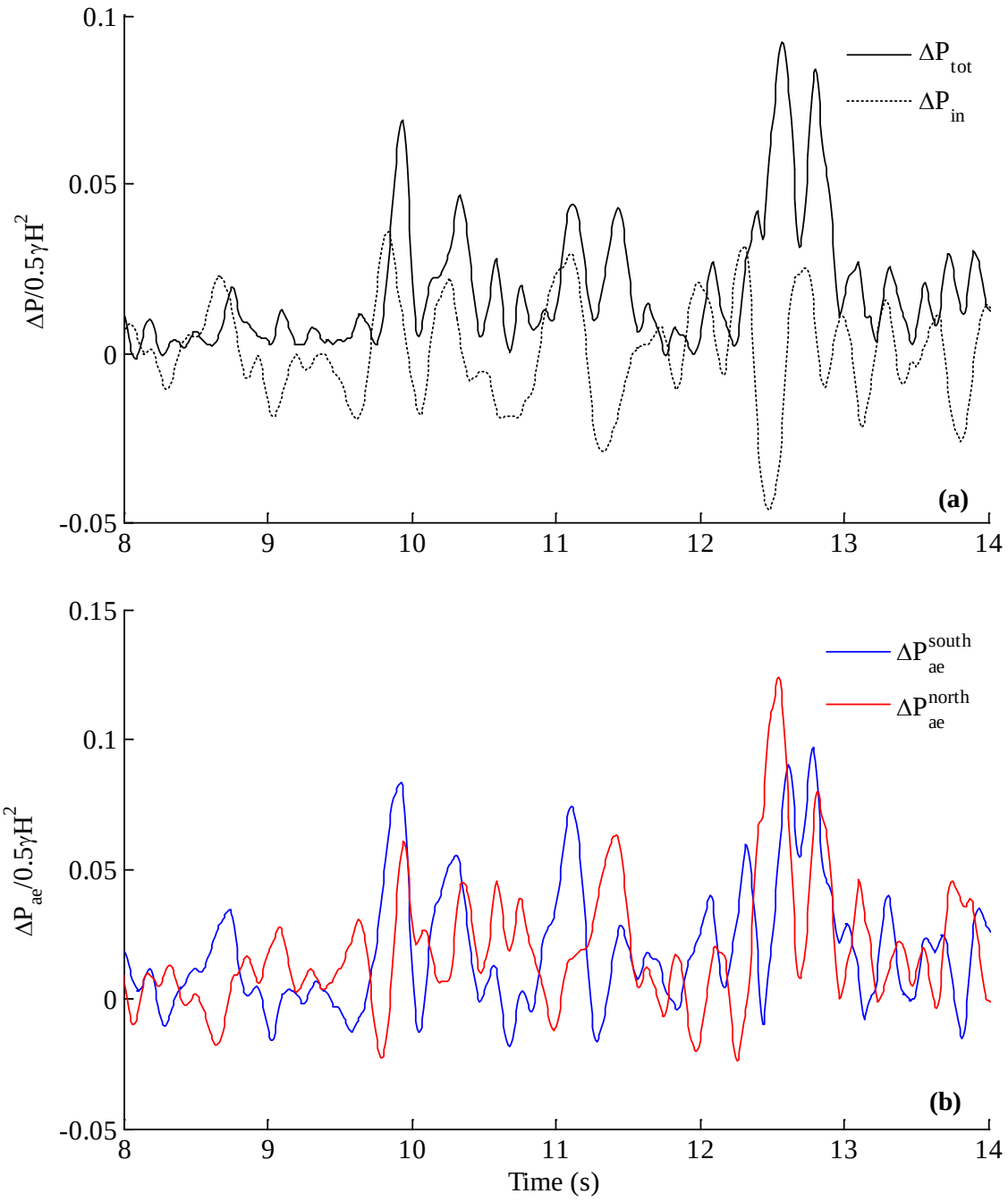

Figure 4.7: Seismic load increment on basement wall during Loma Prieta SC - 2
(a) basement compression and inertial load, (b) soil induced loads on north and south walls
($H = 13.47$ m, $0.5\gamma H^2 \approx 1500$ kN/m)

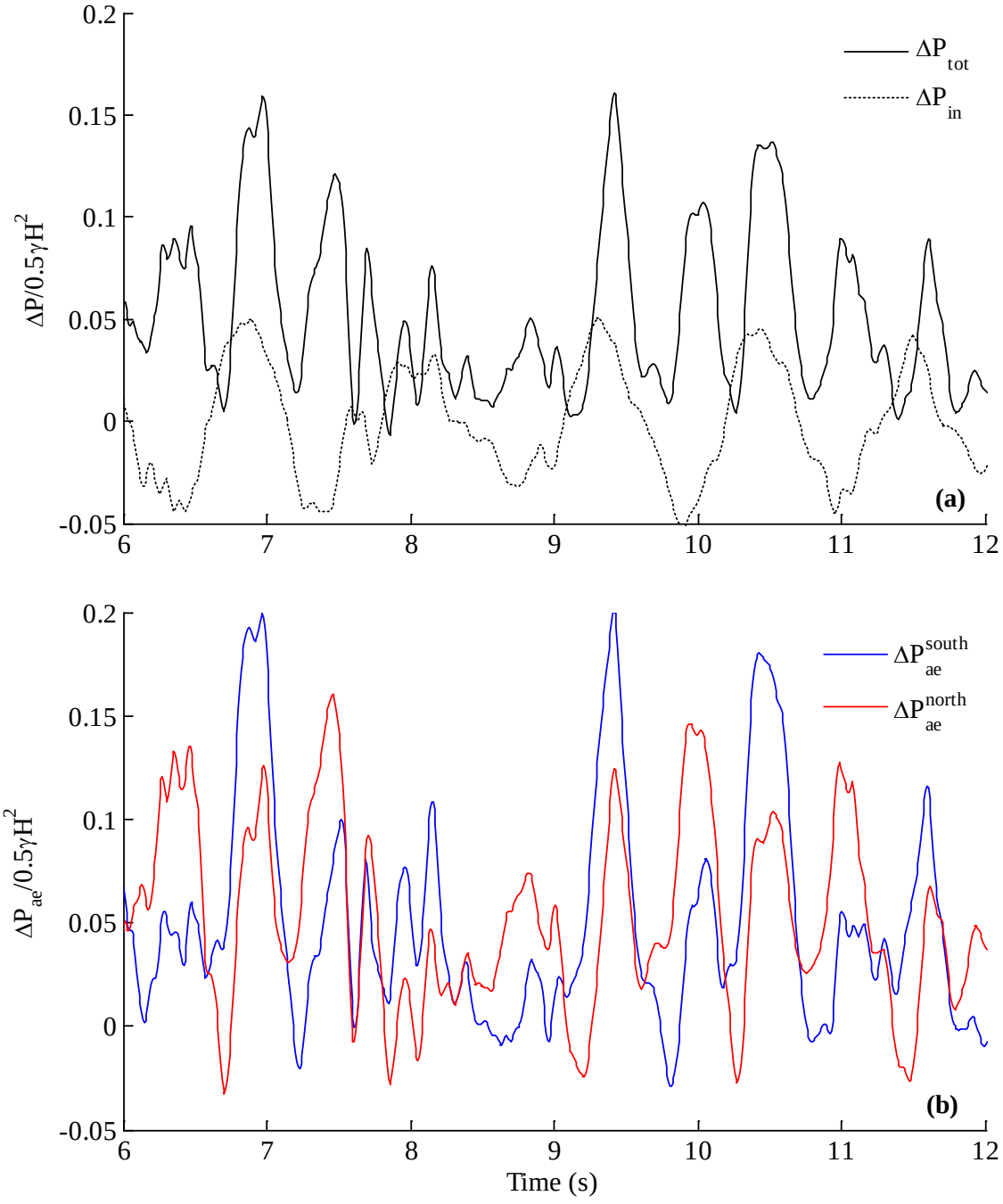

Figure 4.8: Seismic load increment on basement wall during Kobe TAK090 - 3
(a) basement compression and inertial load, (b) soil induced loads on north and south walls
($H = 13.47$ m, $0.5\gamma H^2 \approx 1500$ kN/m)

A summary of the maximum basement loads measured on the structure is shown in Table 4.3, decomposed into static and dynamic components. The results show that approximately 75-90% of the maximum net load comes from static earth pressure, 2-7% comes from inertial loads of the basement wall, and the remaining 5-15% comes from the seismic earth pressure. Note that these

peak values do not occur simultaneously, so the relative percentages may not be accurate at every instance in time. Using linear regression, the coefficient of dynamic earth pressure (removing inertial effects) for the 13.3 m tall structure can be approximated as Equation 4.2:

$$\Delta K_{ae} = 0.57\left(PGA_{ff,surface}/g - 0.19\right) \pm \epsilon \qquad \textbf{(4.2)}$$

where $\epsilon = 0$ represents the mean and $\epsilon \approx 0.055$ represents the 95% confidence intervals. A plot of the data, the regression, the semi-empirical Seed & Whitman (1970) method, the Wood (1973) solution, and the M-O solution for clean sand for estimating the coefficient of dynamic earth pressure is shown in Figure 4.9. The data and regression from Mikola & Sitar (2013) and Candia & Sitar (2013) for 6.5 m tall braced walls in cohesionless and cohesive backfill, respectively, are also shown for comparison.

Table 4.3: Free field acceleration coefficients and measured basement loads loads normalized by $0.5\gamma H^2 \approx 1500$ kN/m

Ground Motion	PGA^n	PGA^s	P_a	ΔP_{ae}	ΔP_{in}	ΔP_{ae}^n	P_{ae}^n	ΔP_{ae}^s	P_{ae}^s
1) Kocali YPT060	0.36	0.30	0.47	0.07	0.04	0.07	0.53	0.10	0.57
2) Kocali YPT330	0.33	0.26	0.47	0.04	0.03	0.05	0.52	0.06	0.52
3) Loma Prieta SC	0.38	0.35	0.48	0.09	-0.04	0.12	0.59	0.09	0.56
4) Loma Prieta WVC270	0.29	0.26	0.47	0.02	-0.03	0.04	0.51	0.03	0.50
5) Kobe TAK090	0.53	0.47	0.47	0.16	-0.05	0.16	0.63	0.20	0.67
6) Loma Prieta SC	0.39	0.37	0.48	0.09	-0.05	0.12	0.59	0.10	0.57
7) Loma Prieta WVC270	0.30	0.27	0.48	0.02	-0.03	0.04	0.52	0.04	0.51

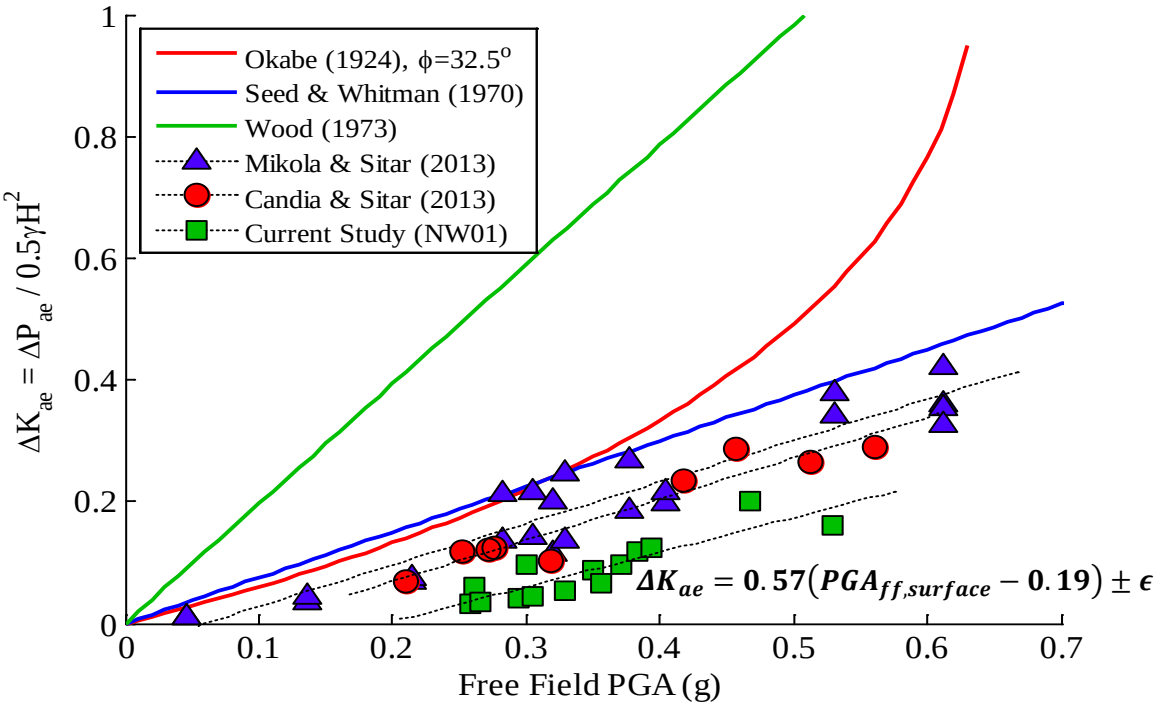

Figure 4.9: Coefficient of dynamic earth pressure versus free field PGA at the surface

The results demonstrate some of the issues with analytic and empirical solutions at present. The limit equilibrium solutions overestimate actual observations of dynamic earth pressure on retaining structures. In this regard, it should not be surprising that structures designed for moderate ground acceleration (< 0.2 g) with a reasonable factor of safety for static conditions (FS ~ 1.5) perform well, as discussed by Mikola & Sitar (2013). As already concluded by Mikola & Sitar (2013), the Seed & Whitman (1970) solution represents a reasonable upper bound, and the Wood (1973) solution is a significant overestimate even for very stiff walls, such as those in this study. Another issue with these solutions is that the location at which the PGA is measured or how the seismic coefficient is related to the PGA is not directly specified. While using free field PGA at the surface may be reasonable for relatively short walls (Mikola & Sitar, 2013; Candia & Sitar, 2013), deeper or taller walls will experience lower average acceleration due their physical length and incoherency. The alternative then is to consider the average acceleration over the depth of the wall. To alleviate both issues, that of using a high PGA when most of the wall is subjected to a reduced acceleration and the incoherency of the backfill acceleration that increases with increasing depth of the wall, a different measure of ground response is desirable. Bray et al. (1998) use maximum horizontal equivalent acceleration, $MHEA = |\tau_h/\sigma_v|_{max} g$, to estimate the seismic displacement of a slope. The measure of ground response incorporating depth of embedment and incoherency effects will be referred to as the seismic coefficient k_{MHEA} in this study. The seismic coefficient is computed by averaging the acceleration in the backfill over the depth of embedment of the retaining structure at each instant in time, then selecting the absolute maximum value (Equation 4.3). This is mathematically equivalent to computing $MHEA/g$ for a uniform density backfill. The values of k_{MHEA} for the north and south backfills for the current study and the maximum normalized dynamic load increment are shown in Table 4.4.

$$k_{MHEA} = \left|\frac{\Sigma \Delta z \ddot{u}}{\Sigma \Delta z g}\right|_{max} = PGA_{depth\ averaged}/g \Leftrightarrow MHEA/g = |\tau_h/\sigma_v|_{max} \quad \textbf{(4.3)}$$

Table 4.4: Seismic coefficients, k_{MHEA}, and dynamic load increments loads normalized by $0.5\gamma H^2 \approx 1500$ kN/m

Ground Motion	k_{max}^{north}	k_{max}^{south}	ΔP_{ae}^{north}	ΔP_{ae}^{south}
1) Kocali YPT060	0.23	0.22	0.07	0.10
2) Kocali YPT330	0.21	0.19	0.05	0.06
3) Loma Prieta SC – 1	0.32	0.26	0.12	0.09
4) Loma Prieta WVC270 - 1	0.17	0.17	0.04	0.03
5) Kobe TAK090 - 3	0.35	0.32	0.16	0.20
6) Loma Prieta SC – 2	0.33	0.26	0.12	0.10
7) Loma Prieta WVC270 - 2	0.18	0.17	0.04	0.04

The coefficient of dynamic earth pressure can be approximated as Equation 4.4:

$$\Delta K_{ae} = 0.68(k_{MHEA} - 0.11) \pm \epsilon \quad \textbf{(4.4)}$$

where $\epsilon \approx 0.053$ represents the 95% confidence intervals. A similar analysis was performed with the data from Mikola & Sitar (2013) and Candia & Sitar (2013). A plot of the data and the new regression, the reanalyzed data and new regressions from Mikola & Sitar (2013) and Candia & Sitar (2013), the semi-empirical Seed & Whitman (1970) solution, the Wood (1973) solution, and the M-O solution for clean sand for estimating the coefficient of dynamic earth pressure coefficient are shown in Figure 4.10.

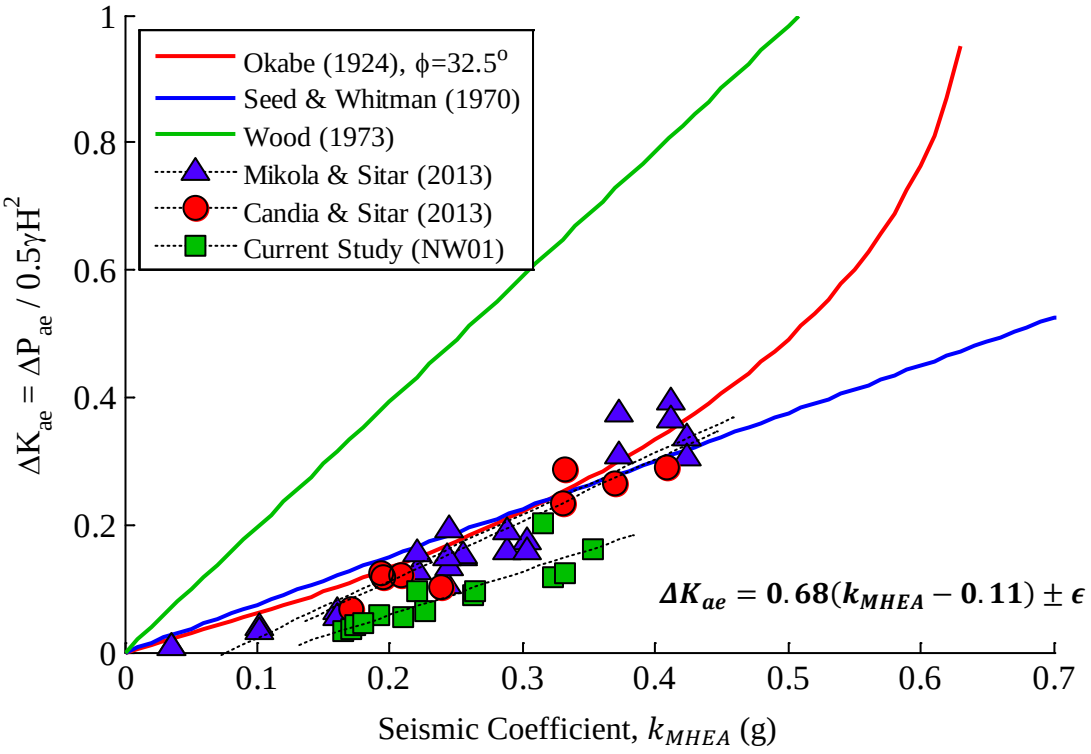

Figure 4.10: Coefficient of dynamic earth pressure versus seismic coefficient, k_{MHEA}

Table 4.5 compares the ratio of the seismic coefficient to the peak free field acceleration. Note that the ratios fall roughly between 0.60 and 0.85 and these values agree well, for example, with those suggested by Anderson et al. (2008), which will be discussed further in Section 7.1.1.

Table 4.5: Ratio of seismic coefficient, k_{MHEA}, to peak free field acceleration at surface

Ground Motion	$k_{MHEA}^{north}/PGA^{north}$	$k_{MHEA}^{south}/PGA^{south}$
1) Kocali YPT060	0.64	0.73
2) Kocali YPT330	0.64	0.73
3) Loma Prieta SC – 1	0.84	0.74
4) Loma Prieta WVC270 - 1	0.59	0.65
5) Kobe TAK090 - 3	0.66	0.67
6) Loma Prieta SC – 2	0.85	0.70
7) Loma Prieta WVC270 - 2	0.60	0.63

5 Numerical Modeling of Centrifuge Experiment

5.1 Introduction

The centrifuge experiment was modeled in FLAC$^{2\text{-D}}$ (Itasca, 2011) using a nonlinear hysteretic soil model. The objective of the modeling effort was to evaluate how well a calibrated numerical model could reproduce the results of the physical experiment. Special attention was given to using soil parameters that could be readily determined through correlations and realistic assumptions and to boundary conditions, soil-structure connectivity, and to the fidelity of representation of the physical experiment.

5.2 Soil Model Definition

Two soil models were considered for use in this study. The first was the elasto-plastic Mohr-Coulomb model with hysteretic damping using a sigmoidal curve representing the secant shear modulus degradation. The input parameters are:

ϕ_f = peak friction angle — c = cohesion intercept

G = elastic (small strain) shear modulus — K = elastic bulk modulus

ψ = dilation angle — σ^t = tension limit

Modulus degradation curves are defined in FLAC assuming that the stress depends only on strain and not on the number of cycles or time. Then, an incremental constitutive relation is defined from the modulus degradation curve by $\bar{\tau}/\gamma = M_s$, where $\bar{\tau} = \tau/G_0$ is the normalized shear stress, G_0 is the small strain shear modulus, γ is the shear strain and M_s is the strain-dependent secant modulus. The normalized tangent modulus, M_t, is obtained using Equation 5.1:

$$M_t = \frac{d\bar{\tau}}{d\gamma} = M_s + \gamma \frac{dM_s}{d\gamma} \quad \textbf{(5.1)}$$

The incremental shear modulus is given by $G_0 M_t$, which is used in place of the shear modulus G_0 to create the "backbone curve". Reversal points are handled by applying two Masing (1926) rules: (1) a new, but inverted, function is started upon reversal with an initial unload modulus G_0; and (2) the first quarter-cycle of loading is scaled by one-half relative to all other cycles. Note that the derivative of the modulus reduction curve is necessary to define the tangent modulus in FLAC. Since degradation curves are typically specified as tables of values spaced logarithmically, continuous functions are needed in FLAC so analytical derivatives can be computed. Four tangent modulus degradation functions are available in FLAC; the three parameter sigmoidal curve is used in this study and is specified in Equation 5.2:

$$M_s = \frac{a}{1 + \exp(-(L - x_0)/b)} \quad \textbf{(5.2)}$$

where $L = \log_{10}(\gamma)$ is the logarithmic strain, a, b, x_0 are the three input parameters, and M_s represents the secant modulus. This equation has a similar structure as that suggested by Hardin & Drnevich (1972) which is also available in FLAC (Equation 5.3):

$$M_s = \frac{1}{1 + \gamma/\gamma_{ref}} \tag{5.3}$$

where γ_{ref} is the strain at which the modulus reduction curve crosses the $G/G_0 = 0.5$ line. In the case of the three parameter sigmoidal curve with $a = 1.0$, the parameter x_0 represents the base-10 logarithm of the strain at which the modulus reduction curve crosses the $G/G_0 = 0.5$ line $\left(x_0 = \log_{10}(\gamma_{ref})\right)$ and the parameter b adjusts the curvature of the modulus degradation curve. For this study $a = 1.0$ was specified, and b and x_0 were determined in the calibration process.

The second soil model considered in this study was the two-dimensional, hysteretic, total stress soil model UBCHyst (Naesgaard, 2011). The primary processes of interest in this study that can be modeled by UBCHyst are increasing hysteresis and reduction in secant modulus with greater strain and number of cycles, and strength reduction with plastic strain. UBCHyst is formulated to capture the primary features of low permeability clayey or silty soil or high permeability granular soil subject to cyclic shearing in the horizontal plane where liquefaction is not considered. The model utilizes a Mohr-Coulomb failure criterion with a shear modulus reduction factor that is a function of the stress ratio and the change in stress ratio to reach failure to produce hysteretic cycles that reduce the mechanical damping required in a computer model (Figure 5.1). The tangent shear modulus reduction equation is defined in Equation 5.4.

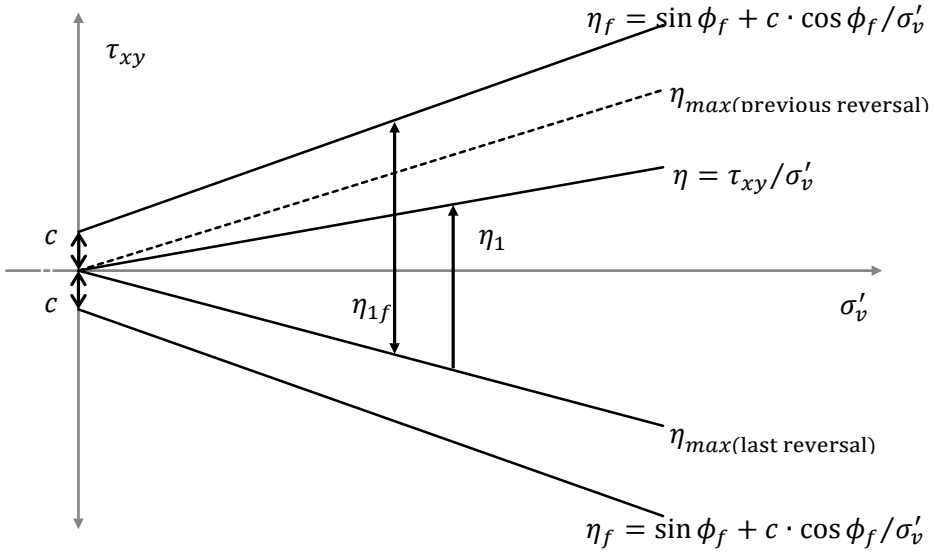

Figure 5.1: UBCHyst model key variables (adapted from Naesgaard, 2011)

$$G_t = G_r \left(\frac{P}{P_a}\right)^m \left(1 - \left(\frac{\eta_1}{\eta_{1f}}\right)^{n1} R_f\right)^n \cdot \text{mod1} \cdot \text{mod2} \quad \textbf{(5.4)}$$

where:

ϕ_f = peak friction angle

c = cohesion intercept

σ_v' = vertical effective stress

τ_{xy} = shear stress in horizontal plane

P = mean effective confining stress

P_a = reference atmospheric pressure

G_r = reference shear modulus

K_r = reference bulk modulus

η = current stress ratio = τ_{xy}/σ_v'

η_{max} = maximum η at last reversal

$\eta_f = \eta$ at failure envelope = $\sin\phi_f + c \cdot \cos\phi_f/\sigma_v'$

η_1 = change in η since last reversal = $\eta - \eta_{max}$

η_{1f} = change in η to reach failure envelope in direction of loading = $\eta_f - \eta_{max}$

mod1 = first time loading reduction factor; usually 0.6 to 0.8

mod2 = permanent modulus reduction with large strain = $1 - \left|\frac{\eta}{\eta_f}\right|^{rm} \cdot dfac \geq 0.2$

m = shear modulus exponent = 0.5

R_f = stress rate factor; usually 1

n = stress rate exponent; usually 2

$n1$ = (not in original model); usually 1

rm = large strain exponent

$dfac$ = large strain factor

5.3 Numerical Model Definition

5.3.1 Mesh Generation

A two-dimensional plain strain finite difference model of centrifuge experiment NW01 was developed and consisted of 3552 quadrilateral zones (of which 336 were null zones) and 100 structural elements (Figure 5.2). The size of the zones in the model was selected based on stability requirements for the finite difference scheme, as recommended in the FLAC User's Manual (Itasca, 2011). This recommendation is based on that of Kuhlemeyer & Lysmer (1973), wherein the maximum length of the zones Δl should be smaller than one-tenth to one-eighth of the wavelength λ associated with the highest frequency $f_{max}$of the input motion. Since the frequencies of the input motions are filtered above 15 Hz and the estimated average shear wave velocity of the soil during intense shaking was $V_s \approx 150 \pm 15$ m/s, the maximum element size was estimated to be:

$$\Delta l < \frac{\lambda}{10} = \frac{V_s}{10 f_{max}} = \frac{150 \pm 15 \text{ m/s}}{10 \cdot 15 \text{ Hz}} = 0.9 \text{ to } 1.1 \text{ m}$$

Based on this estimate and employing conservatism with the estimated shear wave velocity, the maximum zone length in the model was selected to be $\Delta l = 0.555$ m.

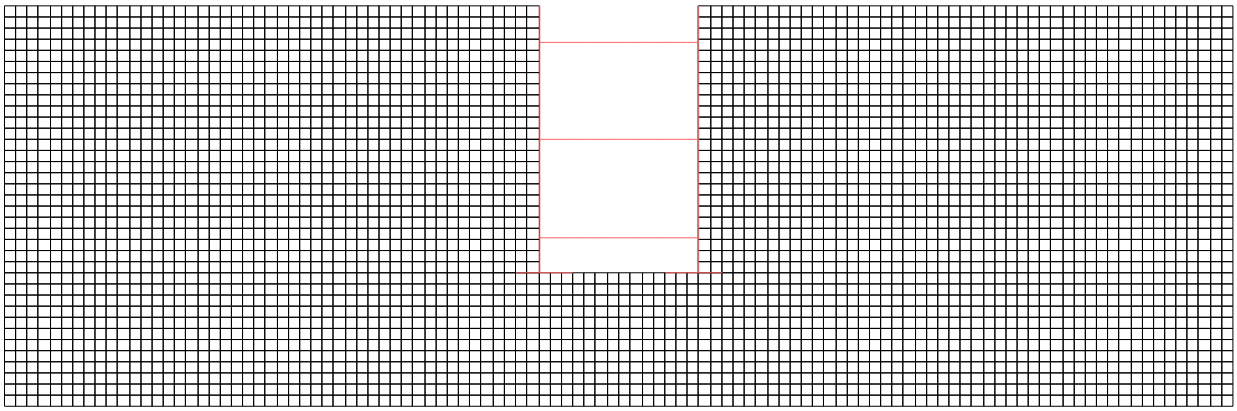

Figure 5.2: Two-dimensional finite difference mesh of centrifuge experiment developed in FLAC

5.3.2 Boundary Conditions

The base of the model was fixed both horizontally and vertically to reproduce the fixed-base condition of the laminar container of the experiment. The surface of the model was traction free and acceleration histories were applied to the base of the model after static equilibrium was achieved. The lateral boundaries of the model were tied together both horizontally and vertically using the ATTACH command in FLAC to simulate the laminar container. The effect of modeling the laminar container was considered in a previous study (Candia & Sitar, 2013), and the ground motion was essentially identical at a distance greater than 9 m from the boundary for the case of a centrifuge experiment similar in dimensions to that of this study. Since the structure is located at the center of the model zone, approximately 25 m from the boundary in prototype scale, modeling the laminar container was deemed unnecessary. Additionally, it was determined that modeling the container increases the run time of the simulation considerably.

5.3.3 Input Ground Motions

Input ground motions for the numerical model were obtained from the acceleration histories recorded at the base of the centrifuge experiment. The direct application of the acceleration history corresponds to a rigid base, which is appropriate in the case of the centrifuge experiment. These ground motions were used to calibrate the soil model because the numerical results could be directly compared to the results from the centrifuge.

5.3.4 Mechanical Damping

Elasto-plastic soil models provide hysteretic damping at moderate to large strains upon yielding, but provide little to no damping at small strains. This is unrealistic as most soils exhibit

measurable damping even at small strains. Additionally, this can cause numerical instability since energy may not be dissipated, leading to unrealistic accelerations. To prevent this from occurring, mechanical (viscous) damping is defined in FLAC, and can be specified as mass proportional, stiffness proportional, or a combination of the two with Rayleigh damping. Rayleigh damping was used in this study to produce approximately frequency independent mechanical damping over the frequency range of interest. In the original formulation, the damping matrix $\boldsymbol{C}$ is assumed to be proportional to the mass and stiffness matrices of the system as $\boldsymbol{C} = \alpha \boldsymbol{M} + \beta \boldsymbol{K}$. In FLAC, the mass proportional term is equivalent to a dashpot connecting each grid point to "ground" and the stiffness proportional term is equivalent to a dashpot connecting across zones. For multiple degree-of-freedom systems, the damping ratio ξ_i at the i^{th} angular frequency ω_i can be computed from (Bathe & Wilson, 1976) as $2\xi_i = \alpha/\omega_i + \beta\omega_i$. The parameters α and β can be determined by specifying the damping at two prescribed angular frequencies or by specifying the minimum damping ratio ξ_{min} and its corresponding angular frequency ω_{min}. FLAC uses the latter approach by solving for α and β with Equation 5.5 (Chopra, 2011):

$$\begin{bmatrix} 1/\omega_{min} & \omega_{min} \\ -1/\omega_{min}^2 & 1 \end{bmatrix} \begin{bmatrix} \alpha \\ \beta \end{bmatrix} = \begin{bmatrix} 2\xi_{min} \\ 0 \end{bmatrix} \quad \textbf{(5.5)}$$

The choice of ξ_{min} and ω_{min} depends on the frequency content of the input ground motion; therefore, it is impractical to specify a single set of parameters. Note that in FLAC, the frequency must be input as the circular frequency $f_{min} = \omega_{min}/2\pi$ with units of Hertz. f_{min} was selected to be equal to the natural frequency of the free field soil deposit in the numerical model, which was approximately 3.0 Hz. When using the Mohr-Coulomb model with sigmoidal modulus degradation a value of ξ_{min}= 0.002 (0.2%) was used and when using UBCHyst a value of ξ_{min}= 0.02 (2.0%) was used.

5.3.5 Structural Elements

Linear elastic beam elements were used to model the walls, cross bracing and footings of the basement. The equivalent plain strain properties are summarized in Table 5.1 for a unit width in prototype scale. All components of the basement were discretized into element lengths of approximately 0.555 m to coincide with the soil grid. The wall and footing nodes were rigidly attached to the soil grid, and the connections between the walls and footings, and the walls and cross braces were modeled as shear connections with no moment transfer.

The geometric properties of the cross bracing accounts for the equivalent stiffness of the load cells and the steel rods used in the centrifuge experiment. Also, the plain strain elastic modulus $\mathrm{E}^* = \mathrm{E}/(1-\nu^2)$ of aluminum was used for all elements. Rayleigh damping is included in the beam elements to reduce high frequency noise; ξ_{min} is set to 0.001 (0.1%) and the corresponding frequency coincides with that defined for the soil (3.0 Hz).

Table 5.1: Structural element properties used in FLAC model

Property per unit width	Units	Basement Wall	Cross Braces	Footing
Elastic Modulus	E^* (kPa)	7.68 E+07	7.68 E+07	7.68 E+07
Unit mass	ρ (Mg/m^3)	2.84 E+00	3.34 E+01	2.72 E+00
Cross Section	A (m^2/m)	5.75 E-01	9.53 E-03	9.14 E-01
Second Moment of Area	I (m^4/m)	2.97 E-02	9.17 E-04	6.43 E-02

5.4 Soil Model Calibration

The input parameters for the Mohr-Coulomb soil model with hysteretic damping and the UBCHyst soil model were determined in four steps. The steps for both models are described in parallel below, and then the final soil parameters are listed.

First, it is desirable to have a "reasonable" selection process for parameters that could be repeated. Therefore, basic parameters were selected based on documented correlations and some simple assumptions. The density of the soil was assumed to have a square root distribution with normalized depth, with a minimum value at the top and a maximum value at the bottom. The density at the top was computed based on the initial density measured in the centrifuge. The density at the bottom was computed by equating the vertical pressure at the base of the model to that measured in the centrifuge when assuming a uniform density. In general, any distribution involving the normalized depth raised to an arbitrary power could be selected and computing the density at the base would be as follows for $x > 0$ (Equation 5.6):

$$\sigma_v(H) = \rho_{avg} g H = g \int_0^H \left(\rho_{min} + (\rho_{max} - \rho_{min}) \left(\frac{z}{H} \right)^x \right) dz \Rightarrow$$
$$\rho_{max} = \rho_{avg} + x \cdot (\rho_{avg} - \rho_{min}) \quad \textbf{(5.6)}$$

The void ratio was estimated at the i^{th} layer using the density at the center of the layer (Equation 5.7a). Then, the reference shear modulus was estimated using the Hardin (1978) relationship (Equation 5.7b). Next, the shear modulus and shear wave velocity were computed using Equation 5.7c and Equation 5.7d, respectively. Plots of the density, reference shear modulus and interpreted shear wave velocity distributions with depth are shown in Figure 5.3.

$$e_i = \frac{G_s}{\rho_i} - 1 \quad \text{(a)} \qquad G_{r,i} = \frac{625}{0.3 + 0.7 e_i^2} P_a \quad \text{(b)}$$
$$G_{max,i} = G_{r,i} \left(\frac{\sigma_{m,i}}{P_a} \right)^{0.5} \quad \text{(c)} \qquad V_{s,i} = \left(\frac{G_{max,i}}{\rho_i} \right)^{0.5} \quad \text{(d)} \quad \textbf{(5.7)}$$

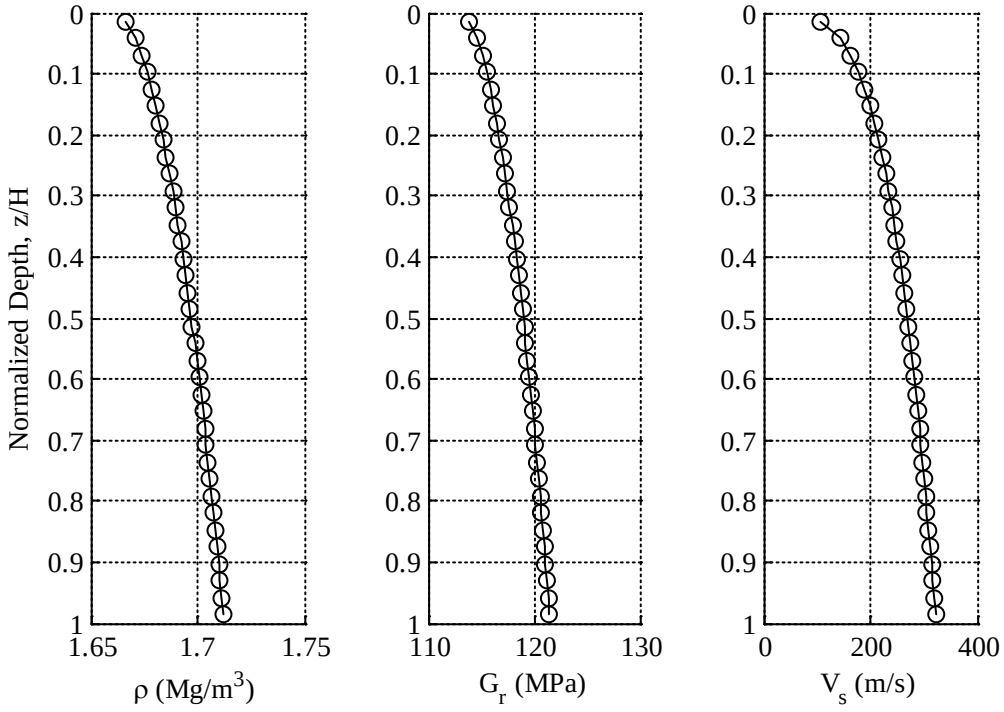

Figure 5.3: Assumed density, reference shear modulus, and shear wave velocity distributions

A constant friction angle of $\phi_f = 32.5°$ was assumed for all depths. This particular value was selected to match the implied static earth pressure distribution measured in the load cells during the centrifuge experiment assuming a linear distribution of at-rest horizontal pressure, as shown in Section 4.3. Note that, in general, the apparent friction angle should vary with confining pressure, as shown by Bolton (1986). However, a key assumption of that study was that the specimens underwent large strains to failure to determine the friction angle. In this study large deformations in the soil mass were not observed, nor was failure. Thus, the shear stiffness of the soil mass is more relevant for this study than the shear strength of individual soil elements. Also, note that because the shear modulus, and thus the shear wave velocity, is expected to degrade during dynamic excitation, the previous analysis to determine the maximum size of the soil zones based on the average shear wave velocity estimated during the centrifuge test in Section 5.3.1 is valid.

Second, a single soil element was modeled in FLAC and subjected to a cyclic shear test resembling a direct simple shear test in the laboratory. Initially, the effect of each parameter associated with shear modulus reduction in the UBCHyst model was determined by setting all values to those recommended by Naesgaard (2011) and perturbing the parameters one at a time. From this analysis, the effect each parameter had on the shape of the shear modulus degradation curve with varying confining stress and maximum shear modulus could be determined. Then, the strain level, confining pressure and its corresponding reference shear modulus were varied to obtain normalized shear modulus degradation curves (Figure 5.4) and true shear modulus

degradation curves (Figure 5.5), which were compared to Darendeli (2001) curves obtained using the default modulus degradation curves in DEEPSOIL (Hashash et al., 2015). The confining pressures correspond to the average confining pressure that would be measured at the center of a soil zone in the full numerical model based on the density and coefficient of horizontal at-rest earth pressure. The corresponding damping curves were also obtained (Figure 5.6), although the damping at high strains (>0.1%) was unrealistic when compared to those from Darendeli (2001) due to the wide hysteretic loops at high strains. For this study, large strains were not observed in the centrifuge experiment or the numerical analyses. Therefore, the large strain regime is not an issue. The necessary input files for the direct simple shear simulation were obtained from the Itasca user-defined models webpage (*http://www.itasca-udm.com/index.html*). The effects of each parameter of the three parameter sigmoidal curve were determined analytically. It was determined that $b = -1/(0.9190 \cdot \ln 10) \approx -0.4726$ provided a good fit for the curvature at all depths and x_0 increased with confining pressure to correspond with the increased strain at which the modulus reduction curve crosses the $G/G_0 = 0.5$ line.

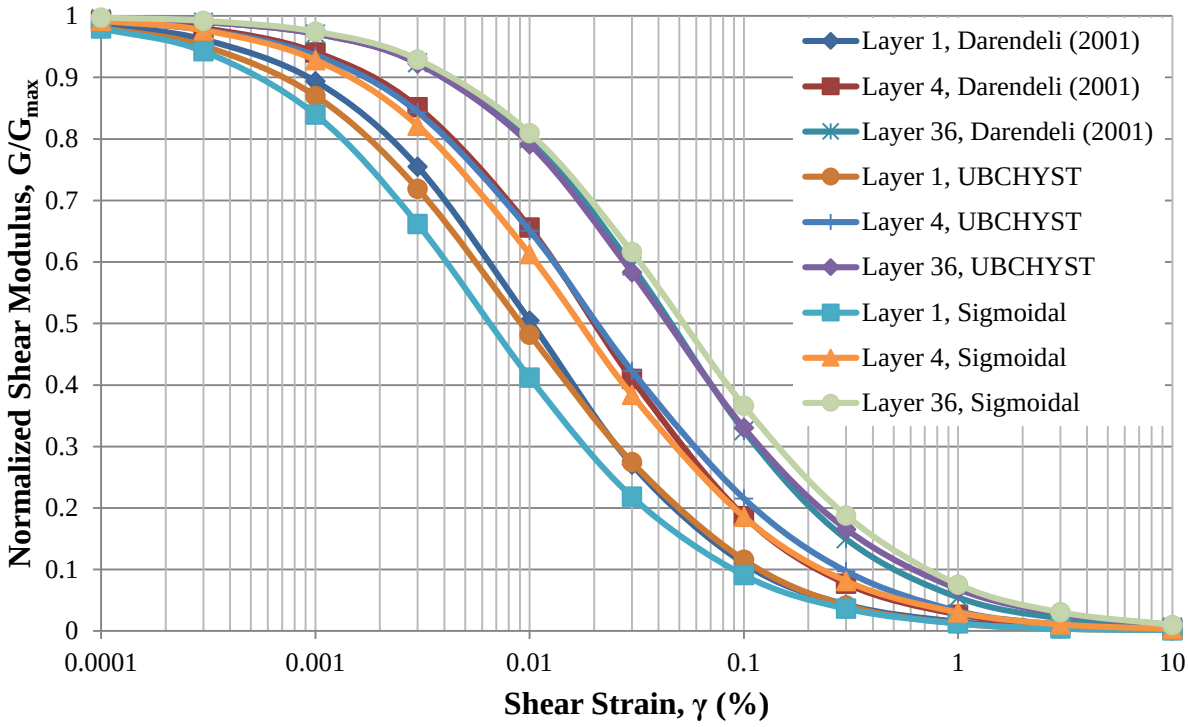

Figure 5.4: Normalized shear modulus degradation vs shear strain

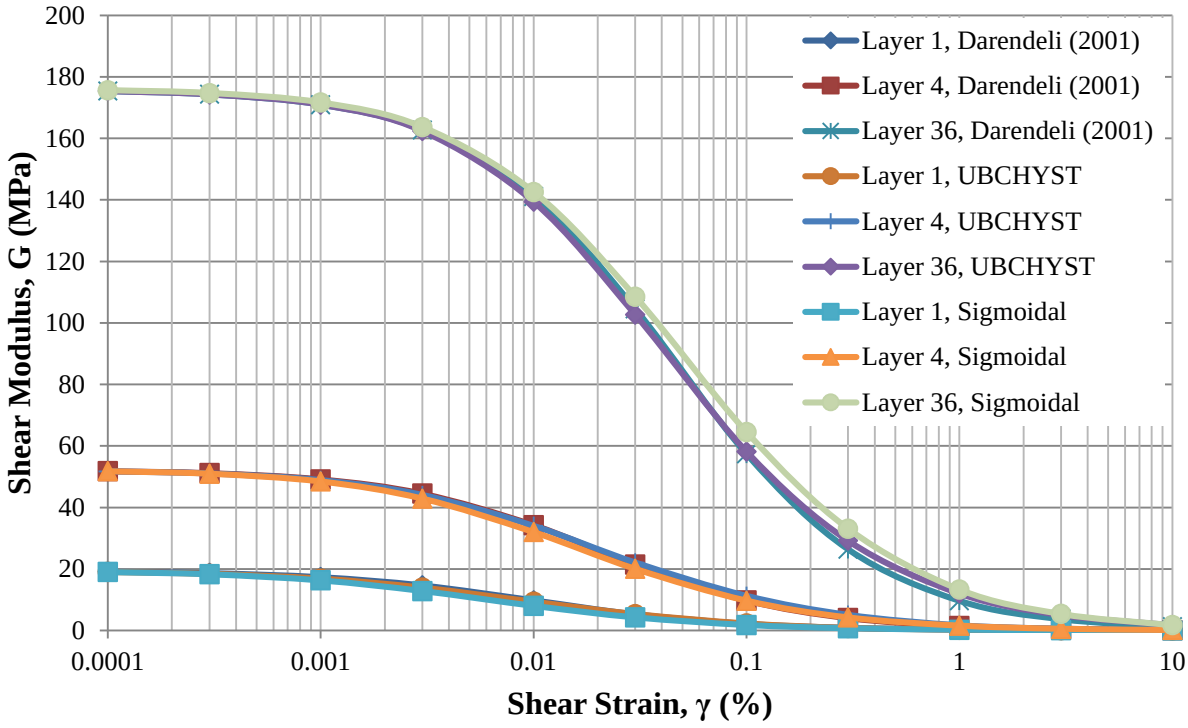

Figure 5.5: Shear modulus degradation vs shear strain

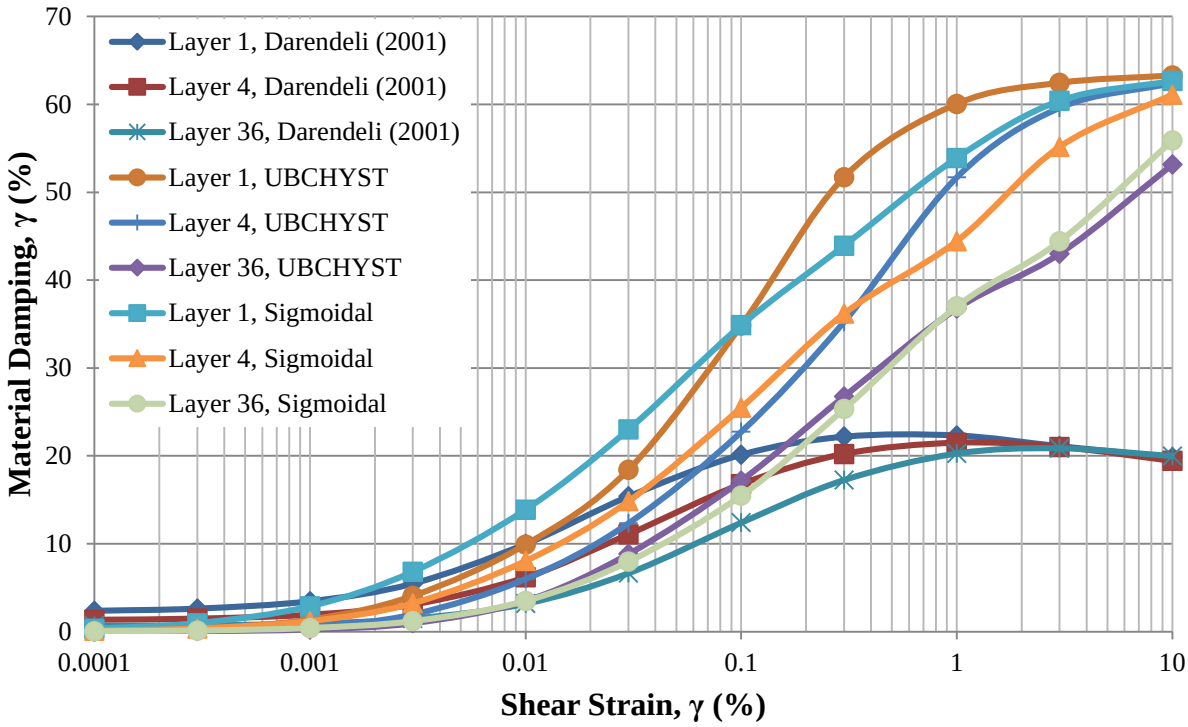

Figure 5.6: Material damping vs shear strain

Third, a soil column representing the free field in the centrifuge container was modeled in FLAC using the initial parameters determined in the first part of the calibration process. The input ground motions were those obtained from the filtered records of the accelerometer at the base of the centrifuge container. The acceleration response of the soil column at various depths was compared to that of the centrifuge experiment and the Rayleigh damping parameters were adjusted to obtain a better match with the acceleration histories. The boundary conditions in the soil column were designed to mimic the analysis performed by SHAKE; i.e., the sides of the column were attached together and forced to translate horizontally by the same amount at each time step while maintaining no vertical displacement and the bottom of the column was fixed horizontally and vertically. The soil column was two zones wide and 36 zones tall, with grid dimensions corresponding to that in the full model.

It is necessary to have a stress profile to compute the shear modulus in the soil zones using Equation 5.7c. In order to do this, the soil is first treated as a linear elastic medium in order to establish the stress profile based on the initial density profile. Then, the model has to come to equilibrium using the Mohr-Coulomb relationship with the shear modulus calculated for each zone to initialize the strains. Only then can the non-linear dynamic analysis start using the hysteretic soil model. In FLAC, "fictitious" mass is used to compute equilibrium in static mode and true mass is used in dynamic mode. Switching from a static to a dynamic analysis will induce small numerical vibrations. Therefore, a period of 0.2 seconds of computational time without dynamic input was used to still the initial vibrations and then the dynamic excitation was applied to the model. The same procedure was used in Mikola & Sitar (2013) and Candia & Sitar (2013). The intent at this stage was to obtain initial Rayleigh damping values (discussed in Section 5.3.4) that would expedite calibration in the full prototype model. Ahmadi et al. (2015) concluded that soil damping has a greater effect on the displacement response of a soil-structure system than the force response. Thus, calibrating Rayleigh damping to accurately model the acceleration response in the backfill without the influence of the structure is valid.

The final step of the calibration process consisted of modeling the centrifuge experiment at prototype scale and comparing the acceleration response in the free field at various depths and the magnitude of the maximum seismic earth pressure increment to that observed in the physical experiment. The same modeling sequence used for the soil column was used again, i.e., the soil model was initially linear elastic, then Mohr-Coulomb, then non-linear hysteretic. Prior to initiating dynamic mode, the empty space of the structure was removed, the structure was installed, and the model was re-equilibrated. This has the effect of "wishing" the structure into place, which mimics the construction in the centrifuge experiment. The final calibrated parameters selected for use in the UBCHyst soil model and the Mohr-Coulomb soil model with hysteretic damping are shown in Table 5.2. For clarity, note that the density, ρ, varies as a square root distribution with depth for both soil models according to Equation 5.8a. The reference bulk modulus is assumed to be twice the reference shear modulus at each depth, with the reference shear modulus determined as described earlier. The stress rate exponent, n, and the large strain

factor, $dfac$, vary with confining pressure according to Equation 5.8b and Equation 5.8c, respectively. The reference logarithmic strain for the sigmoidal hysteretic model, x_0, varies with confining pressure according to Equation 5.8d. All other parameters are constant with depth.

$$\rho = \rho_{min} + (\rho_{max} - \rho_{min})\left(\frac{z}{H}\right)^{1/2} \quad \text{(a)} \qquad n = n_{min} + \Delta n\left(\frac{\sigma_m}{P_a}\right)^{1/2} \quad \text{(b)}$$
$$dfac = dfac_{min} + \Delta dfac\left(\frac{\sigma_m}{P_a}\right)^{1/2} \quad \text{(c)} \qquad x_0 = \log_{10}\left(\gamma_{ref,1}\left(\frac{\sigma_m}{P_a}\right)^{n_\gamma}\right) \quad \text{(d)} \qquad \textbf{(5.8)}$$

Table 5.2: Calibrated soil model properties used in FLAC model

ρ_{min}	= 1.66	Mg/m^3	P_a	= 100	kPa	n_{min}	= 1.75	rm	= 0.75
ρ_{max}	= 1.7125	Mg/m^3	ψ	= 0.0	deg	Δn	= 1.884	$n1$	= 1.25
c	= 0.0	kPa	R_f	= 0.75		$dfac_{min}$	= 0.00	$\gamma_{ref,1}$	= 0.0352
ϕ_f	= 32.5	deg	mod1	= 0.75		$\Delta dfac$	= 0.5657	n_γ	= 0.3483

One of the issues with the sigmoidal hysteretic model is that permanent shear modulus degradation cannot be modeled. This affects the acceleration response of the backfill when comparing the numerical results to the experimental results. The peak values are matched approximately, but the frequency content of the accelerations is poorly matched. UBCHyst is able to account for this with parameter $dfac$, which incorporates permanent modulus degradation with increasing maximum stress ratio. By setting $dfac$ = 0, no permanent modulus reduction can be modeled, with similar results as with the sigmoidal hysteretic model. Therefore, the effects of modulus degradation on the acceleration response are modest, but clearly important, in this particular study. It is difficult to calibrate this parameter in a simple shear test as was done in the second step of the calibration process. This is mainly due to the limited number of cycles performed in the numerical direct simple shear tests and the use of one strain amplitude for each test. Note that previous studies using the UBCHyst model (Candia & Sitar, 2013; Mikola & Sitar, 2013) used values of $dfac$ equal to 0 and 0.8 when modeling centrifuge experiments with compacted clay and Nevada sand, respectively. Clearly, this parameter is important and must be determined on a project specific basis as the amount of potential modulus degradation will be a function of many parameters, most importantly the soil type and the intensity and duration of ground shaking.

Another issue that was observed when using either soil model was that the normalized recorded static load at the start of the numerical simulation was lower than that recorded in the centrifuge, and at the end of the numerical simulation was equal to or higher than that recorded in the centrifuge. To alleviate this issue, the soil grid was softened in the region around the sides of the structure by reducing the maximum shear modulus and bulk modulus by 50%. The effect was that the softened soil grid would more accurately model “failed” or “highly strained” soil next to the structure and the static offset would be reduced. As this issue is more pronounced for the sigmoidal modulus degradation model, and considering the aforementioned issues, it was

decided that the sigmoidal model would not be used further in this study and the UBCHyst model would be used.

5.5 Accelerations in Soil and Structure

The acceleration histories were filtered in the frequency domain to remove spurious noise resulting from the explicit integration process in FLAC. Amplification of the peak ground acceleration in the backfill and the basement structure is shown in Figure 5.7; the results are similar to those measured in the centrifuge (Section 4.1).

Examples of acceleration histories and response spectra computed at various locations in the numerical model and compared to the acceleration histories measured with accelerometers at the corresponding locations in the centrifuge experiment are shown in Figure 5.8 to Figure 5.13. The plots show the responses in the north and south free field at the surface, mid-height of the wall, and base of the wall; the north and south soil adjacent to the structure at the surface, mid-height of the structure, and base of the structure; and the north and south wall at the surface, mid-height of the structure, and base of the structure. Additional plots are shown in Appendix A. In general, the response of the free field computed in the numerical model matches well with that measured in the centrifuge experiment at all levels in both amplitude and spectral amplification. The computed spectral response in the soil adjacent to the structure is slightly amplified at all periods at the surface compared to the measured response; the responses at depth match well. The computed spectral response in the wall matches well with that measured in the centrifuge experiment, with some slight deamplification at the surface for the larger ground motions (Loma Prieta SC-1, Loma Prieta SC-2, Kobe TAK 090-3).

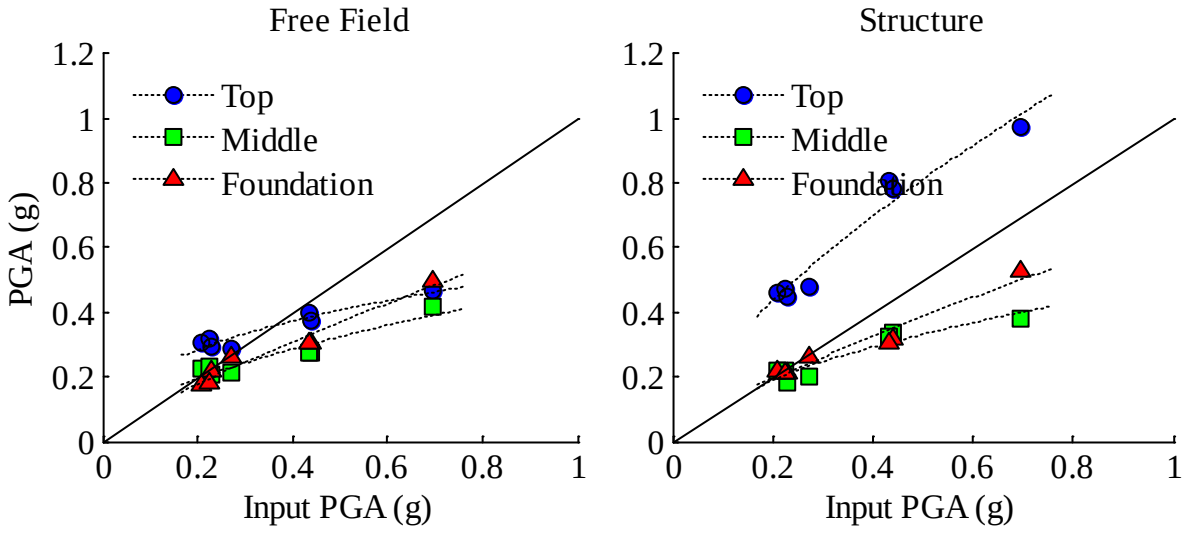

Figure 5.7: Computed ground motion amplification in free field and structure

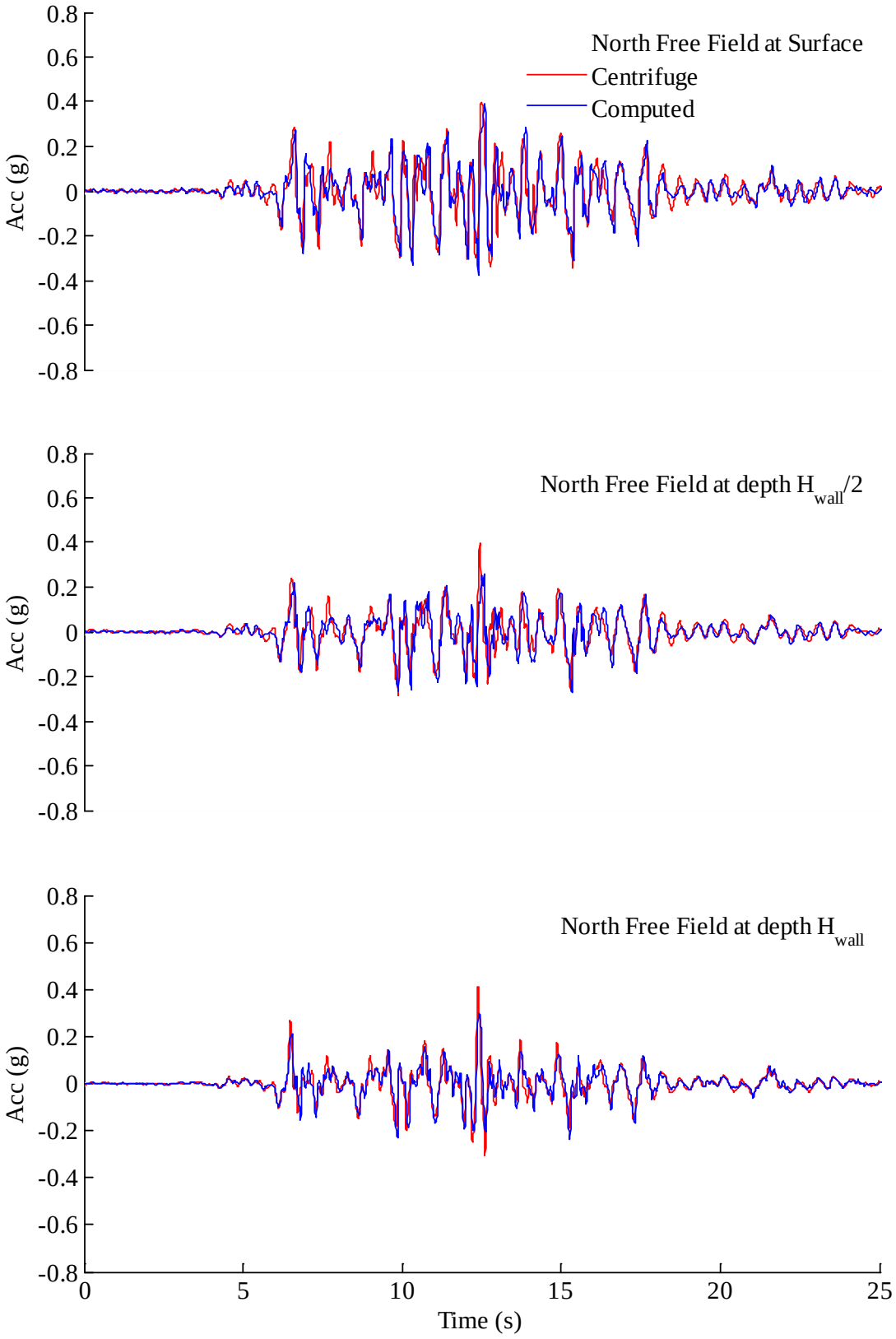

Figure 5.8: Measured and computed accelerations in north free field during Loma Prieta SC-2

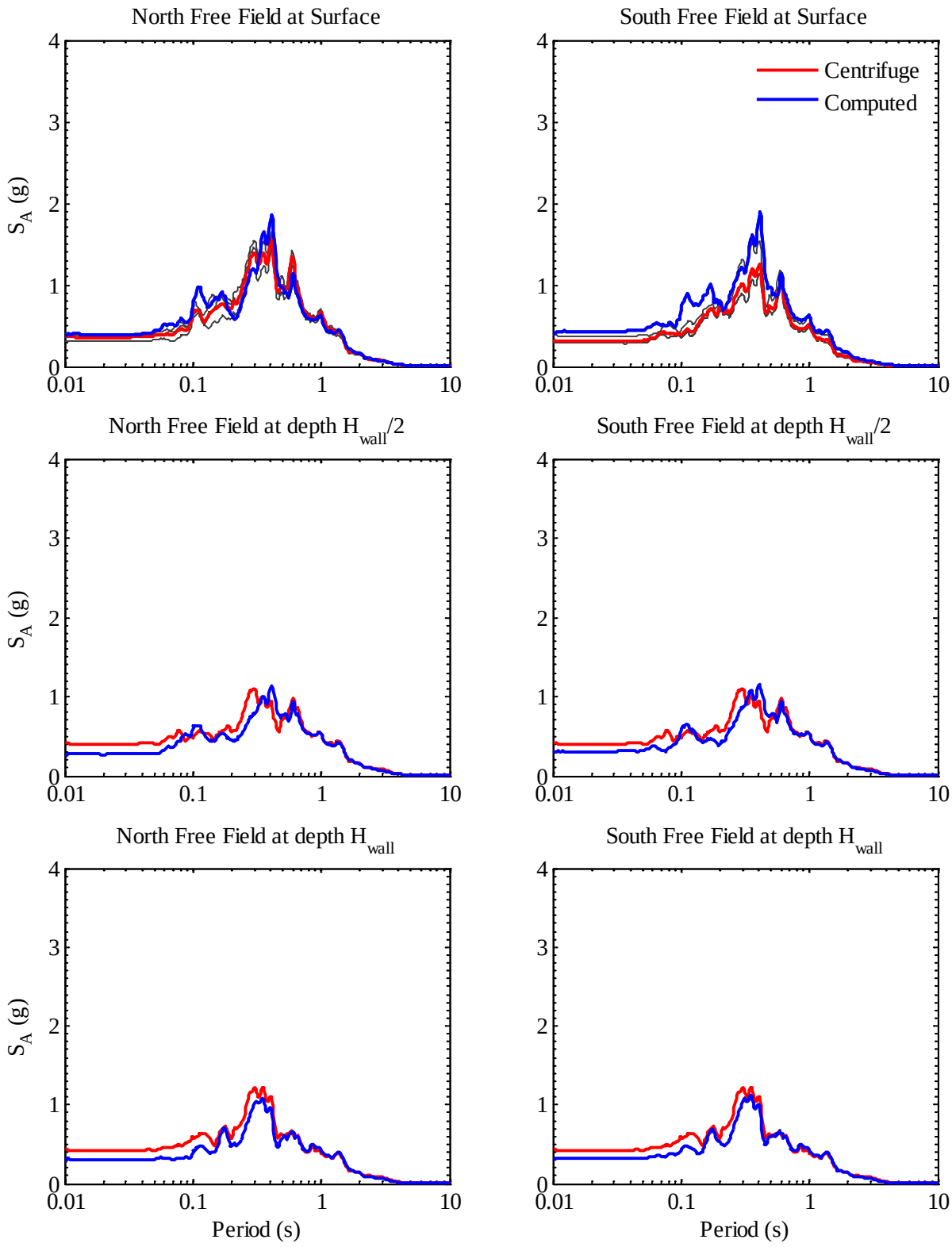

Figure 5.9: Measured and computed acceleration response spectra in free field at 5% damping during Loma Prieta SC-2

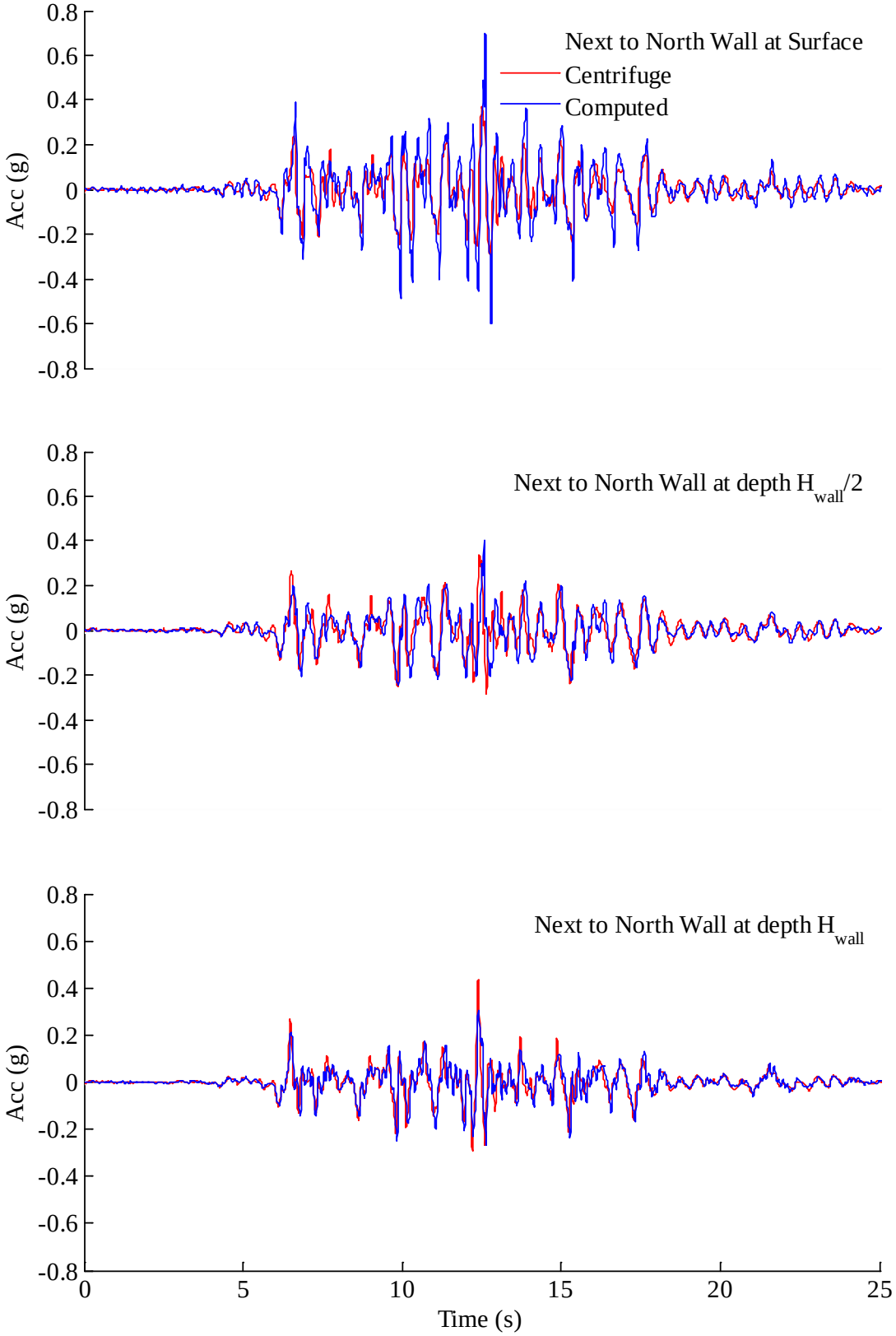

Figure 5.10: Measured and computed accelerations next to north wall during Loma Prieta SC-2

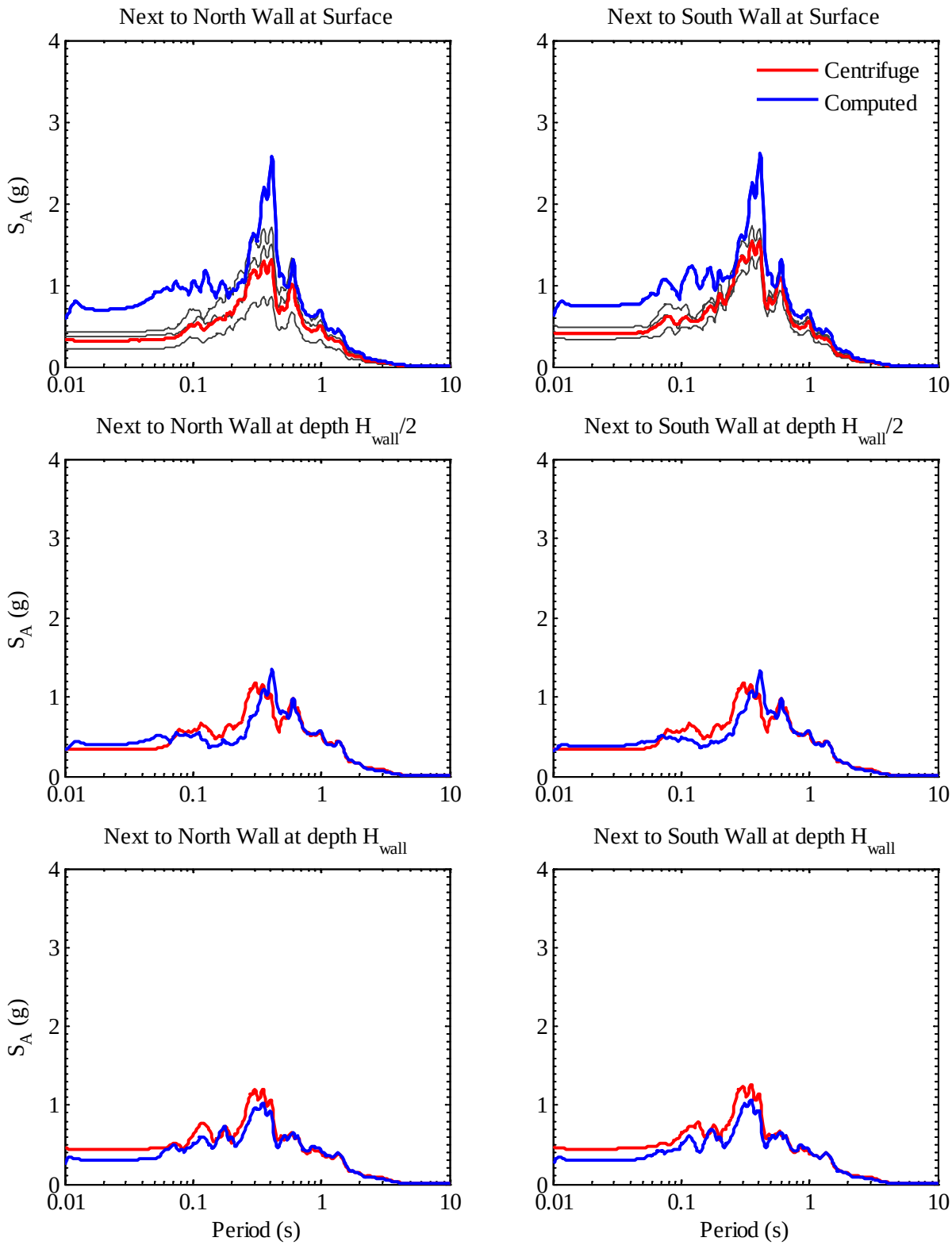

Figure 5.11: Measured and computed acceleration response spectra in soil next to structure during Loma Prieta SC-2

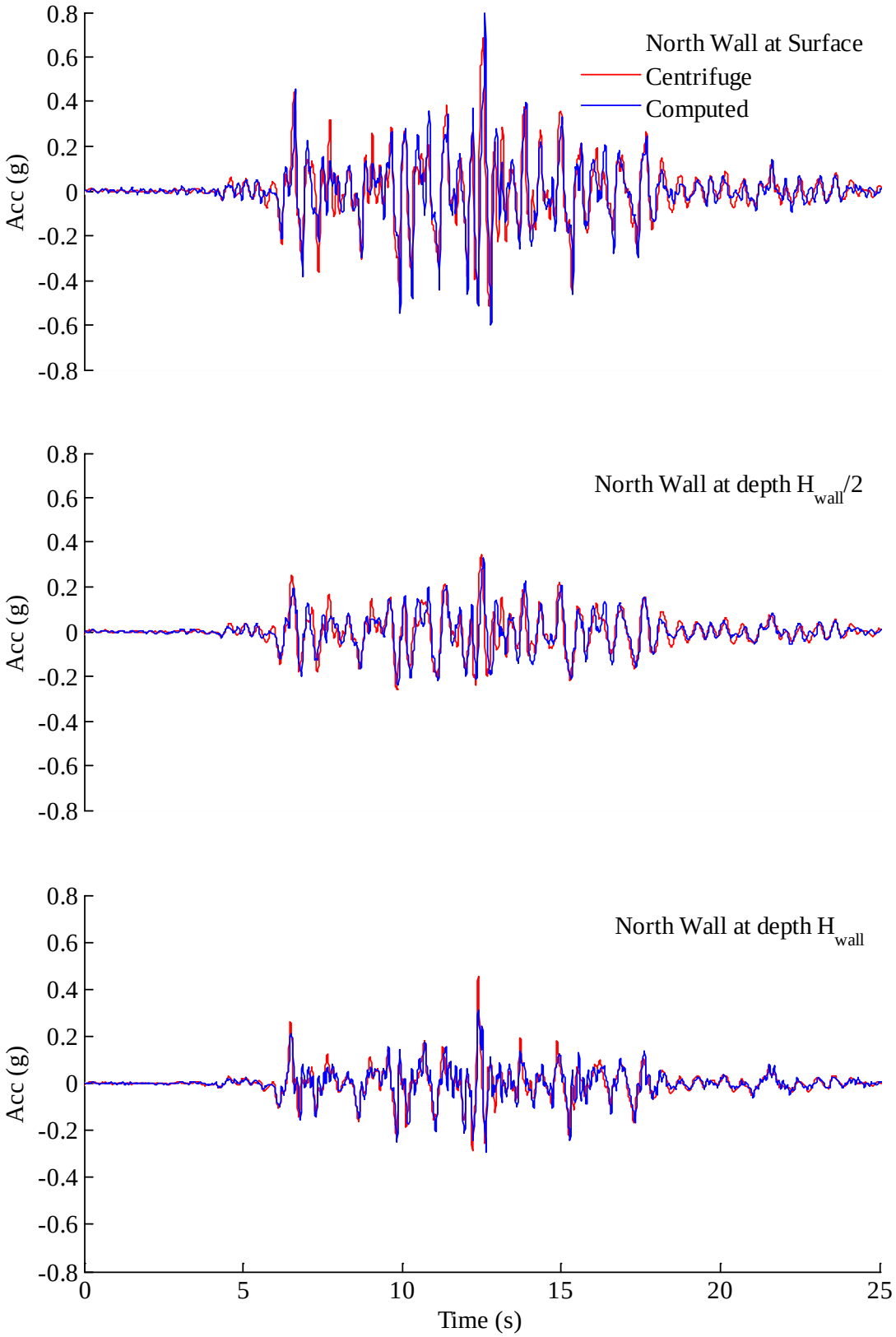

Figure 5.12: Measured and computed accelerations in north wall during Loma Prieta SC-2

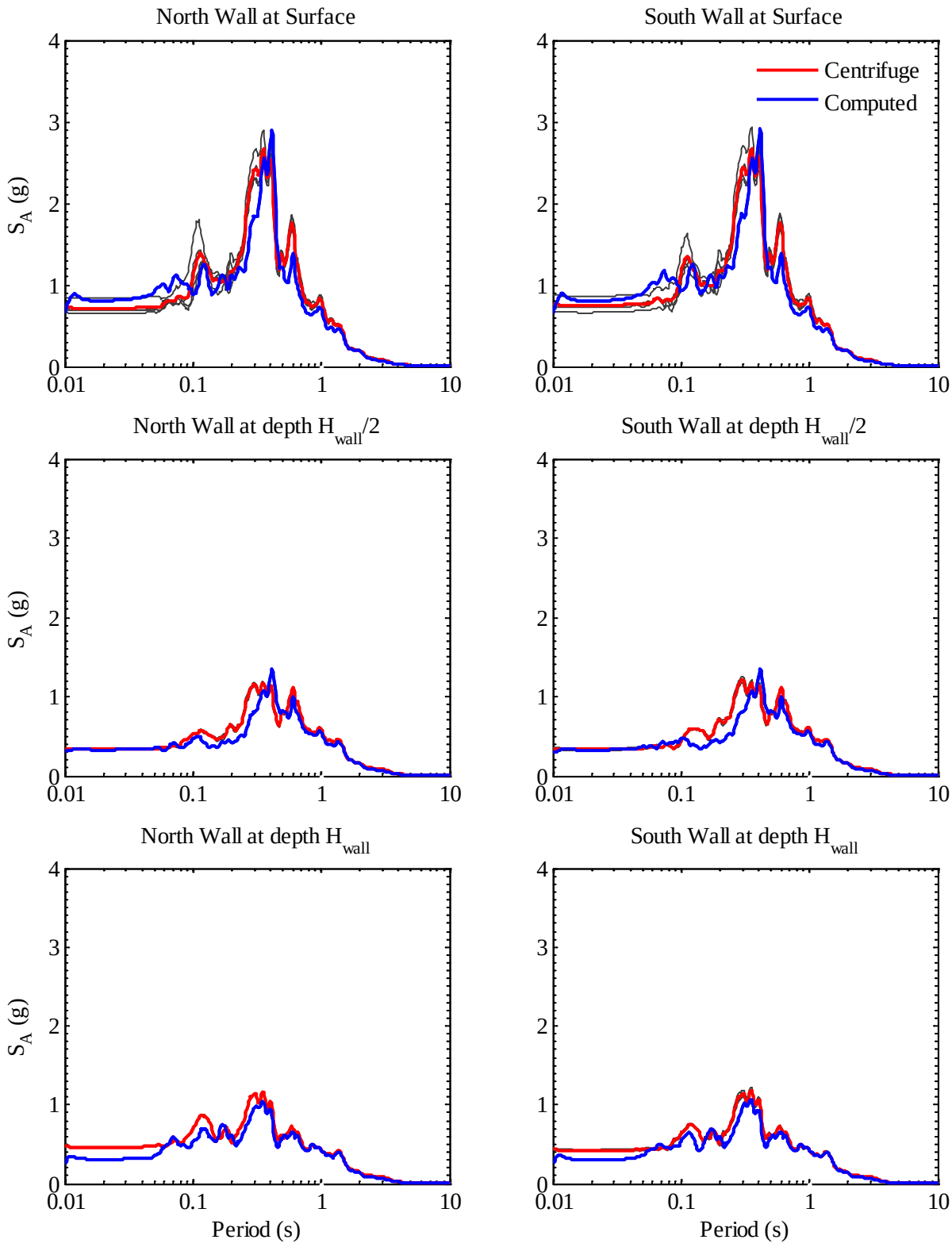

Figure 5.13: Measured and computed acceleration response spectra in structure at 5% damping during Loma Prieta SC-2

5.6 Basement Wall Response

Two measures were used to compute the loads acting on the basement wall in the numerical model. First, the axial load in the beam elements at the ends of the cross bracing were recorded and analyzed in the same manner as the load cells in the centrifuge experiment. The total load was summed, giving the total load, and then the static and dynamic parts were separated as discussed in Section 3.4. Then, the inertia component of the load was added or subtracted as $\Delta P_{ae} = \Delta P_{tot} \pm \Delta P_{in}$, where the inertia load was computed from the mass of the wall and the accelerations acting on the wall.

In the second method, the horizontal stress in the soil zones adjacent to the wall were used to compute the load on the structure. The static and dynamic components of the stress were separated as discussed in Section 3.4 and then integrated along the height. The total load was computed using Equation 5.9, where σ_x^i is the horizontal stress in zone i, H is the total height of the wall, and N is the total number of soil zones. The static and dynamic components of the total load were computed similarly.

$$P_{ae} = \int_0^H \sigma_x dz \approx \frac{H}{N} \sum_{i=1}^{N} \sigma_x^i \qquad \textbf{(5.9)}$$

Examples of the measured and computed normalized loads on the structures are shown in Figure 5.14. Additional plots are shown in Appendix A. The total soil induced load (i.e., removing the inertial loads) are shown first, then the inertia loads, and finally the dynamic soil induced load for the north and south wall for each ground motion considered. The computed soil induced load histories, whether total or dynamic, do not accurately resemble the measured load histories. This is due to the complicated interaction between the soil and structure, including the compaction sequence at the beginning of the centrifuge experiment. The inertia load histories do match well, which is to be expected given the good agreement of the accelerometer histories discussed in Section 5.5. The peak loads do match well between the centrifuge experiment and the two measures computed in the numerical model; this demonstrates that computing the dynamic load using the soil stresses is comparable to using the axial loads in the struts.

Typical instantaneous dynamic earth pressure distributions corresponding to the maximum dynamic earth pressure increment (ΔK_{ae}) are shown in Figure 5.15. Additional plots of the instantaneous dynamic earth pressure distributions corresponding to both the maximum and minimum ΔK_{ae} are shown in Appendix A. The dynamic load measured in the top strut was assumed to correspond to a dynamic pressure distribution starting at zero at the surface and increasing linearly with depth until the depth at the midpoint between the top and middle rows of load cells. The dynamic load measured in the middle and bottom struts was then combined and distributed linearly from the midpoint between the top and middle struts to the base of the wall. The dynamic earth pressure distribution at the time of the maximum dynamic earth pressure increment (ΔK_{ae}) suggest a non-linear distribution, contrary to what is typically assumed using

the M-O or the Seed & Whitman (1970) method. In particular, the distribution is (near) zero at the surface, increases rapidly with depth, and then decreases to essentially zero at the base of the wall for most of the ground motions. For comparison, the interpreted dynamic earth pressure from the load cells in the centrifuge experiment were processed in the same manner as described above. Lastly, the dynamic earth pressure distributions computed in the soil zones corresponding to the maximum and minimum dynamic earth pressure increments are plotted. Note that the dynamic earth pressure distribution predicted by the M-O method is computed using the seismic coefficient, k_{MHEA}, and that predicted by the Seed & Whitman (1970) method is computed using 80% of the peak ground acceleration at the surface. Based on the figures, it is clear that the computed pressure distribution in the soil grid is complex, but is reasonably represented by the assumed distribution of the loads measured in the load cells (for the centrifuge experiment) or the strut loads (for the numerical simulation).

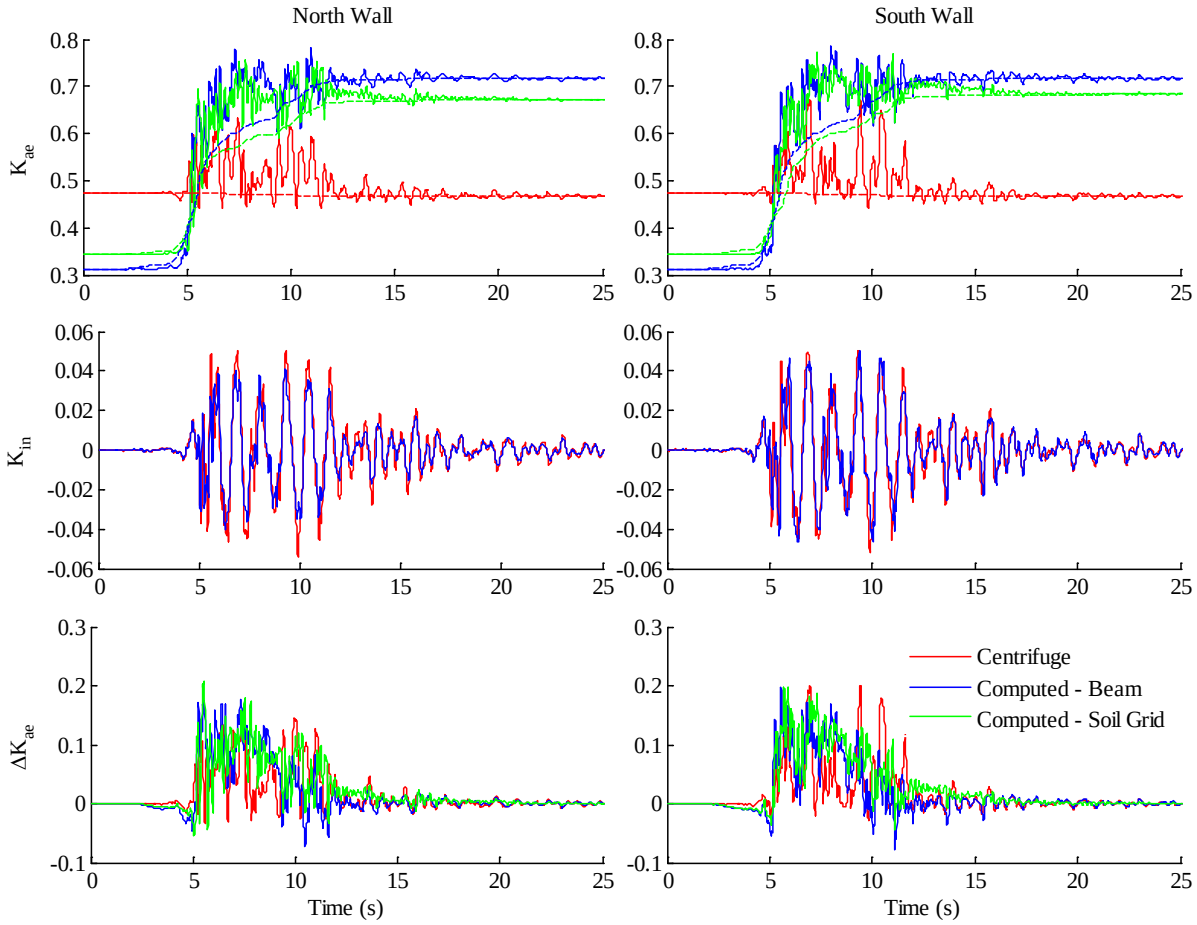

Figure 5.14: Measured and computed normalized loads on structure during Kobe TAK 090-3

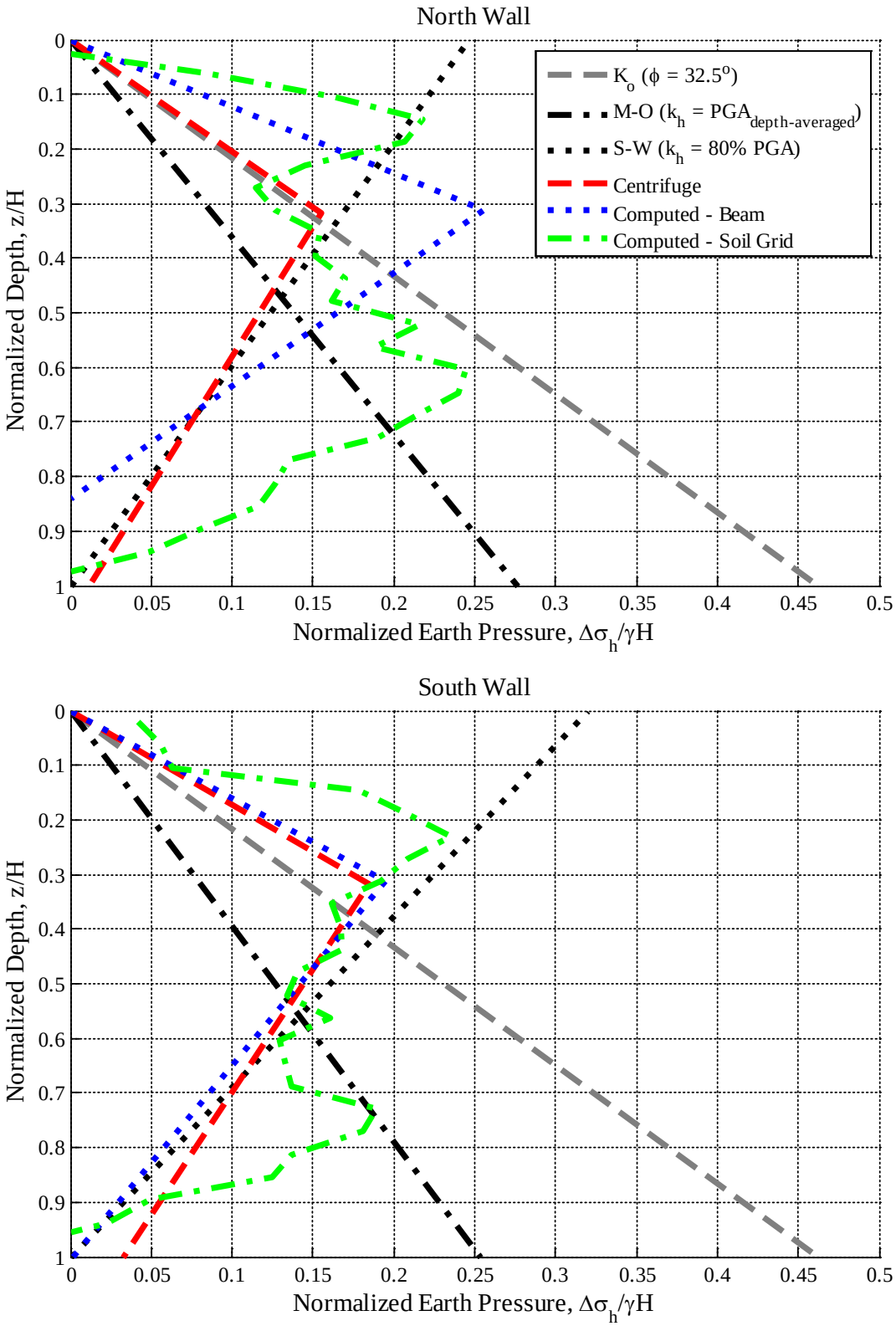

Figure 5.15: Measured and computed normalized dynamic earth pressure distributions at maximum ΔK_{ae} during Kobe TAK 090-3

The chosen method of separating the dynamic and static components of the earth pressure (as described in Section 3.4) in the numerical simulation has some unavoidable consequences. The total earth pressure load tends to drift in the numerical simulation, therefore the initial and final loads are not equal. Consequently, the static and dynamic components will be different if the total earth pressures are summed and then separated into components, or if the total earth pressures are separated into components and then summed. The order of computations wherein the total earth pressures are separated into components first and then summed provided a more conservative estimate of the dynamic load (i.e., the computed ΔK_{ae} is higher for a given seismic coefficient) was selected herein.

The dynamic increment of earth pressure versus k_{MHEA} computed in the numerical model is compared with the experimental results in Figure 5.16. The numerical results interpreted from the interface elements and the beam elements representing the cross braces are both shown. Results from analytical solutions (Okabe, 1924; Seed & Whitman, 1970; Wood, 1973) are also shown for reference, as before. Overall, the results from the numerical model reflect the trend of increasing dynamic earth pressure with increasing peak average free field acceleration and show that a numerical model is well capable of reproducing experimental results when the model is properly calibrated and realistic soil behavior and soil properties are used. Additionally, using an average measure of acceleration in the free field over the depth of the embedded structure seems more appropriate than a single measure from the surface or at the depth of the structure. This produces better agreement between the observed and computed dynamic load compared to the dynamic load predicted with the Okabe (1924) and Seed & Whitman (1970) methods for $k_{MHEA} \lesssim 0.4$ and for deep structures.

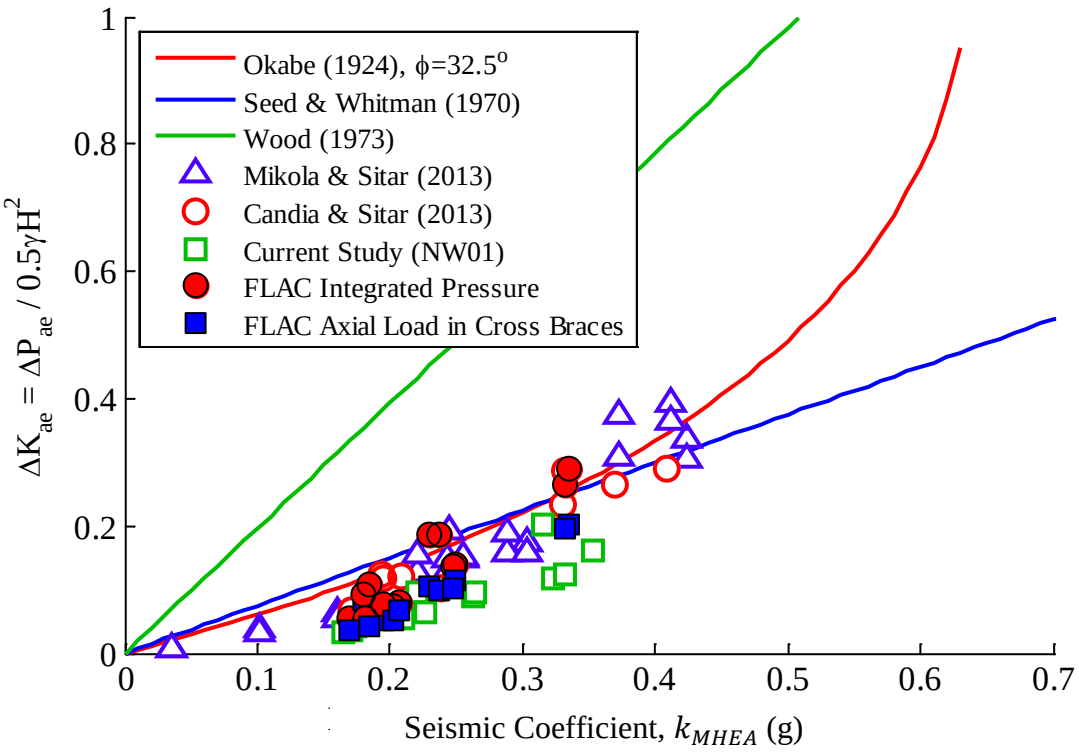

Figure 5.16: Computed and observed coefficient of dynamic earth pressure increment versus seismic coefficient, k_{MHEA}

An alternative is to characterize the load temporally, with the realization that the peak load does not occur uniformly throughout the earthquake excitation. In reality, some lesser value of load could be used for design that reflects the rather modest loads that occur for the majority of the excitation. In fact, the reduction in seismic coefficient on account of the seismic demand occurring for only a brief period of time suggested by Seed & Whitman (1970) is based on this idea. With this in mind, a measure of the "average" and "variation" of the dynamic load and the pressure distribution was sought for the numerical simulation. First, the average acceleration record in the free field at the surface was computed and the time at which the record first exceeds 0.05 g ($t_{i,>0.05g}$) and the time at which the record last exceeds 0.05 g ($t_{f,>0.05g}$) are noted. The dynamic pressure record at each soil grid adjacent to the wall was then truncated before $t_{i,>0.05g}$ and after $t_{f,>0.05g}$, and the resulting record was then split into positive (total pressure greater than static pressure) and negative (total pressure less than static pressure) lists. Assuming that the values in the list of positive dynamic earth pressures are normally distributed, the mean and standard deviation of the values was computed at each depth. For each earthquake, an envelope of mean (μ) values of positive dynamic earth pressure at each depth was constructed, as well as an envelope of mean-plus-one-standard deviation ($\mu + \sigma$) values of positive dynamic earth pressure. Examples of the envelopes are shown in Figure 5.17. Additional plots are shown in Appendix A.

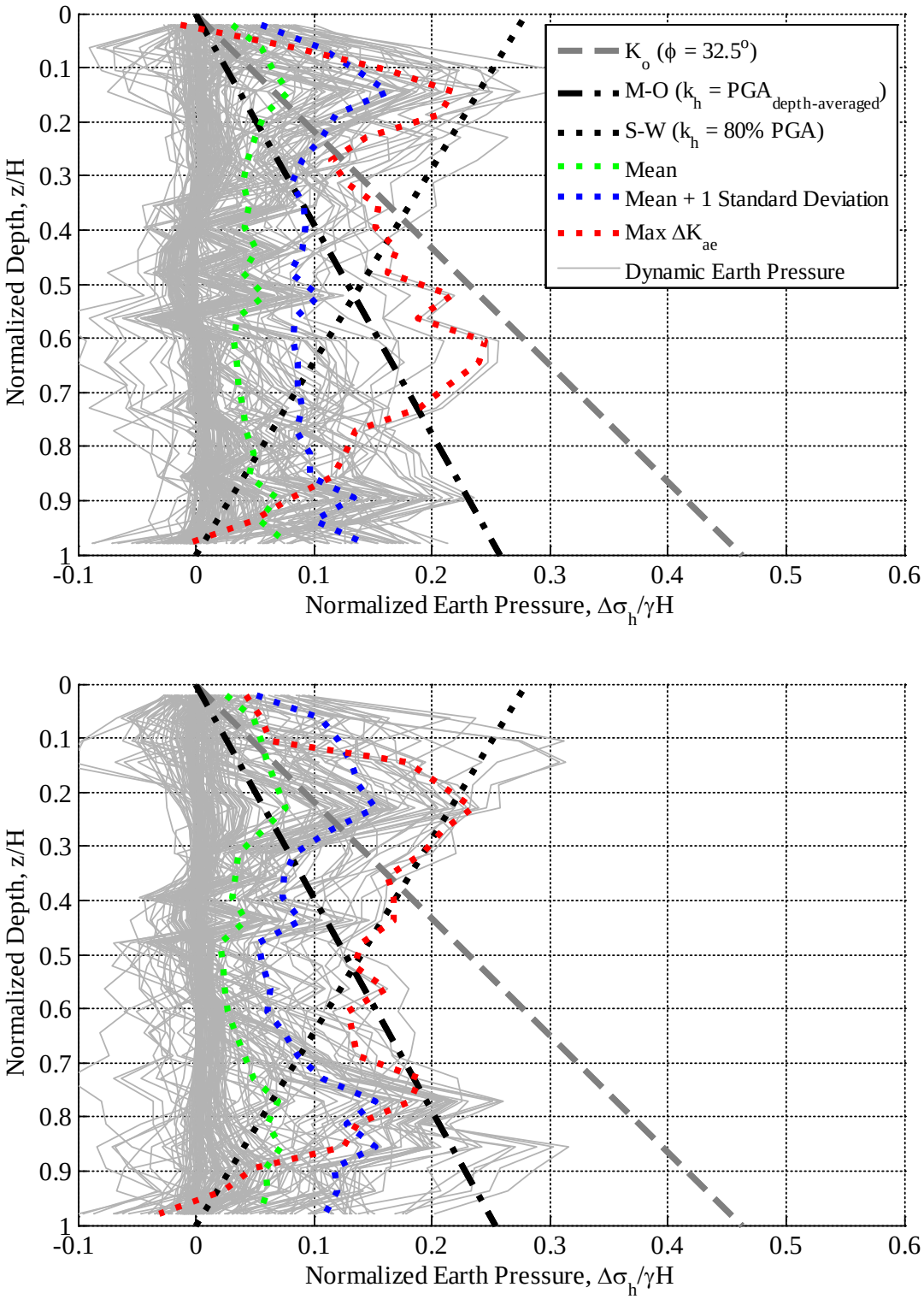

Figure 5.17: Mean envelope and mean-plus-one-standard-deviation envelopes of normalized dynamic earth pressure, and computed normalized dynamic earth pressure distributions at maximum ΔK_{ae} during Kobe TAK 090-3

Using these envelopes, dynamic earth pressure increment coefficients were computed representing (approximately) the 50th (μ) and 84th ($\mu + \sigma$) percentile level of exceedance of the static earth pressure. These values are plotted in Figure 5.18, along with the maximum computed seismic earth pressure increment coefficient from FLAC measured in the soil grid adjacent to the structure, as well as the Okabe (1924), Seed & Whitman (1970), and Wood (1973) solutions.

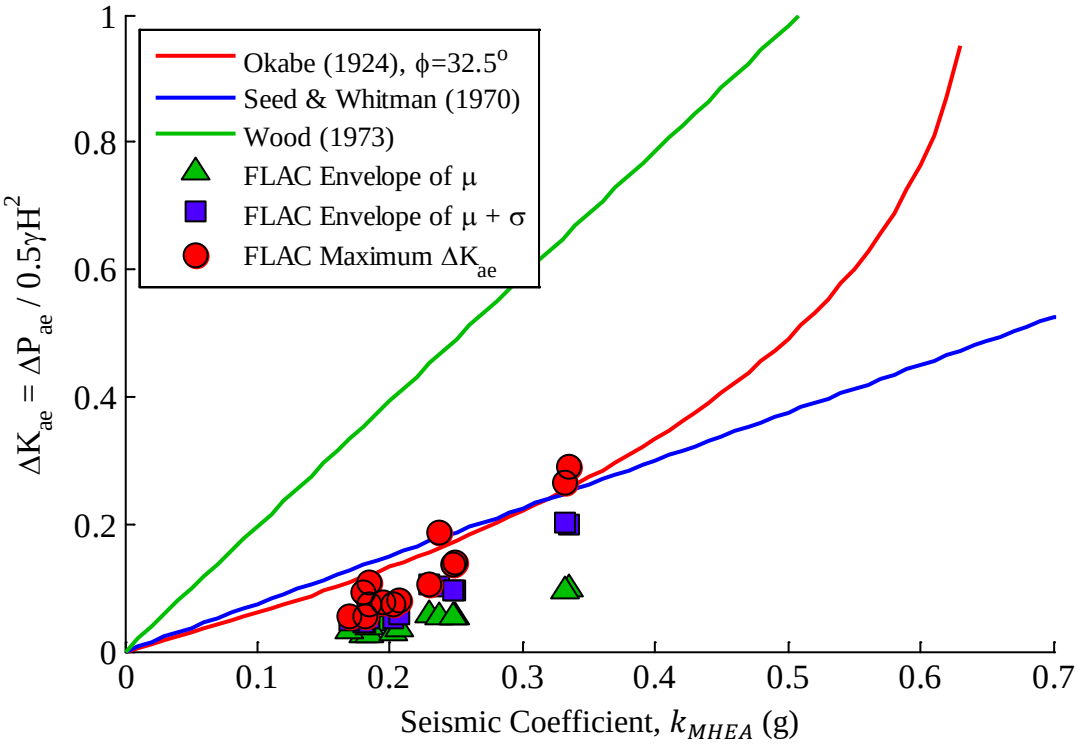

Figure 5.18: Computed mean, mean-plus-one-standard-deviation, and maximum coefficient of dynamic earth pressure increment versus seismic coefficient, k_{MHEA}

Obviously, the ΔK_{ae} associated with the mean and mean-plus-one-standard-deviation envelopes of dynamic earth pressure are lower than the peak measured coefficients. Thus, the issue of using an appropriate, reduced, value of the seismic coefficient arises again. However, in this instance the issue is no longer associated with incoherency or wave scattering due to the depth of embedment of the retaining structure, but rather with the average seismic demand on the wall during excitation. With this in mind, the ΔK_{ae} corresponding to the mean envelope of dynamic earth pressure correlates with 60% of the seismic coefficient and the ΔK_{ae} corresponding to the mean-plus-one-standard-deviation envelope of dynamic earth pressure correlates with 80% of the seismic coefficient. These values are plotted in Figure 5.19, along with the maximum computed seismic earth pressure increment coefficient from FLAC measured in the soil grid adjacent to the structure, as well as the Okabe (1924), Seed & Whitman (1970), and Wood (1973) solutions.

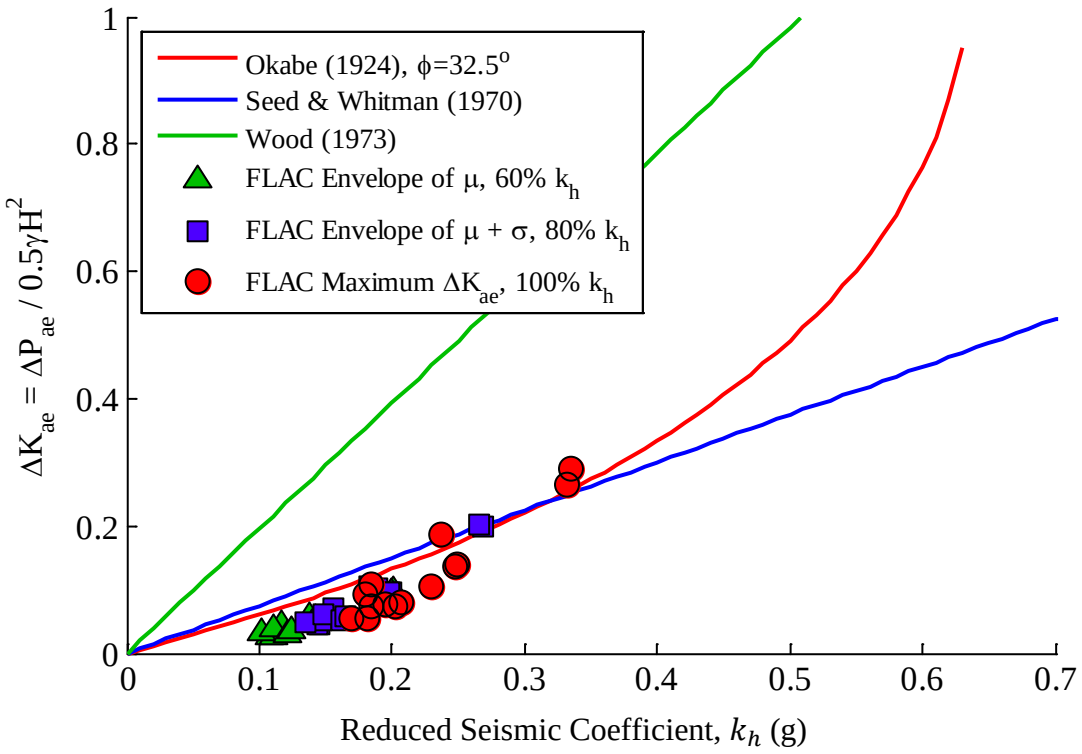

Figure 5.19: Computed mean, mean-plus-one-standard-deviation, and maximum coefficient of dynamic earth pressure increment versus reduced seismic coefficient, k_h

Almost all of the data plot below the Mononobe-Okabe and Seed & Whitman (1970) analytical solutions. The method of characterizing the dynamic load demonstrated herein has the feature of allowing a designer to select a desired level of certainty based on the importance of the project. For a retaining structure with large consequences as a result of failure, 100% or the maximum value of the seismic coefficient can be used. Decreases in the severity and number of consequences can be used to justify a reduction in the seismic coefficient at the expense of an increased potential for failure. Note that the reductions of the seismic coefficient are analogous to the Noda et al. (1975) recommendations (for 60%) and Seed & Whitman (1970) recommendations (for 80%) of the maximum value of the seismic coefficient, as discussed further in Section 7.1.1.

6 Numerical Modeling of Seismic Response of Basement Structures

The ultimate objective of this research has been the development of general recommendations for the evaluation of seismic loading on basement walls with different amounts of embedment. To this end an extensive series of numerical analyses of basement structures with different levels of embedment and different depth to width ratios was performed using FLAC$^{2\text{-}D}$. Five different structures were considered: a three-bay basement with one to four levels and a single bay, single level basement. The basic parameters for the soil model were the same as used in modeling the centrifuge experiments in order to maintain consistency. Thus, unless otherwise mentioned, the parameters used for the numerical simulation of the centrifuge experiment were used in this part of the study.

6.1 Numerical Model Properties

The basement structure was centered in a 30 m deep and 120 m wide soil domain in order to prevent the structure from interacting with the boundaries. As already described in Section 5.4, in order to achieve the desired initial condition the soil was initially linearly elastic and then the Mohr-Coulomb relationship was used. The final step was to switch the constitutive model to the non-linear hysteretic UBCHyst. Once the model was equilibrated, an excavation was simulated in 3 m lifts until the specified depth of embedment was achieved. The excavation was "braced" with pressure equivalent to at-rest static pressure estimated using Coulomb (1776) theory. The structure was installed and the interaction between the soil and structure was allowed to equilibrate. Next, the dynamic mode of the code was initiated and mechanical damping was specified, as described in Section 5.3.4. A period of 0.2 sec of computational time without dynamic input was specified, and then dynamic excitation was applied to the model.

6.1.1 Structure Model

Linear elastic beam elements were used to model the walls and floors of the prototype structures. The properties were selected in the same manner as by Taiebat et al. (2014), namely that the material was normal weight $w_c = 23.6$ kN/m^3 (~150 pcf) concrete with compressive strength $f_c' = 34$ MPa (~5000psi). The elastic modulus was determined using the empirical relationship $E_c = 0.043(w_c)^{1.5}\sqrt{f_c'} \approx 4700\sqrt{f_c'}$ (for normal weight concrete) and converted to a plain strain modulus using $E^* = E/(1-\nu^2)$ and $\nu = 0.2$. The thickness of the walls, base, and floors of the basement structure were selected to provide a stiff structure and to avoid the necessity of incorporating inelastic bending (Taiebat et al., 2014; Tabatabaiefar & Fatahi, 2014). The equivalent plain strain properties for the basement structures are summarized in Table 6.1 for a unit width in prototype scale. All components of the basement were discretized into element lengths of 0.5 m to coincide with the soil grid. Rayleigh damping with $\xi_{min} = 0.0001$ (0.01%) is included in the beam elements to reduce high frequency noise.

Table 6.1: Structural element properties used in FLAC model of prototype basement structure

Property per unit width	Units	Walls	Base	Floors
Elastic Modulus	E^* (kPa)	2.85 E+07	2.85 E+07	2.85 E+07
Unit mass	ρ (Mg/m^3)	2.40 E+00	2.40 E+00	2.40 E+00
Cross Section	A (m^2/m)	6.00 E-01	6.00 E-01	4.00 E-01
Second Moment of Area	I (m^4/m)	1.80 E-02	1.80 E-02	5.33 E-03

Each level of the structure was 3 m high and each bay was 8 m wide in the 3-bay structures (Figure 6.1 to Figure 6.4). The single bay structure was 3 m deep and 6 m wide, or one-quarter the size of the largest structure (Figure 6.5).

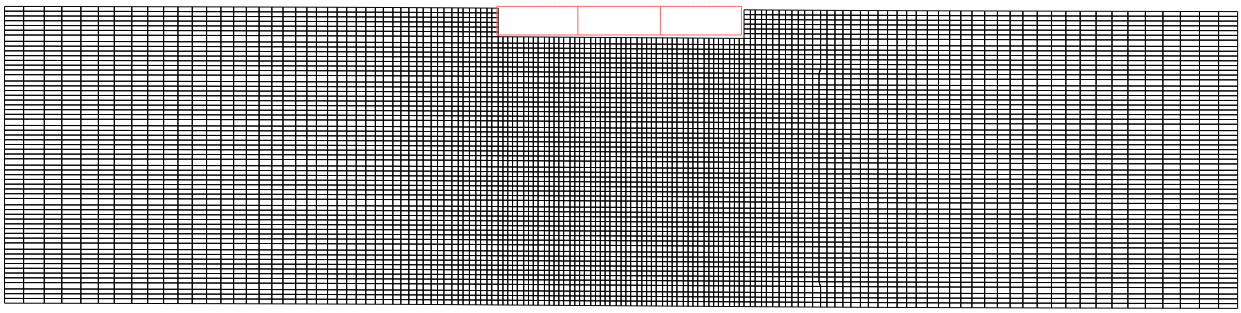

Figure 6.1: Finite difference mesh of one-level, three-bay prototype basement developed in FLAC

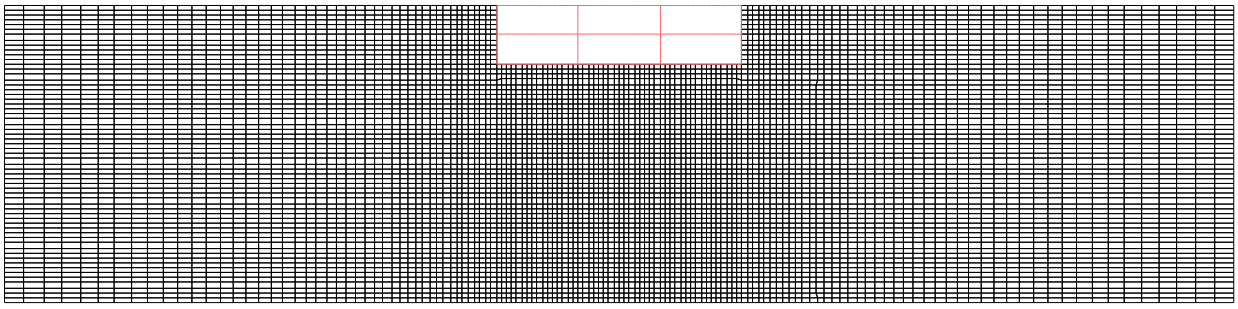

Figure 6.2: Finite difference mesh of two-level, three-bay prototype basement developed in FLAC

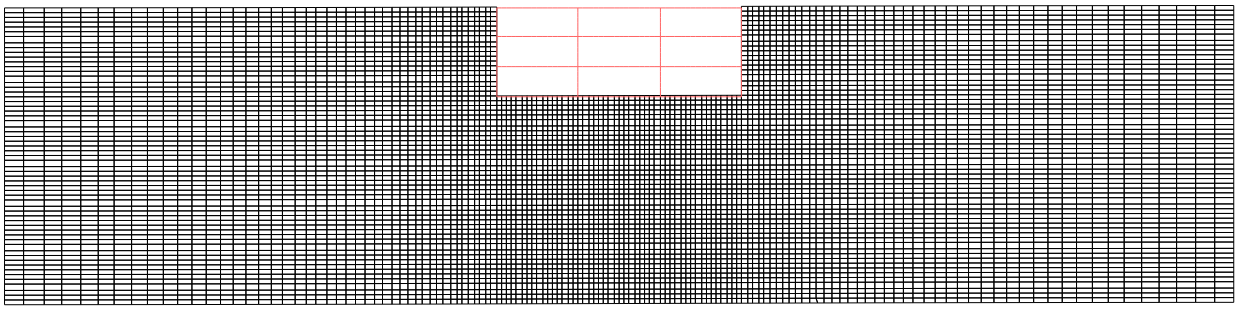

Figure 6.3: Finite difference mesh of three-level, three-bay prototype basement developed in FLAC

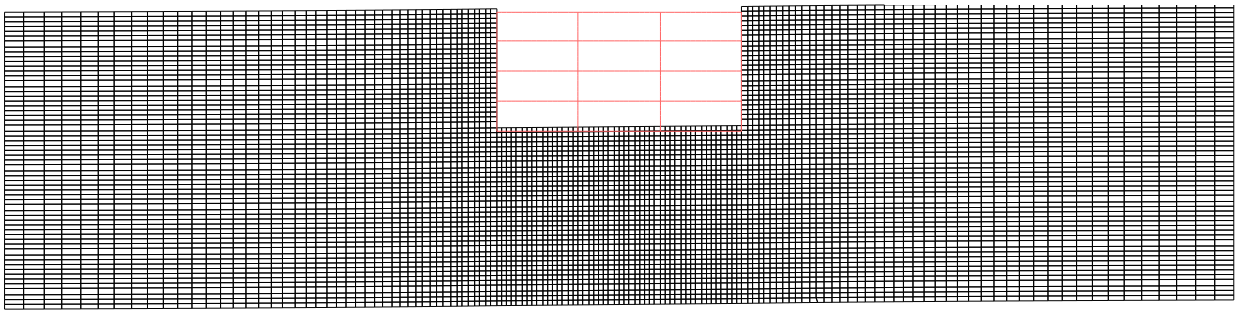

Figure 6.4: Finite difference mesh of four-level, three-bay prototype basement developed in FLAC

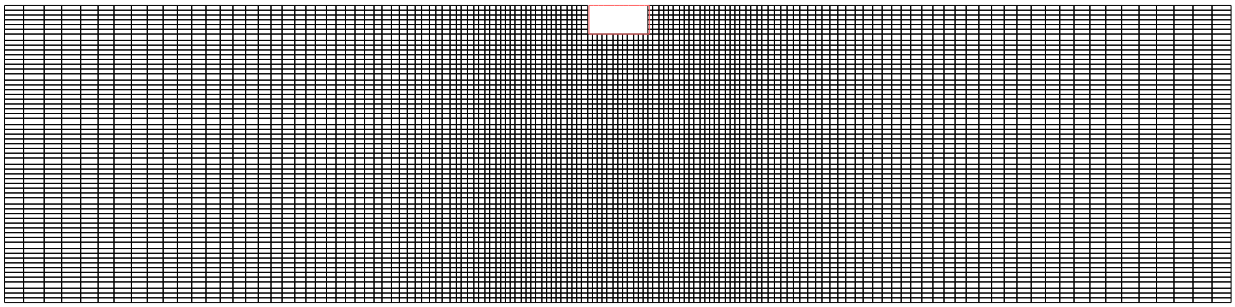

Figure 6.5: Finite difference mesh of one-level, one-bay prototype basement developed in FLAC

6.1.2 Boundary Conditions and Mechanical Damping

A quiet (absorbing) boundary was specified at the base of the model to allow energy to radiate away from the model structure. The viscous boundary developed by Lysmer & Kuhlemeyer (1969), which is based on independent dashpots in the normal and shear directions at the boundaries, is used in FLAC. The dashpots provide viscous normal and shear tractions as Equation 6.1:

$$t_n = -\rho C_p v_n \qquad t_s = -\rho C_s v_s \tag{6.1}$$

where v_n and v_s are the normal and shear components of the velocity at the boundary, ρ is the mass density, and C_p and C_s are the *p*- and *s*-wave velocities of the zones at the boundary. The normal and shear tractions are then applied to the model in the same manner as boundary loads.

The lateral boundaries of the model were modeled using the free-field boundary option in FLAC. In this scheme, a one-dimensional "column" of unit width is analyzed on each side of the domain and coupled to the main grid with viscous dashpots. If there is relative motion between the free-field grid and the main grid, the dashpots absorb the energy. Also, the unbalanced forces from the free field grids are applied to the main grid at the lateral boundaries. The calculations for the free field column are performed in small-strain mode; this can cause some distortion of the interaction at the boundary unless the deformations near the boundary are relatively small compared to grid dimensions.

When using a quiet boundary at the base, free field boundaries on the sides, and applying dynamic loading along the base, rotation of the model may occur in FLAC. To prevent this, FLAC allows the reaction forces along the side boundaries (obtained from static equilibrium prior to adjusting the boundaries for dynamic conditions) to be updated at every time step to satisfy global force and moment equilibrium. This method to prevent rotation was chosen as opposed to the alternative where the depth of the model is increased, thereby increasing the model execution time.

The boundary conditions as described allow for radiation damping in the plane of the analysis. However, a realistic soil-structure system will radiate energy in the out-of-plane direction as well. In FLAC, this effect of three-dimensional radiation damping can be approximated with dashpots connecting all grid points in the main grid to the corresponding grid points in the free field, while the viscous force is not applied to the free field grid. The dashpot acts on the difference between the velocity in the main grid and the free field velocity as Equation 6.2:

$$c = \frac{2\rho C_s^{ff}}{W} \tag{6.2}$$

where c is the coefficient of three-dimensional damping, C_s^{ff} is the free field shear wave velocity and W is the out-of-plane width of the structure (taken equal to the in-plane width of the prototype structure). This formulation is identical to that described by Lysmer et al. (1975).

Rayleigh damping was defined as in Section 5.3.4, with the minimum frequency $f_{min} = 2.22$ Hz.

6.1.3 Input Ground Motions

Due to the quiet boundary specified at the base of the model, input ground motions could not be applied as acceleration histories as in the rigid base case for the simulation of the centrifuge experiment. Instead, a stress wave history derived from a velocity record was required, as discussed in Mejia & Dawson (2006). Additionally, it was desirable to simulate realistic seismic conditions; thus, ground motions from depth were required. Therefore, input ground motions for the numerical model were obtained in a three step process.

First, a suite of target ground motions were selected from the Pacific Earthquake Engineering Research (PEER) Center Ground Motion Database with a $V_{s,30}$ between 250 m/s and 290 m/s to correspond approximately with the initial $V_{s,30}$ = 267 m/s of the numerical model. Note that this corresponds to a Site Class D according to the International Building Code (ICC, 2014). The earthquakes from which ground motions were selected corresponded to the source earthquakes of the ground motions in the centrifuge experiment. Table 6.2 lists the ground motions and various characteristics as obtained from the PEER Database.

Table 6.2: Ground motion records obtained from PEER Ground Motion Database for Site Class D

Event	M_w	Station	R_{jb} (km)	R_{rup} (km)	$V_{s,30}$ (m/s)	PGA (g)
Loma Prieta	6.93	Richmond City Hall (RCH)	87.78	87.87	260	0.13
		Gilroy Array #2 (GA2)	10.38	11.07	271	0.37
		Capitola (CAP)	8.65	15.23	289	0.52
Kobe	6.90	Sakai (SKI)	28.08	28.08	256	0.15
		Amagasaki (AMA)	11.34	11.34	256	0.28
Kocaeli	7.51	Bursa Tofas (BUR)	60.43	60.43	290	0.10
		Duzce (DUZ)	13.6	15.37	282	0.36

Next, a one-dimensional soil column was developed for use in an equivalent-linear deconvolution analysis. The height, density and maximum shear modulus of the layers in the soil column were selected based on the values intended for the free field in the FLAC model; i.e., the layers were all 0.5 m thick with density increasing as a square root with depth and Equation 5.7a,b and c from Section 5.4 were used to determine the maximum shear modulus. The values for the upper 20 m are the same as from the numerical model simulating the centrifuge experiment, and the bottom 10 m simply continue the same trends, as shown in Figure 6.6.

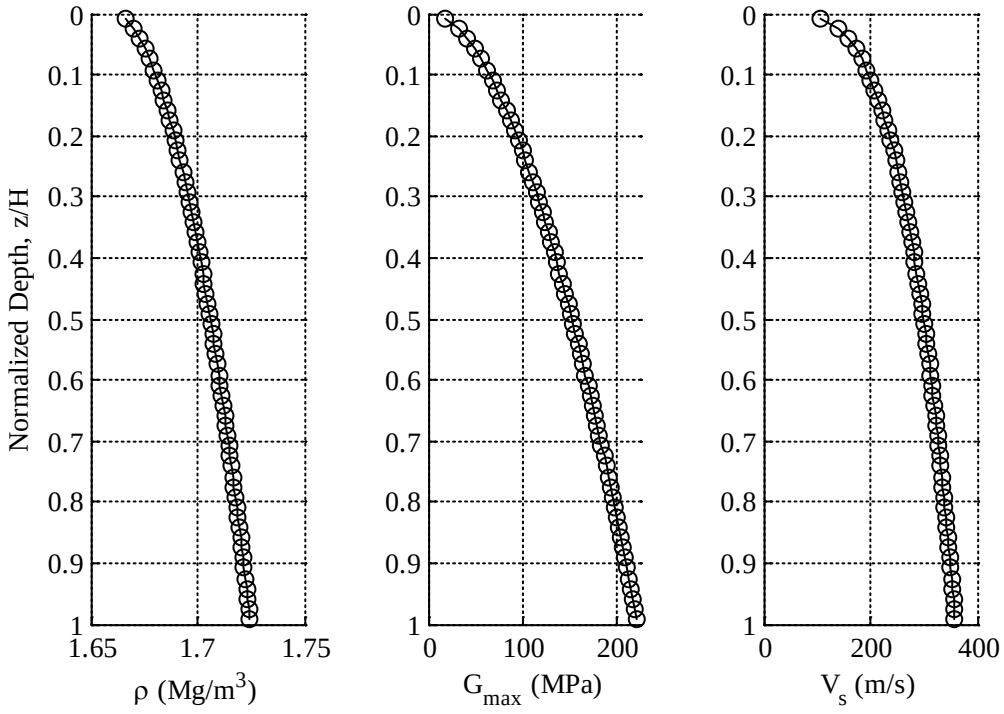

Figure 6.6: Assumed density, shear modulus, and shear wave velocity distributions, Site Class D

The normalized shear modulus degradation curve for each layer was determined using the Darendeli (2001) formulation with a strength adjustment at large strain according to Yee et al. (2013). The corresponding damping curve for each layer was determined using the Darendeli

(2001) procedure but with the adjusted normalized shear modulus degradation curve instead of the unadjusted form.

Lastly, a deconvolution analysis was performed in SHAKE2000 (Ordoñez, 2000) to obtain the outcropping ground motion at depth. The procedure suggested by Silva (1998) was used for the deconvolution. The upward propagating motion was extracted, and then converted to a velocity wave, which was converted to a shear stress wave using Equation 6.3:

$$\sigma_s = 2C_s\rho\sqrt{G/G_{max}}\,v_s \qquad \textbf{(6.3)}$$

where $C_s = \sqrt{G_{max}/\rho}$ is the initial shear wave velocity at the base of the numerical model and the factor of two accounts for the fact that half of the input energy is absorbed by the quiet boundary. The acceleration record obtained from SHAKE2000 was processed in a linear deconvolution process; however, the shear modulus at the base of the soil column in the analysis was the degraded shear modulus G, not G_{max}. Also, continuity of shear stresses is utilized in the formulation of the frequency domain solution, so the additional factor $\sqrt{G/G_{max}}$ is necessary to obtain the strain compatible shear stress wave. Thus, the conversion from a velocity wave to a shear stress wave must include the additional factor. Further details of the ground motion processing procedure are explained in Appendix C.

The deconvolution procedure was checked by applying the shear stress wave input at the base of a soil domain equivalent to the backfill dimensions of the full FLAC prototype model; i.e., 30 m deep and 48 m wide, with a quiet (absorbing) boundary at the base, lateral free field boundaries, and utilizing the base rotation correction. Three-dimensional radiation damping was not included in this check since a structure was not present in the calibration model.

A second suite of input ground motions corresponding to a Site Class C was selected from the Pacific Earthquake Engineering Research (PEER) Center Ground Motion Database with a $V_{s,30}$ between 550 m/s and 580 m/s to correspond approximately with an initial $V_{s,30}$ = 564 m/s. Table 6.3 lists the ground motions and various characteristics as obtained from the PEER Database.

Table 6.3: Ground motion records obtained from PEER Ground Motion Database for Site Class C

Event	M_w	Station	R_{jb} (km)	R_{rup} (km)	$V_{s,30}$ (m/s)	PGA (g)
Northridge	6.69	Palmdale HWP (PHP)	41.37	41.67	551.56	0.06, 0.07
		Big Tujunga (TUJ)	19.1	19.74	550.11	0.17, 0.26
Chi Chi	7.62	TCU 105	17.16	17.16	575.54	0.11
		TCU 075	0.89	0.89	573.02	0.26

Next, a one-dimensional soil column was developed for use in an equivalent-linear deconvolution analysis. The heights of the layers remained the same as in the previous model (0.5 m thick). The density increased as a square root with depth, but the minimum and maximum densities were larger than the previous model. Instead of correlating maximum shear modulus to

the void ratio as was done previously, a target shear wave velocity profile with a $V_{s,30} = 564$ m/s was selected as a fourth-root distribution with depth and the inferred shear modulus profile was calculated. The computations are detailed in Equation 6.4a and b, and the profiles are shown in Figure 6.7.

$$V_{s,i} = V_{s,min} + \left(V_{s,max} - V_{s,min}\right)\left(\frac{z}{H}\right)^{0.25} \quad \text{(a)} \qquad G_{max,i} = \rho_i V_{s,i}^2 \quad \text{(b)} \qquad \textbf{(6.4)}$$

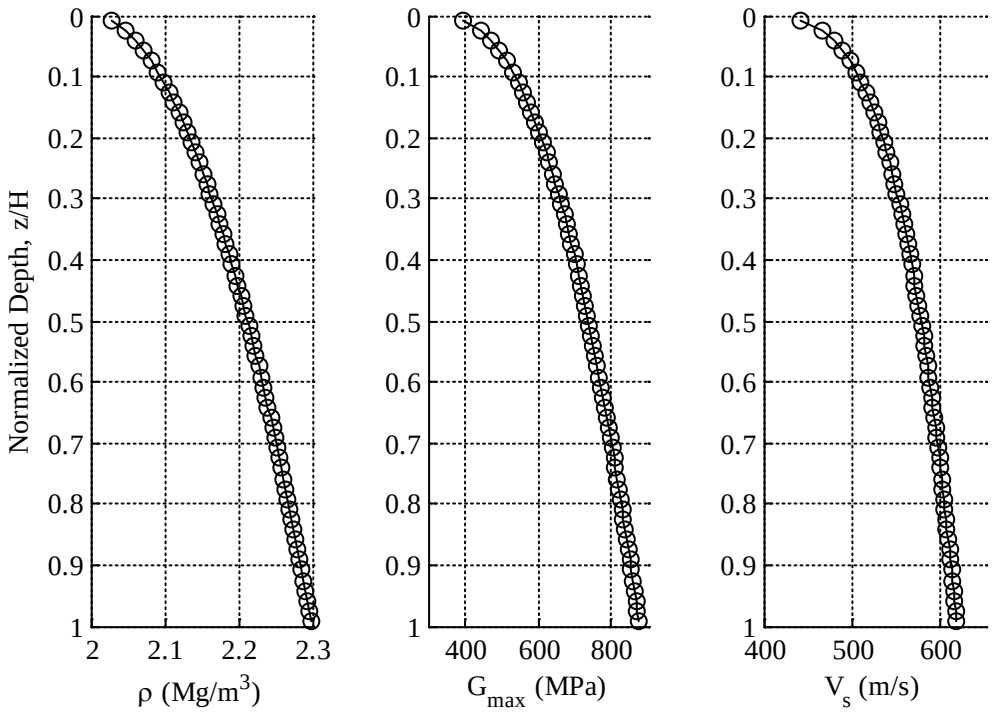

Figure 6.7: Assumed density, shear modulus, and shear wave velocity distributions, Site Class C

The normalized shear modulus degradation curve for each layer was determined using the Menq (2001) formulation with a strength adjustment at large strain according to Yee et al. (2013). The corresponding damping curve for each layer was determined using the Darendeli (2001) procedure but with the adjusted normalized shear modulus degradation curve instead of the unadjusted form. The final calibrated parameters selected for use in the UBCHyst soil model are shown in Table 6.4. As before, the strain level, confining pressure and its corresponding reference shear modulus were varied to obtain the normalized shear modulus degradation curves (Figure 6.8) and true shear modulus degradation curves (Figure 6.9), which were compared to Menq (2003) curves. The confining pressures correspond to the average confining pressure that would be measured at the center of a soil zone in the prototype numerical model based on the density and coefficient of horizontal at-rest earth pressure. The corresponding damping curves were also obtained (Figure 6.10), although the damping at high strains (>0.1%) was unrealistic when compared to those from Menq (2003); this is expected based on the previous calibrations to Darendeli (2001) curves.

A deconvolution analysis was performed for the second suite of ground motions in SHAKE 2000 using the aforementioned procedure. Similarly, the validity of the procedure was checked by applying the shear stress wave input at the base of a soil domain equivalent to the backfill dimensions of the full FLAC prototype model.

Table 6.4: Calibrated soil model properties used in FLAC model for Site Class C profile

ρ_{min}	=	2.00	Mg/m^3	P_a	=	100	kPa	n_{min}	=	0.50	rm = 1.00
ρ_{max}	=	2.30	Mg/m^3	ψ	=	0.0	deg	Δn	=	1.50	$n1$ = 1.00
c	=	5.0	kPa	$V_{s,min}$	=	365.0	m/s	$dfac_{min}$	=	0.00	R_f = 1.00
ϕ_f	=	40.0	deg	$V_{s,max}$	=	617.8	m/s	$\Delta dfac$	=	0.80	mod1 = 0.75

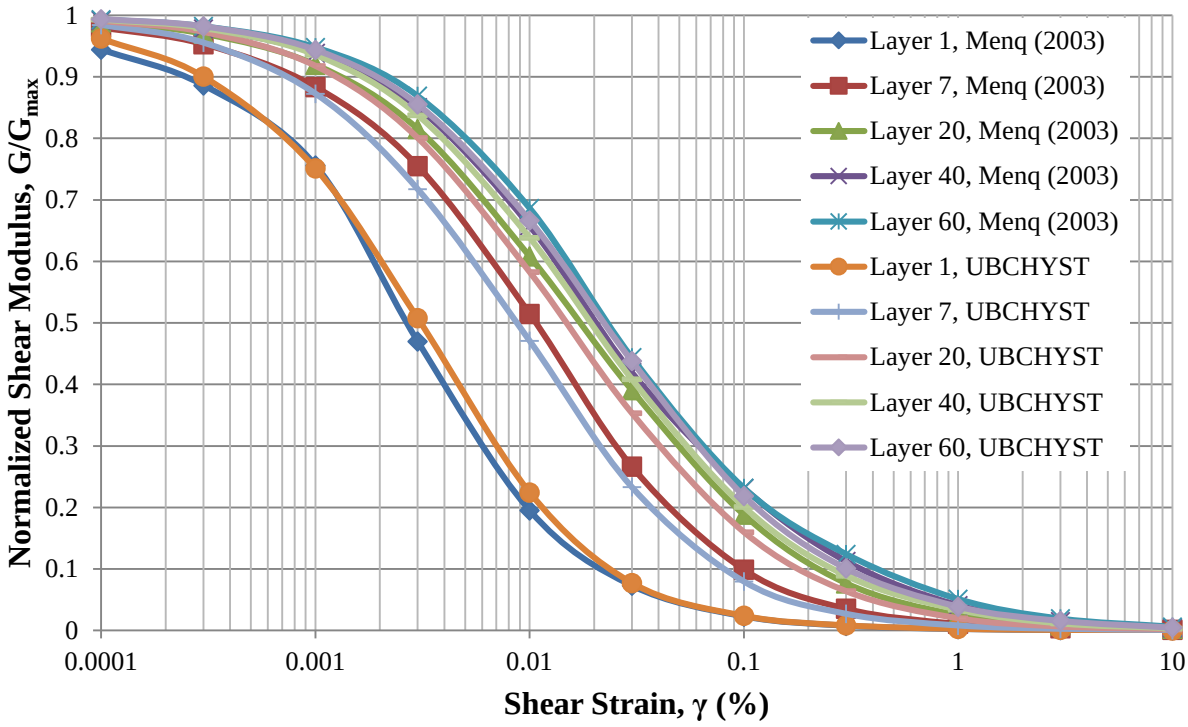

Figure 6.8: Normalized shear modulus degradation vs shear strain for Site Class C

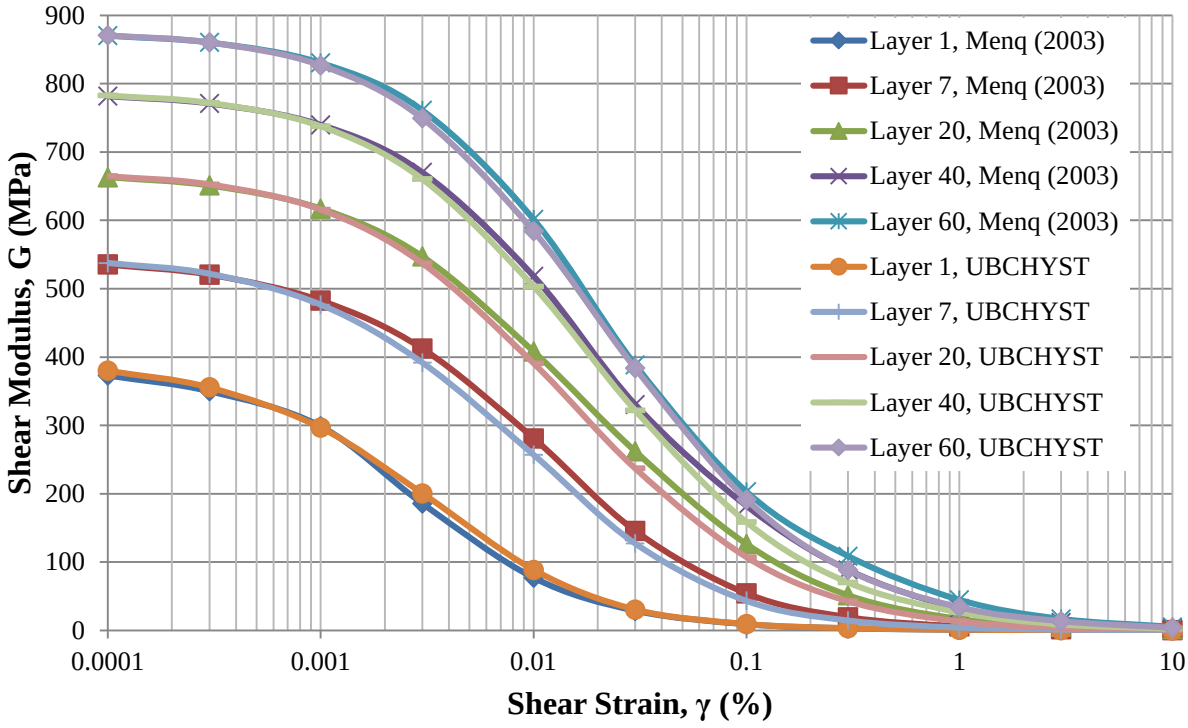

Figure 6.9: Shear modulus degradation vs shear strain for Site Class C

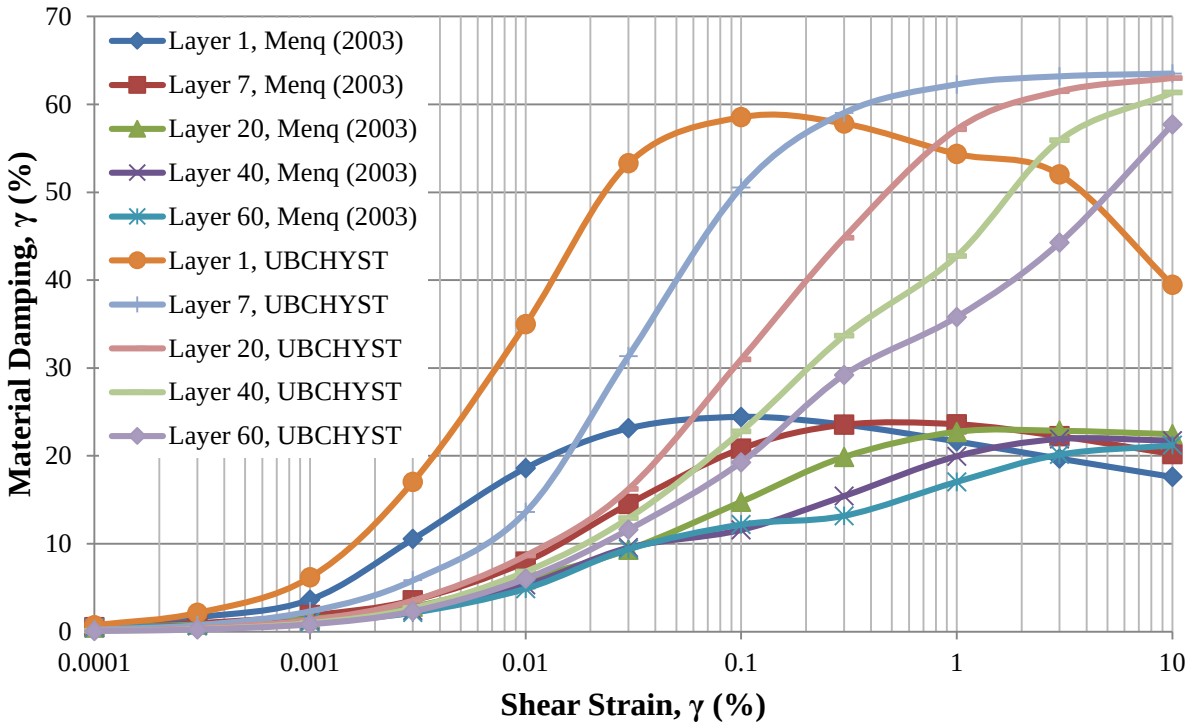

Figure 6.10: Material damping vs shear strain for Site Class C

6.2 Accelerations in Soil and Structures

The acceleration time histories were filtered in the frequency domain to remove spurious noise resulting from the explicit integration process in FLAC. Examples of acceleration histories and response spectra computed at various locations in the numerical models compared to the target surface records obtained from PEER are shown in Figure 6.11 to Figure 6.15. Additional plots are shown in Appendix B. The plots show the response in the free field at the surface and at the level of the base of the prototype basement structure; and at the prototype basement structure at the surface and at the base of the structure. In general, the response of the free field at the surface computed in the numerical model matches well with the target ground motion in the free field from PEER. With increasing depth of the prototype basement structure, the phase difference between the acceleration record at the surface and the depth of the structure increases as would be expected. Also, there is clear evidence of amplification in the backfill and the prototype basement structures from the depth of the structure to the surface based on the response spectra.

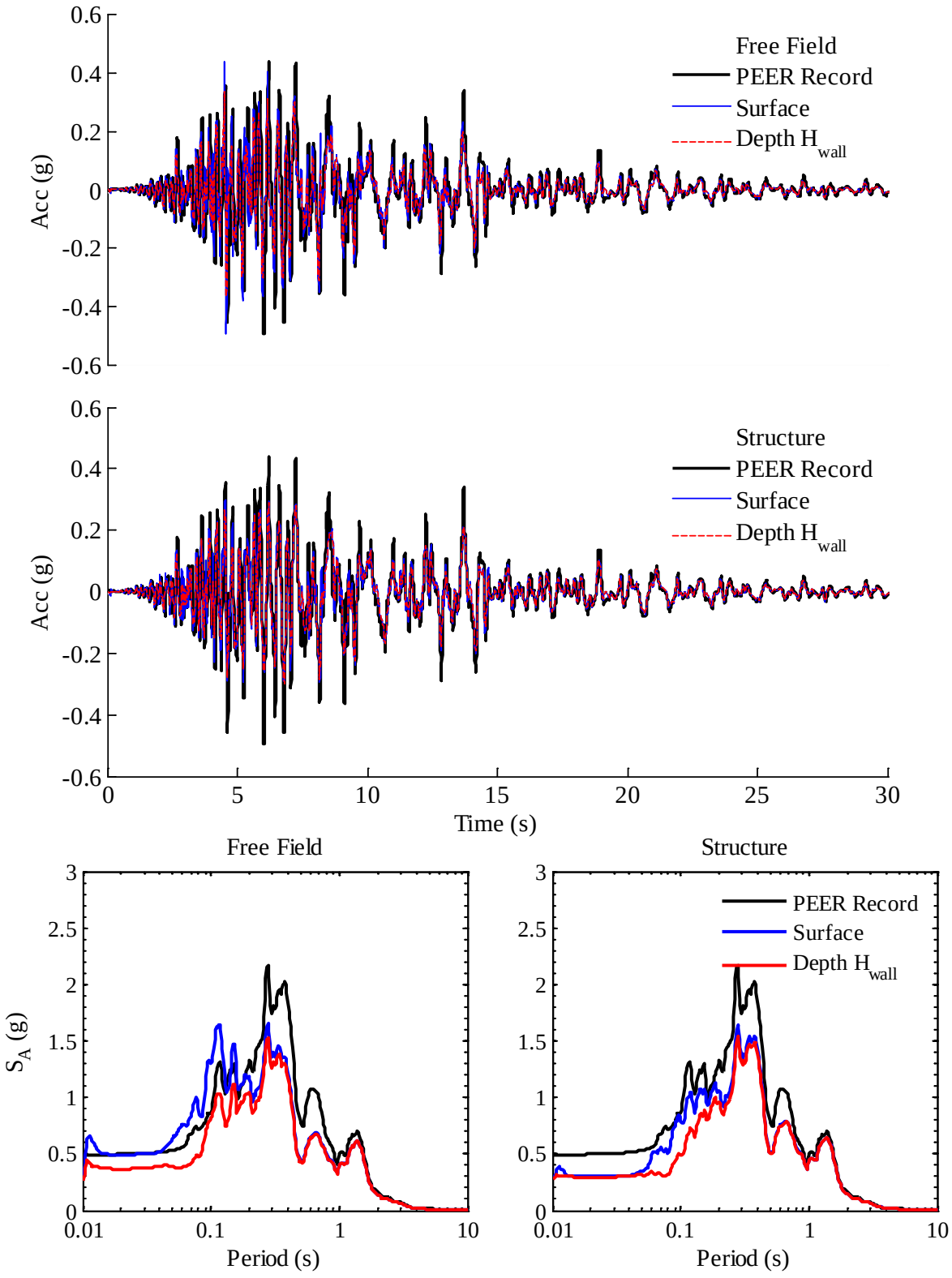

Figure 6.11: Computed accelerations and response spectra at 5% damping in free field and structure during Loma Prieta CAP 000 for one level basement; Site Class D

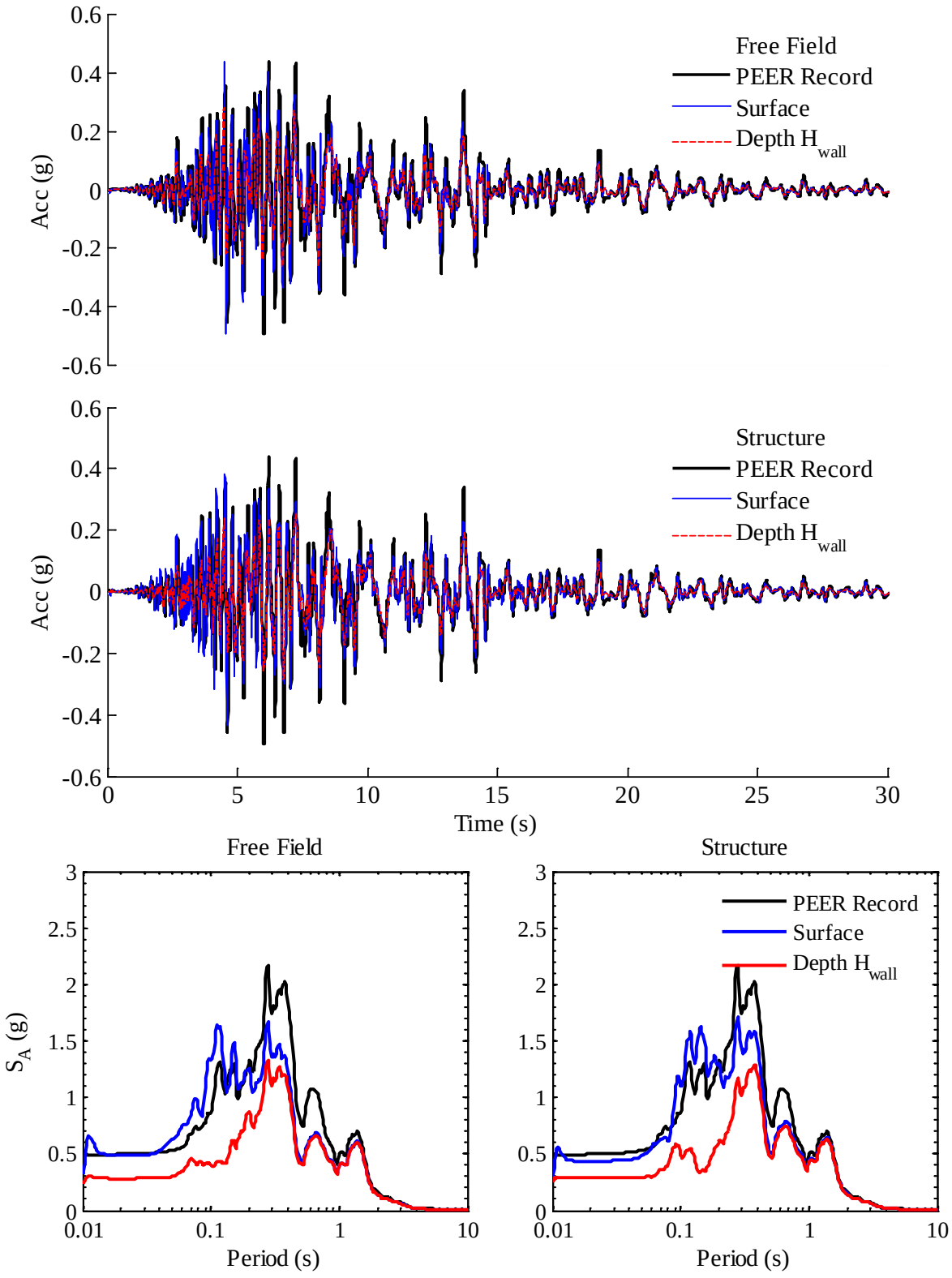

Figure 6.12: Computed accelerations and response spectra at 5% damping in free field and structure during Loma Prieta CAP 000 for two level basement; Site Class D

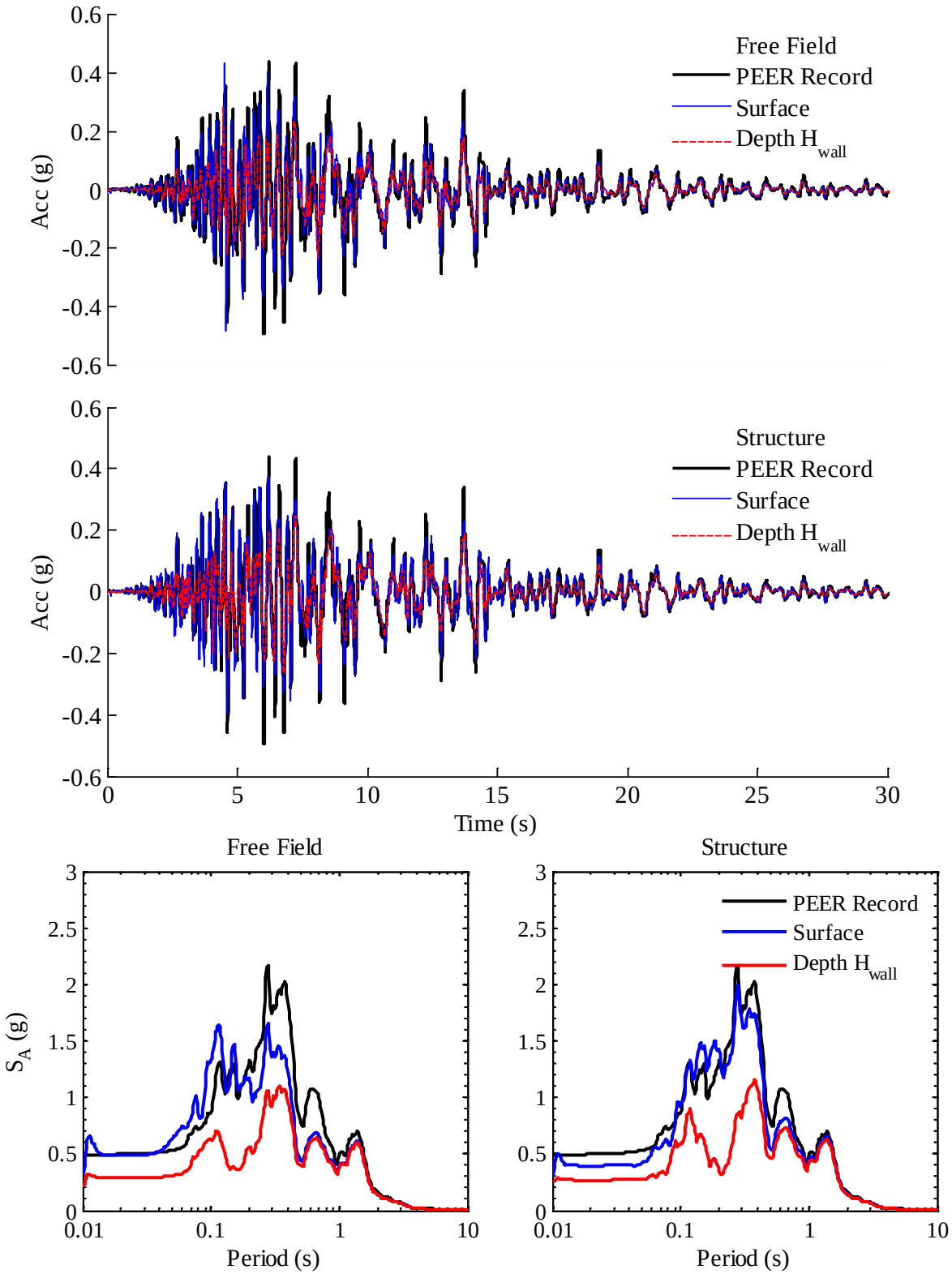

Figure 6.13: Computed accelerations and response spectra at 5% damping in free field and structure during Loma Prieta CAP 000 for three level basement; Site Class D

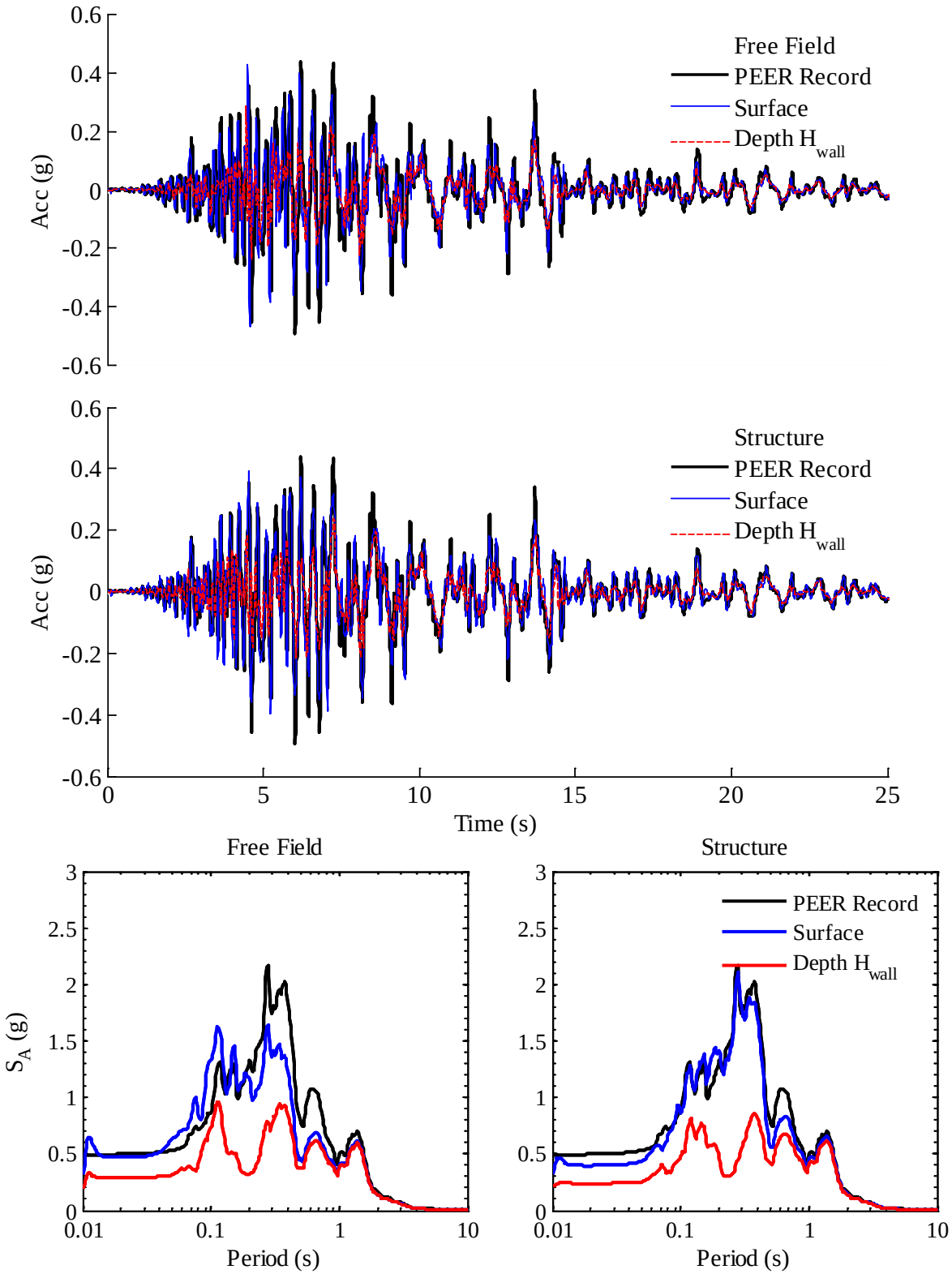

Figure 6.14: Computed accelerations and response spectra at 5% damping in free field and structure during Loma Prieta CAP 000 for four level basement; Site Class D

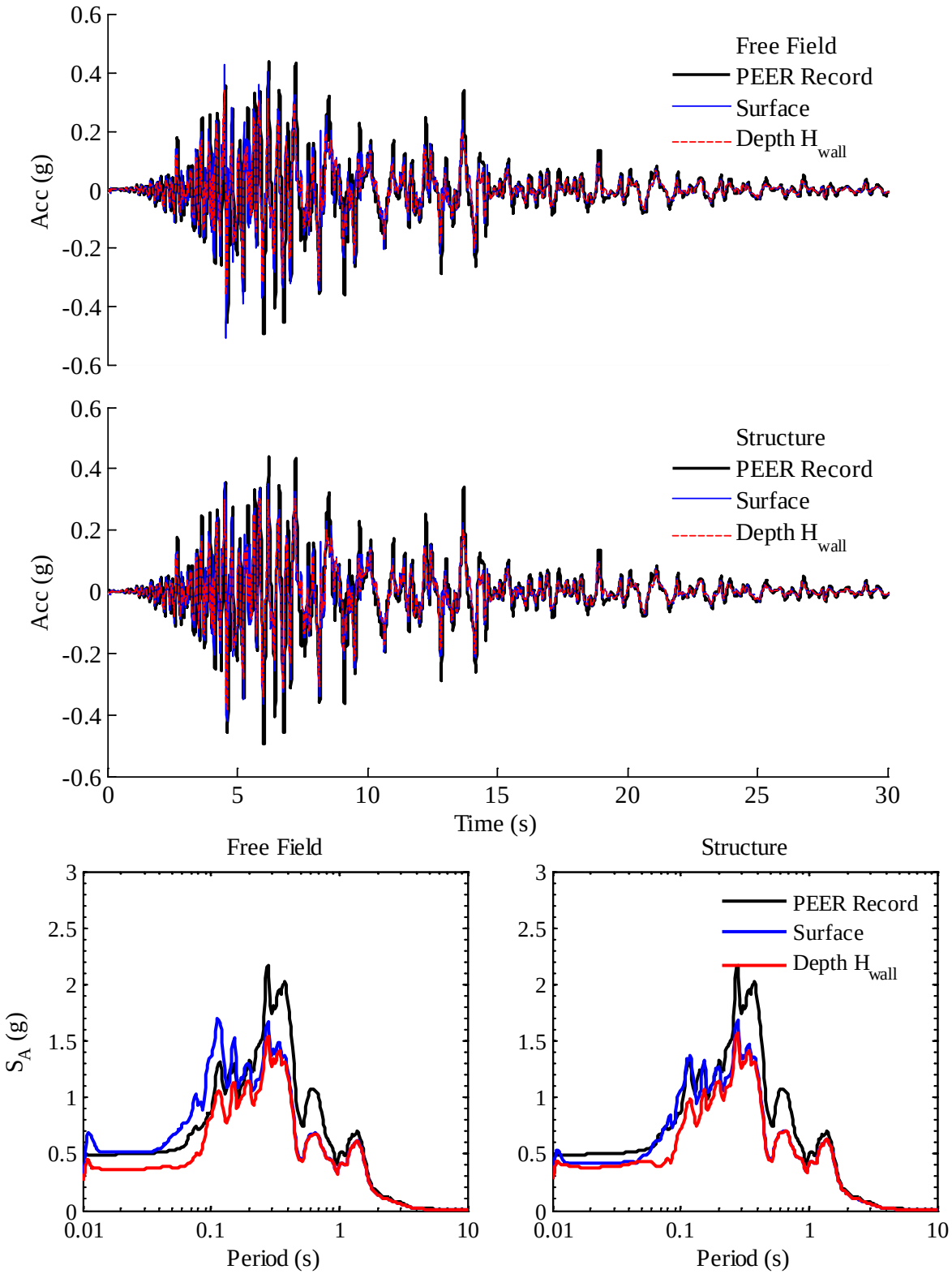

Figure 6.15: Computed accelerations and response spectra at 5% damping in free field and structure during Loma Prieta CAP 000 for one bay, one level basement; Site Class D

6.3 Prototype Basement Structure Response

The loads acting on the prototype basement structure in the numerical model were computed by integrating the horizontal stresses in the soil along the height of the basement structure, as in the numerical simulation of the centrifuge experiment discussed in Section 5.6.

The instantaneous dynamic earth pressure distributions computed in the soil zones corresponding to the maximum ΔK_{ae} are shown in Figure 6.16 to Figure 6.20. Additional plots of the instantaneous dynamic earth pressure distributions corresponding to both the maximum and minimum ΔK_{ae} are shown in Appendix B. Note that the dynamic earth pressure distribution predicted by the M-O method is computed using the corresponding value of the seismic coefficient, k_{MHEA}, and that predicted by the Seed & Whitman (1970) method is computed using 80% of the peak ground acceleration at the surface (as described previously in Section 5.6). Based on the figures, it is clear that the computed pressure distribution in the soil grid is complex and depends on the depth of embedment of the prototype basement structure. For the three-bay prototype basement structures with one (3 m) or two levels (6 m), the pressure distribution is reasonably represented by a triangular distribution similar to that used in the M-O method. For the three (9 m) and four level (12 m) prototype basement structures, the pressure distribution is reasonably represented by a uniform distribution or the assumed distribution developed in Section 5.6, namely that the pressure increases linearly to a depth of about one-third of the depth of embedment, then decreases linearly to zero at the base of the prototype basement. Note that the magnitude of the seismic coefficient decreases with increasing depth of embedment for the same input ground motion.

For the one bay, one level (3 m) prototype basement structure, the dynamic pressure is negligible. This is due to the low lateral stiffness of the structure and the shallow embedment that allows it to move with the soil during shaking. Additionally, this may be a result of the computation procedure, the consequences of which were described previously in Section 5.6.

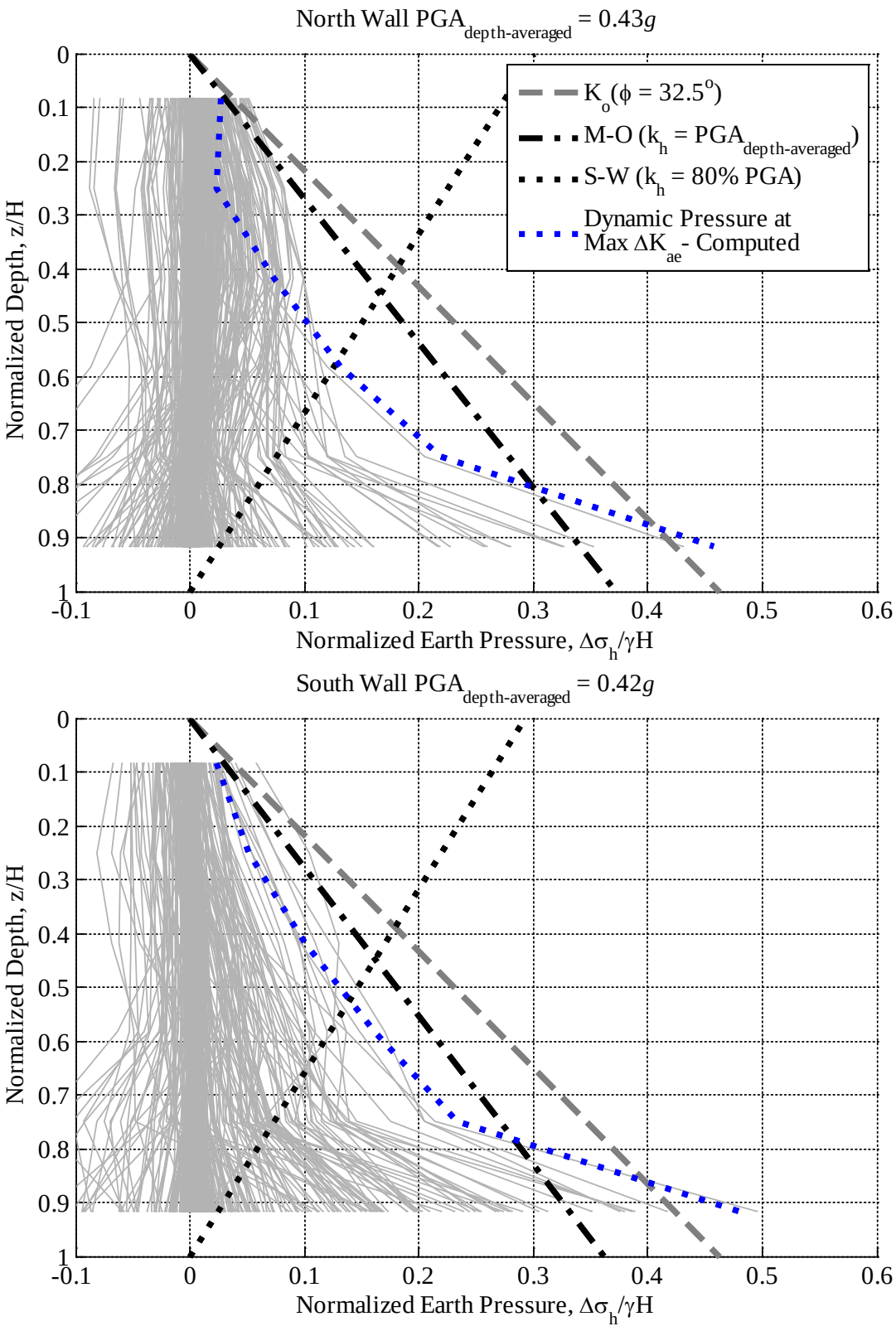

Figure 6.16: Computed normalized dynamic earth pressure distributions at maximum ΔK_{ae} during Loma Prieta CAP 000 for one level basement; Site Class D

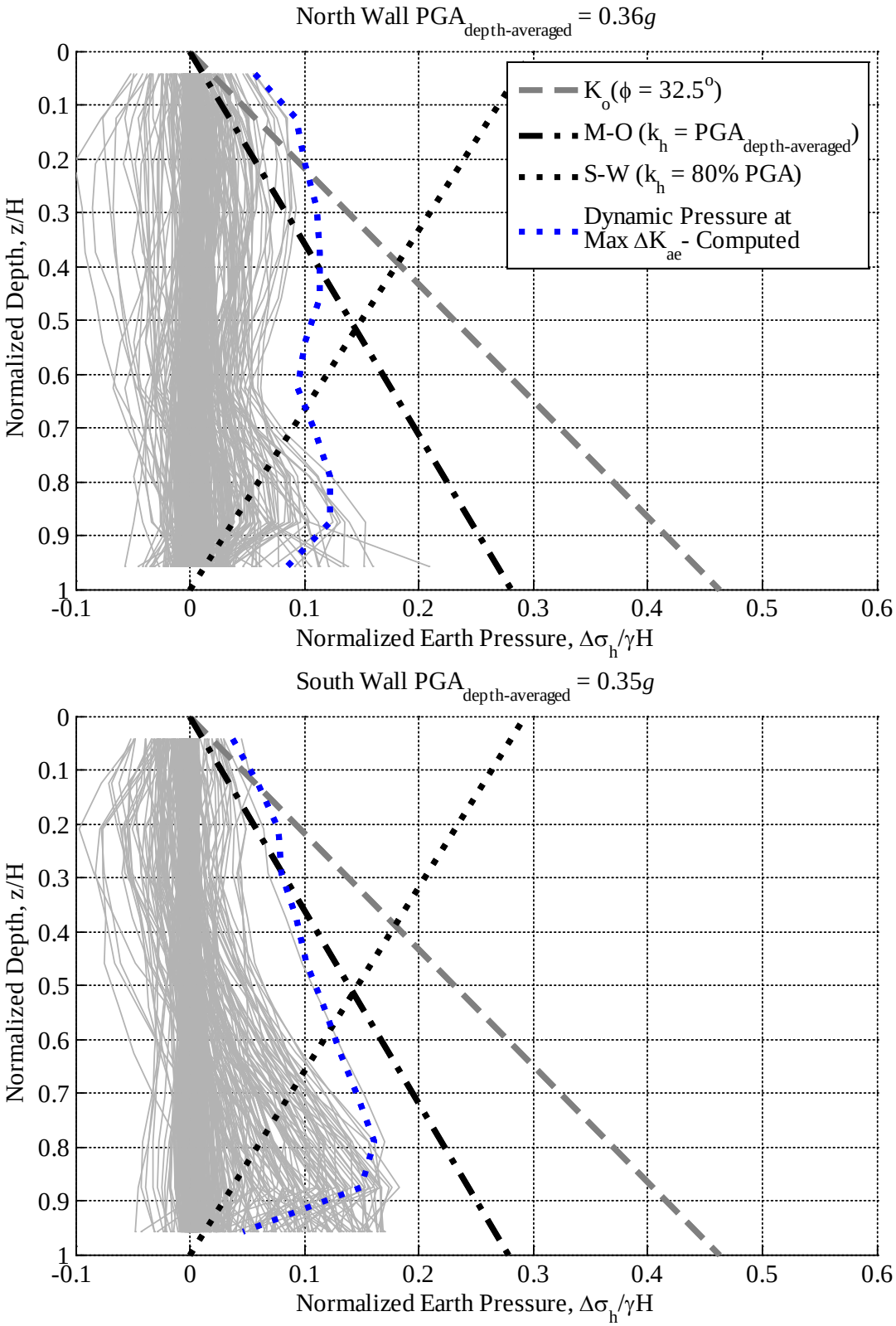

Figure 6.17: Computed normalized dynamic earth pressure distributions at maximum ΔK_{ae} during Loma Prieta CAP 000 for two level basement; Site Class D

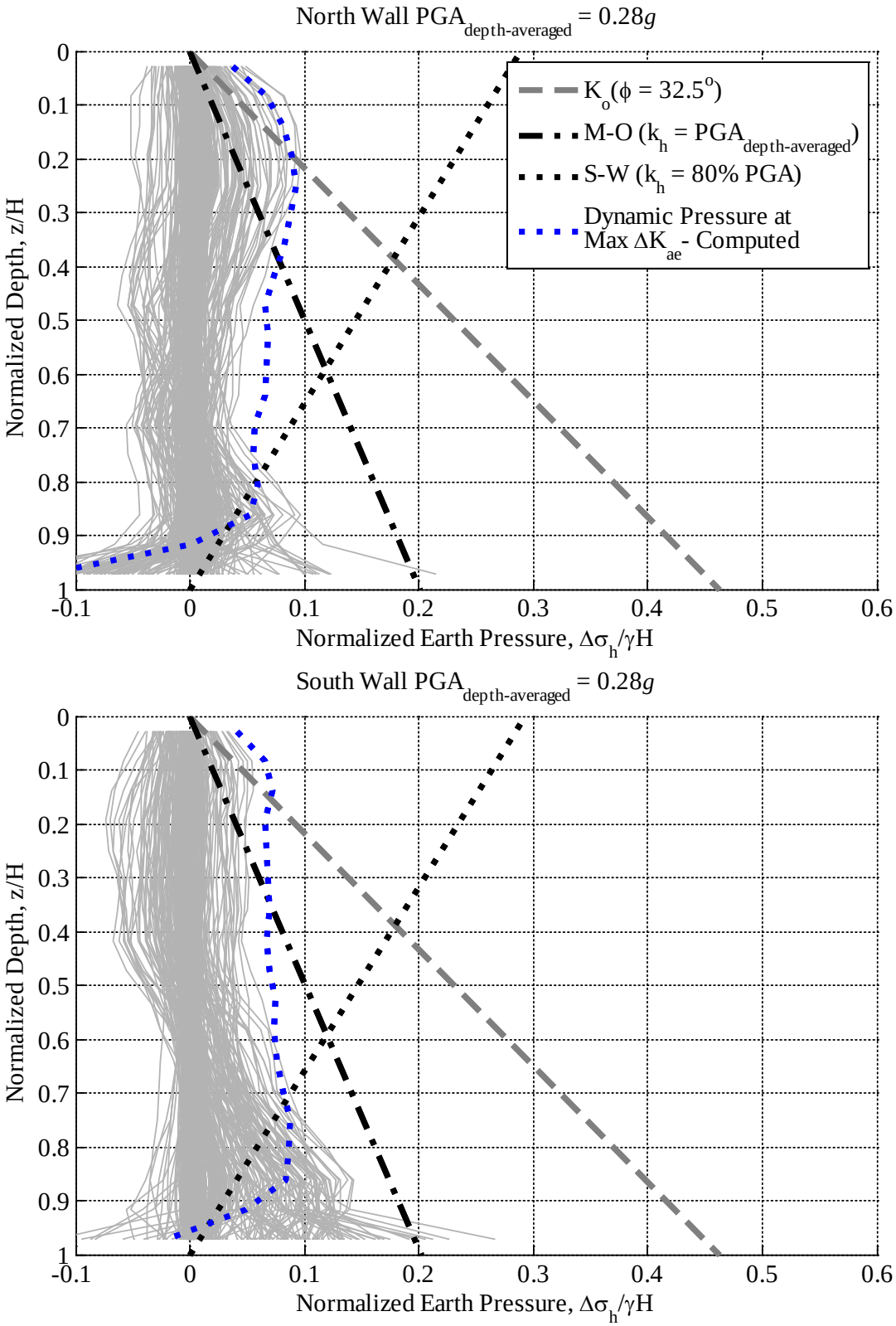

Figure 6.18: Computed normalized dynamic earth pressure distributions at maximum ΔK_{ae} during Loma Prieta CAP 000 for three level basement; Site Class D

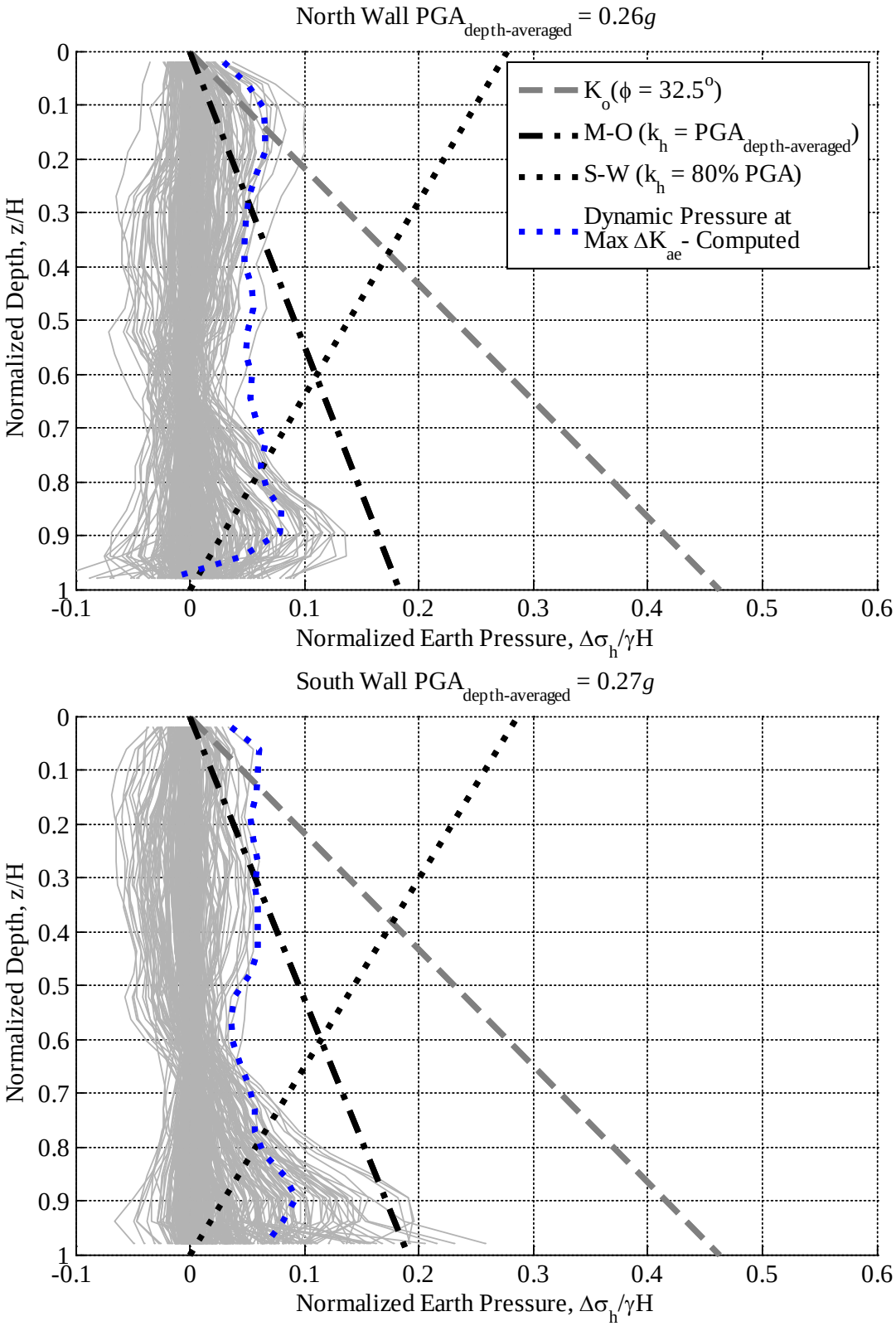

Figure 6.19: Computed normalized dynamic earth pressure distributions at maximum ΔK_{ae} during Loma Prieta CAP 000 for four level basement; Site Class D

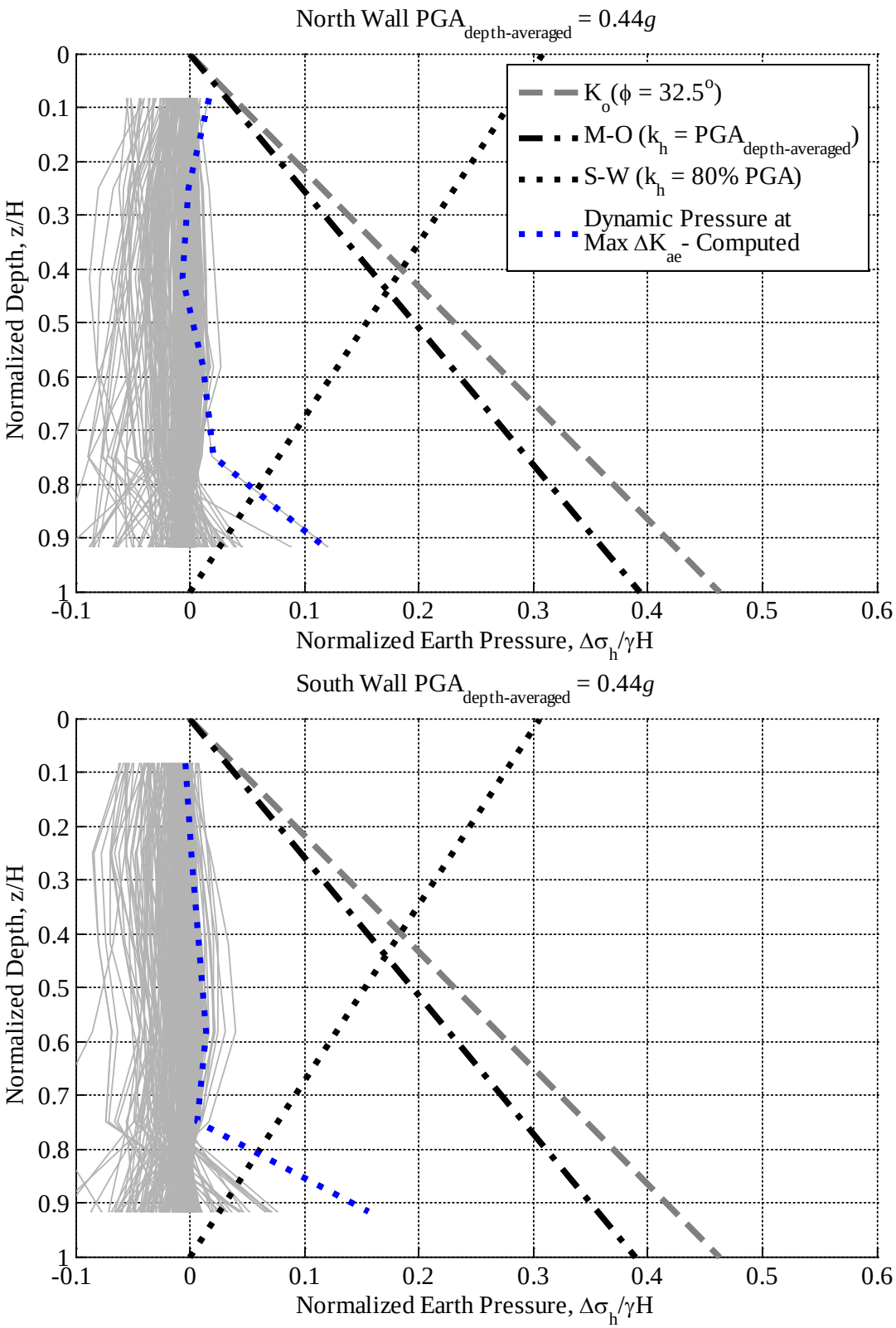

Figure 6.20: Computed normalized dynamic earth pressure distributions at maximum ΔK_{ae} during Loma Prieta CAP 000 for one bay, one level basement; Site Class D

The dynamic increment of earth pressure versus the seismic coefficient, k_{MHEA}, computed in the numerical model of the prototype basement structures with three bays are shown in Figure 6.21 and Figure 6.22 for Site Class D and C, respectively. Results from analytical solutions (Okabe, 1924; Seed & Whitman, 1970; Wood, 1973) are also shown, as before. The results from the numerical model accurately reflect the trend of increasing dynamic earth pressure with increasing values of the seismic coefficient for the prototype structures with three bays and different depths of embedment for both site classes. Again, using an average measure of acceleration in the free field over the depth of the embedded structure seems more appropriate than a single measure from the surface or at the depth of the structure.

For the one bay, one level, prototype basement structure, the results are quite different. Due to the increased flexibility of the structure, the dynamic load from seismic earth pressure is essentially negligible up to about 0.4*g*, as shown in Figure 6.23 and Figure 6.24 for Site Class D and C, respectively. This is expected based on the computed dynamic earth pressure distributions. For comparison, the average trend from the centrifuge tests conducted by Al Atik & Sitar (2010) is presented as well. As can be seen, the numerical results are consistent with these previously obtained experimental results.

6.4 Summary of Observations

The results presented herein demonstrate the efficacy of numerical analyses to reasonably represent the response of basement structures. The results are consistent with centrifuge experiments and calibrated numerical analyses thereof. Based on the results, the dynamic earth pressure increment on stiffer and wider structures that do not undergo significant racking deformation or rigid body rotations can be reasonably approximated using the M-O method with the seismic coefficient, k_{MHEA}. Alternatively, using the Seed & Whitman (1970) method with either 80% of the PGA or the seismic coefficient as defined herein seems a reasonable simplification.

The dynamic earth pressure increment on flexible and thin structures that may undergo significant racking deformation or rigid body rotations and translations is negligible for the range of ground motion intensities that were investigated. The limiting criterion for such cases is the deformation capacity of the structure rather than the strength capacity. This aspect of the problem was not investigated in this study.

Note that the calculated seismic coefficient, k_{MHEA}, did not exceed ~0.45 for any of the analyses; the conclusions herein therefore may not necessarily apply to more intense ground excitation.

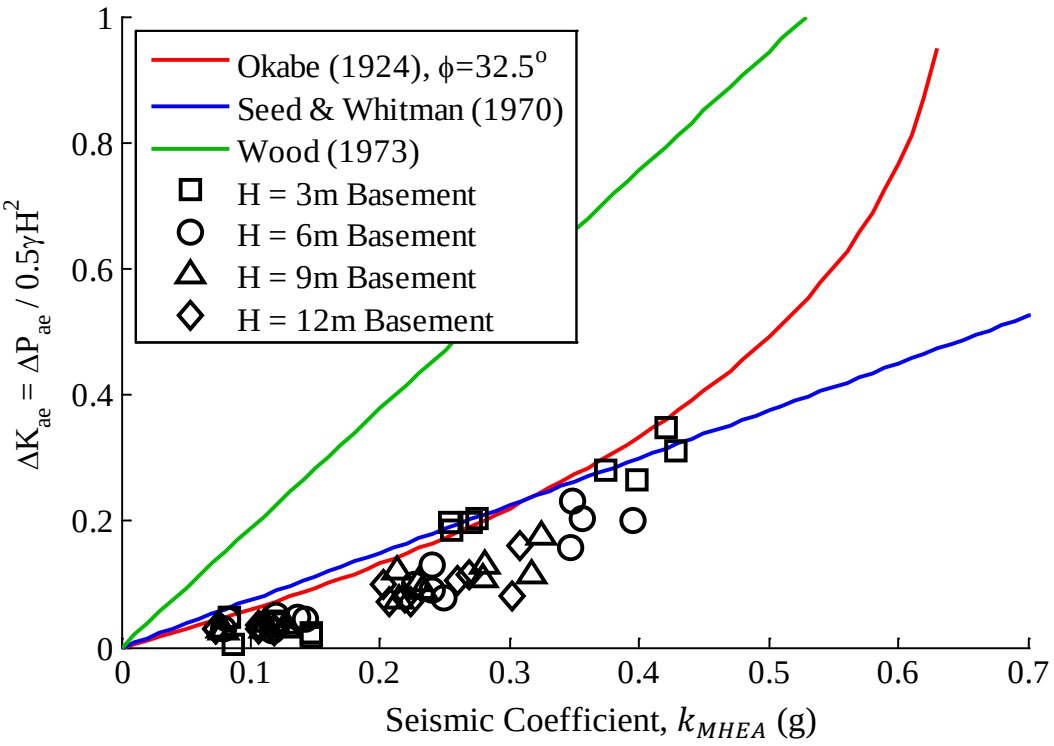

Figure 6.21: Computed coefficient of dynamic earth pressure increment versus seismic coefficient, k_{MHEA}, for three-bay, prototype basement structures, Site Class D

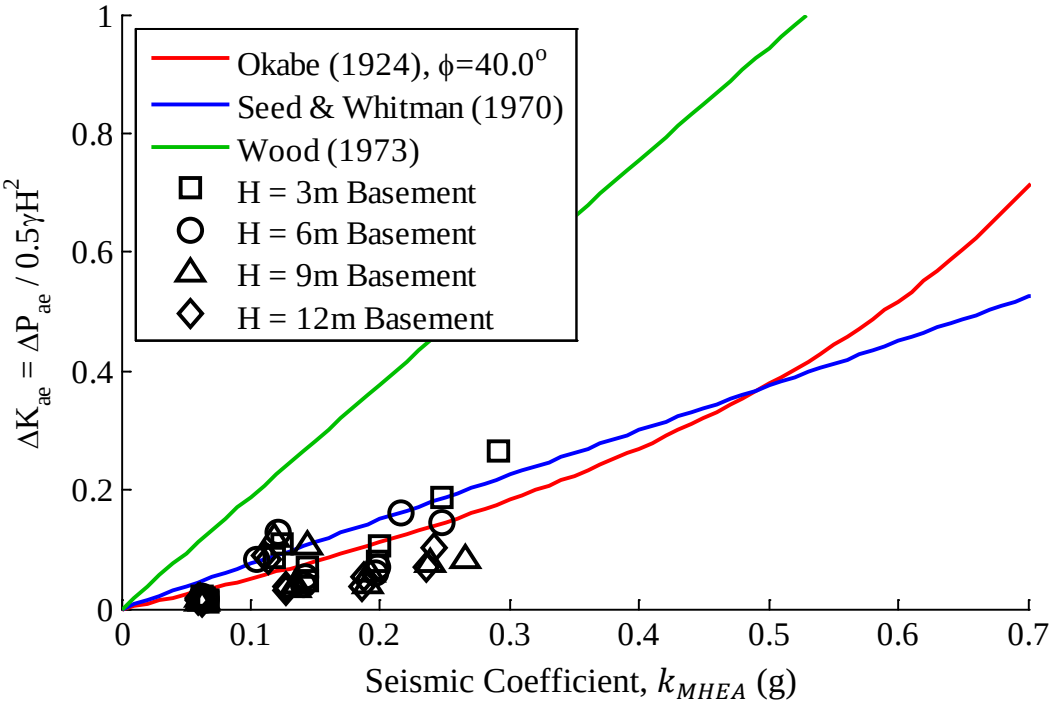

Figure 6.22: Computed coefficient of dynamic earth pressure increment versus seismic coefficient, k_{MHEA}, for three-bay, prototype basement structures, Site Class C

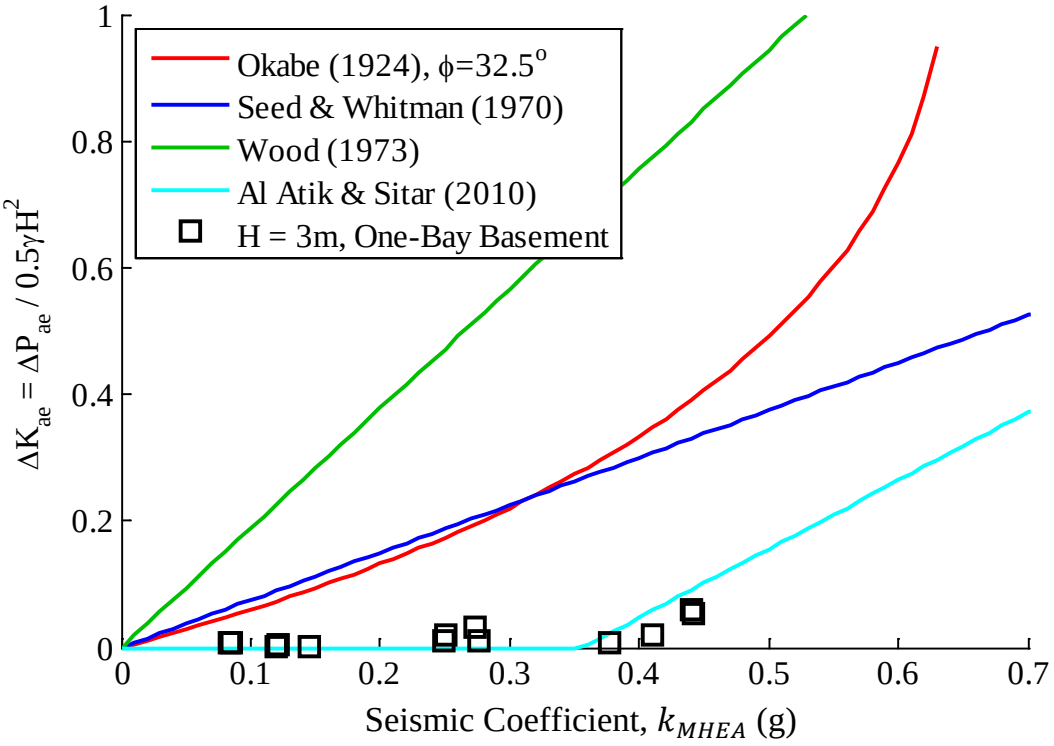

Figure 6.23: Computed coefficient of dynamic earth pressure increment versus seismic coefficient, k_{MHEA}, for one-bay, one-level prototype basement structure, Site Class D

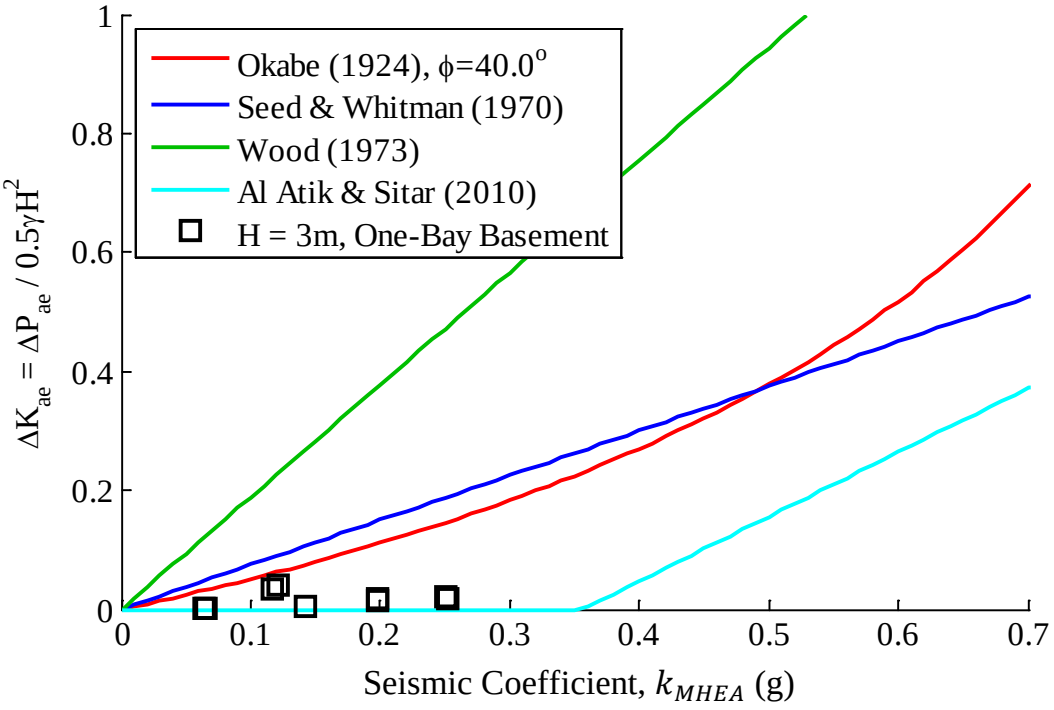

Figure 6.24: Computed coefficient of dynamic earth pressure increment versus seismic coefficient, k_{MHEA}, for one-bay, one-level prototype basement structure, Site Class C

7 Discussion, Conclusions & Design Recommendations

This research was comprised of three components: (1) physical modeling of seismically induced earth pressure on basement structures using a centrifuge experiment, (2) numerical modeling of the centrifuge experiment, and (3) numerical modeling of a series of prototype basement structures. The physical model consisted of a scaled model basement structure with dry, dense sand backfill. The physical model was densely instrumented with accelerometers, pressure transducers, load cells, and displacement transducers, and was subjected to a series of processed and filtered shaking events. The recorded data were then used to obtain static and dynamic loads, accelerations, velocities, and displacements and to infer dynamic earth pressure on the basement structure. The centrifuge experiment provided a well-documented case history to calibrate a two-dimensional finite difference model in FLAC^{2D}. The purpose of the numerical analysis was to validate the use of numerical models to capture the response of the soil-structure system and to calibrate the model for use in the analysis of the prototype structures. The numerical modeling of the prototype structures linked the findings from the centrifuge experiment to previous experimental studies. In this section, the results of the centrifuge experiment and numerical modeling are discussed in relation to current design recommendations.

7.1 Simplified Design Recommendations

7.1.1 Seismic Coefficient

Seed & Whitman (1970) proposed a seismic earth pressure coefficient $\Delta K_{ae} \approx 0.75 k_h$ where $k_h g$ is the horizontal acceleration. In their recommendations, they observed that "the peak ground acceleration occurs for only an instant and thus does not have sufficient duration to cause significant wall displacement" with the conclusion that the effective seismic coefficient (ground acceleration in the paper) should be (Equation 7.1)

$$k_h \approx 0.8 \frac{a_{max}}{g} \tag{7.1}$$

Noda et al. (1975), as summarized by Nozu et al. (2004), proposed an upper bound envelope for the equivalent seismic coefficient. Threshold seismic coefficients were obtained by back-analysis of 129 case histories of damaged and non-damaged quay walls at sites of non-liquefiable soils during 12 earthquakes (Figure 7.1). The equivalent seismic coefficient was defined as Equation 7.2:

$$k_e = \frac{a_{max}}{g}, \quad a_{max} < 0.2g; \qquad k_e = \frac{1}{3}\left(\frac{a_{max}}{g}\right)^{\frac{1}{3}}, \quad a_{max} \geq 0.2g \tag{7.2}$$

with an average relationship between equivalent seismic coefficient and PGA Equation 7.3:

$$k_e = 0.6 \frac{a_{max}}{g} \tag{7.3}$$

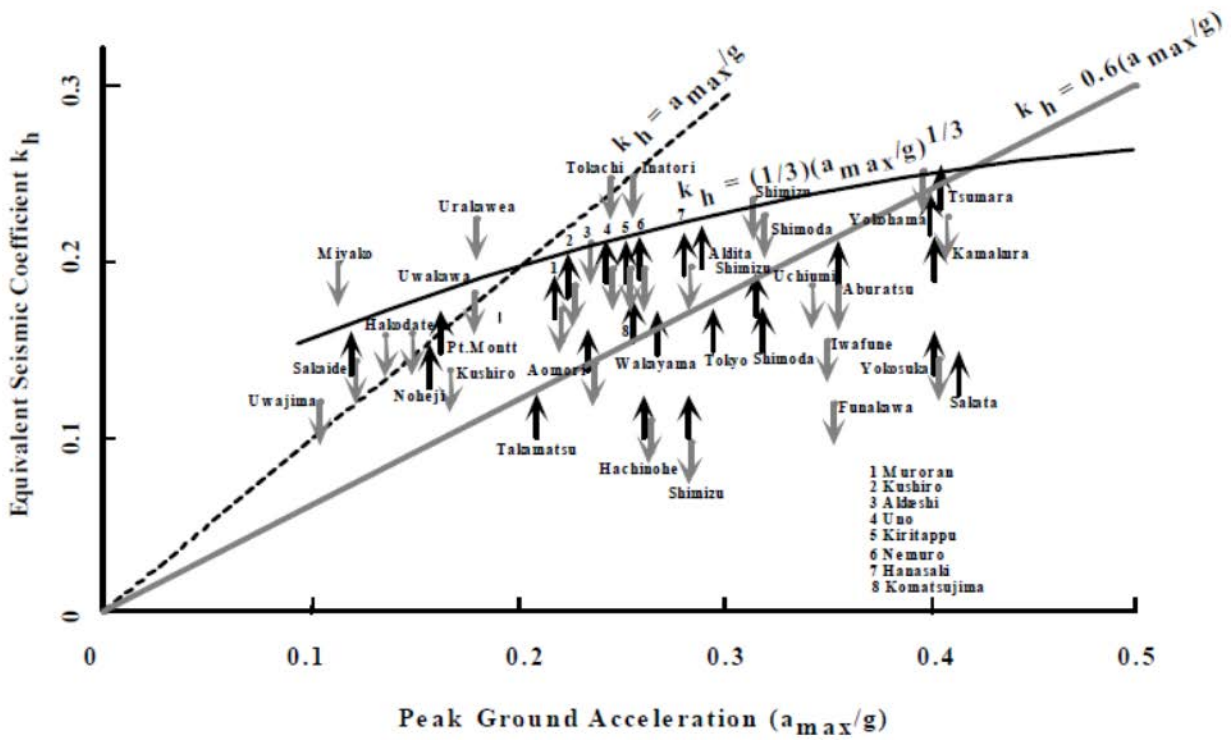

Figure 7.1: Equivalent seismic coefficient for gravity-type quay walls from Noda et al. (1975) (adapted from Nozu et al. (2004))

The equations for effective seismic coefficient proposed by Seed & Whitman (1970) and equivalent seismic coefficient proposed by Noda et al. (1975) are based on empirical studies of case histories of gravity and cantilever retaining walls, and quay walls of moderate (up to about 20 ft or 6 m) height and also on the results of shaking table tests of walls up to about 3 ft high. The profile of ground acceleration over a shallow depth is likely to be essentially uniform, as observed by Seed & Whitman (1970). Therefore, the approximations of Noda et al. (1975) and Seed & Whitman (1970) account for the necessary reduction of ground acceleration based on the peak acceleration occurring for only a short instant. The approximations do not account for incoherency of the ground motion throughout the depth of the backfill, which, for relatively short retaining structures, is essentially negligible. For deeper retaining structures and basement walls extending to greater depths (more than about 20 ft or 6 m), incoherency of the ground motion becomes more apparent and should be considered.

The National Cooperative Highway Research Program (NCHRP) Report 611 (Anderson et al., 2008) provides a procedure for assessing height-dependent seismic coefficients in Sections 6.1.2 and 7.5 of the report. Section 6.1.2 “Scattering Analysis for Retaining Walls” describes a numerical study using QUAD-4M of four retaining walls of varying heights (20 ft, 40 ft, 80 ft, 150 ft) with a sloped, uniform, linear elastic backfill on a uniform, linear elastic foundation subject to nine input motions separated into three categories based on spectral shape. The scaling factor α was computed by calculating the peak average seismic coefficient in three assumed

failure blocks per analysis and then dividing that result by the PGA at the surface. The values of α for each category of input motion (lower bound, mid-level, upper bound) were averaged together and these values were used to construct a graphical selection procedure based on wall height. Section 7.5 "Height-Dependent Seismic Design Coefficients" describes additional numerical studies of retaining walls with non-linear soil properties and an impedance contrast between the backfill and the foundation. The final recommendation for seismic coefficients to be used in seismic earth pressure calculations are based on a straight line approximation to the data for Site Class C, D, and E foundation soils (Equation 7.4a, b):

$$k_{avg} = \alpha k_{max} \quad \text{(a)} \qquad \alpha = 1 + 0.01H[(0.5\beta) - 1] \quad \text{(b)} \qquad \textbf{(7.4)}$$

where k_{max} is the peak seismic coefficient measured at the ground surface $(= F_{PGA}PGA)$, α is the fill height-dependent reduction factor, H is the fill height in feet, $\beta = F_v S_1 / k_{max}$, F_{PGA} is the short (0-2 second) period range site coefficient from NCHRP 20-07 $\left(= F_a = f(S_s, \text{site class})\right)$, F_v is the 1-second period site coefficient from NCHRP 20-07 $\left(= f(S_1, \text{site class})\right)$, S_s is the mapped short period spectral acceleration, and S_1 is the 1-second period spectral acceleration. For Site Class A and B foundation soils, the value of α should be increased by 20 percent, and for walls greater than 100 ft the value of α should be the value for H =100 ft. The values of α computed using Equation 7.4b are shown in Figure 7.2 with the recommendations of Seed & Whitman (1970) and Noda et al. (1975) for the effective seismic coefficient. For comparison, the measured data from the free field accelerometers in the centrifuge tests of Mikola & Sitar (2013), Candia & Sitar (2013), and the current study are shown.

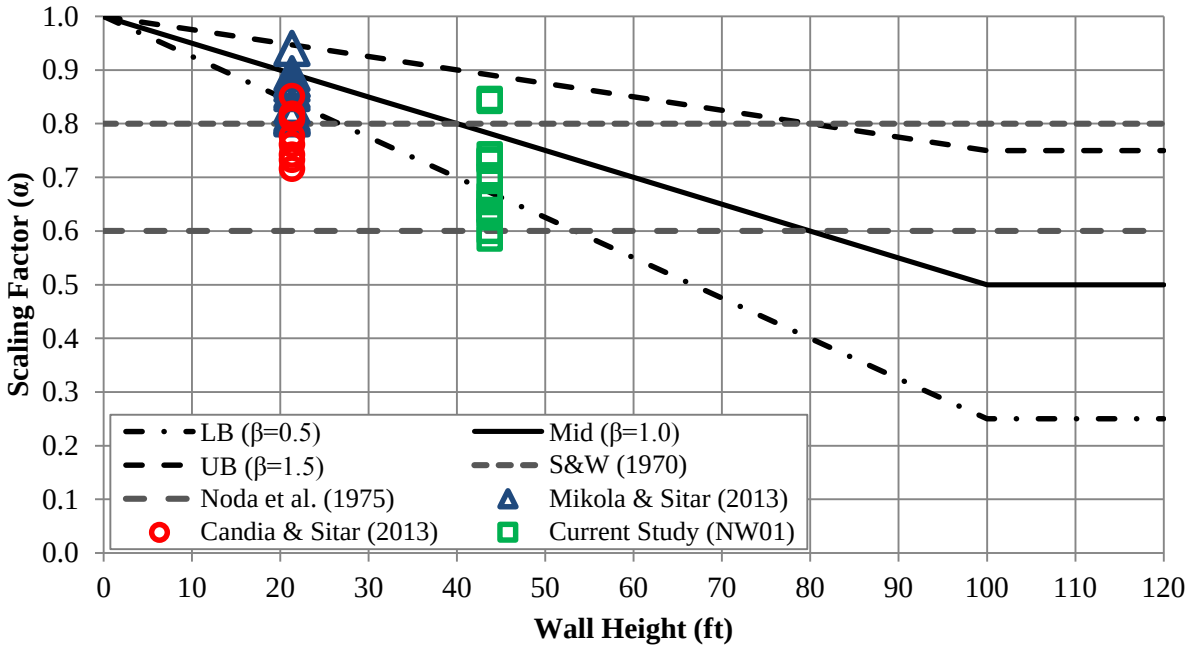

Figure 7.2: NCHRP Report 611 and observed height-dependent reduction factor versus wall height

Although the procedure is simple, NCHRP Report 611contains a few comments regarding the use of the procedure that are addressed herein. First, for walls less than 20 ft in height on firm ground (B/C foundation condition) the traditional assumption for design $(k_{avg} \approx k_{max})$ is recommended. Second, the height-dependent reduction accounts for wave scattering in the backfill but does not incorporate the difference between peak dynamic load and the average dynamic load. Therefore, an additional reduction may be justified and applied to the effective seismic coefficient provided the resulting seismic coefficient is very clearly defined for structural design purposes. Lastly, wall movements are not considered in the M-O method nor are they considered in the NCHRP Report 611 recommendations. For retaining walls that are allowed to translate and rotate a further reduction in the seismic coefficient may be justified. In fact, the FHWA-NHI-11-032 report (Kavazanjian et al., 2011) suggests modifying the design seismic coefficient, which has already been adjusted by α, as $k_s = 0.5k_{avg}$ to account for 1 to 2 inches of permissible permanent displacement. For non-displacing structures this reduction is likely unjustified, as no appreciable deformation is allowed or expected.

Candia, Sanhueza & Sitar (2014) computed the dynamic earth pressure coefficient using an equivalent-linear site response analysis combined with a rigid failure block retained by a rigid gravity wall. The total dynamic load was computed using Equation 7.5 and Equation 7.6, where the first is maximized with respect to the angle of inclination of the assumed failure wedge and the second is approximated based on the free field discretization (Figure 7.3). The seismic coefficient, k_h, can be computed as Equation 7.7.

$$P_{ae} = \frac{Q_h \cos(\alpha - \phi) + W \sin(\alpha - \phi) - C \cos\phi - C' \sin(\alpha - \phi)}{\cos(\alpha - \delta - \phi)} \tag{7.5}$$

$$Q_h = \int_0^{H_{wall}} \rho \frac{H_{wall} - z}{\tan\alpha} \ddot{u}_t(z,t)dz \approx \frac{\rho}{\tan\alpha} \sum_{i=1}^{N} (H_{wall} - z_i)\ddot{u}_t(z_i,t)\Delta z_i \tag{7.6}$$

$$k_h = \frac{Q_h}{W} = \frac{2}{H^2} \sum_{i=1}^{N} (H_{wall} - z_i) \frac{\ddot{u}_t(z_i,t)}{g} \Delta z_i \tag{7.7}$$

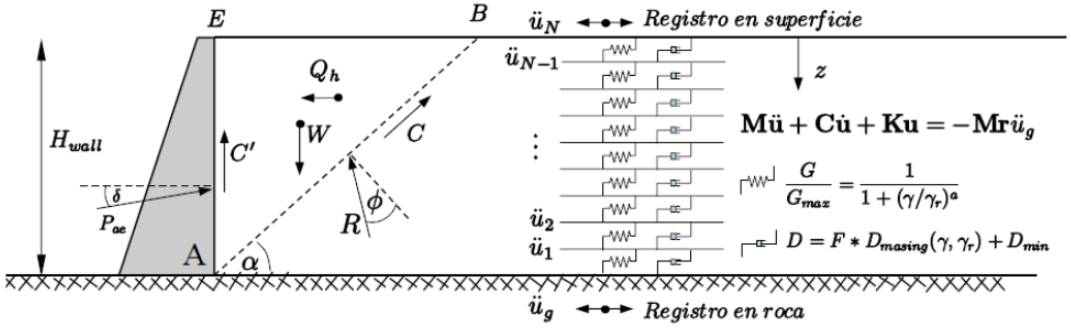

Figure 7.3: Simplified model of a retaining wall and viscoelastic backfill (from Candia, Sanhueza & Sitar, 2014)

Candia, Sanhueza & Sitar (2014) then compared the computed dynamic earth pressure coefficient measured in the equivalent-linear analysis to that estimated using the M-O method in a series of plots. However, the abscissa in the plots was the PGA measured at the surface rather than the seismic coefficient, k_h. It can be shown that if the data from the equivalent-linear analysis is correlated with k_h instead of the PGA measured at the surface, then the data from the equivalent-linear analysis will exactly coincide with the M-O method.

In light of these observations and analyses, two options are recommended as potential methods to compute the seismic coefficient for non-displacing basement structures: (1) obtain a design PGA and design site-specific response spectrum from a chart or code requirement and use the equations or chart in NCHRP Section 7.5 to obtain an appropriate height-dependent reduction factor for the PGA; or (2) perform a site response analysis including the backfill of the site and use the peak depth-averaged acceleration over the embedment depth of the structure as the equivalent seismic design coefficient. It can be shown that the code-based estimate is conservative compared to the results from the centrifuge for almost all of the cases considered. For this analysis, the code-based α is determined using two methods. In the first method, the response spectrum of the base input record in the centrifuge experiments is scaled according to the code procedure, and S_s and S_1 are selected from the measured response spectrum of the base input. The site-specific factors F_{PGA} and F_v are selected assuming Site Class D, and then the computed values of β and α are determined (Figure 7.4). In the second method, the response spectrum of the surface recording in the centrifuge experiments is used; the site-specific factors F_{PGA} and F_v are not included since the response spectrum is already scaled to the surface (Figure 7.5). Thus, two modifications to the equations are necessary, namely $k_{max} = PGA_{surface}$ and $\beta = S_1/k_{max}$. As before, the measured values of α are computed by dividing the seismic coefficient by the peak acceleration at the surface. For a displacing retaining structure, an alternative method proposed by Bray et al. (2010) incorporating allowable displacement is recommended.

A possible explanation for the conservatism is due to the formulation of the problem in the NCHRP Report 611. The seismic coefficient, whether it was for the case of an embankment slope or a retaining wall with a sloping backfill, was computed by dividing the seismic force induced by the earthquake in the assumed failure block by the weight of the failure block. The failure block is defined to start at the toe of the slope or the heel of the retaining wall, thus it approximately resembles an inverted triangle. This definition of the seismic coefficient is therefore biased toward the accelerations at the top of the assumed failure block, thus producing a higher predicted height-dependent reduction factor. The same is true for the analysis conducted by Candia, Sanhueza & Sitar (2014). For the experimental results, there is no assumed failure block because the retaining structures are not free to displace. Therefore, the accelerations at various depths are uniformly weighted in the evaluation of the seismic coefficient as defined herein. This causes the measured height-dependent reduction factor to be lower for a non-displacing retaining structure compared to a displacing retaining structure.

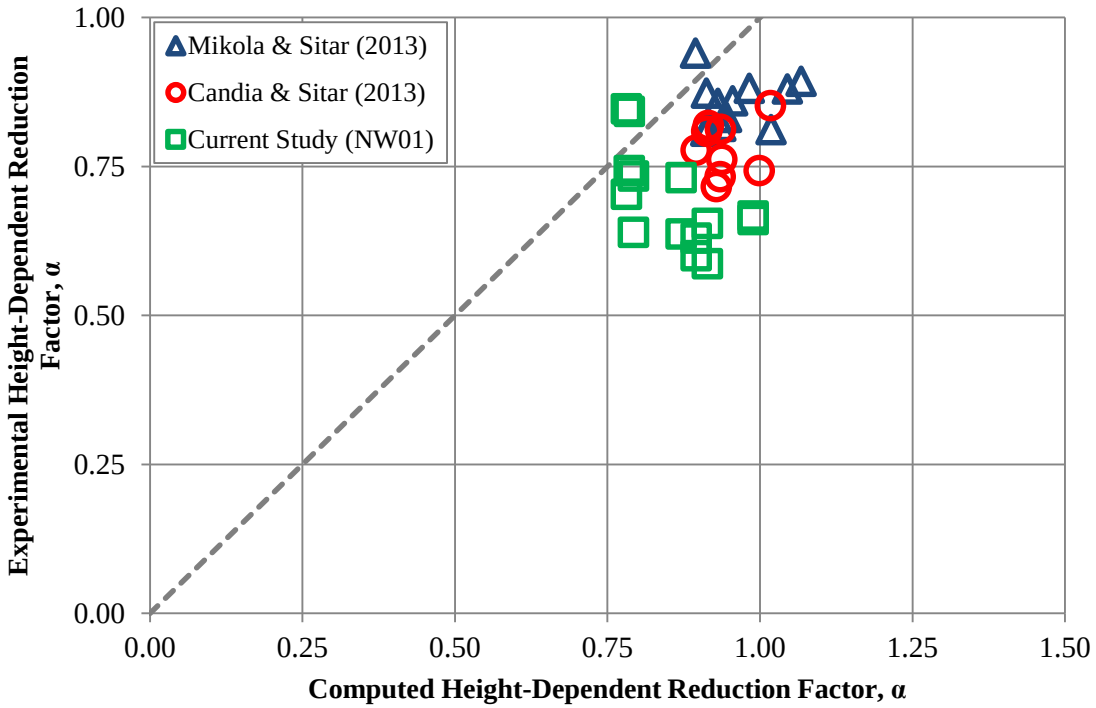

Figure 7.4: Experimental versus NCHRP Report 611 height-dependent reduction factor using base input

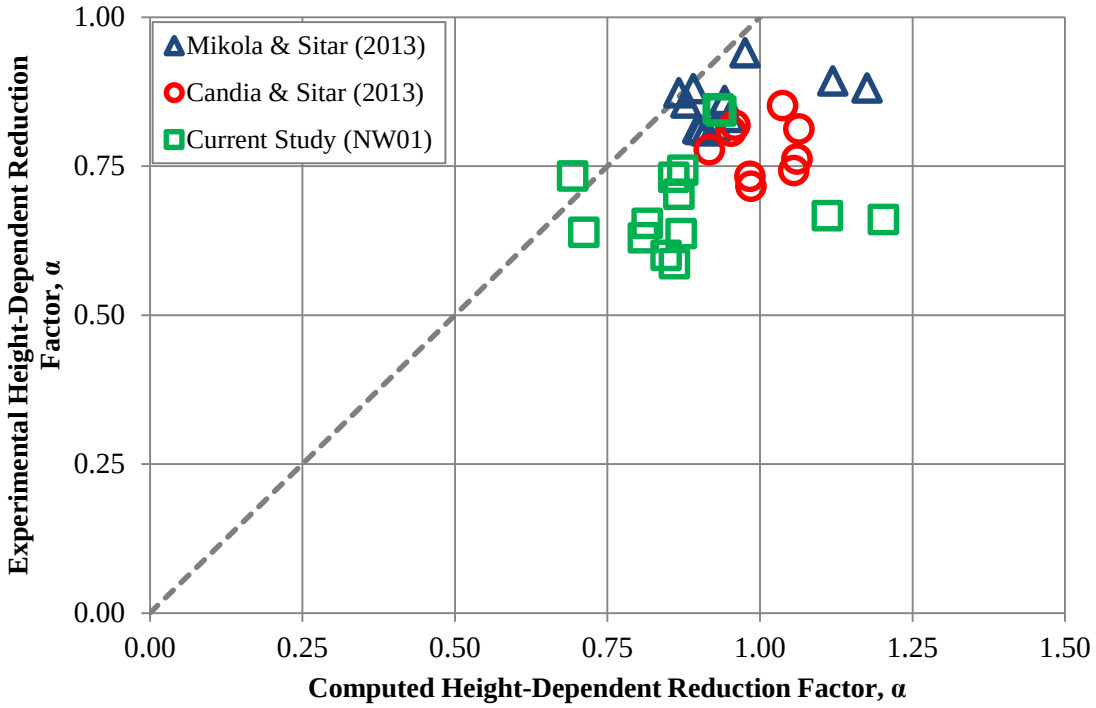

Figure 7.5: Experimental versus NCHRP Report 611 height-dependent reduction factor using surface recording

A final historical note worth revisiting concerns the use of height-dependent seismic coefficients in other geotechnical earthquake engineering applications. Makdisi & Seed (1978) extended the findings of Seed & Martin (1966) and developed a procedure for estimating permanent seismic deformation of embankment dams based on case histories and finite element analyses where the seismic coefficient is reduced depending on the assumed depth of sliding (Figure 7.6). In fact, Section 8.2.2 of the NCHRP Report 611 comments that this reduction should be considered equivalent to α in terms of its use, namely that wave scattering effects need to be considered for deep slides and structures. More recent studies (Bray et al., 1998; Bray & Travasarou, 2007) also account for non-uniform acceleration throughout the depth of sliding as MHEA; however, the computation is embedded within other correlations in the procedures.

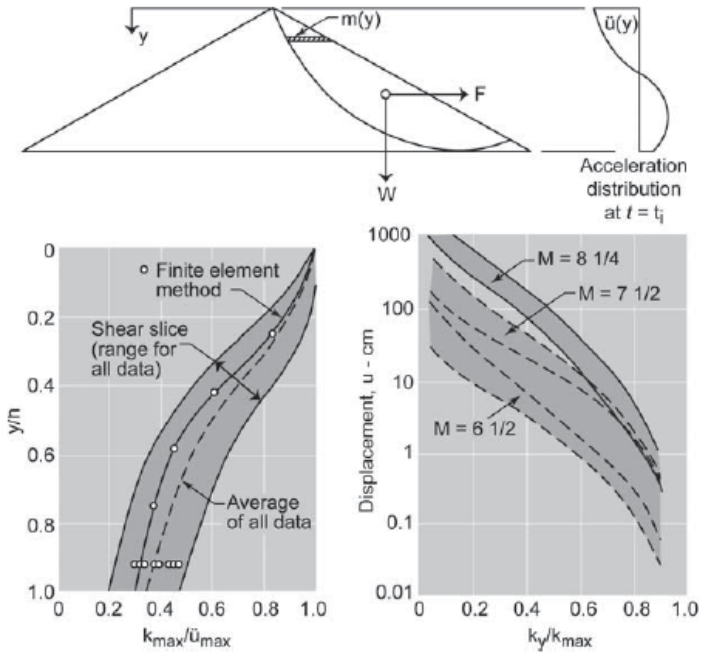

Figure 7.6: Permanent seismic deformation charts from Makdisi & Seed (1978) (adapted from Anderson et al. (2008))

Seed & Idriss (1971) developed a procedure for estimating the cyclic stress ratio for liquefaction hazard assessment. The procedure computes the cyclic stress ratio as Equation 7.8:

$$CSR_{eq} = 0.65 \cdot CSR_{peak} = 0.65 \left(\frac{a_{max}}{g}\right)\left(\frac{\sigma_v}{\sigma_v'}\right) r_d \qquad \textbf{(7.8)}$$

where $r_d = (\tau_{max})_{real}/(\tau_{max})_{rigid\ body}$ is a non-linear shear mass participation factor (or shear stress reduction parameter). More recent studies (Golesorkhi, 1989; Idriss, 1999; Cetin et al., 2004; Kishida et al., 2009) have correlated r_d with depth, earthquake and ground motion characteristics, and the dynamic soil properties of the deposit. Similar to the work of Makdisi & Seed (1978), a non-linear reduction in demand with increasing depth aligns with the results of the experiments and analyses performed as a part of this study.

7.1.2 Seismic Earth Pressure Resultant

To determine the magnitude of the seismic earth pressure resultant, it is recommended to use the M-O method with an appropriate value of the seismic coefficient (from Section 7.1.1), selecting the friction angle (ϕ_f) to correspond with the expected deformation level. This accounts for the friction angle not being fully mobilized. Displacing retaining structures are generally designed for active earth pressure, which assumes full mobilization of the frictional resistance of the backfill. Non-displacing retaining structures may not move away from the backfill far enough to fully mobilize the frictional resistance of the soil, so some reduction of the friction angle could be warranted. For a low value of the seismic coefficient ($k_{MHEA} \lesssim 0.3$), the selection of ϕ_f does not significantly affect the estimated value of dynamic earth pressure resultant. For higher values of the seismic coefficient, selecting ϕ_f too small will cause the M-O equation to be undefined. At this time, the data are insufficient to fully characterize an appropriate mobilized friction angle for design purposes. Therefore, it is recommended for now that the peak friction angle should be used in the computation to maintain consistency with current design approaches.

7.1.3 Seismic Earth Pressure Distribution

The M-O method states that the resultant of the total (static and dynamic) earth pressure acts at a point one-third the distance from the base of the wall ($h = H/3$), following Coulomb (1776). After subtracting out the static earth pressure, the resultant of which acts at $h = H/3$ as well, it is obvious that the dynamic earth pressure resultant acts at the same location. The implication is that the dynamic earth pressure distribution is assumed to linearly increase with depth, hence a triangular distribution starting at zero at the top of the wall. If the dynamic horizontal earth pressure is assumed to be governed by a relationship similar to that of static horizontal earth pressure (i.e., $K = \sigma_h/\sigma_v$) and the vertical stress is linearly increasing with depth as $\sigma_v = \gamma z$, it is possible to infer a functional form of a coefficient of dynamic horizontal earth pressure, ΔK, as a function of depth. For the case of the M-O method, $\Delta K(z)$ must be constant and equal to ΔK_{ae}; this is consistent with assuming a constant static active, passive, or at-rest coefficient of horizontal earth pressure. The graphical relationship is shown in Figure 7.7.

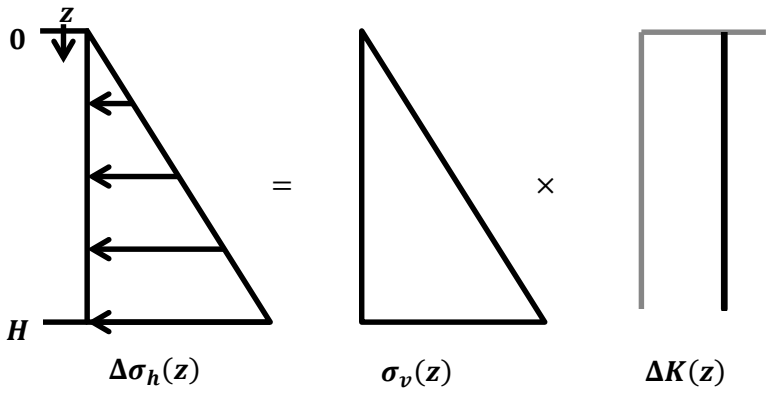

Figure 7.7: Dynamic earth pressure coefficient ΔK implied by triangular distribution

Seed & Whitman (1970) proposed that the resultant of the dynamic earth pressure acts at a point $h = 0.6H$ from the base of the wall. What has been assumed in practice is that this implies an inverted triangular distribution starting at zero at the base of the wall. For this case, the implied functional form of $\Delta K(z)$ is not constant with depth; the coefficient must be zero at the base of the wall and infinite at the surface. While this analysis extends the assumptions of soil mechanics beyond their intended use, the implications that result are worth exploring. The graphical relationship is shown in Figure 7.8; the equations are shown in Equation 7.9 and Equation 7.10.

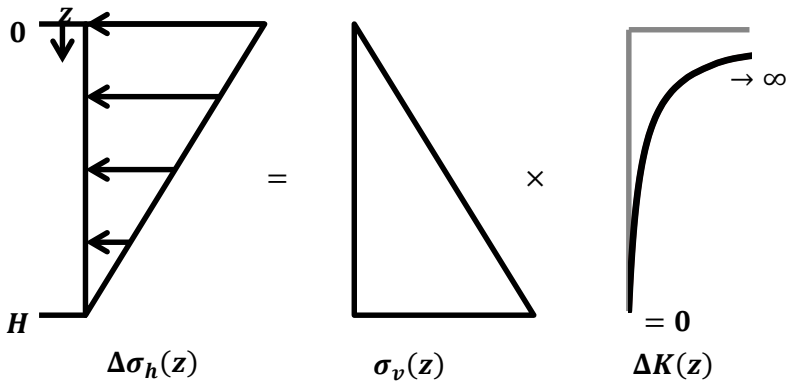

Figure 7.8: Dynamic earth pressure coefficient ΔK implied by inverted triangular distribution

$$\Delta\sigma_h(z) = \Delta K_{ae}\gamma(H - z) \quad \textbf{(7.9)}$$

$$\Delta K(z) = \Delta K_{ae}\left(\frac{H}{z} - 1\right) \quad \textbf{(7.10)}$$

For the case of the dynamic load being applied at $h = 0.5H$, a potential solution is such that the distribution of dynamic earth pressure is uniform. At first glance, the functional form of $\Delta K(z)$ may seem to be simple, but in fact it is just as intriguing as for the inverted triangular distribution; the coefficient is non-zero at the base of the wall and infinite at the surface. The graphical relationship is shown in Figure 7.9; the equations are shown in Equation 7.11and Equation 7.12.

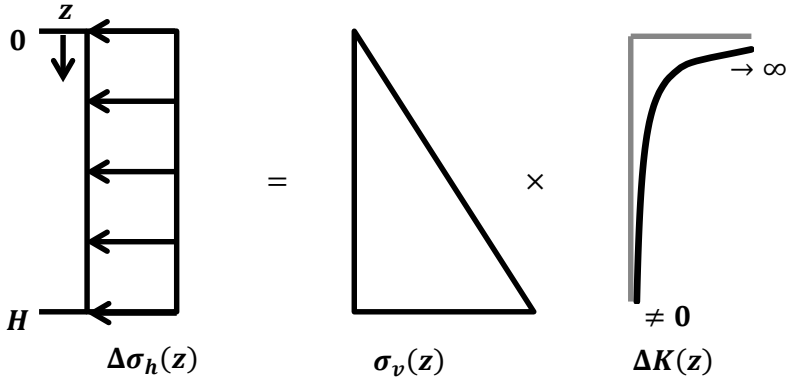

Figure 7.9: Dynamic earth pressure coefficient ΔK implied by uniform distribution

$$\Delta\sigma_h(z) = \frac{1}{2}\Delta K_{ae}\gamma H \tag{7.11}$$

$$\Delta K(z) = \frac{1}{2}\Delta K_{ae}\frac{H}{z} \tag{7.12}$$

In light of this analysis, it is clear that an assumed non-zero dynamic earth pressure at the surface level of a wall implies an unrealistic solution with regards to the ratio of the horizontal stress and vertical stress. Additionally, it is important to note that the Seed & Whitman (1970) method does not make an assumption about the distribution of the earth pressure, but instead only specifies the point of application of the dynamic component for design purposes; the implied distribution is purely a mathematical construction. However, recall that the point of application of the resultant is specified at $h = 0.6H$, which does not correspond to a triangular distribution. To alleviate this inconsistency, a cubic distribution of earth pressure was developed. The graphical relationship is shown in Figure 7.10; the equations are shown in Equation 7.13 and Equation 7.14.

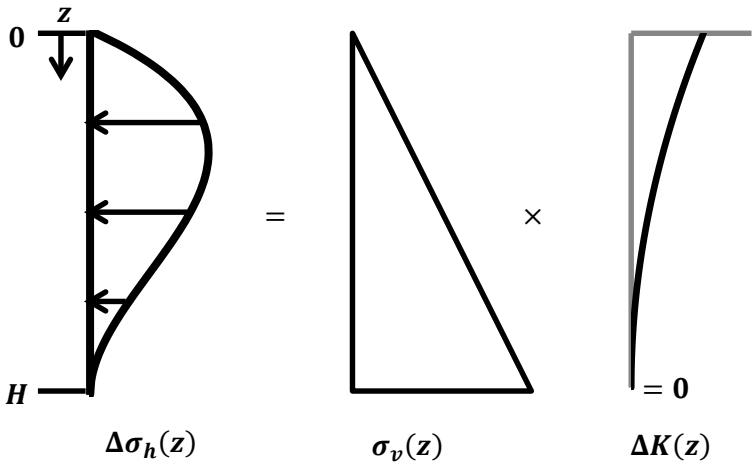

Figure 7.10: Dynamic earth pressure coefficient ΔK implied by cubic distribution

$$\Delta\sigma_h(z) = 6\Delta K_{ae}\gamma z\left(1 - \frac{z}{H}\right)^2 \tag{7.13}$$

$$\Delta K(z) = 6\Delta K_{ae}\left(1 - \frac{z}{H}\right)^2 \tag{7.14}$$

While more complicated than an inverted triangular distribution, the cubic distribution of dynamic earth pressure has two advantages. First, the implied coefficient of dynamic horizontal earth pressure is finite at the boundaries. Second, the point of application of the resultant of the dynamic earth pressure distribution is $h = 0.6H$ from the base of the retaining structure (Equation 7.15). Also, the resultant of the dynamic earth pressure distribution is directly comparable to the (inverted) triangular distribution (Equation 7.16).

$$h = H - \frac{\int_0^H z\sigma_{h,D}(z)dz}{\int_0^H \sigma_{h,D}(z)dz} = H - \frac{\int_0^H z\left[z\left(1-\frac{z}{H}\right)^2\right]dz}{\int_0^H \left[z\left(1-\frac{z}{H}\right)^2\right]dz} = 0.6H \quad \textbf{(7.15)}$$

$$\Delta P_{ae} = \int_0^H \Delta\sigma_h(z)dz = 6\Delta K_{ae}\gamma \int_0^H \left[z\left(1-\frac{z}{H}\right)^2\right]dz = \frac{1}{2}\gamma H^2 \Delta K_{ae} \quad \textbf{(7.16)}$$

Alternatively, an "inverted" cubic distribution was developed that merely inverts the previous cubic distribution (Equation 7.17 and Equation 7.18). This is analogous to including some curvature in the Mononobe-Okabe method, and consequently shifts the point of application of the resultant to $h = 0.4H$. In fact, a static distribution of this form was proposed, but not expressed mathematically, in Terzaghi (1934b).

$$\Delta\sigma_h(z) = 6\Delta K_{ae}\gamma z\left(1-\frac{z}{H}\right)\frac{z}{H} \quad \textbf{(7.17)}$$

$$\Delta K(z) = 6\Delta K_{ae}\left(1-\frac{z}{H}\right)\frac{z}{H} \quad \textbf{(7.18)}$$

A piecewise linear approximation to the cubic distribution was developed such that the implied coefficient of dynamic horizontal earth pressure is finite at the boundaries and the point of application of the resultant of the dynamic earth pressure distribution is $h = 0.6H$. Note that this distribution is essentially a hybrid between the implied distributions of the Mononobe-Okabe and Seed & Whitman (1970) methods. The graphical relationship is shown in Figure 7.11; the equations are shown in Equation 7.19 and Equation7.20. The piecewise linear distribution can be adjusted to provide any desired point of application of the resultant.

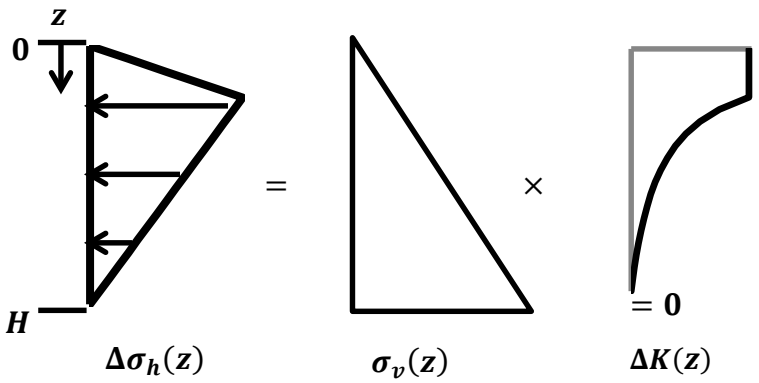

Figure 7.11: Dynamic earth pressure coefficient ΔK implied by piecewise linear distribution

$$\begin{aligned} \Delta\sigma_h(z) &= 5\Delta K_{ae}\gamma z \quad z/H < 0.2 \\ \Delta\sigma_h(z) &= \frac{5}{4}\Delta K_{ae}\gamma(H-z) \quad z/H \geq 0.2 \end{aligned} \quad \textbf{(7.19)}$$

$$\begin{aligned} \Delta K(z) &= 5\Delta K_{ae} \quad z/H < 0.2 \\ \Delta K(z) &= \frac{5}{4}\Delta K_{ae}\left(\frac{H}{z}-1\right) \quad z/H \geq 0.2 \end{aligned} \quad \textbf{(7.20)}$$

Lastly, a parabolic distribution was developed such that the implied coefficient of dynamic horizontal earth pressure is finite at the boundaries and the point of application of the resultant of the dynamic earth pressure distribution is $h = 0.5H$. Note that this distribution is essentially an extension of the uniform distribution that alleviates the issues of an infinite coefficient at the surface. The graphical relationship is shown in Figure 7.12; the equations are shown in Equation 7.21 and Equation 7.22. A half-period sinusoidal distribution could also be used to produce an equivalent distribution.

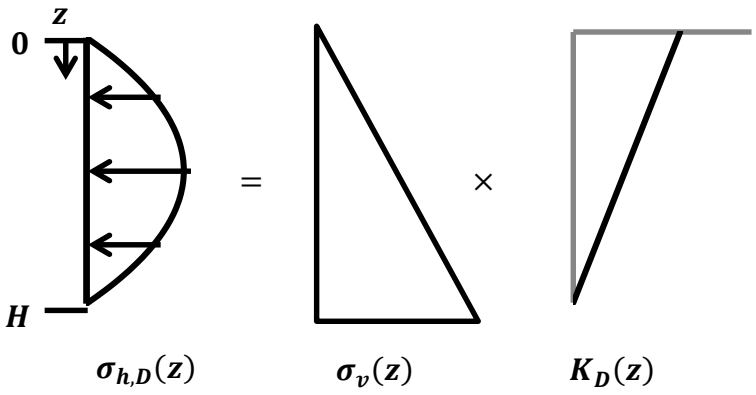

Figure 7.12: Dynamic earth pressure coefficient ΔK implied by parabolic distribution

$$\Delta\sigma_h(z) = 3\Delta K_{ae}\gamma z\left(1 - \frac{z}{H}\right) \quad \textbf{(7.21)}$$

$$\Delta K(z) = 3\Delta K_{ae}\left(1 - \frac{z}{H}\right) \quad \textbf{(7.22)}$$

For comparison, the six dynamic earth pressure distributions are normalized by $\Delta K_{ae}\gamma H$ and plotted in Figure 7.13. Also, the total earth pressure distributions for $K_A = 0.27$ (static active earth pressure with $\phi = 35°$) and $\Delta K_{ae} = 0.2$ (corresponding to a seismic coefficient $k_h \approx 0.25 - 0.30$ using M-O or Seed & Whitman, 1970) are normalized by γH and plotted in Figure 7.14.

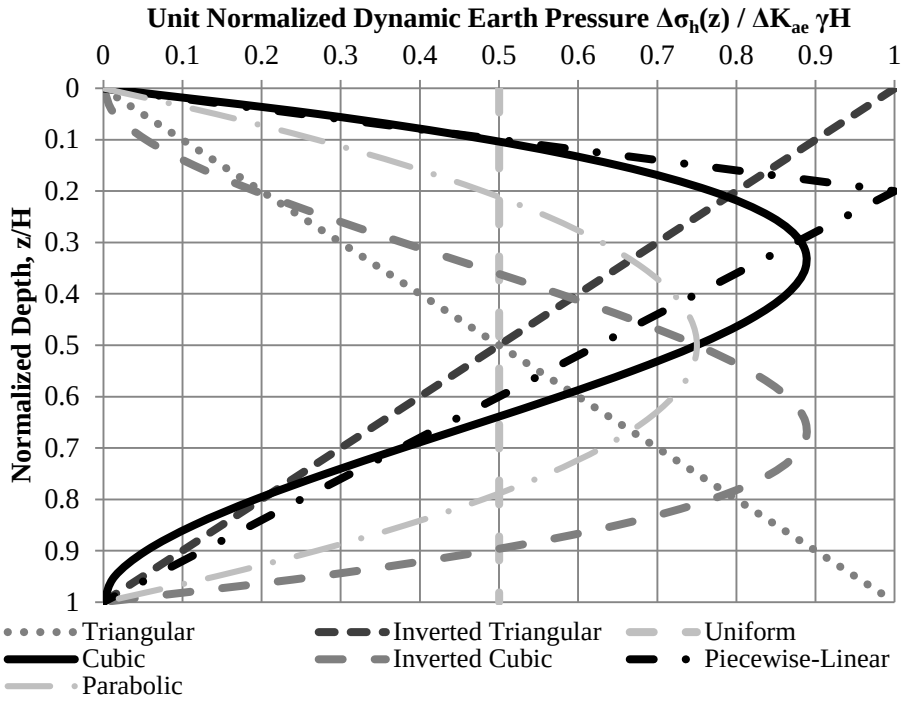

Figure 7.13: Unit normalized dynamic earth pressure versus normalized depth

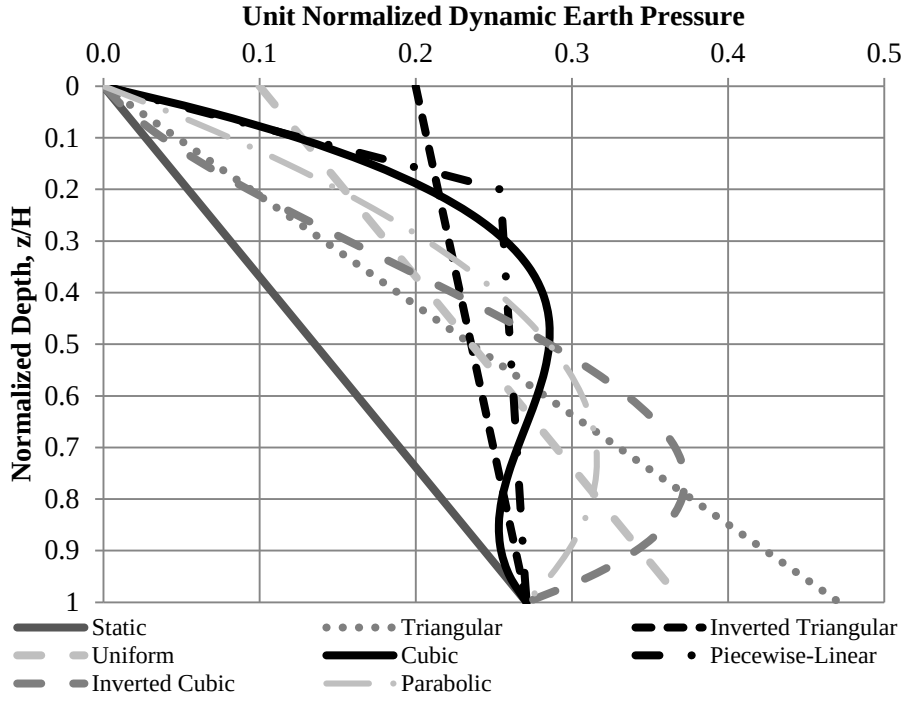

Figure 7.14: Normalized total earth pressure versus normalized depth for K_A= 0.27 (static active pressure with $\phi = 35°$) and ΔK_{ae}= 0.2

For the deep basement structure seismic earth pressure distribution in the centrifuge and the corresponding numerical model in FLAC is complex, but approximately bilinear. In the numerical models the pressure increased linearly from zero at the surface until a depth of approximately 1/3 *H*, where *H* is the depth of embedment of the basement wall, and then decreased to approximately zero at the base of the wall. For the prototype basement structure, the seismic earth pressure distribution depends on the depth of embedment of the structure. For the one- and two-level basement structures, the seismic earth pressure distribution is approximately linear. This is consistent with previous studies regarding seismic earth pressure on braced basement structures up to 6m in height (Mikola & Sitar, 2013; Candia & Sitar, 2013). For the three- and four-level basement structures, the seismic earth pressure distribution is approximately linear for low to moderate intensity ($\mathrm{PGA}_{ff} \lesssim 0.3g$) ground excitation and approximately uniform for high intensity ($\mathrm{PGA}_{ff} \gtrsim 0.4g$) ground excitation.

The difference between the two observed distributions for deep basement structures seems to come from the relative stiffness of the structures compared to the soil profile. The structure in the centrifuge and the corresponding numerical model were made of aluminum and were quite thick whereas the prototype structure had properties corresponding to a reasonably sized concrete basement. The numerical model of the centrifuge structure used a flexural rigidity of $(EI)_{centrifuge} = 2.28 \times 10^6$ kN $\cdot$ m^2/m and the numerical model of the prototype structure used $(EI)_{prototype} = 5.14 \times 10^5$ kN $\cdot$ m^2/m. The effective lateral stiffness (k_{lat}) of the prototype basement structures using a simple frame model and static condensation (Chopra, 2011) are listed in Table 7.1. Additionally, relative flexibility values $d_w = G_{avg}/k_{lat}$ (modified from Veletsos & Younan, 1997) are shown for the two site classes prior to dynamic excitation (the values of d_w decreases as the shear modulus of the backfill degrades).

Table 7.1: Effective lateral stiffness of prototype basement structure and relative flexibility

Structure Geometry	k_{lat} $(MN/m/m)$	d_w Site Class D	d_w Site Class C
1 level, 3 bays	210.0	0.21	2.27
2 levels, 3 bays	210.8	0.29	2.50
3 levels, 3 bays	252.9	0.30	2.22
4 levels, 3 bays	137.8	0.65	4.30
1 level, 1 bay	80.2	0.54	5.94

Using the definition of relative wall flexibility from Veletsos & Younan (1997), the prototype structures are very stiff when embedded in the Site Class D profile and are somewhat flexible when embedded in the Site Class C profile. Thus, the relative stiffness of the structure compared to the surrounding medium is very important to understand how to classify a structure as “rigid” or “flexible”. Jung & Bobet (2008), utilizing the problem formulation of Veletsos & Younan (1997), computed dynamic earth pressure distributions for “extreme” cases of wall-soil systems in ABAQUS, as shown in Figure 7.15.

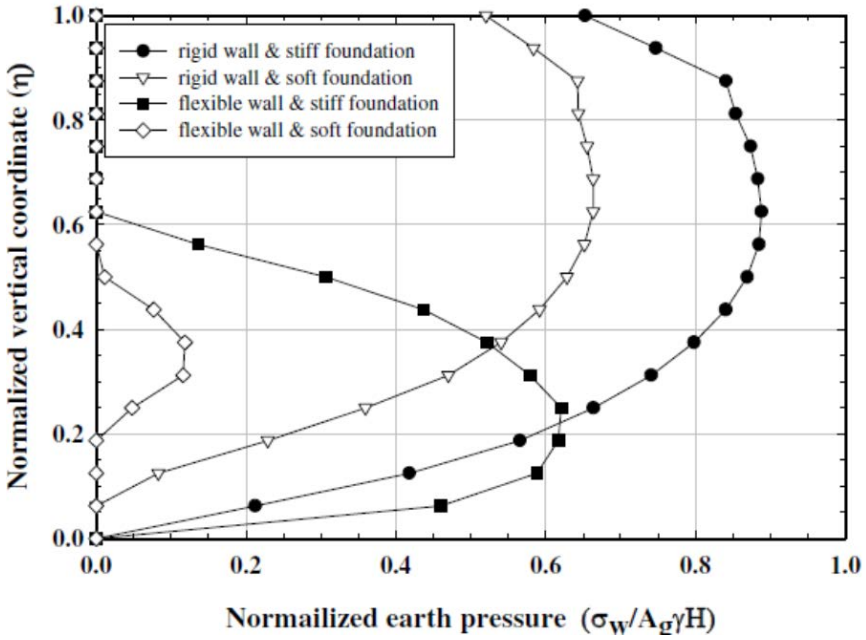

Figure 7.15: Distribution of normalized seismic earth pressure (from Jung & Bobet, 2008)

The cases considered are 1) a rigid wall on a stiff foundation, 2) a rigid wall on a soft foundation, 3) a flexible wall on a stiff foundation, and 4) a flexible wall on a soft foundation. The effects of foundation flexibility on the shape of the distribution are not as significant as the effects of the wall flexibility. Increasing flexibility of the entire system tends to decrease the magnitude of the earth pressure, regardless of the source. Considering the distributions developed by Jung & Bobet (2008) and the results of the numerical modeling of the tall basement walls ($\gtrsim$ 6 m) presented in this study, the normalized analytic distributions developed previously are recommended. For a relatively rigid wall ($d_w < 1$), the cubic distribution of dynamic earth pressure with the point of application at $h = 0.6H$ (Equation 7.14) is recommended. For a relatively flexible wall ($d_w > 5$), the cubic distribution of dynamic earth pressure with the point of application at $h = 0.4H$ (Equation 7.18) is recommended. For a wall in the transition regime ($1 < d_w < 5$), the parabolic distribution of dynamic earth pressure with the point of application at $h = 0.5H$ (Equation 7.22) is recommended.

Note that sliding deformation of the retaining structure relative to the soil foundation was not assessed in Veletsos & Younan (1994a, 1994b, 1997), which also neglects the ability of a shorter basement wall ($\lesssim$ 6 m) to translate as a rigid body with the backfill and soil foundation. Similar to the case of static earth pressure, a rigid body translation of the wall induces an approximately triangular distribution of dynamic earth pressure. This reasonably explains the dynamic earth pressure distribution computed in the numerical analyses of the short basement walls and observed by Mikola & Sitar (2013) and Candia & Sitar (2013).

7.2 Numerical Modeling Recommendations

Computed dynamic earth pressures are highly sensitive to input soil properties, the constitutive model that is used, the interface stiffness, and formulation of the contact law. It is important to use a rational approach to assign soil properties based on a realistic soil profile; i.e., increasing density, bulk and shear stiffness with increasing depth in a soil stratum. For shallow basement structures, this is not as important since the variation in soil properties from the top to the bottom of the wall is generally not that large; however, this is not the case for deep basement structures.

The constitutive model governing the shear modulus degradation and damping characteristics of the soil are important, as demonstrated in Section 5.4. While modulus degradation due to monotonic loading was reasonably well captured by both the sigmoidal model and UBCHyst, the former did not account for permanent modulus reduction upon strain reversal. UBCHyst did provide a means to account for such a phenomenon. However, the modulus degradation and permanent modulus reduction were related to the development of shear stress instead of the development and accumulation of shear strain. A more sophisticated constitutive model would be more appropriate, but the development and calibration thereof was beyond the scope of work.

Although ultimately not used in the numerical modeling, interface elements can cause problems for determining both static and dynamic earth pressures. The interface through which the stress is transferred has a large effect on the measured loads. In FLAC, for instance, the forces in the interfaces are calculated based on the amount of displacement occurring across elastic normal and shear springs with specified tensile and shear strengths. One of the limitations in FLAC is that a constant stiffness must be specified for each interface; the reality of increasing soil stiffness with increasing depth is therefore tedious, but not especially difficult, to model. For shallow basement structures, this is not of much concern as the variation of soil properties over the depth of the structure is not particularly great. However, this becomes important when increasing the depth of embedment in a soil profile with stiffness increasing with depth or a layered soil profile with different soil types. In light of this, connecting the structure elements rigidly to the soil grid, while refining the soil grid in close proximity to the structure, allowed for nonlinear stiffness. One may argue that this connection does not allow sliding or separation between the structure elements and the soil grid; however, in this study neither of these issues was applicable because the basement structures essentially moved with the soil.

Not quite as important, but noteworthy nonetheless, is the modeling sequence itself. In the analyses performed in this study the numerical model of the centrifuge experiment was initialized by first defining and equilibrating the soil domain within the model, and then removing the void and installing the structure (as if it were “wished” into place). A 0.2 sec period of “quiet time” allowed slight numerical oscillations from switching between static and dynamic calculation modes in FLAC to dissipate. Then, a design motion was applied to measure dynamic earth pressures. This sequence provided good agreement between the numerical models and the physical experiments, but the rationale behind it may be lacking. If a different problem

were to be analyzed or if different constitutive models for the soil or interface were used, perhaps a different modeling sequence would be more suitable. For the prototype structures, an excavation sequence was utilized wherein each 3 m level was excavated and allowed to equilibrate with horizontal earth pressure equal to static at-rest pressure applied to the sides of the excavation. This type of modeling sequence (i.e., excavation) was utilized in Taiebat et al. (2014); however, the results of that study were not calibrated with any physical models or case histories.

The structural model was not given much attention in this study beyond matching properties and dimensions of the centrifuge experiment and selecting typical values of the prototype structures. The connection between elements influenced the calculated earth pressure. In the numerical model of the centrifuge experiment, the connections were restrained in the translational directions, allowing force transfer from the walls to the struts and footings; rotational restraints were not included, so moment transfer was not allowed. The connections in the prototype basements were restrained in both the translational and rotational degrees of freedom. Initial trials of the numerical model of the prototype basement structures did not have rotational constraints between the walls and the floor slabs, and excessively large dynamic earth pressures were computed. When the rotational constraints between the walls and floor slabs were enabled, the computed dynamic earth pressures agreed well with the trends of the experimental results.

7.3 Recommended Procedures

Based on the above, the following procedures are recommended to calculate the dynamic loading of a retaining structure or basement due to seismic earth pressure in the order of increasing complexity:

1. Obtain the peak ground acceleration in the free field at the surface according to the regional design requirements. Use this value and the Seed & Whitman (1970) method to compute the seismic earth pressure resultant.
2. Obtain the peak ground acceleration in the free field at the surface according to the regional design requirements and reduce this value by the computed height-dependent reduction factor α according to NCHRP Report 611 Section 7.5. A further reduction may be used to account for displacement of the retaining structure according to the guidelines outlined in NCHRP Report 611. Alternatively, use the procedure described in Bray et al. (2010) to incorporate allowable displacements as well as incoherency of the backfill simultaneously to compute the seismic coefficient. Use this value and the M-O method to compute the seismic earth pressure resultant.
3. Perform a 1D site-response analysis and compute an “appropriate” value of the seismic coefficient over the depth of embedment of the retaining structure. For a displacing retaining structure, the seismic coefficient should be the average over an assumed failure wedge. For a non-displacing retaining structure, the seismic coefficient should be the average over the depth of embedment in the free field. Use this value and the M-O method to compute the

seismic earth pressure resultant. Further reductions are possible based on the allowable displacements.

4. Perform a calibrated dynamic analysis of the problem using a numerical analysis tool (e.g., finite elements, finite differences, etc.) and compute the demands on the structure.

For procedures 1, 2 and 3, the seismic earth pressure resultant should be located according to the normalized pressure distributions defined in Equation 7.14, 7.18 or 7.22 depending on the relative stiffness of the structure compared to the surrounding medium. Additionally, the depth of the structure should be considered. For short basement walls $\lesssim$ 6 m and for walls able to displace or slide (i.e. cantilever walls or gravity walls), the seismic pressure distribution is approximately triangular. For procedure 4, the seismic earth pressure distribution is determined in the numerical analysis directly.

For embedded structures, the dynamic earth pressure should be determined using a calibrated dynamic analysis of the problem using a numerical analysis tool (e.g., finite elements, finite differences, etc.). The relative mass and stiffness of the superstructure compared to the basement will introduce further soil-structure interaction (SSI) effects that cannot be adequately characterized in a simplified model. Although the present study offers a starting point for what the distribution of seismically induced loads might be for basement structures, extrapolating the findings to general embedded structures is not appropriate at this time given the simplicity of the structures that were modeled. For example material nonlinearities in the structure were not considered. These have the potential to allow energy dissipation within the structure, further reducing the loads. Alternatively, material nonlinearities in the structure may increase the response of the superstructure, thus increasing the inertial interaction in the entire system. This issue does not lend itself to simplified chart solutions or simplified procedures.

7.4 Limitations & Suggestions for Future Work

Numerical modeling can provide insight into the fundamental mechanisms that are important for determining seismic earth pressure. However, the results are highly sensitive to every aspect of the modeling process. Additionally, three dimensional effects should be explicitly incorporated into the numerical model when possible. Two dimensional analyses, specifically those of partially embedded structures, are inadequate for representing truly three dimensional problems. Nonlinearity should be incorporated into both the soil and structure to properly simulate the energy dissipation in the global system. Therefore, more case histories and experimental, centrifuge, work with deeper basement walls and partially embedded structures are essential to use as calibration benchmarks.

It is also necessary to investigate the effect of wall movement during dynamic excitation on the seismic loads. This will inherently include the mobilized friction angle in the soil. The Mononobe-Okabe method, by extension of the Coulomb (1776) analysis, assumes that the retaining structure has moved sufficiently to fully engage the frictional resistance of the backfill

material. Even in static tests performed by Terzaghi (1934a), back-calculated friction angles corresponding to the measured loads implied a lower friction angle. Arching effects in the soil prior to slip were thought to be the likely cause of the reduced loads, as well as the higher point of application of the observed static earth pressure.

Finally, the effect of frequency content of the ground motion on the seismic loads should be investigated further. Shallow embedded structures are more susceptible to higher frequency motion and deep embedded structures are more susceptible to lower frequency motion. The seismic coefficient as defined herein does not explicitly account for the frequency content of the ground motion. However, larger ground motions generally have more low frequency content due to the seismological aspects of ground motion propagation, so this effect is implicitly included. The analytic elastic solutions of Veletsos & Younan (1994a, 1994b, 1997) and Younan & Veletsos (2000) offer a starting point that can be compared to centrifuge tests to investigate the effects of real soil behavior in combination with the frequency content.

References

Ahmadi, E., Khoshnoudian, F., Hosseini, M. (2015). "Importance of soil material damping in seismic response of soil-MDOF structure systems." *Soils and Foundations*, Japanese Geotechnical Society, Vol. 55, No. 1, pp. 35-44.

Al Atik, L., Sitar, N. (2010). "Seismic earth pressures on cantilever retaining structures." *Journal of Geotechnical and Geoenvironmental Engineering*, Vol. 136, No. 10, pp. 1324-1333.

Al-Homoud, A.S., Whitman, R.V. (1999). "Seismic analysis and design of rigid bridge abutments considering rotation and sliding incorporating non-linear soil behavior." *Soil Dynamics and Earthquake Engineering*, Vol. 18, No. 4, pp. 247-277.

American Society of Civil Engineers. (2005). *Minimum Design Loads for Buildings and Other Structures*. ASCE Standard ASCE/SEI 7-05, ASCE, Reston, Virginia.

American Society of Civil Engineers. (2010). *Minimum Design Loads for Buildings and Other Structures*. ASCE Standard ASCE/SEI 7-10, ASCE, Reston, Virginia.

Anderson, D.G., Martin, G.R., Lam, I., Wang, J.N. (2008). *Seismic Analysis and Design of Retaining Walls, Buried Structures, Slopes, and Embankments (NCHRP Report 611)*. Transportation Research Board, Washington, DC.

Bathe, K.J., Wilson, E.L. (1976). *Numerical Methods in Finite Element Analysis*, Prentice Hall Inc., Englewood Cliffs, New Jersey.

Benuska, L. (1990). "Loma Prieta Earthquake Reconnaissance Report." *Earthquake Spectra*, Supplement to Vol. 6.

Bolton, M.D., Steedman, R.S. (1982). "Centrifugal testing of micro-concrete retaining walls subject to base shaking." *Proceedings of Conference on Soil Dynamics and Earthquake Engineering*, Southampton, Vol. 1, 13-15 July, pp 311-329, Rotterdam: Balkema.

Bolton, M.D., Steedman, R.S. (1984). "The behavior of fixed cantilever walls subject to lateral shaking." *Proceedings of Symposium on the Application of Centrifuge Modeling to Geotechnical Design*, University of Manchester, pp. 302-314, Rotterdam: Balkema.

Bolton, M.D. (1986). "The strength and dilatency of sands." *Geotechnique*, Vol. 36, No. 1, pp. 65-78, DOI: 10.1680/geot.1986.36.1.65.

Bonneville, D., Shuck, A. (2014). "The NEHRP Recommended Seismic Provisions – 2015 Update." Network for Earthquake Engineering Simulation (distributor), Paper, DOI: 10.4231/D3T727G79, https://nees.org/resources/11811.

Bray, J.D., Rathje, E.M., Augello, A.J., Merry, S.M. (1998). "Simplified seismic design procedures for geosynthetic-lined, solid waste landfills." *Geosynthetics International*, Vol. 5, No. 1-2, pp. 203-235.

Bray, J.D., Travasarou, T. (2007). "Simplified procedure for estimating earthquake-induced deviatoric slope displacements." *Journal of Geotechnical and Geoenvironmental Engineering*, Vol. 133, No. 4, pp. 381-392. DOI: 10.1061/(ASCE)1090-0241 (2007) 133:4 (381).

Bray, J.D., Travasarou, T., Zupan, J. (2010). "Seismic Displacement Design of Earth Retaining Structures." *Earth Retention Conference 3*, Bellavue, Washington, pp. 638-644, DOI: 10.1061/41128(384)65

Building Seismic Safety Council. (2009). *NEHRP Recommended Seismic Provisions for New Buildings and Other Structures (FEMA P-750), 2009 Edition*. BSSC, Washington, DC.

Building Seismic Safety Council. (2015). *NEHRP Recommended Seismic Provisions for New Buildings and Other Structures (FEMA P-1050-1), 2015 Edition*. BSSC, Washington, DC.

California Building Standards Commission. (2013). *2013 California Existing Building Code*, Sacramento, California.

Candia, G. (2013). "Experimental and Numerical Modeling of Seismic Earth Pressure on Retaining Walls with Cohesive Backfills." Ph.D. thesis, Department of Civil & Environmental Engineering, University of California, Berkeley.

Candia, G., Sitar, N. (2013). "Seismic Earth Pressures on Retaining Structures in Cohesive Soils." Report No. UCB GT 13-02, August 2013, p. 161.

Candia, G., Mikola, R.G., Sitar, N. (2013). "Seismic earth pressures on braced wall and displacing retaining wall in clay (GC01)." Network for Earthquake Engineering Simulation (database), Dataset, DOI: 10.4231/D37W67572

Candia, G., Sanhueza, C., Sitar, N. (2014). "Evaluación del empuje sísmico en muros de contención en base a un perfil de aceleraciones de campo libre." *VIII Congreso Chileno de Ingeniería Geotécnica*, Santiago, Chile, November 26-28, 2014.

Cetin, K.O., Seed, R.B., Der Kiureghian, A., Tokimatsu, K., Harder L.F., Kayen, R.E., Moss, R.E.S. (2004). "Standard penetration test-based probabilistic and deterministic assessment of seismic soil liquefaction potential." *Journal of Geotechnical and Geoenvironmental Engineering*, Vol. 130, No. 12, pp. 1314-1340.

Chang, C.Y., Mok, C.M., Power, M.S., Tang, Y.K., Tang, H.T., Stepp, J.C. (1990). "Analysis of Dynamic Lateral Earth Pressures Recorded on Lotung Reactor Containment Model Structure." *Proceedings of the Fourth U.S. National Conference on Earthquake Engineering*, Palm Springs, California, May 20-24, 1990.

Chang, C.Y., Mok, C.M., Power, M.S. (1991). "Analysis of Ground Response Data at Lotung Large-Scale Soil-Structure Interaction Experiment Site." Geomatrix Consultants Final Report for EPRI, EPRI-NP-7306-M.

Chopra, A.K. (2011). *Dynamics of Structures: Theory and Applications to Earthquake Engineering*, Fourth Edition, Prentice Hall, Upper Saddle River, New Jersey.

Clough, G.W., Duncan, J.M. (1971). "Finite element analyses of retaining wall behavior." *Journal of the Soil Mechanics and Foundation Division*, ASCE, Vol. 97, No. 12, pp. 1657-1673.

Clough, G.W., Fragaszy, R.J. (1977). "A Study of Earth Loadings on Floodway Retaining Structures in the 1971 San Fernando Valley Earthquake." *Proceedings, 6th World Conference on Earthquake Engineering*. Vol. 3, pp. 2455-2460.

Coulomb, C.A. (1776). “Essai sur une application des règles de maximis et minimis à quelques problèmas de statique, relatifs à l’architecture.” Memoires de l’Academie Royale pres Divers Savants, Vol. 7, pp. 343-387.

Darendeli, M. (2001). “Development of a new family of normalized moduli reduction and material damping curves.” Ph.D. thesis, University of Texas at Austin.

Das, B.M., Puri, V.K. (1996). “Static and dynamic active earth pressure.” *Geotechnical & Geological Engineering*, Vol. 14, No. 4, pp. 353-366.

De Pascale, G., Montalva, G., Candia, G., Ledezma, C. (2015). *Geotechnical Reconnaissance of the 2015 M_w8.3 Illapel, Chile Earthquake* (GEER Association Report No. GEER-043). Geotechnical Extreme Events Reconnaissance. Retrieved December 17, 2015, from http://www.geerassociation.org/GEER_Post%20EQ%20Reports/Illapel_Chile_2015/index.html

Dewoolkar, M.M, Ko, H.Y., Pak, R.Y. (2001). “Seismic behavior of cantilever retaining walls with liquefiable backfills.” *Journal of Geotechnical and Geoenvironmental Engineering*, Vol. 125, No. 5, pp. 424-435.

Dobry, R., Liu, L. (1994). “Centrifuge modeling of soil liquefaction.” *Proceedings of the Tenth World Conference on Earthquake Engineering*, Rotterdam: Balkema, pp. 6801-6809.

Fang, Y.S. (1983). “Dynamic Earth Pressures Against Rotating Walls.” Ph.D. thesis, Department of Civil Engineering, University of Washington, Seattle, Washington.

Finn, W.D.L., Wu, G., Ledbetter, R.H. (1994). “Problems in seismic soil-structure interaction.” *Proceedings of the 8th International Conference on Computer Methods and Advances in Geomechanics*, Morgantown, W.Va., pp. 139-152.

Gazetas, G. (1982). “Vibrational characteristics of soil deposits with variable wave velocity.” *International Journal for Numerical and Analytical Methods in Geomechanics*, Vol. 6, No. 1, pp. 1-20.

Gazetas, G., Psarropoulos, P.N., Anastasopoulos, I., Gerolymos, N. (2004). “Seismic behavior of flexible retaining systems subjected to short-duration moderately strong excitation. *Soil Dynamics and Earthquake Engineering*, Vol. 24, No. 7, pp. 537-550.

Gazetas, G., Garini, E., Zafeirakos, A. (2015) “Seismic Analysis of Anchored Sheet-Pile Walls: Are we Over-designing?” *Proceedings of the 6th International Conference on Earthquake Geotechnical Engineering (6ICEGE)*, Christchurch, NZ, November 1-4, 12 pp.

Giarlelis, C., Mylonakis, G. (2011). “Interpretation of dynamic retaining wall model tests in light of elastic and plastic solution.” *Soil Dynamics and Earthquake Engineering*, Vol. 31, No. 1, pp. 16-24, DOI: 10.1016/j.soildyn.2010.07.002

Golesorkhi, R. (1989) “Factors Influencing the Computational Determinations of Earthquake-Induced Shear Stresses in Sandy Soils.” Ph.D. thesis, Department of Civil & Environmental Engineering, University of California, Berkeley.

Goodman, R.E., Taylor, R.L., Brekke, T.L. (1968). “A Model for the Mechanics of Jointed Rock.” *Journal of the Soil Mechanics and Foundations Division*, ASCE, Vol. 94, No. 3, ASCE, pp. 637-659.

Green, R.A., Ebeling, R.M. (2002). “Seismic analysis of cantilever retaining walls, Phase I.” Report ERDC/ITL TR-02-3, Information Technology Laboratory, US Army Corps of Engineers, Engineer Research and Development Center, Vicksburg, MS.

Gur, T., Pay, A.C., Ramirez, J.A., Sozen, M.A., Johnson, A.M., Irfanoglu, A., Bobet, A. (2009). “Performance of School Buildings in Turkey During the 1999 Düzce and the 2003 Bingöl Earthquakes.” *Earthquake Spectra*, Vol. 25, No. 2, pp. 239-256.

Hall, J.F. (1995). “Northridge Earthquake of January 17, 1994 Reconnaissance Report – Volume 1.” *Earthquake Spectra*, Supplement C to Vol. 11.

Hardin, B.O. (1978) “The nature of stress-strain behavior of soils.” *Proceedings of Earthquake Engineering and Soil Dynamics*, ASCE, Pasadena, California, Vol. 1, pp. 3-89.

Hashash, Y., Tiwari, B., Moss, R., Assimaki, D., Clahan, K., Kieffer, D., Dreger, D., Macdonald, A., Madugo, C., Mason, H., Pehlivan, M., Rayamajhi, D., Acharya, I., Adhikari, B. (2015). *Geotechnical Field Reconnaissance: Gorkha (Nepal) Earthquake of April 25 2015 and Related Shaking Sequence* (GEER Association Report No. GEER-040). Geotechnical Extreme Events Reconnaissance. Retrieved December 17, 2015, from http://www.geerassociation.org/GEER_Post%20EQ%20Reports/Nepal_2015/index.html

Hashash, Y.M.A., Musgrove, M.I., Harmon, J.A., Groholski, D., Phillips, C.A., Park, D. (2015). “DEEPSOIL Version 6.1,” [computer software]. Board of Trustees of University of Illinois at Urbana-Champaign, Urbana, Illinois.

Hashash, Y.M.A., Musgrove, M.I., Harmon, J.A., Groholski, D., Phillips, C.A., Park, D. (2015). “DEEPSOIL Version 6.1, User Manual,” Board of Trustees of University of Illinois at Urbana-Champaign, Urbana, Illinois.

Hausler, E. (2002). “Influence of ground improvement on settlement and liquefaction: a study based on field case history evidence and dynamic geotechnical centrifuge tests.” Ph.D. thesis, University of California, Berkeley.

Holmes, W.T., Sommers, P. (1996). “Northridge Earthquake of January 17, 1994 Reconnaissance Report – Volume 2.” *Earthquake Spectra*, Supplement C to Vol. 11.

Huang, C. (2000). “Investigations of Soil Retaining Structures Damaged During the Chi-Chi (Taiwan) Earthquake.” *Journal of the Chinese Institute of Engineers*, Vol. 23, pp. 417-428.

Hushmand, A., Dashti, S., Zhang, M., McCartney, J.S., Ghayoomi, M., Hushmand, B., Mokarram, N., Davis, C., Lee, Y., Hu, J. (2014). “Seismic Soil-Structure-Interaction and Lateral Earth Pressures on Buried Reservoir Structures.” Technical Paper from GeoCongress 2014, GSP 234, ASCE, 2014, pp. 1215-1224, DOI: 10.1061/9780784413272.118

Ichihara, M., Matsuzawa, H. (1973). “Earth Pressure During Earthquake.” *Soil and Foundations*, Japanese Society of Soil Mechanics and Foundation Engineering, pp. 75-86.

Idriss, I.M., Sun, J.I. (1992). “SHAKE91: A Computer Program for Conducting Equivalent Linear Seismic Response Analysis of Horizontally Layered Soil Deposits.” Center for Geotechnical Modeling, Department of Civil & Environmental Engineering, University of California, Davis, November 1992.

Idriss, I.M. (1999). “An update to the Seed-Idriss simplified procedure for evaluating liquefaction potential.” *Proceedings, TRB Workshop on New Approaches to Liquefaction*, Pblication NO. FHWA-RD-99-165, Federal Highway Administration, January.

Iida, H., Hirota, T., Yoshida, N., Iwafuji, M. (1996). “Damage to Daikai Subway Station.” *Soils and Foundations Special Issue on Geotechnical Aspects of the January 17, 1995 Hyogoken-Nambu Earthquake*, Japanese Geotechnical Society.

International Code Council (ICC). (2011). *International Existing Building Code*, Country Club Hills, Illinois.

International Code Council (ICC). (2014). *International Existing Building Code*, Country Club Hills, Illinois.

Ishibashi, I. Fang, Y.S. (1987). “Dynamic earth pressures with different wall movement modes.” *Soils and Foundations*, Japanese Society of Soil Mechanics and Foundation Engineering, Vol. 27, No. 4, pp. 11-22.

Ishibashi, I., Osada, M., Uwabe, T. (1994). “Dynamic Lateral Pressures Due to Saturated Backfills on Rigid Walls.” *Journal of Geotechnical Engineering*, Vol. 120, No. 10, pp. 1747-1766.

Ishii, Y., Arai, H., Tsuchida, H. (1960). “Lateral earth pressure in an earthquake.” *Proceedings of the Second World Conference on Earthquake Engineering*, Tokyo, Japan, July 11-18, 1960, pp. 211-230.

Itasca Consulting Group, Inc. (2011). “Fast Lagrangian Analysis of Continua, Version 7.0.” [computer software]. Itasca Consulting Group, Inc., Minneapolis, Minnesota.

Itasca Consulting Group, Inc. (2011). “Fast Lagrangian Analysis of Continua, Version 7.0 User’s Guide.” Itasca Consulting Group, Inc., Minneapolis, Minnesota.

Jacobsen, L.S. (1939). Described in Appendix D of “The Kentucky Project” Technical Report No. 12 TVA, 1951.

Jung, C., Bobet, A. (2008). “Seismic Earth Pressures Behind Retaining Walls: Effects of Rigid-body Motions,” *Proceedings of Geotechnical Earthquake Engineering and Soil Dynamics IV*, D. Zeng, M. Manzari & D. Hiltunen, eds., ASCE, Sacramento, CA.

Kavazanjian, E., Wang, J.N., Martin, G.R., Shamsabadi, A., Lam, I., Dickenson, S.E., Hung, C.J., (2011). *LRFD Seismic Analysis and Design of Transportation Geotechnical Features and Structural Foundations (FHWA-NHI-11-032)*. National Highway Institute, Washington, DC.

Kendal Riches, L. (2015). “Observed Earthquake Damage to Christchurch City Council Owned Retaining Walls and the Repair Solutions Developed.” *Proceedings of the 6th International Conference on Earthquake Geotechnical Engineering (6ICEGE)*, Christchurch, NZ, November 1-4, 10 pp.

Kishida, T., Boulanger, R.W., Abrahamson, N.A., Driller, M.W., Wehling, T.M. (2009). “Seismic response of levees in Sacramento-San Joaquin Delta.” *Earthquake Spectra*, EERI, Vol. 25, No. 3, pp. 557-582.

Kloukinas, P., Mylonakis, G., Papantonopoulos, C. (2008). "Distribution of Seismic Earth Pressures on Gravity Walls by Wave-Based Stress Limit Analysis." *Geotechnical Earthquake Engineering and Soil Dynamics IV*, ASCE GSP 181, Sacramento, CA, May 18-22, 10 pp., DOI: 10.1061/40975(318)148

Kloukinas, P., Langousis, M., Mylonakis, G. (2012). "Simple Wave Solution for Seismic Earth Pressures on Nonyielding Walls." *Journal of Geotechnical and Geoenvironmental Engineering*, ASCE, Vol. 138, No. 12, pp. 1514-1519.

Kuhlemeyer, R.L., Lysmer, J. (1973). "Finite element method accuracy for wave propagation problems." *Journal of Soil Mechanics and Foundations*, ASCE, Vol. 9, No. SM5, pp. 421-427.

Kutter, B.L. (1995). "Recent advances in centrifuge modeling of seismic shaking." *Proceedings of Third International Conference on Recent Advances in Geotechnical Earthquake Engineering and Soil Dynamics*, University of Missouri, Rolla, Vol. 2, pp. 927-942.

Lew, M., Simantob, E., Hudson, M.B. (1995). "Performance of Shored Earth Retaining Systems During the January 17, 1994 Northridge Earthquake." *Proceedings, Third International Conference on Recent Advances in Geotechnical Earthquake Engineering and Soil Dynamics*, St. Louis, Missouri, Vol. 3, pp. 1417-1422.

Lew, M., Sitar, N., Al Atik, L. (2010a). "Seismic earth pressures: fact of fiction." Invited Keynote Paper, Earth Retention Conference, ER.

Lew, M., Sitar, N., Al-Atik, L., Pourzanjani, M., Hudson, M.B. (2010b). "Seismic Earth Pressures on Deep Building Basements." Structural Engineers Association of California, Proceedings of the Annual Convention.

Liu, M., Gorman, D.G. (1995). "Formulation of Rayleigh damping and its extensions." *Computers and Structures*, Elsevier Science Ltd., Vol. 57, No. 2, pp. 277-285.

Lysmer, J., Kuhlemeyer, R.L. (1969). "Finite Dynamic Model for Infinite Media." *Journal of Engineering Mechanics*. Vol. 95, No. EM4, pp. 859-877.

Lysmer, J., Udaka, T., Tsai, C.F., Seed, H.B. (1975). "FLUSH – A Computer Program for Approximate 3-D Analysis of Soil-Structure Interaction Problems." University of California, Berkeley, Earthquake Engineering Research Center, Report No. EERC 75-30.

Makdisi, F.I., Seed, H.B. (1978). "Simplified Procedure for Estimating Dam and Embankment Earthquake-Induced Deformations." *Journal of Geotechnical Engineering*, ASCE, Vol. 104, No. GT7, pp. 849-867.

Massar, M.L., Fickus, M., Bryan, E., Petkie, D.T., Terzuoli Jr., A.J. (2011). "Fast computation of spectral centroids." *Advances in Computational Mathematics*, Vol. 35, No. 1, pp. 83-97.

Mathworks, Inc. (2011). "MATLAB Version 7.12.0 (R2011a)," [computer software]. Mathworks, Inc., Natick, Massachusetts.

Matsuo, H. (1941). "Experimental study on the distribution of earth pressures acting on a vertical wall during earthquakes." *Journal of the Japanese Society of Civil Engineers*, Vol. 27, No. 2.

Matsuo, H., Ōhara, S. (1960). “Lateral earth pressure and stability of quay walls during earthquakes.” *Proceedings of the Second World Conference on Earthquake Engineering*, Tokyo, Japan, July 11-18, 1960.

Matsuo, O., Nakamura, S., Saito, Y. (2002). “Centrifuge tests on seismic behavior of retaining walls.” *Proceedings of the International Conference on Physical Modeling in Geotechnics*, St. Johns, Newfoundland, Canada, 10-12 July, 2002.

Matsuzawa, H., Sugimoto, K., (1984). “Seismic Active Earth Pressure Against Elastically Supported Rigid Wall (in Japanese).” *Tsuchi-to-Kiso*, Japanese Society of Soil Mechnaics and Foundation Engineering, Vol. 32, No. 6, pp. 32-39.

Matsuzawa, H., Ishibashi, I., Kawamura, M. (1985). “Dynamic Soil and Water Pressures of Submerged Soils.” *Journal of Geotechnical Engineering*, Vol. 111, No. 10, pp. 1161-1176.

Mayne, P.W., Kulhawy, F.H. (1982). “K_0-OCR relationships in soil.” *Journal of Geotechnical Engineering Division*, ASCE, Vol. 108, No. 6, pp. 851-872.

Mayniel, K. (1808). “Traite analytique et experimental de la poussee des terres.” Paris.

Mejia, L.H., Dawson, E.M. (2006). “Earthquake Deconvolution for FLAC.” *FLAC and Numerical Modeling in Geomechanics (Proceedings of the 4th International FLAC Symposium, Madrid, Spain, May 2006)*, P. Varona & R. Hart, eds. Minneapolis, Minnesota: Itasca Consulting Group, Inc., pp. 211-219.

Menq, F. (2003). “Dynamic Properties of Sandy and Gravelly Soils.” Ph.D. thesis, University of Texas at Austin.

Mikola, R.G., Sitar, N. (2013). “Seismic earth pressures on retaining structures in cohesionless soils.” Report No. UCB GT 13-01, March 2013, p. 217.

Mikola, R.G., Candia, G., Sitar, N. (2013). “Seismic earth pressures on braced wall in sand (ROOZ01).” Network for Earthquake Engineering Simulation (distributor), Dataset, DOI: 10.4231/D3HD7NS4P

Mock, E., Cheng, L. (2011). “Full-scale shake table test of retaining walls with and without sound wall.” Report No. UCD-SESM-10-03, June 2011, p. 596.

Mononobe, N., Matsuo, H, (1929). “On the determination of earth pressure during earthquakes.” *Proceedings of the World Engineering Conference*, Vol. 9, pp. 179-187.

Mononobe, N., Matsuo, H, (1932). “Experimental Investigation of Lateral Earth Pressure during Earthquakes.” *Earthquake Research Institute and Research Institute of Public Works, Department of Home Affairs*, Japan.

Müller-Breslau, H. (1906). “Erddruck auf stützmauern.” Kroner, Stuttgart.

Murphy, L.M. (1973). *San Fernando, California Earthquake of February 9, 1971 (in three volumes)*. U.S. Department of Commerce, Washington, D.C.

Mylonakis, G., Kloukinas, P., Papantonopoulos, C. (2007). “An alternative to the Mononobe-Okabe equations for seismic earth pressures.” *Soil Dynamics and Earthquake Engineering*, Vol 27, No. 10, pp. 957-969, DOI:10.1016/j.soildyn.2007.01.004

Nadim, F., Whitman, R. (1982). "A numerical model for evaluation of seismic behavior of gravity retaining walls." R82-33. Massachusetts Institute of Technology, Report 1982, pp. 232.

Naesgaard, E. (2011). "A hybrid effective stress – total stress procedure for analyzing soil embankments subjected to potential liquefaction and flow." Ph.D. thesis, University of British Columbia, Vancouver, Canada.

Nakamura, S. (2006). "Reexamination of Mononobe-Okabe theory of gravity retaining walls using centrifuge model tests." *Soils and Foundations*, Japanese Geotechnical Society, Vol. 46, No. 2, pp. 135-146.

Nazarian, H.N., Hadjian, A.H. (1979). "Earthquake Induced Lateral Soil Pressures on Structures." *Journal of Geotechnical Engineering Division*, ASCE, Vol. 105, No. 9, pp. 1049-1066.

Nikolaou, S., Zekkos, D., Assimaki, D., Gilsanz, R. (2014). *GEER/EERI/ATC Earthquake Reconnaissance January 26th/February 2nd 2014 Cephalonia, Greece Events* (GEER Association Report No. GEER-034). Geotechnical Extreme Events Reconnaissance. Retrieved December 17, 2015, from http://www.geerassociation.org/GEER_Post%20EQ%20Reports/Cephalonia_Greece_2014/index.html

Newmark, N.M. (1965). "Effects of earthquakes on dams and embankments." *Geotechnique*, Vol. 15, No. 2, pp. 139-160.

Okabe, S. (1924). "General theory of earth pressure and seismic stability of retaining wall and dam." *Journal of the Japanese Society of Civil Engineers*, Tokyo, Japan, Vol. 10, No. 6, pp. 1277-1323.

Okabe, S. (1926). "General theory of earth pressure and laboratory testings on seismic stability of retaining walls." *Journal of the Japanese Society of Civil Engineers*, Tokyo, Japan, Vol. 12, No. 1, pp. 123-134.

Ordoñez, G. (2000) "SHAKE2000," [computer software]. Geomotions, LLC, Lacey Washington.

Ortiz, L.A. (1982). "Dynamic centrifuge testing of cantilever retaining walls." Ph.D. thesis, California Institute of Technology, Pasadena, California.

Ortiz, L.A., Scott, R.F., Lee, J. (1983). "Dynamic centrifuge testing of a cantilever retaining wall." *Earthquake Engineering and Structural Dynamics*, Vol. 11, pp. 251-268.

Ostadan, F. (2005). "Seismic Soil Pressure for Building Walls – an Updated Approach," *Soil Dynamics and Earthquake Engineering*, Vol. 25, pp. 785-793; also published in *Proceedings of the 11th International Conference on Soil Dynamics and Earthquake Engineering and 3rd International Conference on Earthquake Geotechnical Engineering*, University of California, Berkeley, 2004.

Pathmanathan, R. (2006). "Numerical Modelling of Seismic behavior of Earth-Retaining Walls," Master's Thesis, European School for Advanced Studies in Reduction of Seismic Risk.

PEER Ground Motion Database. Accessed on April 15, 2015. <http://ngawest2.berkeley.edu/>

Prakash, S., Saran, S. (1966). “Static and dynamic earth pressures behind retaining walls.” *Proceedings of the Third Symposium on Earthquake Engineering*. University of Roorkee, Roorkee, India, Vol. 1, pp. 277-288.

Prakash, S., Basavanna, B.M. (1969). “Earth Pressure Distribution behind Retaining Wall during Earthquakes.” *Proceedings of the Fourth World Congress on Earthquake Engineering*, Santiago, Chile.

Prakash, S. (1981). “Dynamic Earth Pressures – State of the Art Report.” *Proceedings of the International Conference on Recent Advances in Geotechnical Earthquake Engineering and Soil Dynamics*, St. Louis, Missouri, Vol. III, pp. 993-1020.

Psarropoulos, P.N., Klonaris, G., Gazetas, G. (2005). “Seismic earth pressures on rigid and flexible retaining walls.” *Soil Dynamics and Earthquake Engineering*, No. 25, pp. 795-809.

Rankine, W.M. (1857). “On the stability of loose earth.” Philosophical Transactions of the Royal Society of London, Vol. 147, 9-27.

Rathje, E.M., Abrahamson, N.A., Bray, J.D. (1998). “Simplified frequency content estimates of earthquake ground motions.” *Journal of Geotechnical and Geoenvironmental Engineering*, Vol. 124, No. 2, pp. 150-159.

Rathje, E.M., Stewart, J.P., Baturay, M.B., Bray, J.D., Bardet, J.P. (2006). “Strong Ground Motions and Damage Patterns from the 1999 Duzce earthquake in Turkey.” *Journal of Earthquake Engineering*, Taylor & Francis, Vol. 10, No. 5, 693-724.

Richards, R., Elms, D.G. (1979). “Seismic Behavior of Gravity Retaining Walls.” *Journal of the Geotechnical Engineering Division*, Vol. 105, No. GT4, pp. 449-464.

Richards, R., Huang, C., Fishman, K. (1999). “Seismic earth pressure on retaining structures.” *Journal of Geotechnical and Geoenvironmental Engineering*. Vol. 125, No. 9, pp. 771-778.

Richards, R., Shi, X. (1994). “Seismic Lateral Pressures in Soils with Cohesion.” *Journal of Geotechnical Engineering*, Vol. 124, No. 2, pp. 150-159.

Rollins, K., Franke, K., Luna, R., Rocco, N., Avila, D., Climent, A. (2013). *Geotechnical Aspects of Sept. 5, 2012 M7.6 Samara, Costa Rica Earthquake* (GEER Association Report No. GEER-031). Geotechnical Extreme Events Reconnaissance. Retrieved December 17, 2015, from http://www.geerassociation.org/GEER_Post%20EQ%20Reports/Costa_Rica_2012/index.html

Rollins, K., Ledezma, C., Montalva, G. (2014). *Geotechnical Aspects of April 1, 2014, M8.2 Iquigue, Chile Earthquake* (GEER Association Report No. GEER-038). Geotechnical Extreme Events Reconnaissance. Retrieved December 17, 2015, from http://www.geerassociation.org/GEER_Post%20EQ%20Reports/Iquique_Chile_2014/index.html

Schnabel, P.B., Lysmer, J., Seed, H.B. (1972). “SHAKE: A Computer Program for Earthquake Response Analysis of Horizontally Layered Sites.” University of California, Berkeley, Earthquake Engineering Research Center, Report No. EERC 72-12, December.

Scott, R.F. (1973). “Earthquake-induced earth pressures on retaining wall.” *Proceedings of the Fifth World Conference on Earth Engineering*, Rome, Italy.

Seed, H.B., Whitman, R.V. (1970). “Design of Earth Retaining Structures for Dynamic Loads.” *ASCE Specialty Conference, Lateral Stresses in the Ground and Design of Earth Retaining Structures*. Cornell University, Ithaca, New York, pp. 103-147.

Seed, H.B., Idriss, I.M. (1971). “Simplified procedure for evaluating soil liquefaction potential.” *Journal of Soil Mechanics and Foundation Division*., Vol. 97, SM9, pp. 1249-1273.

Seed, H.B., Martin, G.R. (1966). “The Seismic Coefficient in Earth Dam Design.” *Journal of the Soil Mechanics and Foundations Division*, ASCE, Vol. 92, No. SM3, May.

Shakal, A., Huang, M., Darragh, R., Cao, T., Sherburne, R., Malholtra, P., Cramer, C., Sydnor, R., Graizer, V., Maldonaldo, G., Petersen, C., Wampole, J. (1994). *CSMIP Strong-Motion Records from the Northridge, California Earthquake of 17 January 1994*, California Strong Motion Instrumentation Program Report No. OSMS 94-07, California Department of Conservation, Sacramento, CA.

Sherif, M.A., Ishibashi, I., Lee, C.D. (1982). “Earth Pressures Against Rigid Retaining Walls.” *Journal of the Geotechnical Engineering Division*, ASCE, Vol. 108, No. GT5, pp. 679-695.

Sherif, M.A., Fang, Y.S. (1984). “Dynamic earth pressures on walls rotating about the top.” *Soils and Foundations*, Vol. 24, No. 4, pp. 109-117.

Siddharthan, R., Maragakis, E.M. (1989). “Performance of flexible retaining walls supporting dry cohesionless soils under cyclic loads.” *International Journal for Numerical and Analytical Methods in Geomechanics*, Vol. 13, pp. 309-326.

Silva, W.J. (1988). “Soil response to earthquake ground motion.” EPRI Report NP-5747, Electric Power Research Institute, Palo Alto, California.

Sitar, N., Mikola, R.G., Candia, G. (2012). “Seismically induced lateral earth pressures on retaining structures and basement walls.” Keynote Lecture, Geotechnical Engineering State of the Art and Practice, Keynote Lectures from GeoCongress 2012, GSP 226, ASCE, 2012.

Stadler, A.T. (1996). “Dynamic centrifuge testing of cantilever retaining wall.” Ph.D. thesis, University of Colorado at Boulder.

Steedman, R.S., Zeng, X. (1990). “The influence of phase on the calculation of pseudo-static earth pressure on a retaining wall.” *Geotechnique*, Vol. 40, No. 1, pp. 103-112.

Stewart, J.P., Bray, J.D., Seed, R.B., Sitar, N., eds. (1994). “Preliminary Report on the Principle Geotechnical Aspects of the January 17, 1994, Northridge Earthquake.” Earthquake Engineering Research Center Report No. UCB/EERC 94/08. University of California, Berkeley.

Structural Engineers Association of California. (2009). *SEAOC Blue Book – Seismic Design Recommendations*. SEAOC, Sacramento, CA.

Tabatabaiefar, H.R., Fatahi, B. (2014). “Idealisation of soil-structure system to determine inelastic seismic response of mid-rise building frames.” *Soil Dynamics and Earthquake Engineering*, Vol. 66, pp. 339-351. DOI: 10.1016/j.soildyn.2014.08.007

Taiebat, M., Amirzehni, E., Finn, W.D.L. (2014). “Seismic design of basement walls: evaluation of current practice in British Columbia.” *Canadian Geotechnical Journal*, Vol. 51, No. 9, pp. 1004-1020. DOI: 10.1139/cgj-2013-0212

Terzaghi, K. (1934a). “Large Retaining-Wall Tests: I-Pressure of Dry Sand.” *Engineering News Record*, February 1, pp. 136-140.

Terzaghi, K. (1934b). “Large Retaining-Wall Tests: II-Pressure of Saturated Sand.” *Engineering News Record*, February 22, pp. 259-262.

Tokida, K., Matsuo, O., Nakamura, S. (2001). “Damage of Earth Retaining Structures in the 1999 Chi-Chi, Taiwan Earthquake.” *Proceedings of the Joint Meeting of the U.S.-Japan Cooperative Program in Natural Resources-Panel on Wind and Seismic Effects*, Vol. 32, pp. 495-512.

Trifunac, M.D., Brady, A.G. (1975). “A study on the duration of strong earthquake ground motion.” *Bulletin of the Seismological Society of America*, Vol. 65, No. 3, pp. 581-626.

Veletsos, A.S., Younan, A.H. (1994a). “Dynamic Soil Pressures on Rigid Vertical Walls.” *Earthquake Engineering and Structural Dynamics*. Vol. 23, No. 3, pp. 275-301.

Veletsos, A.S., Younan, A.H. (1994b). “Dynamic Modeling and Response of Soil-Wall Systems.” *Journal of Geotechnical Engineering*. Vol. 120, No. 12, pp. 2155-2179.

Veletsos, A.S., Parikh, V.H., Younan, A.H. (1995) “Dynamic response of a pair of walls retaining a viscoelastic solid.” *Earthquake Engineering and Structural Dynamics*, Vol. 24, No. 12, pp. 1567-1589.

Veletsos, A.S., Younan, A.H. (1997). “Dynamic response of cantilever retaining wall.” *Journal of Geotechnical and Geoenvironmental Engineering*. Vol. 123, No. 2, pp. 161-172.

Verdugo, R., Sitar, N., Frost, J.D., Bray, J.D., Candia, G., Eldridge, T., Hashash, Y., Olson, S.M., Ursua, A. (2012). “Seismic Performance of Earth Structures: Dams, Levees, Tailings Dams and Retaining Walls.” *Earthquake Spectra*. Vol. 28, No. S1, pp. S75-S96., June.

Wagner, N., Sitar, N. (2013). “Seismic earth pressures in a deep basement wall on dry sand (NW01).” Network for Earthquake Engineering Simulation (distributor), Dataset, DOI: 10.4231/D3D21RJ44

Watanabe, K., Munaf, Y., Koseki, J., Tateyama, M., Kojima, K. (2003). “Behavior of several types of model retaining walls subjected to irregular excitation.” *Soils and Foundations*, Japanese Geotechnical Society, Vol. 43, No. 5, pp. 13-27.

Watanabe, K., Koseki, K., Tateyama, M. (2011). “Seismic earth pressure exerted on retaining walls under a large seismic load.” *Soils and Foundations*, Japanese Geotechnical Society, Vol. 51, No. 3, pp. 379-394.

Whitman, R.V. (1990). “Seismic Design and Behavior of Gravity Retaining Walls.” *Proceedings, Design and Performance of Earth Retaining Structures*, GSP 25, ASCE, NY, pp. 817-842.

Whitman, R.V. (1991). “Seismic Design of Earth Retaining Structures.” *Proceedings, Second International Conference on Recent Advances in Geotechnical Earthquake Engineering and Soil Dynamics*, St. Louis, Missouri, pp. 1767-1778.

Wilson, P.R. (2009). “Large scale passive force-displacement and dynamic earth pressure experiments and simulations.” Ph.D. thesis, Department of Structural Engineering, University of California, San Diego.

Wood, J.H. (1973). “Earthquake-Induced Soil Pressures on Structures.” Earthquake Engineering Research Laboratory Report EERL 73-05, California Institute of Technology, Pasadena, CA.

Wu, G. (1994). “Dynamic soil-structure interaction: pile foundations and retaining structures.” Ph.D. thesis, Department of Civil Engineering, University of British Columbia, Vancouver, B.C.

Wu, G., Finn, W.D.L. (1996). “Seismic pressures against rigid walls.” In *Analysis and Design of Retaining Structures Against Earthquakes*, Proceedings of the American Society of Civil Engineers Convention, Washington, D.C., pp. 1-18.

Wu, G., Finn, W.D.L. (1999). “Seismic lateral pressures for design of rigid walls.” *Canadian Geotechnical Journal*, Vol. 36, No. 3, pp. 509-522. DOI: 10.1139/t99-013

Yee, E., Stewart, J.P., Tokimatsu, K. (2013). “Elastic and Large-Strain Nonlinear Seismic Site Response from Analysis of Vertical Array Recordings.” *Journal of Geotechnical and Geoenvironmental Engineering*. Vol. 139, No. 10, pp. 1789-1801.

Yoshida, N. (2009). “Damage to subway station during the 1995 Hyogoken-Nambu (Kobe) earthquake.” *Earthquake geotechnical case histories for performance-based design – Kokusho (ed)*. © 2009 Taylor & Francis Group, London, ISBN 978-0-415-80484-4

Youd, T.L., Bardet, J.P., Bray, J.D. (2000). “1999 Kocaeli, Turkey, Earthquake Reconnaissance Report.” *Earthquake Spectra*, Supplement to Vol. 16.

Younan, A.H., Veletsos, A.S. (2000). “Dynamic response of flexible retaining walls.” *Earthquake Engineering and Structural Dynamics*, Vol. 29, pp. 1815-1844.

Zhai, E., Davis, C., Yan, L., Hu, J. (2013). “Numerical Simulations of Geotechnical Centrifuge Modeling of Seismic Earth Pressures on an Underground Restrained Structure.” *Proceedings of 6th China-Japan-US Trilateral Symposium on Lifeline Earthquake Engineering*, Chengdu, China, pp. 369-376, DOI: 10.1061/9780784413234.048

Appendices

Appendix A Results from centrifuge experiment and numerical model

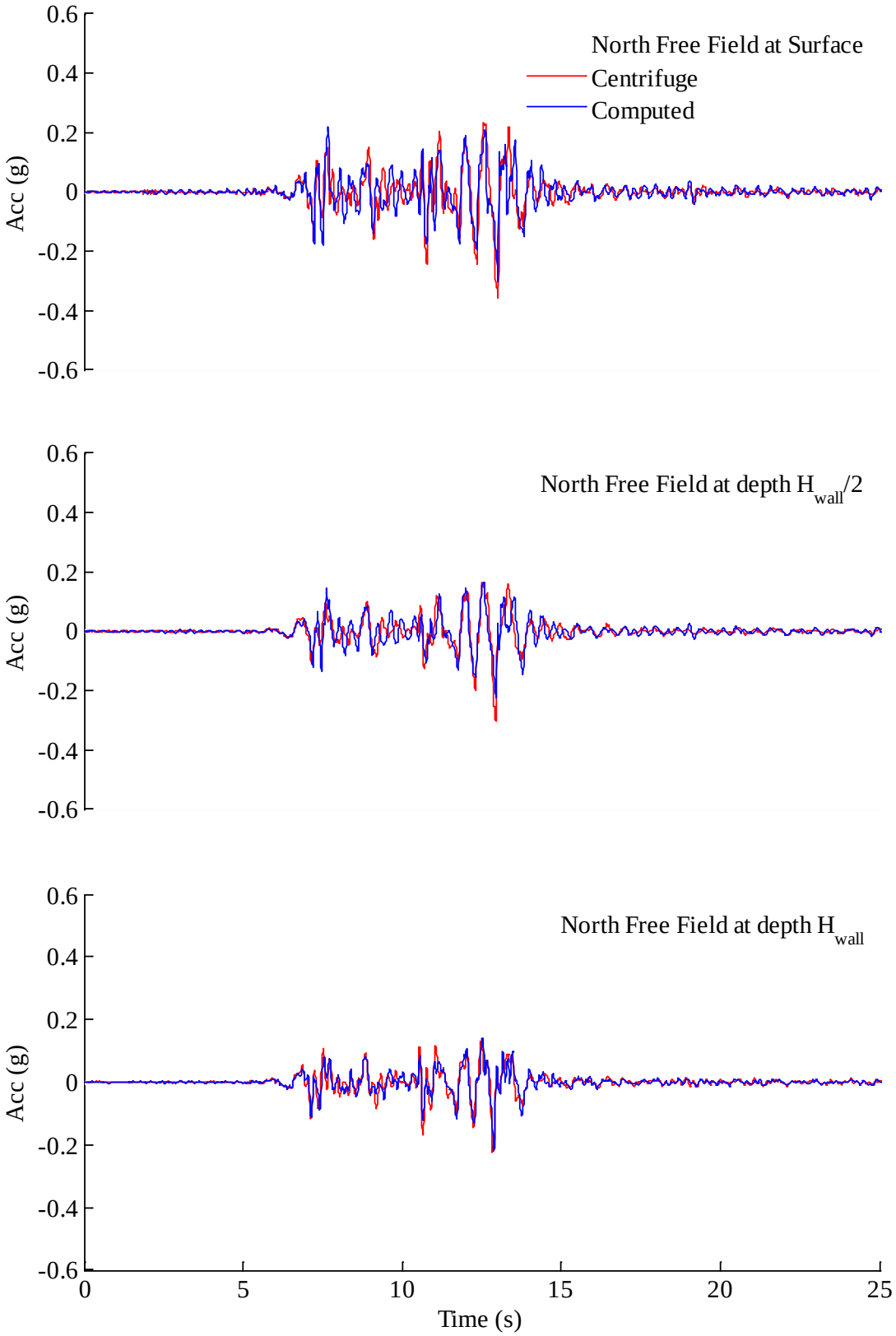

Figure A.1: Measured and computed accelerations in north free field during Kocaeli YPT 060

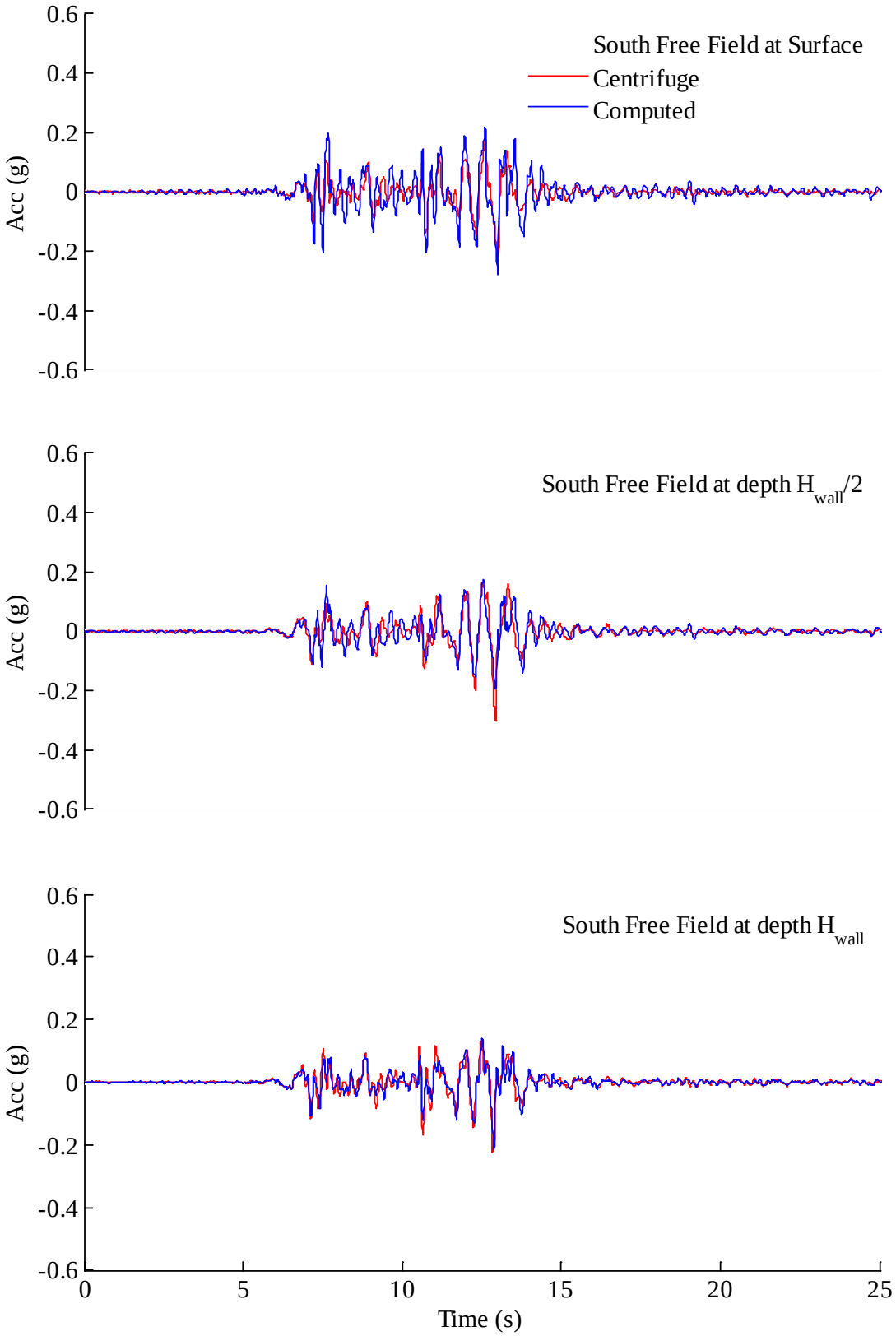

Figure A.2: Measured and computed accelerations in south free field during Kocaeli YPT 060

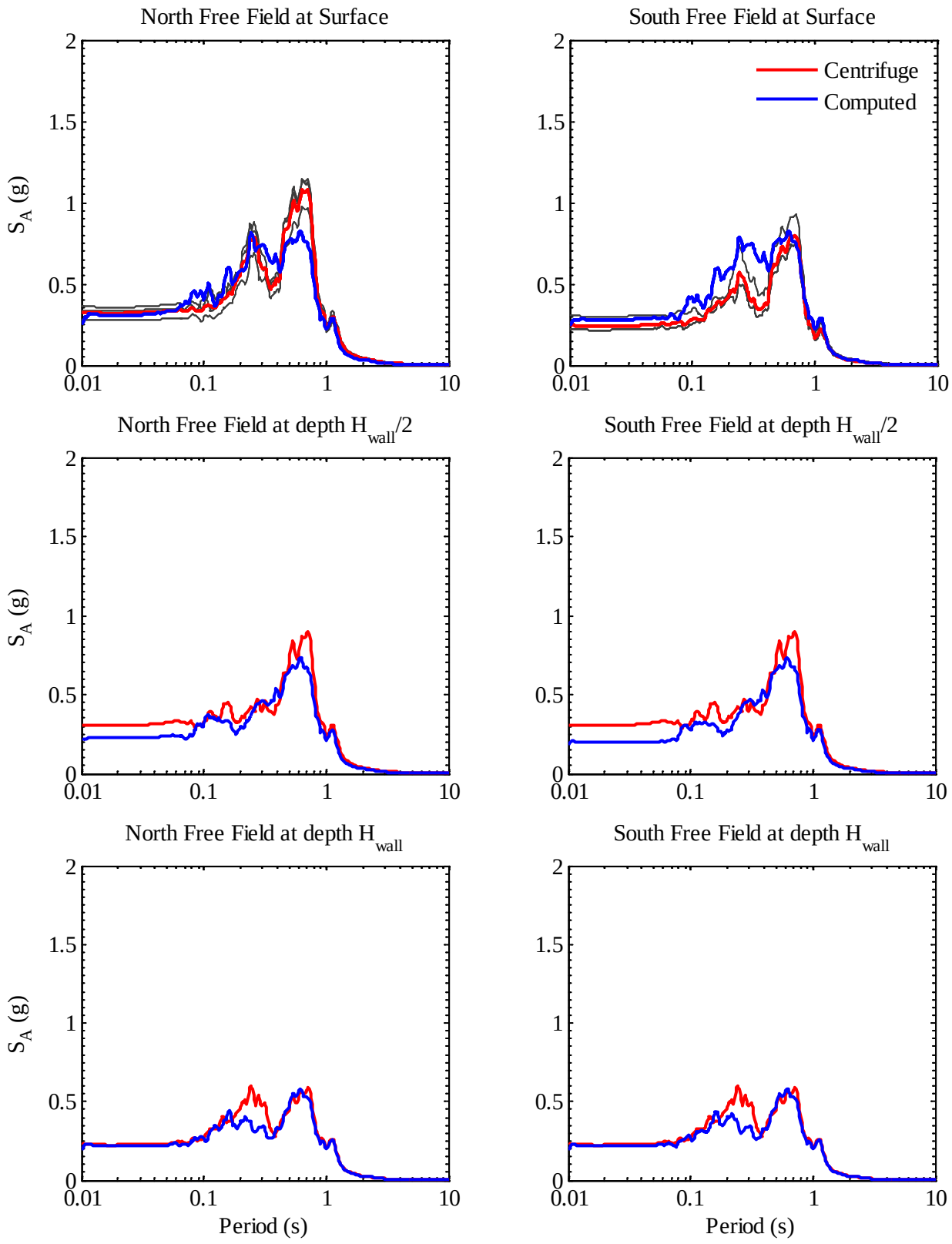

Figure A.3: Measured and computed acceleration response spectra in free field at 5% damping during Kocaeli YPT 060

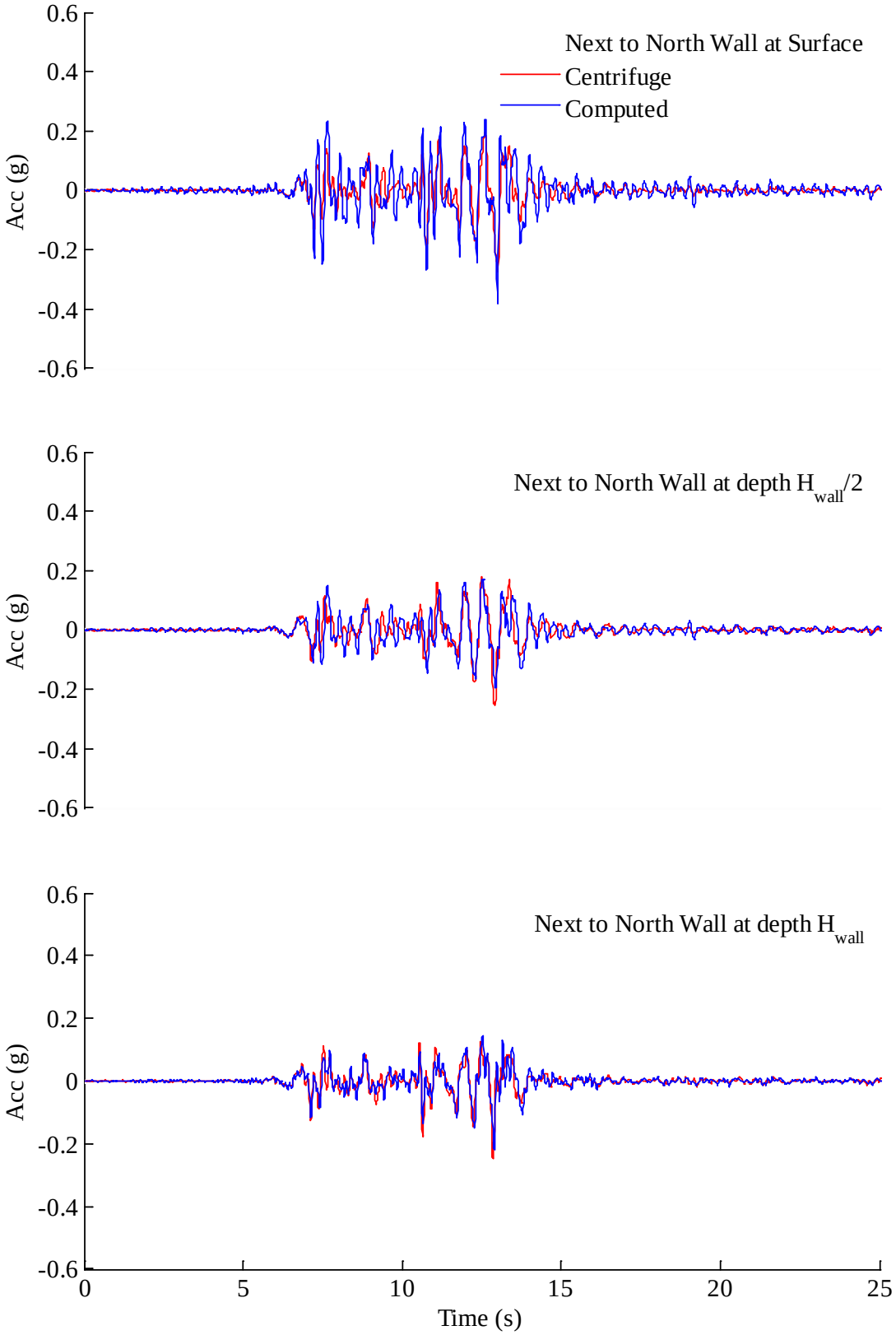

Figure A.4: Measured and computed accelerations next to north wall during Kocaeli YPT 060

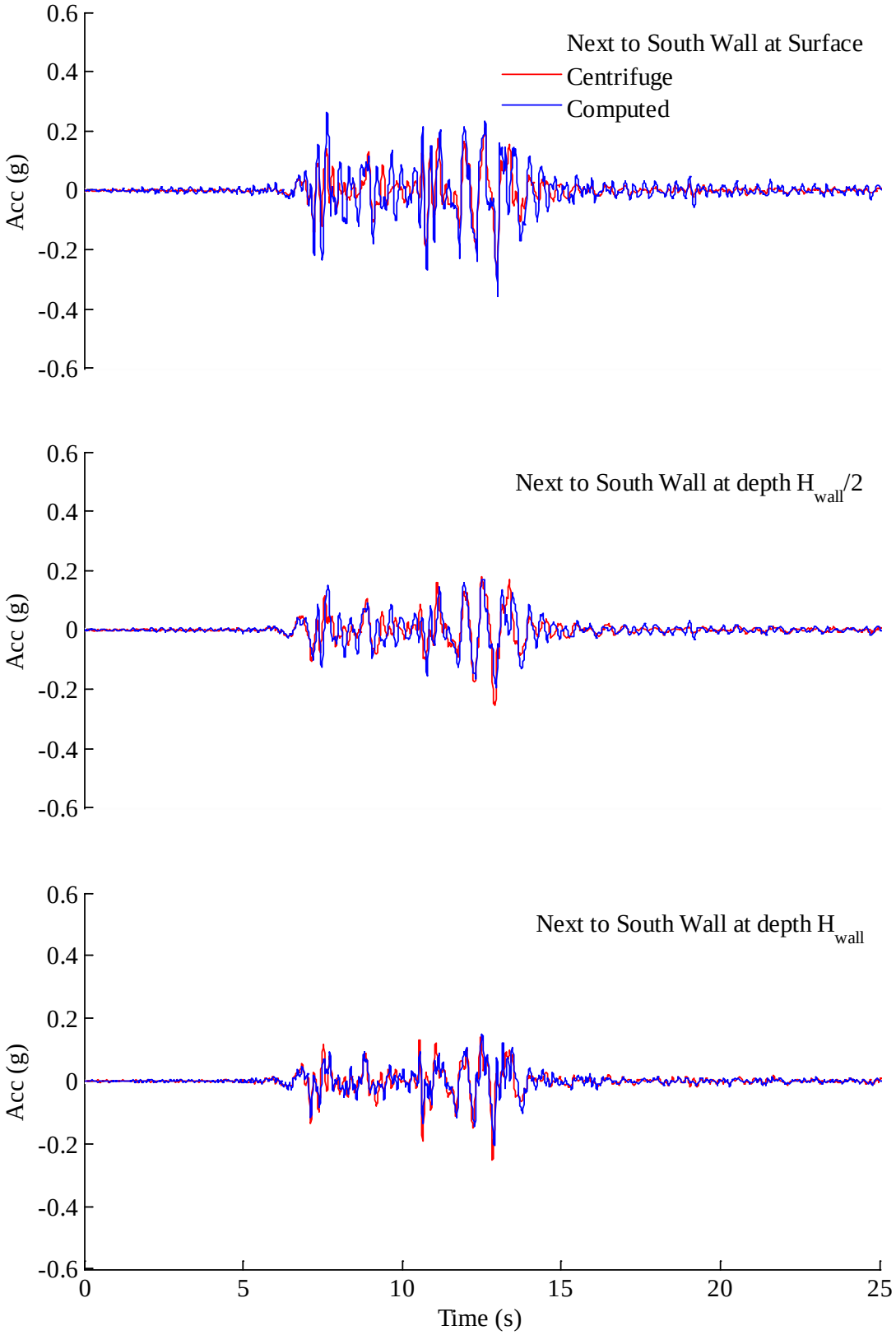

Figure A.5: Measured and computed accelerations next to south wall during Kocaeli YPT 060

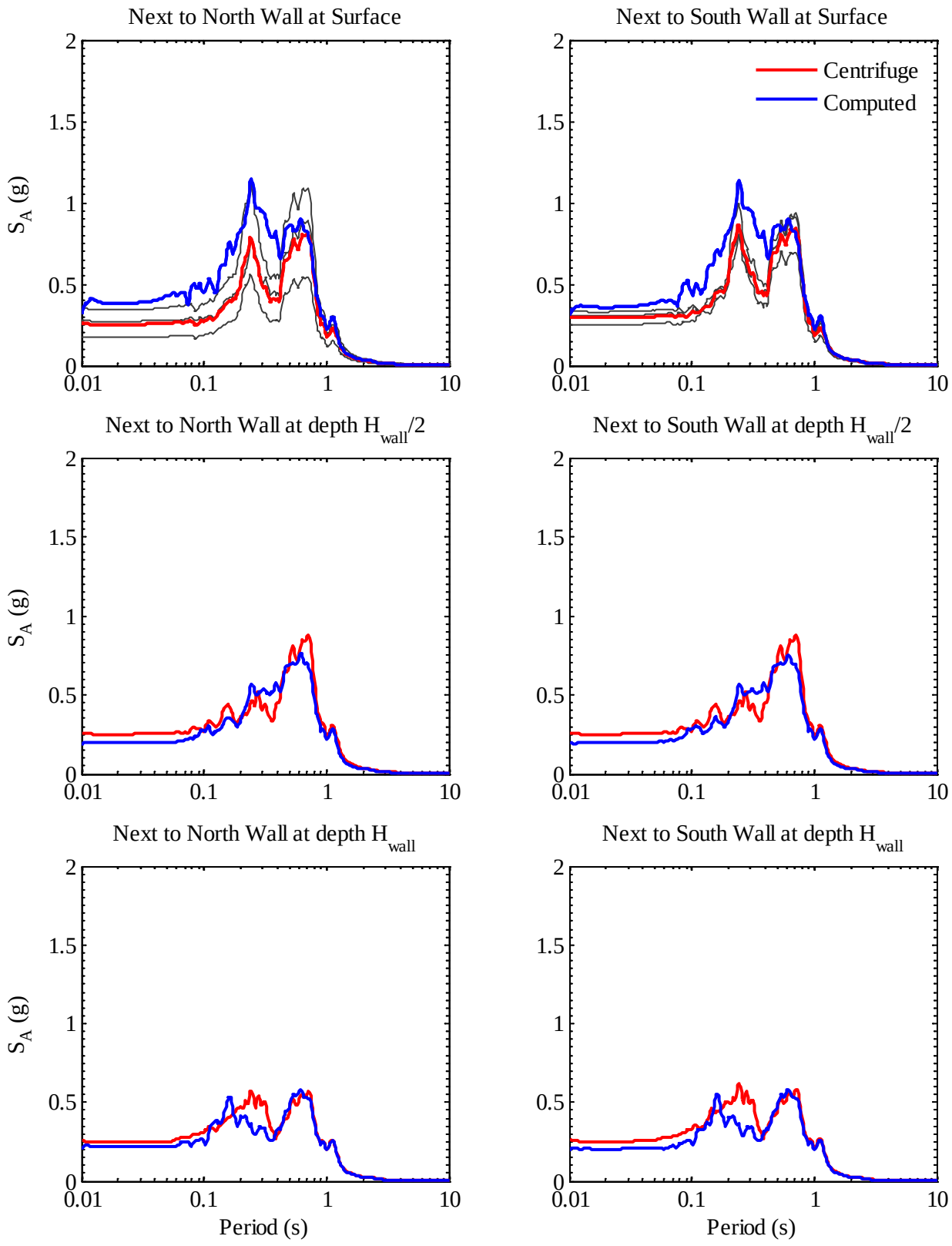

Figure A.6: Measured and computed acceleration response spectra in soil next to structure at 5% damping during Kocaeli YPT 060

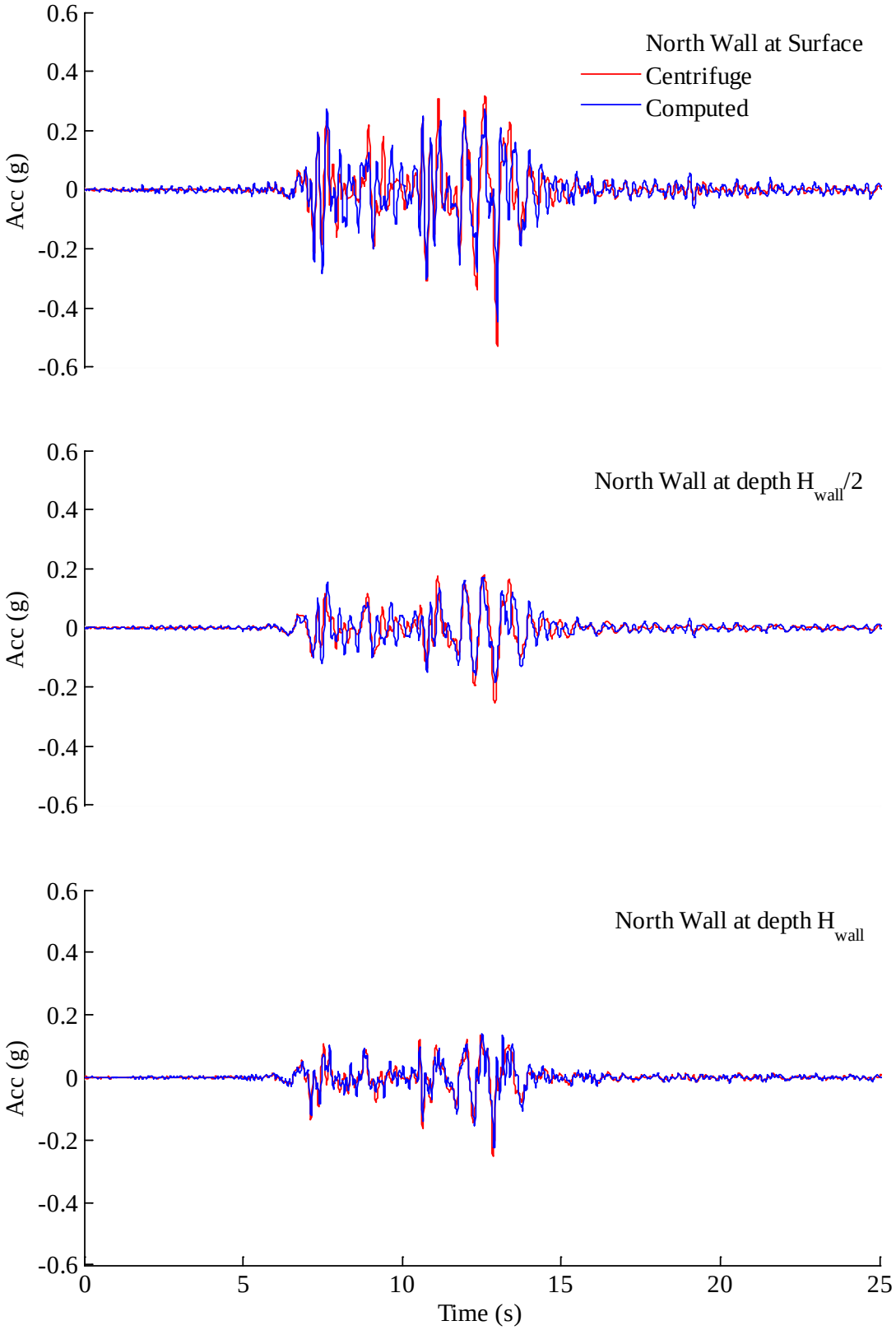

Figure A.7: Measured and computed accelerations in north wall during Kocaeli YPT 060

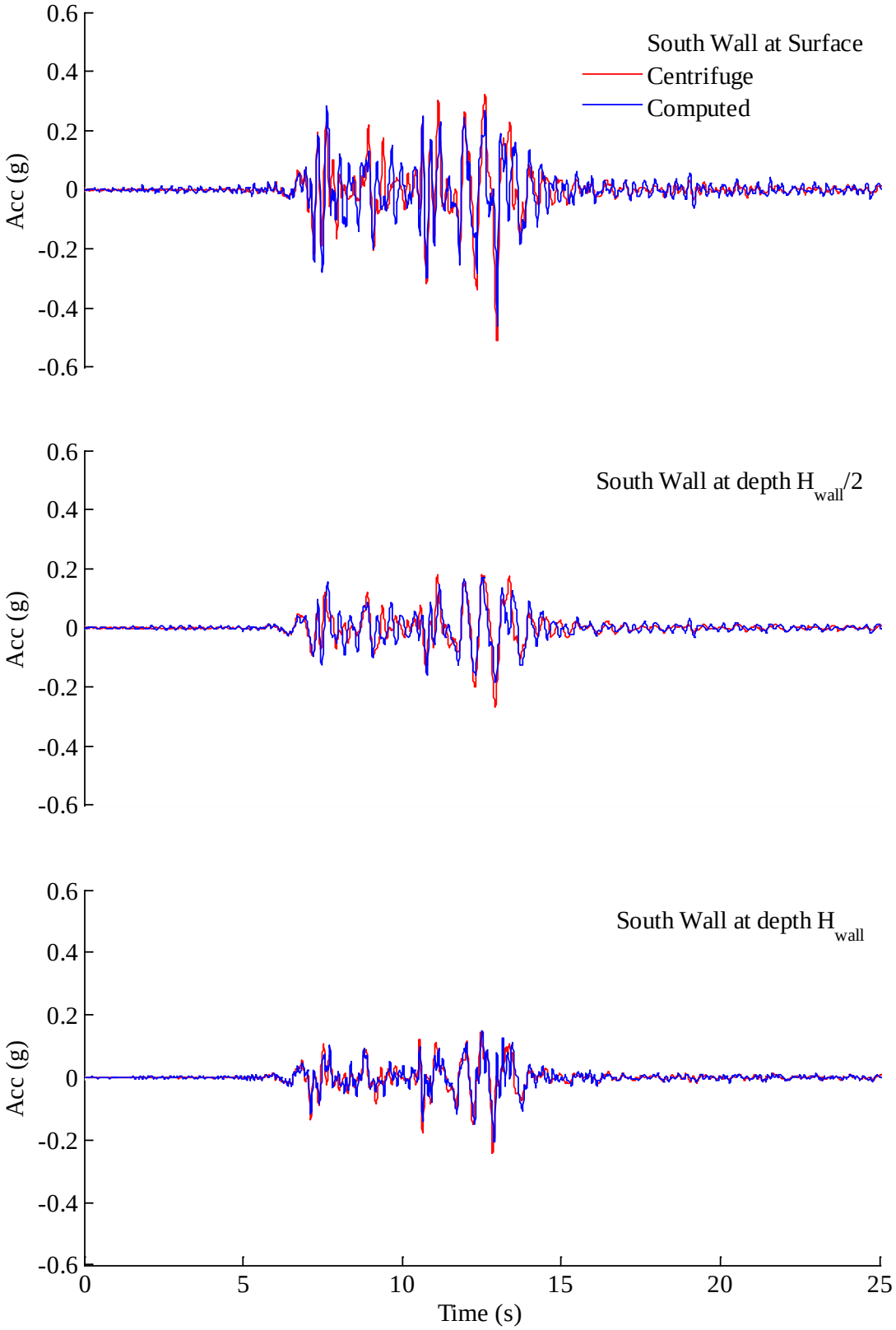

Figure A.8: Measured and computed accelerations in south wall during Kocaeli YPT 060

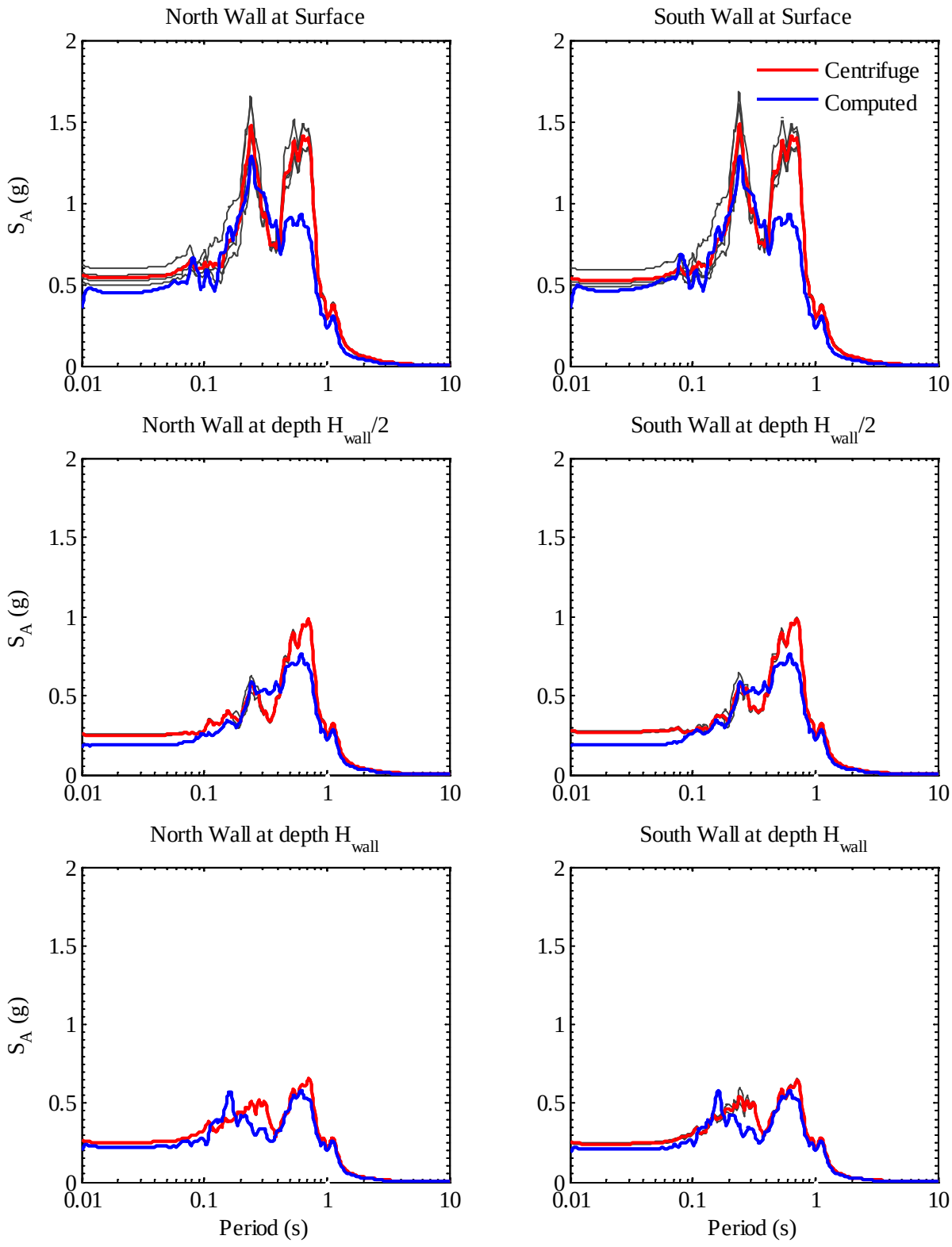

Figure A.9: Measured and computed acceleration response spectra in structure at 5% damping during Kocaeli YPT 060

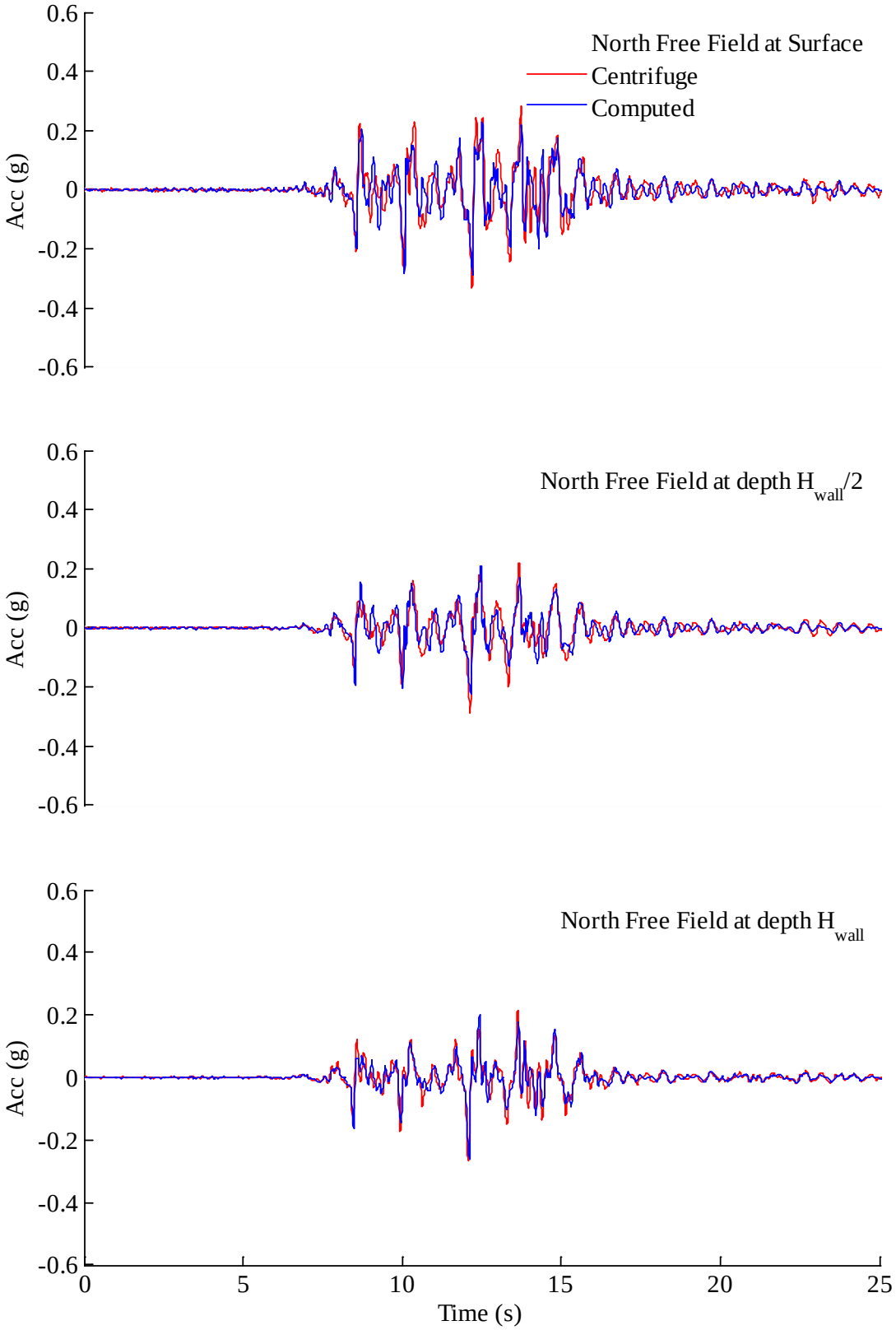

Figure A.10: Measured and computed accelerations in north free field during Kocaeli YPT 330

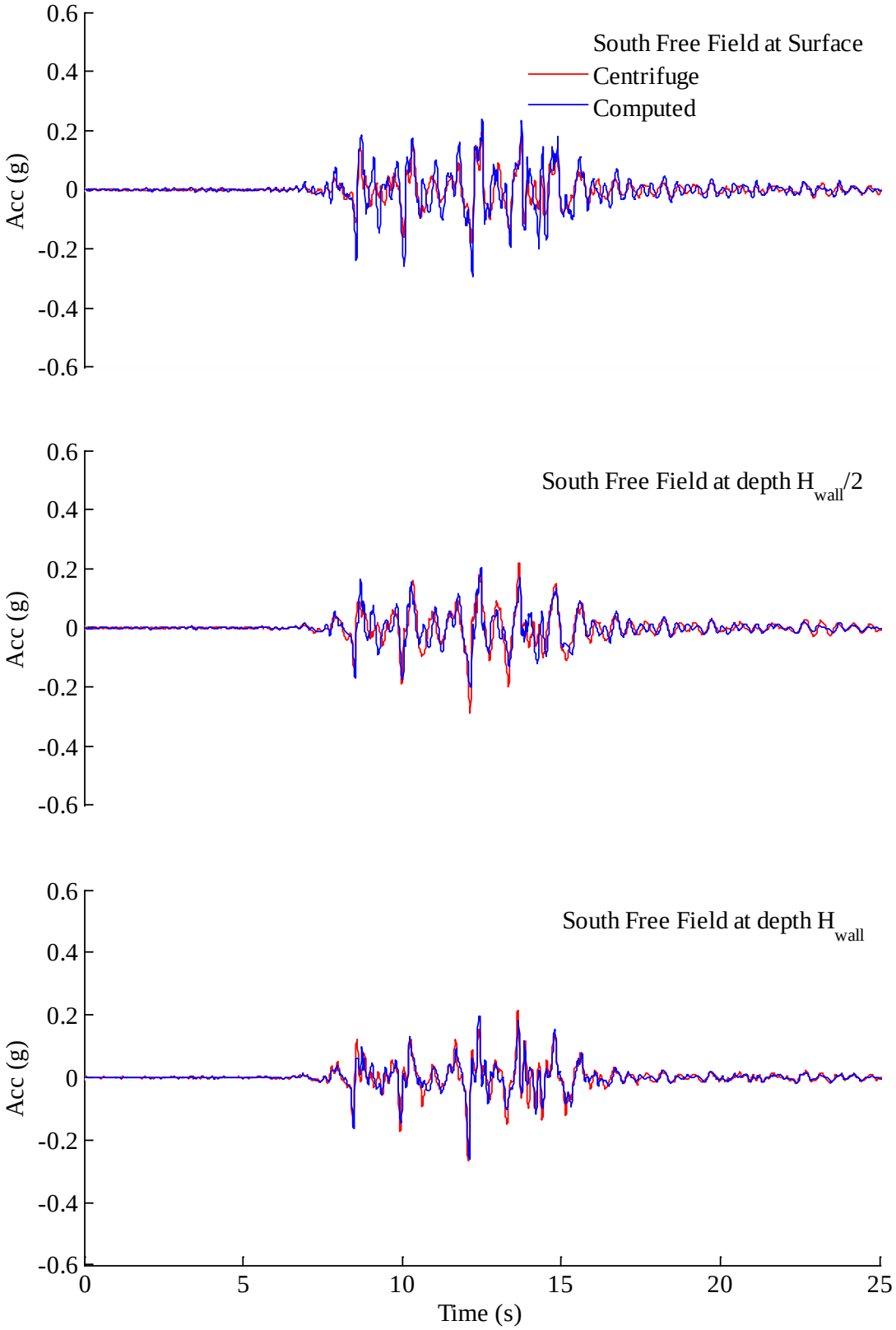

Figure A.11: Measured and computed accelerations in south free field during Kocaeli YPT 330

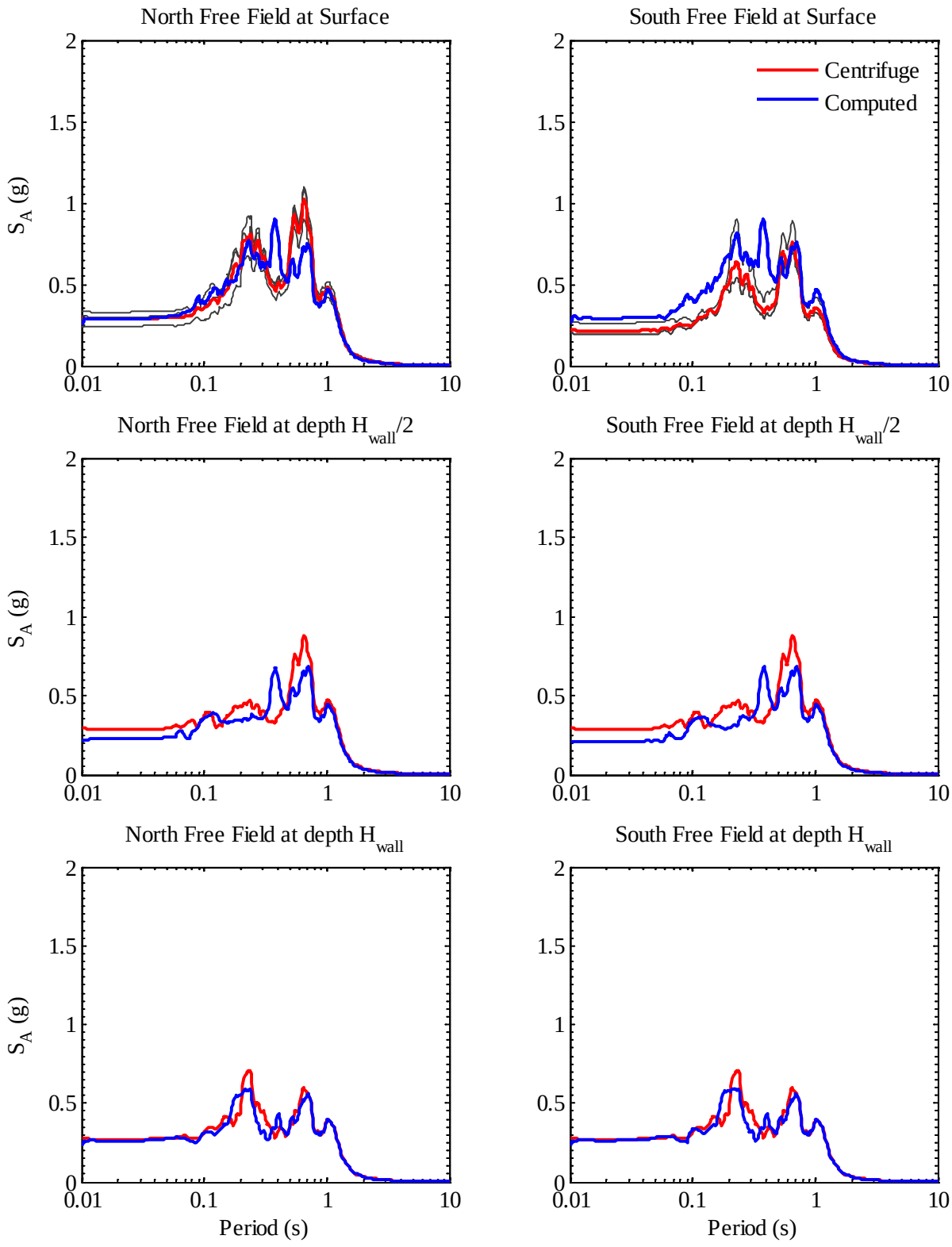

Figure A.12: Measured and computed acceleration response spectra in free field at 5% damping during Kocaeli YPT 330

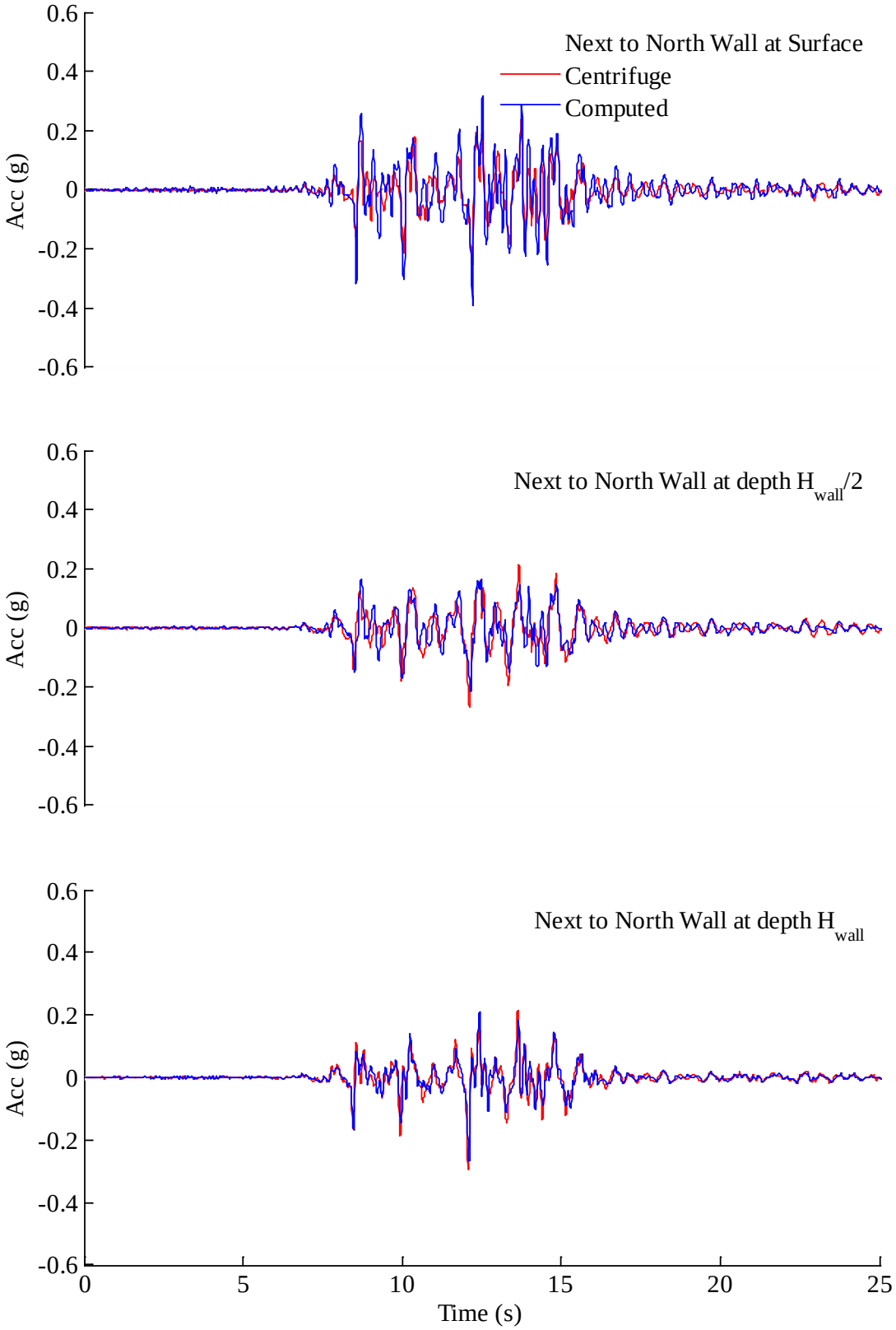

Figure A.13: Measured and computed accelerations next to north wall during Kocaeli YPT 330

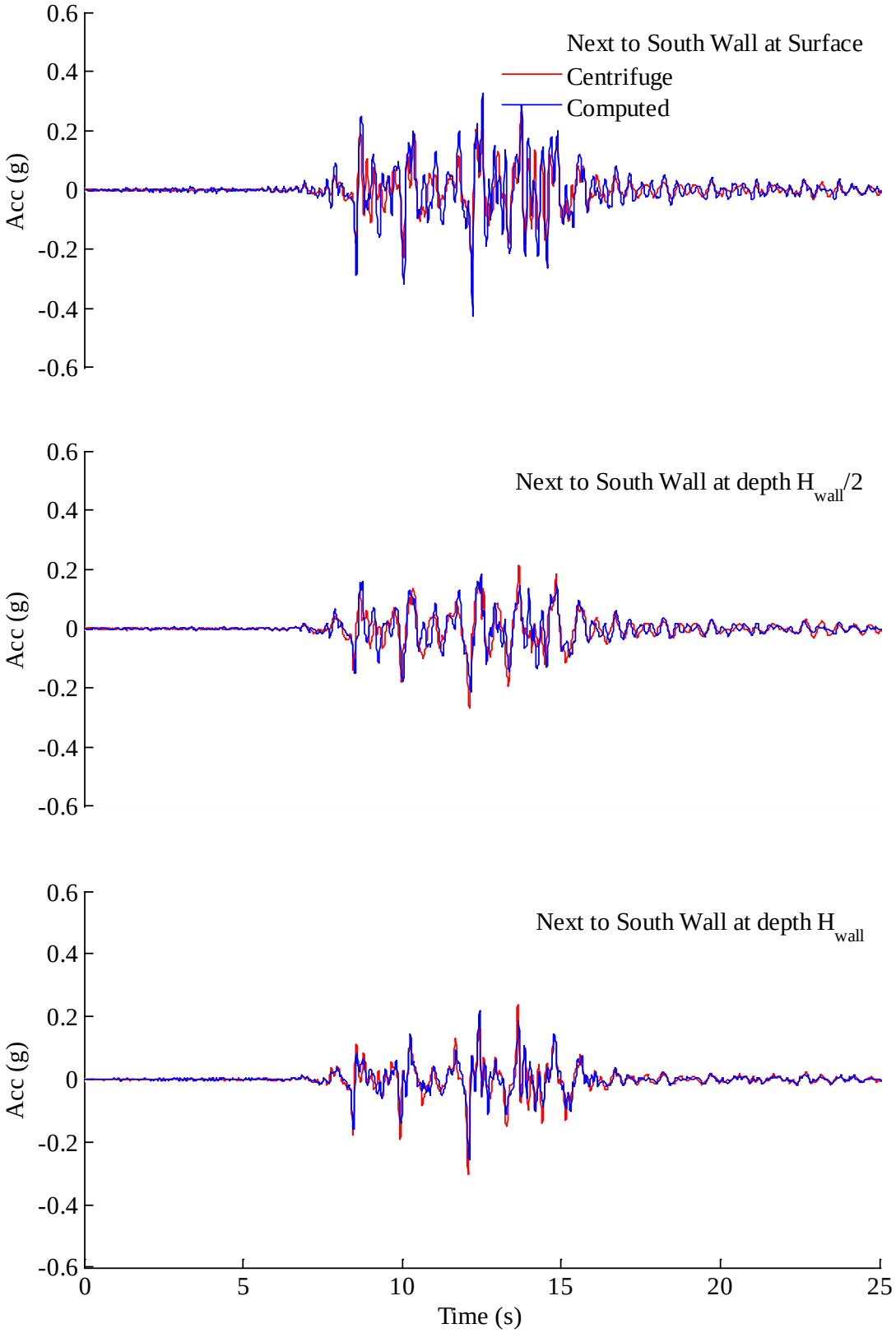

Figure A.14: Measured and computed accelerations next to south wall during Kocaeli YPT 330

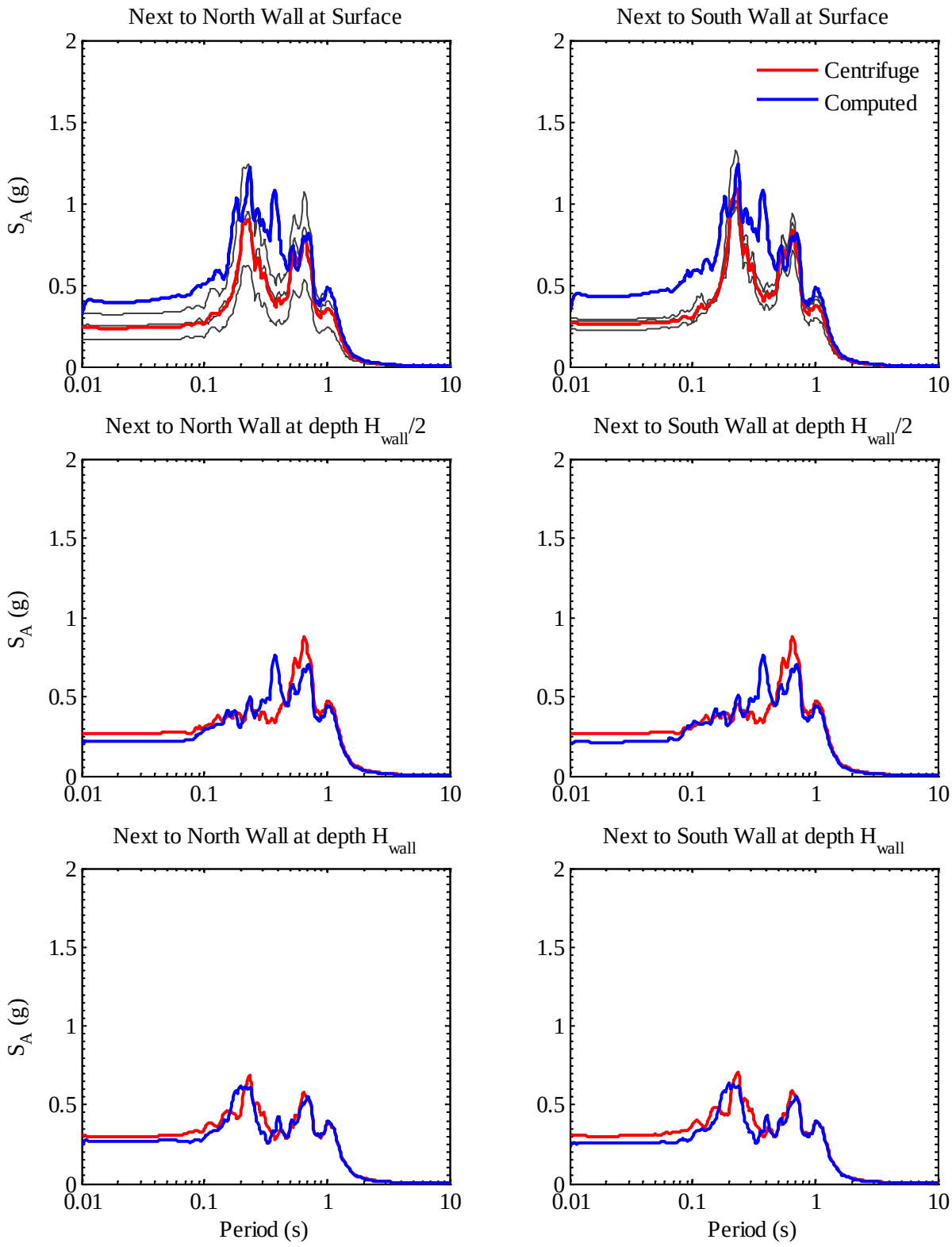

Figure A.15: Measured and computed acceleration response spectra in soil next to structure at 5% damping during Kocaeli YPT 330

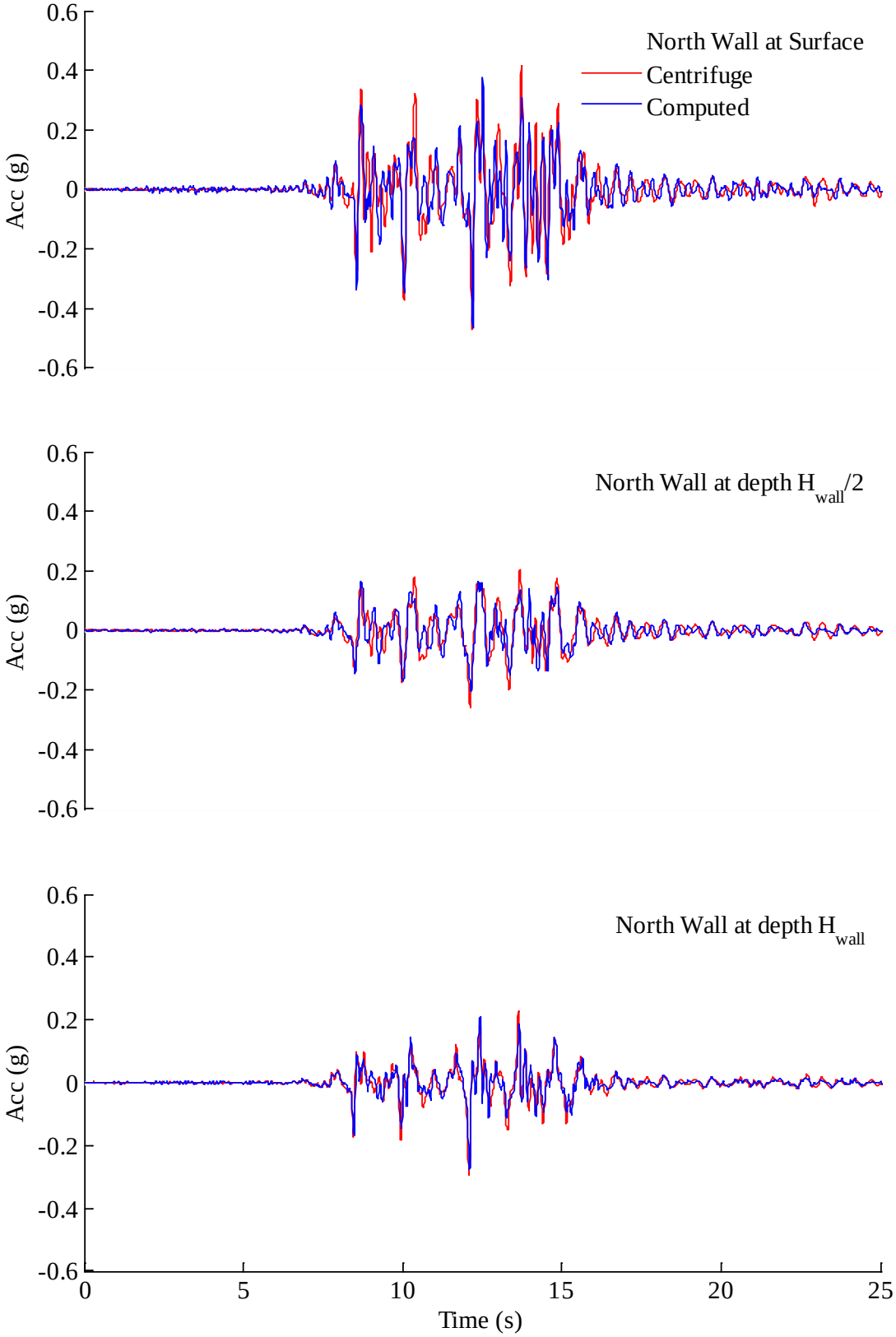

Figure A.16: Measured and computed accelerations in north wall during Kocaeli YPT 330

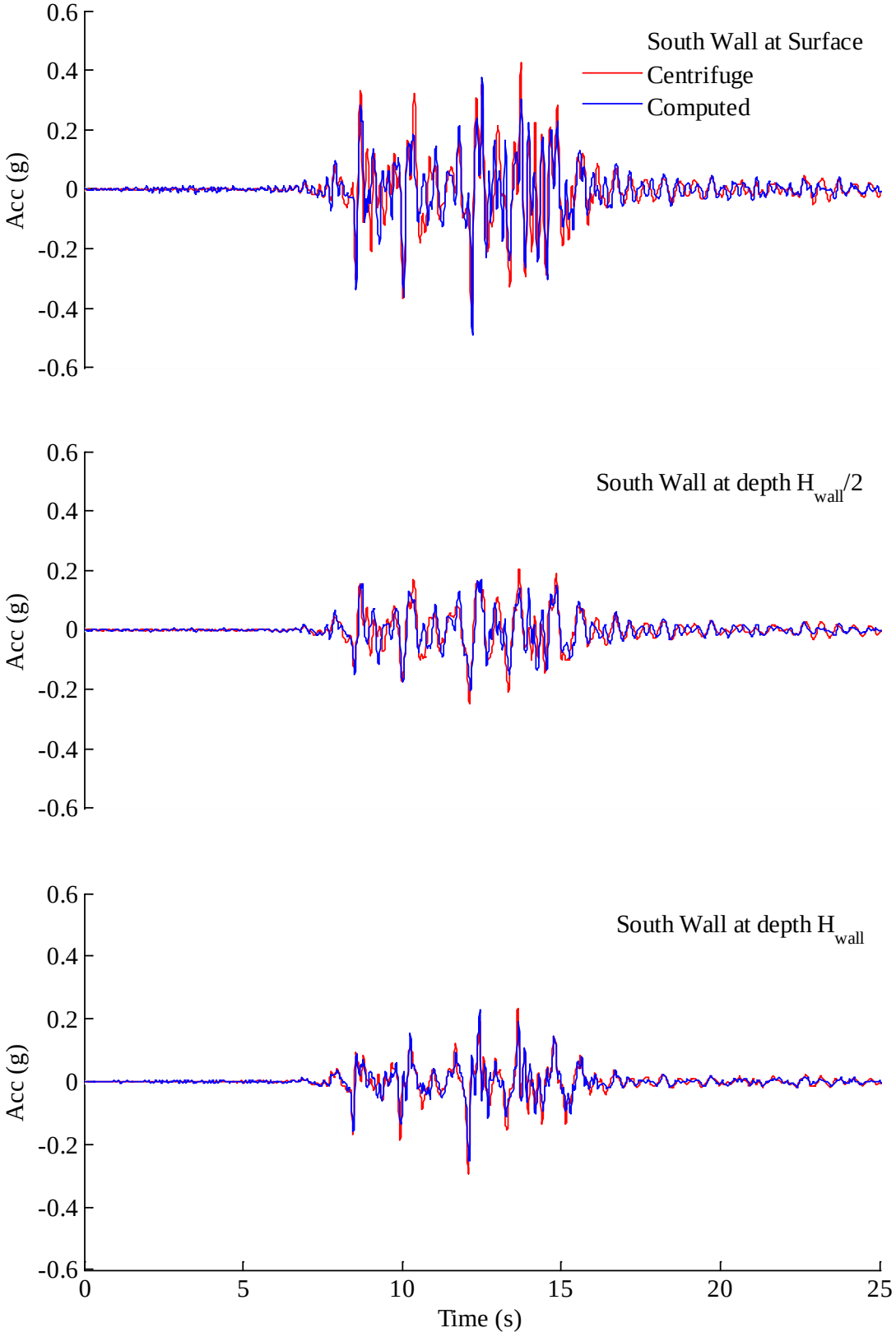

Figure A.17: Measured and computed accelerations in south wall during Kocaeli YPT 330

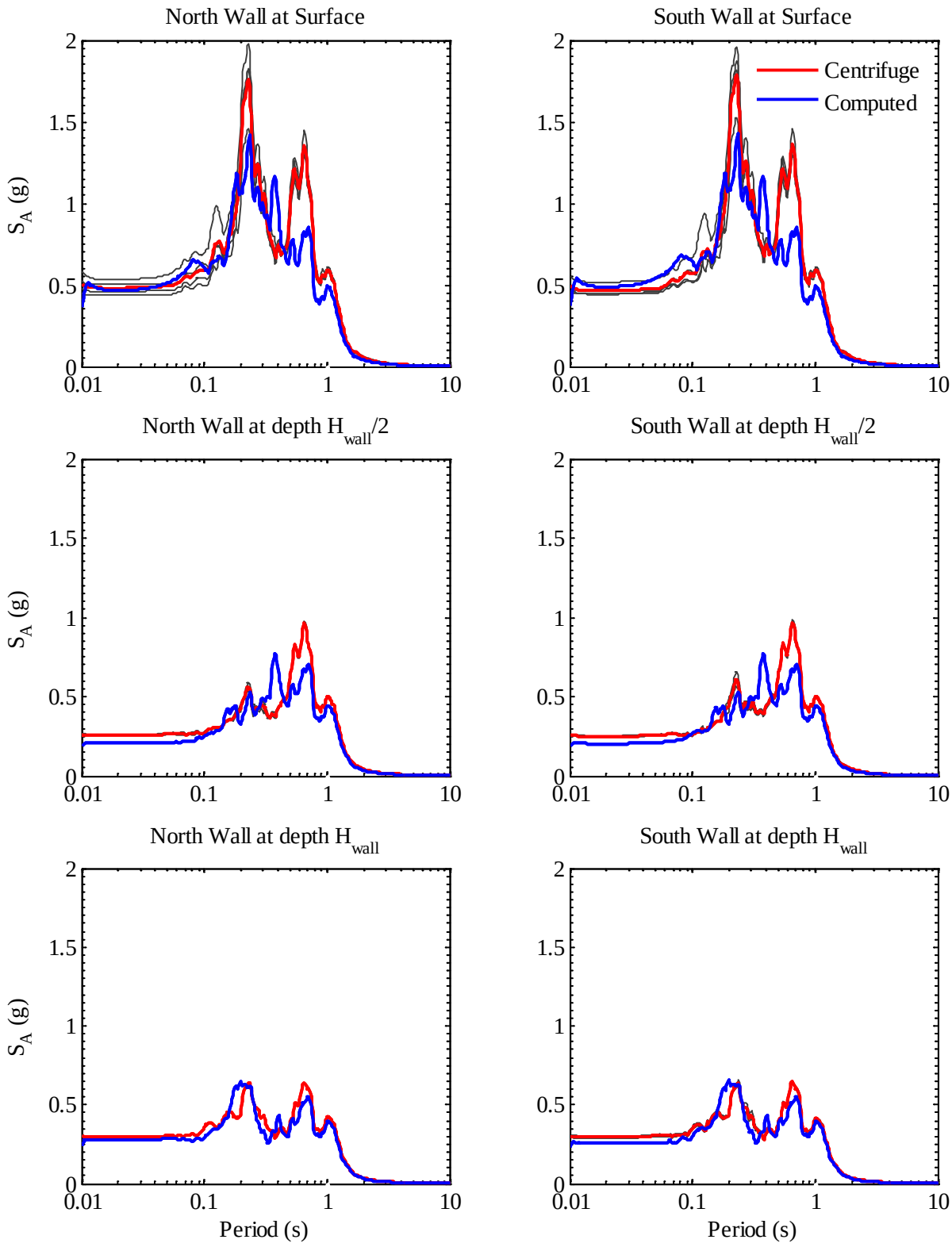

Figure A.18: Measured and computed acceleration response spectra in structure at 5% damping during Kocaeli YPT 330

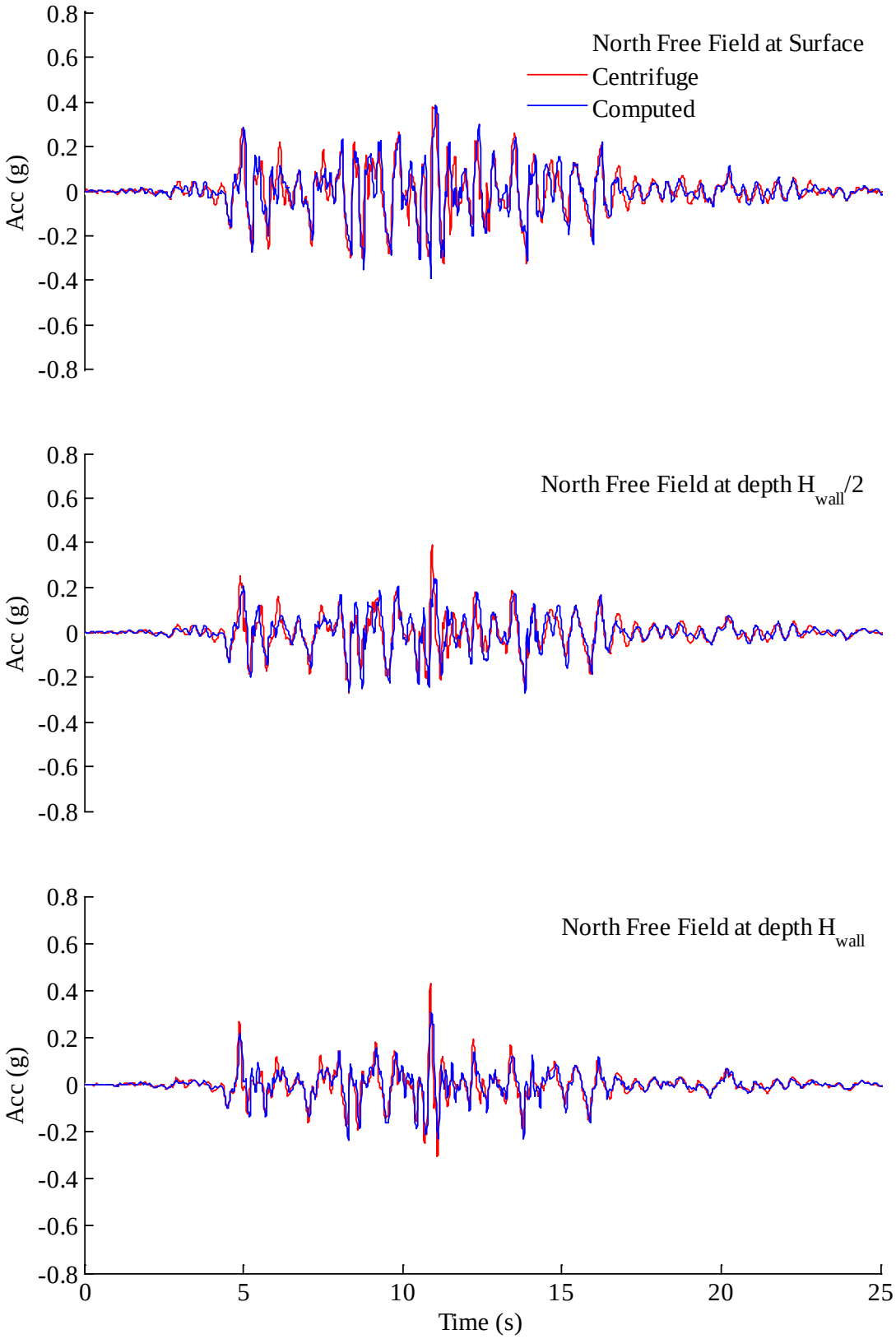

Figure A.19: Measured and computed accelerations in north free field during Loma Prieta SC-1

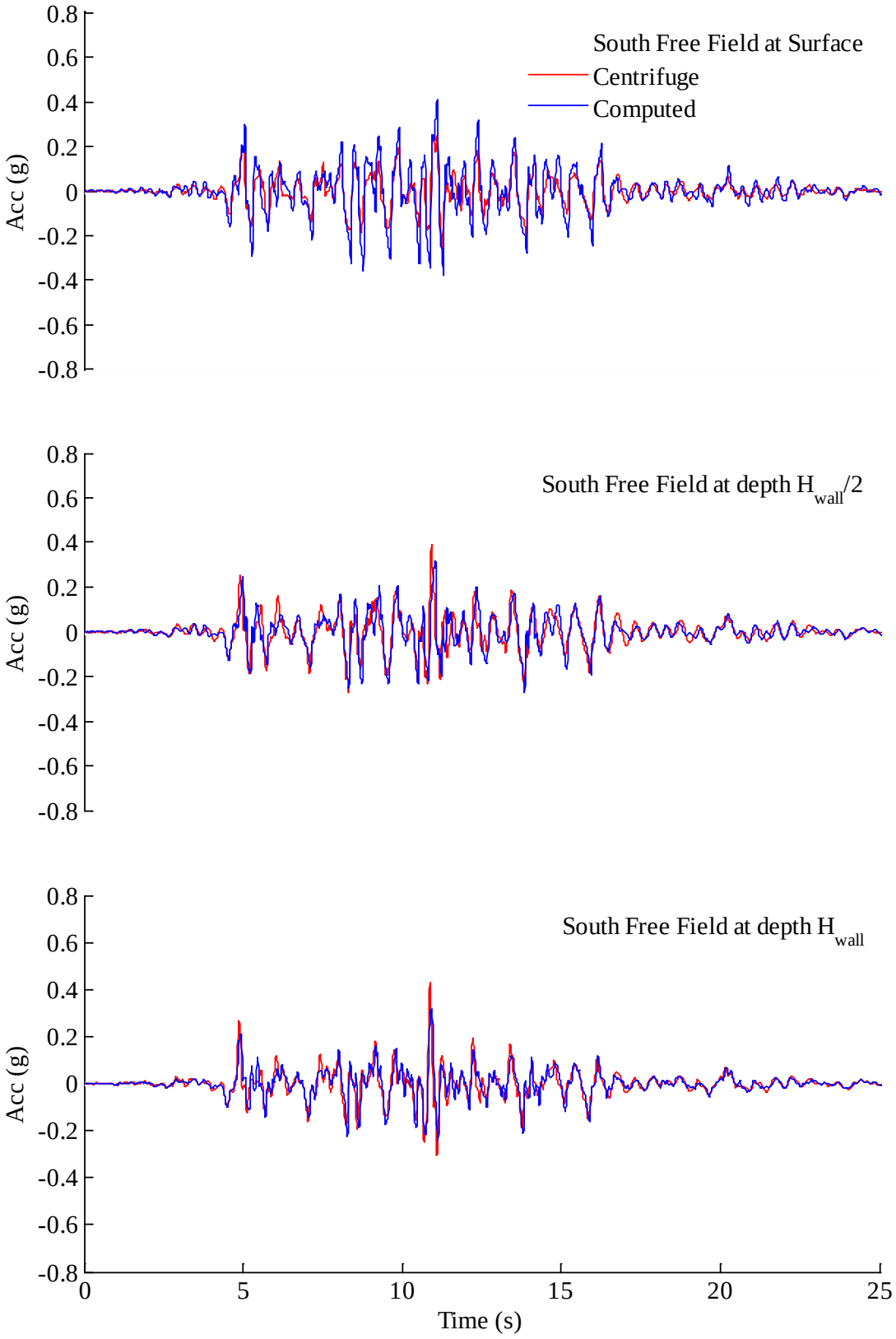

Figure A.20: Measured and computed accelerations in south free field during Loma Prieta SC-1

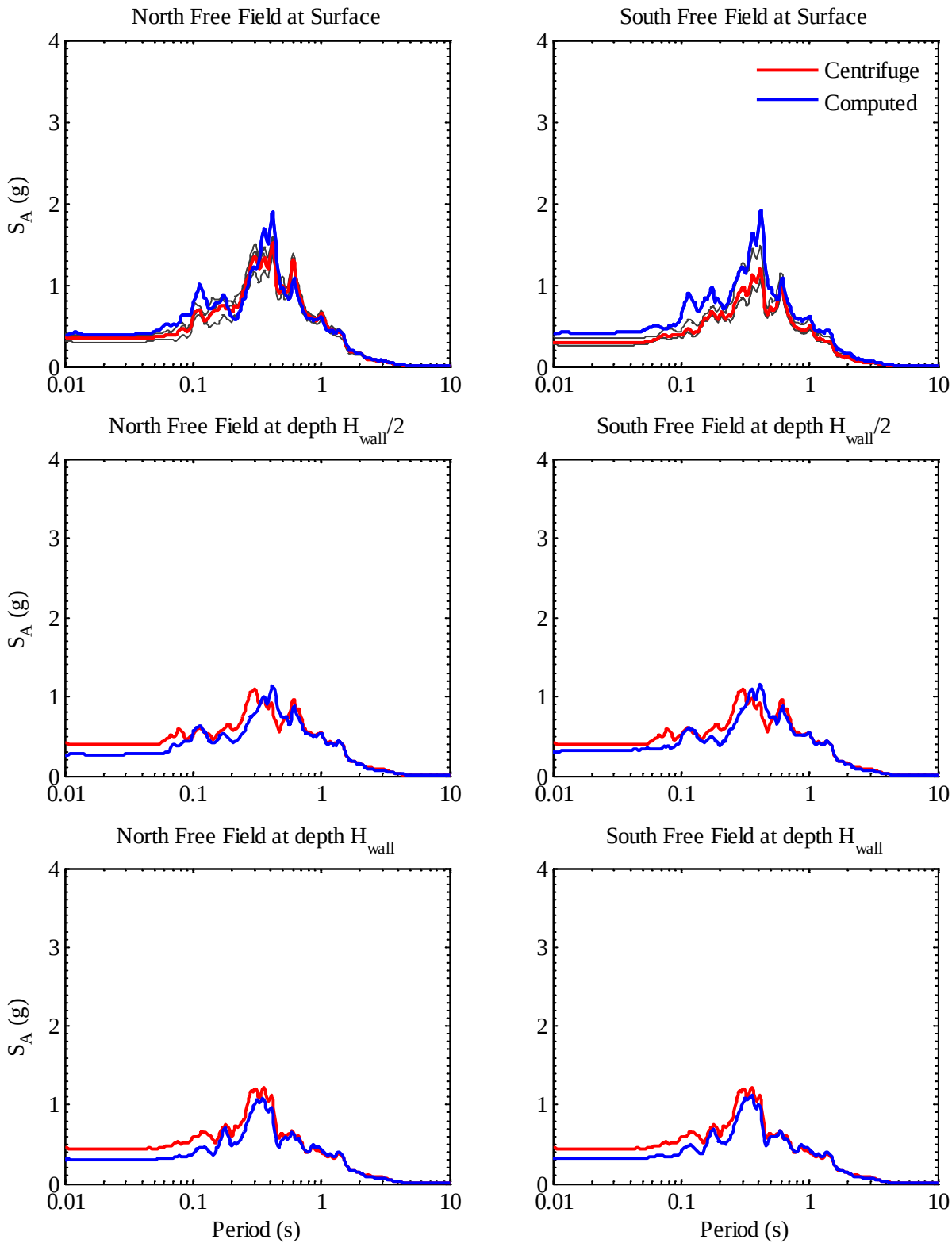

Figure A.21: Measured and computed acceleration response spectra in free field at 5% damping during Loma Prieta SC-1

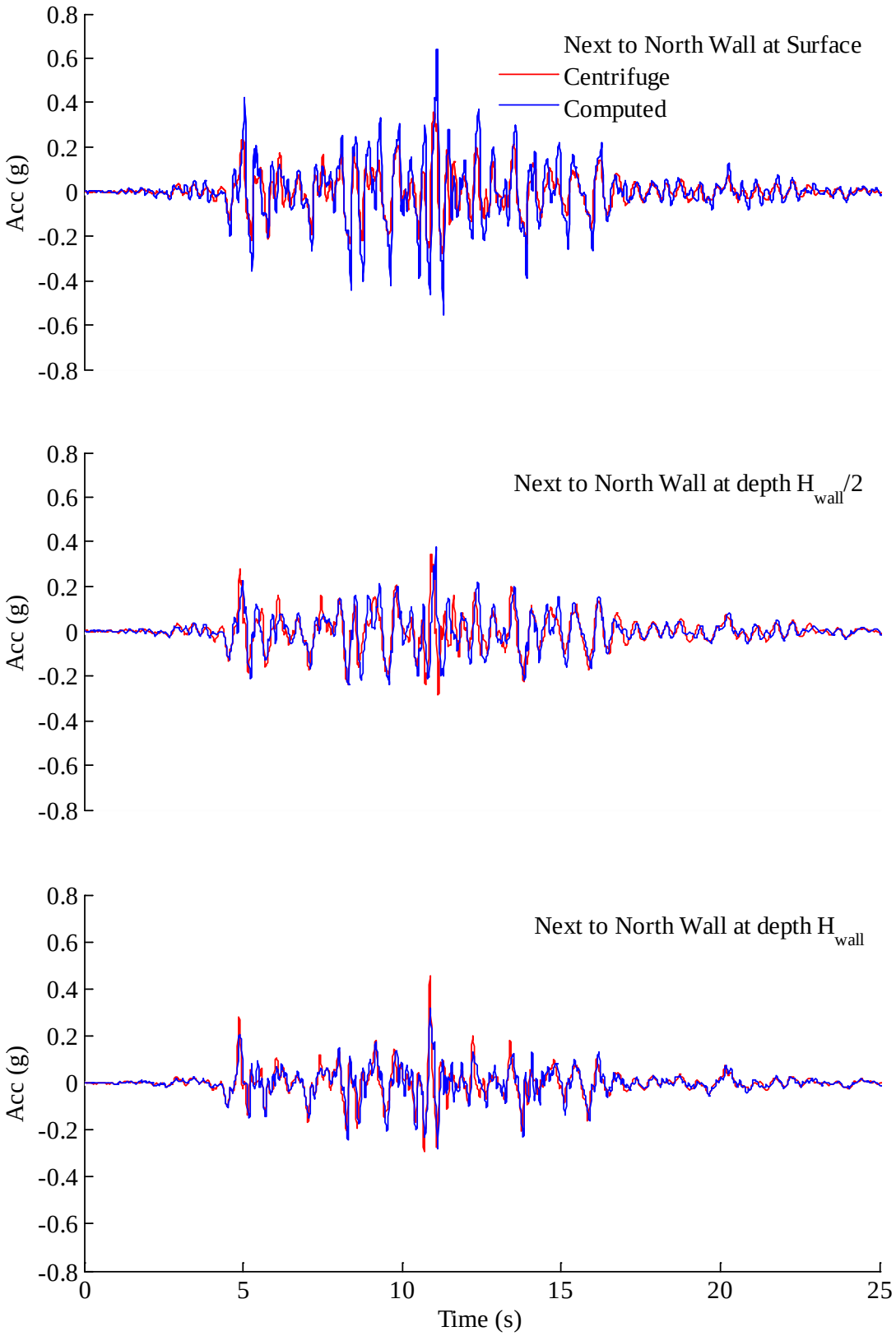

Figure A.22: Measured and computed accelerations next to north wall during Loma Prieta SC-1

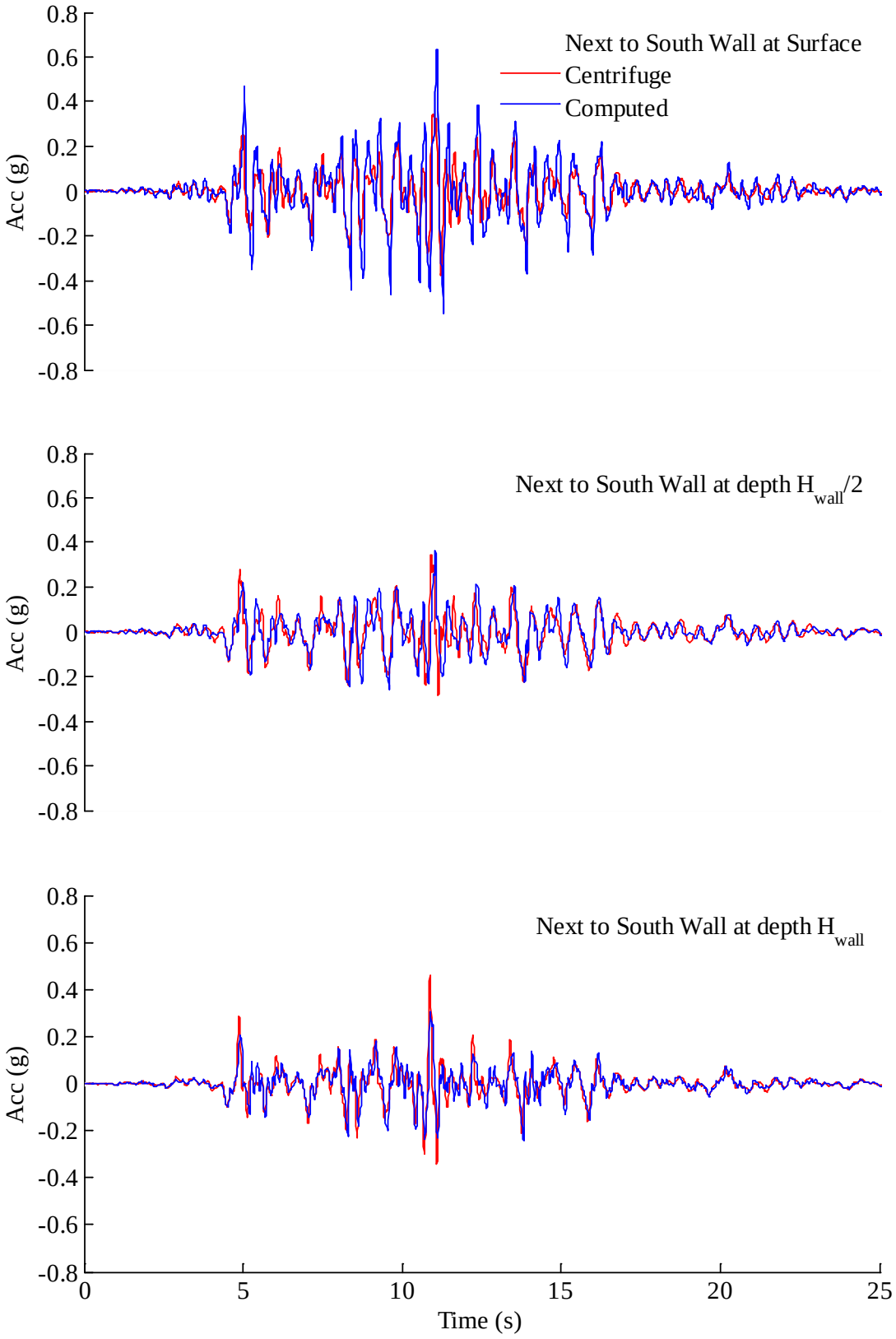

Figure A.23: Measured and computed accelerations next to south wall during Loma Prieta SC-1

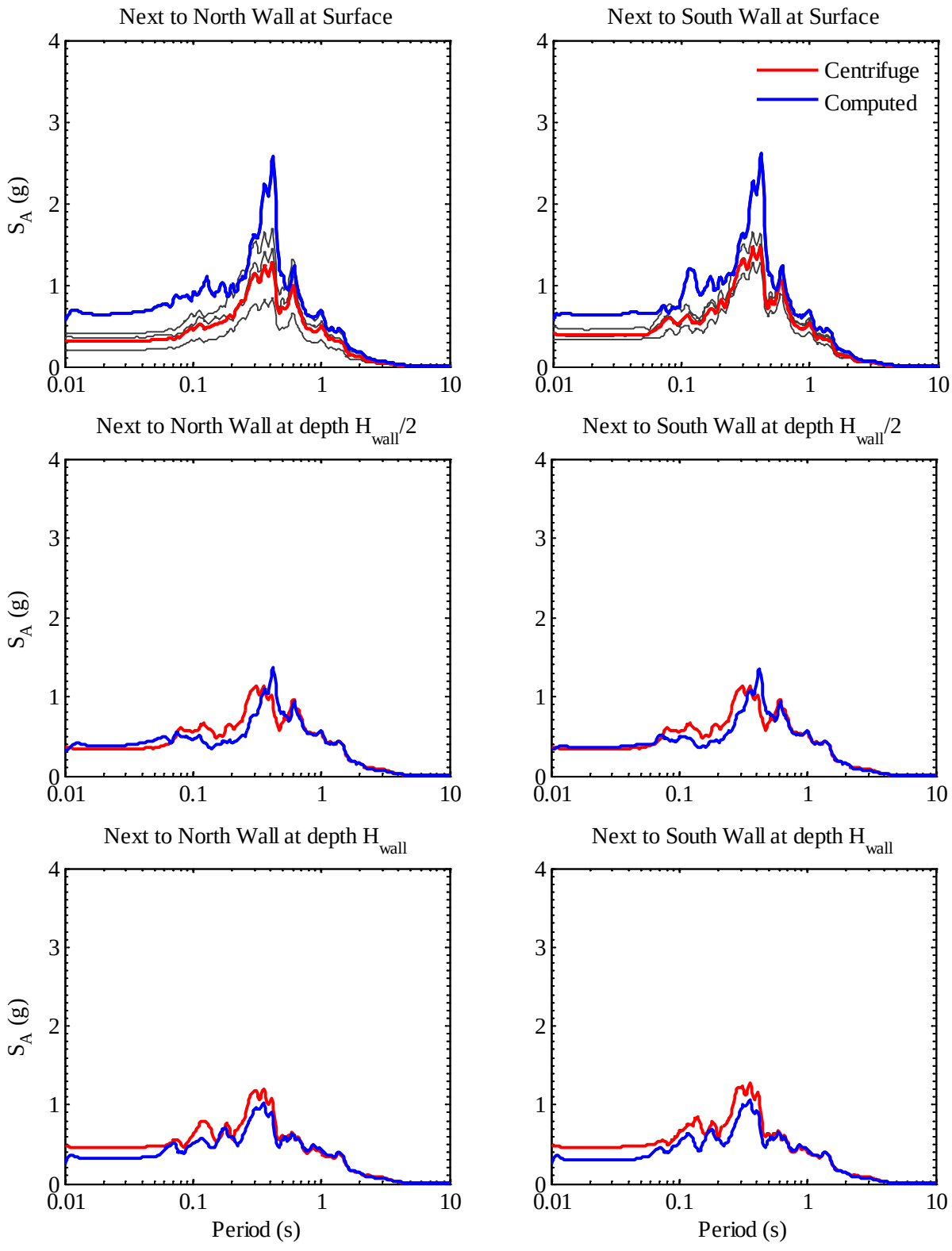

Figure A.24: Measured and computed acceleration response spectra in soil next to structure at 5% damping during Loma Prieta SC-1

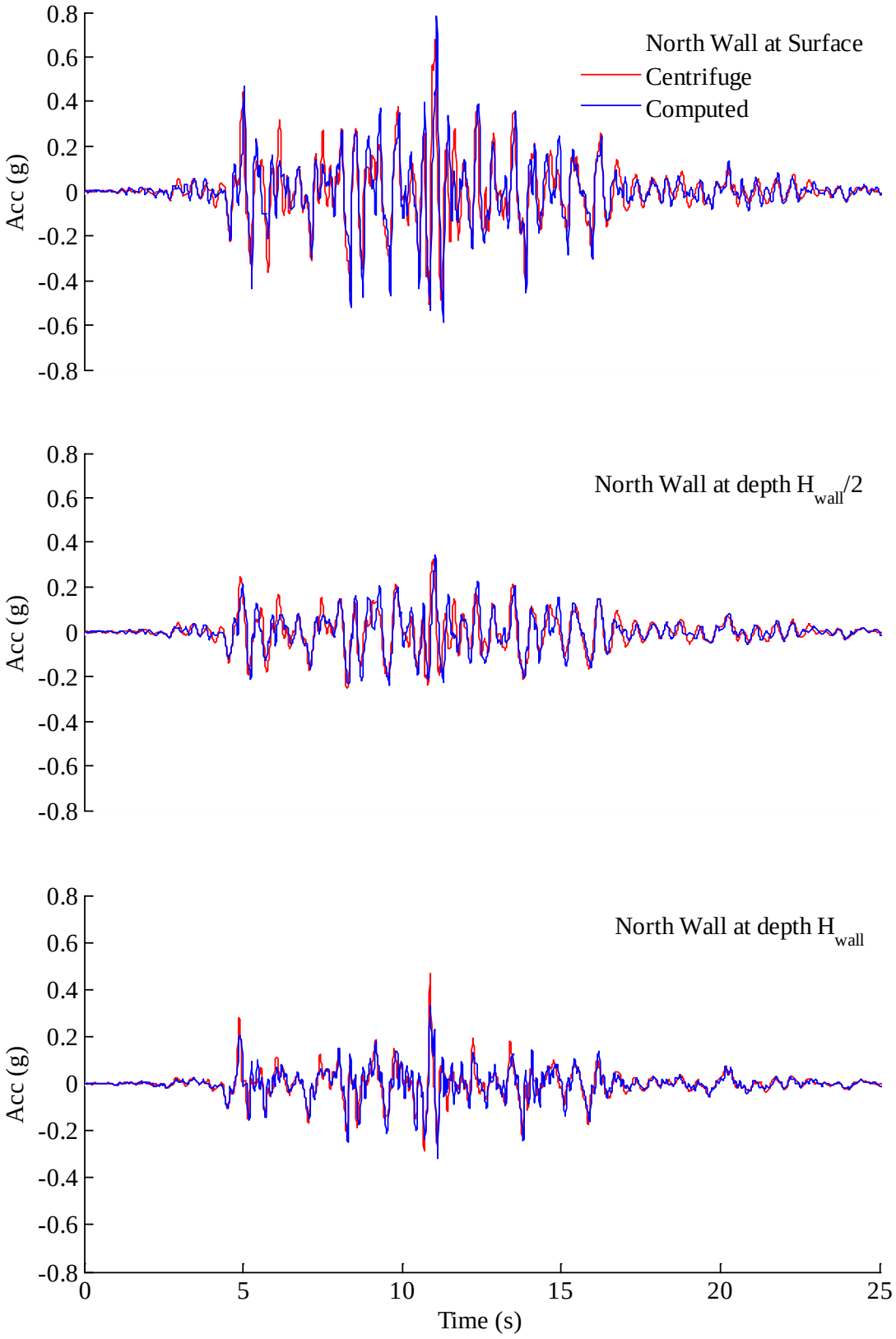

Figure A.25: Measured and computed accelerations in north wall during Loma Prieta SC-1

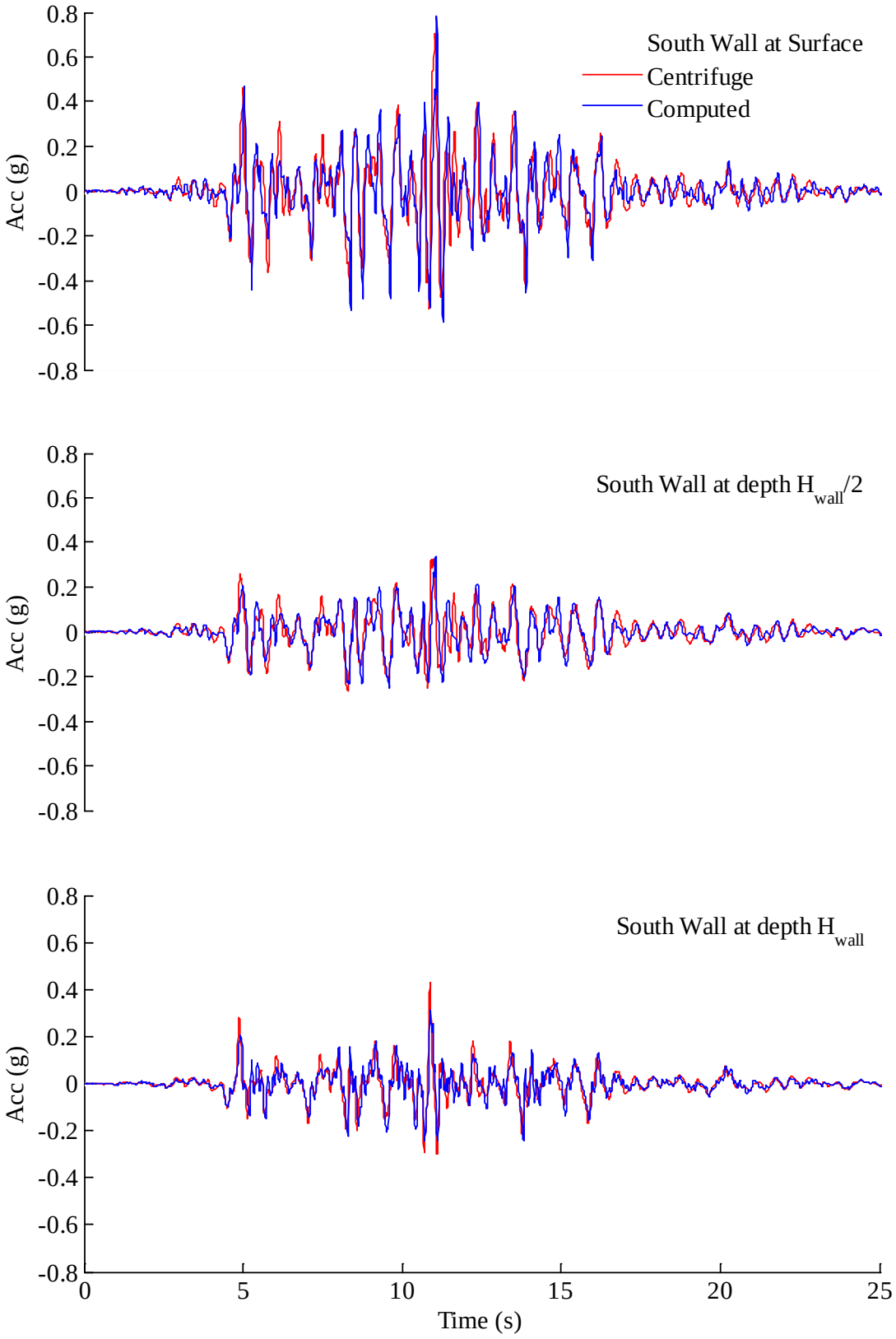

Figure A.26: Measured and computed accelerations in south wall during Loma Prieta SC-1

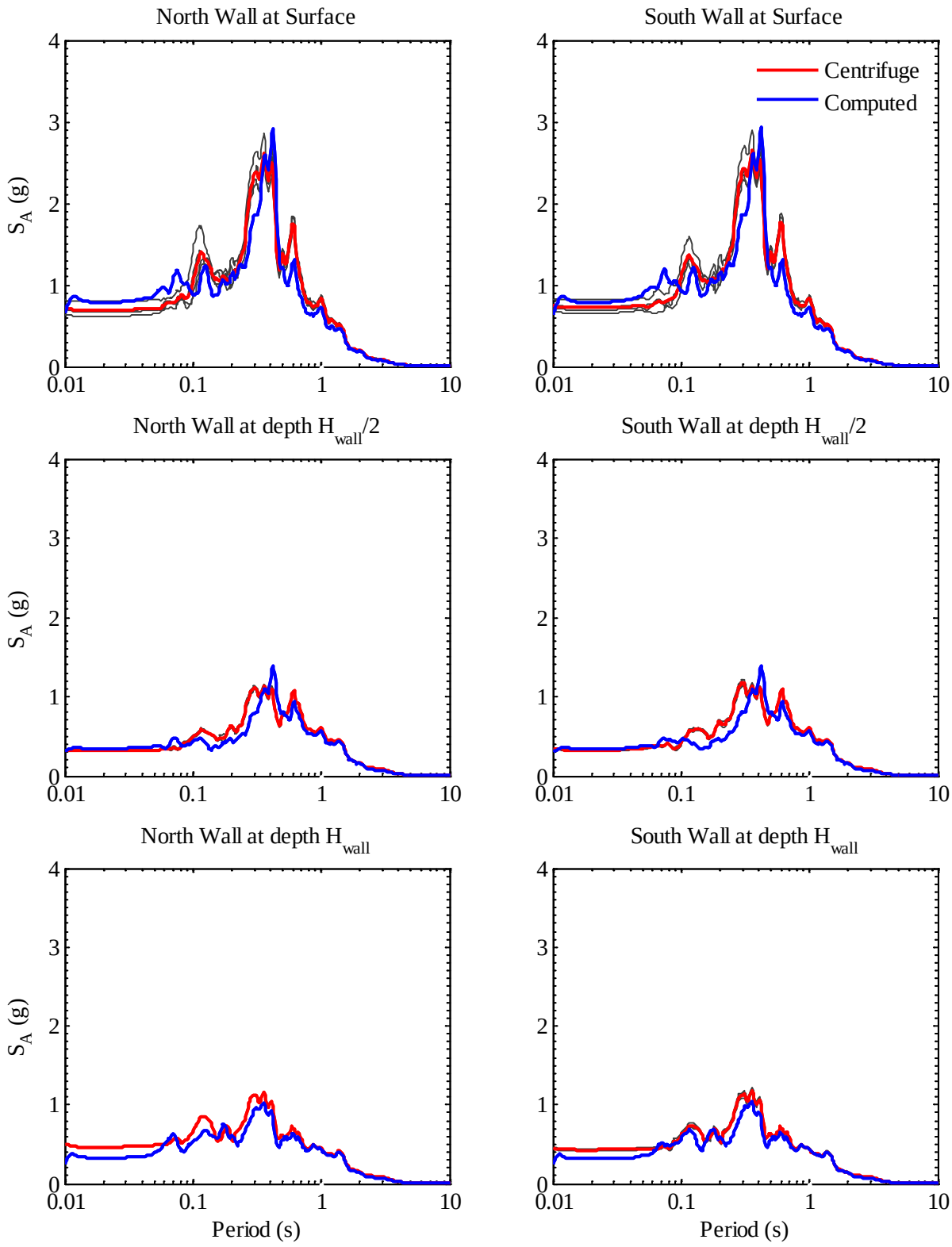

Figure A.27: Measured and computed acceleration response spectra in structure at 5% damping during Loma Prieta SC-1

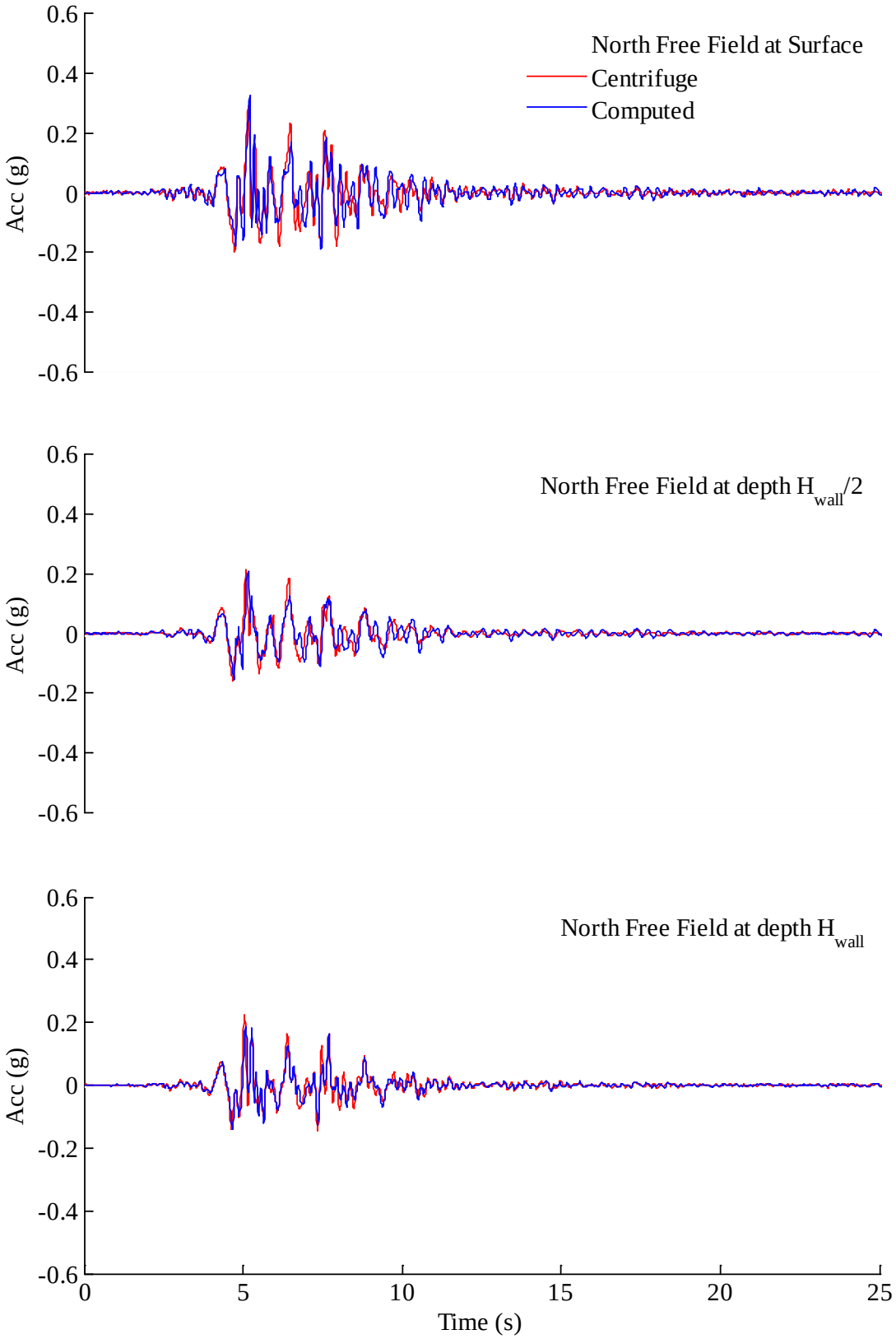

Figure A.28: Measured and computed accelerations in north free field during Loma Prieta WVC-1

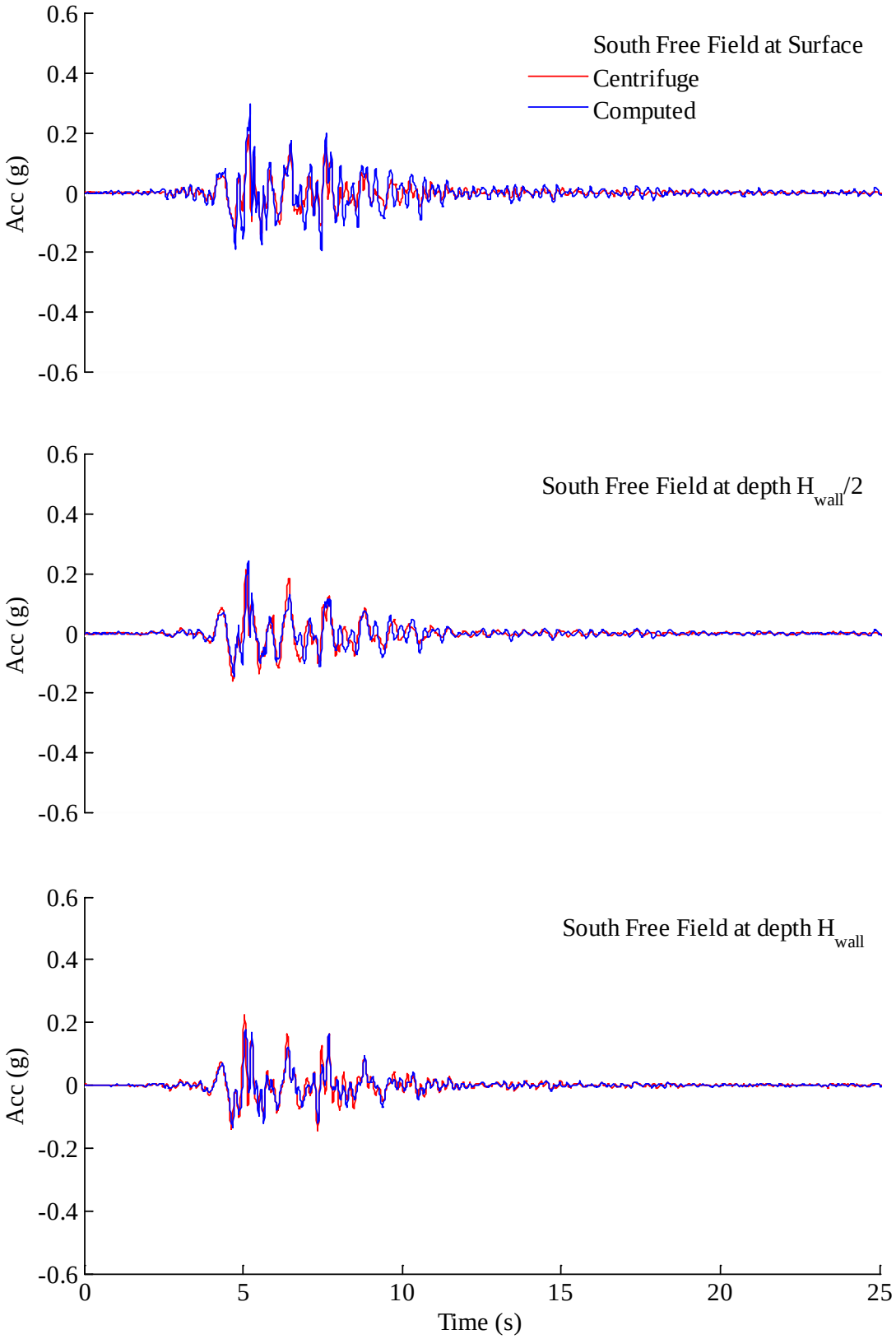

Figure A.29: Measured and computed accelerations in south free field during Loma Prieta WVC-1

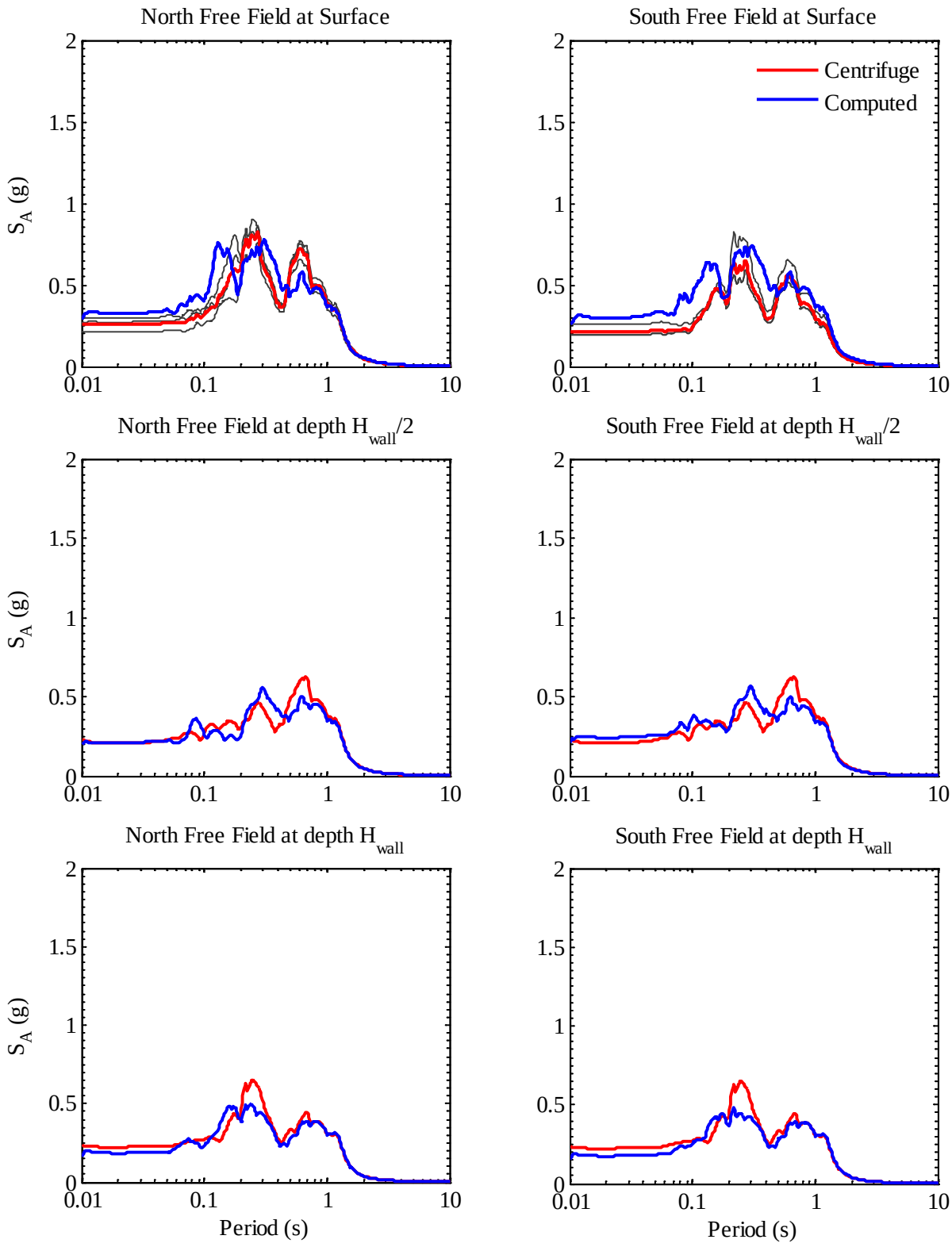

Figure A.30: Measured and computed acceleration response spectra in free field at 5% damping during Loma Prieta WVC-1

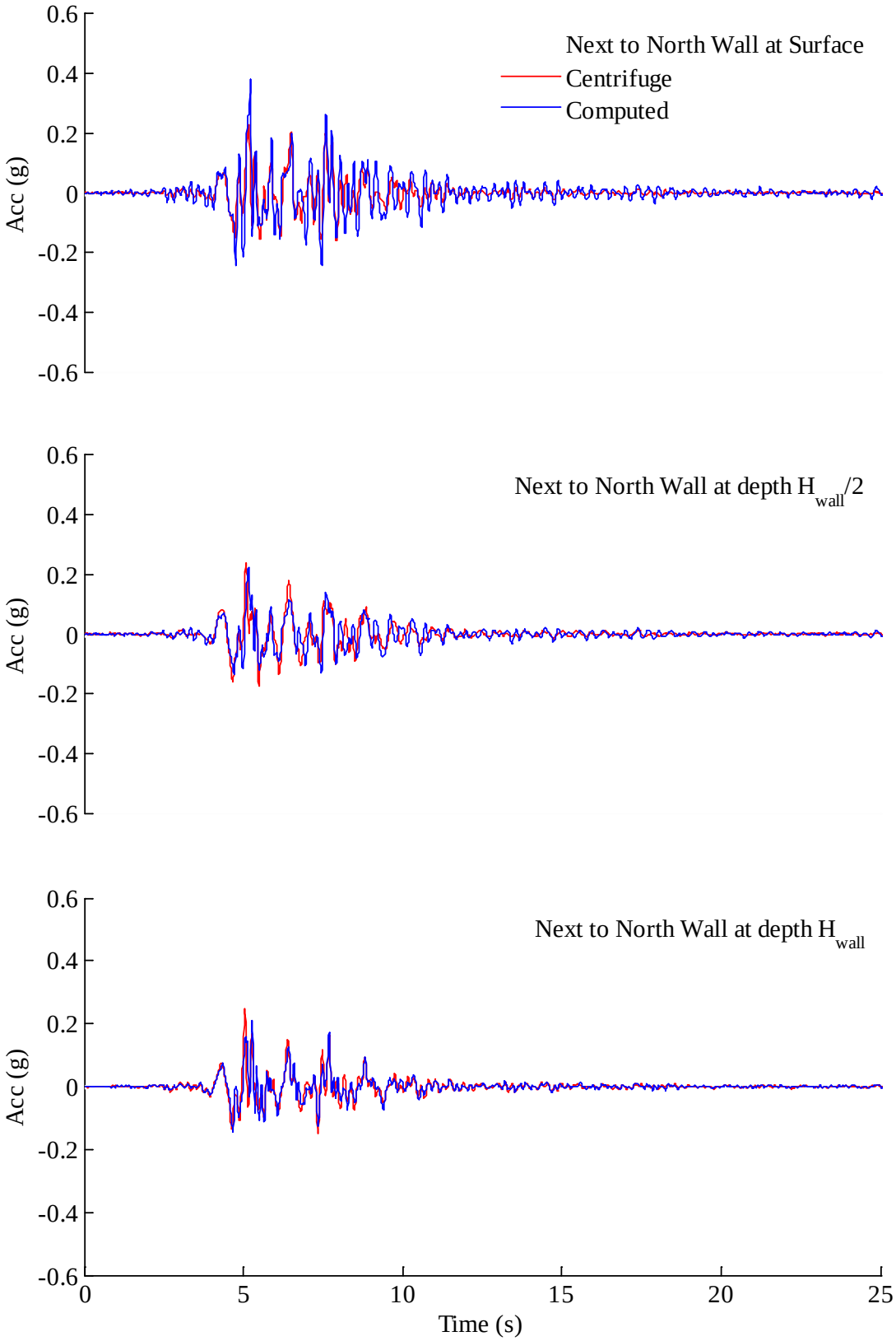

Figure A.31: Measured and computed accelerations next to north wall during Loma Prieta WVC-1

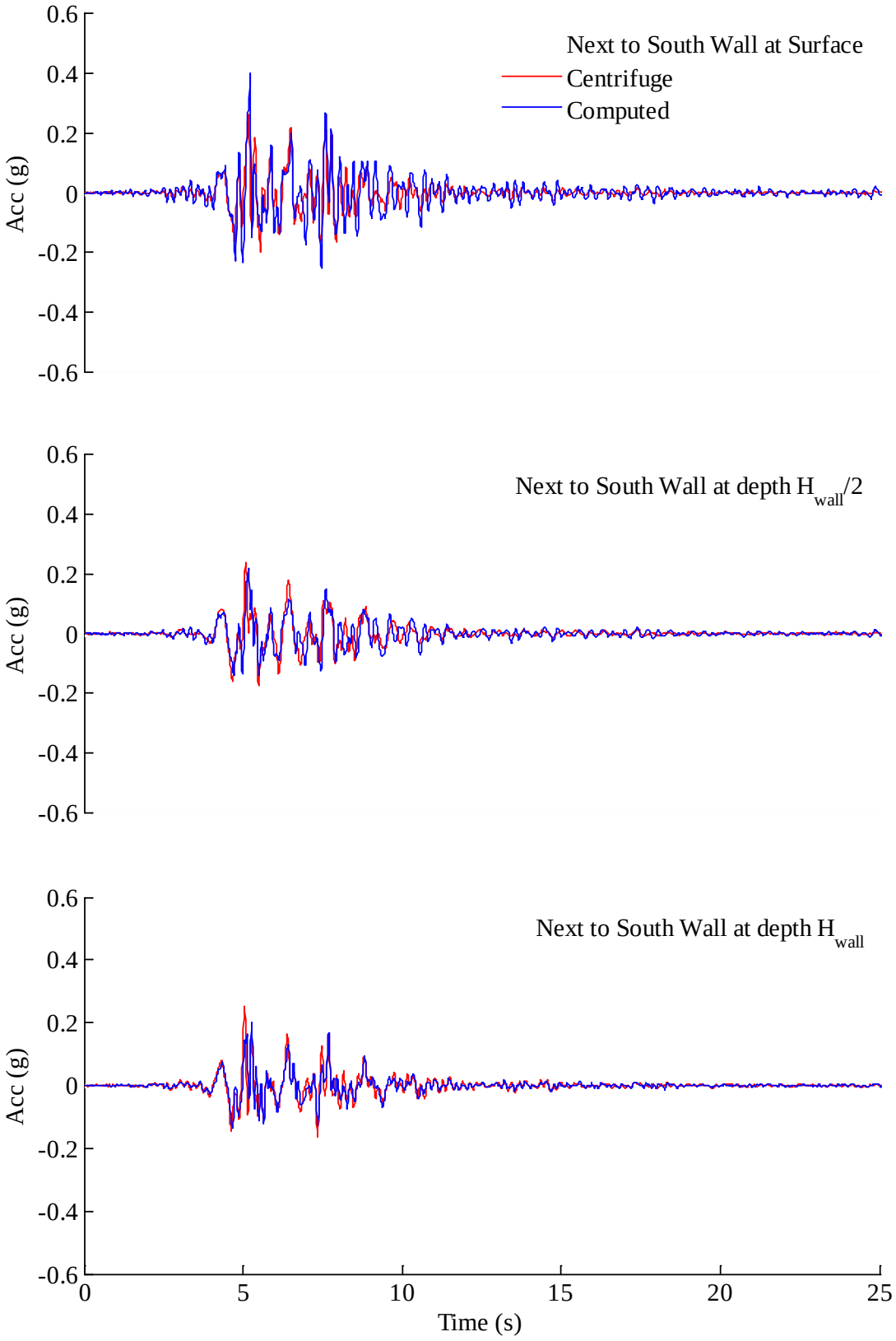

Figure A.32: Measured and computed accelerations next to south wall during Loma Prieta WVC-1

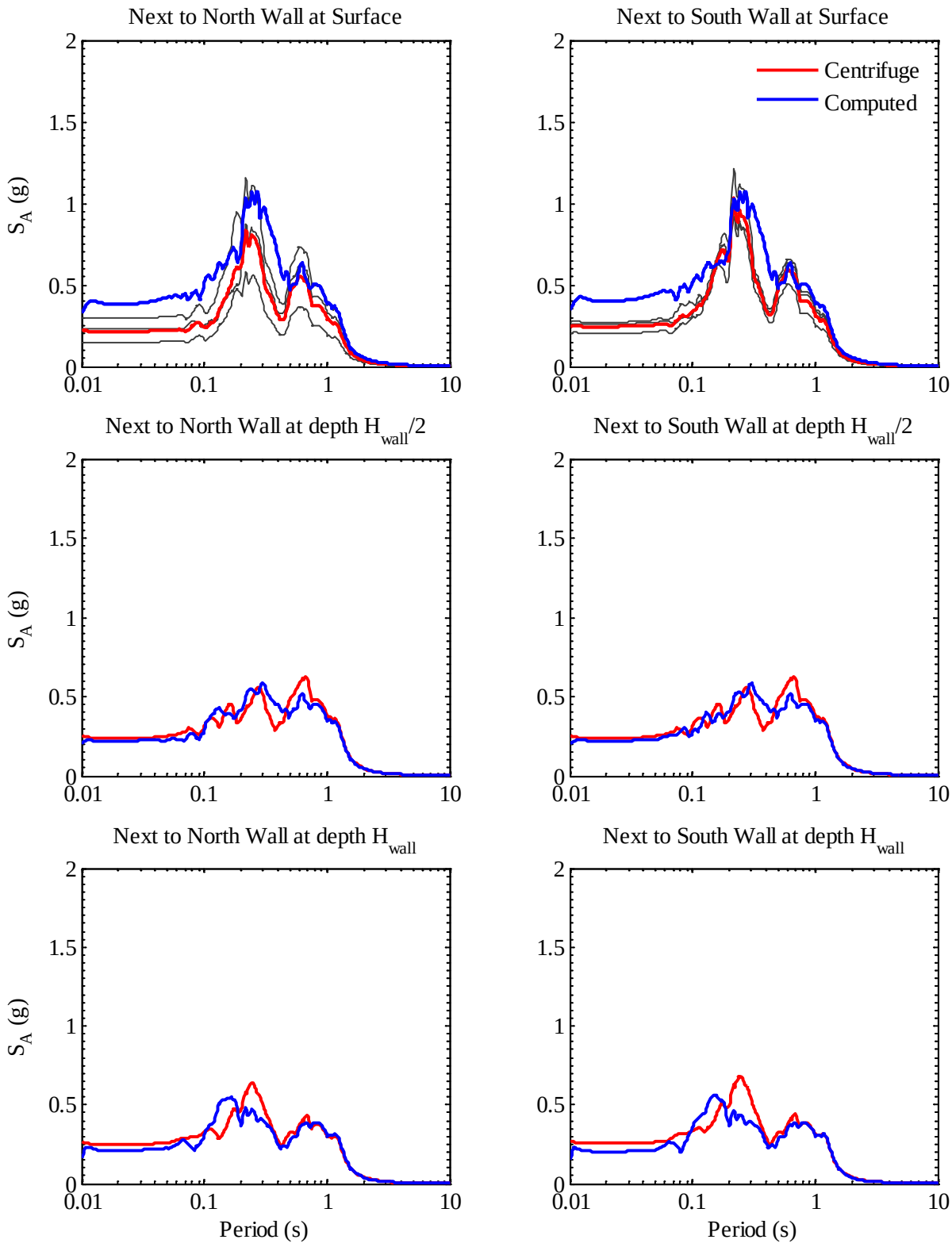

Figure A.33: Measured and computed acceleration response spectra in soil next to structure at 5% damping during Loma Prieta WVC-1

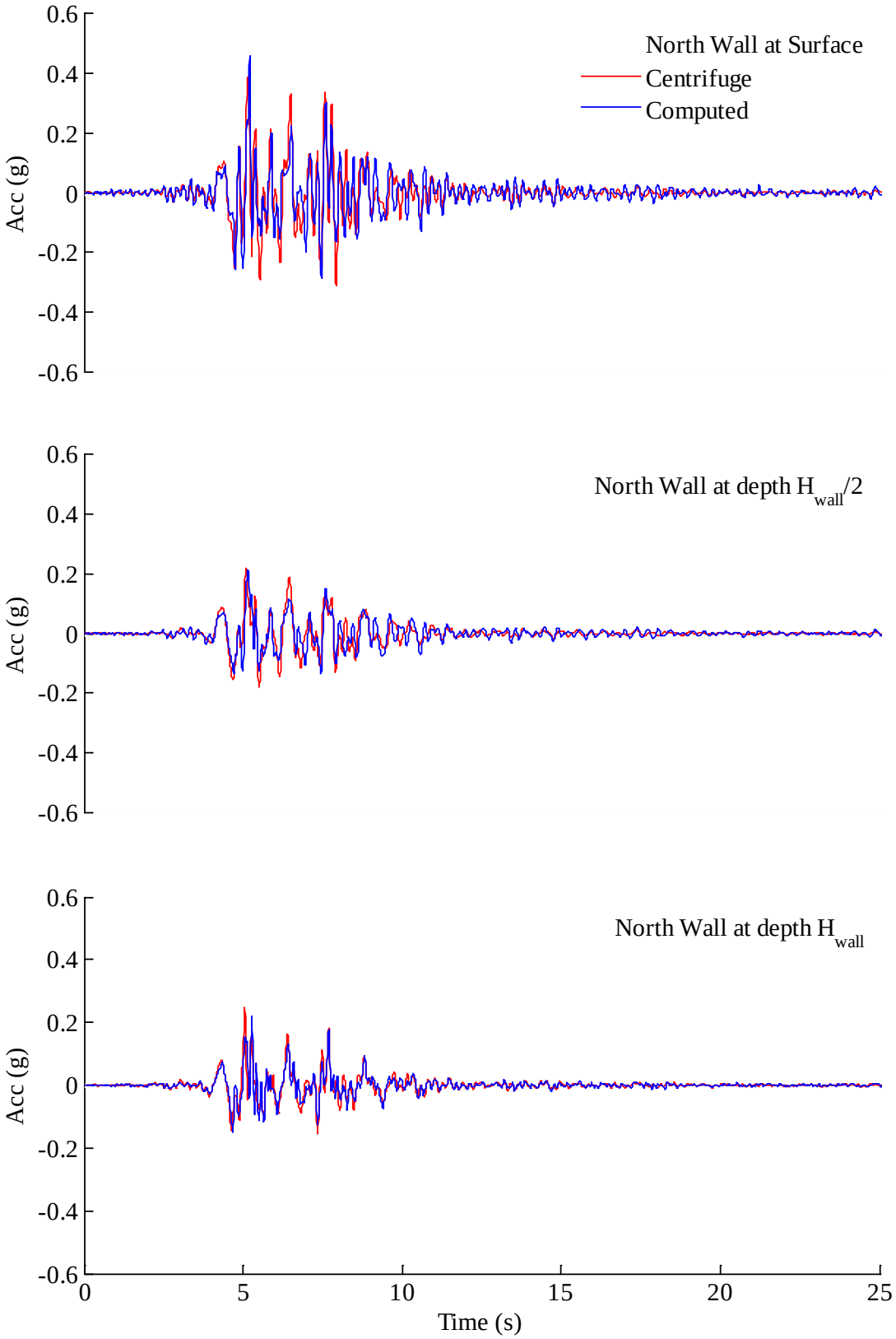

Figure A.34: Measured and computed accelerations in north wall during Loma Prieta WVC-1

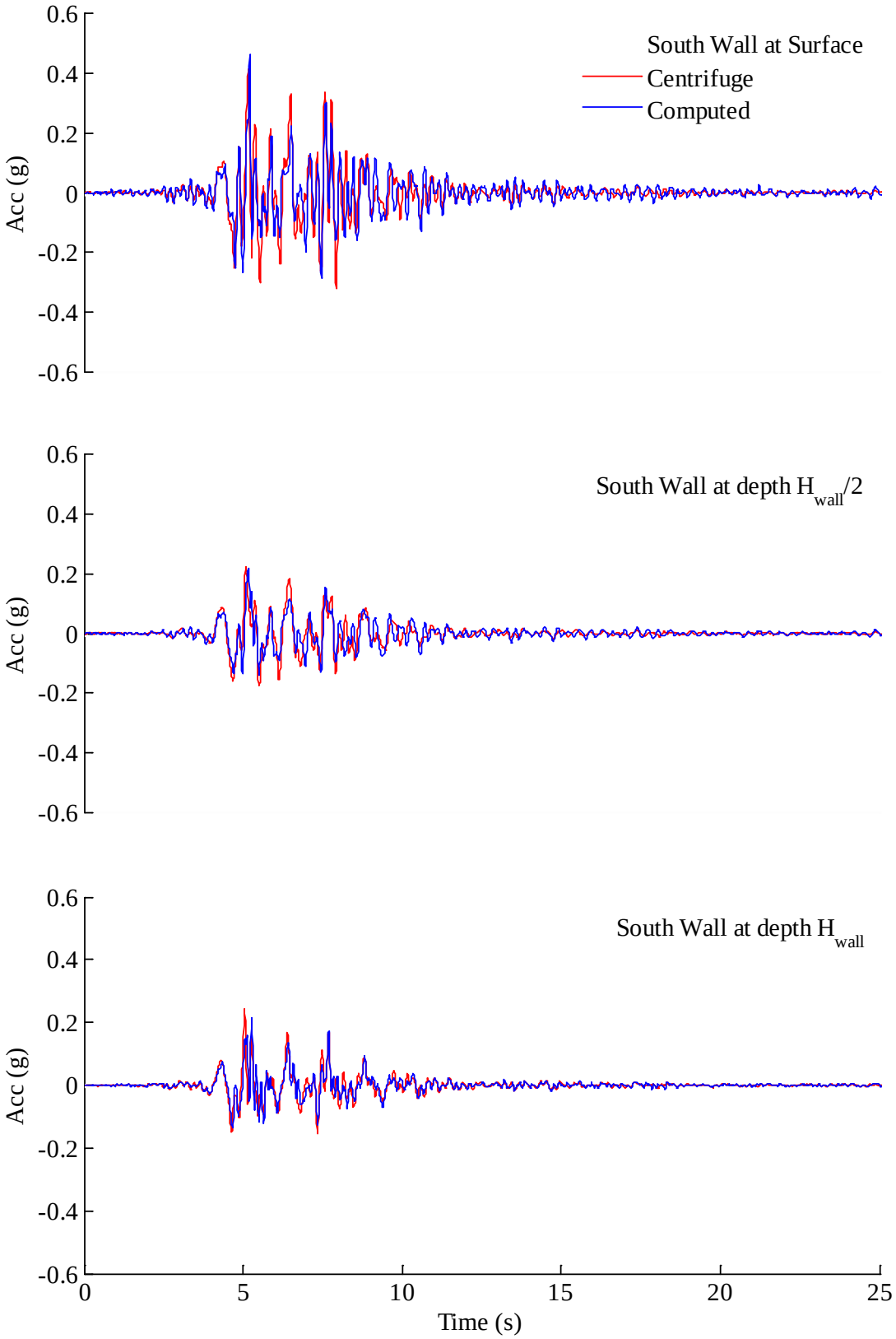

Figure A.35: Measured and computed accelerations in south wall during Loma Prieta WVC-1

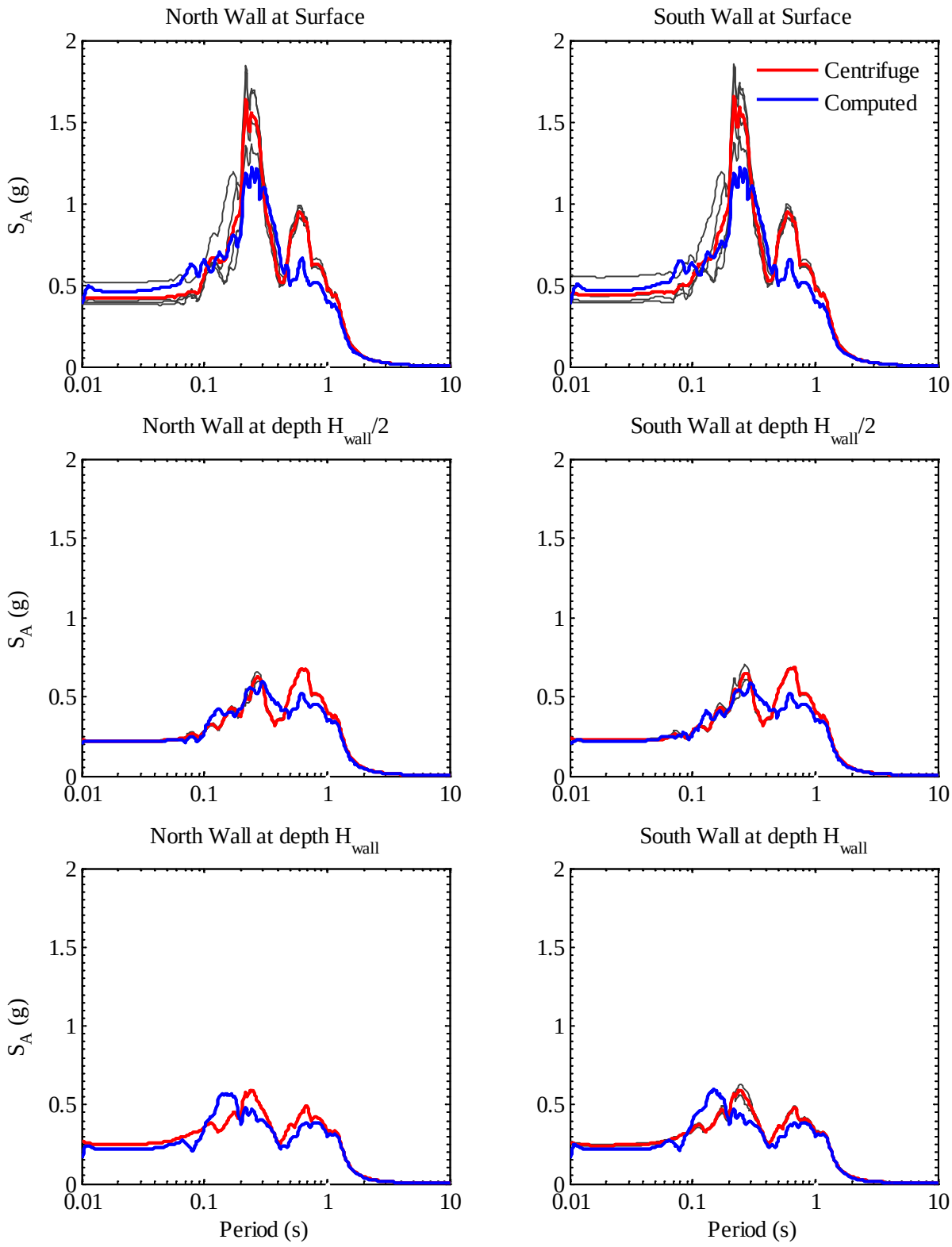

Figure A.36: Measured and computed acceleration response spectra in structure at 5% damping during Loma Prieta WVC-1

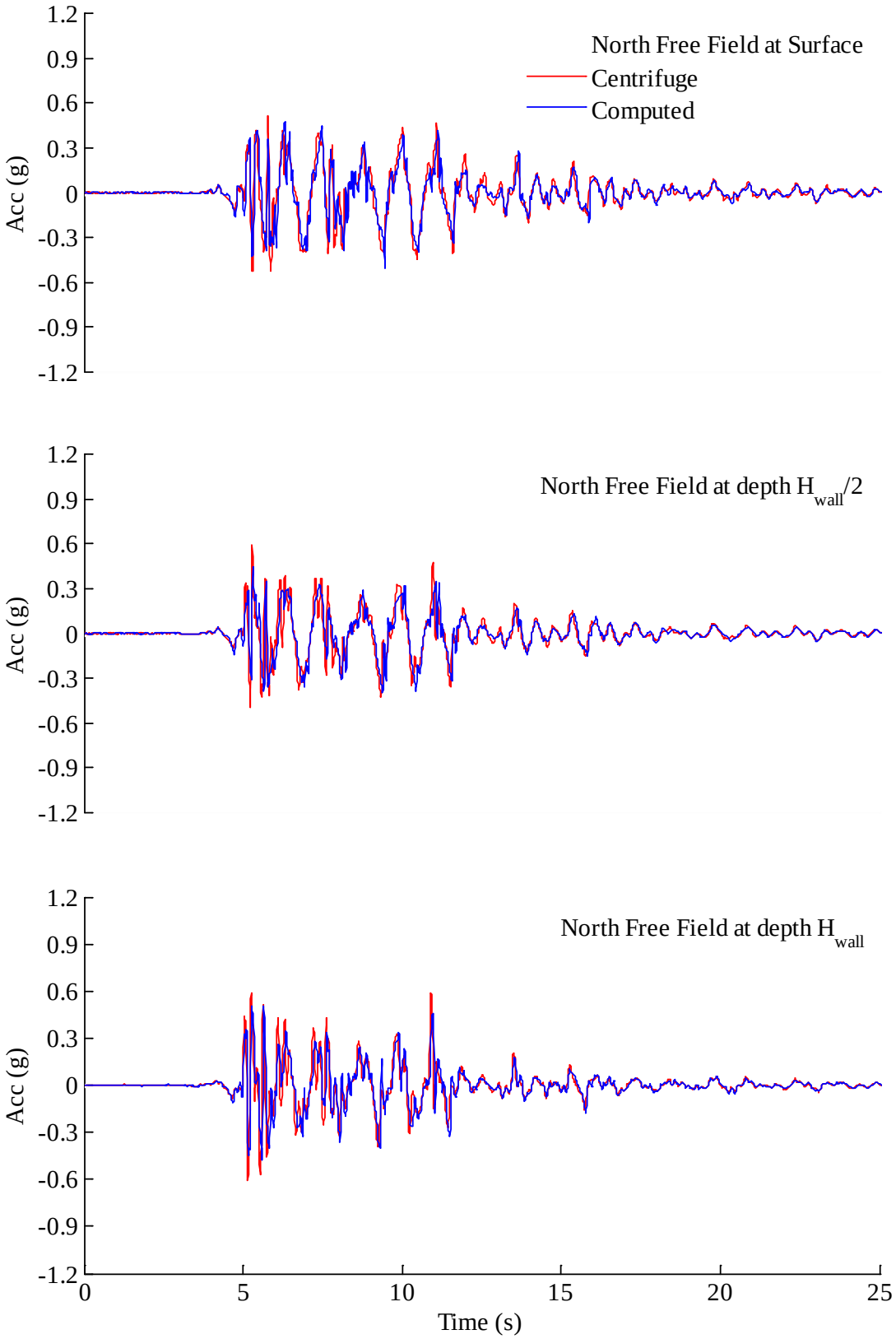

Figure A.37: Measured and computed accelerations in north free field during Kobe TAK 090-3

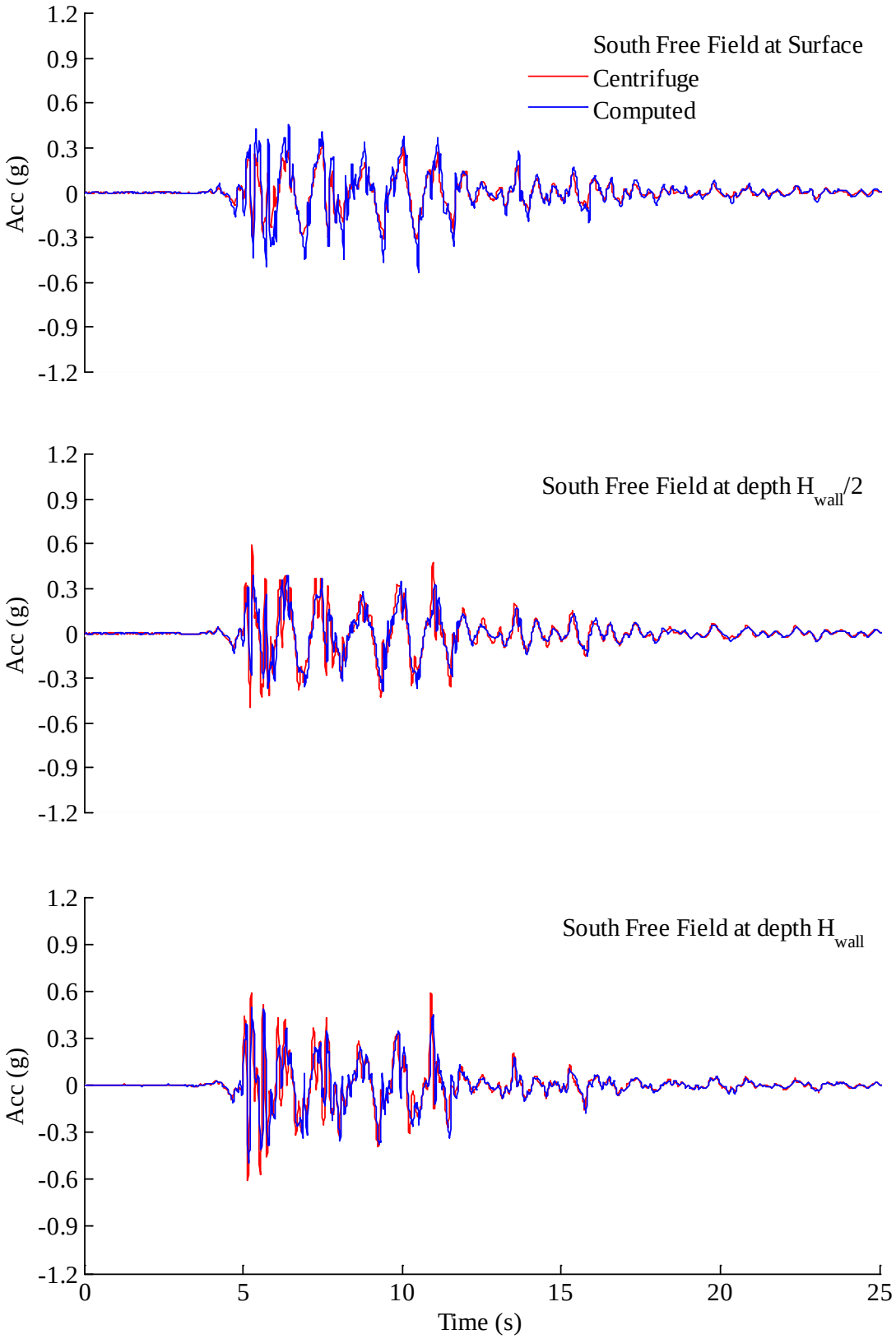

Figure A.38: Measured and computed accelerations in south free field during Kobe TAK 090-3

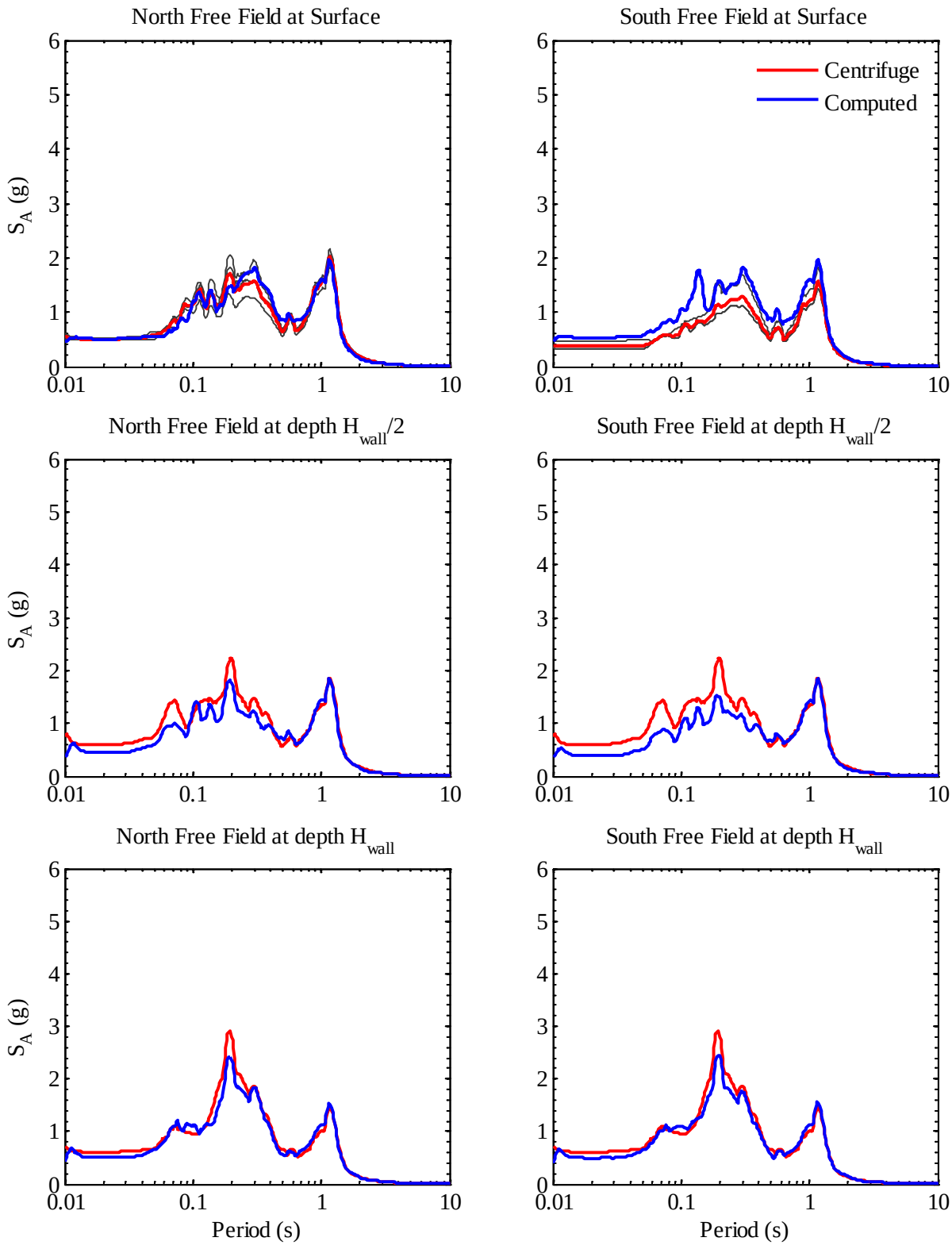

Figure A.39: Measured and computed acceleration response spectra in free field at 5% damping during Kobe TAK 090-3

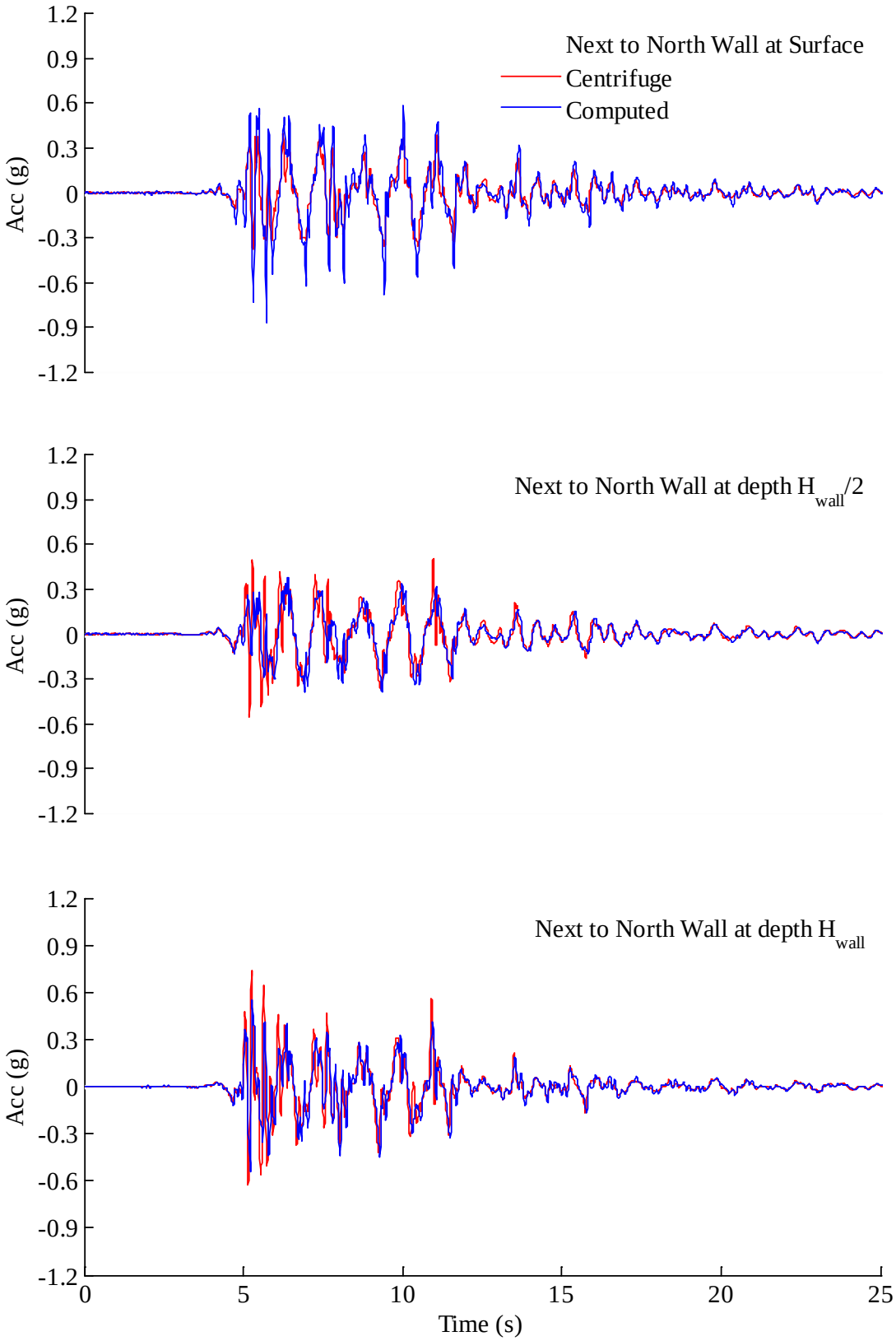

Figure A.40: Measured and computed accelerations next to north wall during Kobe TAK 090-3

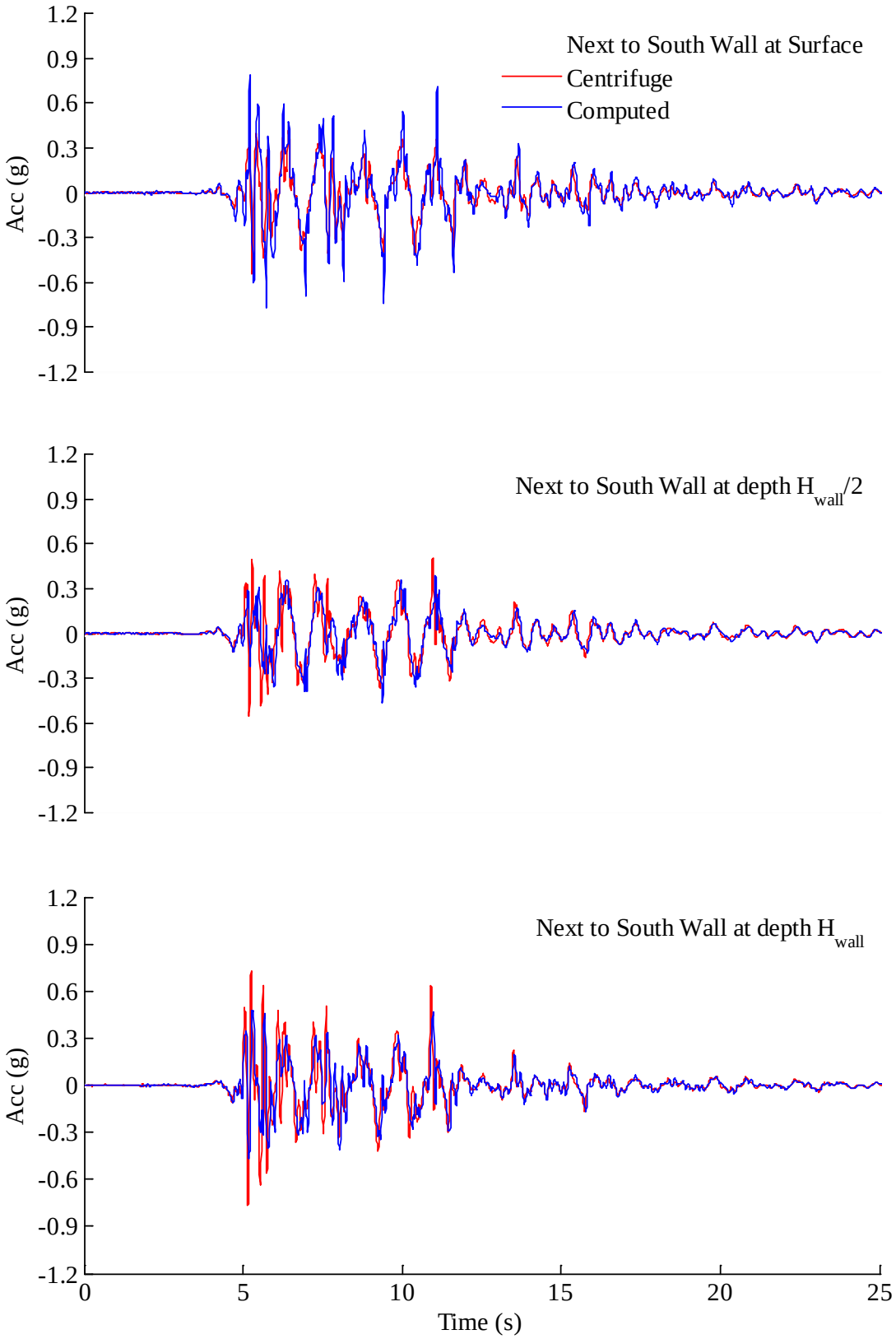

Figure A.41: Measured and computed accelerations next to south wall during Kobe TAK 090-3

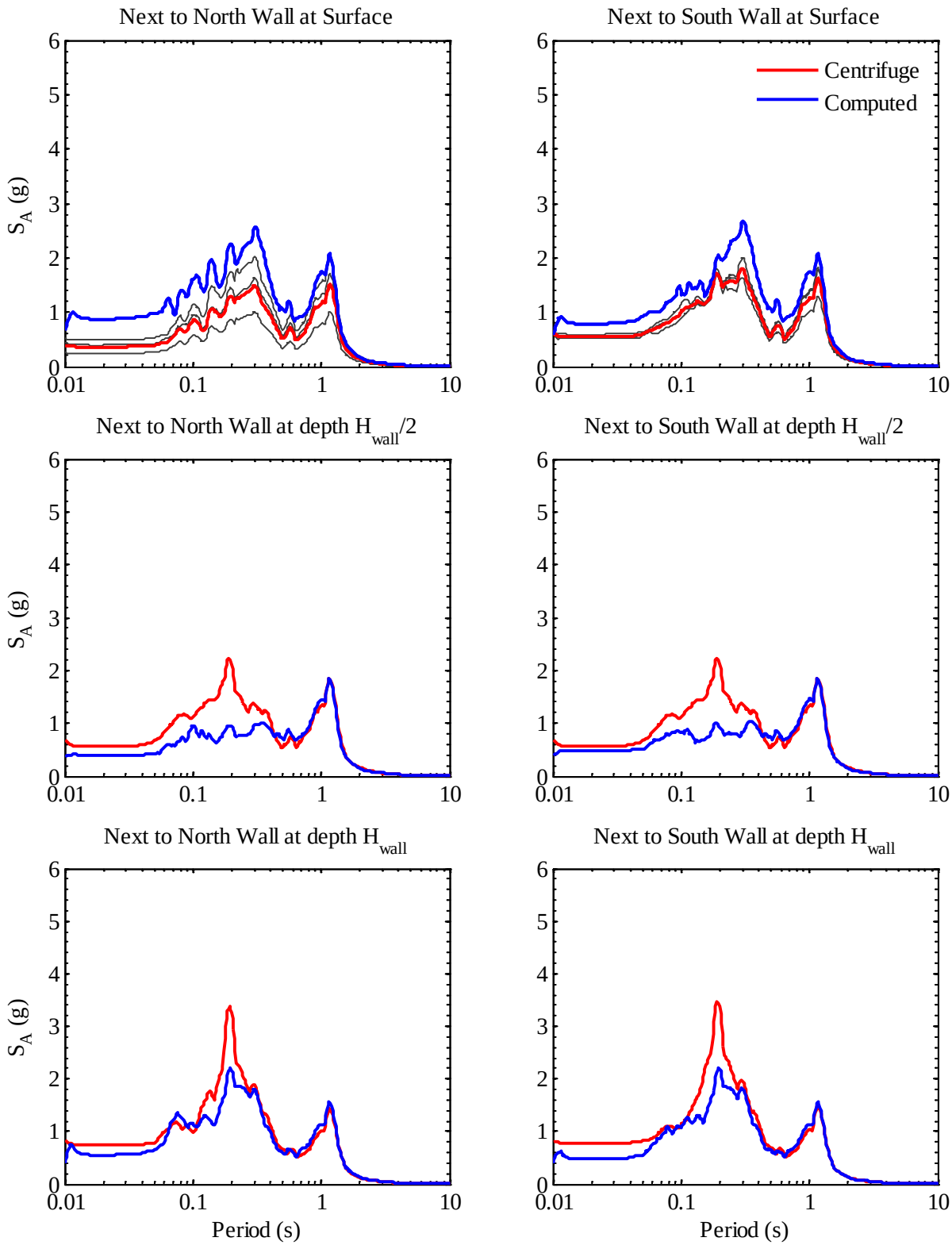

Figure A.42: Measured and computed acceleration response spectra in soil next to structure during Kobe TAK 090-3

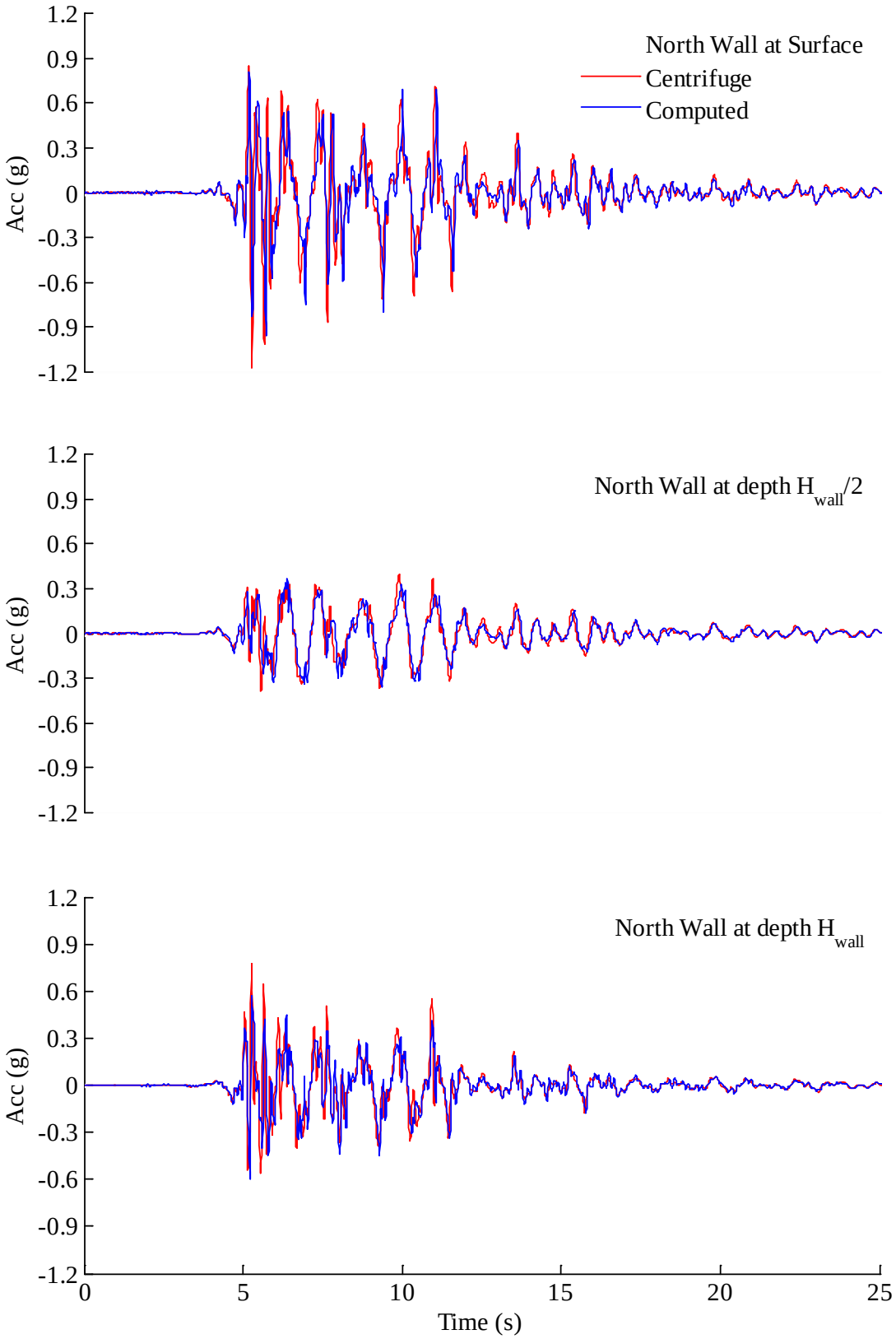

Figure A.43: Measured and computed accelerations in north wall during Kobe TAK 090-3

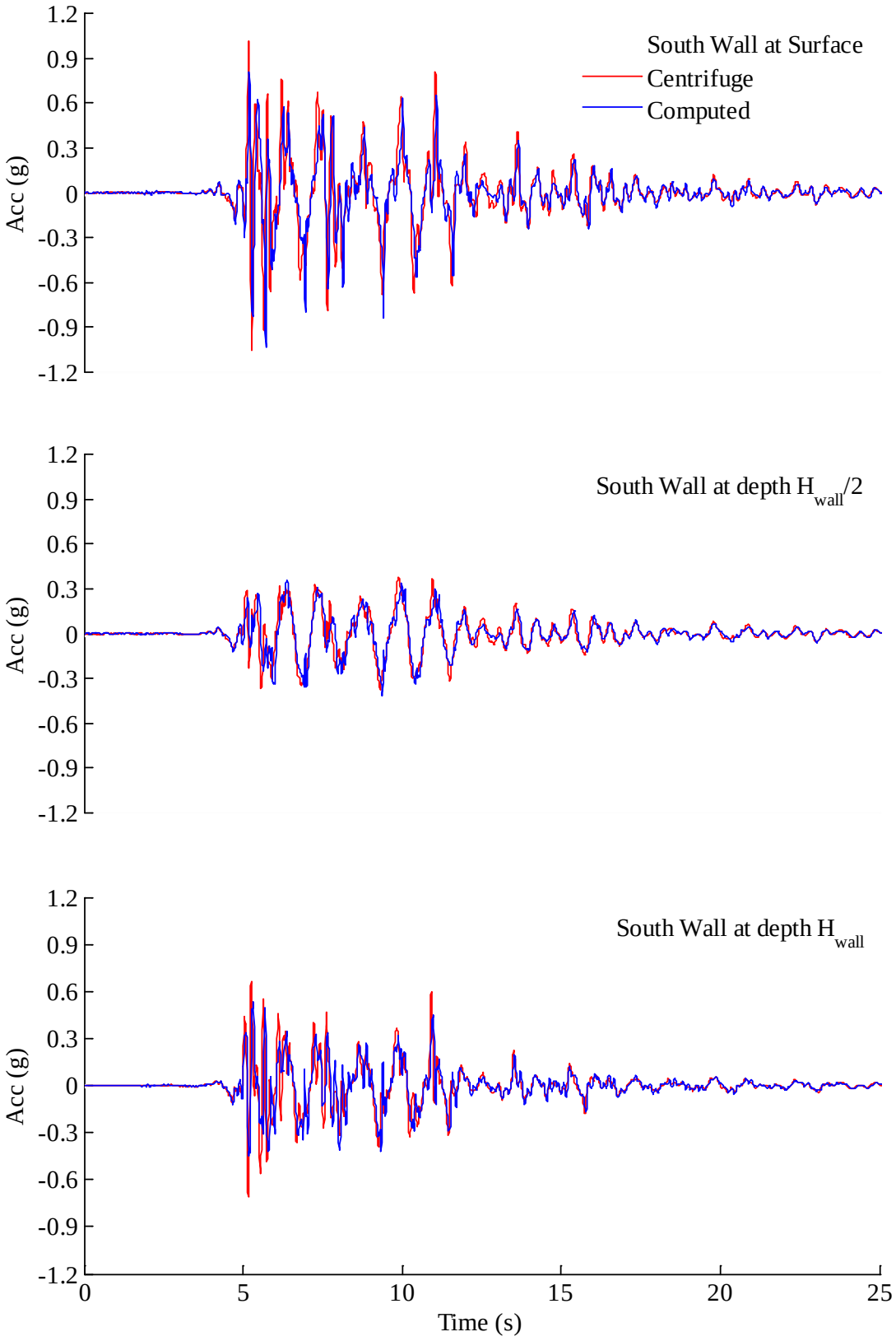

Figure A.44: Measured and computed accelerations in south wall during Kobe TAK 090-3

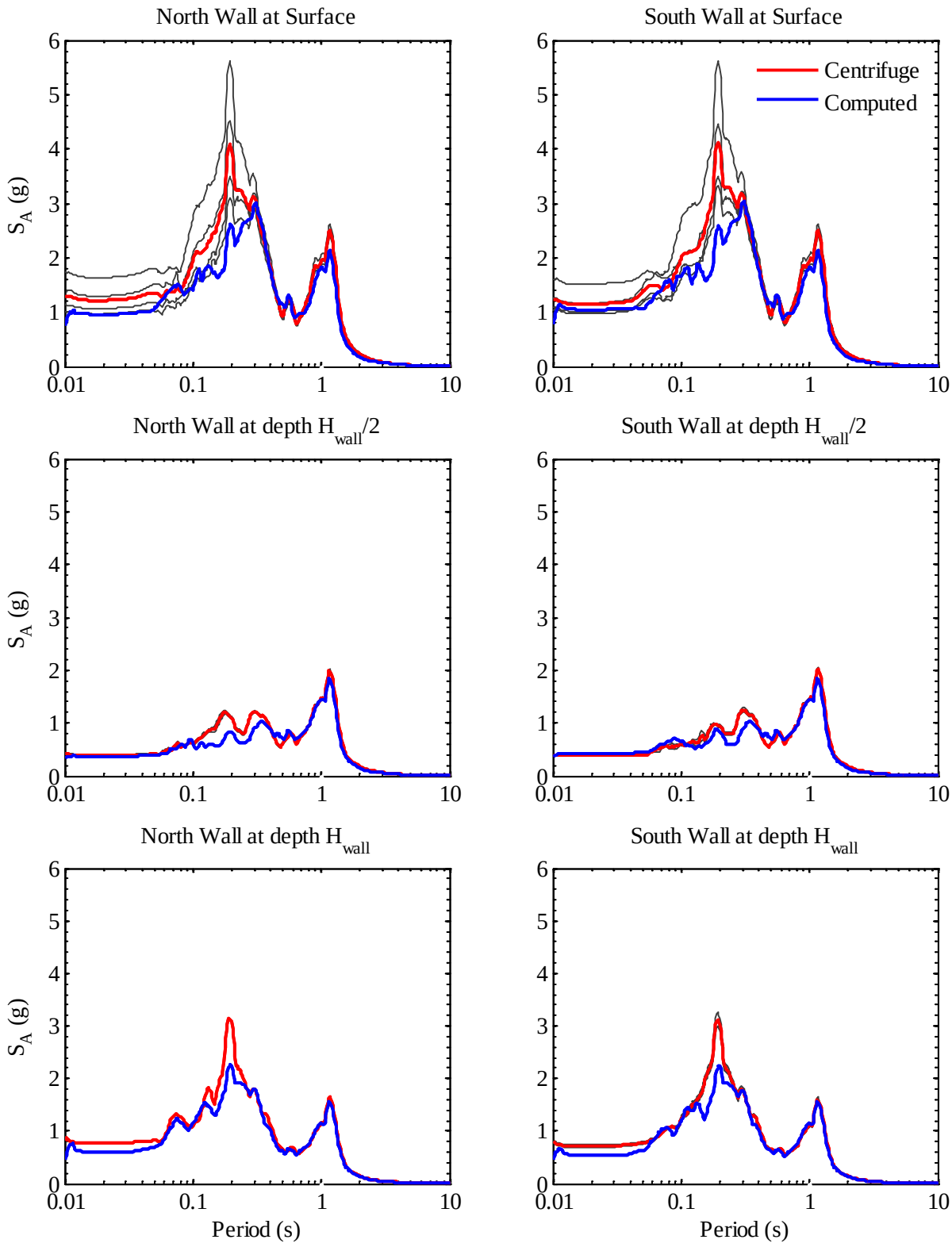

Figure A.45: Measured and computed acceleration response spectra in structure at 5% damping during Kobe TAK 090-3

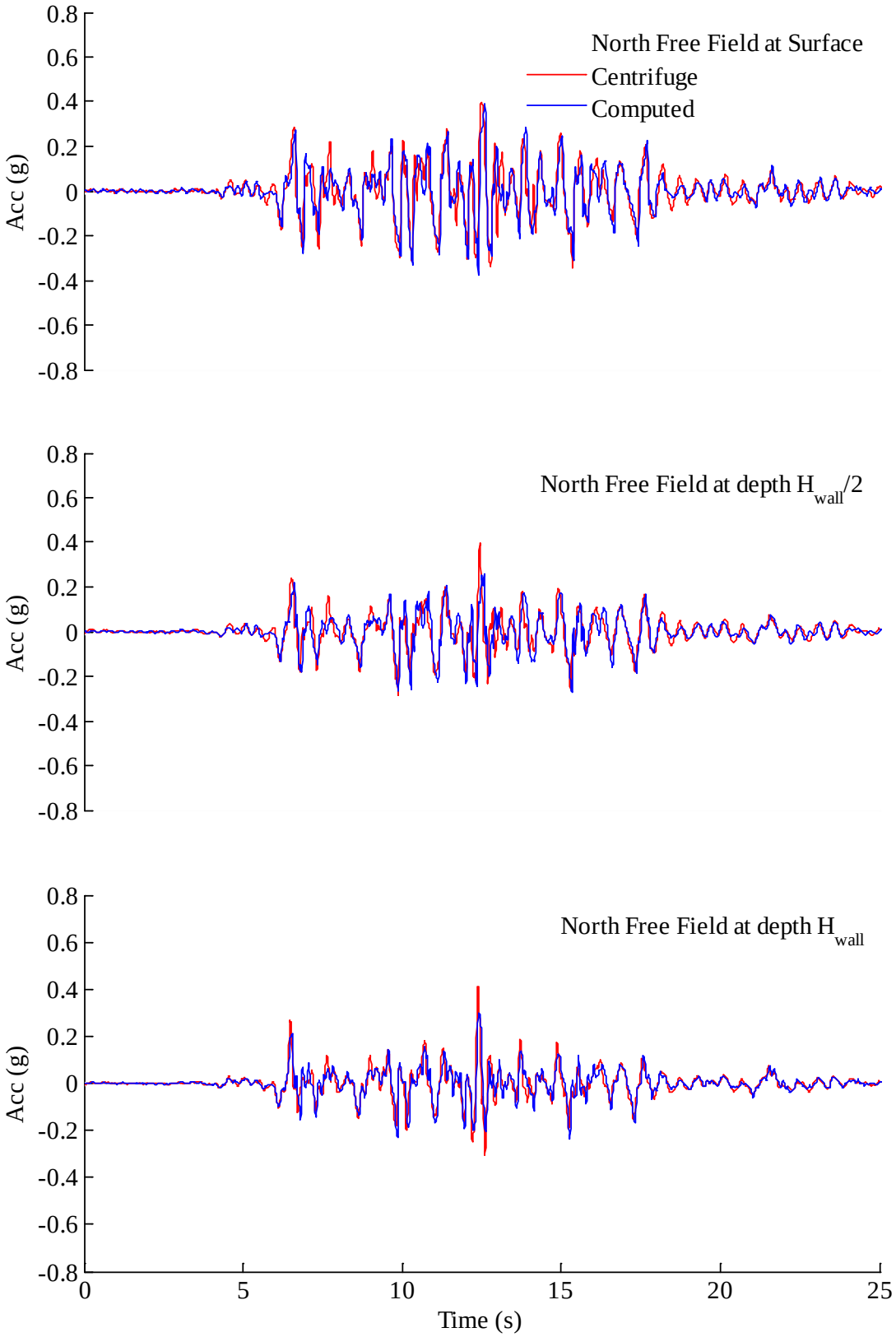

Figure A.46: Measured and computed accelerations in north free field during Loma Prieta SC-2

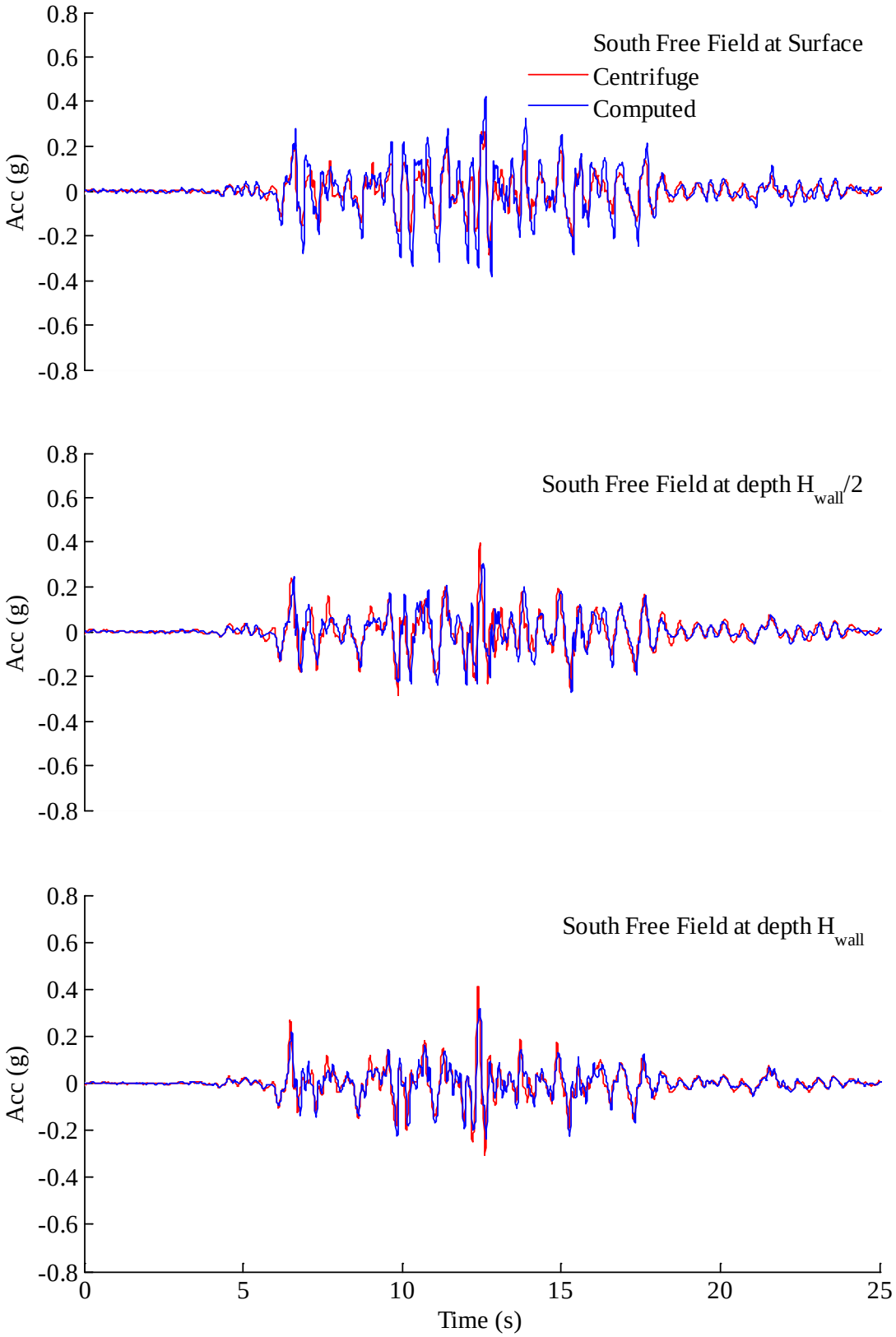

Figure A.47: Measured and computed accelerations in south free field during Loma Prieta SC-2

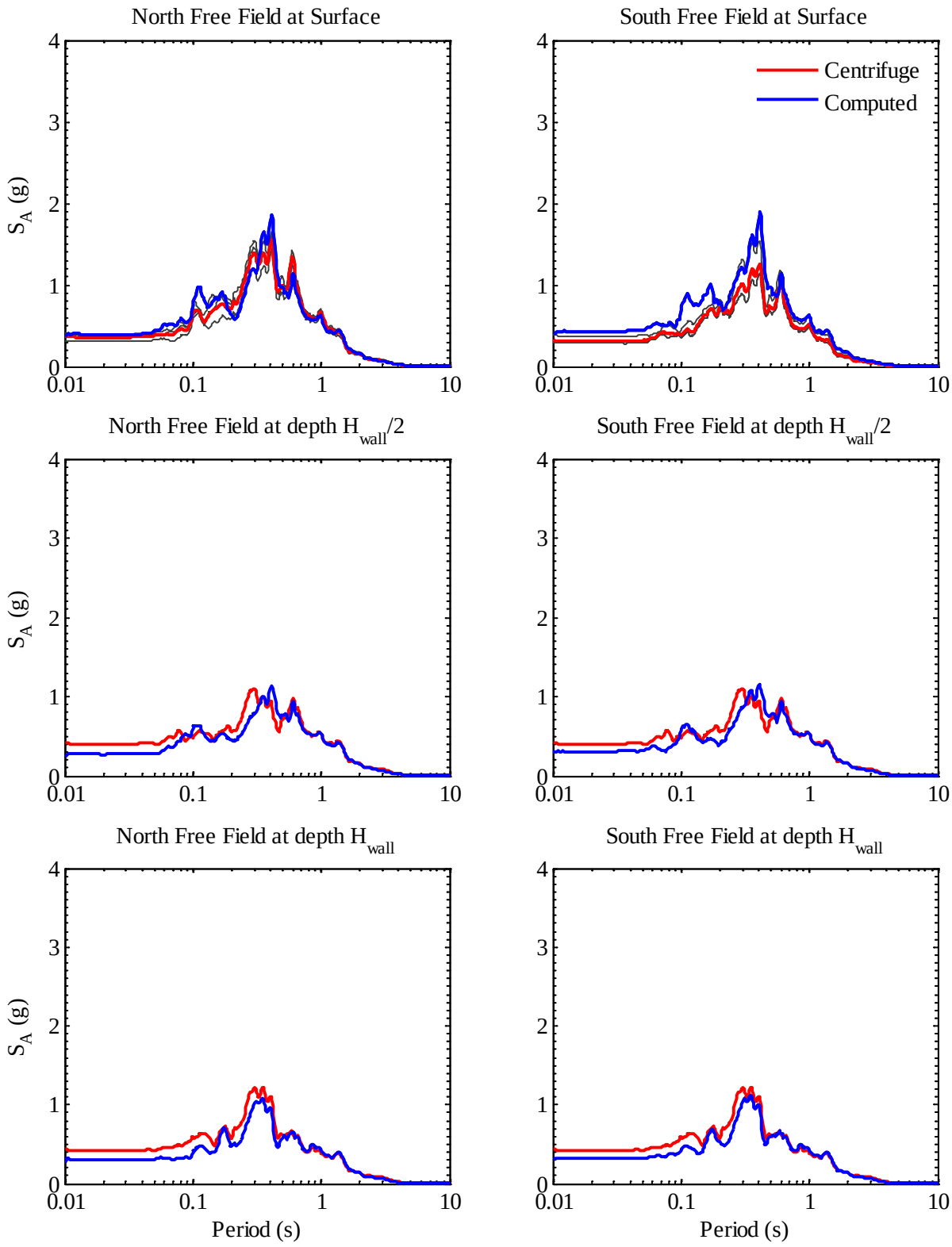

Figure A.48: Measured and computed acceleration response spectra in free field at 5% damping during Loma Prieta SC-2

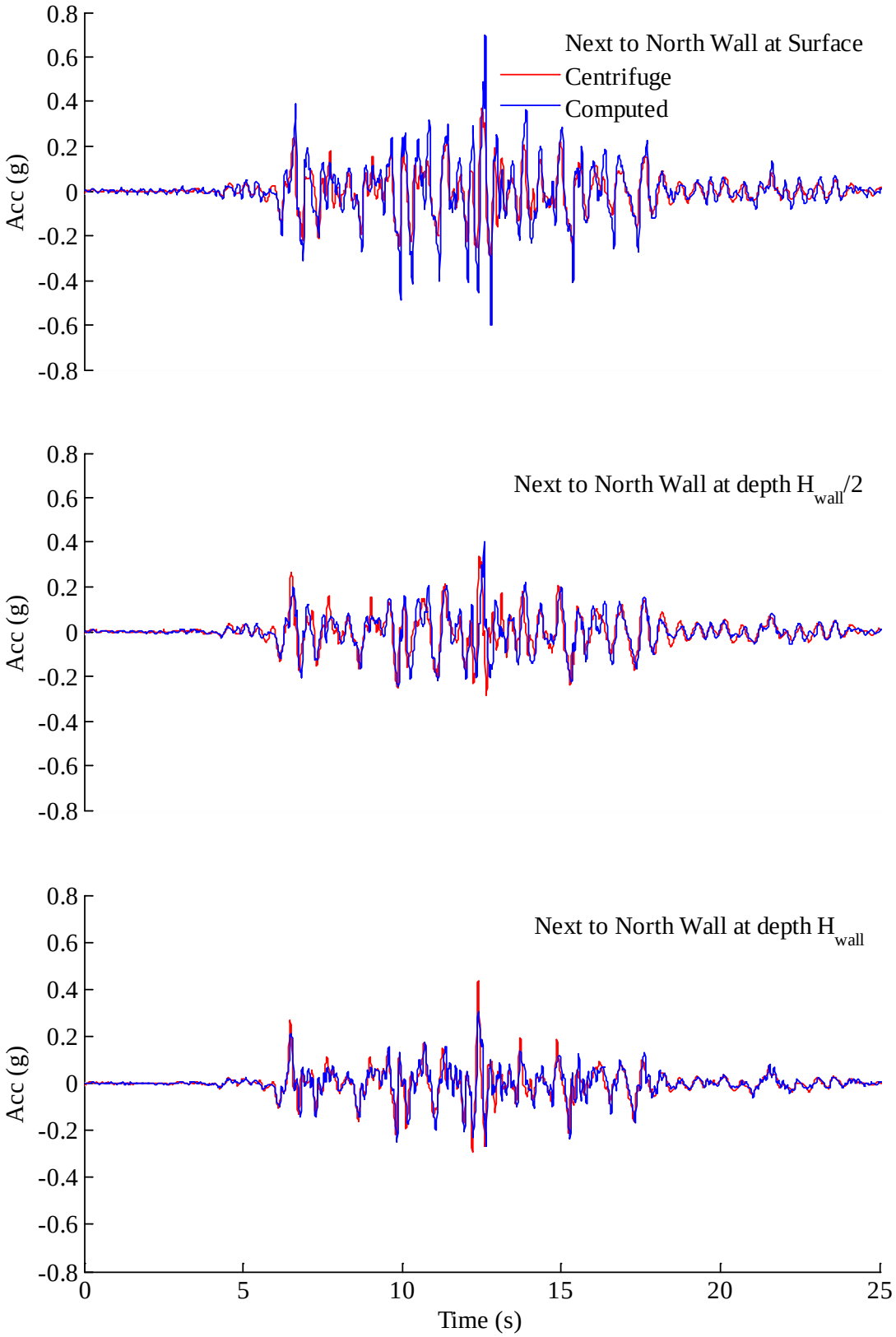

Figure A.49: Measured and computed accelerations next to north wall during Loma Prieta SC-2

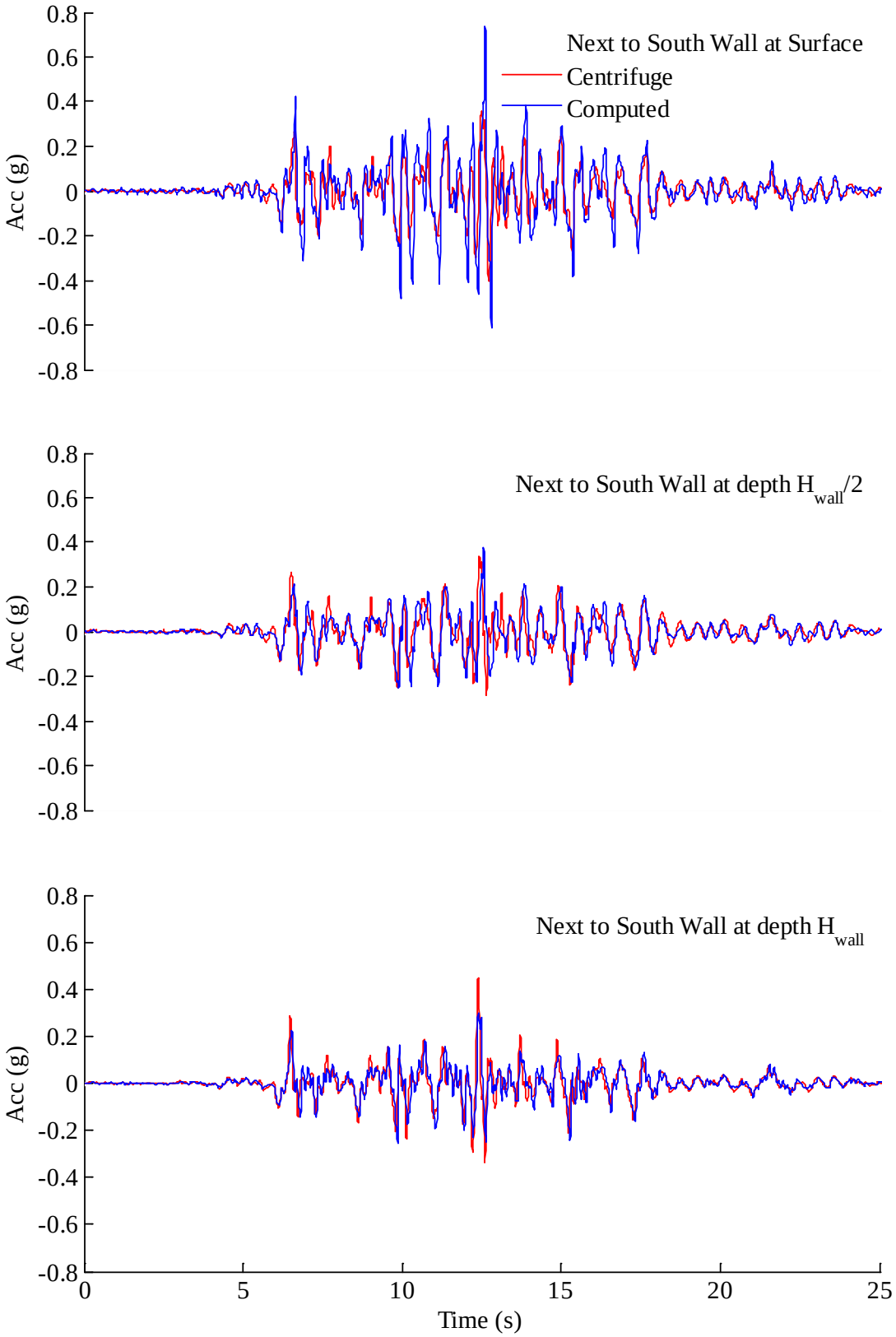

Figure A.50: Measured and computed accelerations next to south wall during Loma Prieta SC-2

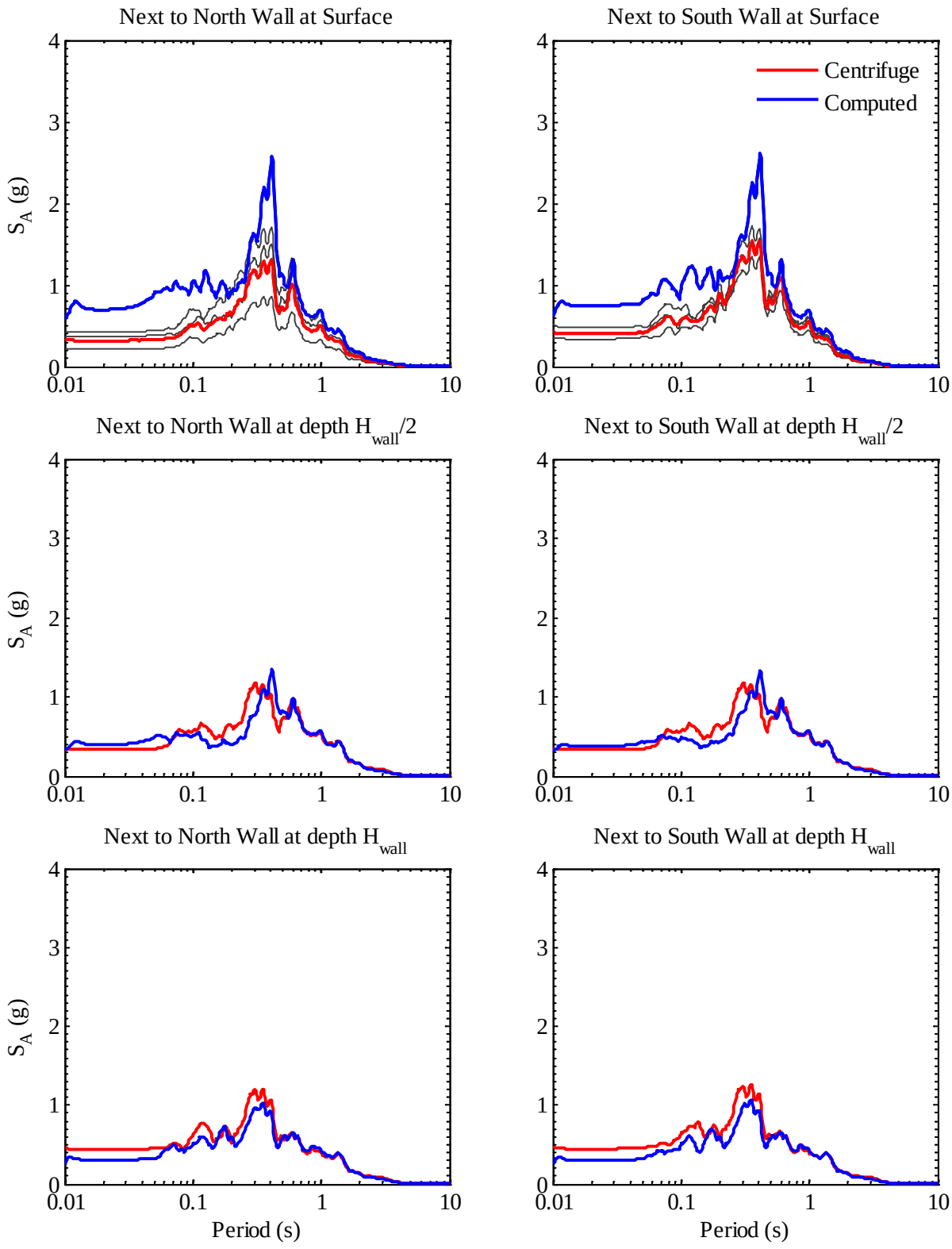

Figure A.51: Measured and computed acceleration response spectra in soil next to structure during Loma Prieta SC-2

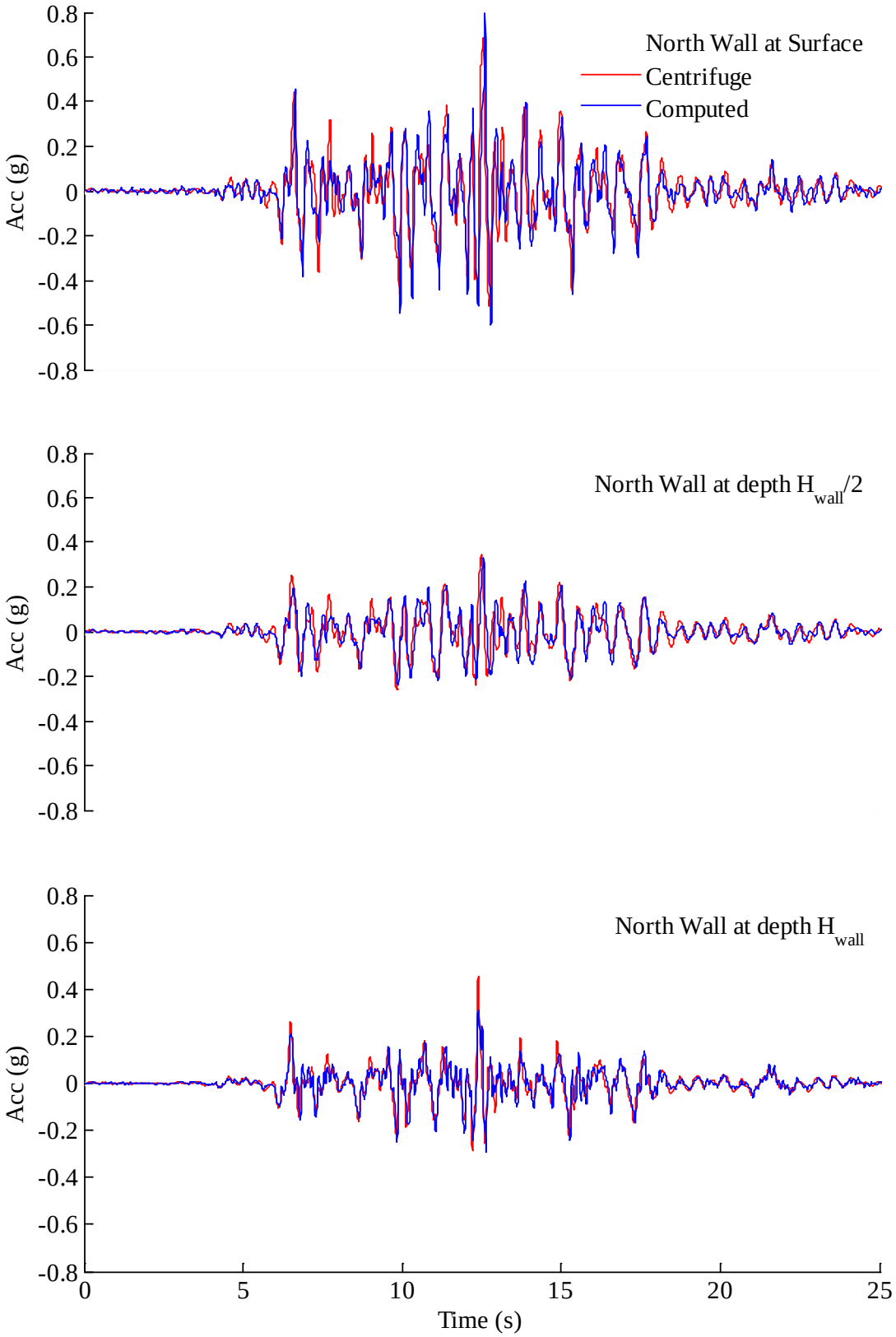

Figure A.52: Measured and computed accelerations in north wall during Loma Prieta SC-2

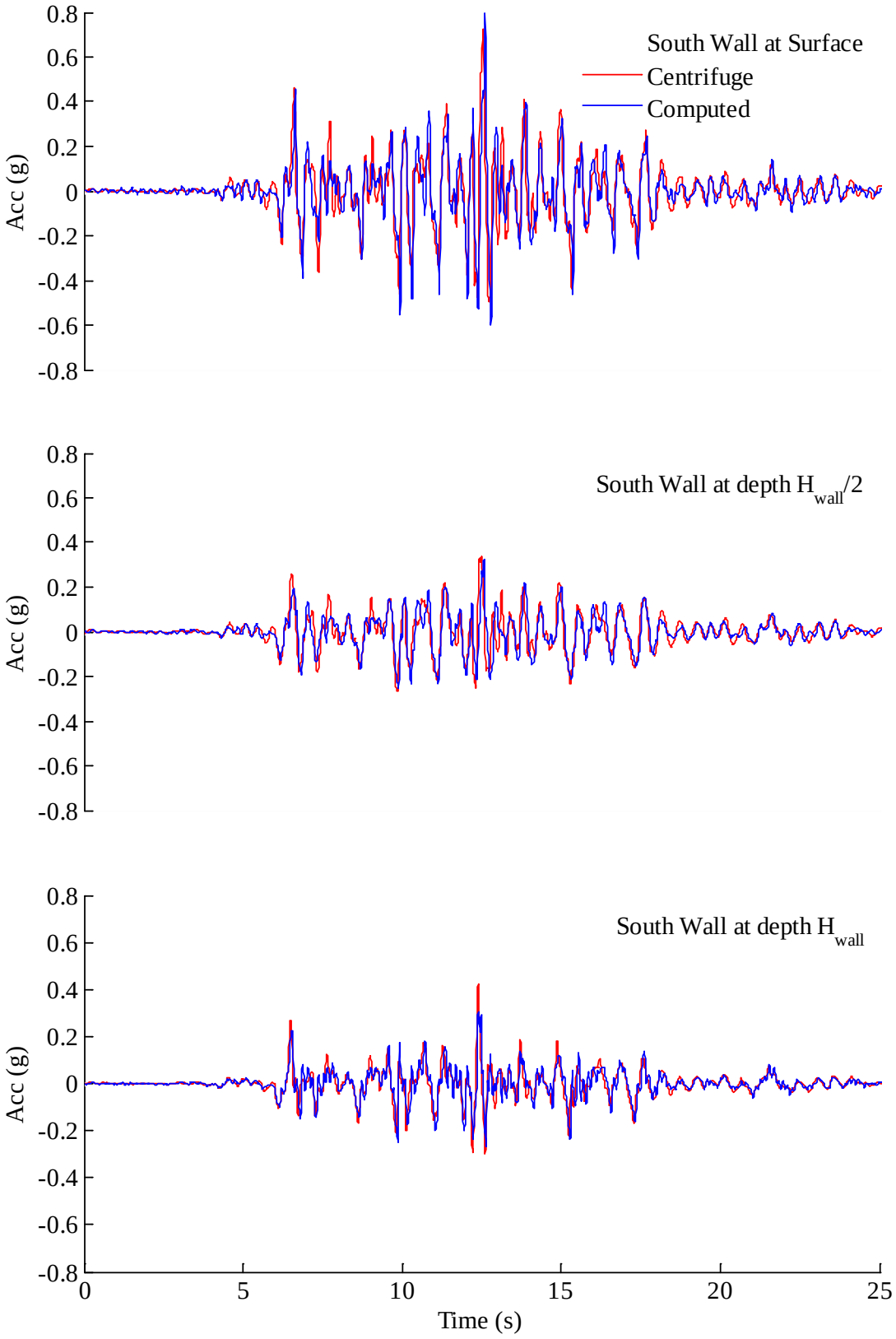

Figure A.53: Measured and computed accelerations in south wall during Loma Prieta SC-2

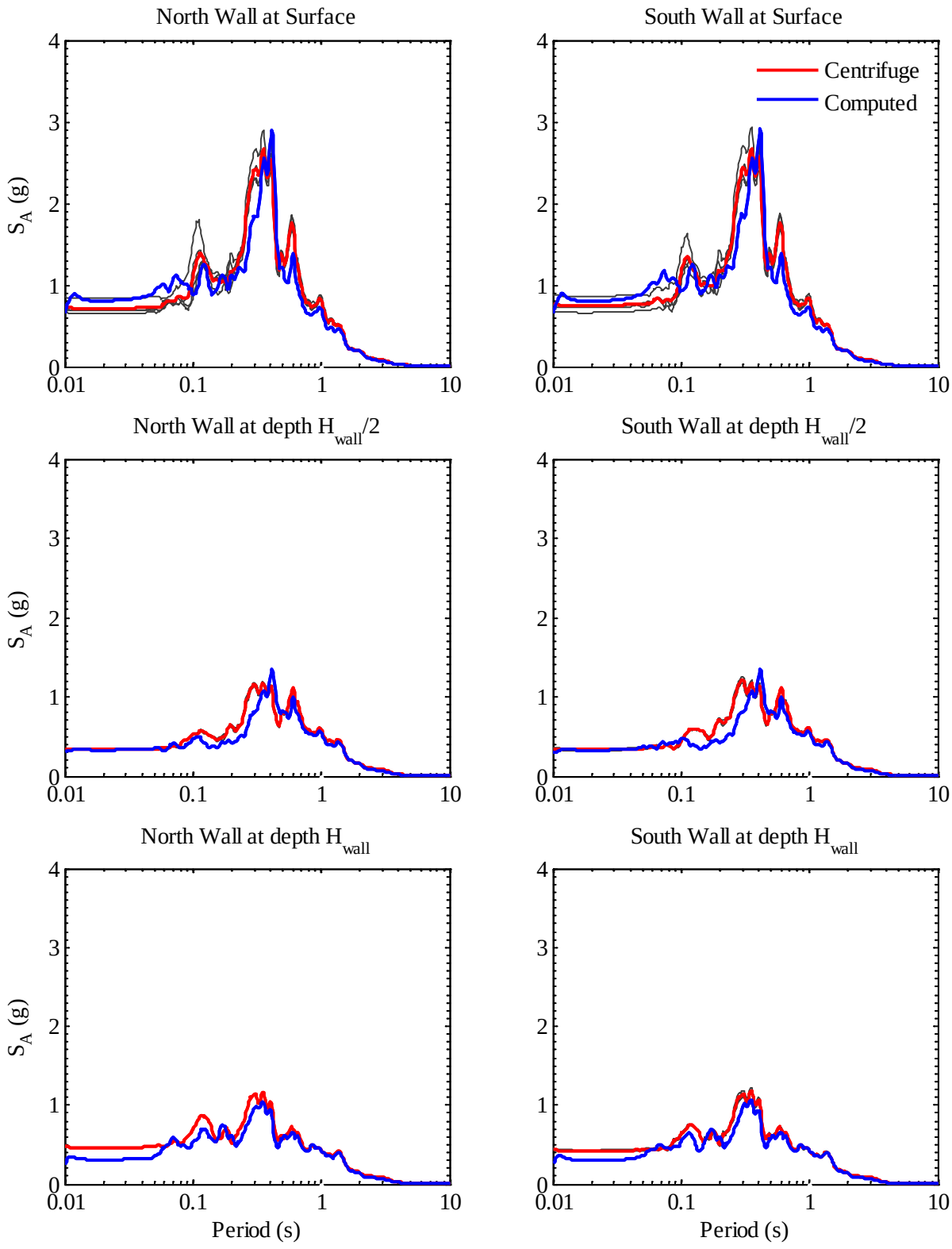

Figure A.54: Measured and computed acceleration response spectra in structure at 5% damping during Loma Prieta SC-2

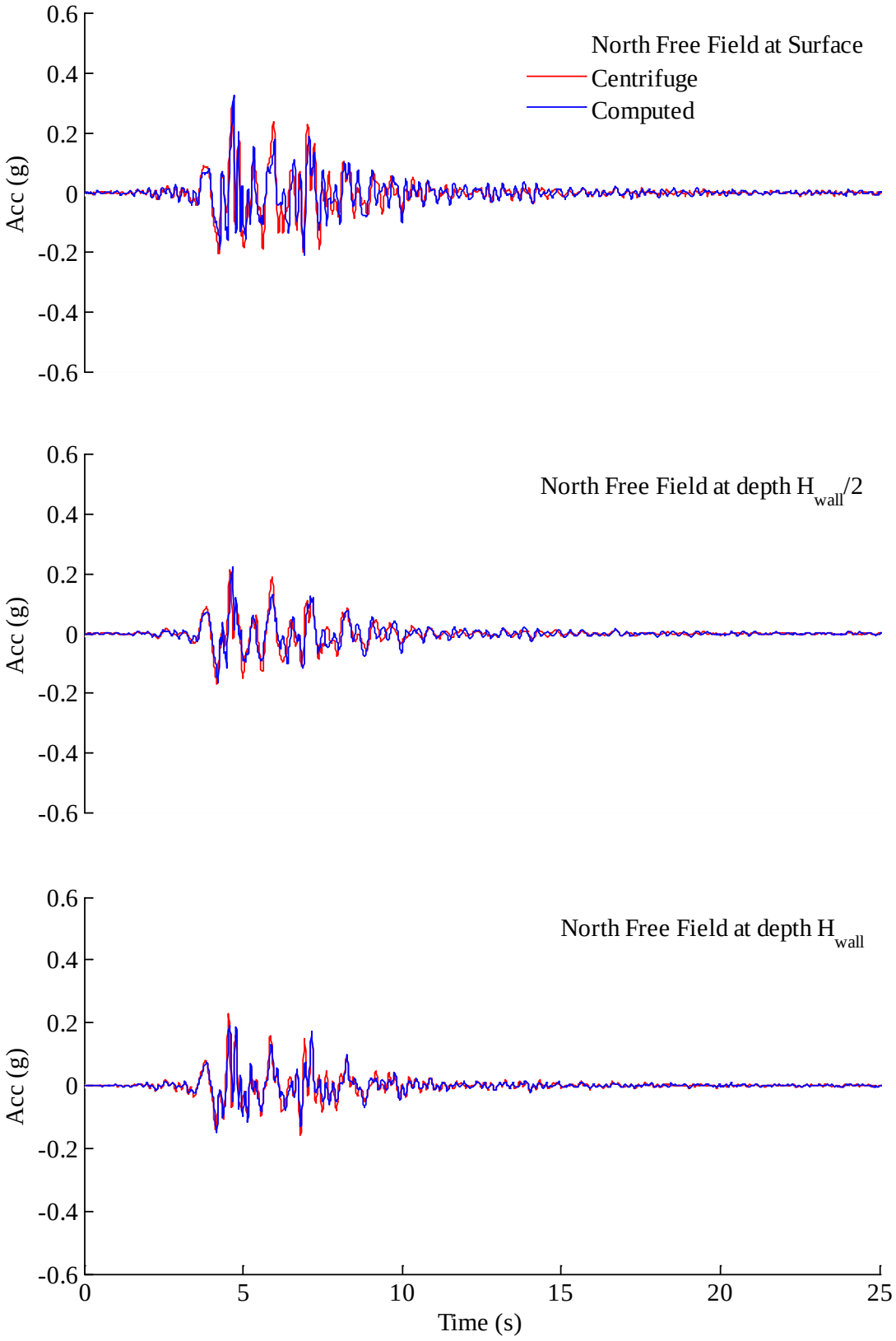

Figure A.55: Measured and computed accelerations in north free field during Loma Prieta WVC-2

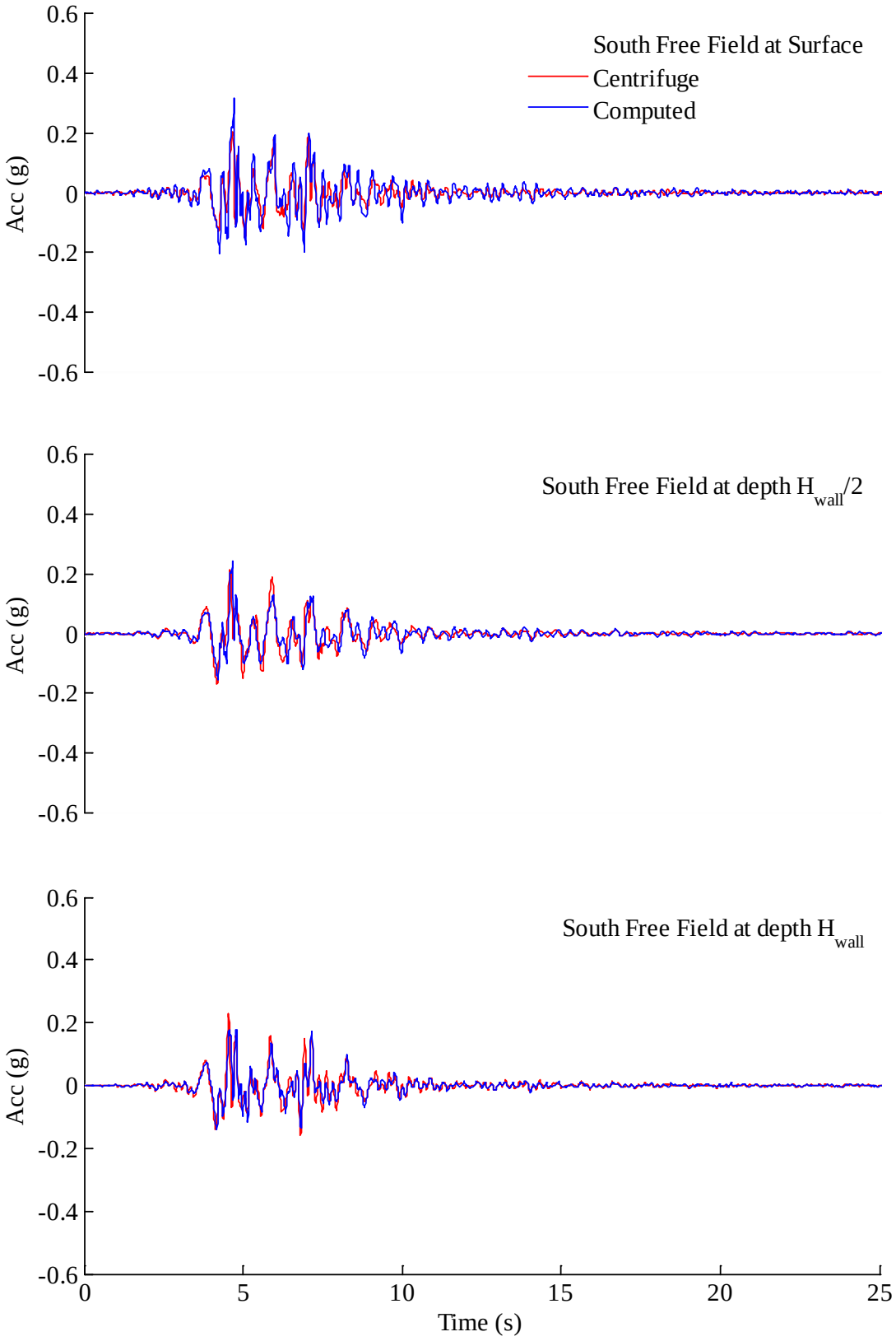

Figure A.56: Measured and computed accelerations in south free field during Loma Prieta WVC-2

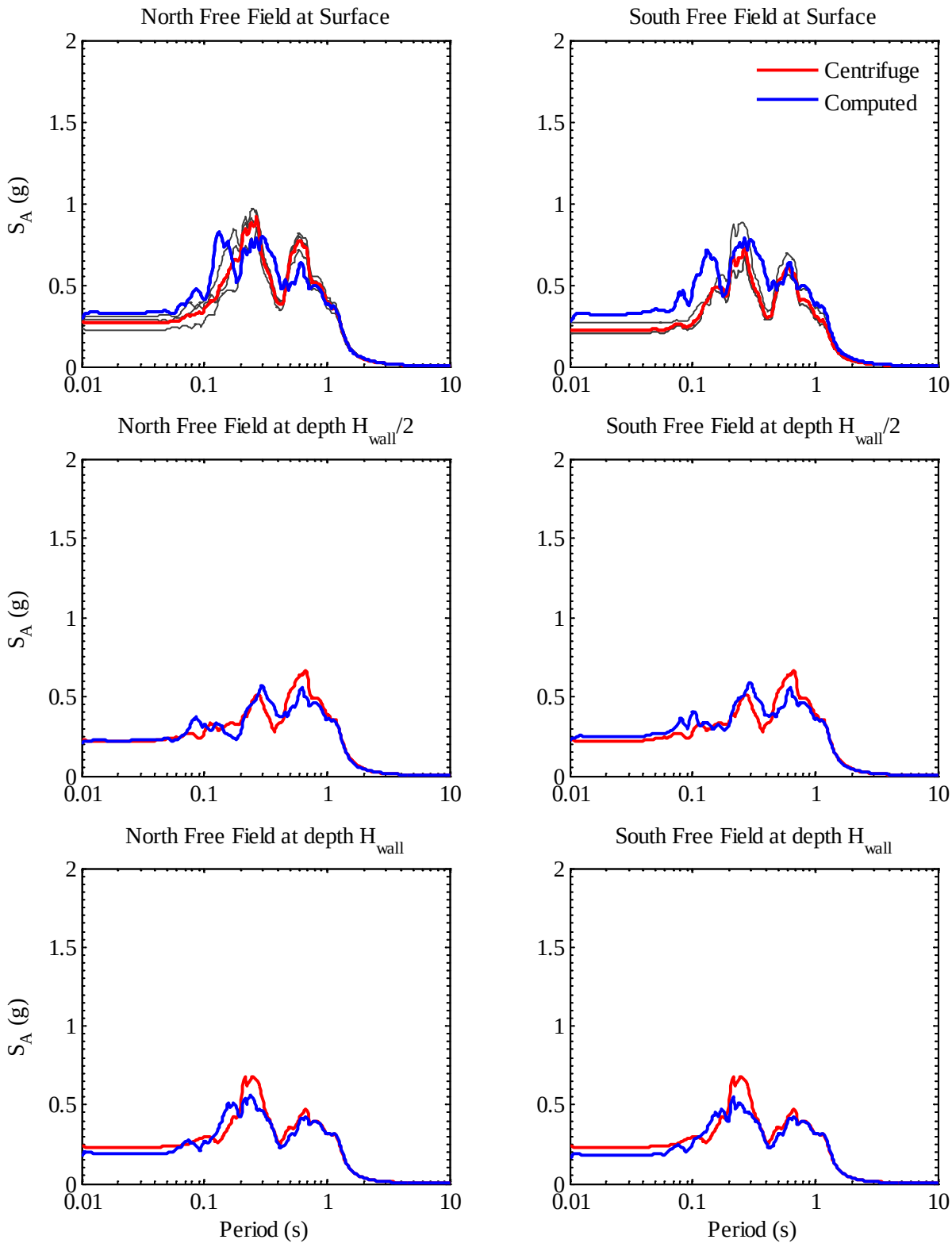

Figure A.57: Measured and computed acceleration response spectra in free field during Loma Prieta WVC-2

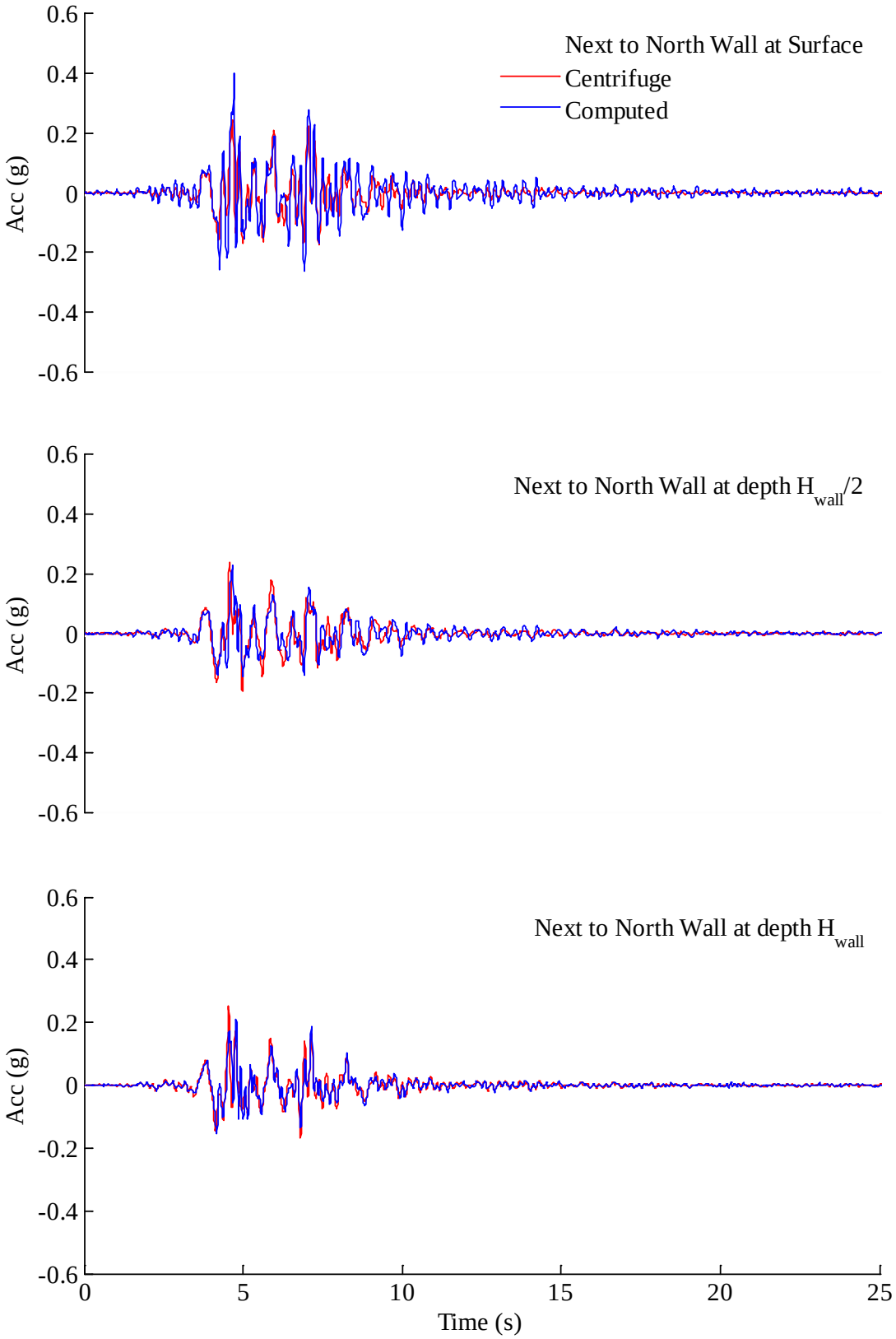

Figure A.58: Measured and computed accelerations next to north wall during Loma Prieta WVC-2

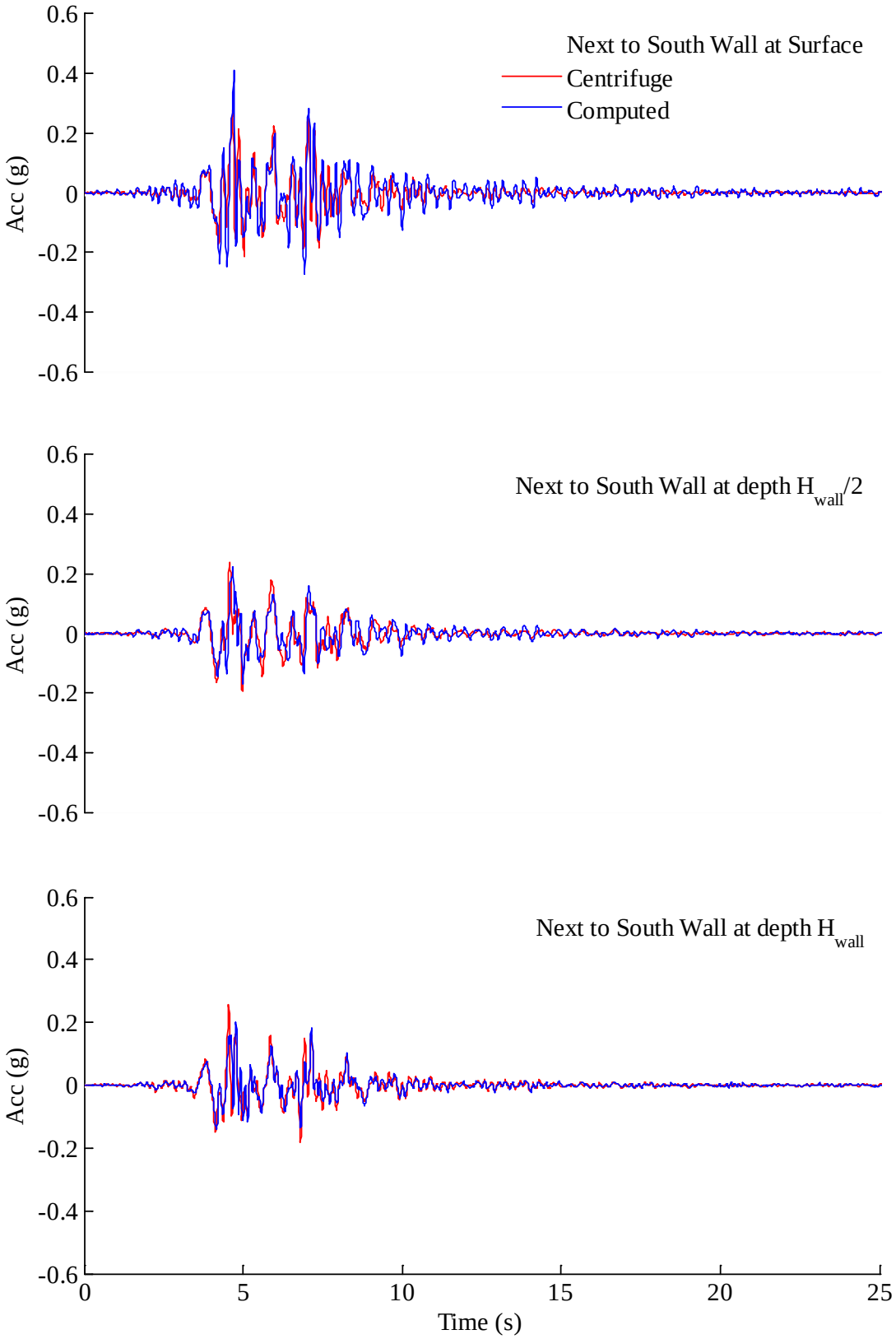

Figure A.59: Measured and computed accelerations next to south wall during Loma Prieta WVC-2

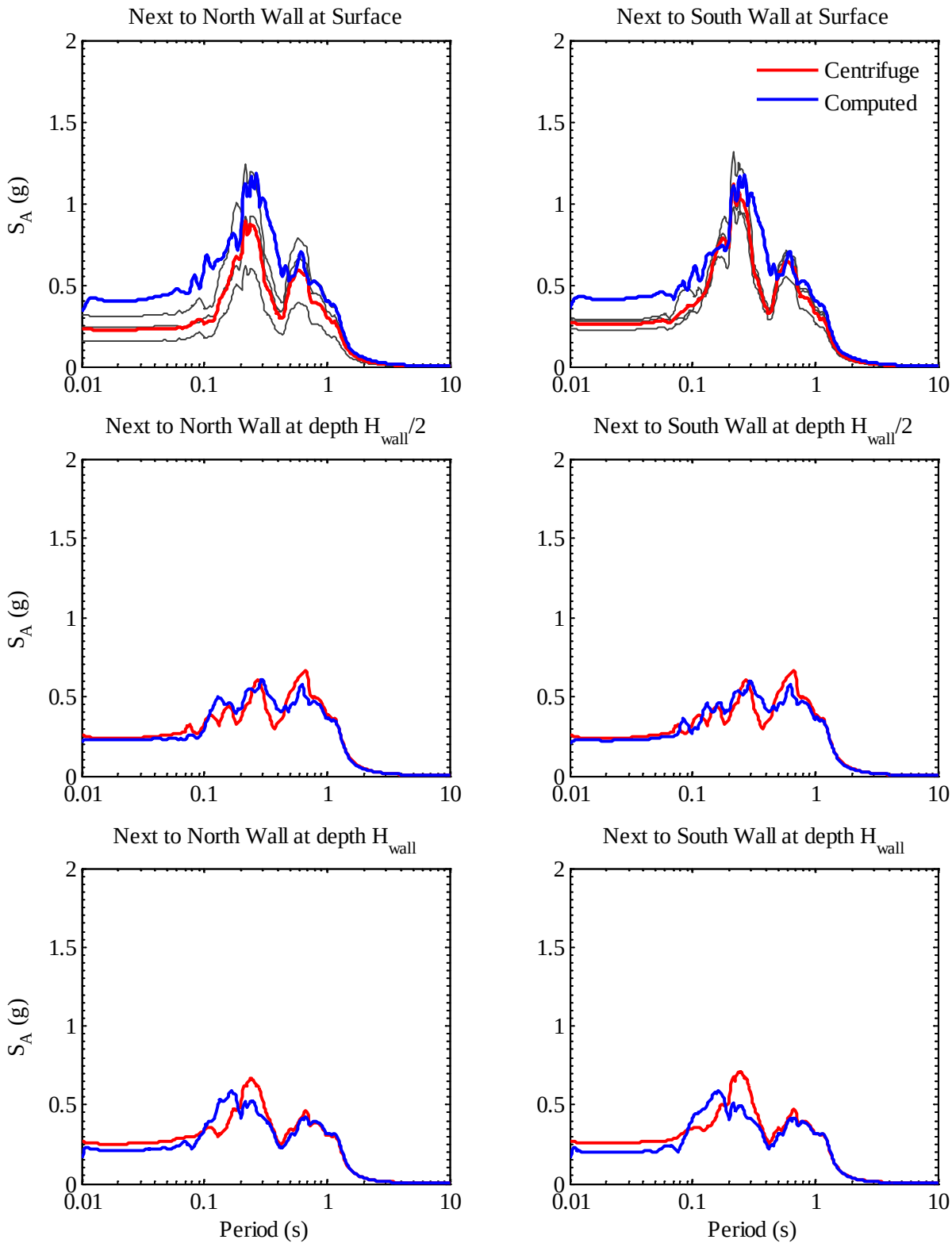

Figure A.60: Measured and computed acceleration response spectra in soil next to structure during Loma Prieta WVC-2

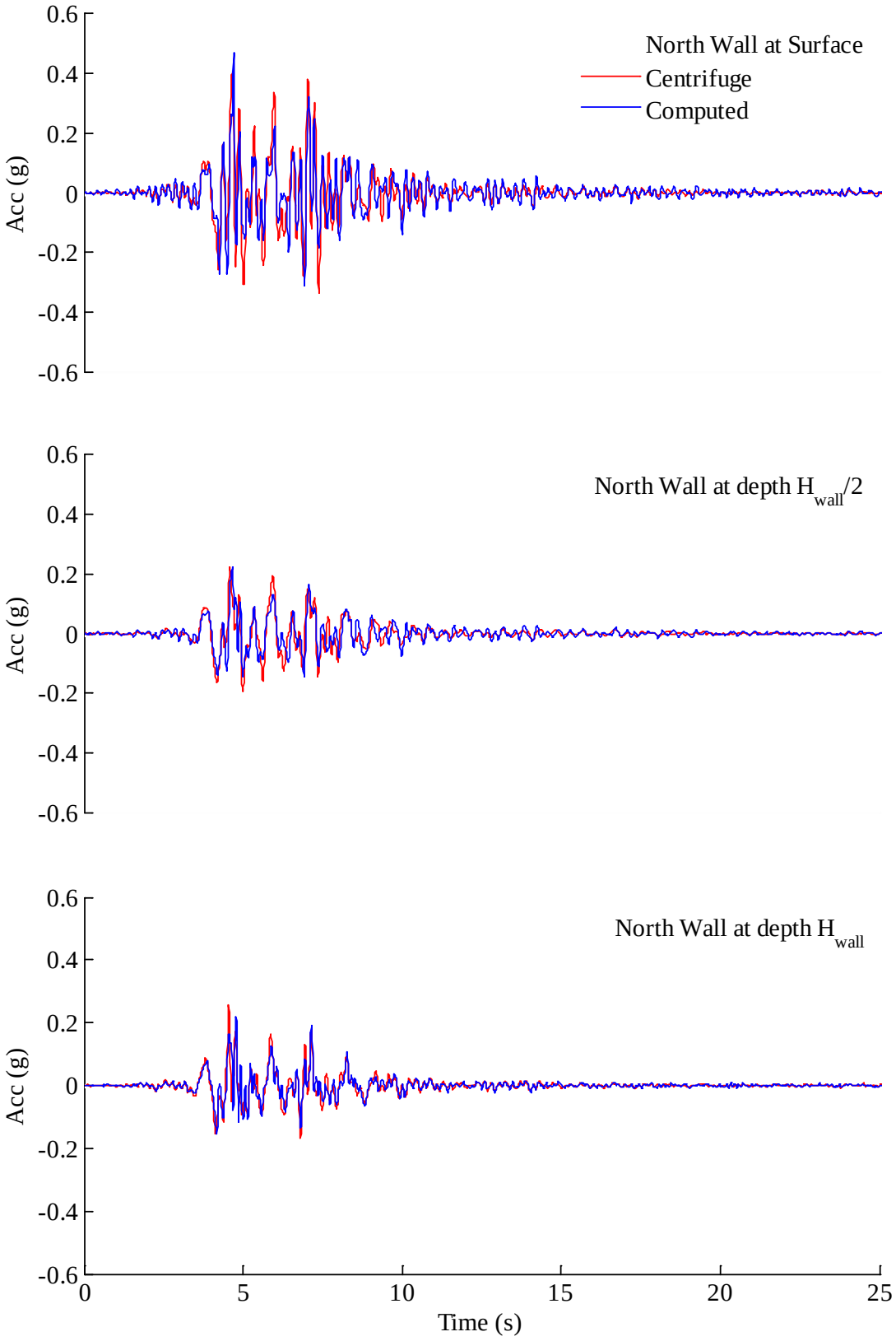

Figure A.61: Measured and computed accelerations in north wall during Loma Prieta WVC-2

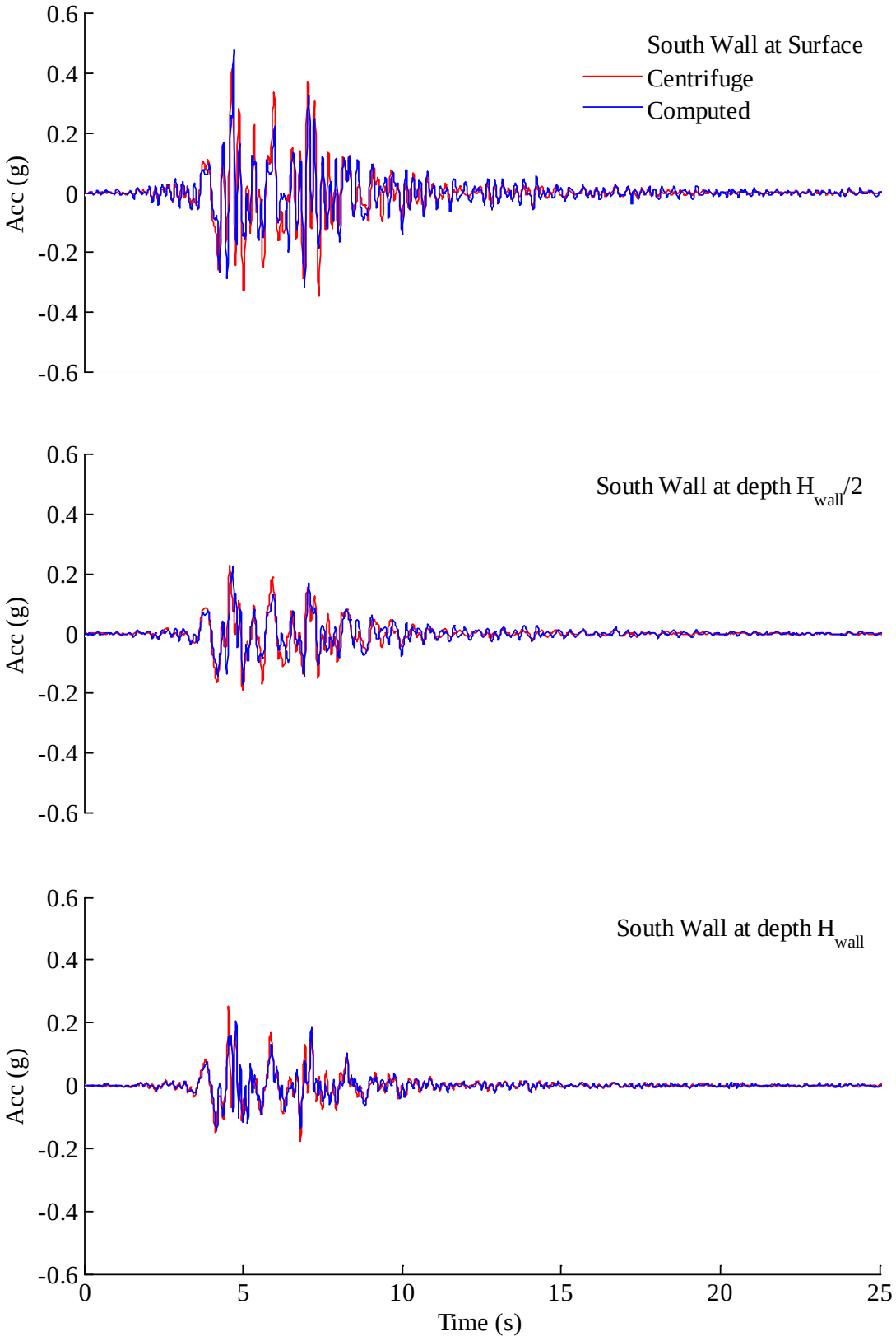

Figure A.62: Measured and computed accelerations in south wall during Loma Prieta WVC-2

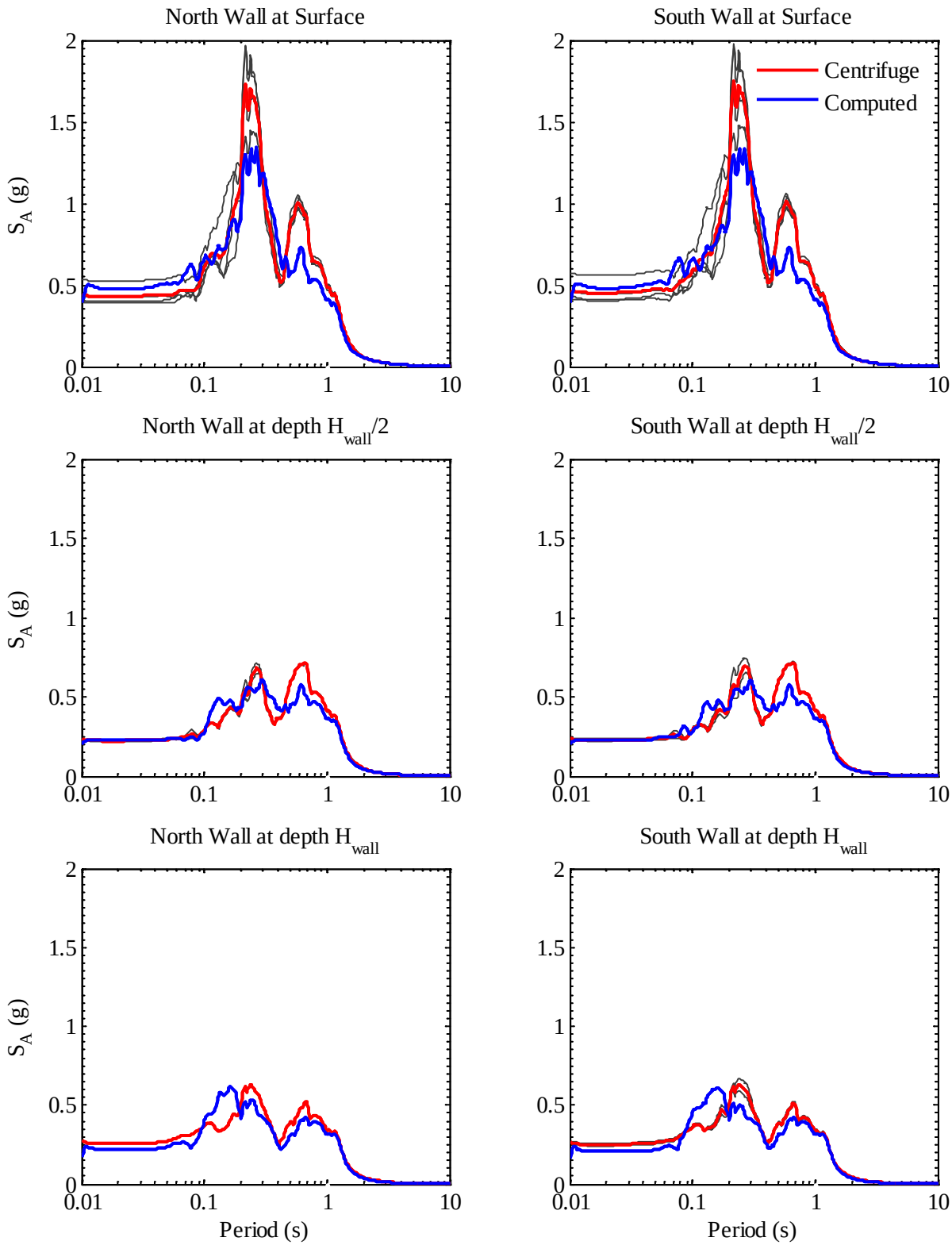

Figure A.63: Measured and computed acceleration response spectra in structure at 5% damping during Loma Prieta WVC-2

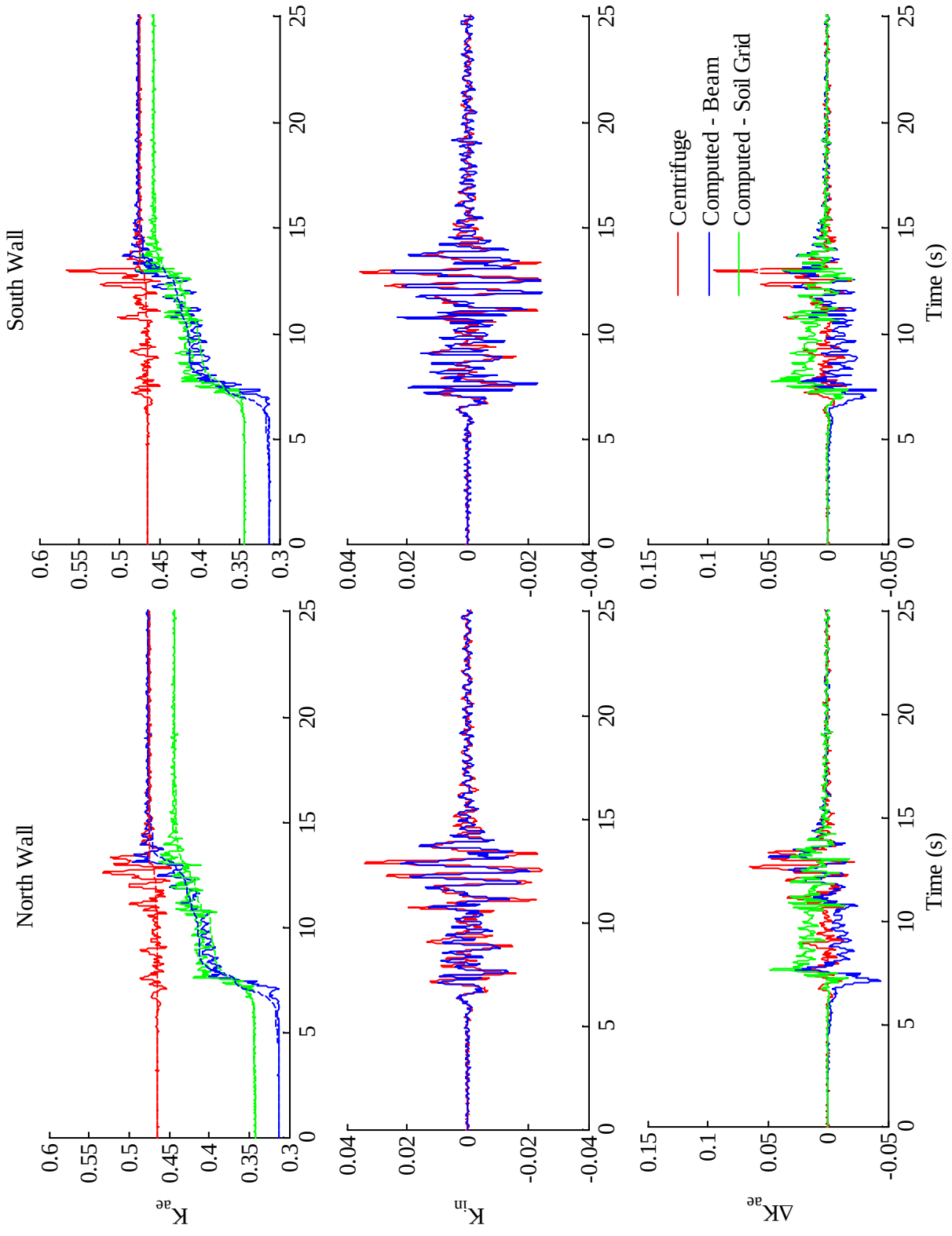

Figure A.64: Measured and computed normalized loads on structure during Kocaeli YPT 060

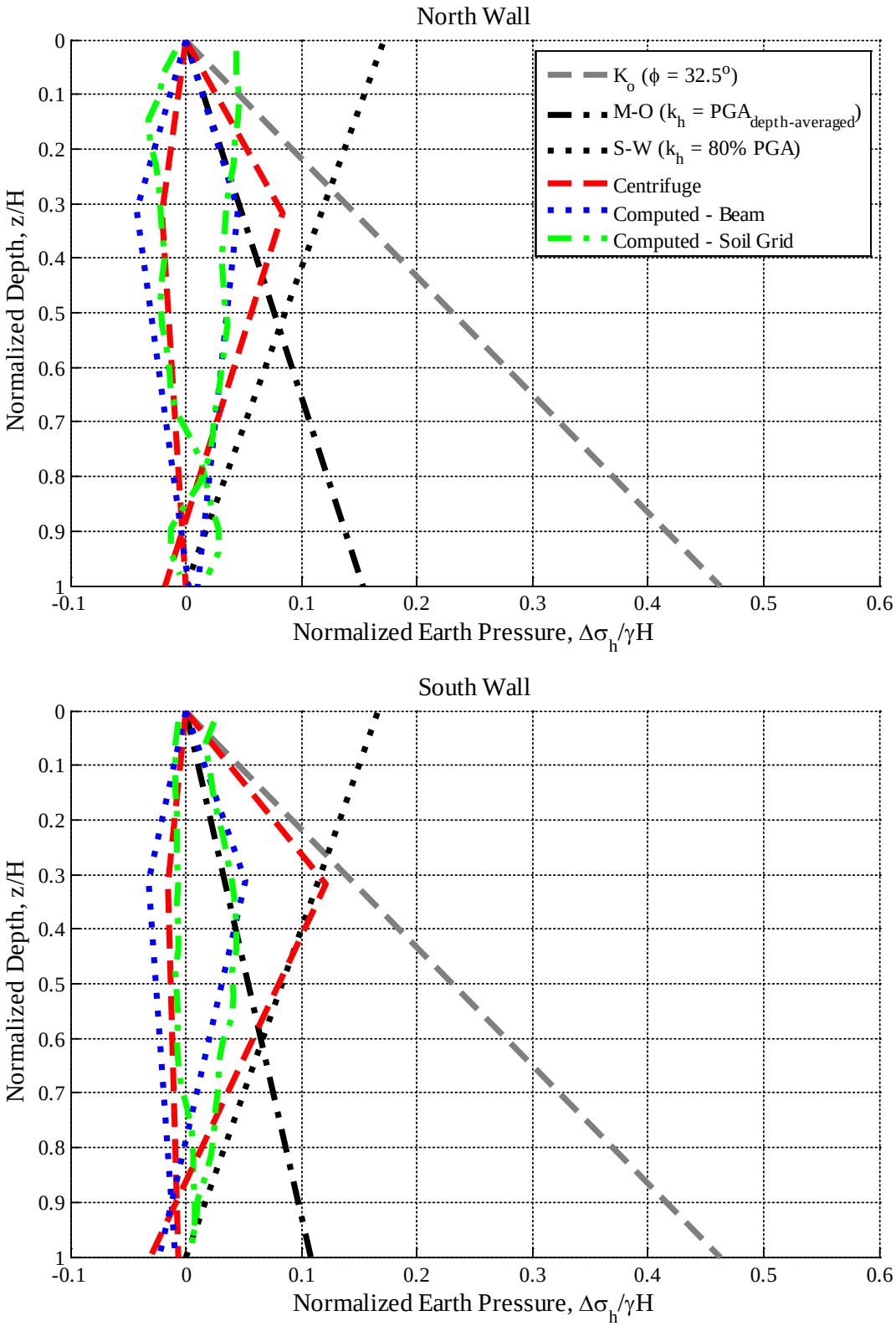

Figure A.65: Measured and computed normalized dynamic earth pressure distributions at maximum and minimum ΔK_{ae} during Kocaeli YPT 060

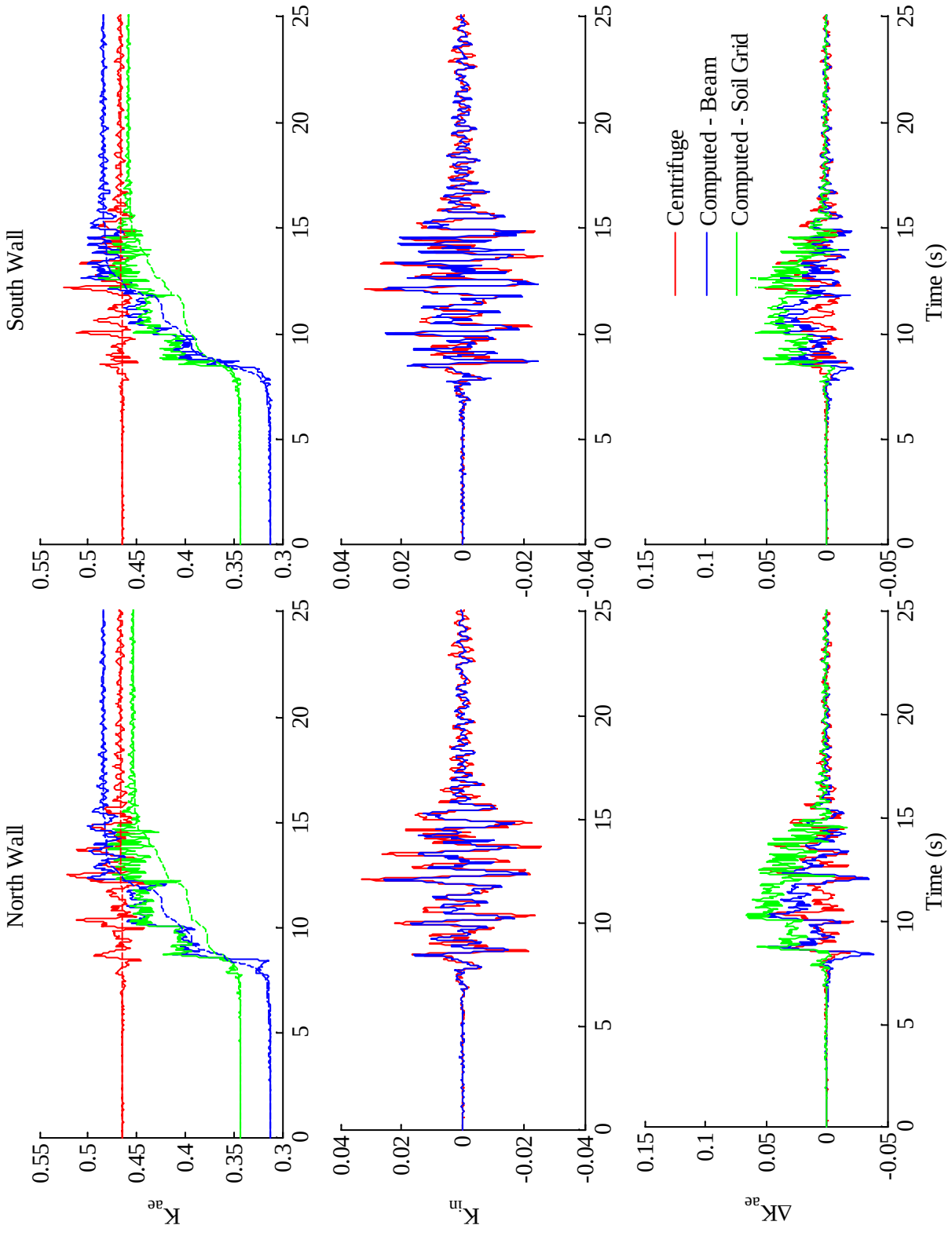

Figure A.66: Measured and computed normalized loads on structure during Kocaeli YPT 330

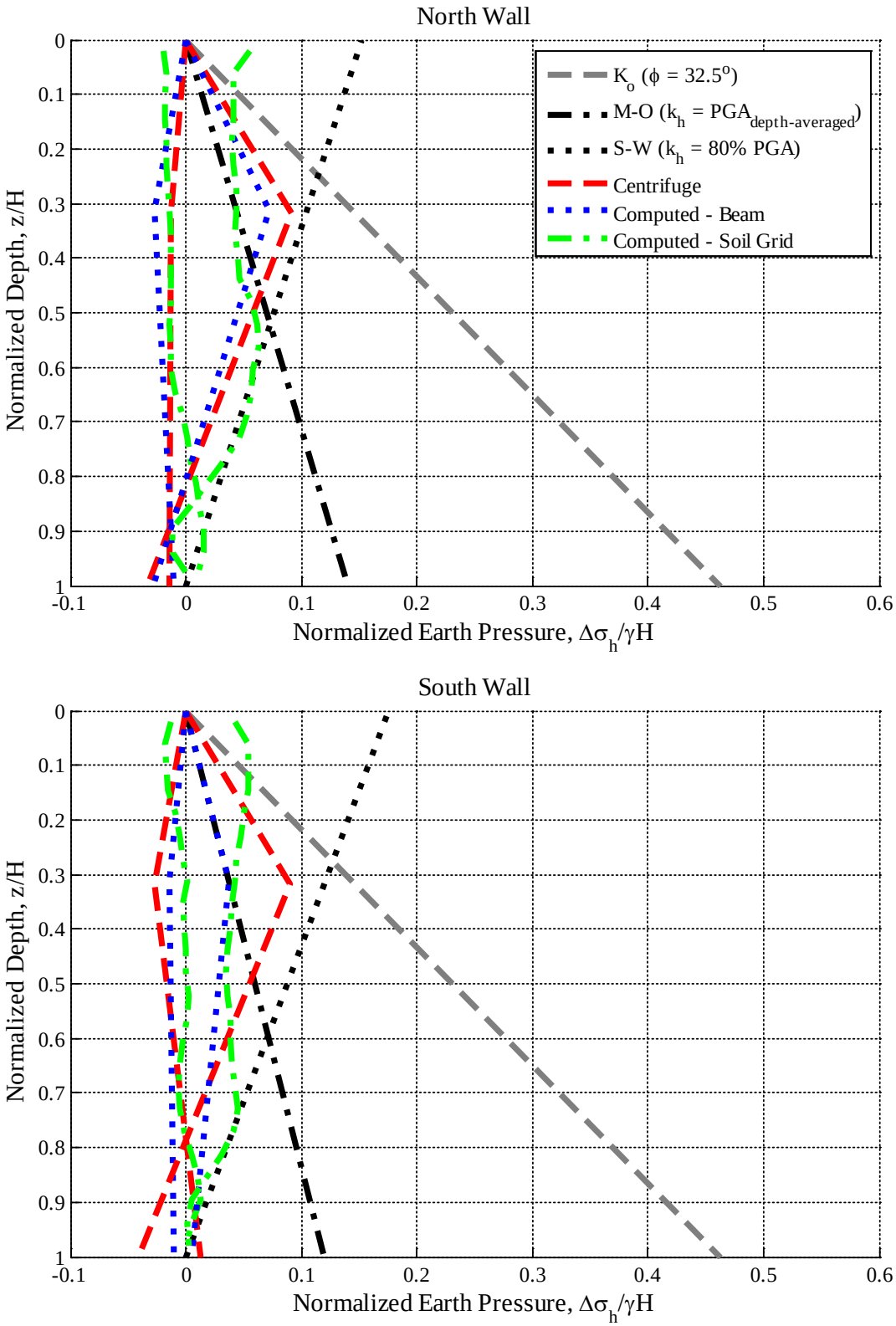

Figure A.67: Measured and computed normalized dynamic earth pressure distributions at maximum and minimum ΔK_{ae} during Kocaeli YPT 330

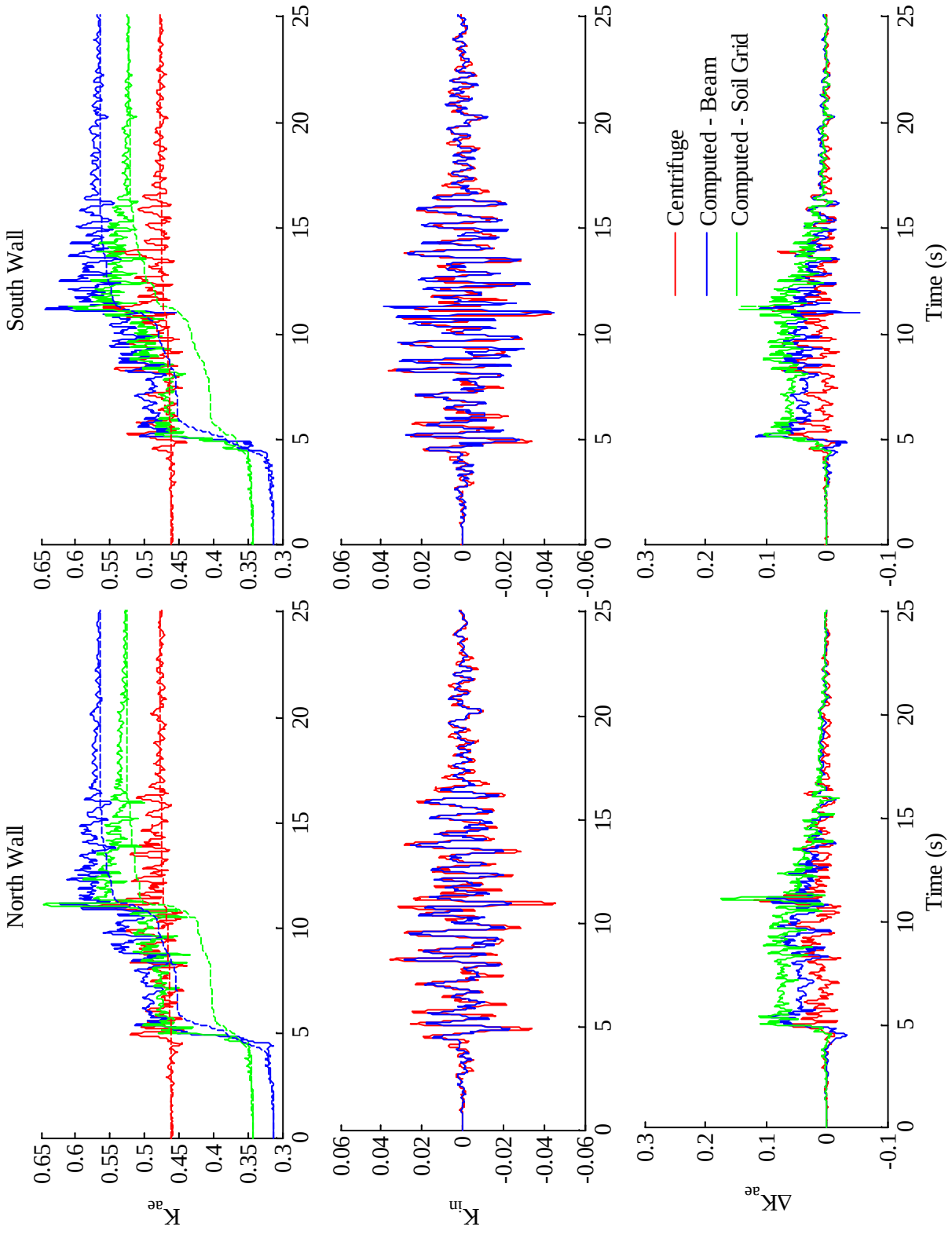

Figure A.68: Measured and computed normalized loads on structure during Loma Prieta SC-1

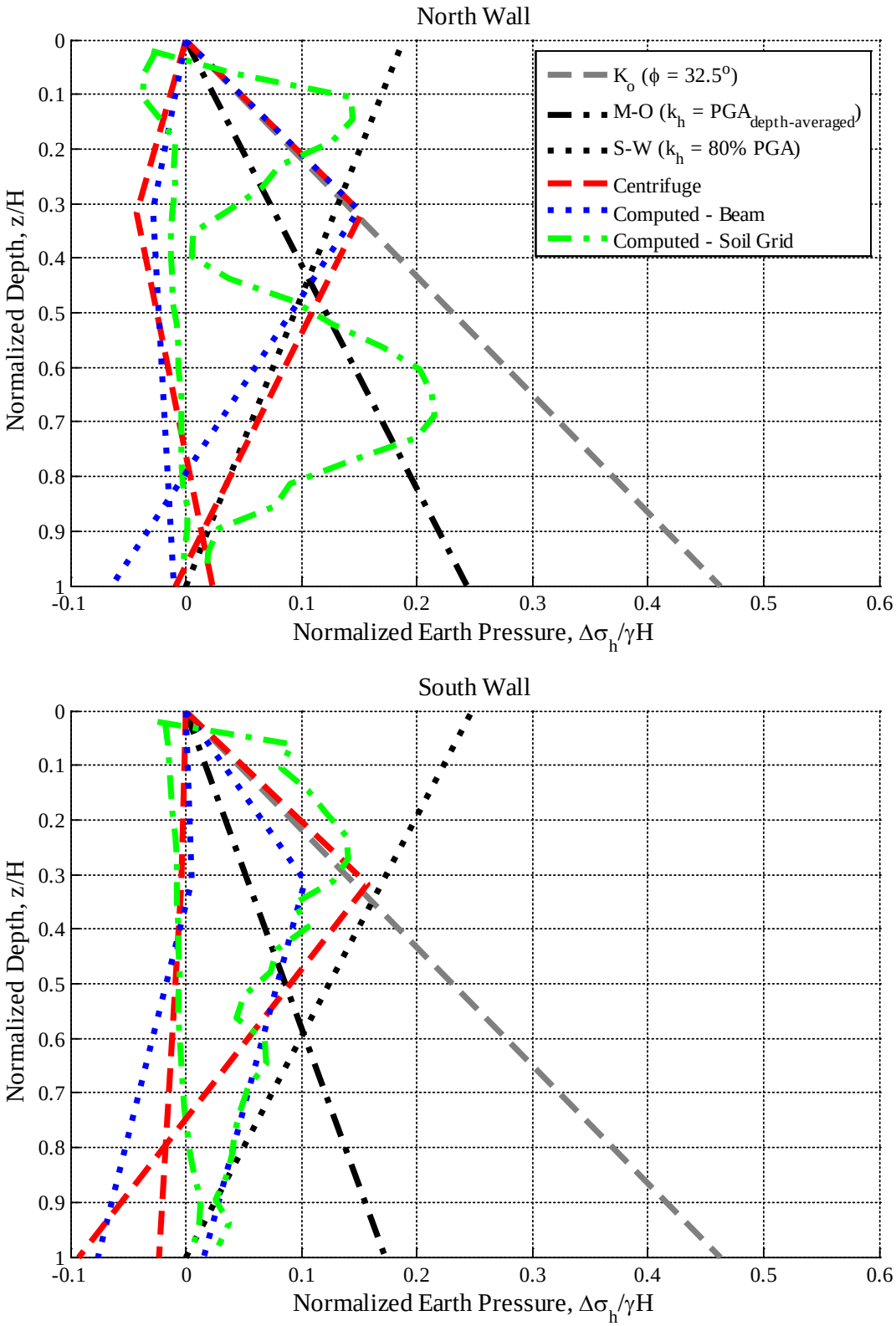

Figure A.69: Measured and computed normalized dynamic earth pressure distributions at maximum and minimum ΔK_{ae} during Loma Prieta SC-1

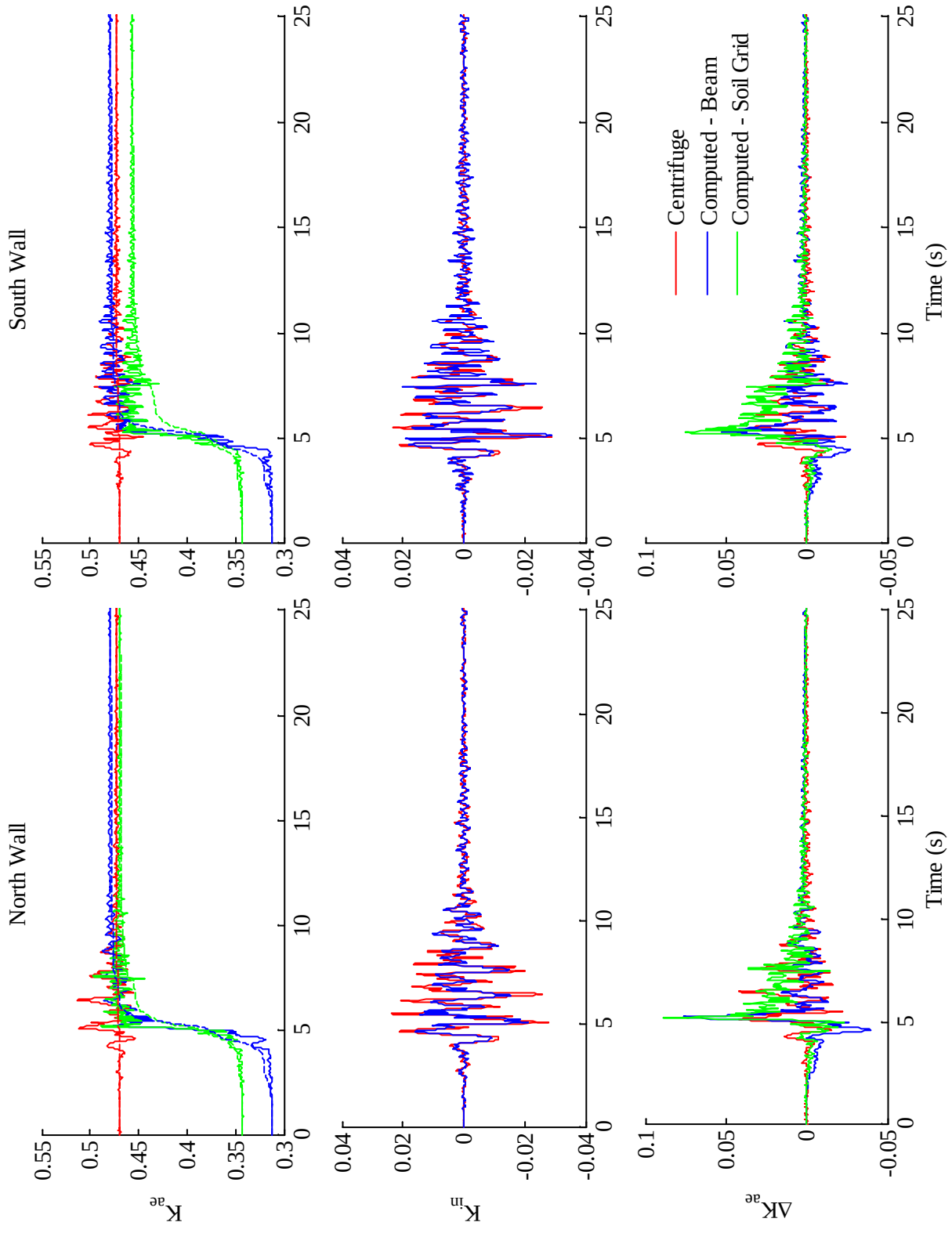

Figure A.70: Measured and computed normalized loads on structure during Loma Prieta WVC-1

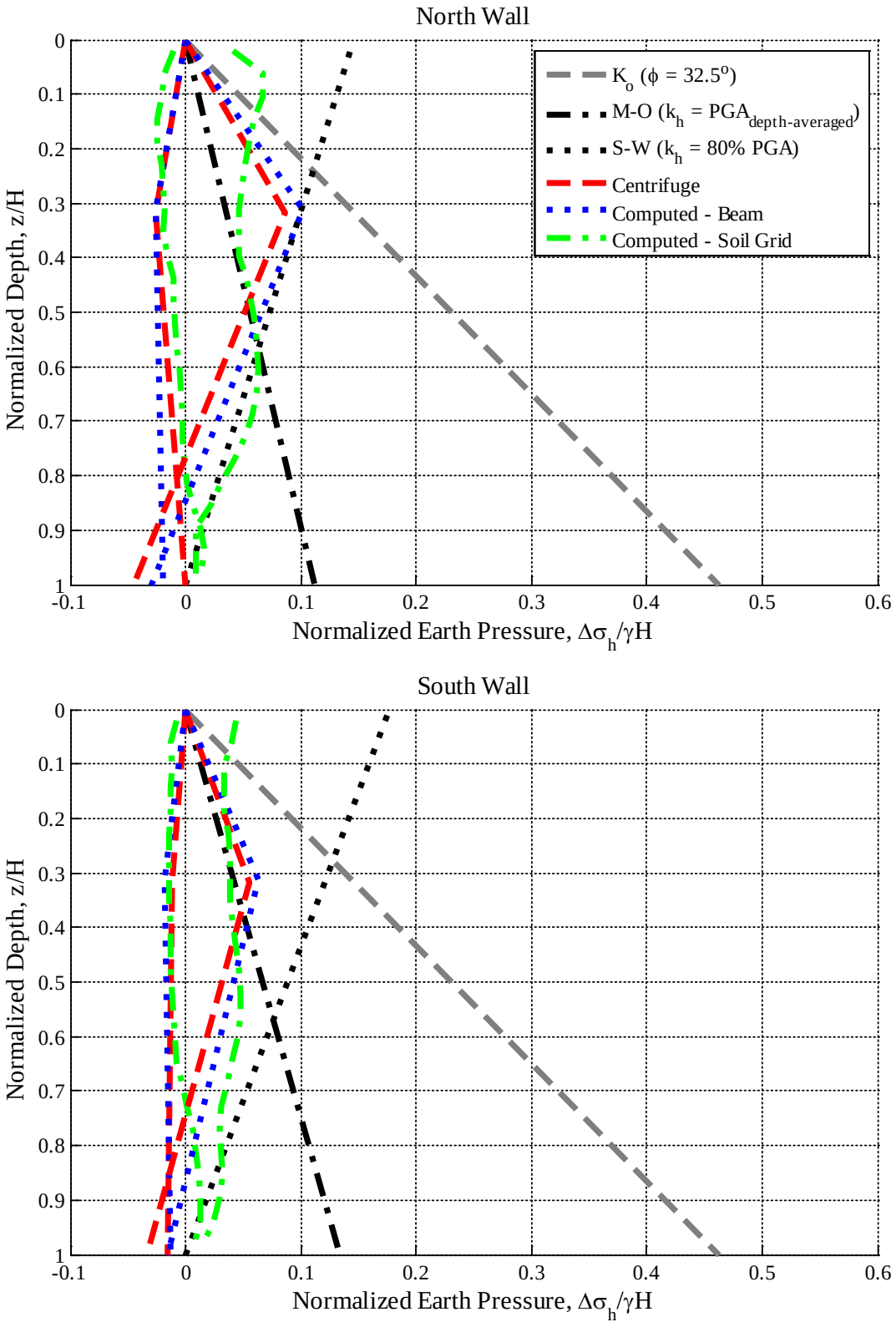

Figure A.71: Measured and computed normalized dynamic earth pressure distributions at maximum and minimum ΔK_{ae} during Loma Prieta WVC-1

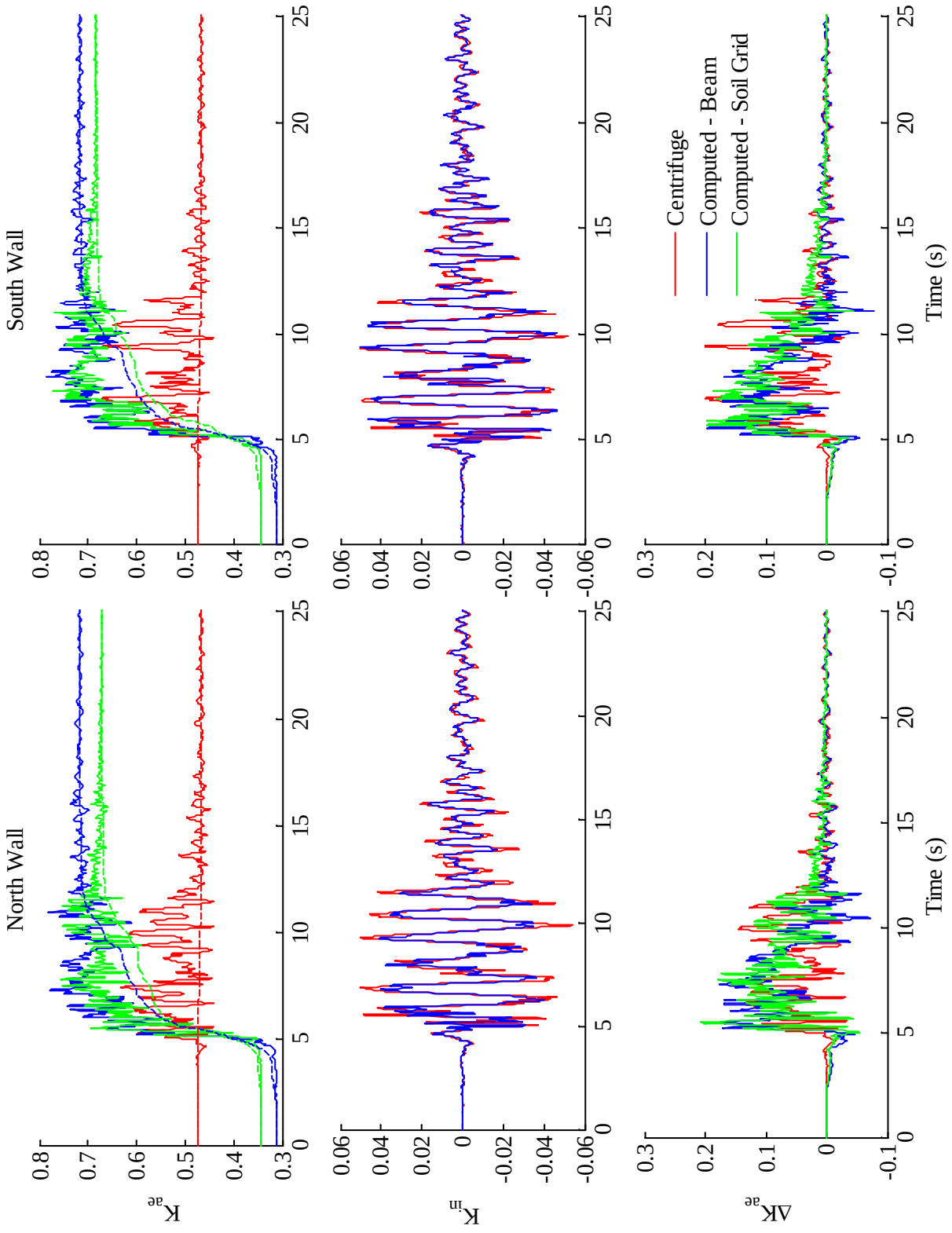

Figure A.72: Measured and computed normalized loads on structure during Kobe TAK 090-3

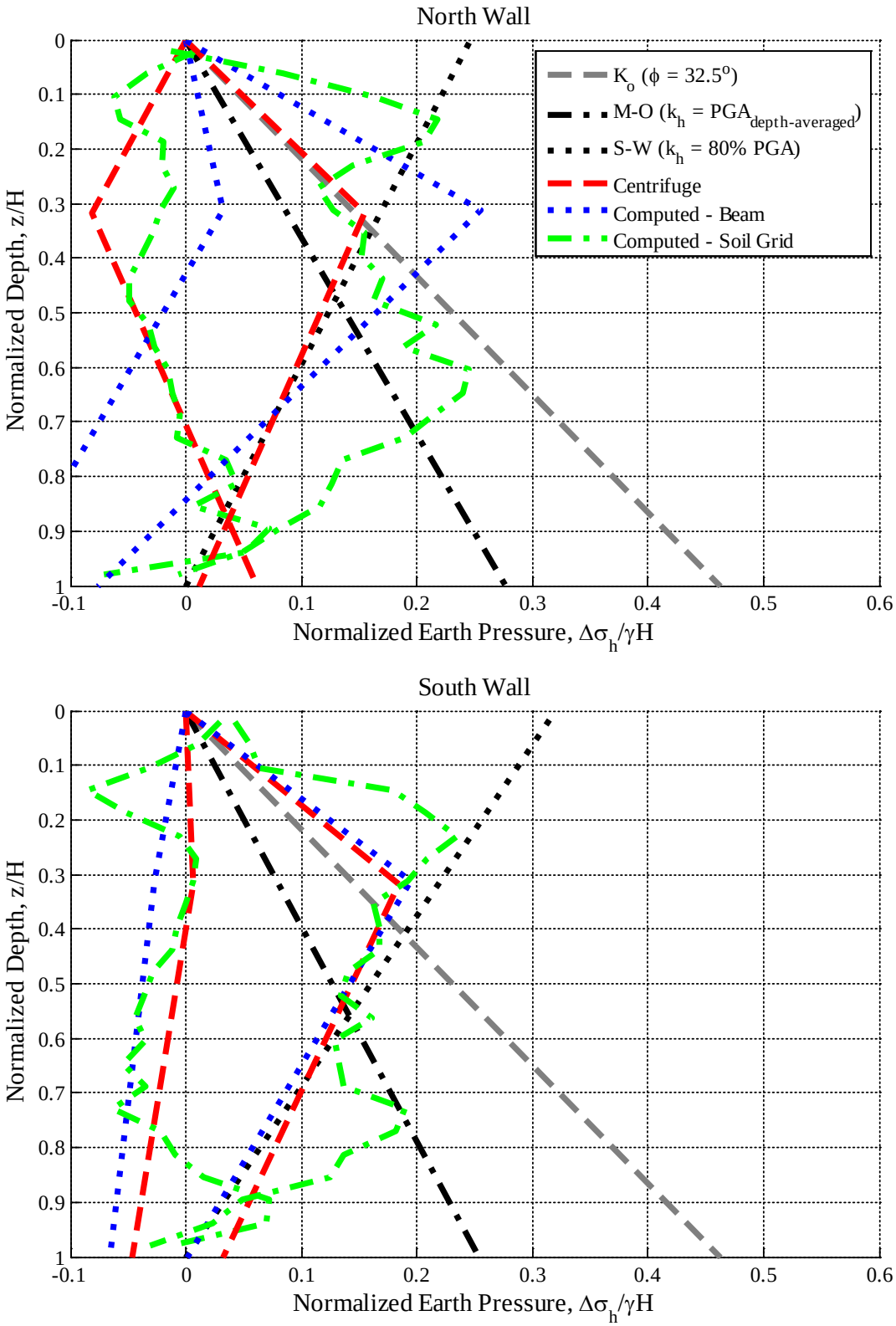

Figure A.73: Measured and computed normalized dynamic earth pressure distributions at maximum and minimum ΔK_{ae} during Kobe TAK 090-3

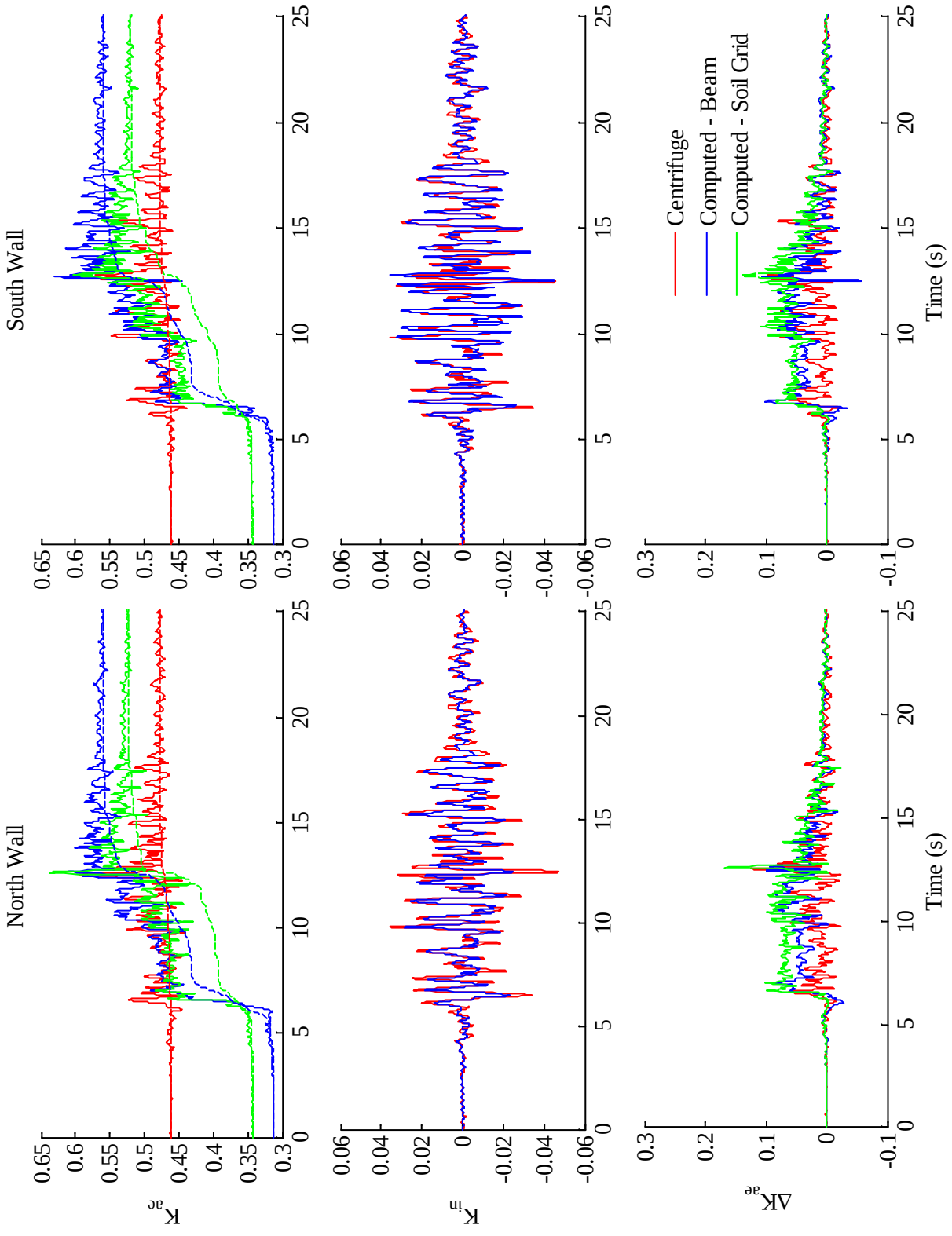

Figure A.74: Measured and computed normalized loads on structure during Loma Prieta SC-2

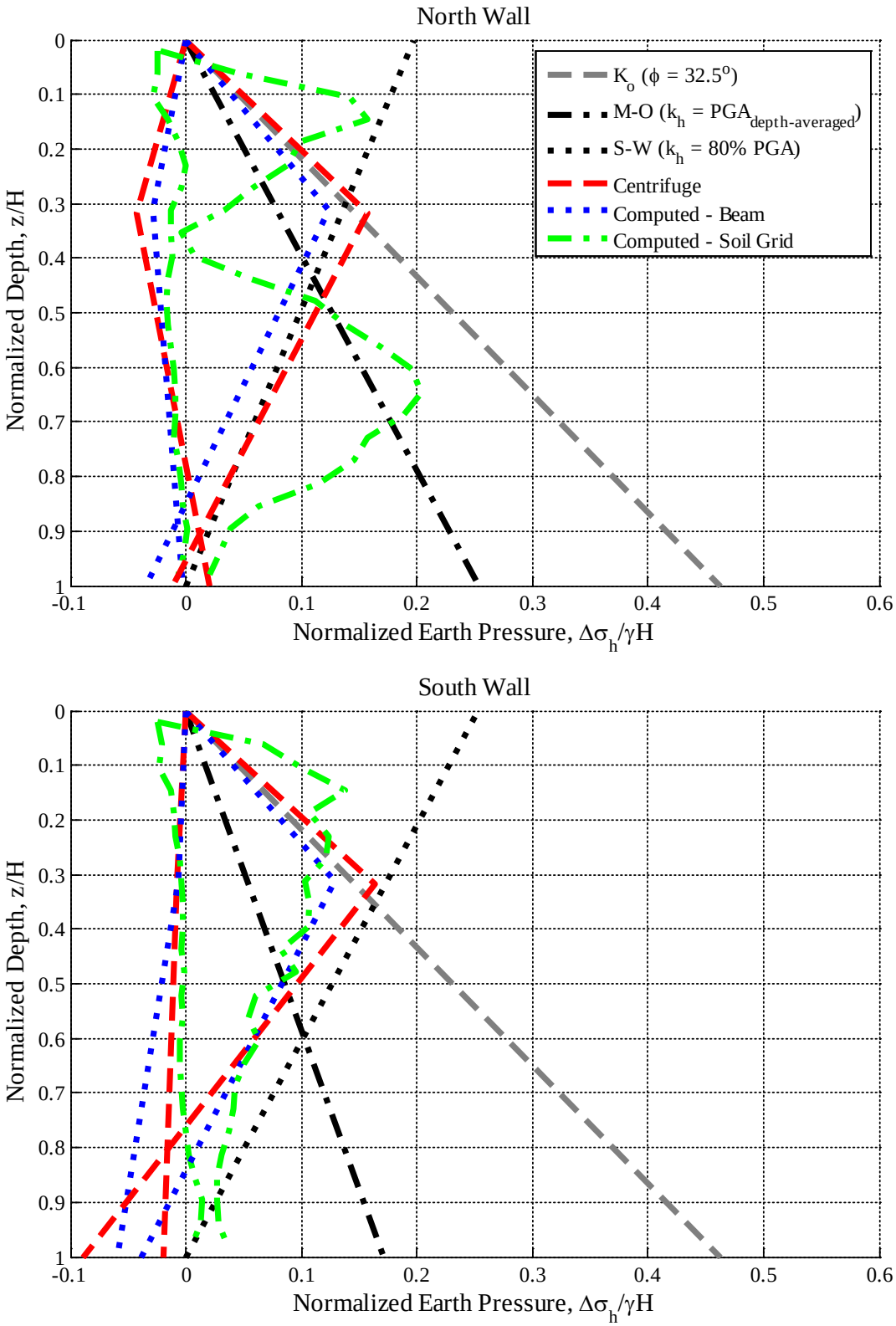

Figure A.75: Measured and computed normalized dynamic earth pressure distributions at maximum and minimum ΔK_{ae} during Loma Prieta SC-2

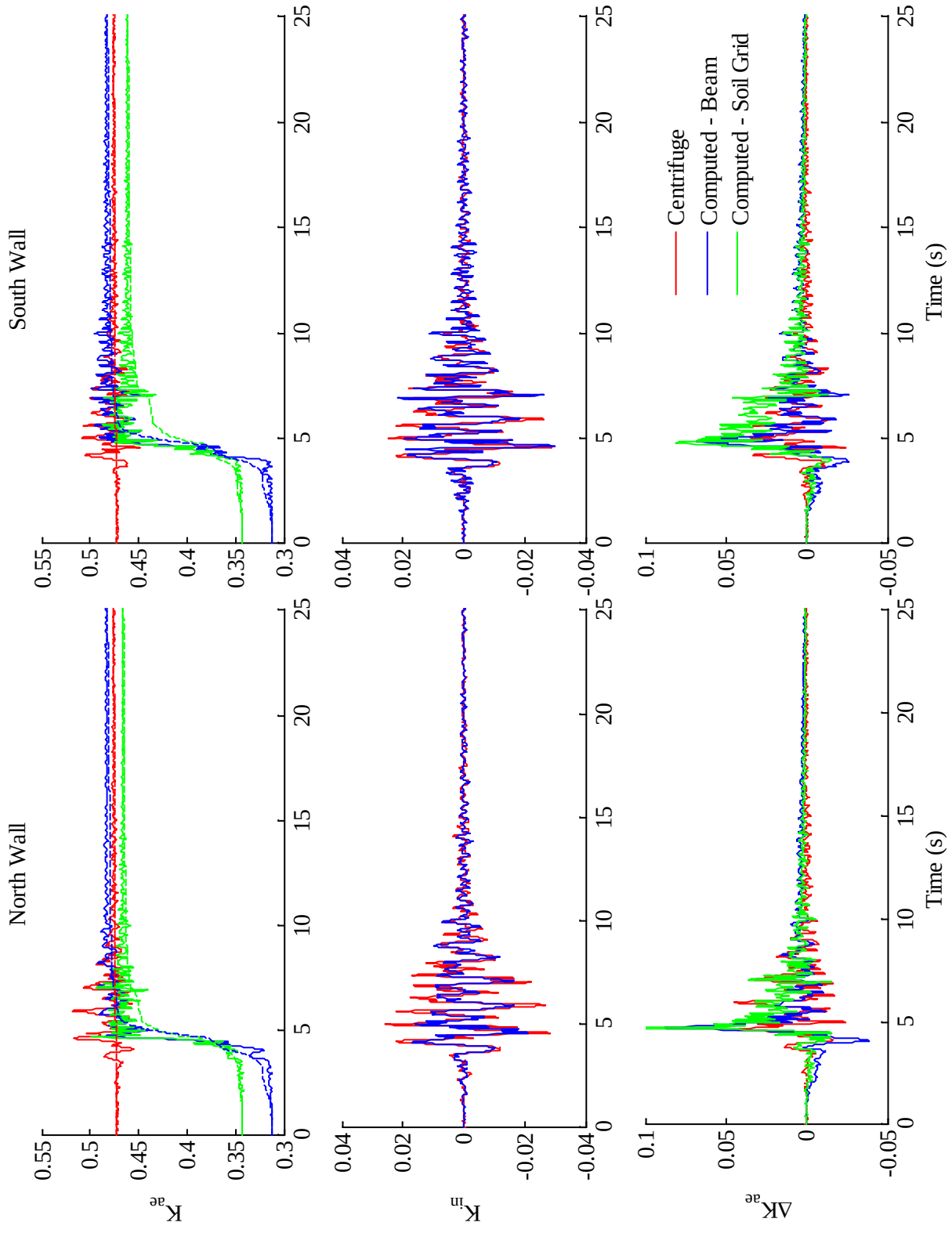

Figure A.76: Measured and computed normalized loads on structure during Loma Prieta WVC-2

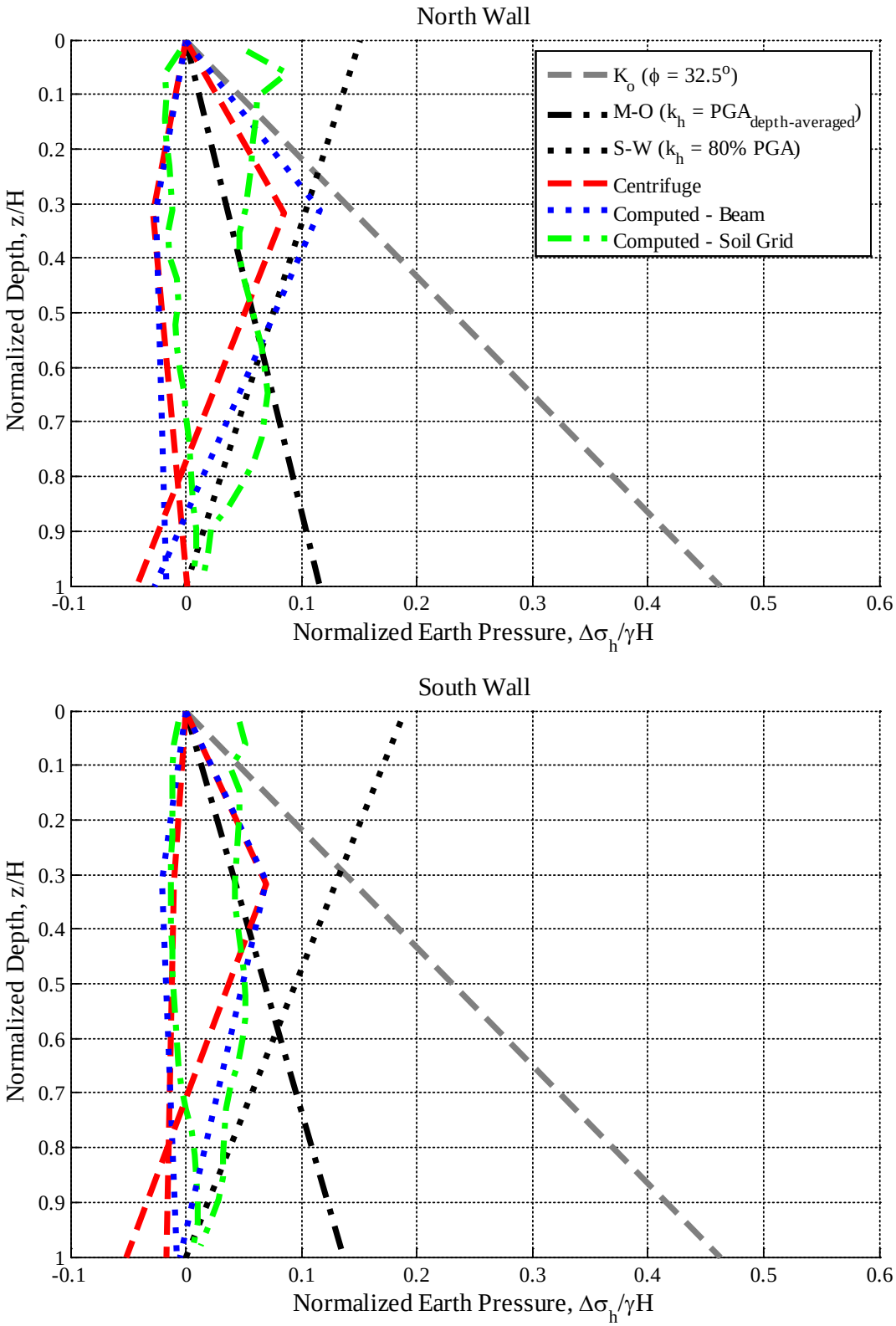

Figure A.77: Measured and computed normalized dynamic earth pressure distributions at maximum and minimum ΔK_{ae} during Loma Prieta WVC-2

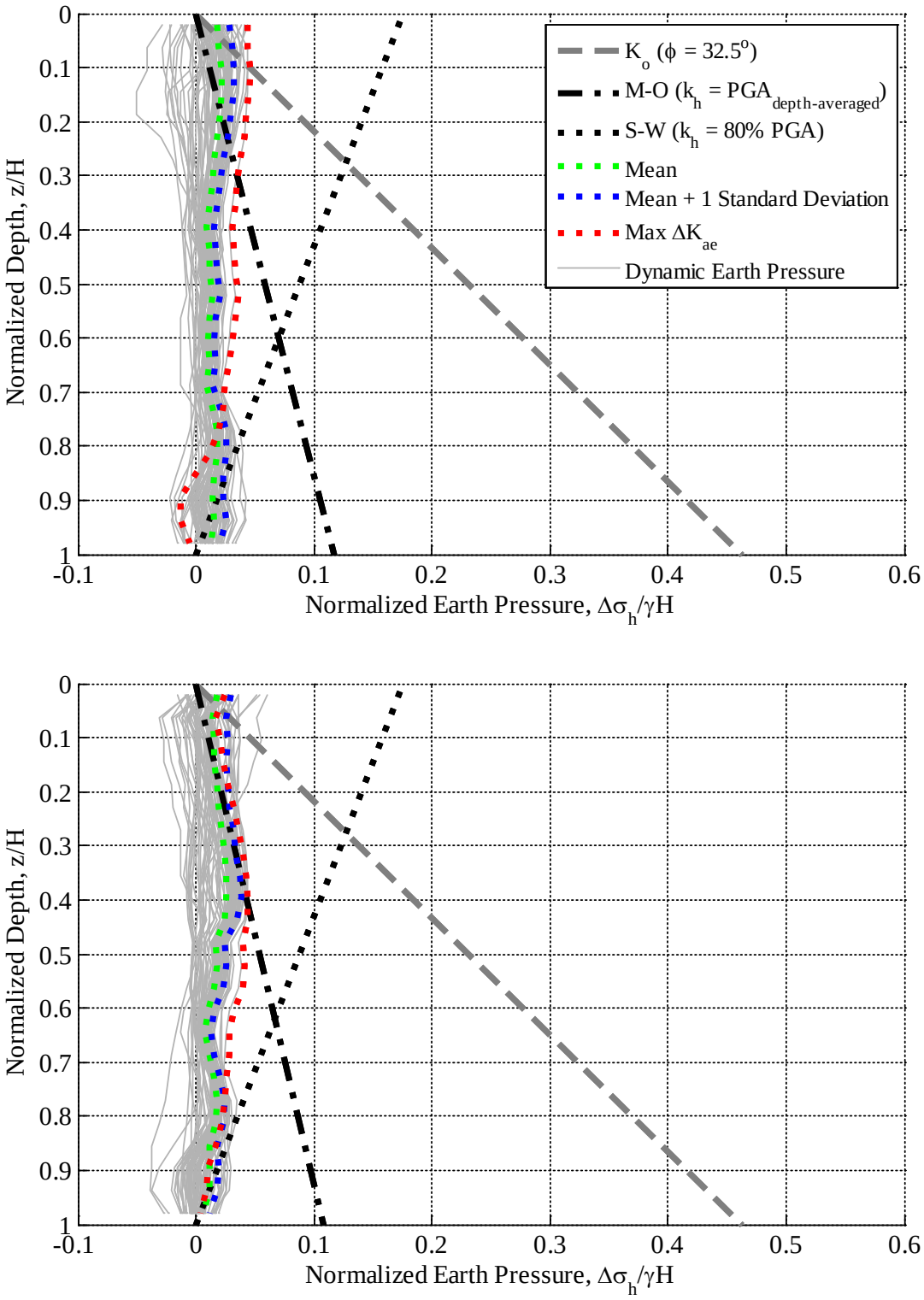

Figure A.78: Mean envelope and mean-plus-one-standard-deviation envelopes of normalized dynamic earth pressure, and computed normalized dynamic earth pressure distributions at maximum ΔK_{ae} during Kocaeli YPT 060

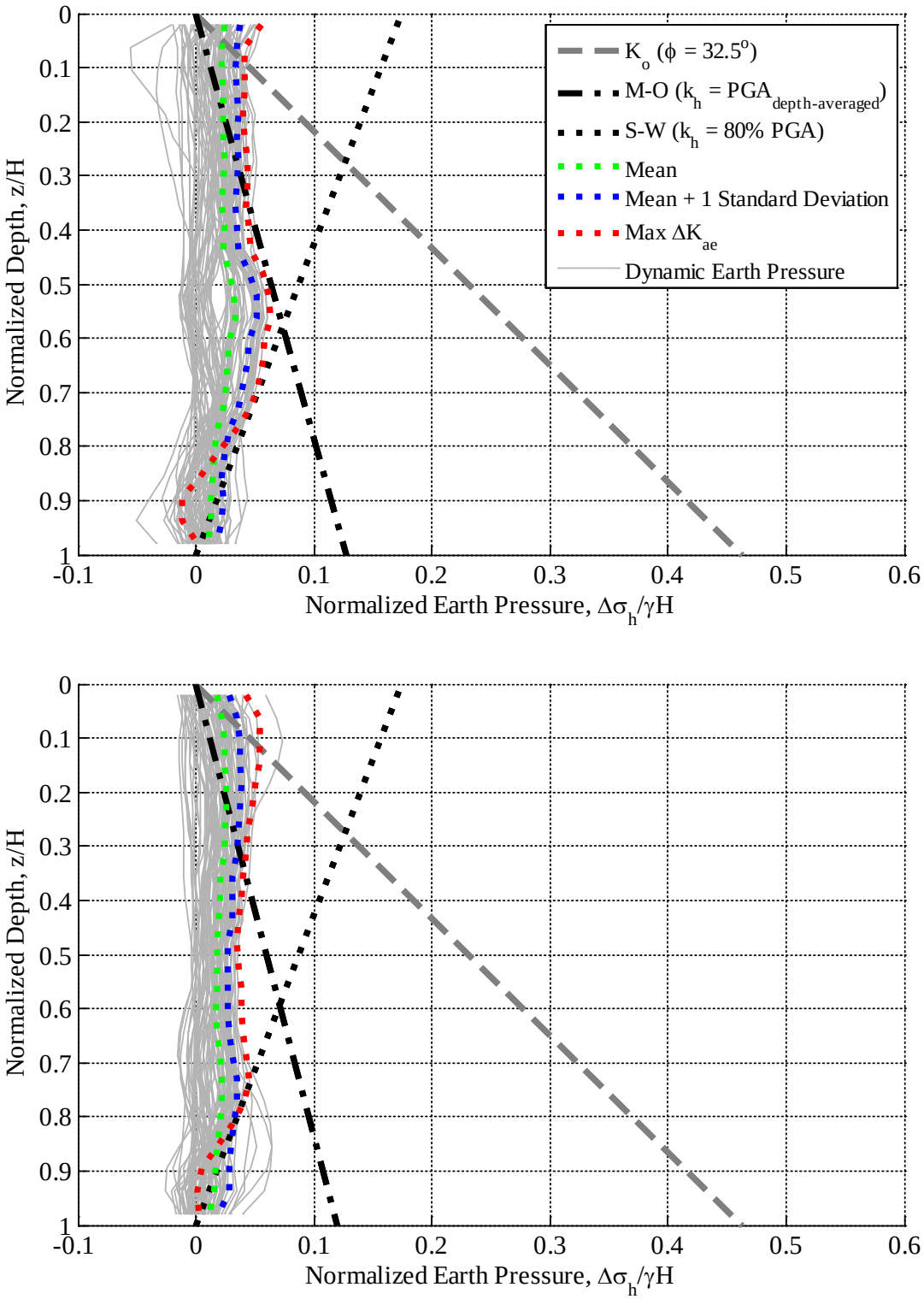

Figure A.79: Mean envelope and mean-plus-one-standard-deviation envelopes of normalized dynamic earth pressure, and computed normalized dynamic earth pressure distributions at maximum ΔK_{ae} during Kocaeli YPT 330

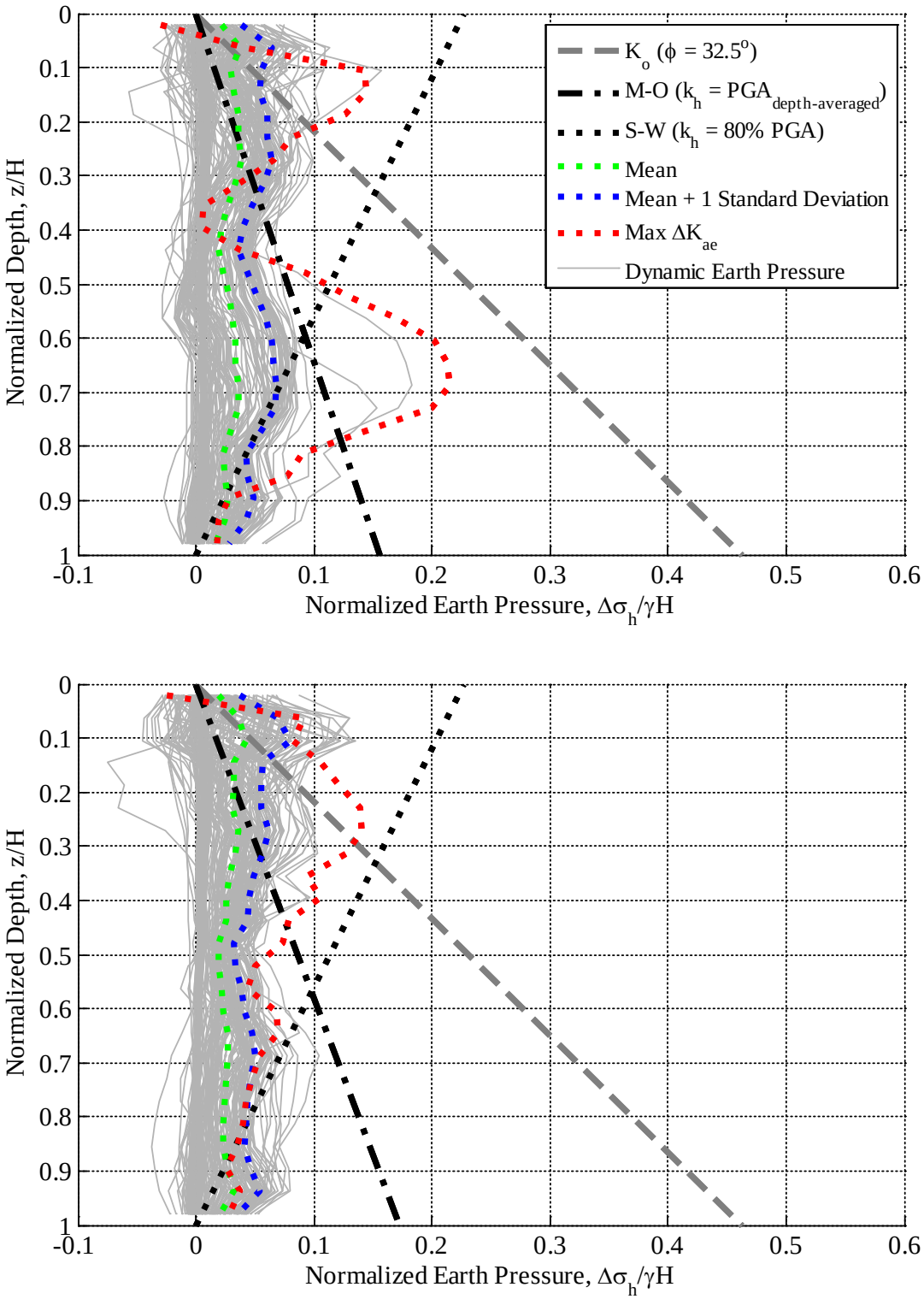

Figure A.80: Mean envelope and mean-plus-one-standard-deviation envelopes of normalized dynamic earth pressure, and computed normalized dynamic earth pressure distributions at maximum ΔK_{ae} during Loma Prieta SC-1

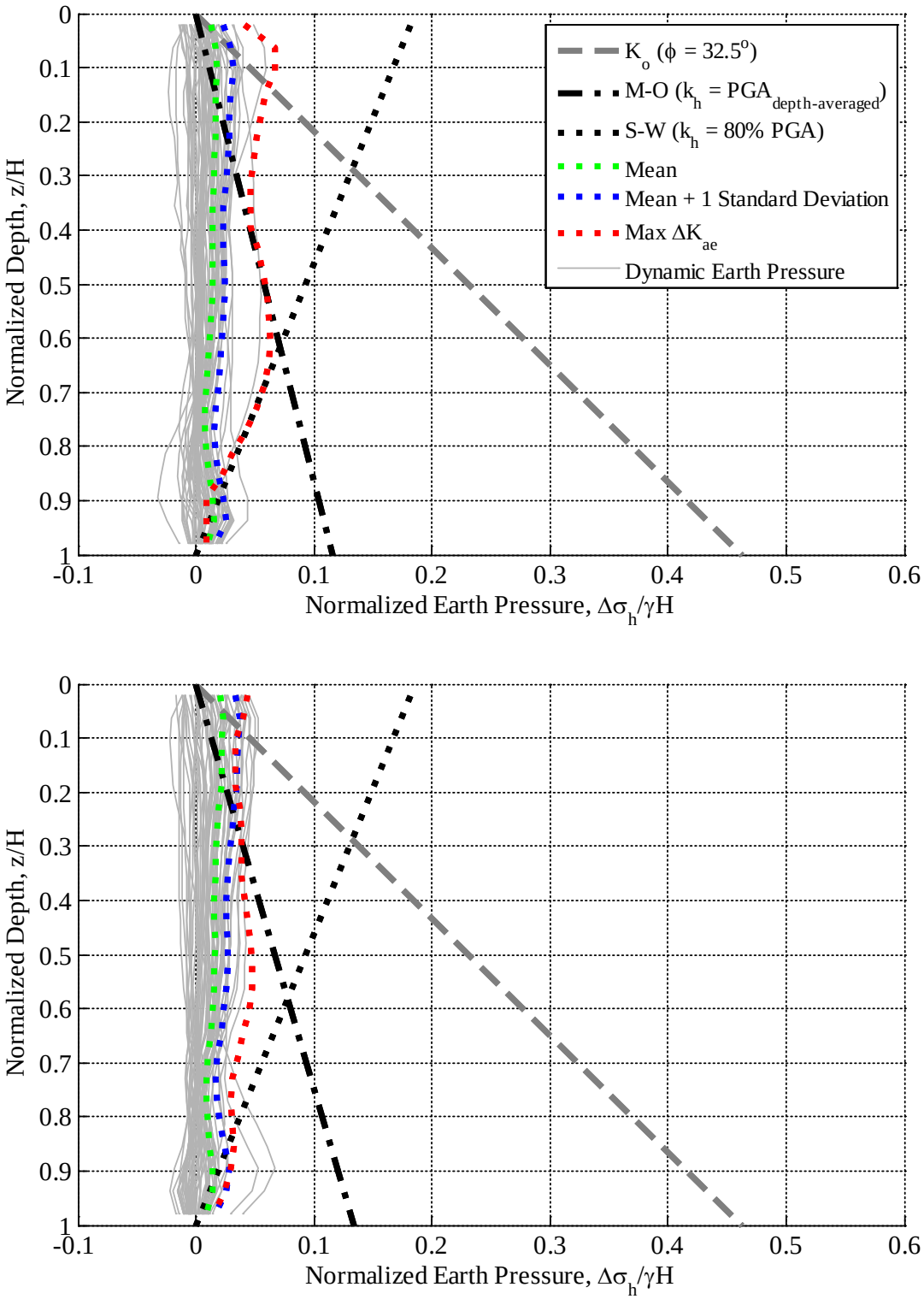

Figure A.81: Mean envelope and mean-plus-one-standard-deviation envelopes of normalized dynamic earth pressure, and computed normalized dynamic earth pressure distributions at maximum ΔK_{ae} during Loma Prieta WVC-1

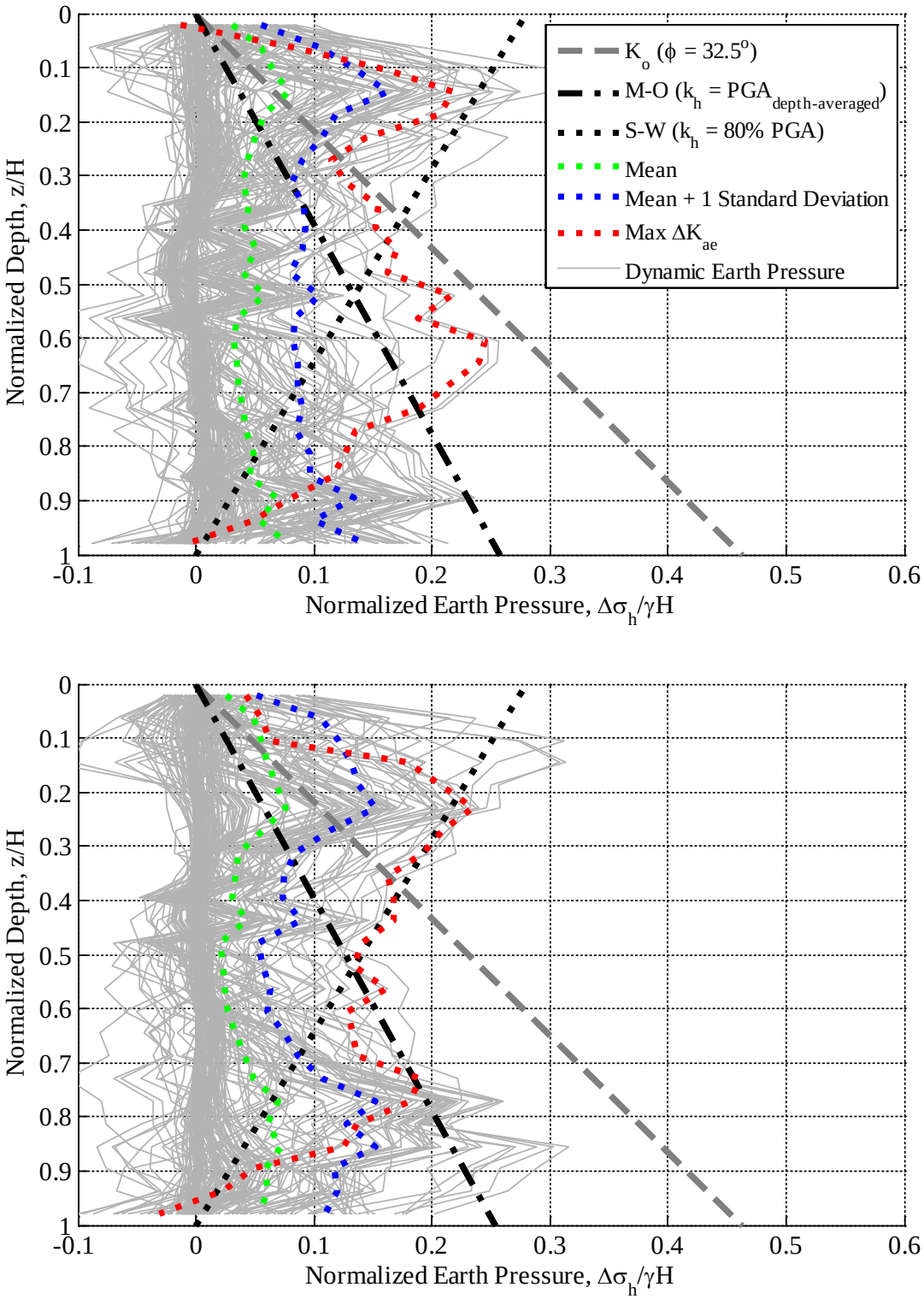

Figure A.82: Mean envelope and mean-plus-one-standard-deviation envelopes of normalized dynamic earth pressure, and computed normalized dynamic earth pressure distributions at maximum ΔK_{ae} during Kobe TAK 090-3

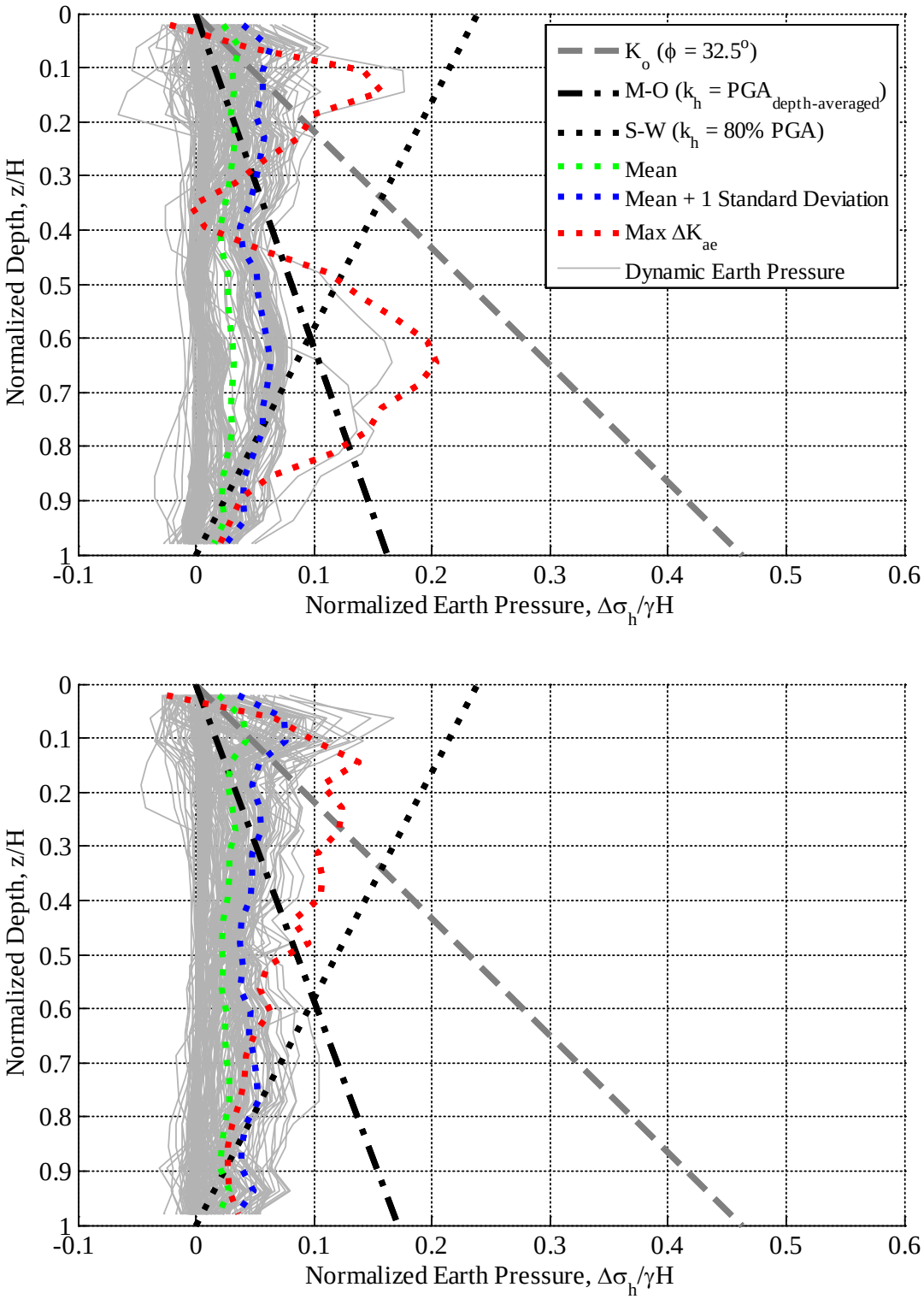

Figure A.83: Mean envelope and mean-plus-one-standard-deviation envelopes of normalized dynamic earth pressure, and computed normalized dynamic earth pressure distributions at maximum ΔK_{ae} during Loma Prieta SC-2

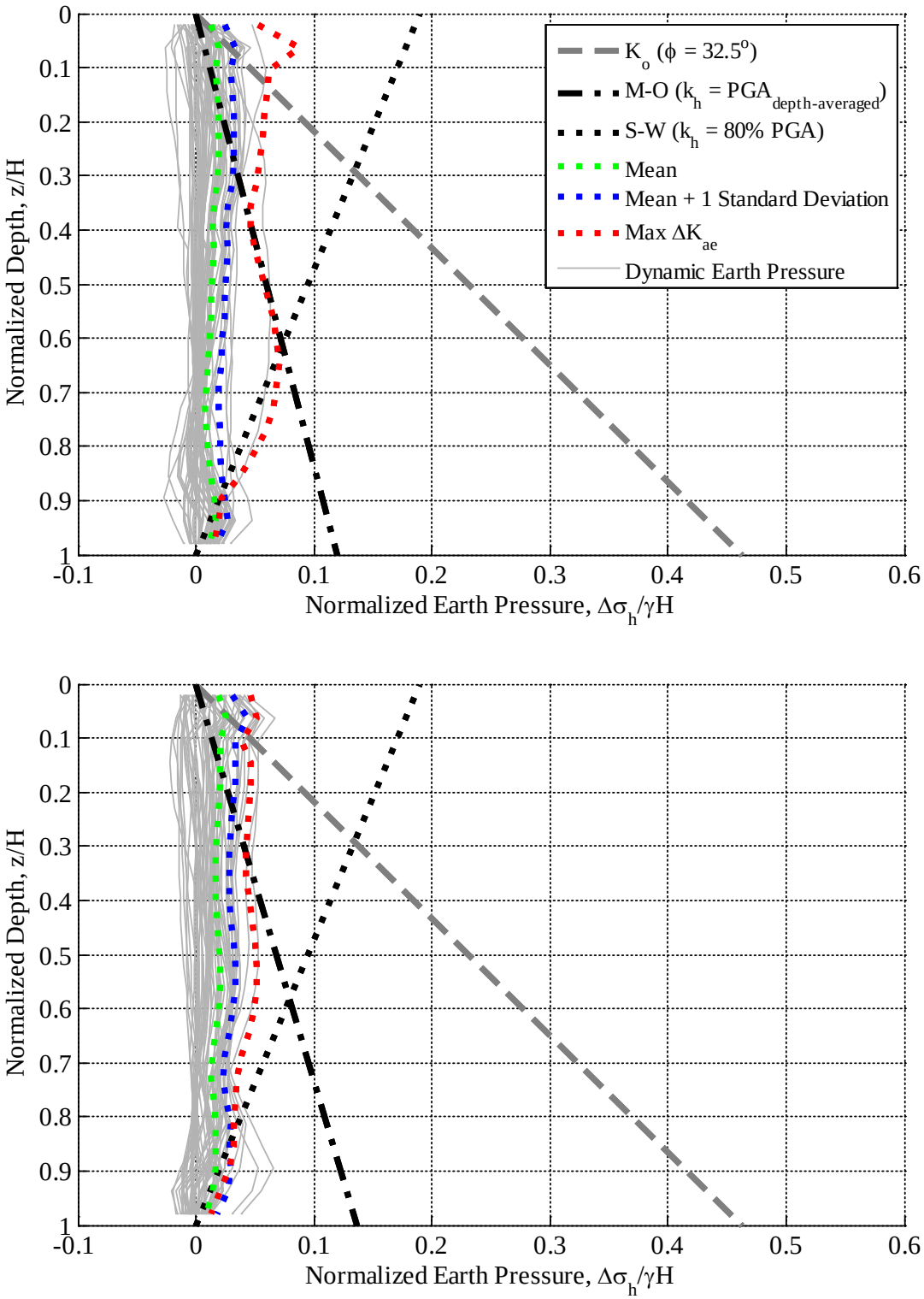

Figure A.84: Mean envelope and mean-plus-one-standard-deviation envelopes of normalized dynamic earth pressure, and computed normalized dynamic earth pressure distributions at maximum ΔK_{ae} during Loma Prieta WVC-2

Appendix B Results from prototype basement structure model

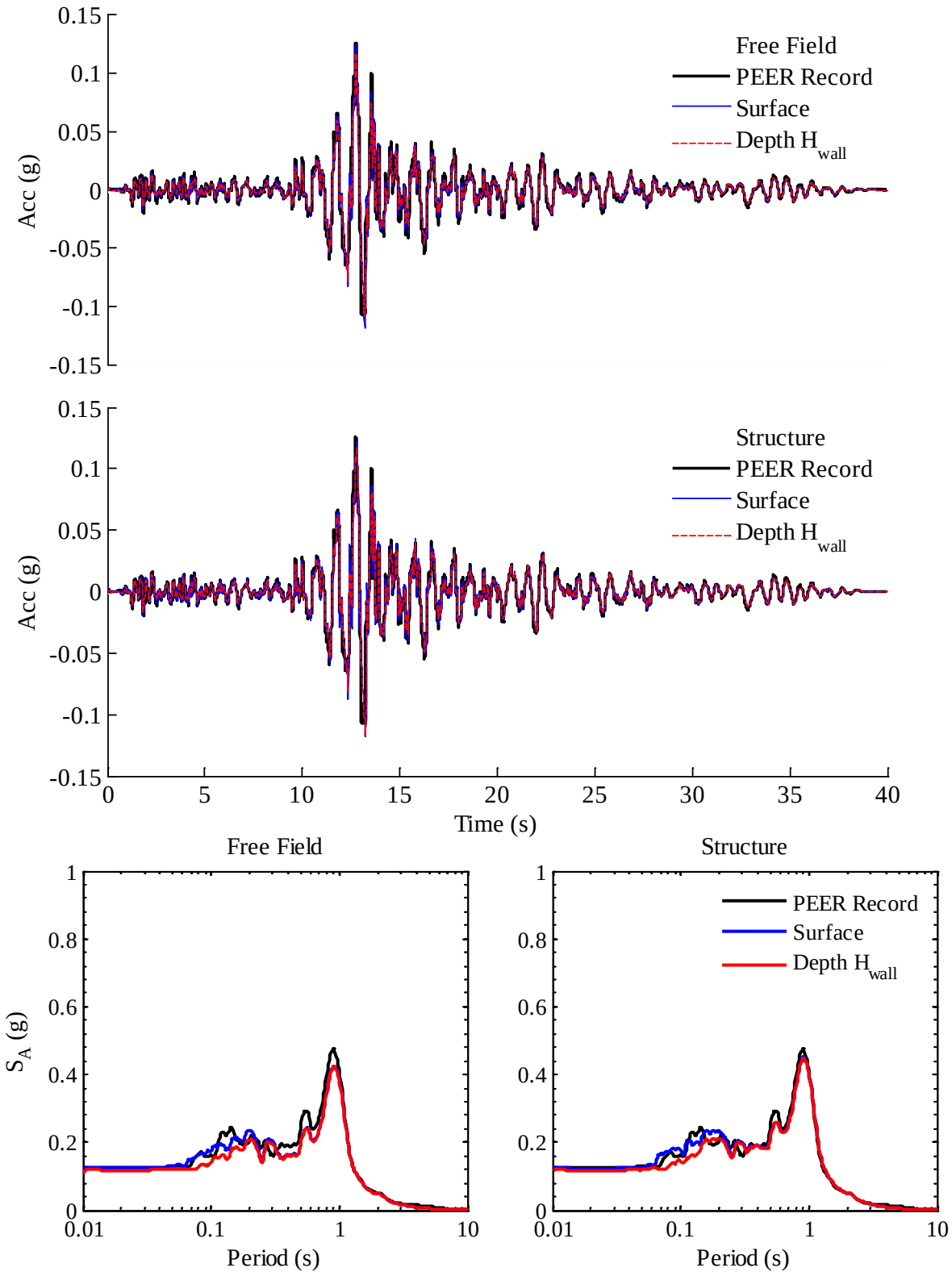

Figure B.1: Computed accelerations and response spectra at 5% damping in free field and structure during Loma Prieta RCH 190 for one level basement; Site Class D

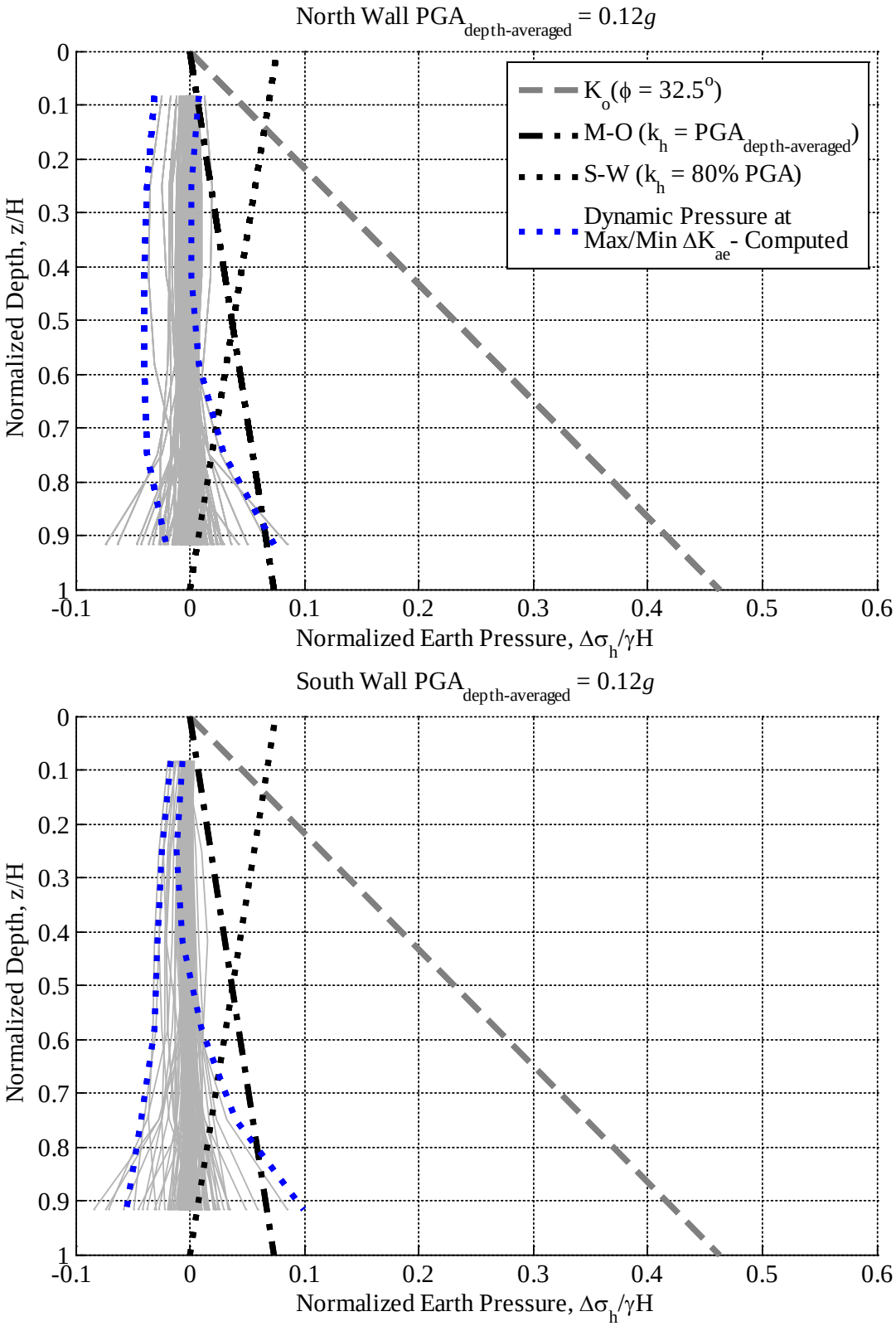

Figure B.2: Computed normalized dynamic earth pressure distributions at maximum and minimum ΔK_{ae} during Loma Prieta RCH 190 for one level basement; Site Class D

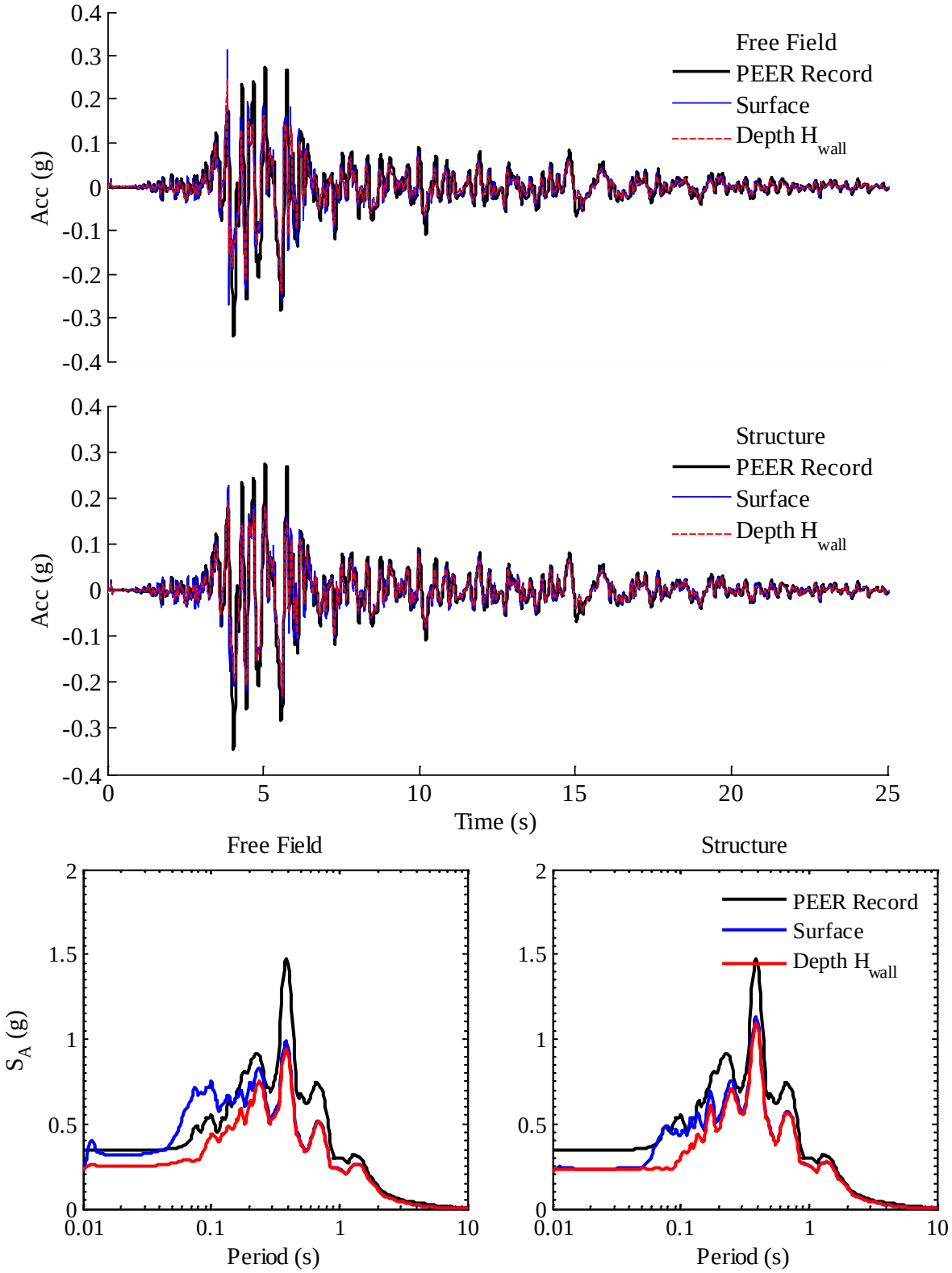

Figure B.3: Computed accelerations and response spectra at 5% damping in free field and structure during Loma Prieta GA2 000 for one level basement; Site Class D

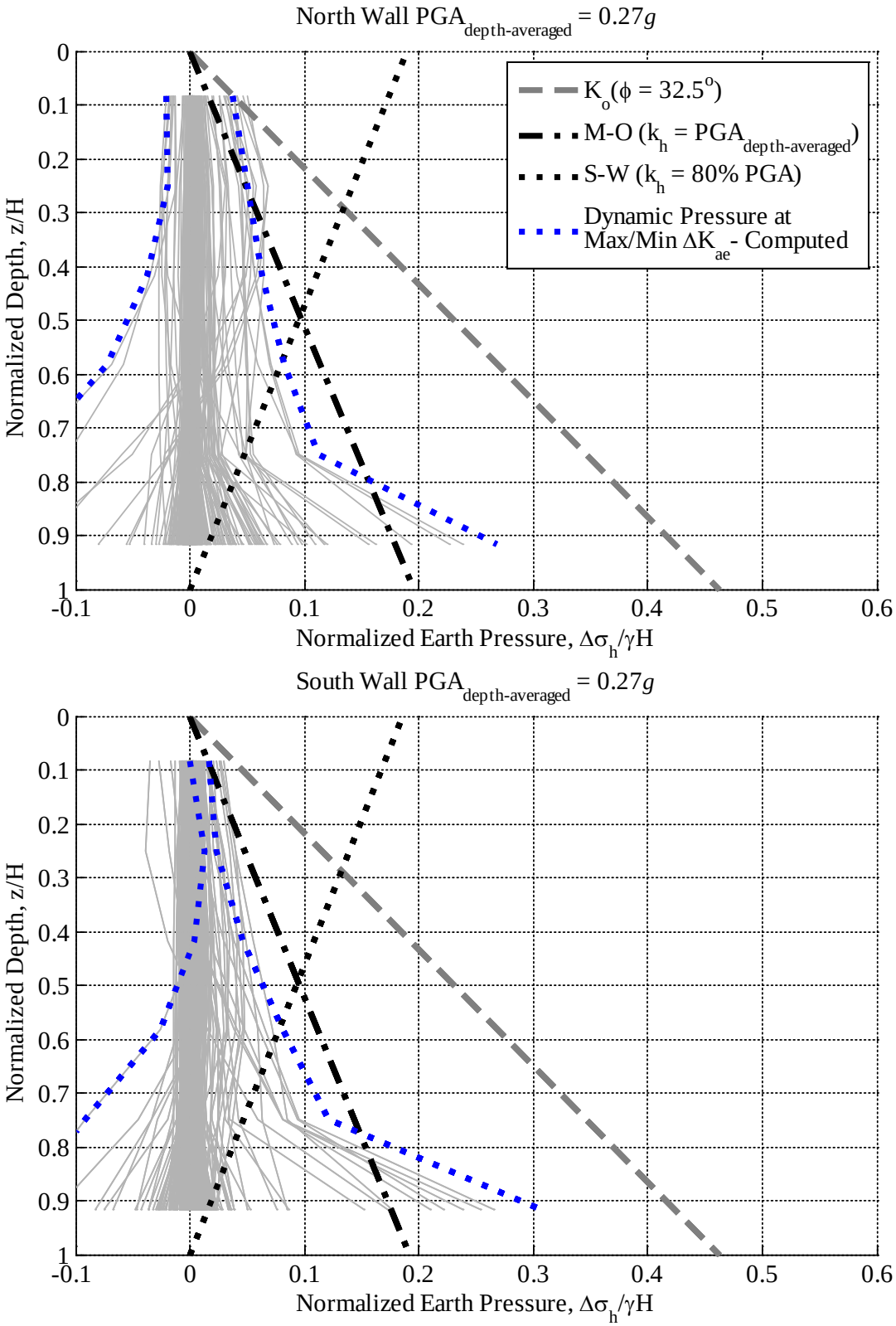

Figure B.4: Computed normalized dynamic earth pressure distributions at maximum and minimum ΔK_{ae} during Loma Prieta GA2 000 for one level basement; Site Class D

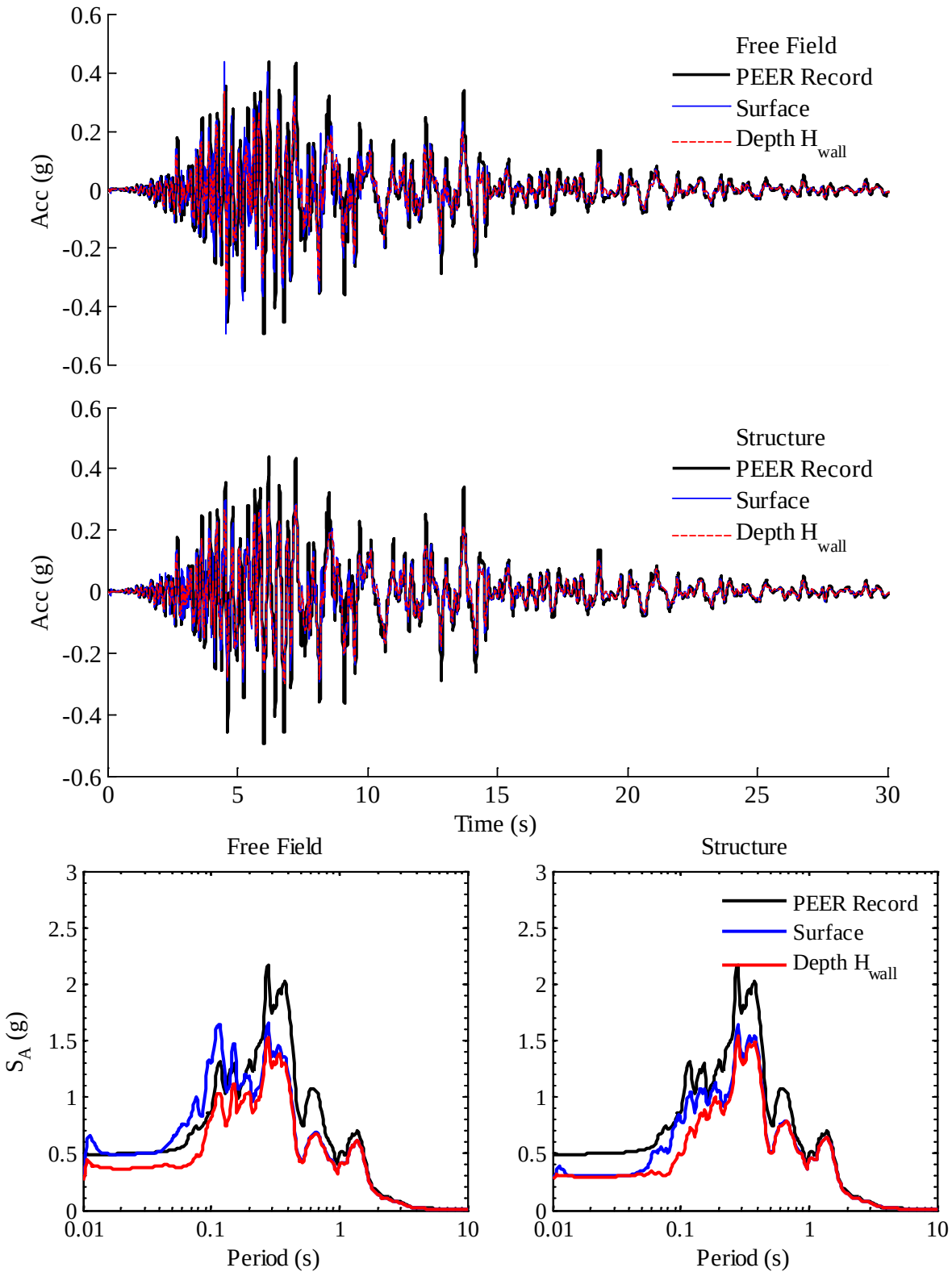

Figure B.5: Computed accelerations and response spectra at 5% damping in free field and structure during Loma Prieta CAP 000 for one level basement; Site Class D

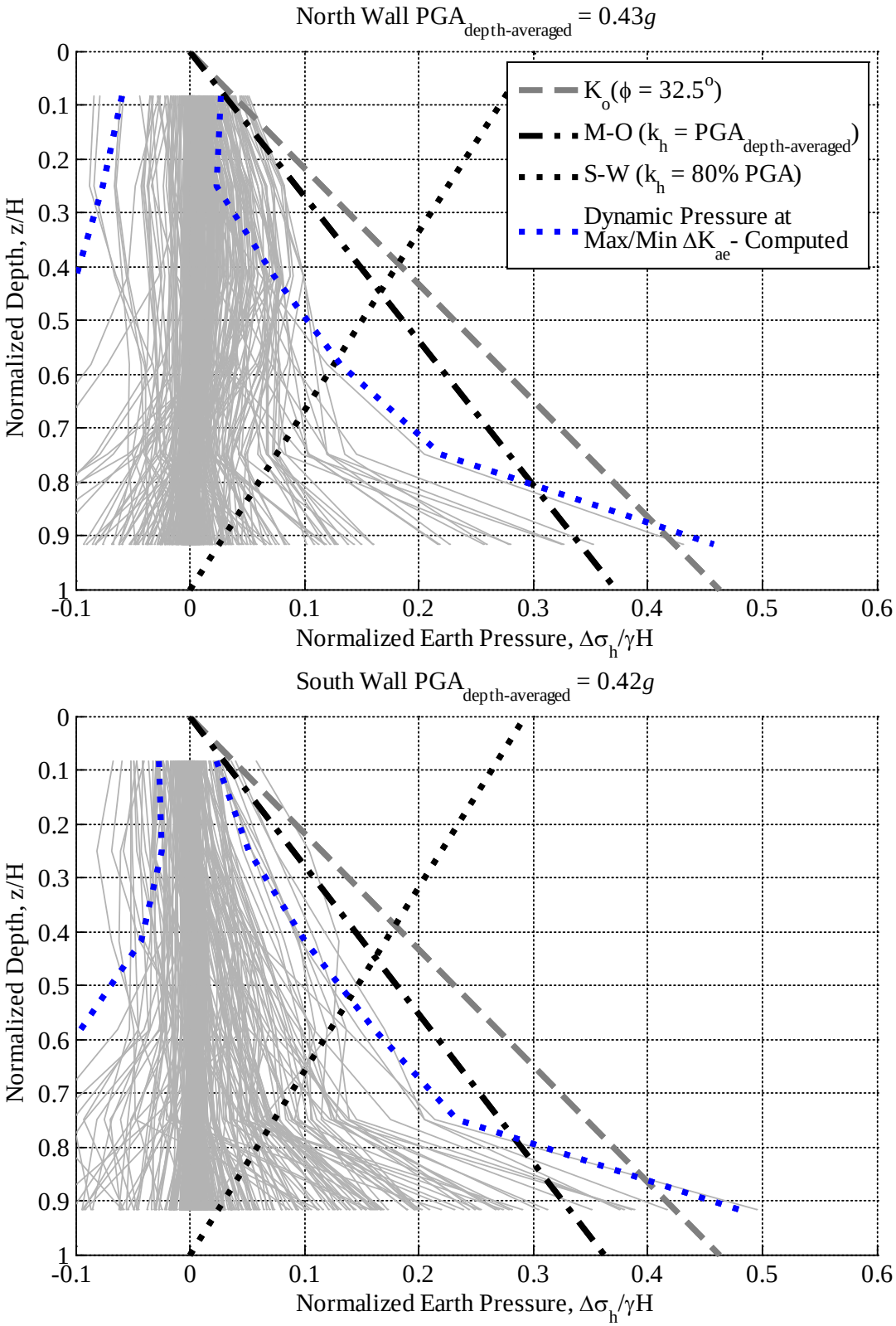

Figure B.6: Computed normalized dynamic earth pressure distributions at maximum and minimum ΔK_{ae} during Loma Prieta CAP 000 for one level basement; Site Class D

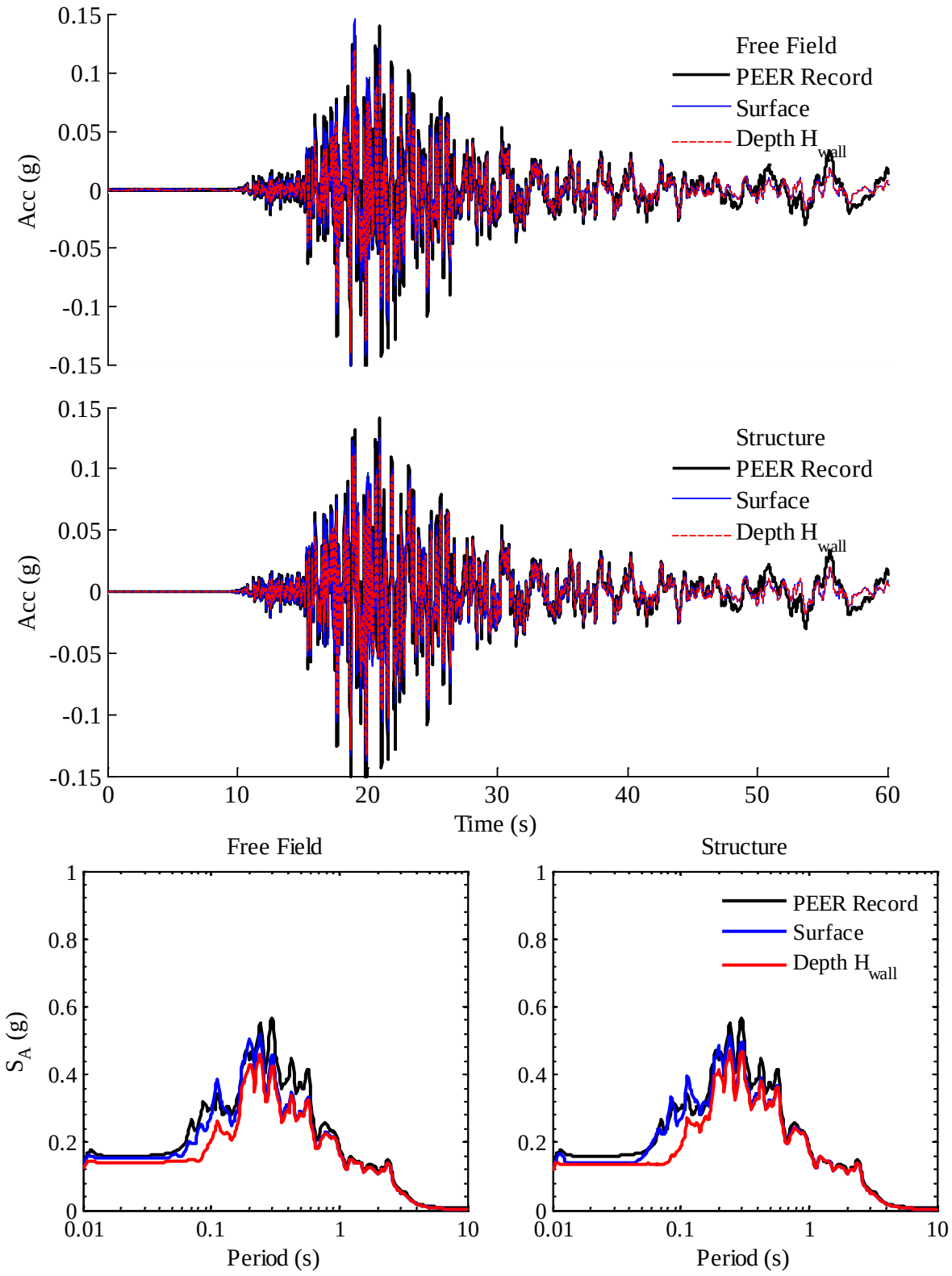

Figure B.7: Computed accelerations and response spectra at 5% damping in free field and structure during Kobe SKI 000 for one level basement; Site Class D

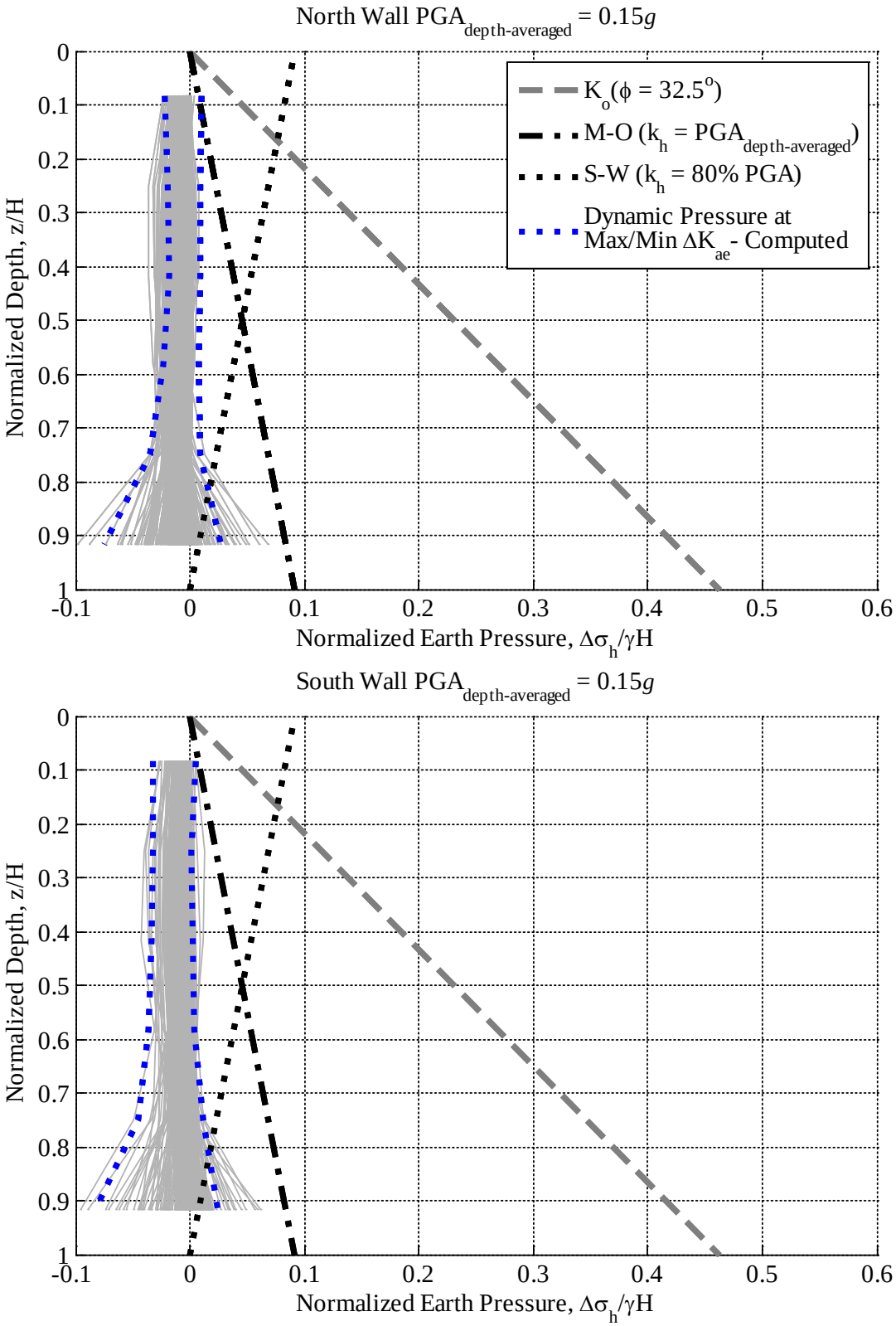

Figure B.8: Computed normalized dynamic earth pressure distributions at maximum and minimum ΔK_{ae} during Kobe SKI 000 for one level basement; Site Class D

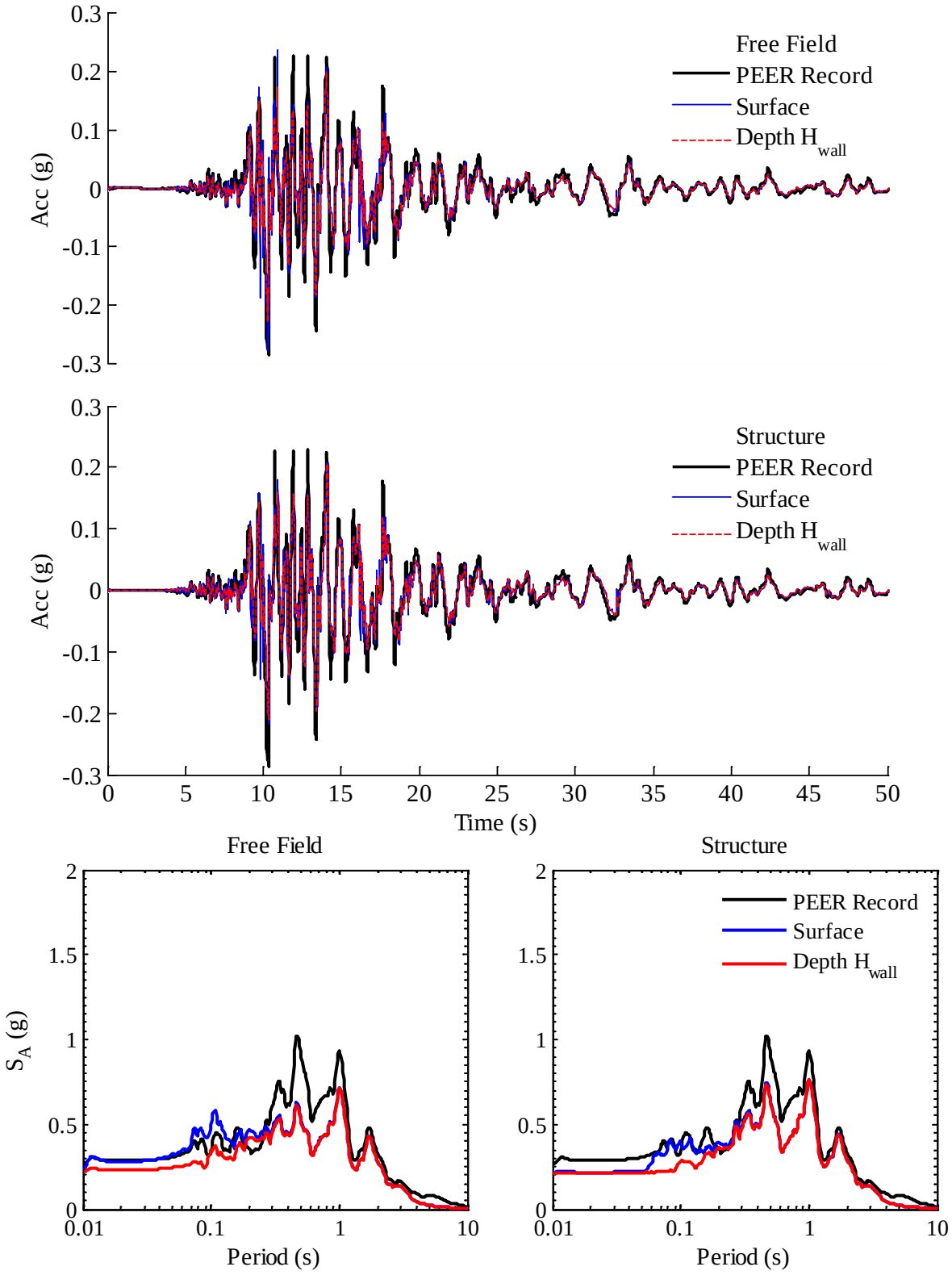

Figure B.9: Computed accelerations and response spectra at 5% damping in free field and structure during Kobe AMA 000 for one level basement; Site Class D

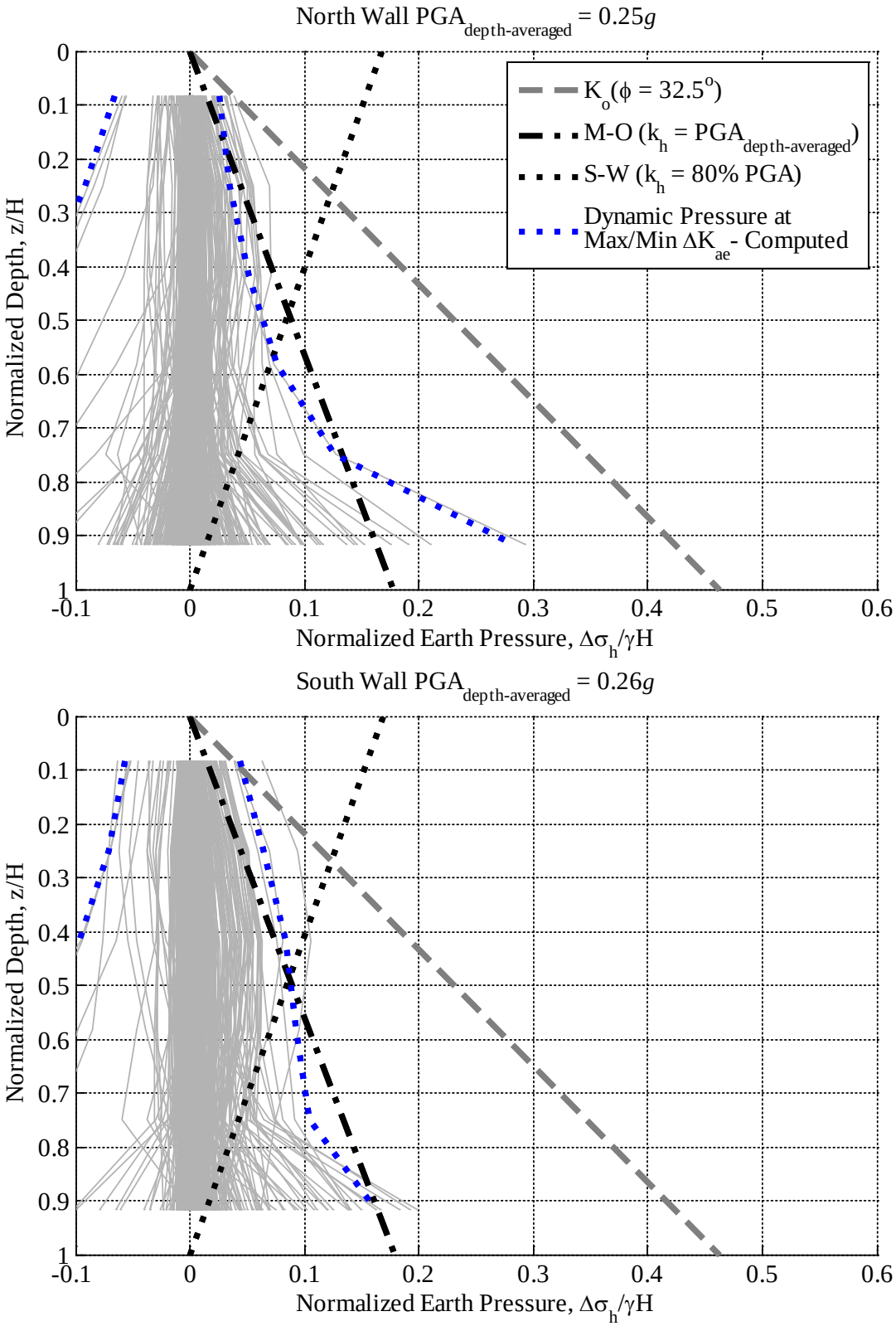

Figure B.10: Computed normalized dynamic earth pressure distributions at maximum and minimum ΔK_{ae} during Kobe AMA 000 for one level basement; Site Class D

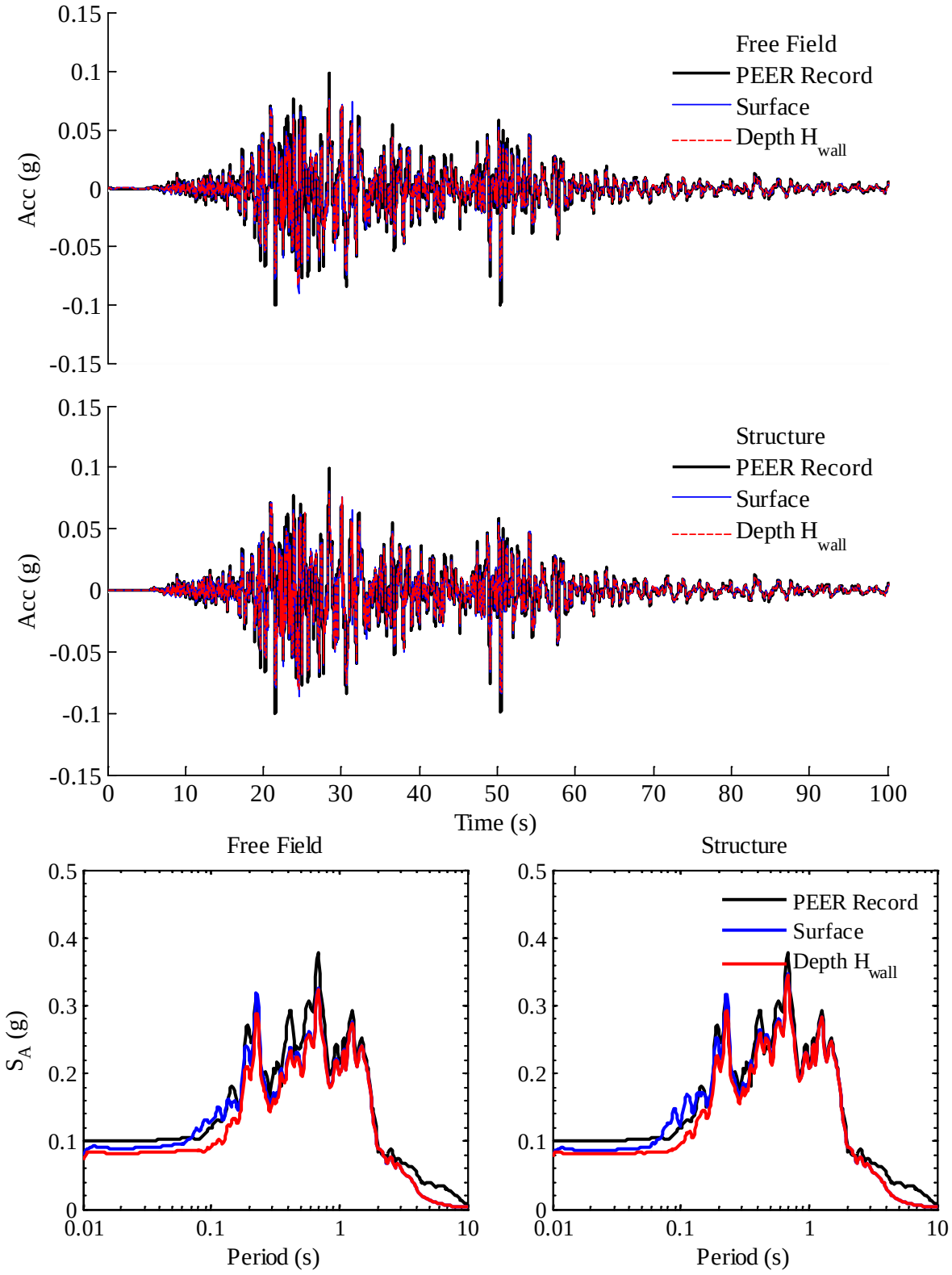

Figure B.11: Computed accelerations and response spectra at 5% damping in free field and structure during Kocaeli BUR 090 for one level basement; Site Class D

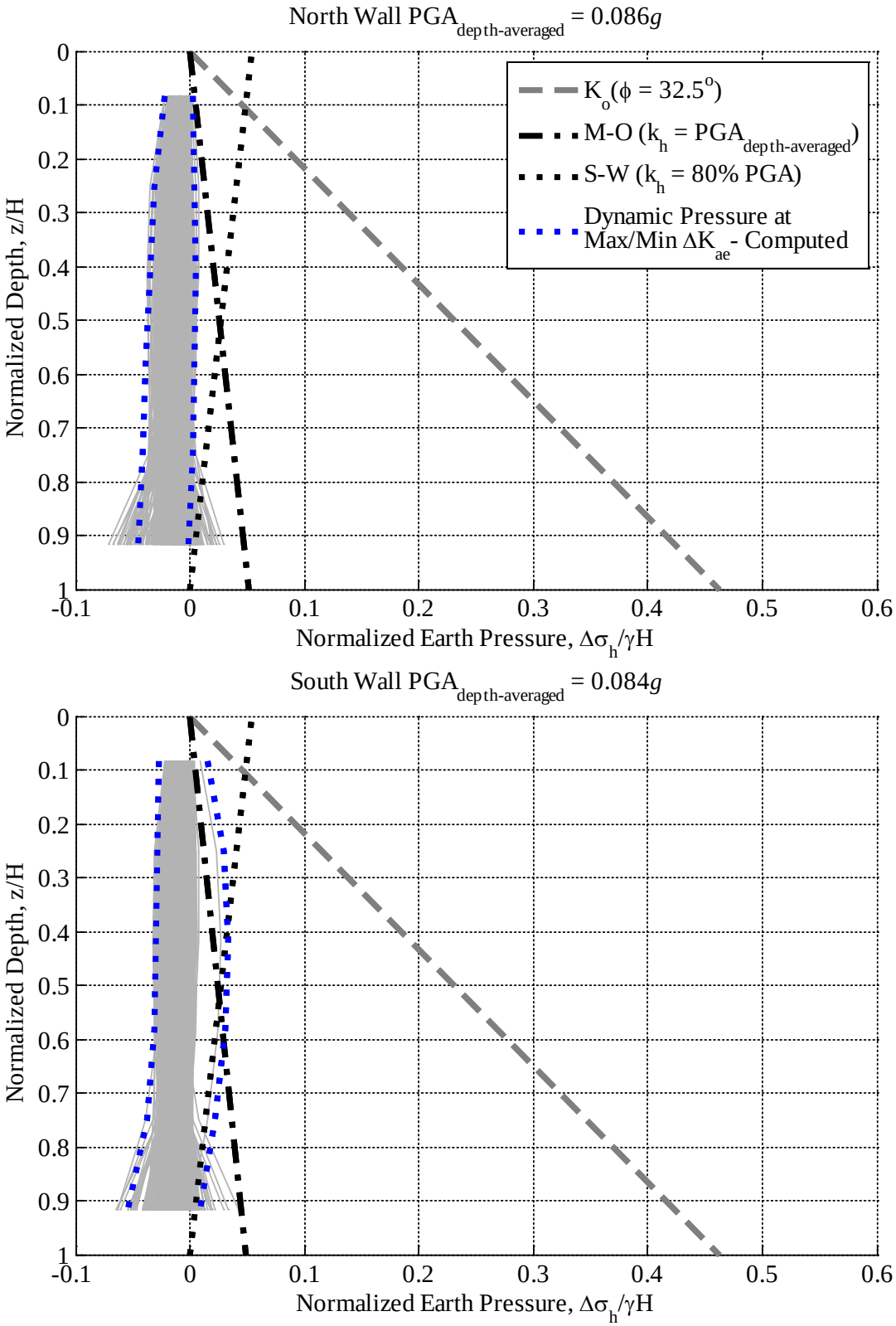

Figure B.12: Computed normalized dynamic earth pressure distributions at maximum and minimum ΔK_{ae} during Kocaeli BUR 090 for one level basement; Site Class D

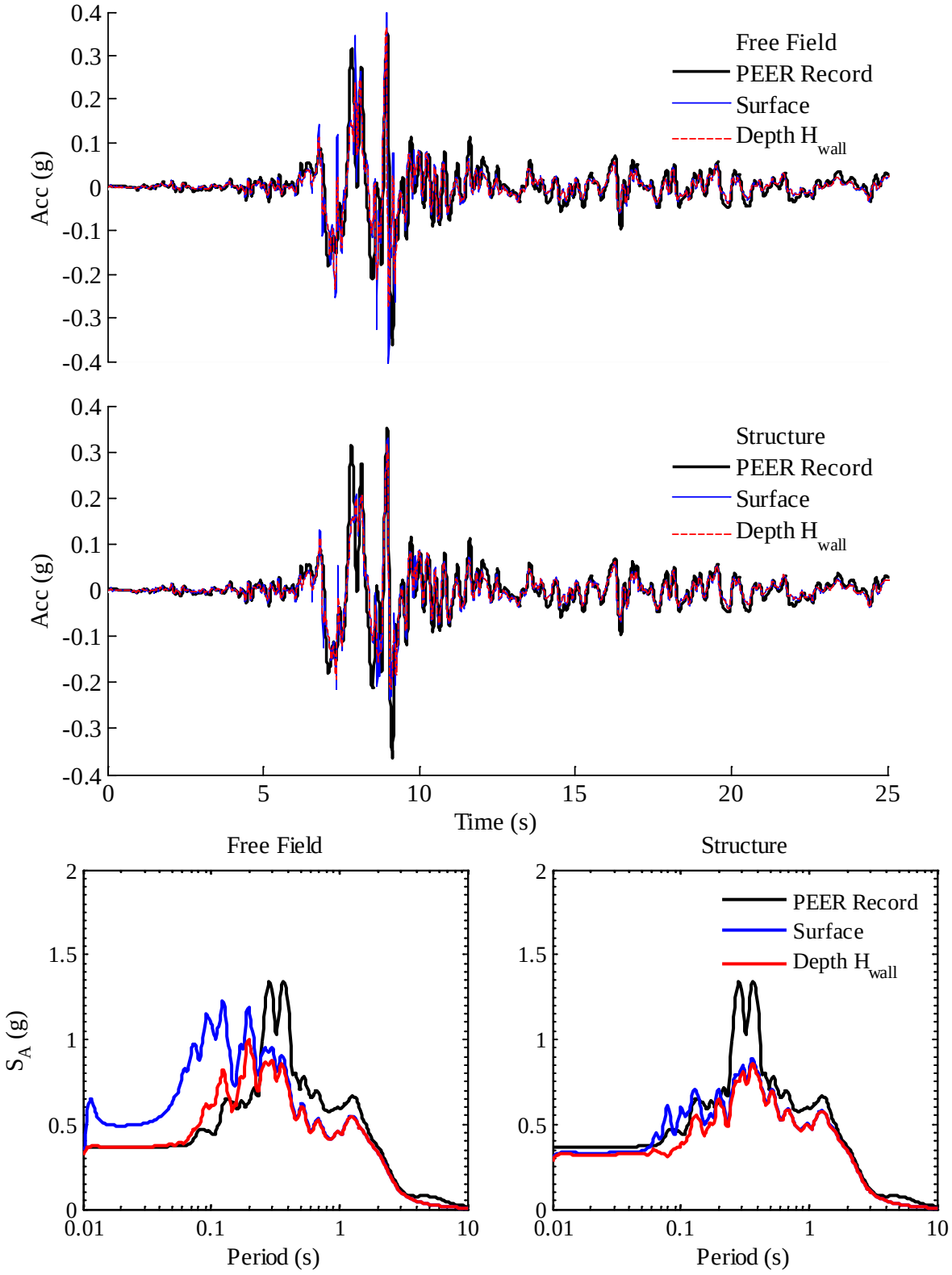

Figure B.13: Computed accelerations and response spectra at 5% damping in free field and structure during Kocaeli DUZ 270 for one level basement; Site Class D

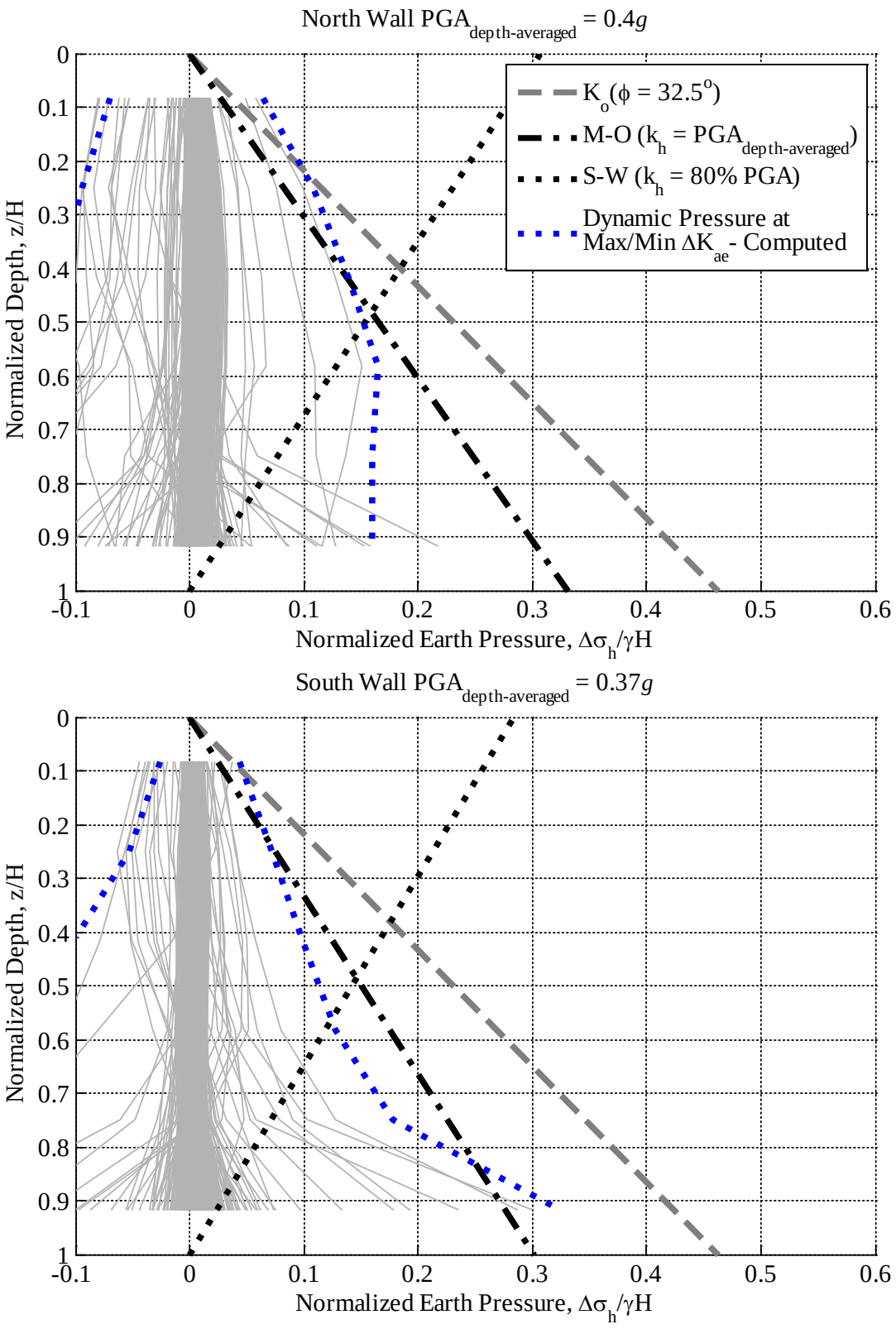

Figure B.14: Computed normalized dynamic earth pressure distributions at maximum and minimum ΔK_{ae} during Kocaeli DUZ 270 for one level basement; Site Class D

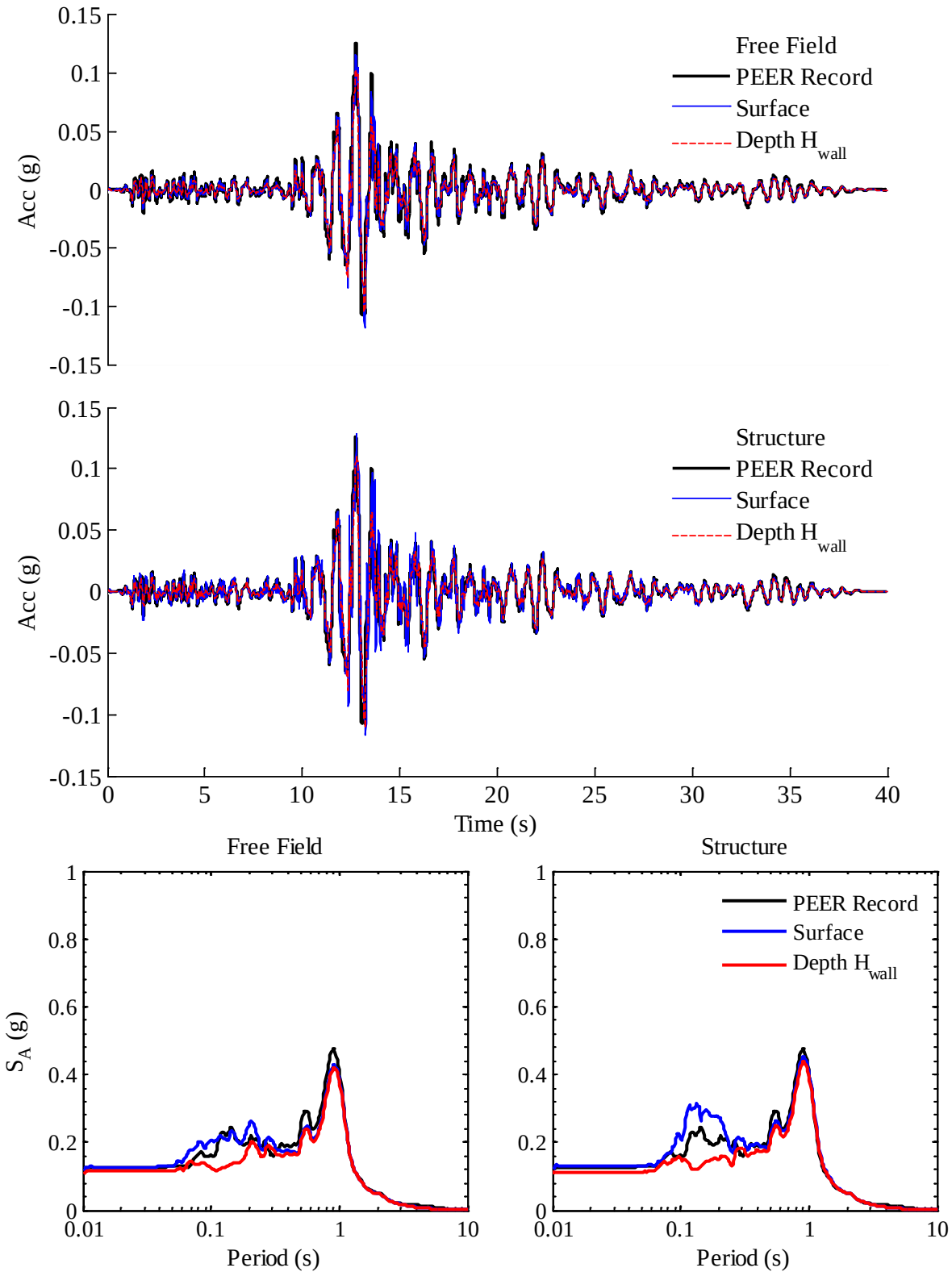

Figure B.15: Computed accelerations and response spectra at 5% damping in free field and structure during Loma Prieta RCH 190 for two level basement; Site Class D

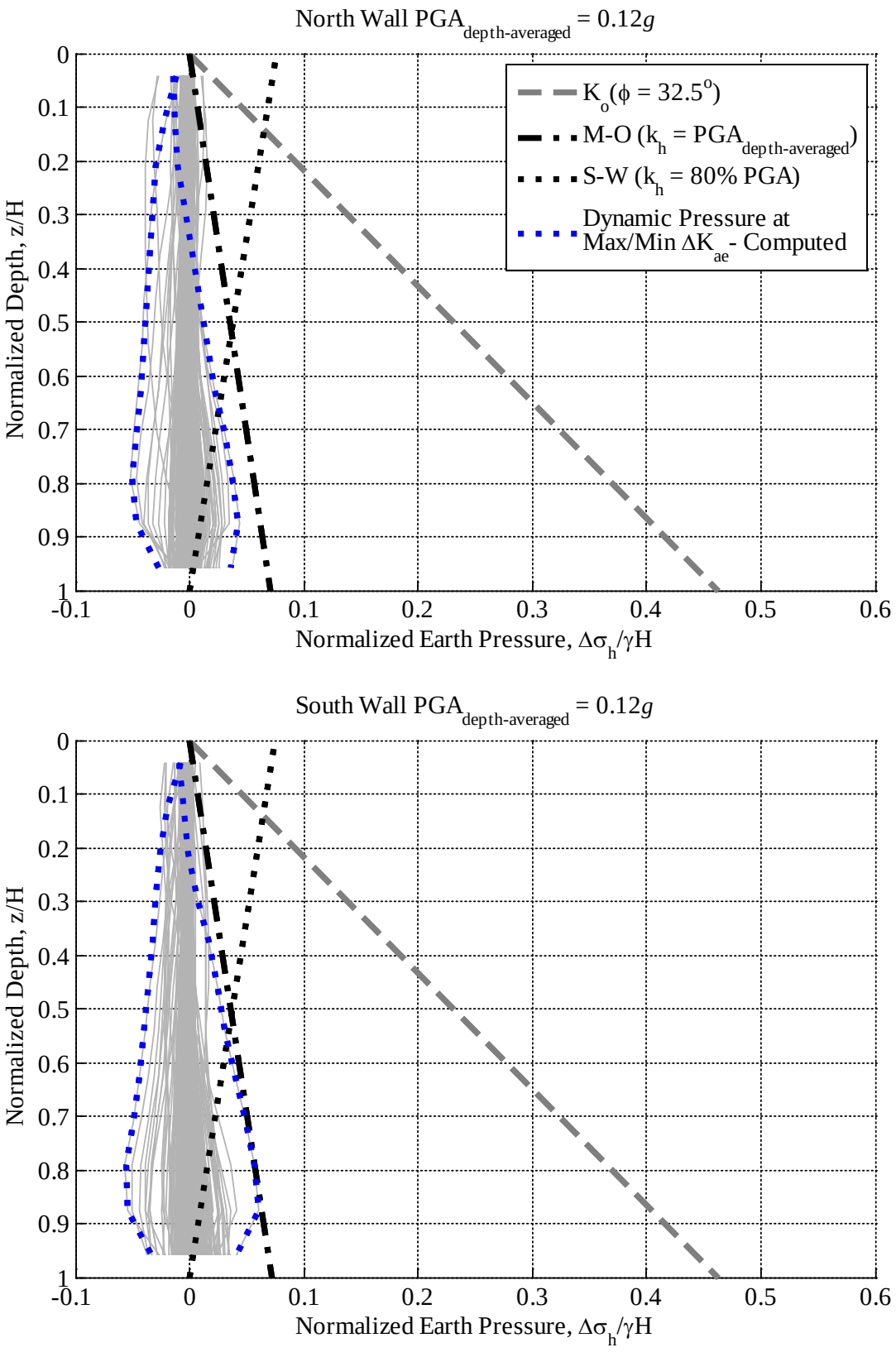

Figure B.16: Computed normalized dynamic earth pressure distributions at maximum and minimum ΔK_{ae} during Loma Prieta RCH 190 for two level basement; Site Class D

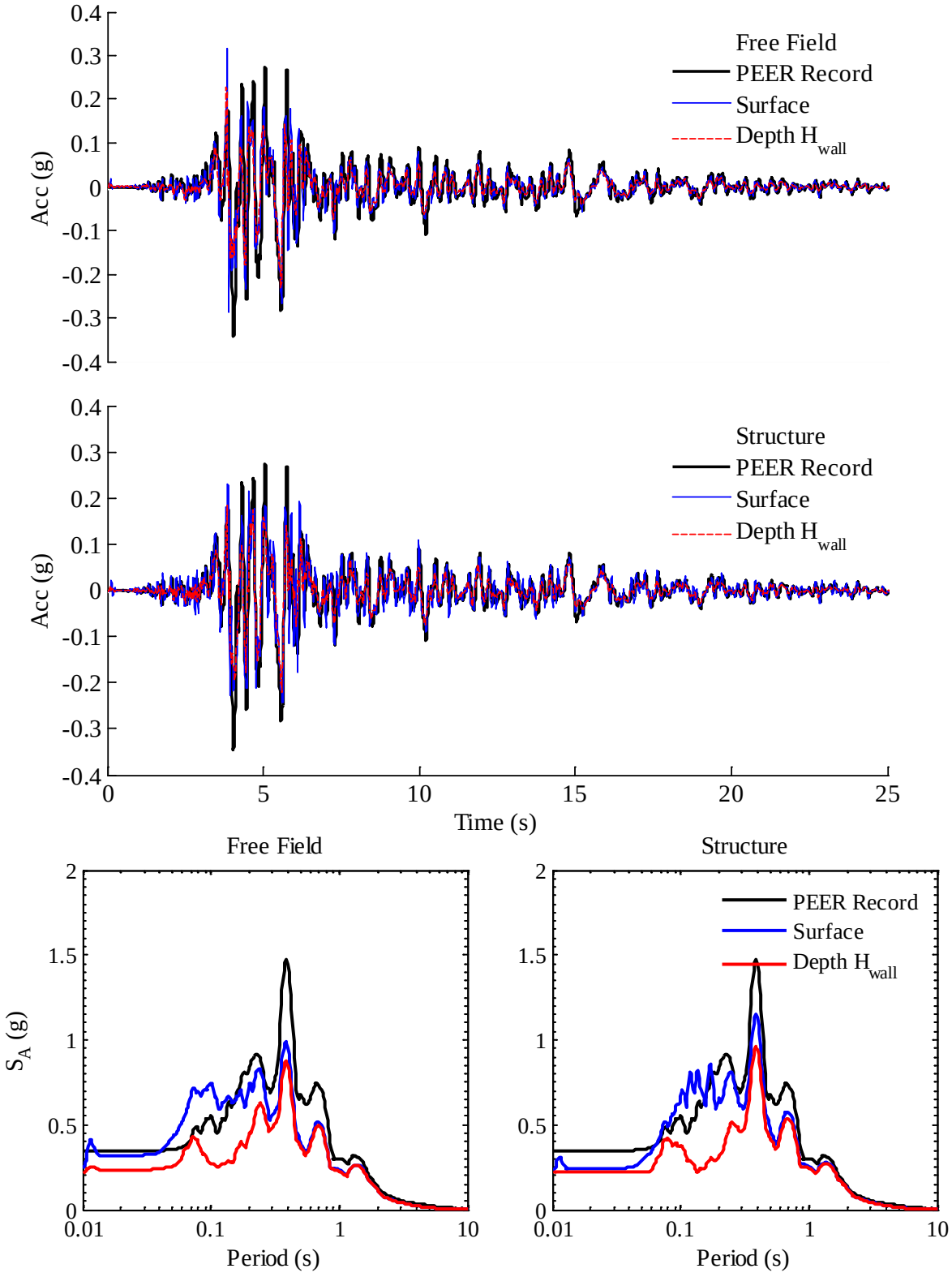

Figure B.17:Computed accelerations and response spectra at 5% damping in free field and structure during Loma Prieta GA2 000 for two level basement; Site Class D

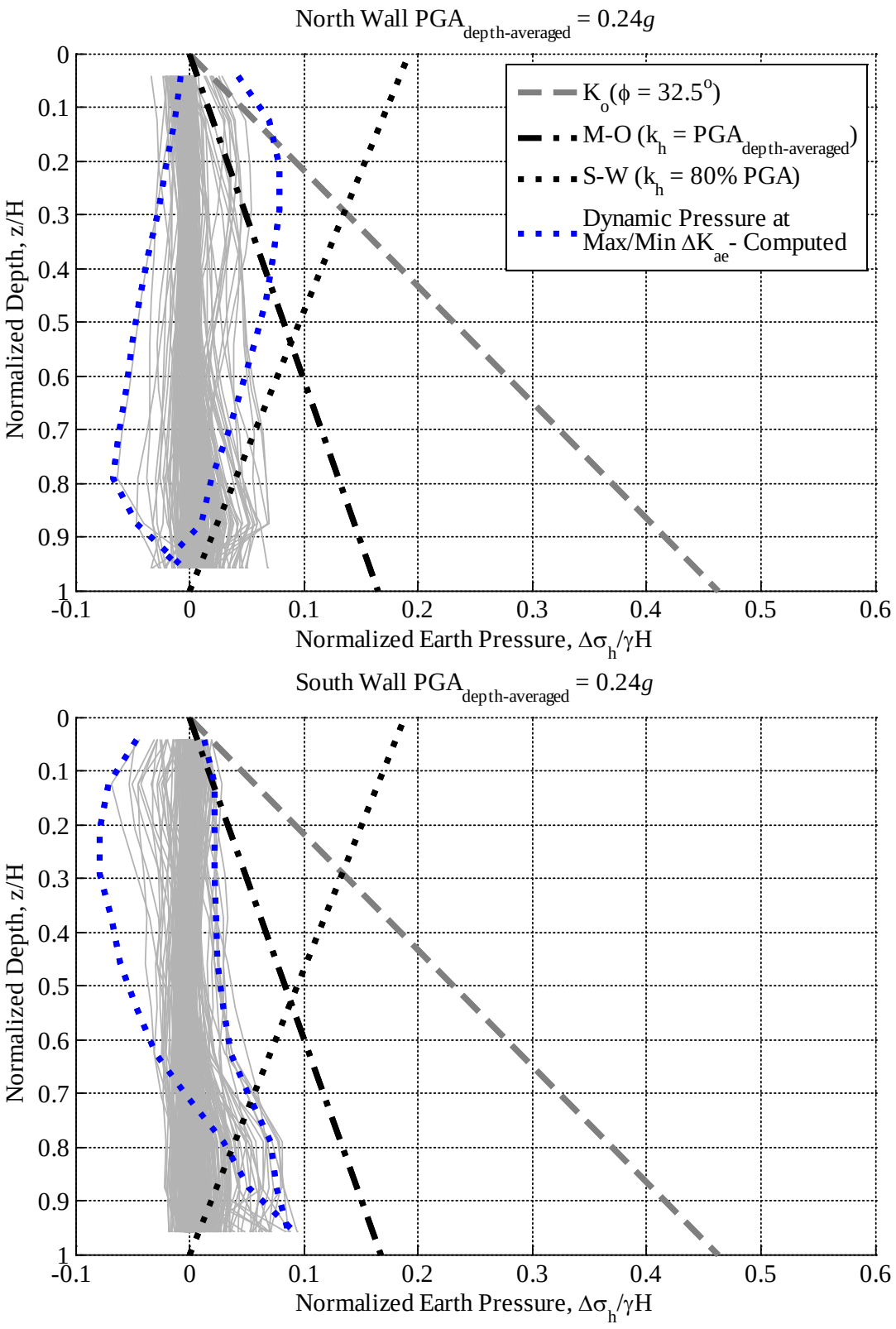

Figure B.18: Computed normalized dynamic earth pressure distributions at maximum and minimum ΔK_{ae} during Loma Prieta GA2 000 for two level basement; Site Class D

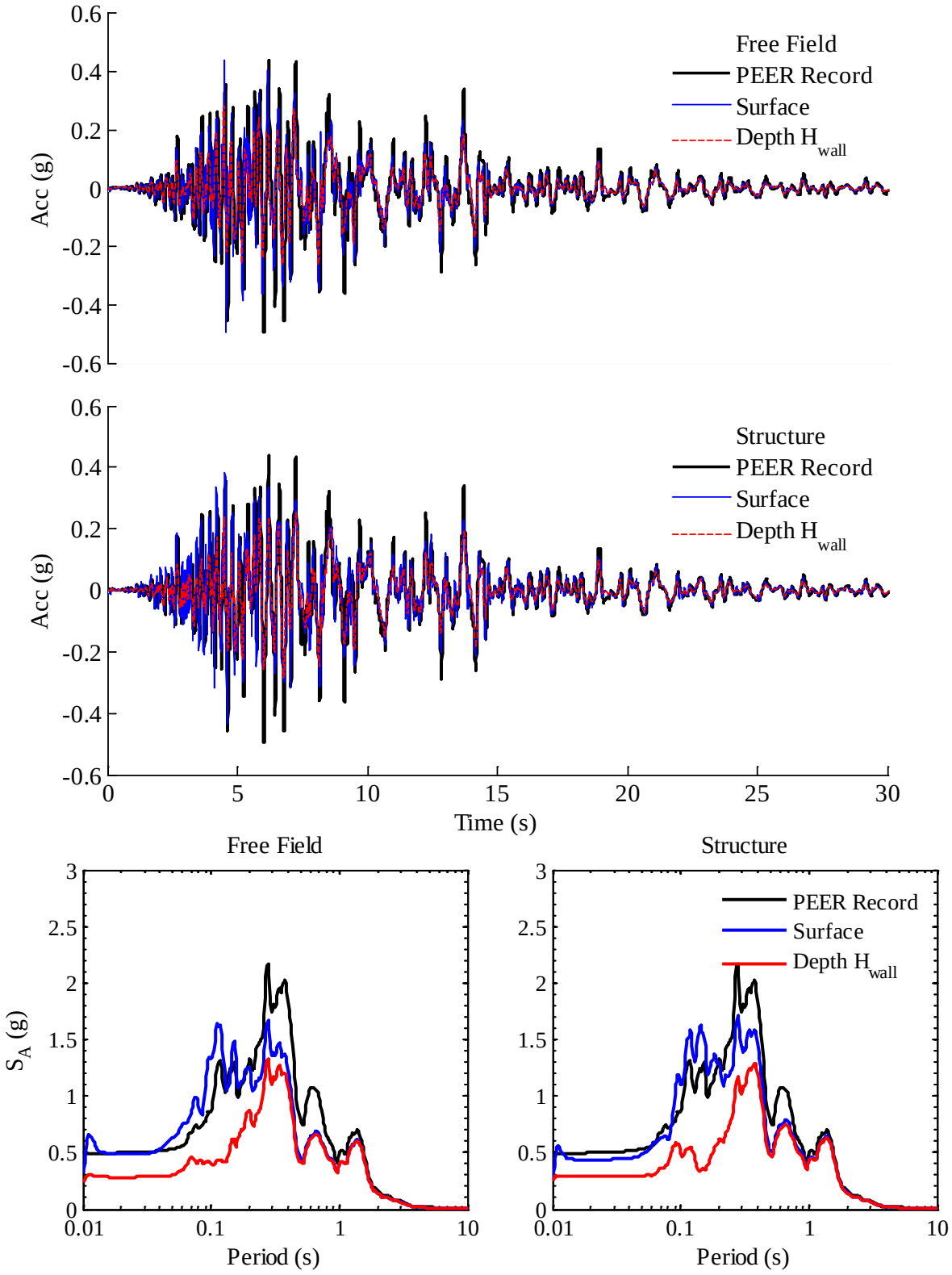

Figure B.19: Computed accelerations and response spectra at 5% damping in free field and structure during Loma Prieta CAP 000 for two level basement; Site Class D

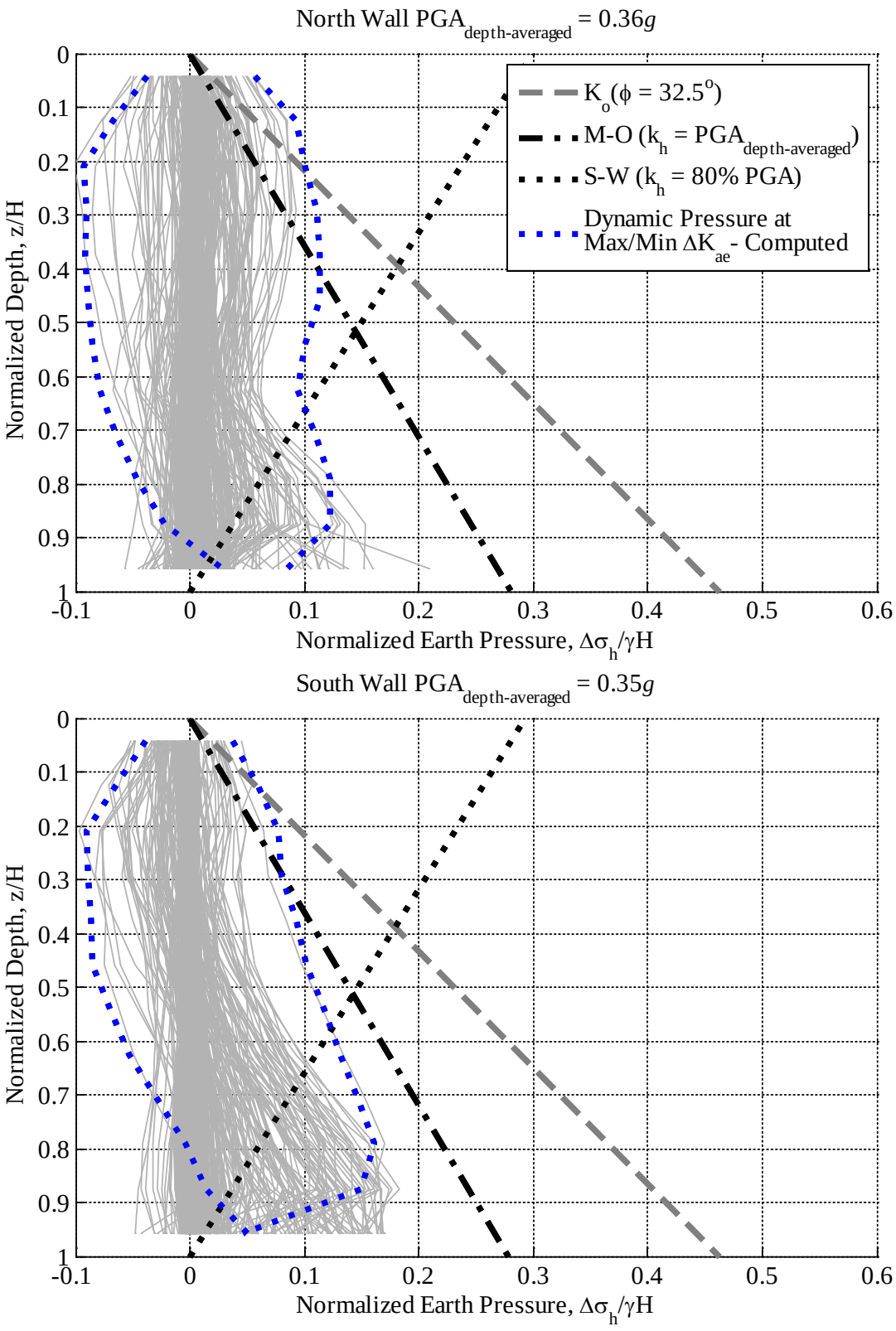

Figure B.20: Computed normalized dynamic earth pressure distributions at maximum and minimum ΔK_{ae} during Loma Prieta CAP 000 for two level basement; Site Class D

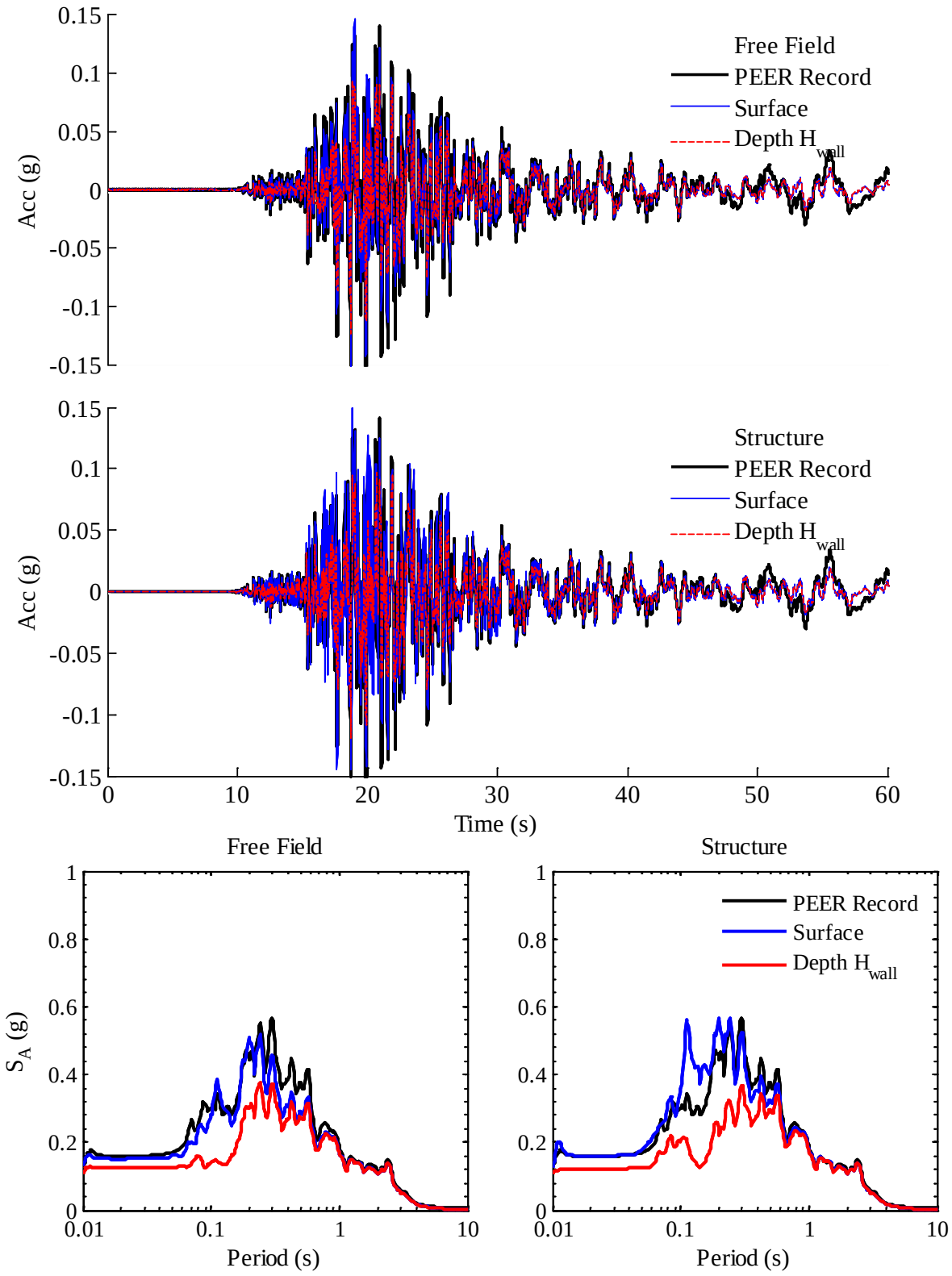

Figure B.21: Computed accelerations and response spectra at 5% damping in free field and structure during Kobe SKI 000 for two level basement; Site Class D

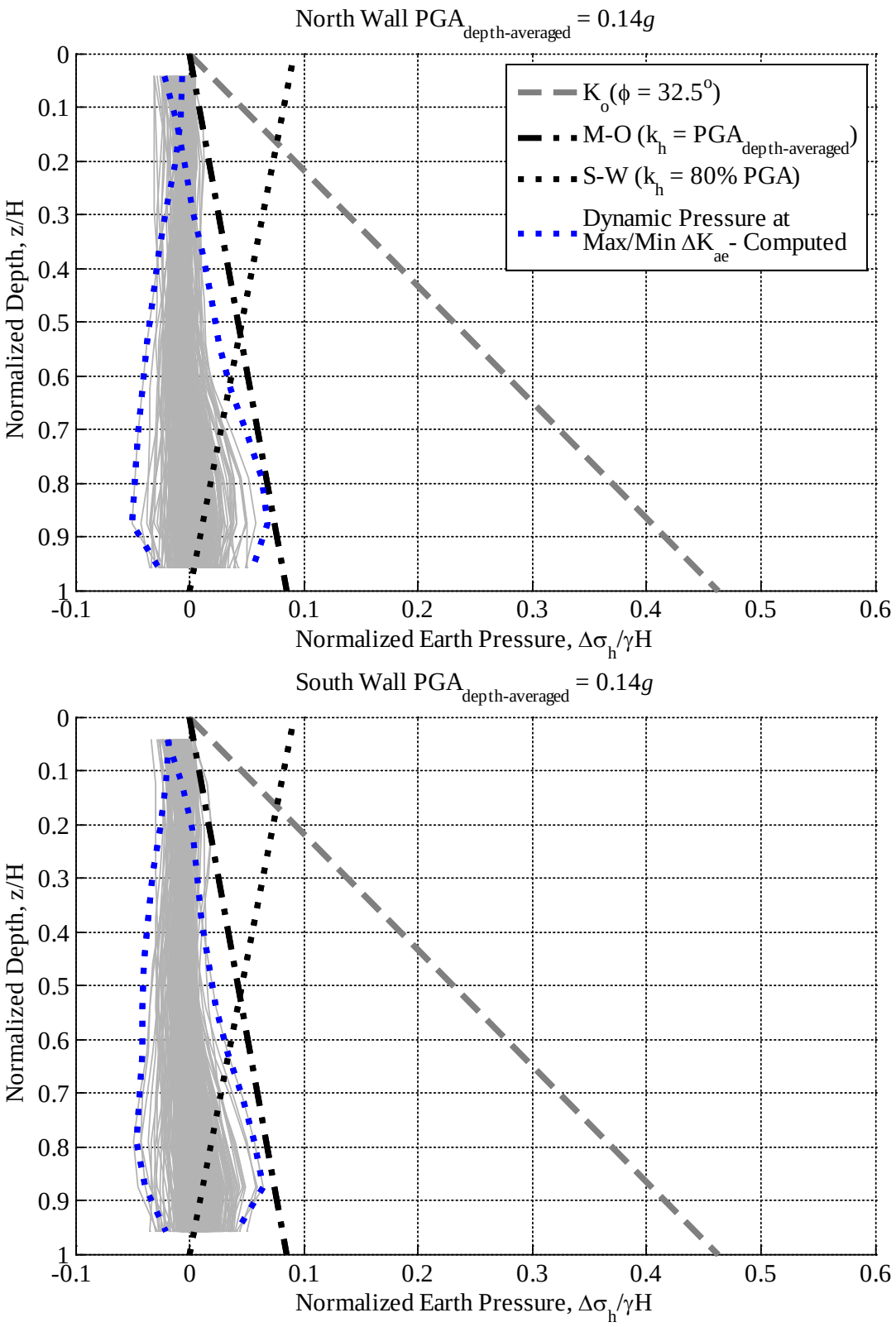

Figure B.22: Computed normalized dynamic earth pressure distributions at maximum and minimum ΔK_{ae} during Kobe SKI 000 for two level basement; Site Class D

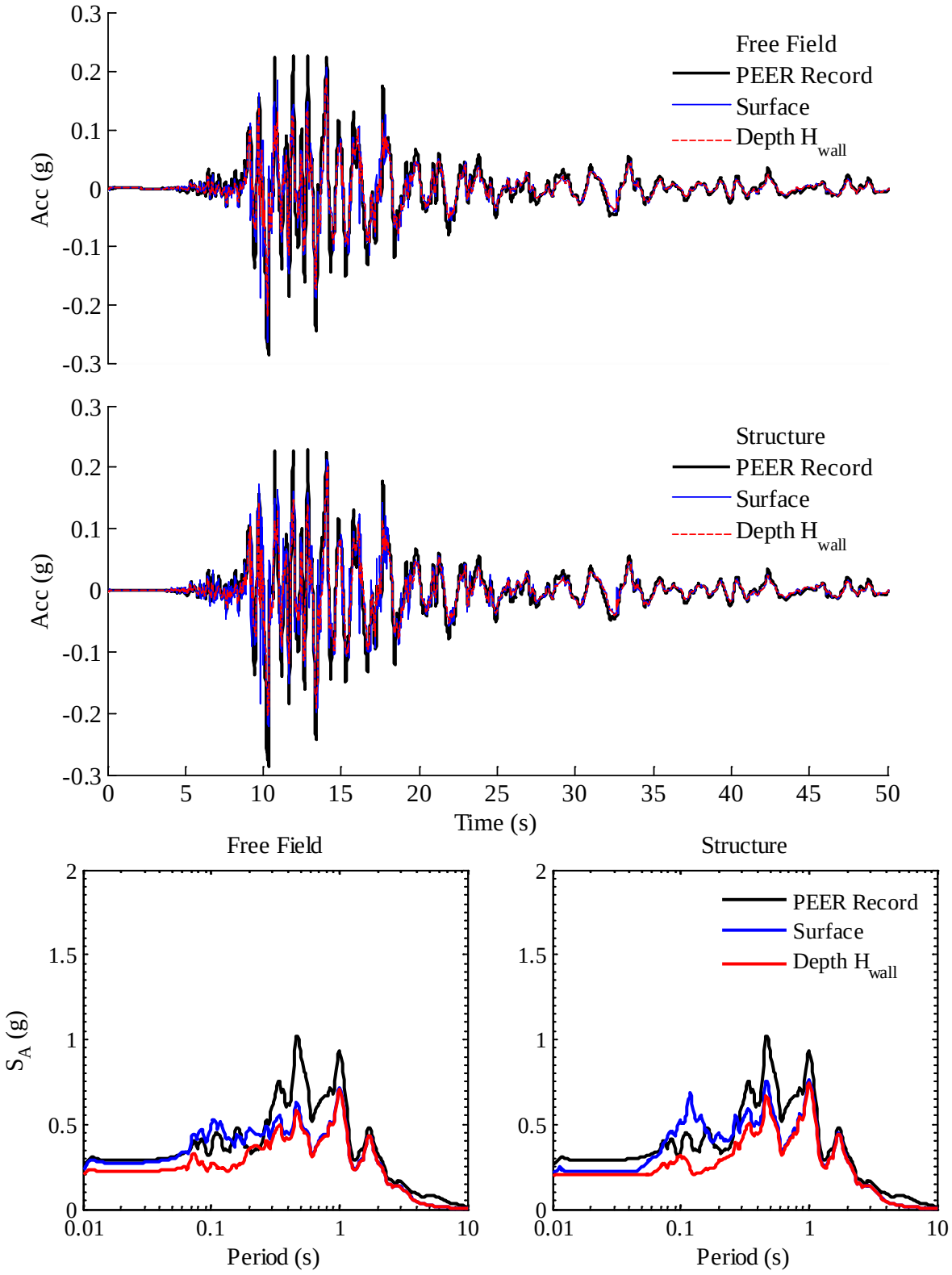

Figure B.23: Computed accelerations and response spectra at 5% damping in free field and structure during Kobe AMA 000 for two level basement; Site Class D

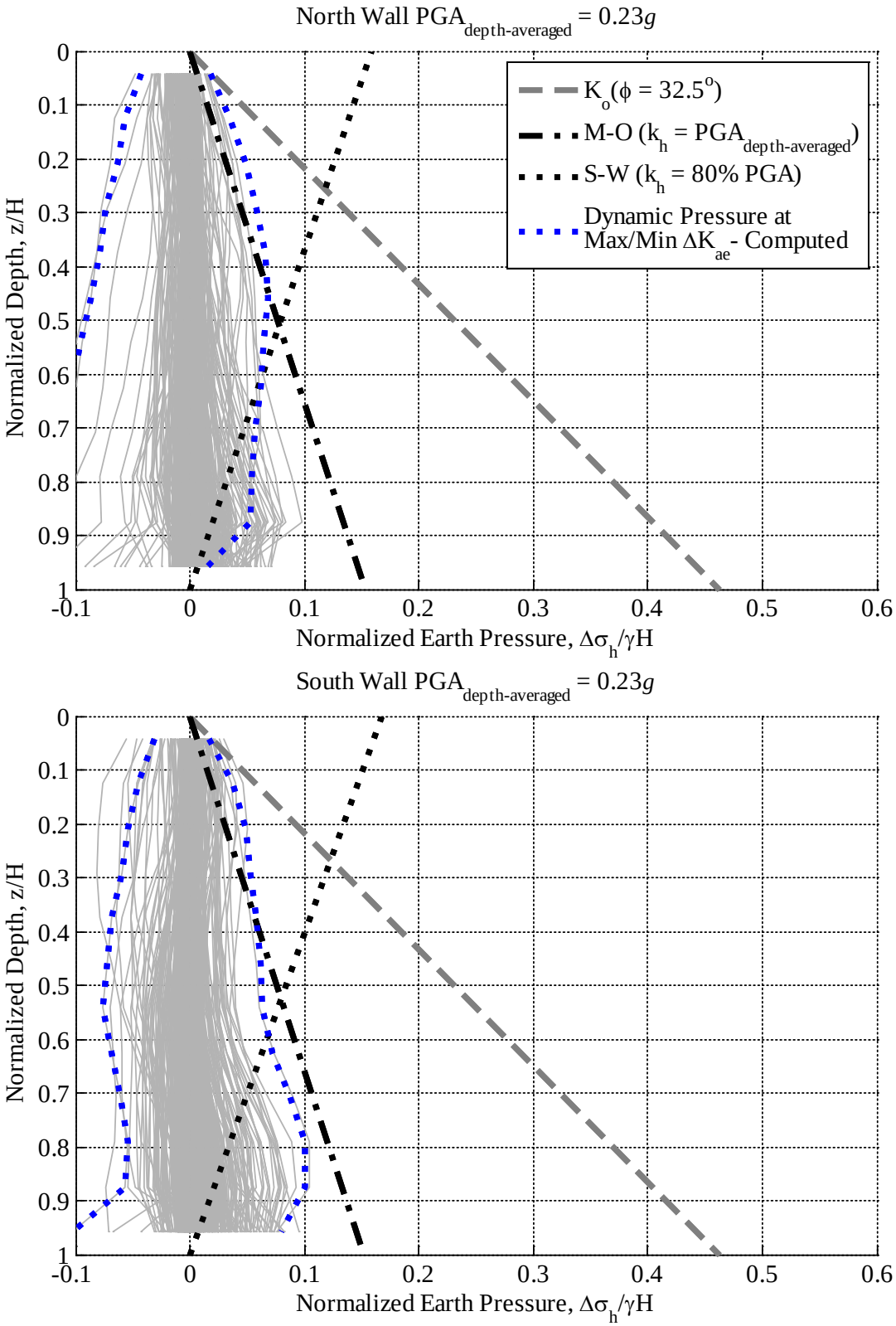

Figure B.24: Computed normalized dynamic earth pressure distributions at maximum and minimum ΔK_{ae} during Kobe AMA 000 for two level basement; Site Class D

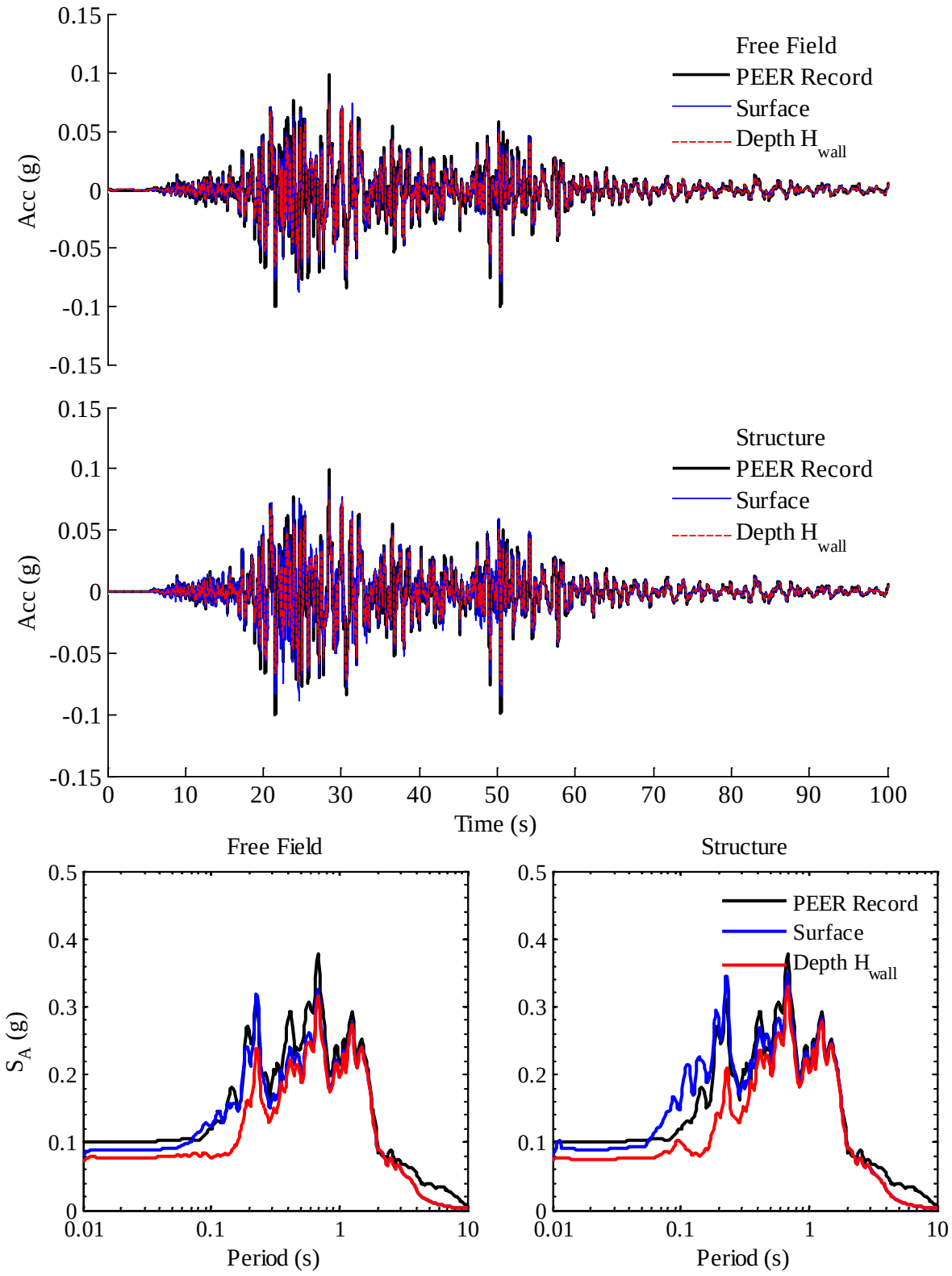

Figure B.25: Computed accelerations and response spectra at 5% damping in free field and structure during Kocaeli BUR 090 for two level basement; Site Class D

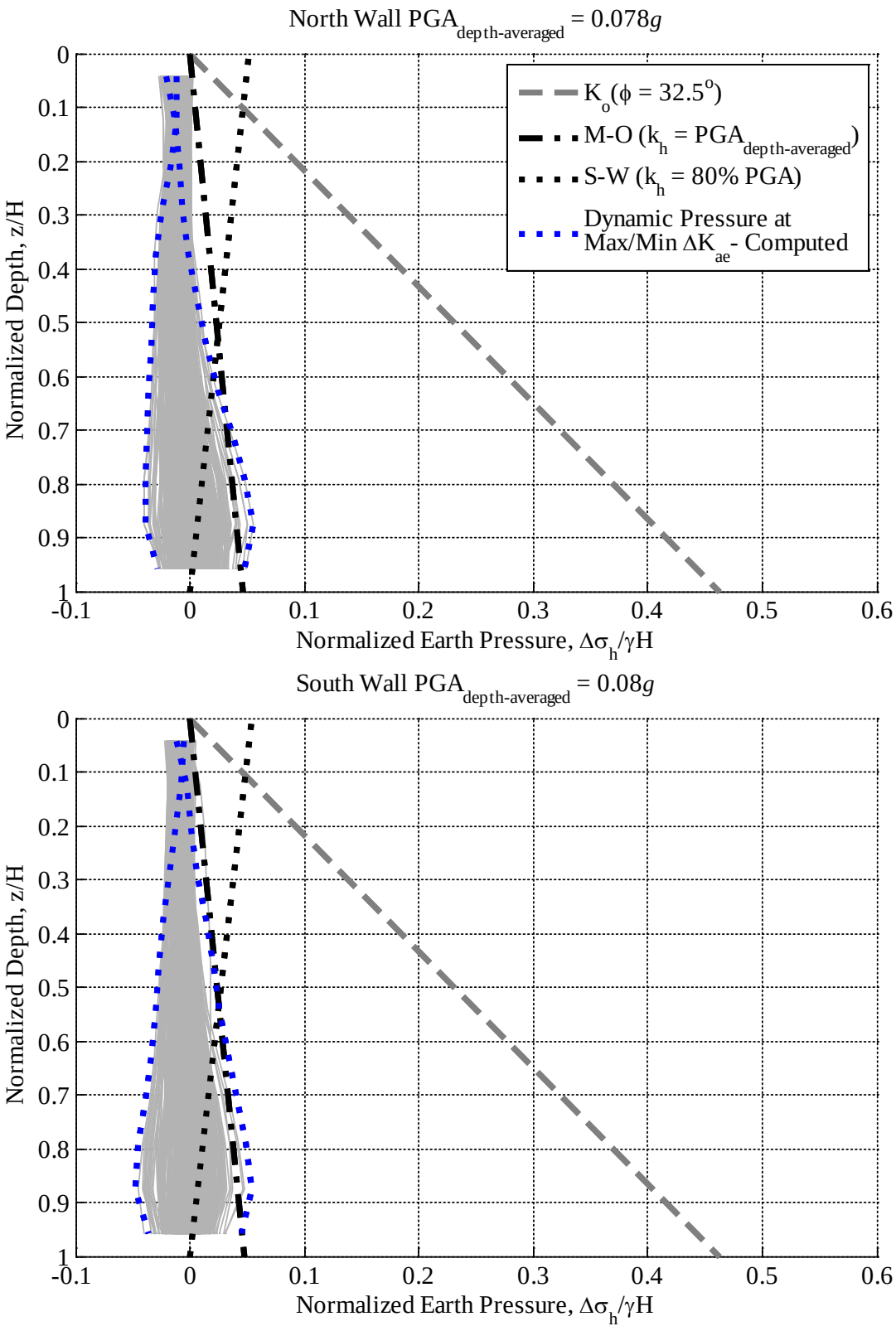

Figure B.26: Computed normalized dynamic earth pressure distributions at maximum and minimum ΔK_{ae} during Kocaeli BUR 090 for two level basement; Site Class D

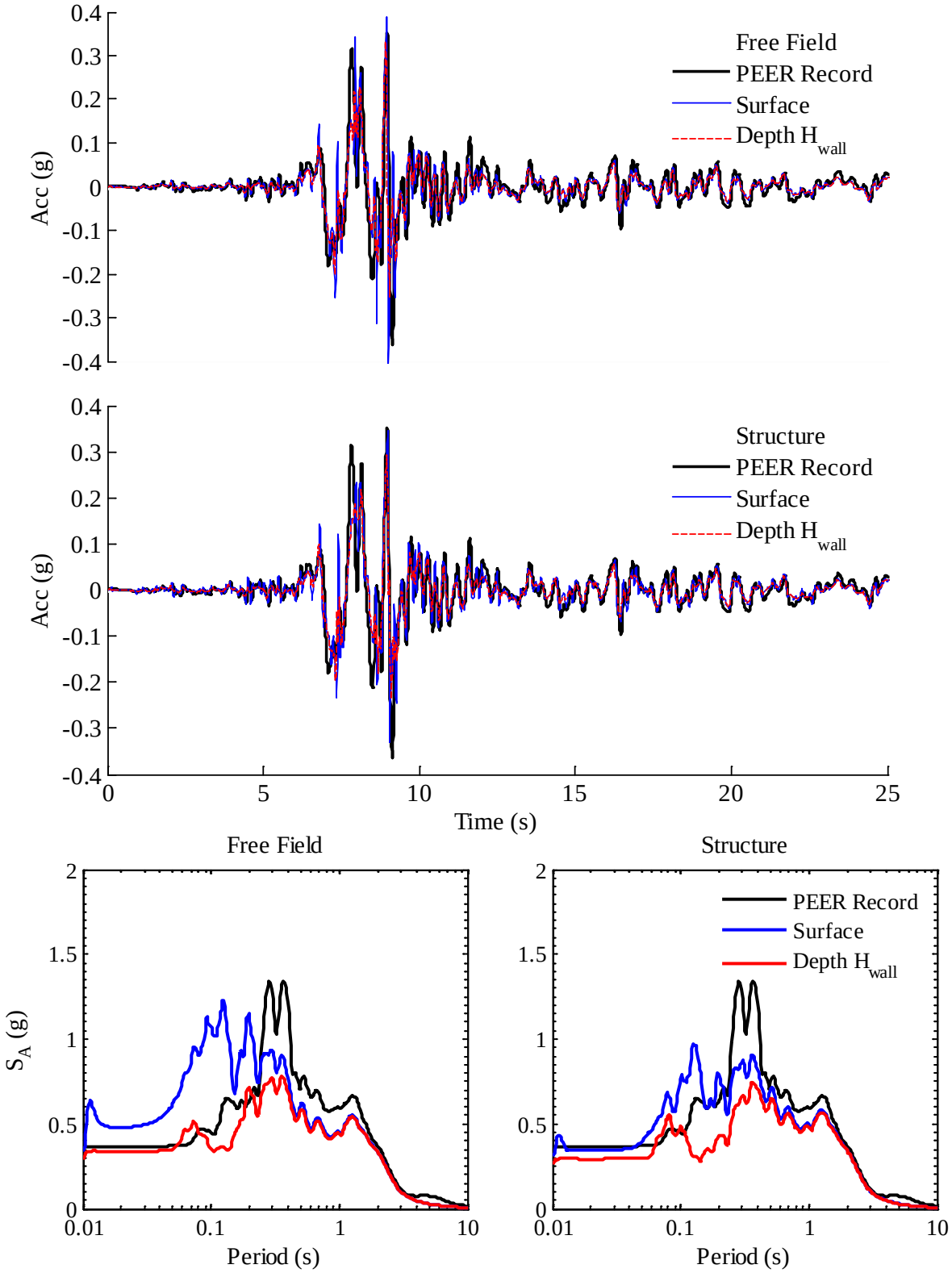

Figure B.27: Computed accelerations and response spectra at 5% damping in free field and structure during Kocaeli DUZ 270 for two level basement; Site Class D

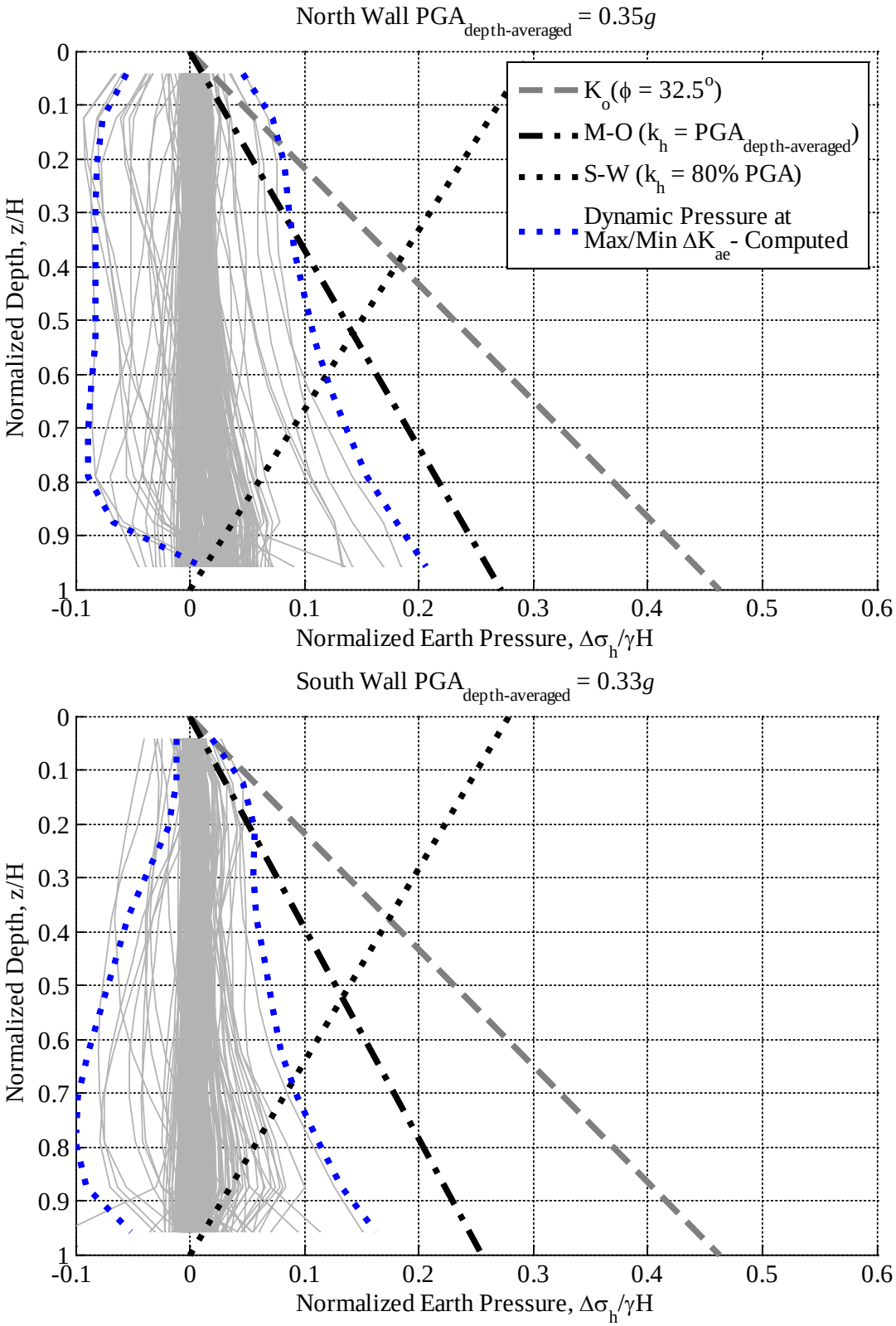

Figure B.28: Computed normalized dynamic earth pressure distributions at maximum and minimum ΔK_{ae} during Kocaeli DUZ 270 for two level basement; Site Class D

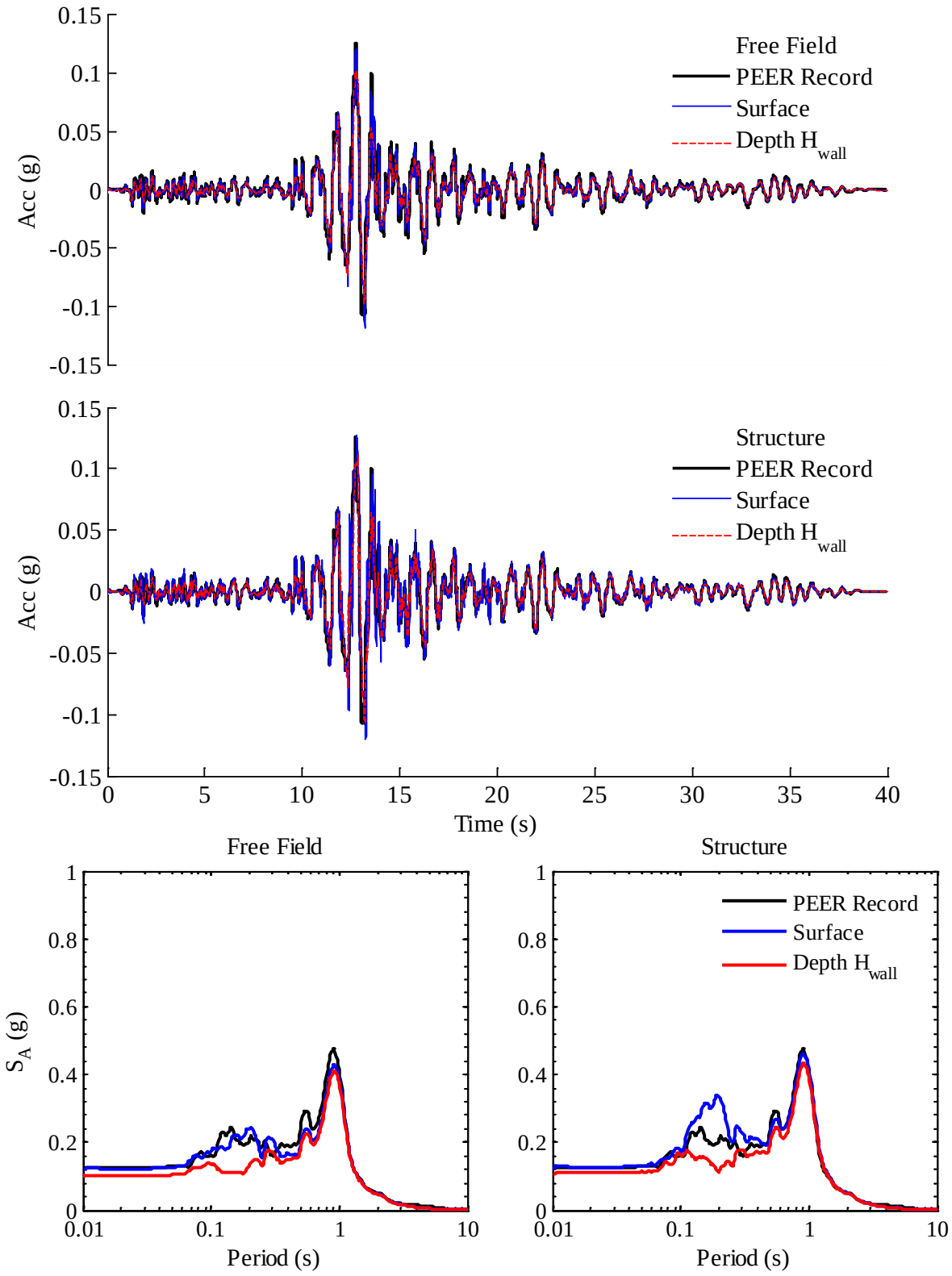

Figure B.29: Computed accelerations and response spectra at 5% damping in free field and structure during Loma Prieta RCH 190 for three level basement; Site Class D

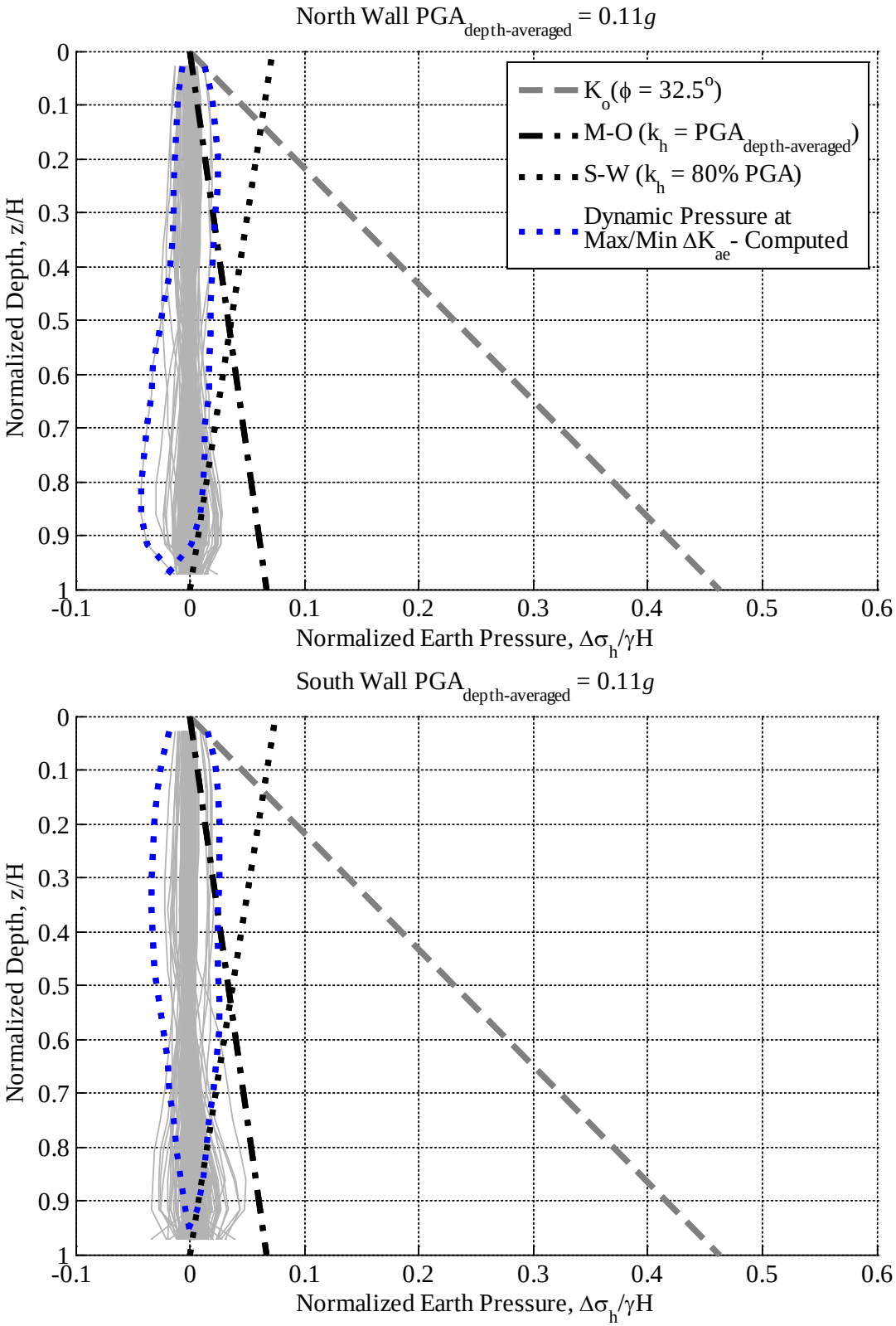

Figure B.30: Computed normalized dynamic earth pressure distributions at maximum and minimum ΔK_{ae} during Loma Prieta RCH 190 for three level basement; Site Class D

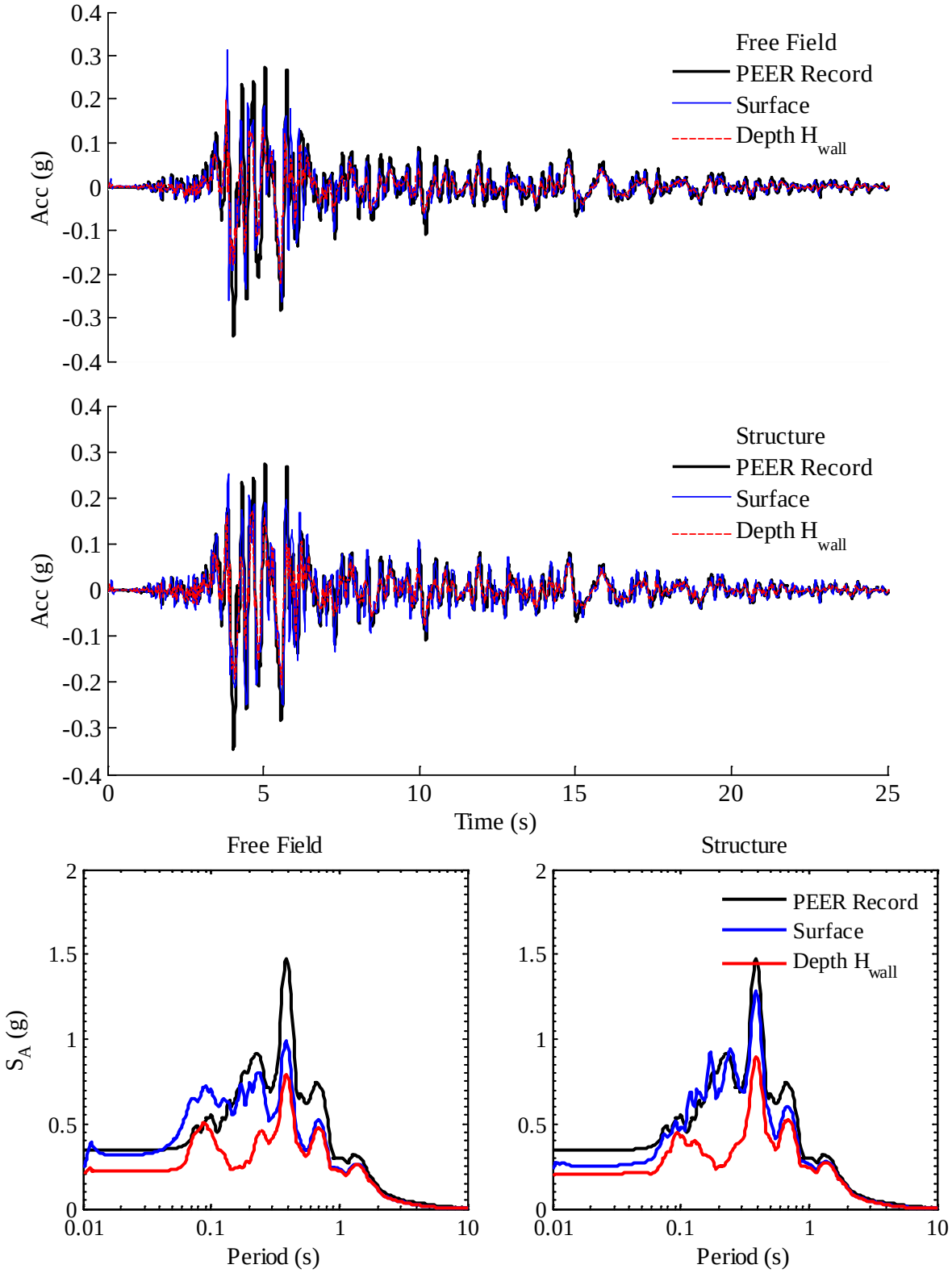

Figure B.31:Computed accelerations and response spectra at 5% damping in free field and structure during Loma Prieta GA2 000 for three level basement; Site Class D

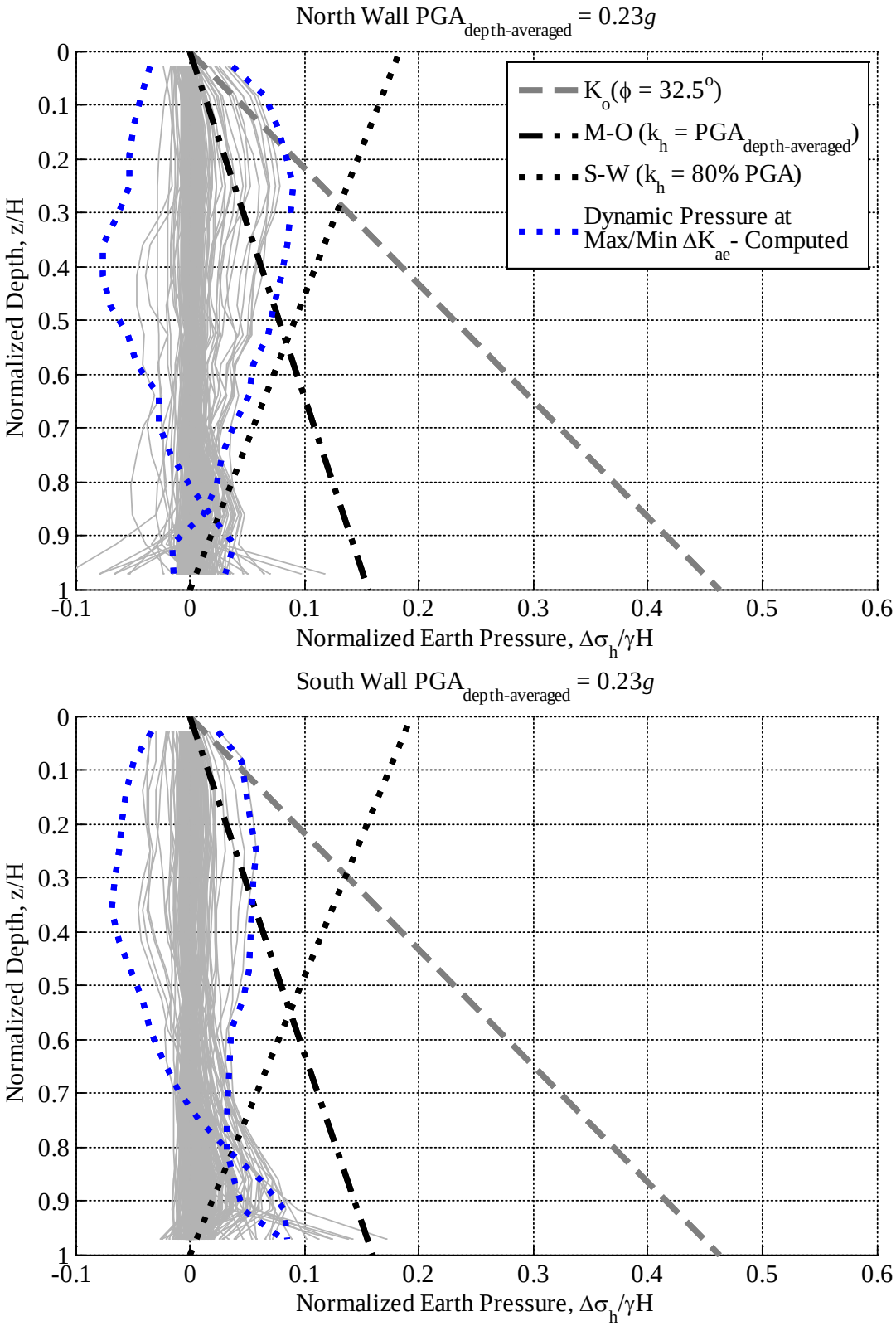

Figure B.32: Computed normalized dynamic earth pressure distributions at maximum and minimum ΔK_{ae} during Loma Prieta GA2 000 for three level basement; Site Class D

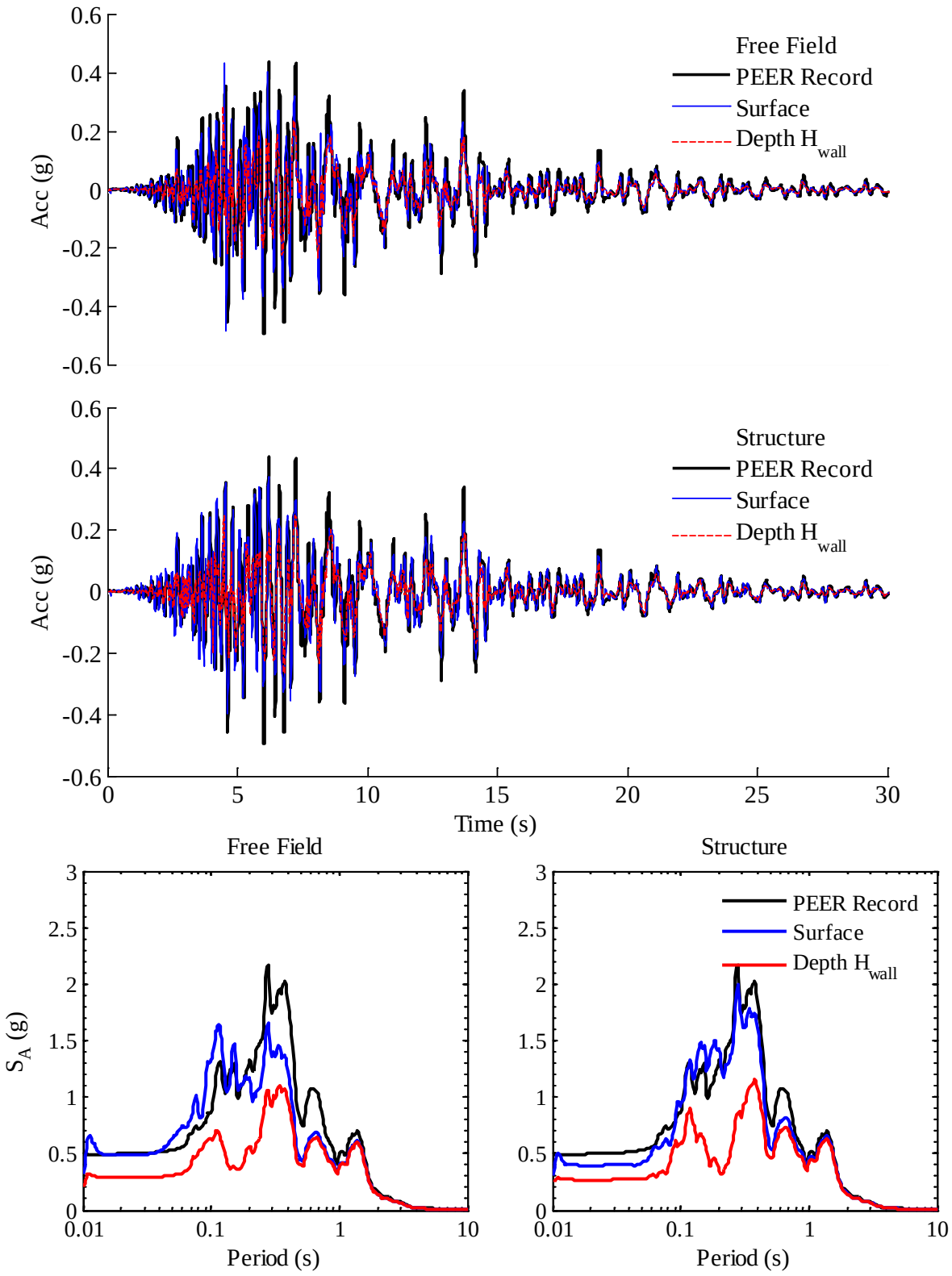

Figure B.33: Computed accelerations and response spectra at 5% damping in free field and structure during Loma Prieta CAP 000 for three level basement; Site Class D

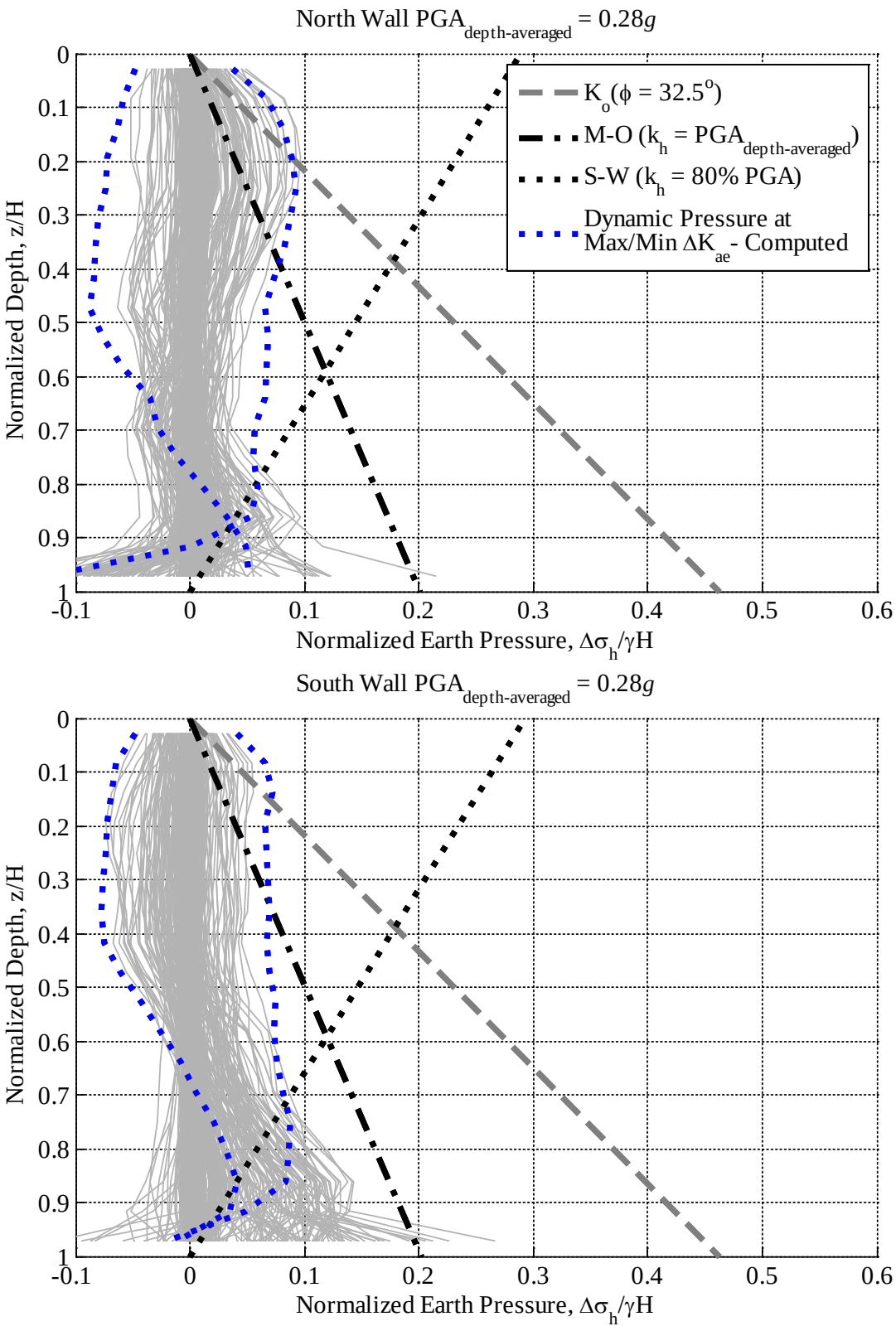

Figure B.34: Computed normalized dynamic earth pressure distributions at maximum and minimum ΔK_{ae} during Loma Prieta CAP 000 for three level basement; Site Class D

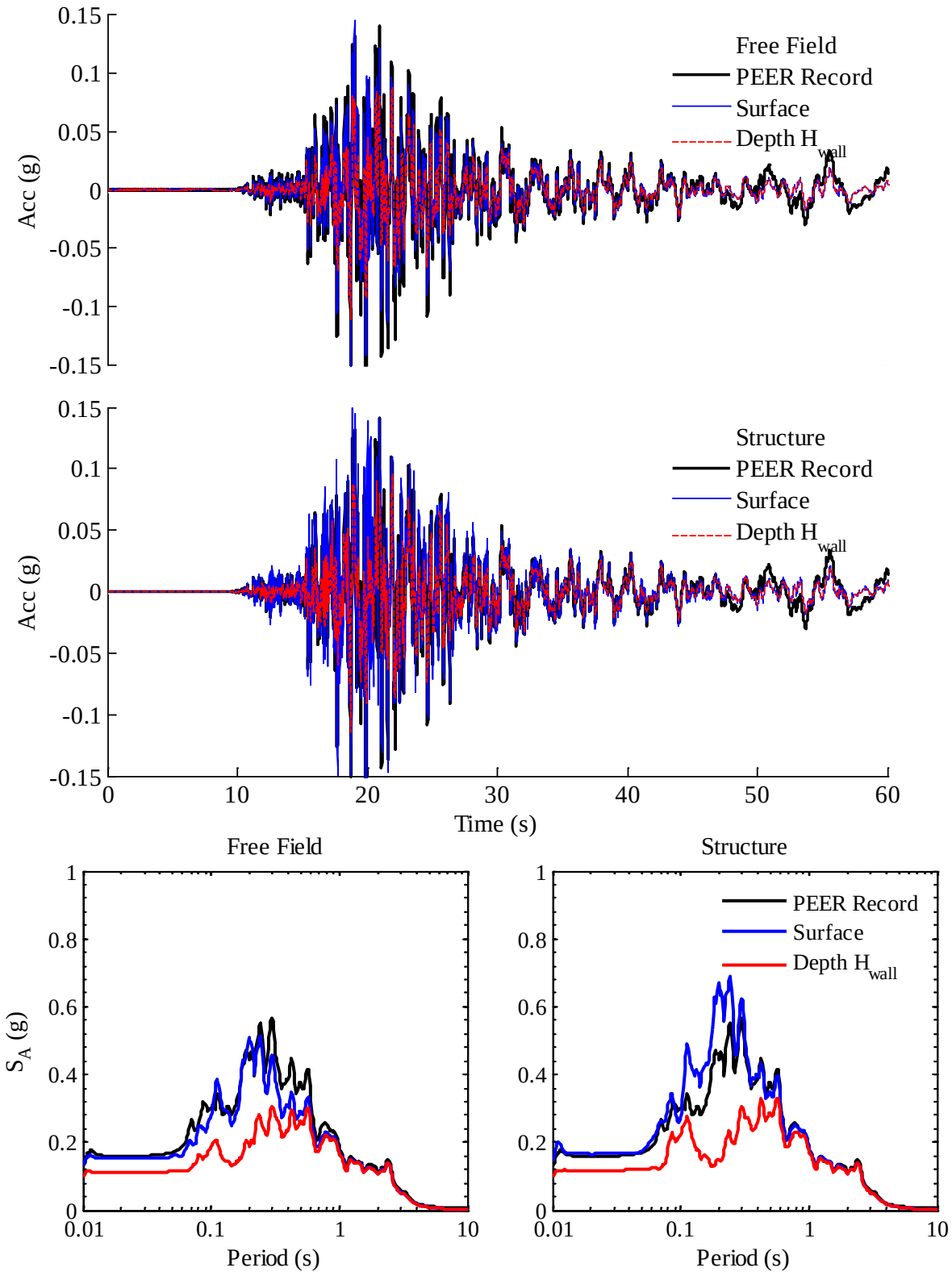

Figure B.35: Computed accelerations and response spectra at 5% damping in free field and structure during Kobe SKI 000 for three level basement; Site Class D

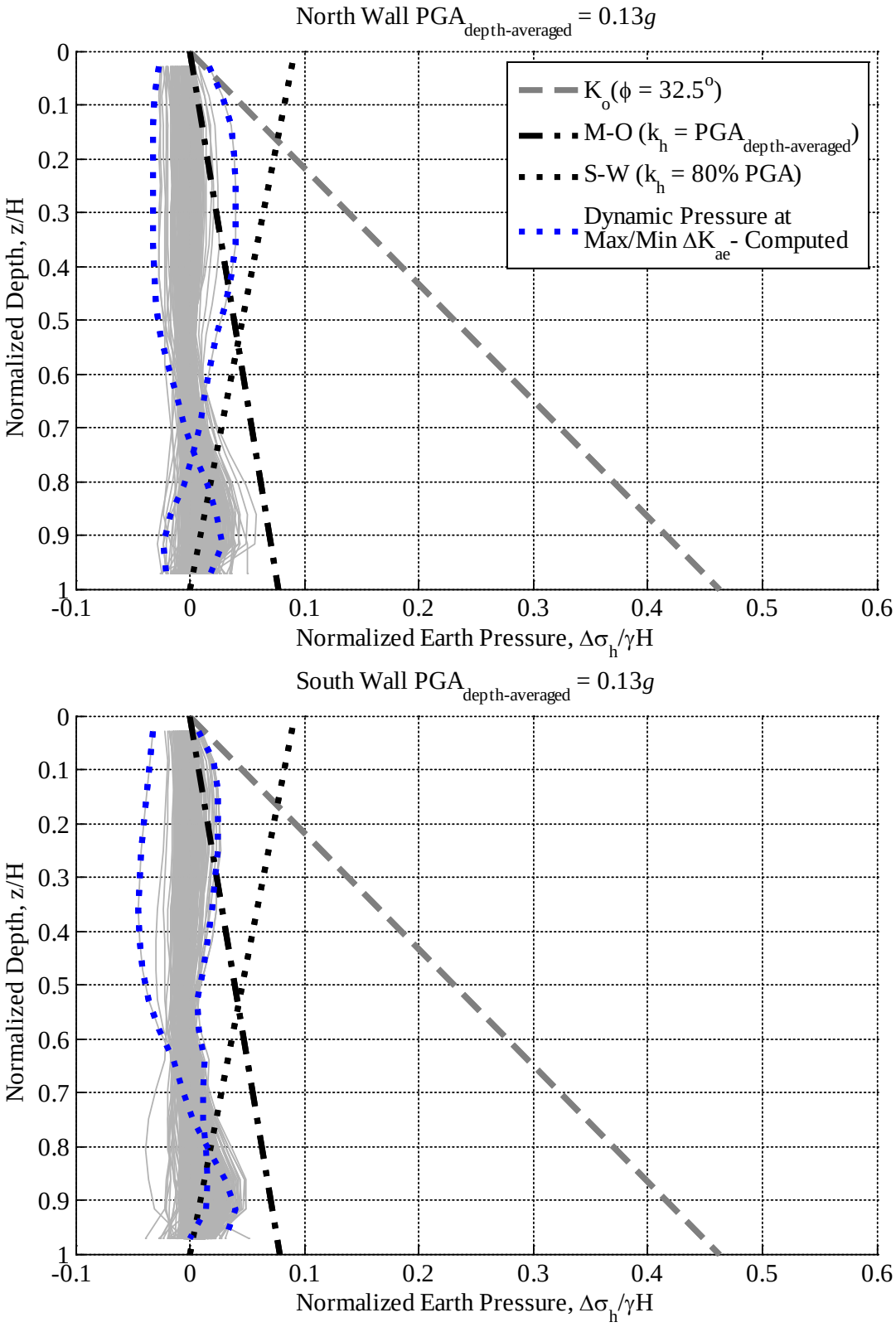

Figure B.36: Computed normalized dynamic earth pressure distributions at maximum and minimum ΔK_{ae} during Kobe SKI 000 three for three level basement; Site Class D

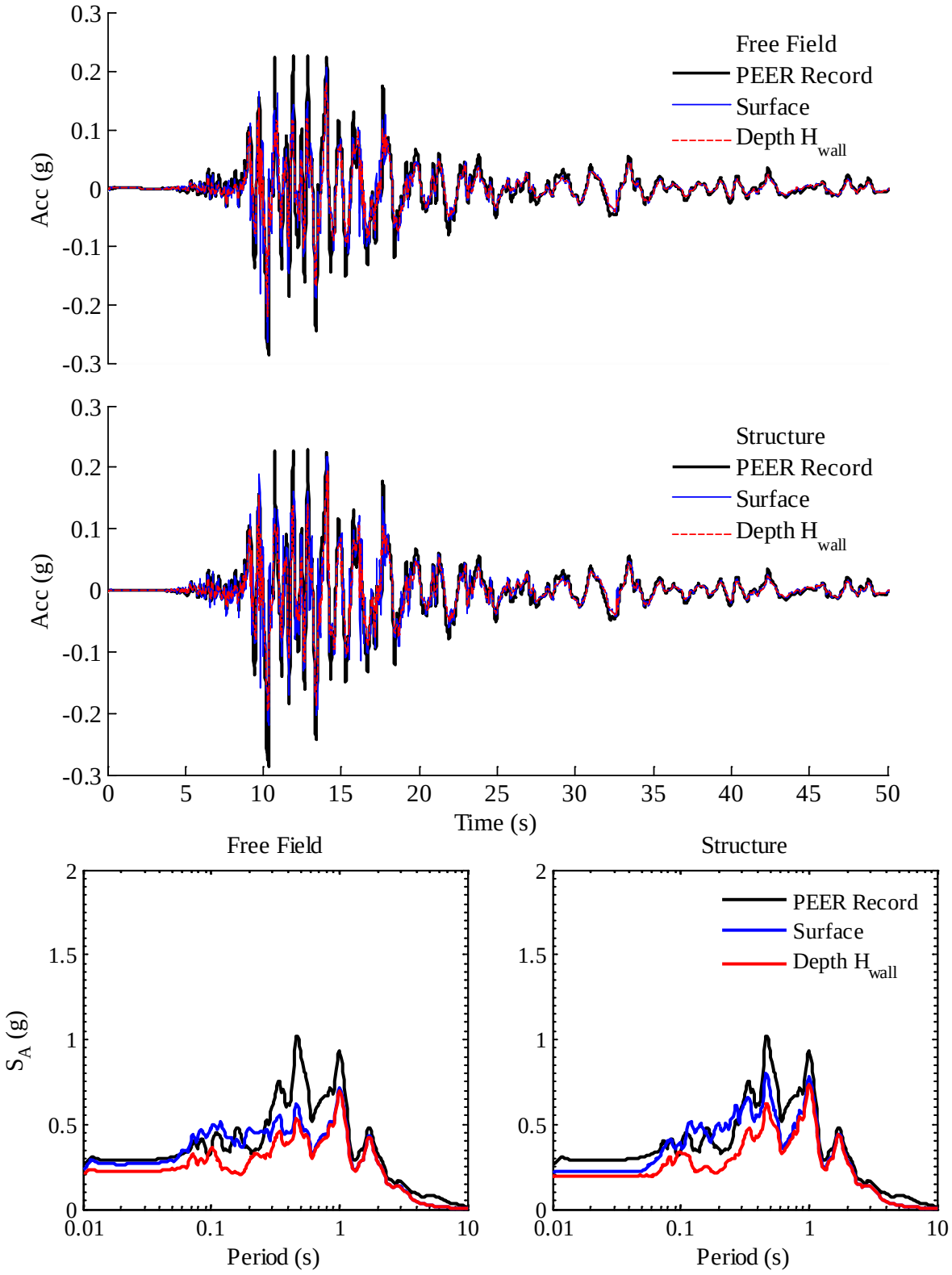

Figure B.37: Computed accelerations and response spectra at 5% damping in free field and structure during Kobe AMA 000 for three level basement; Site Class D

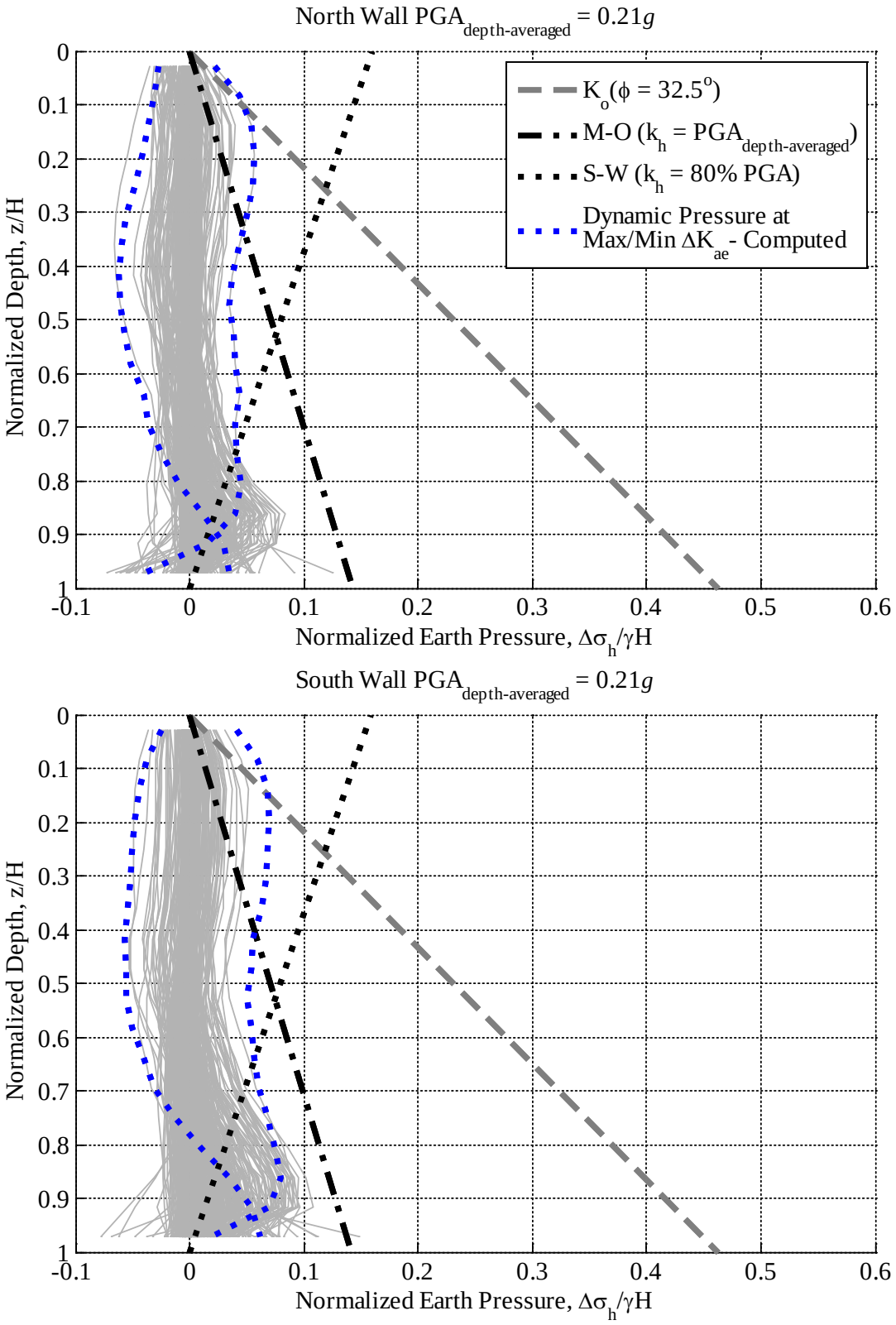

Figure B.38: Computed normalized dynamic earth pressure distributions at maximum and minimum ΔK_{ae} during Kobe AMA 000 for three level basement; Site Class D

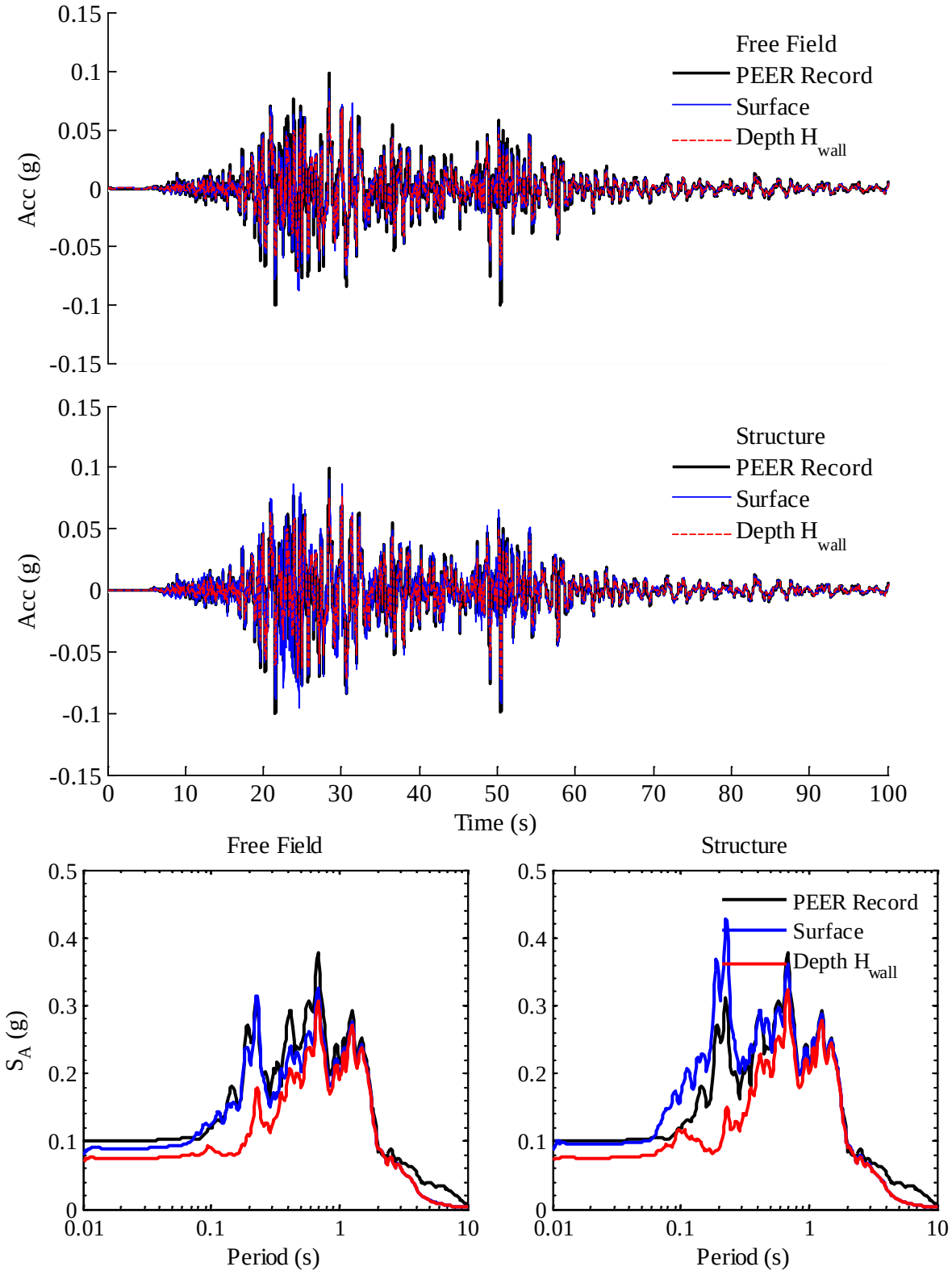

Figure B.39: Computed accelerations and response spectra at 5% damping in free field and structure during Kocaeli BUR 090 for three level basement; Site Class D

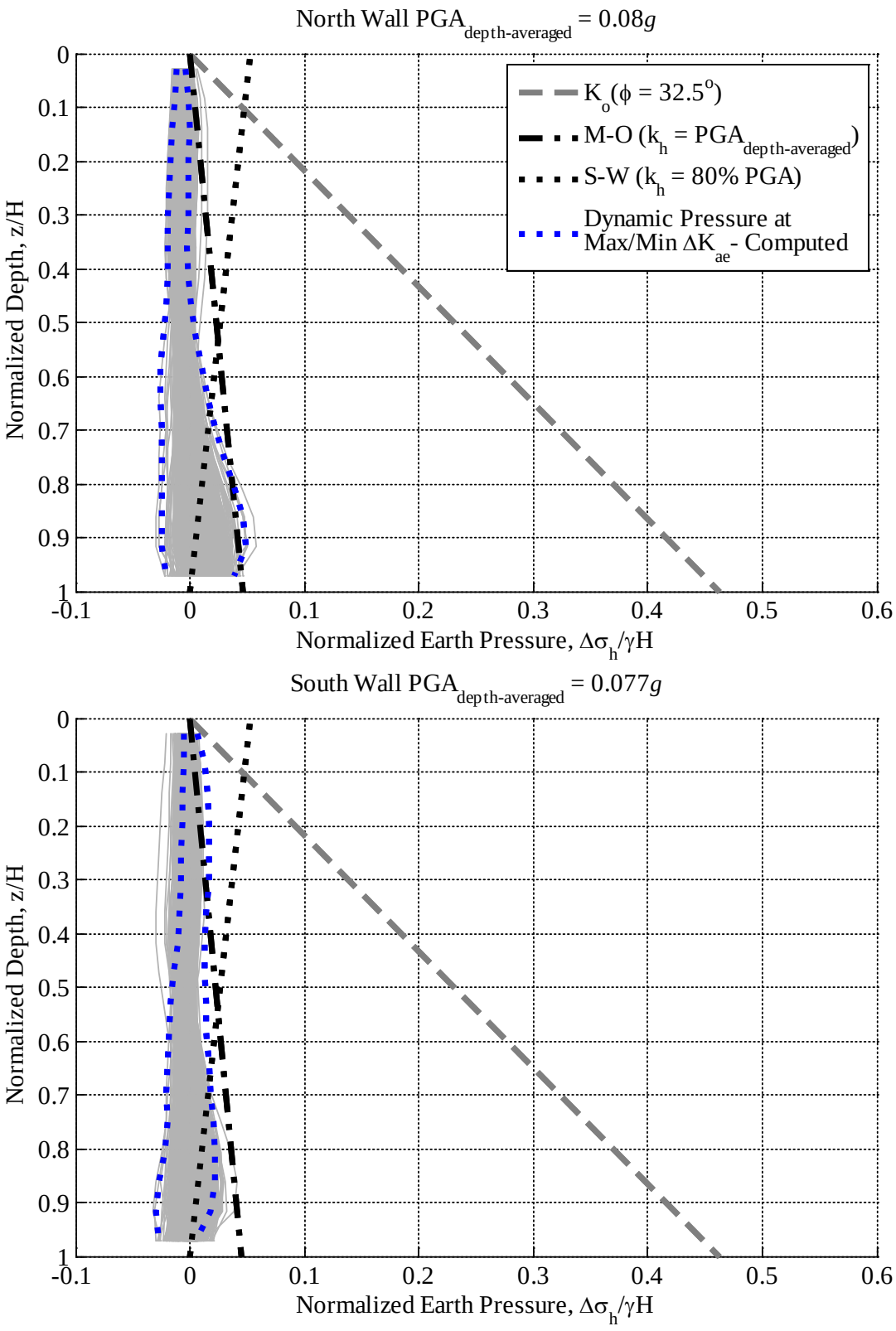

Figure B.40: Computed normalized dynamic earth pressure distributions at maximum and minimum ΔK_{ae} during Kocaeli BUR 090 for three level basement; Site Class D

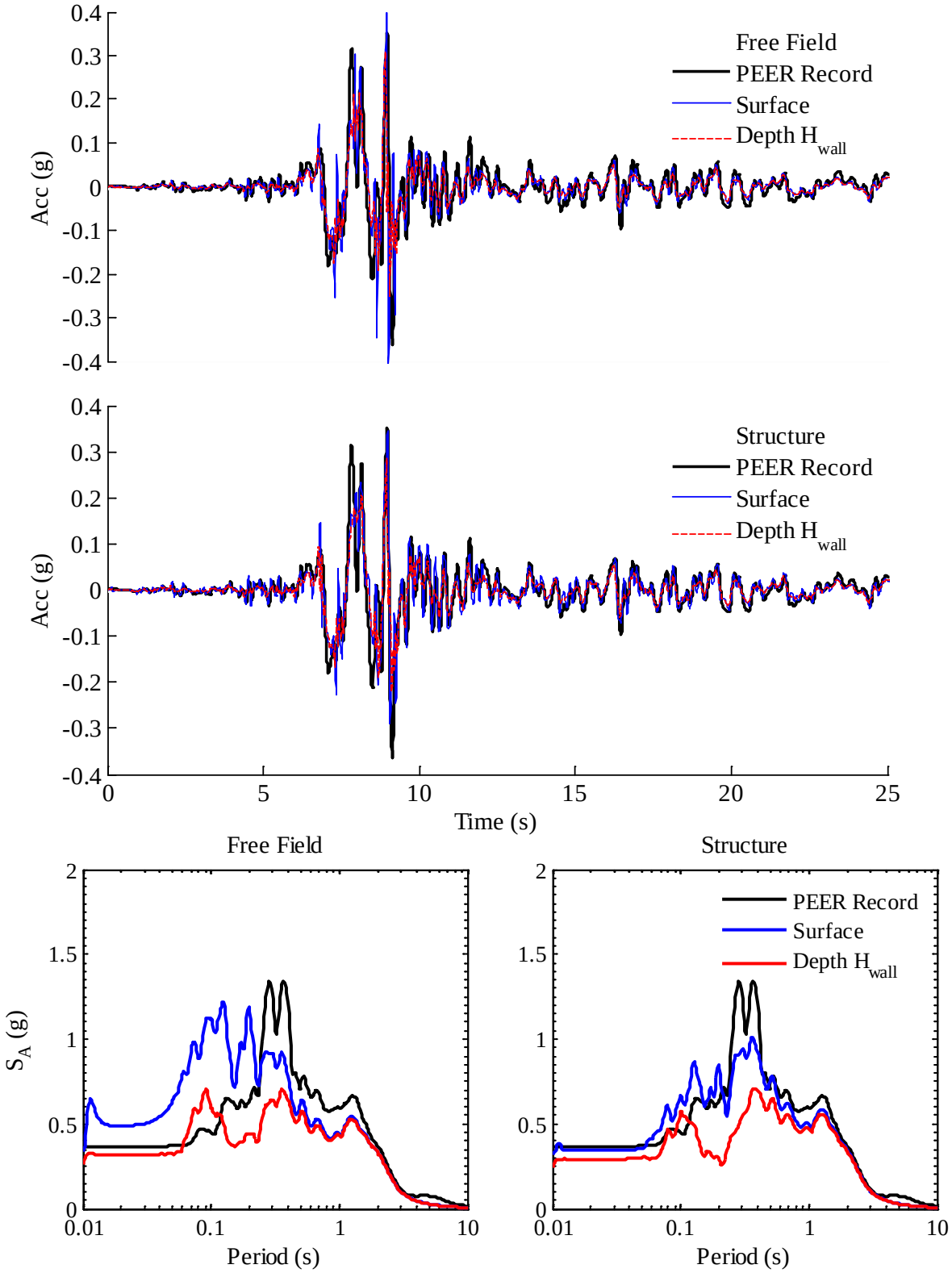

Figure B.41: Computed accelerations and response spectra at 5% damping in free field and structure during Kocaeli DUZ 270 for three level basement; Site Class D

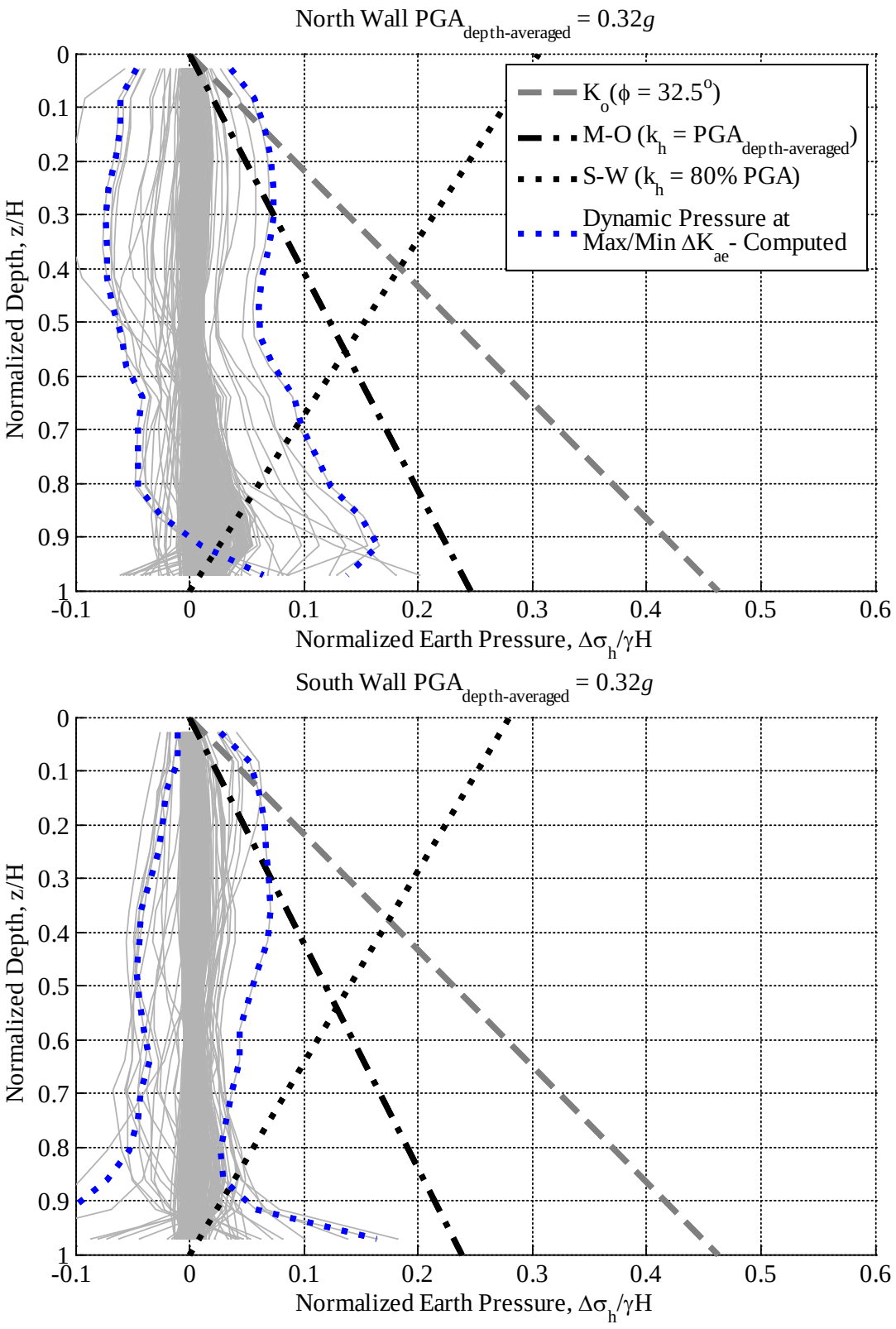

Figure B.42: Computed normalized dynamic earth pressure distributions at maximum and minimum ΔK_{ae} during Kocaeli DUZ 270 for three level basement; Site Class D

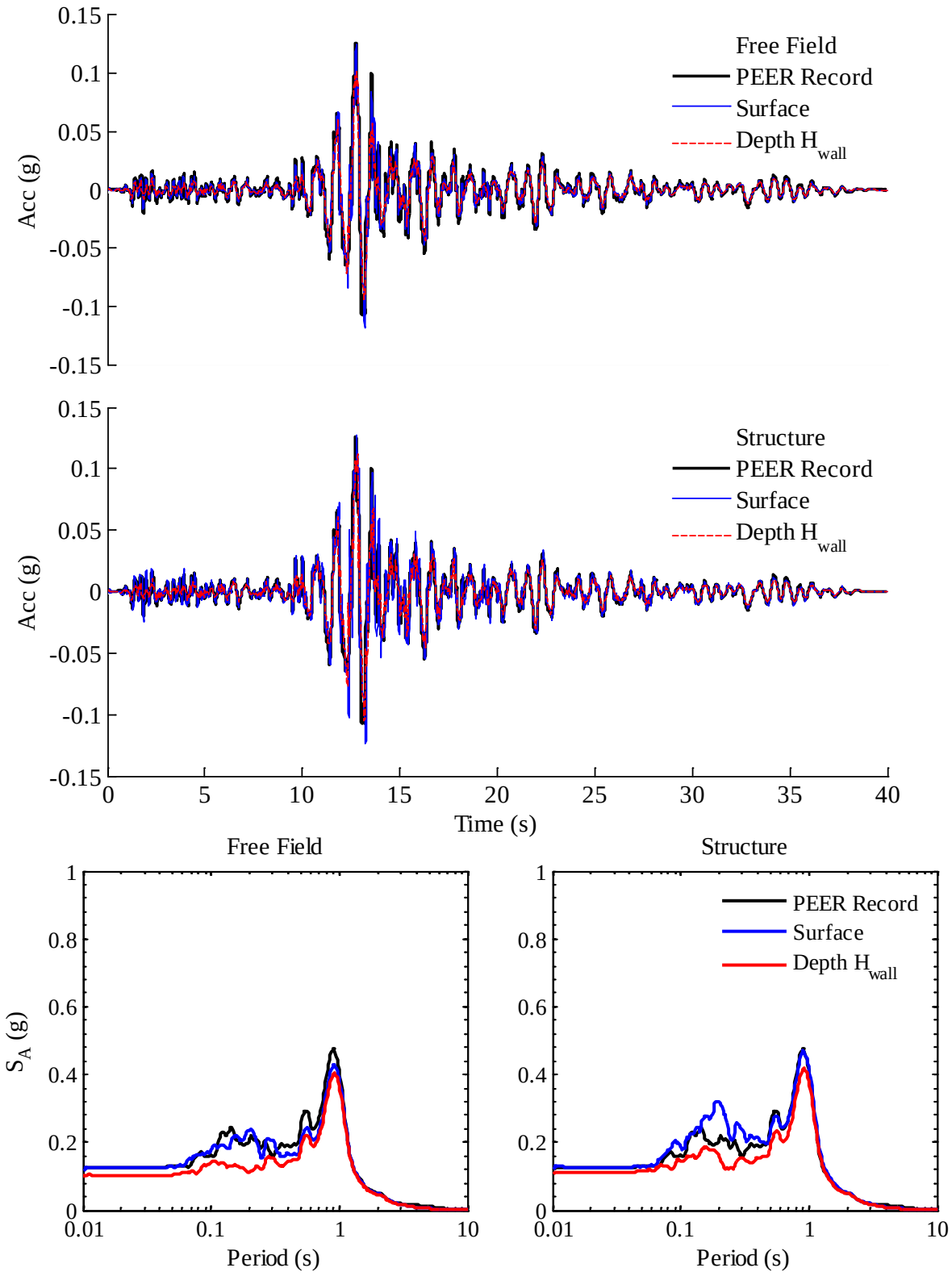

Figure B.43: Computed accelerations and response spectra at 5% damping in free field and structure during Loma Prieta RCH 190 for four level basement; Site Class D

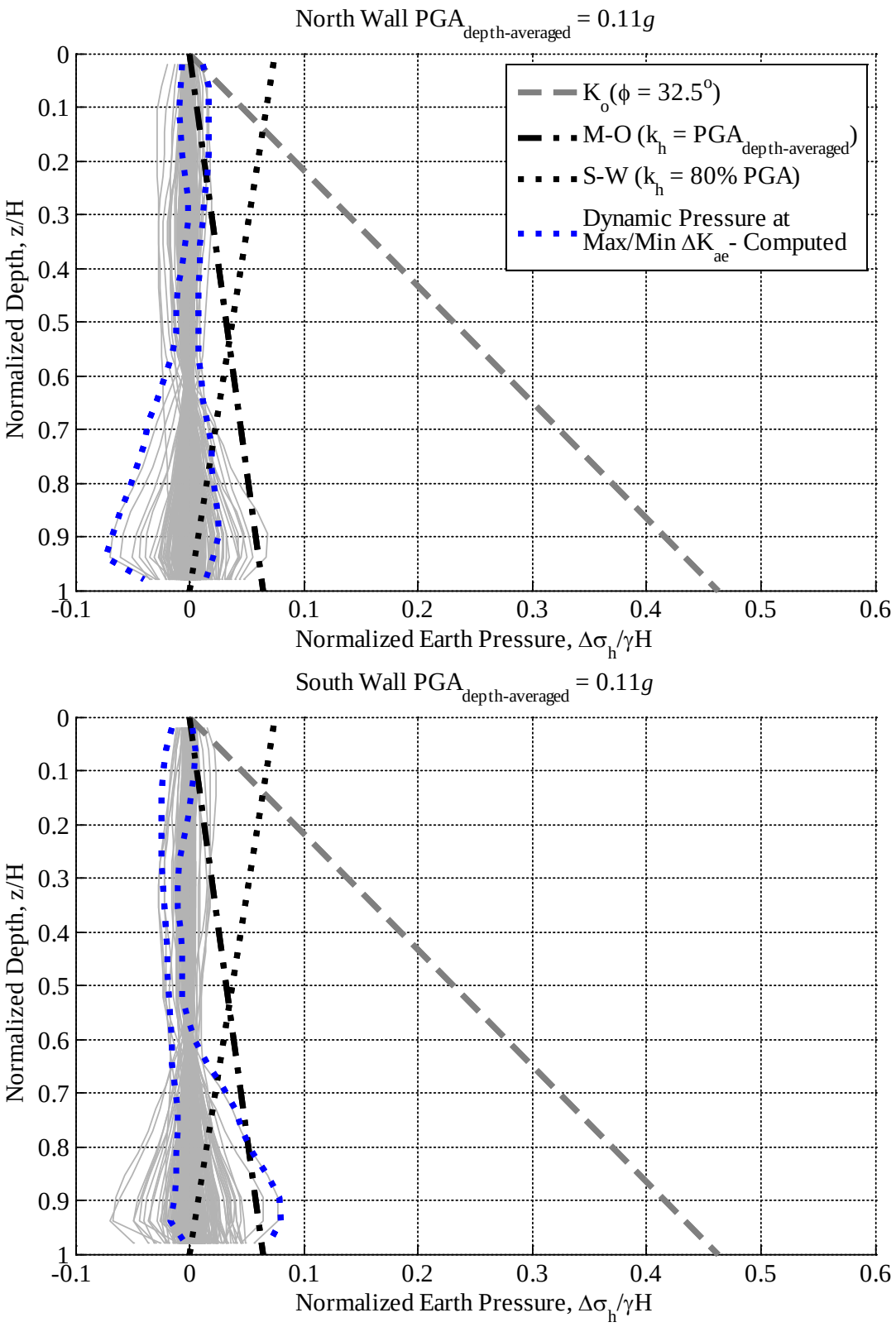

Figure B.44: Computed normalized dynamic earth pressure distributions at maximum and minimum ΔK_{ae} during Loma Prieta RCH 190 for four level basement; Site Class D

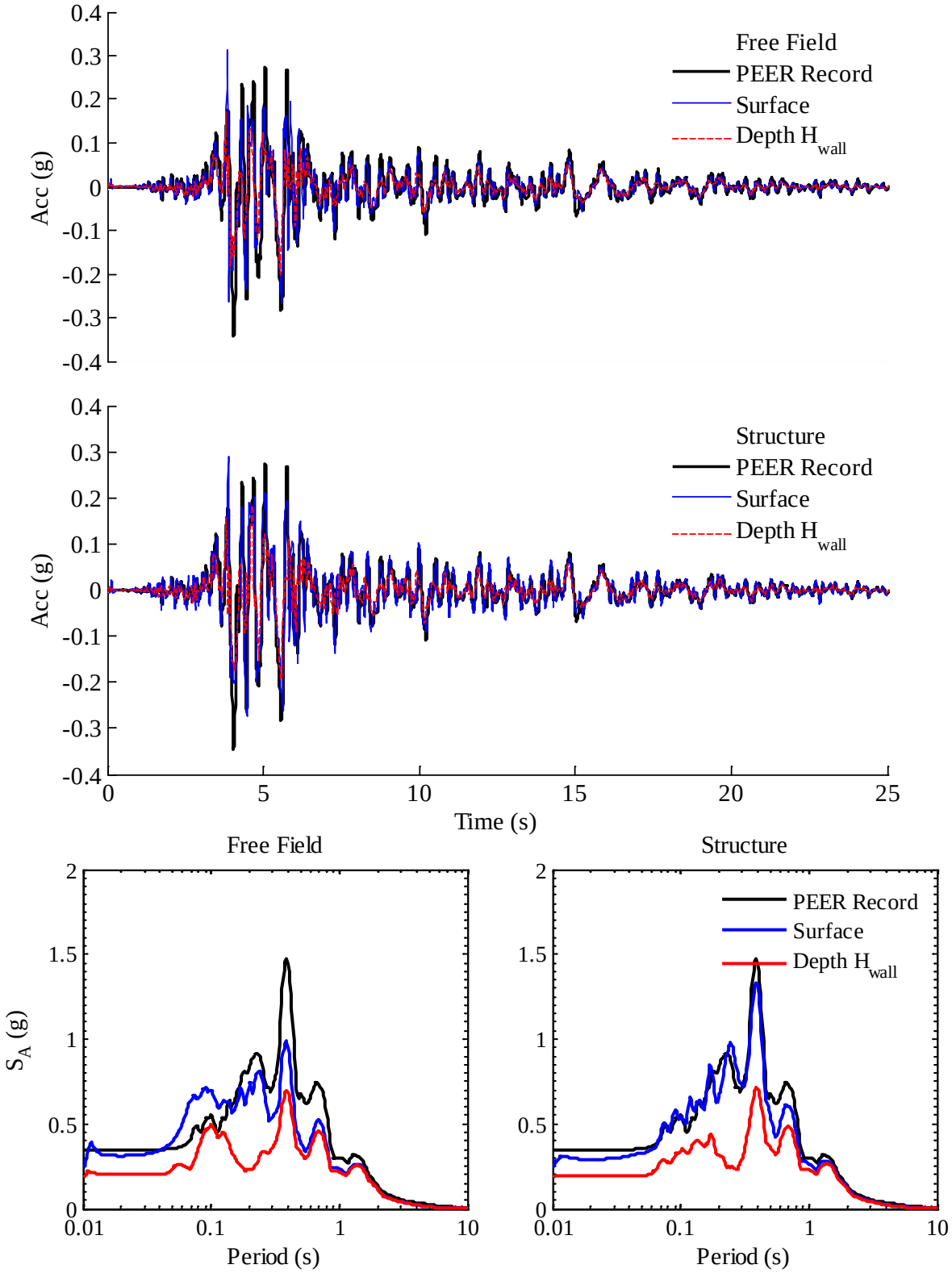

Figure B.45:Computed accelerations and response spectra at 5% damping in free field and structure during Loma Prieta GA2 000 for four level basement; Site Class D

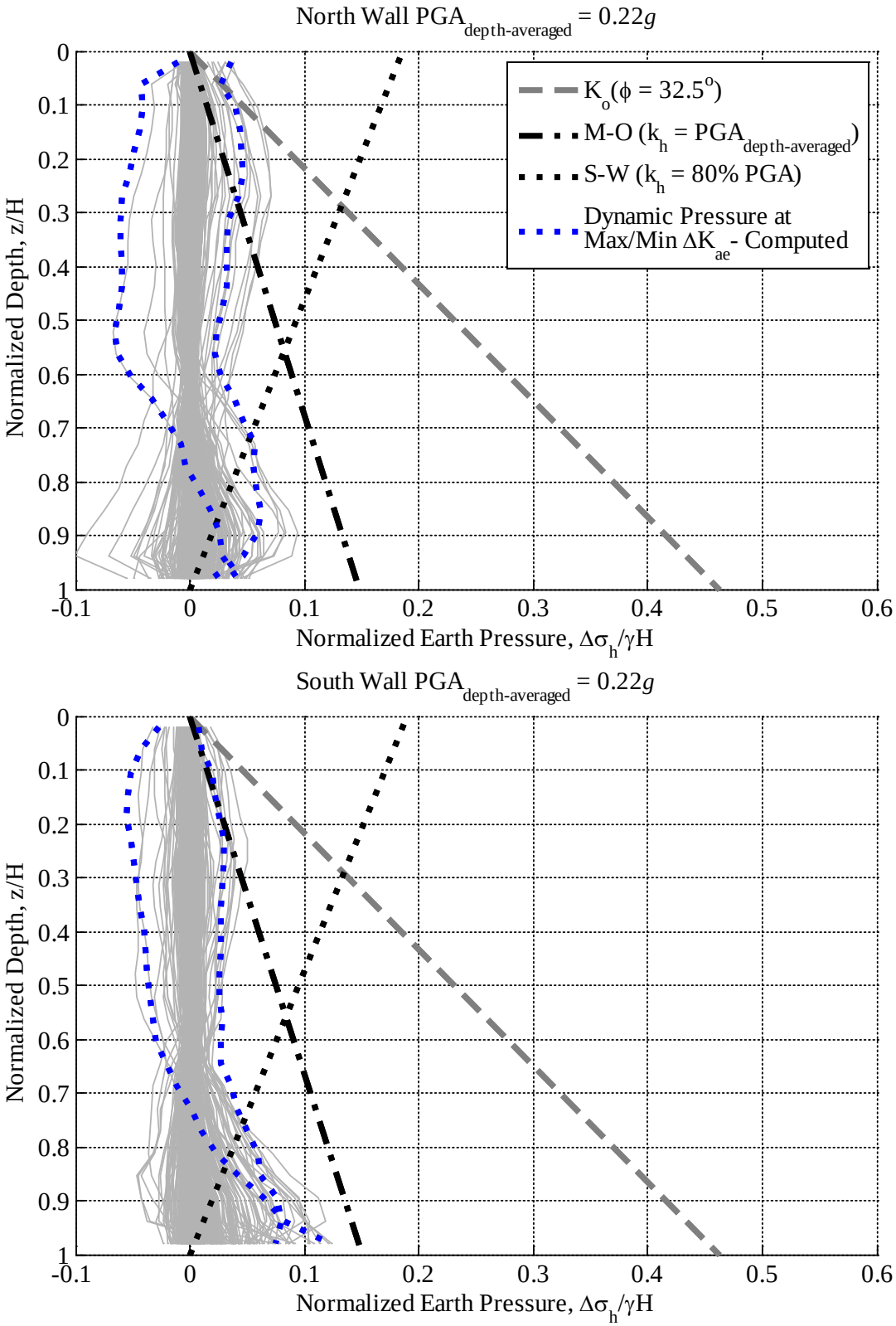

Figure B.46: Computed normalized dynamic earth pressure distributions at maximum and minimum ΔK_{ae} during Loma Prieta GA2 000 for four level basement; Site Class D

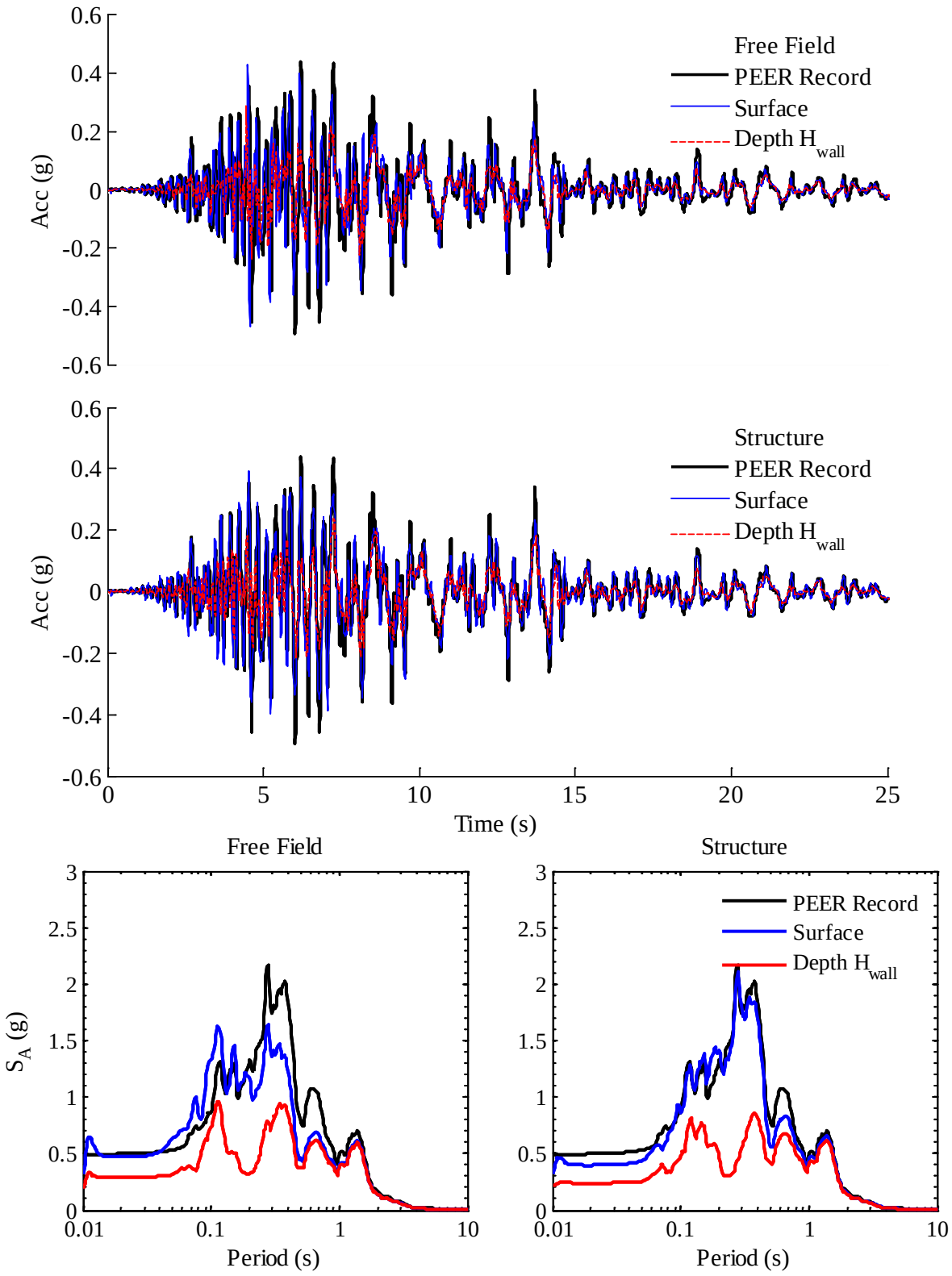

Figure B.47: Computed accelerations and response spectra at 5% damping in free field and structure during Loma Prieta CAP 000 for four level basement; Site Class D

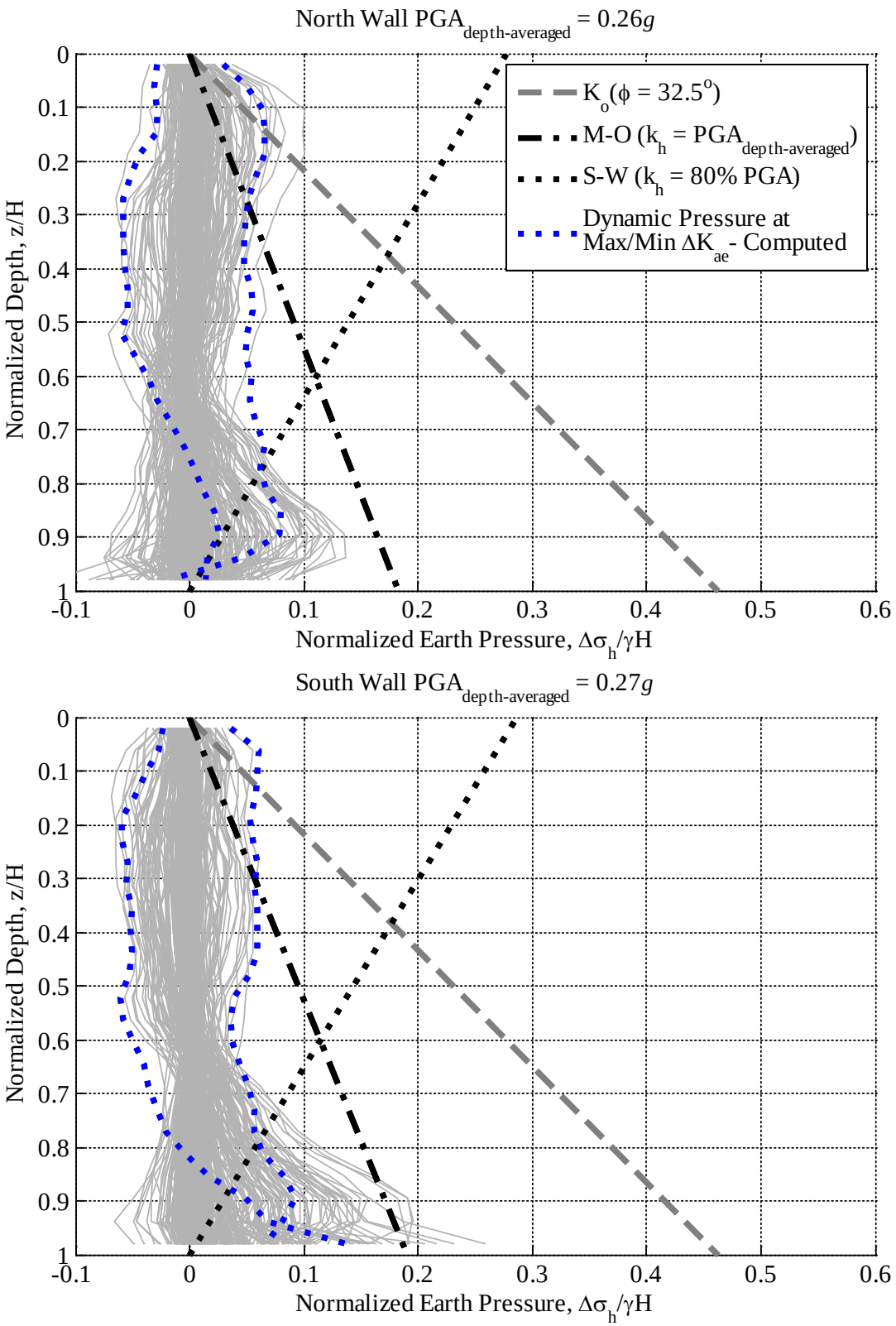

Figure B.48: Computed normalized dynamic earth pressure distributions at maximum and minimum ΔK_{ae} during Loma Prieta CAP 000 for four level basement; Site Class D

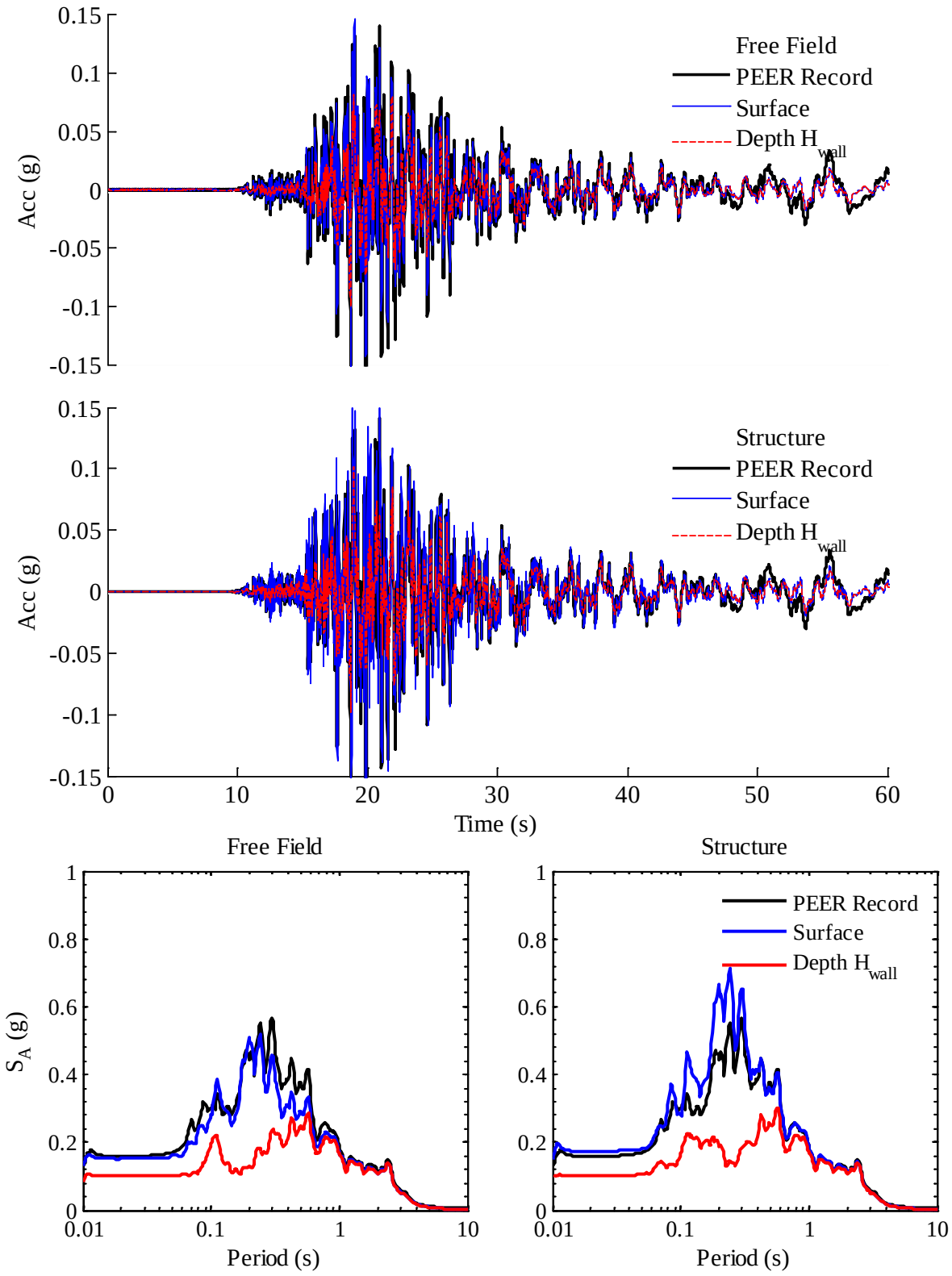

Figure B.49: Computed accelerations and response spectra at 5% damping in free field and structure during Kobe SKI 000 for four level basement; Site Class D

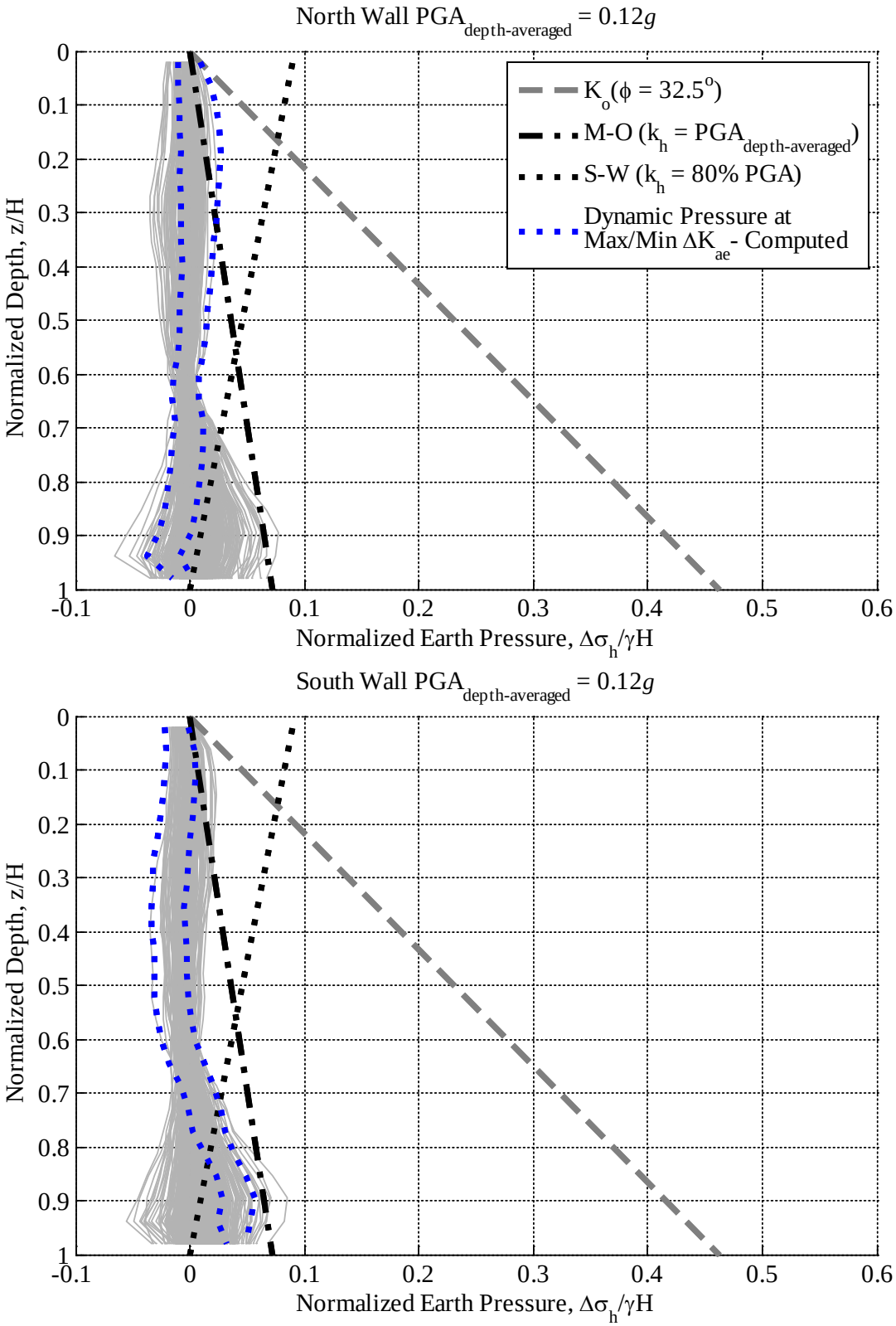

Figure B.50: Computed normalized dynamic earth pressure distributions at maximum and minimum ΔK_{ae} during Kobe SKI 000 for four level basement; Site Class D

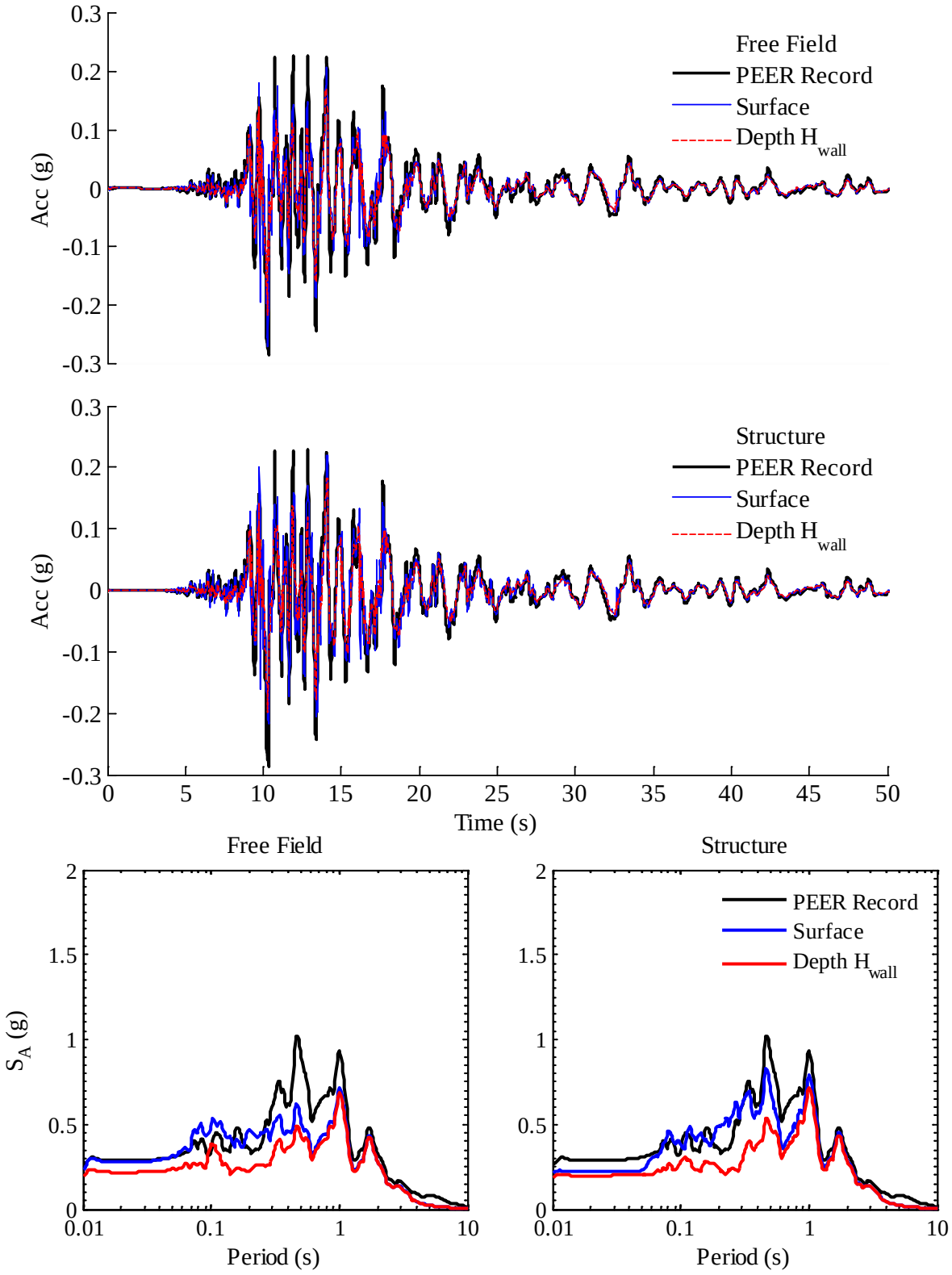

Figure B.51: Computed accelerations and response spectra at 5% damping in free field and structure during Kobe AMA 000 for four level basement; Site Class D

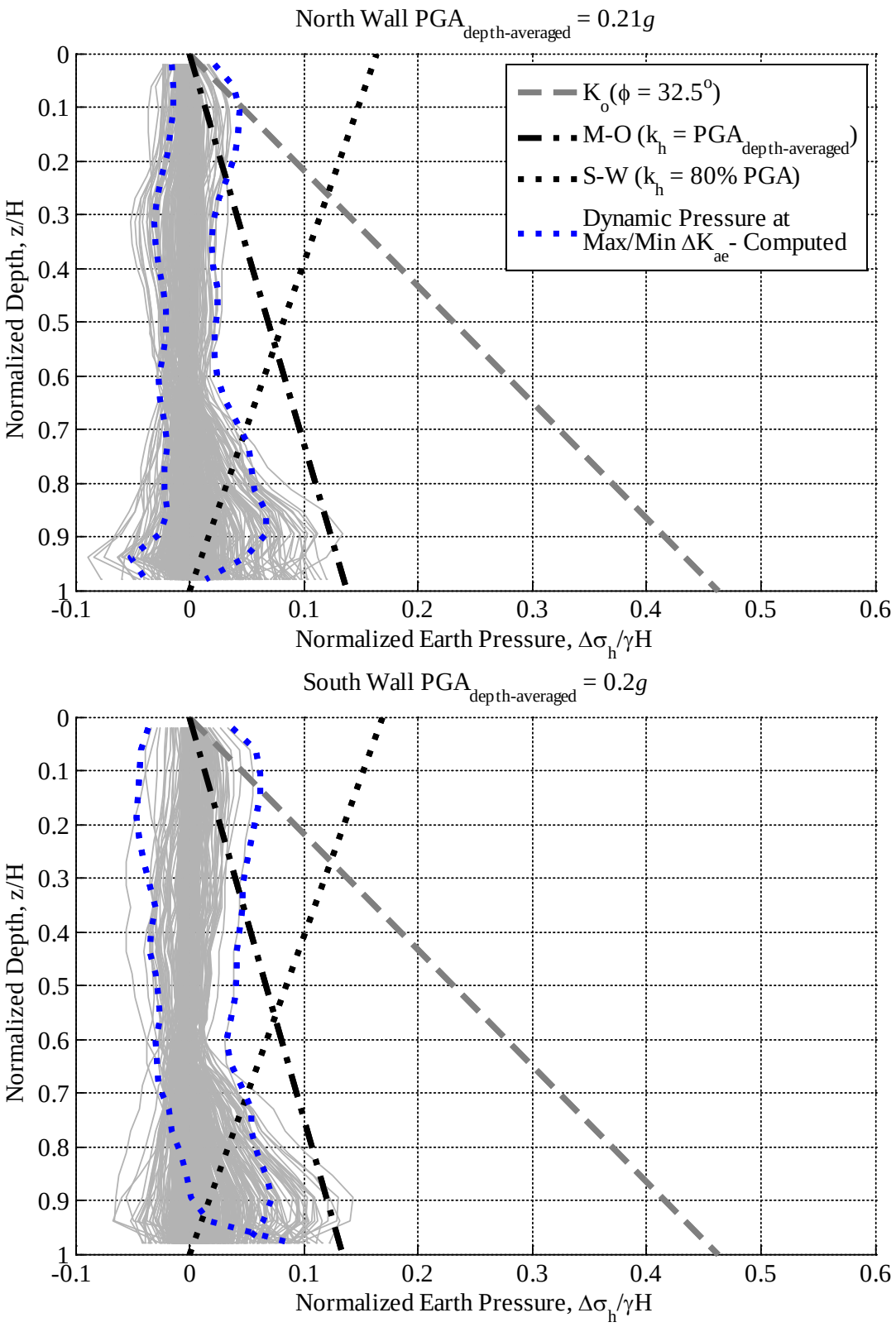

Figure B.52: Computed normalized dynamic earth pressure distributions at maximum and minimum ΔK_{ae} during Kobe AMA 000 for four level basement; Site Class D

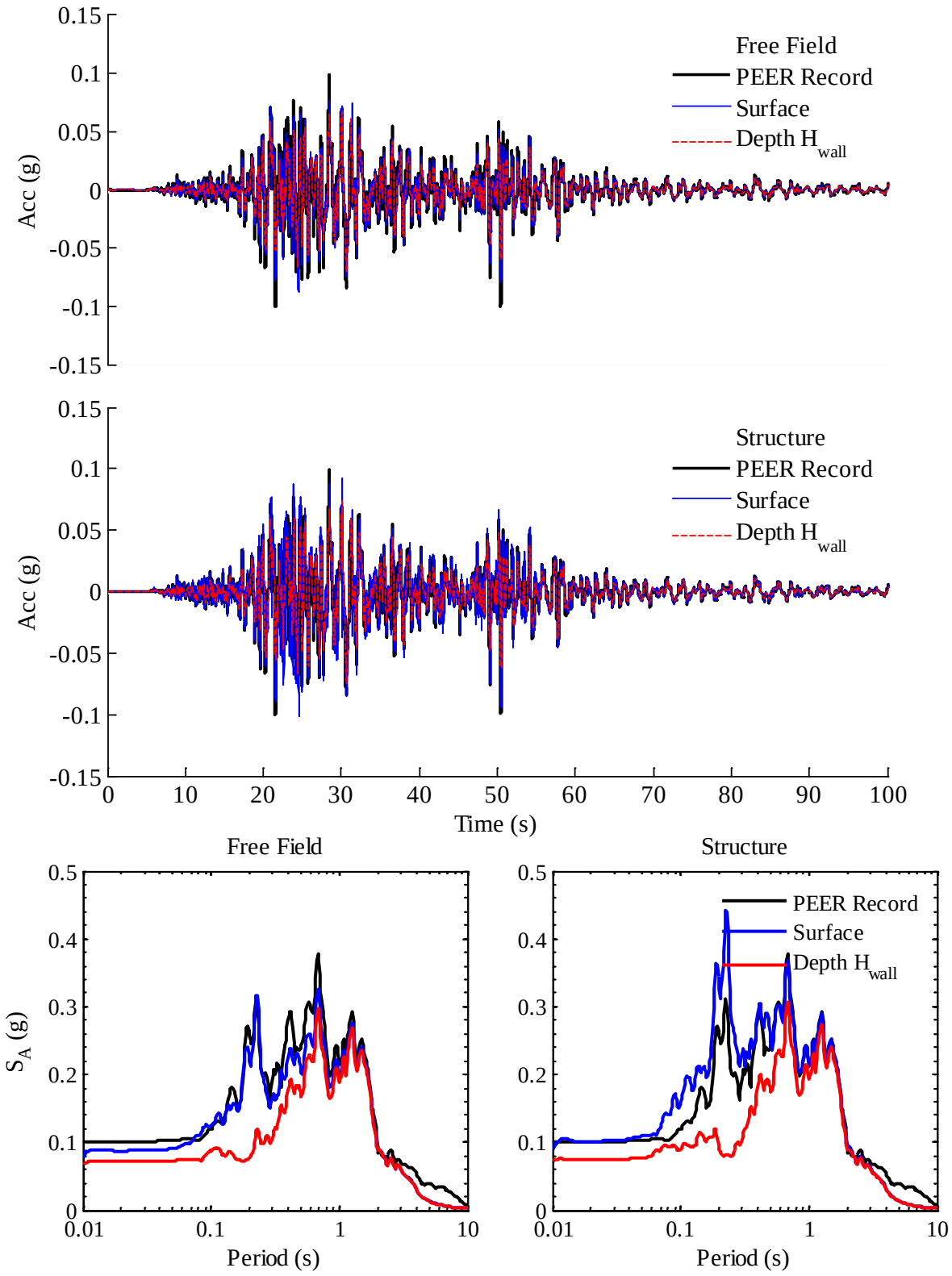

Figure B.53: Computed accelerations and response spectra at 5% damping in free field and structure during Kocaeli BUR 090 for four level basement; Site Class D

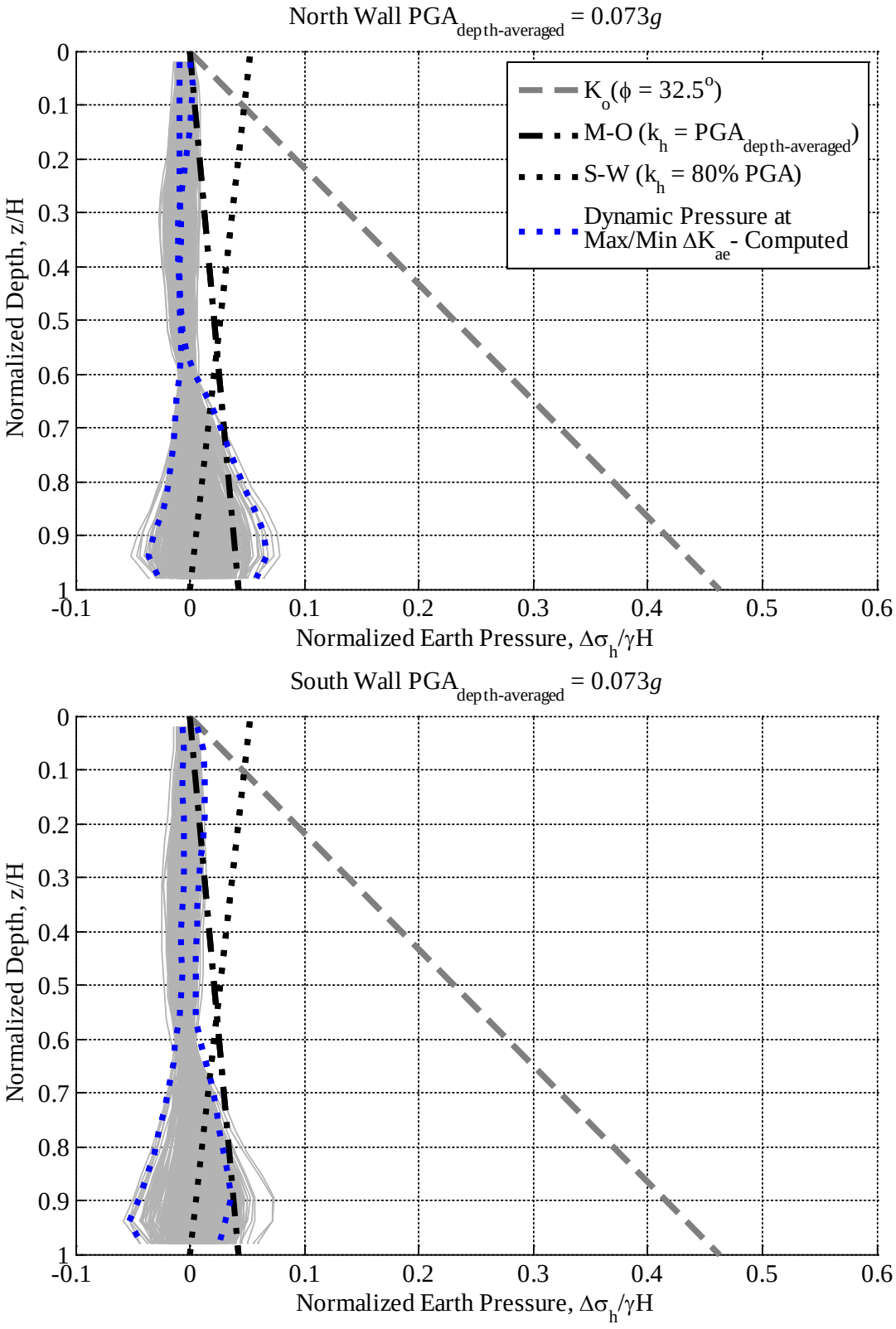

Figure B.54: Computed normalized dynamic earth pressure distributions at maximum and minimum ΔK_{ae} during Kocaeli BUR 090 for four level basement; Site Class D

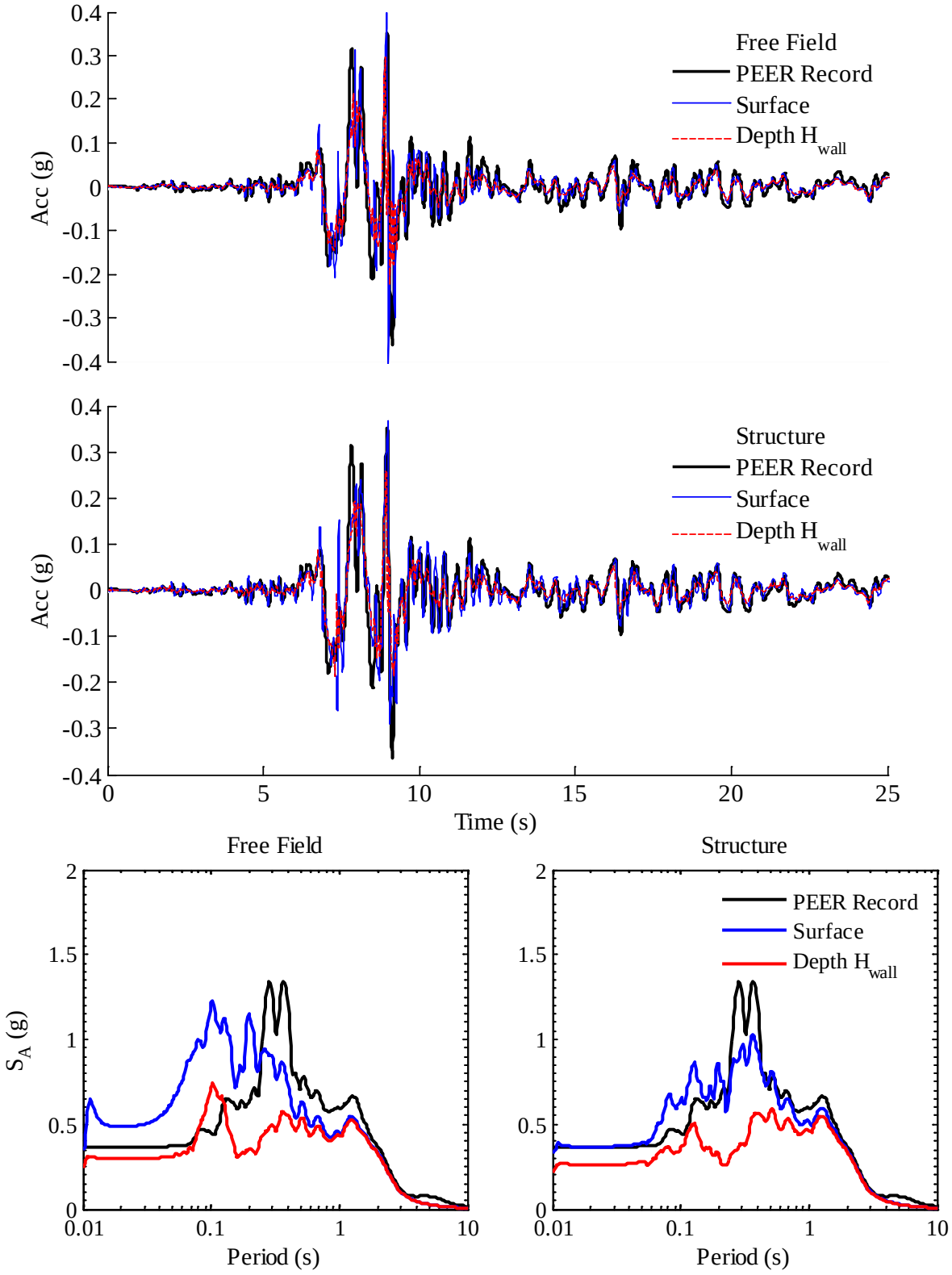

Figure B.55: Computed accelerations and response spectra at 5% damping in free field and structure during Kocaeli DUZ 270 for four level basement; Site Class D

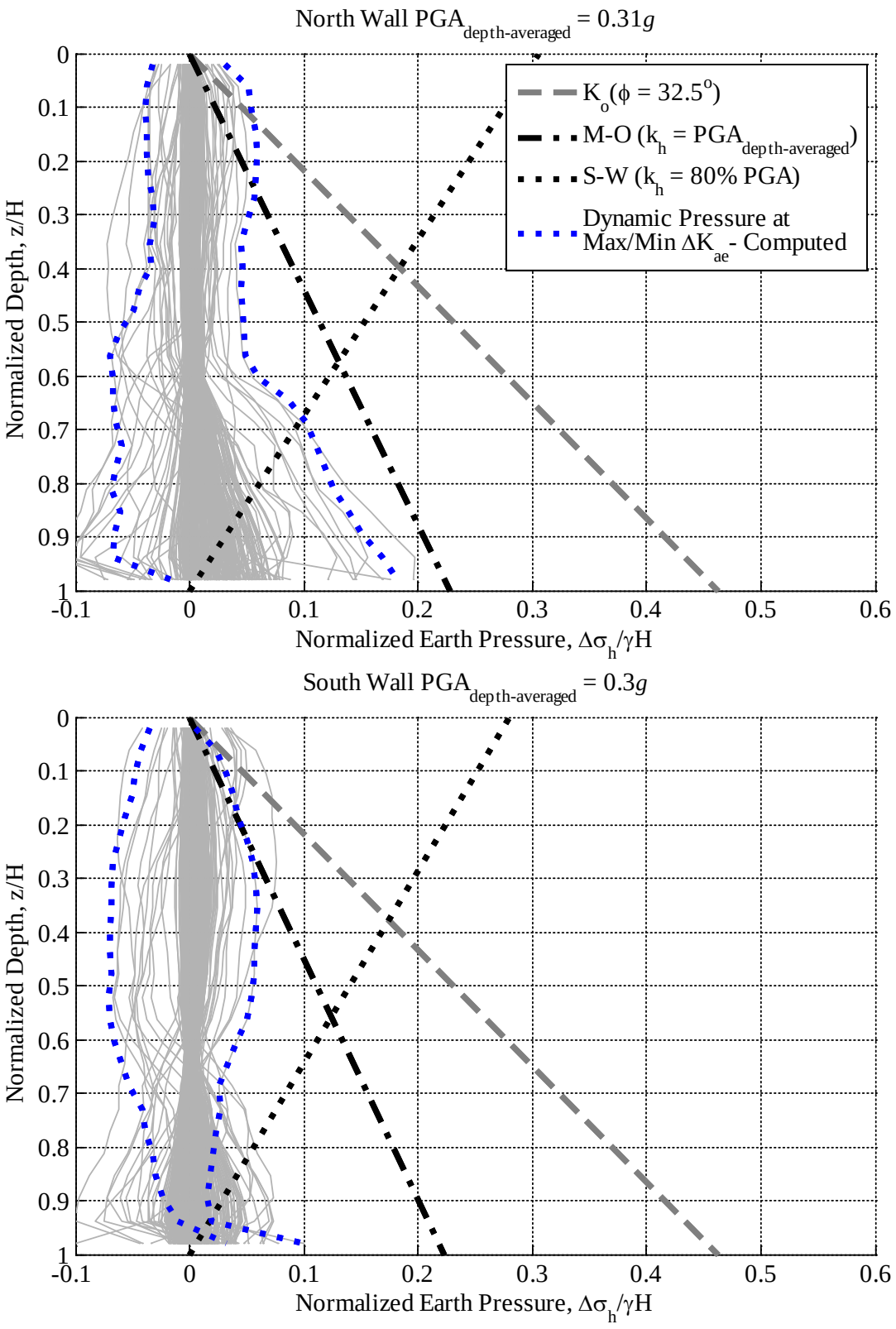

Figure B.56: Computed normalized dynamic earth pressure distributions at maximum and minimum ΔK_{ae} during Kocaeli DUZ 270 for four level basement; Site Class D

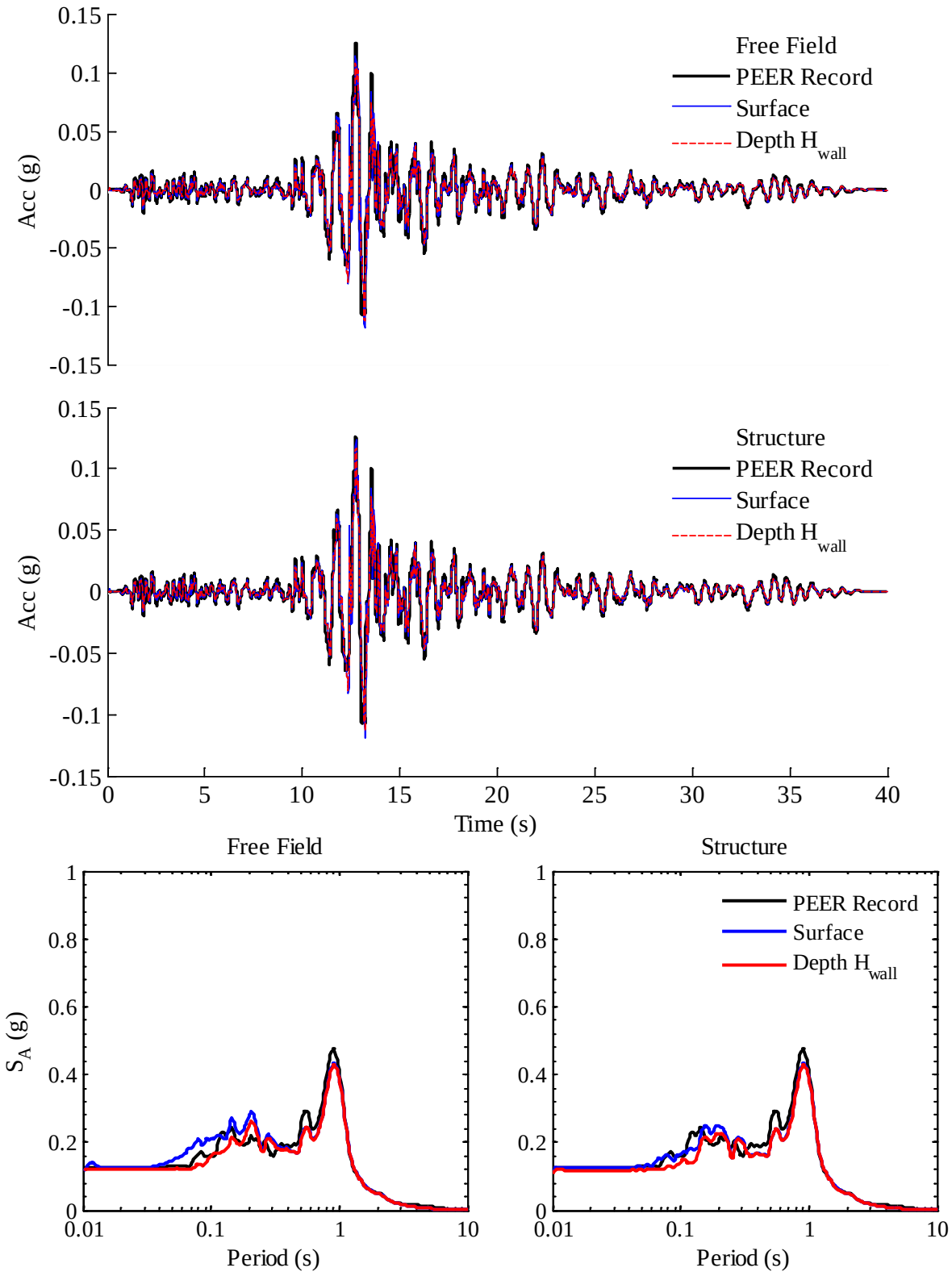

Figure B.57: Computed accelerations and response spectra at 5% damping in free field and structure during Loma Prieta RCH 190 for one bay, one level basement; Site Class D

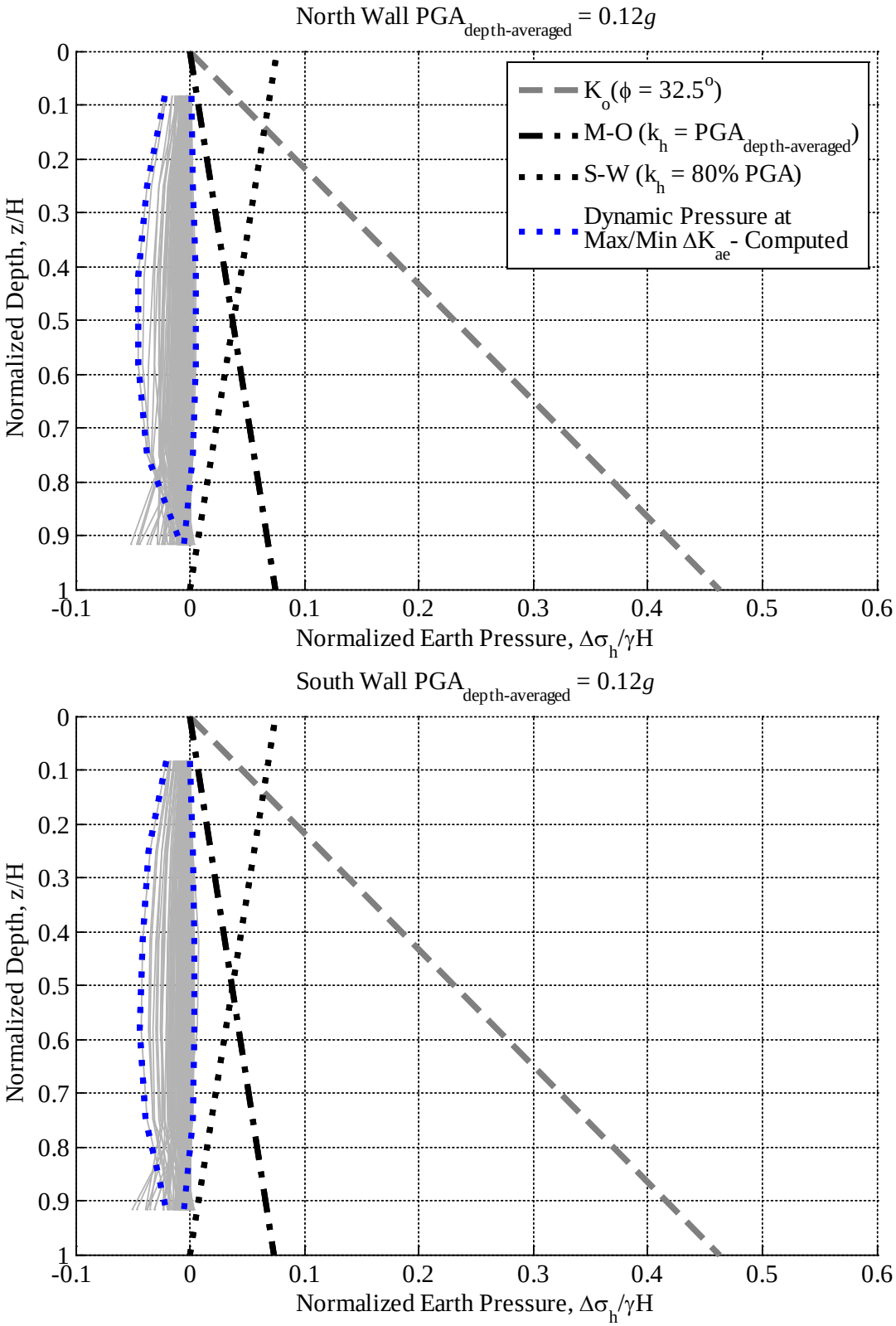

Figure B.58: Computed normalized dynamic earth pressure distributions at maximum and minimum ΔK_{ae} during Loma Prieta RCH 190 for one bay, one level basement; Site Class D

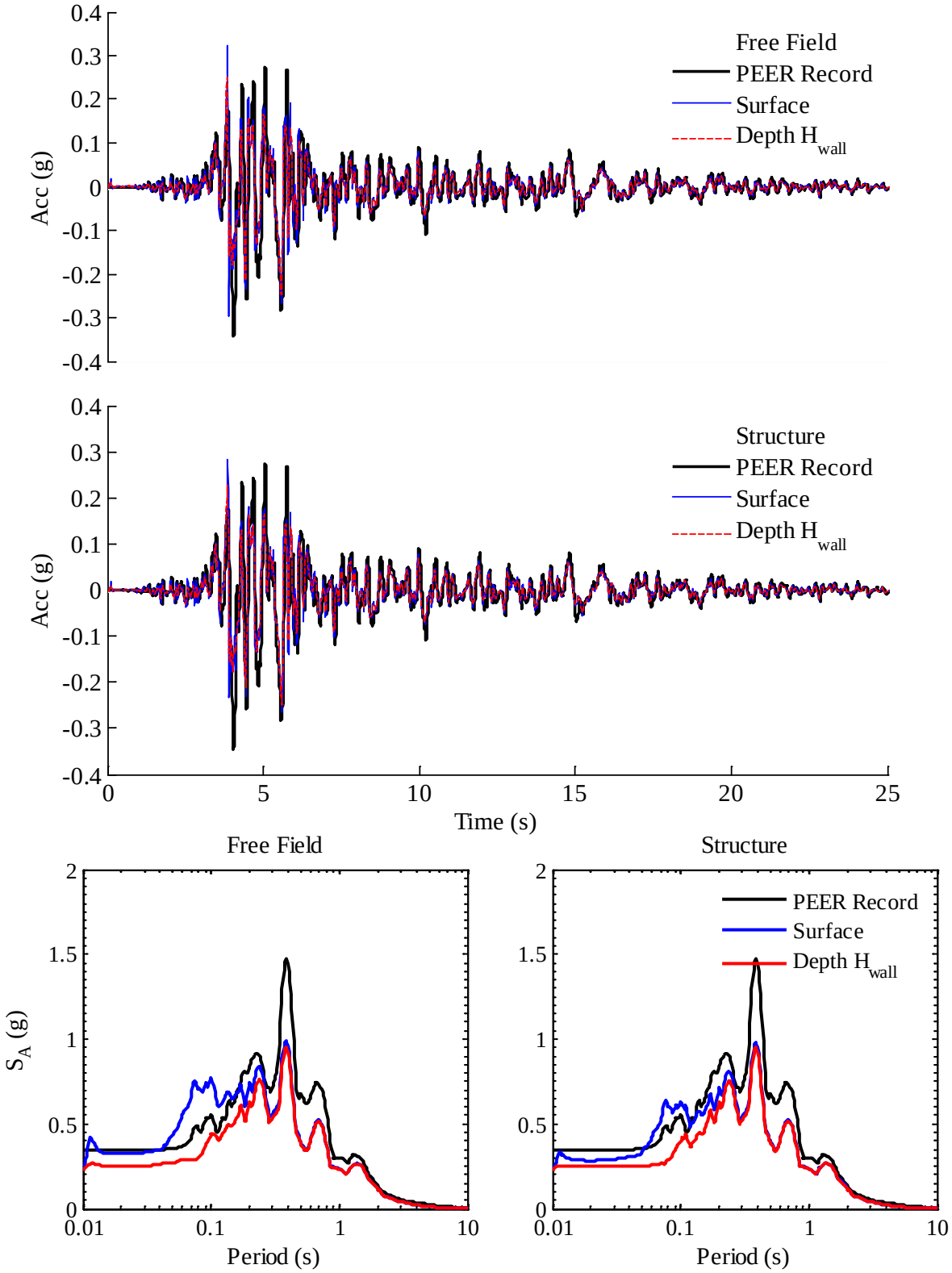

Figure B.59:Computed accelerations and response spectra at 5% damping in free field and structure during Loma Prieta GA2 000 for one bay, one level basement; Site Class D

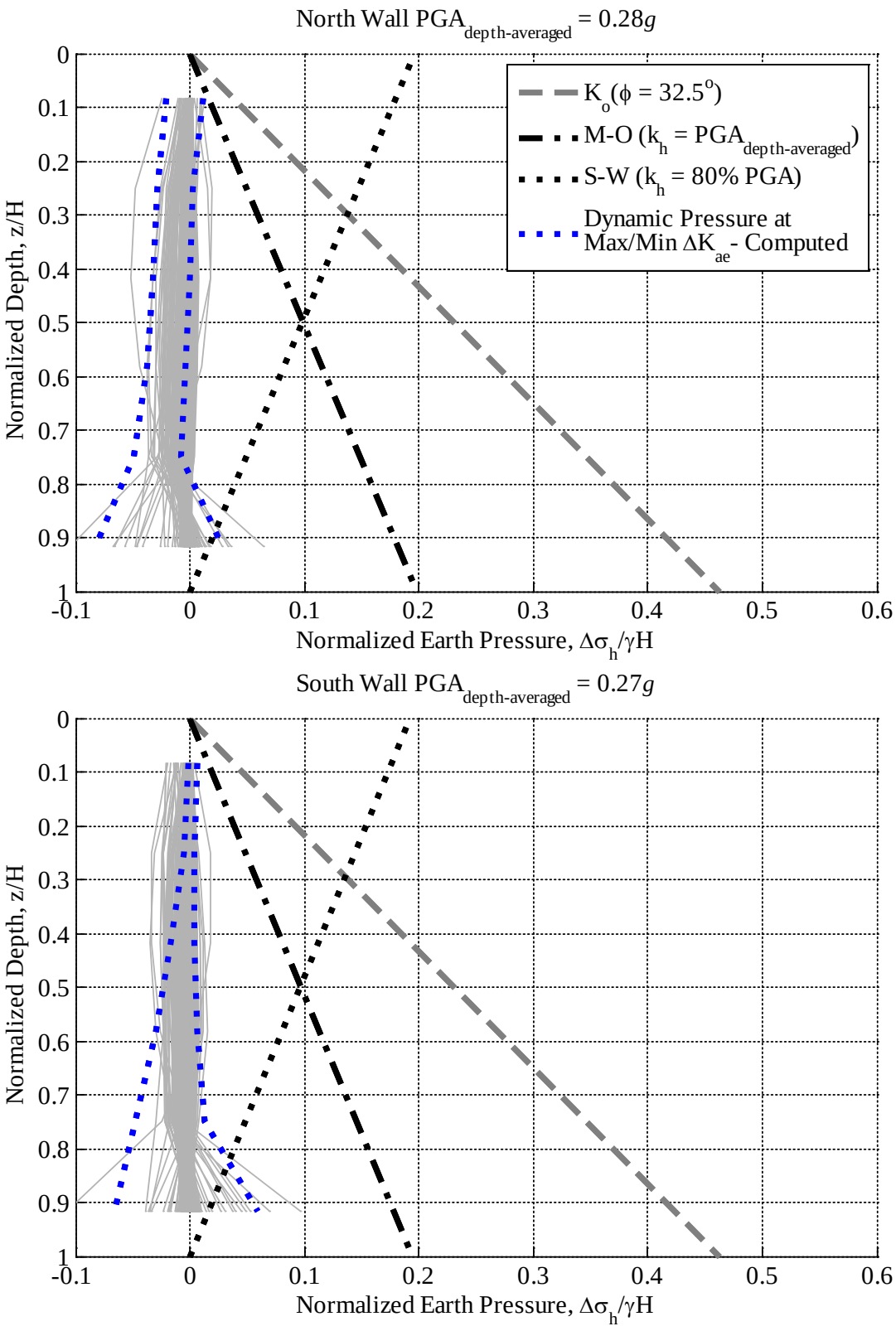

Figure B.60: Computed normalized dynamic earth pressure distributions at maximum and minimum ΔK_{ae} during Loma Prieta GA2 000 for one bay, one level basement; Site Class D

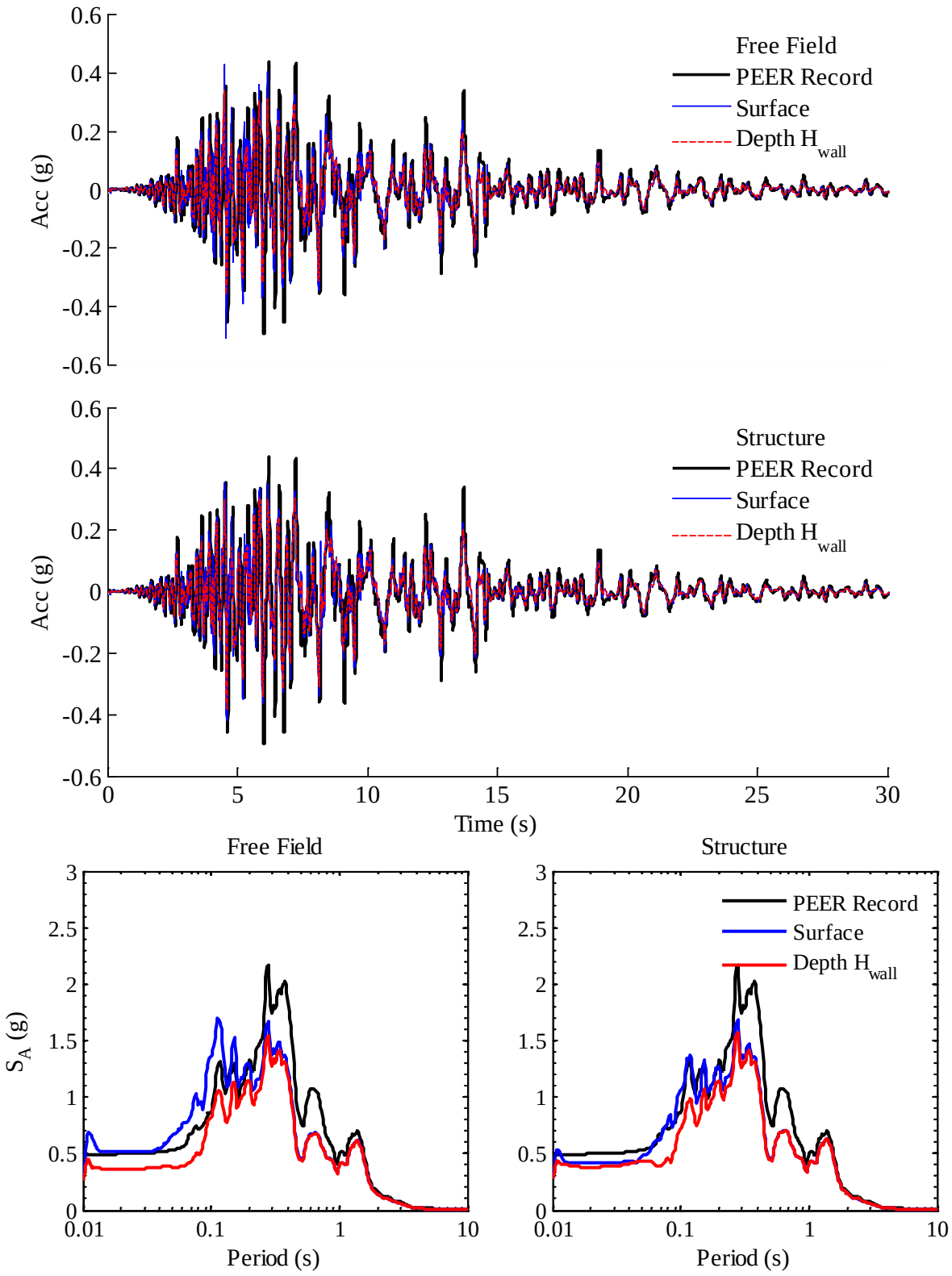

Figure B.61: Computed accelerations and response spectra at 5% damping in free field and structure during Loma Prieta CAP 000 for one bay, one level basement; Site Class D

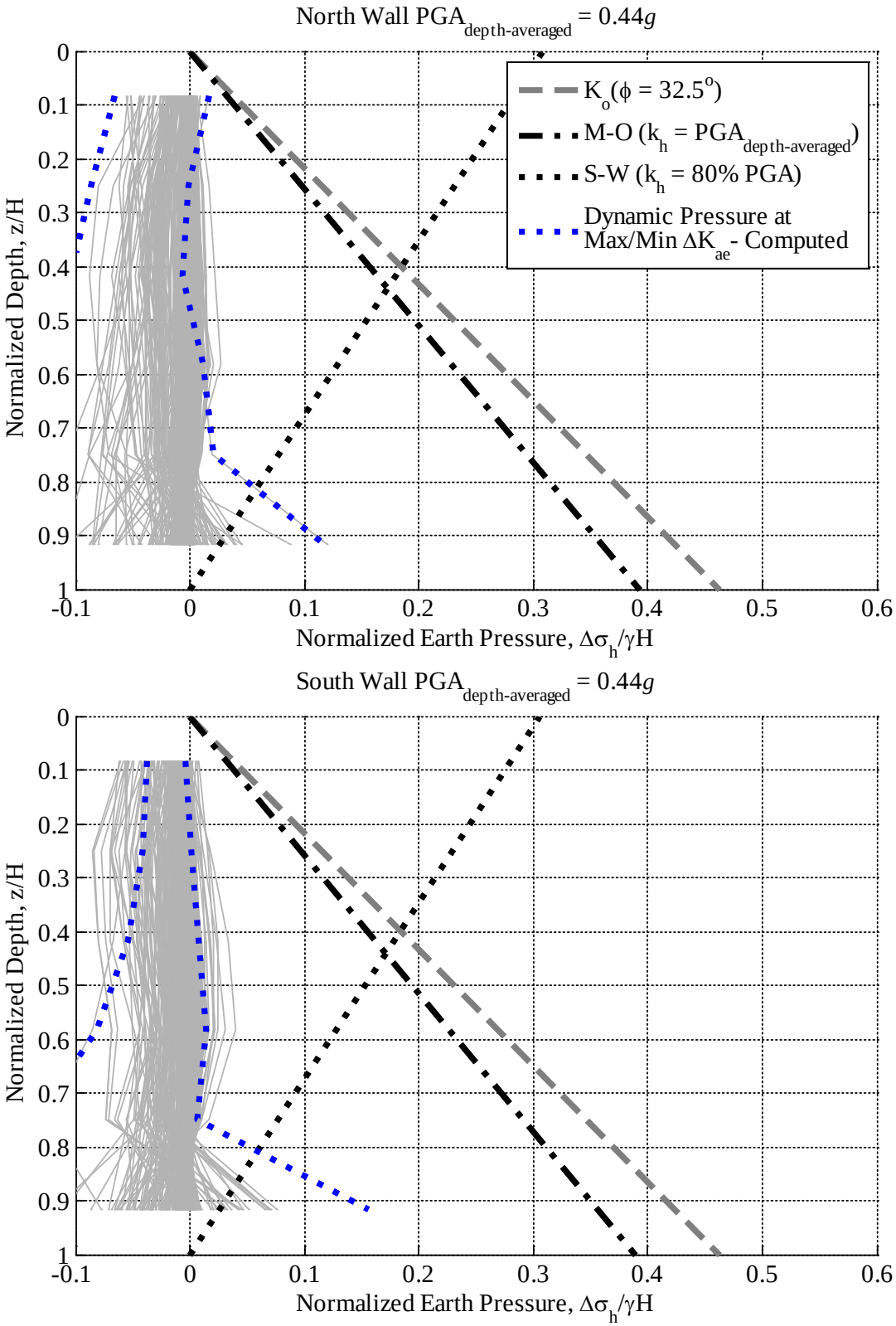

Figure B.62: Computed normalized dynamic earth pressure distributions at maximum and minimum ΔK_{ae} during Loma Prieta CAP 000 for one bay, one level basement; Site Class D

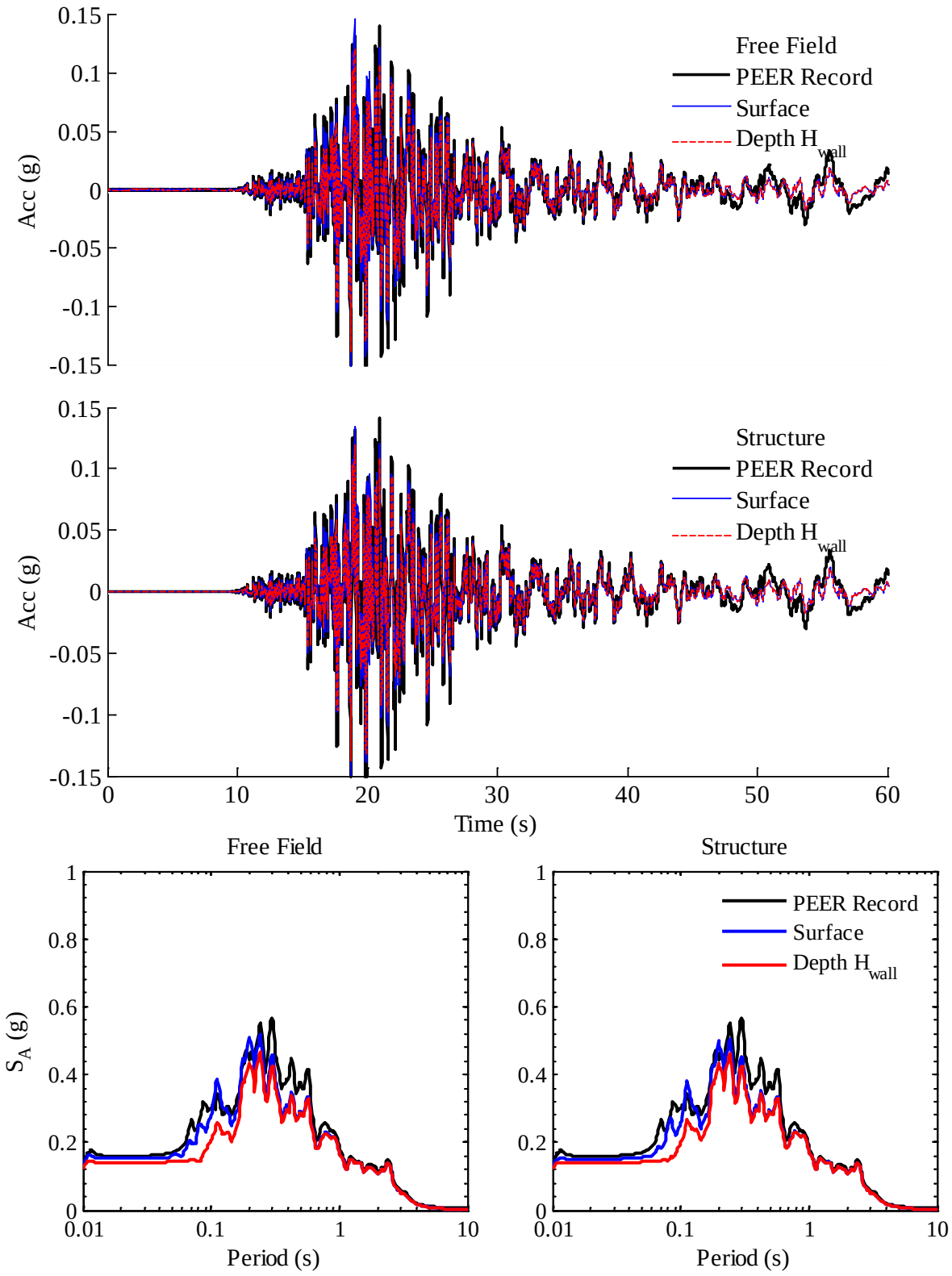

Figure B.63: Computed accelerations and response spectra at 5% damping in free field and structure during Kobe SKI 000 for one bay, one level basement; Site Class D

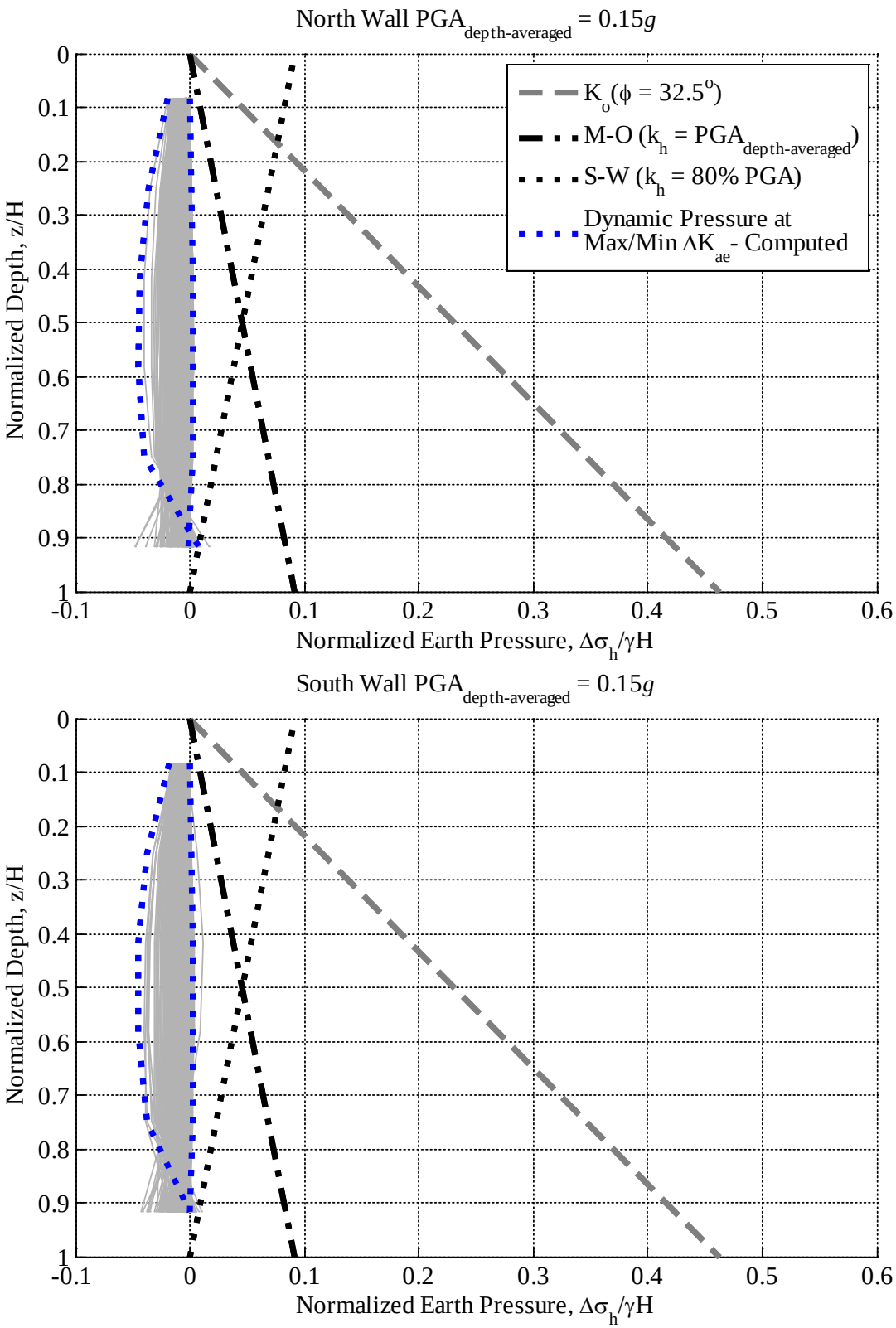

Figure B.64: Computed normalized dynamic earth pressure distributions at maximum and minimum ΔK_{ae} during Kobe SKI 000 for one bay, one level basement; Site Class D

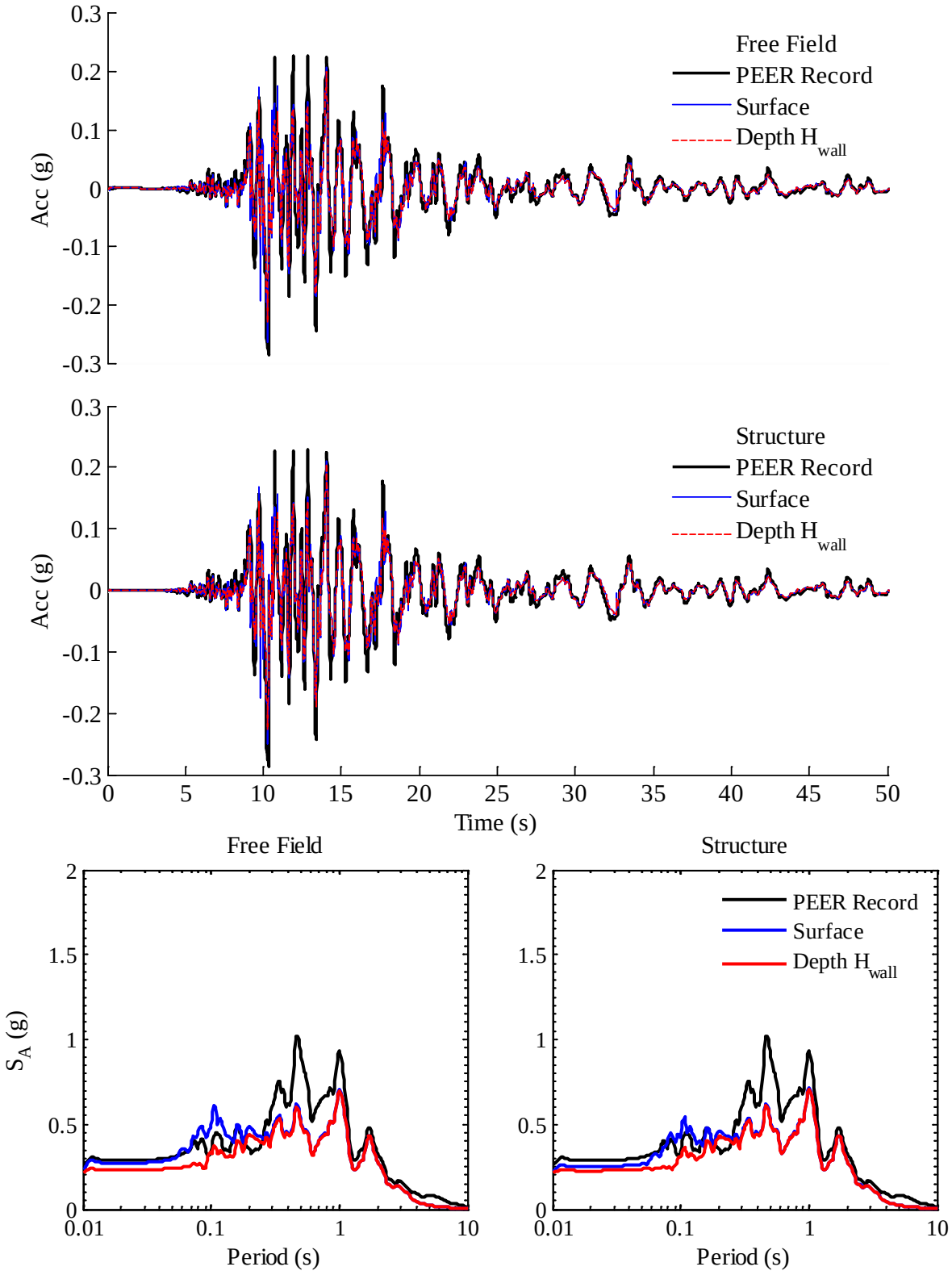

Figure B.65: Computed accelerations and response spectra at 5% damping in free field and structure during Kobe AMA 000 for one bay, one level basement; Site Class D

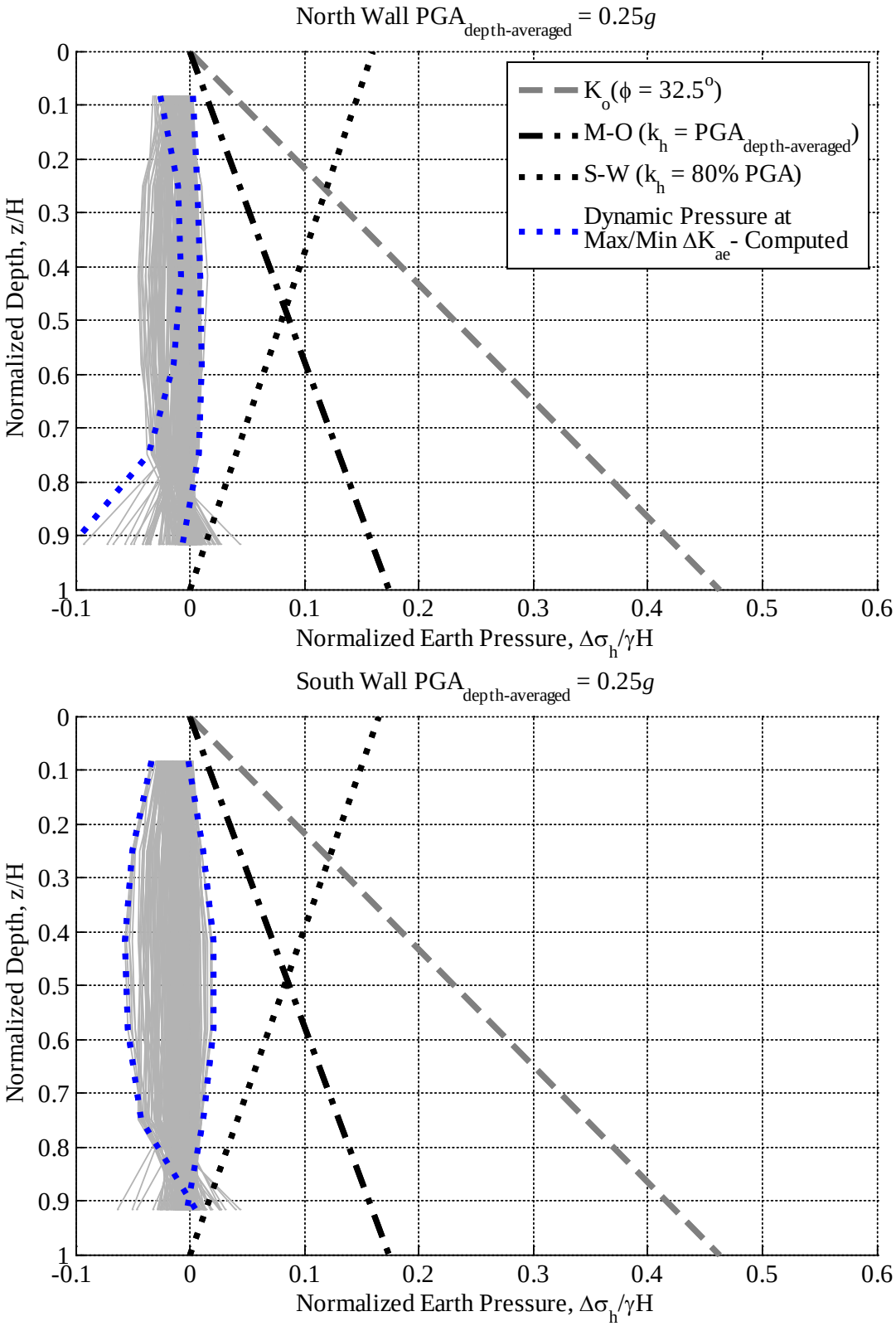

Figure B.66: Computed normalized dynamic earth pressure distributions at maximum and minimum ΔK_{ae} during Kobe AMA 000 for one bay, one level basement; Site Class D

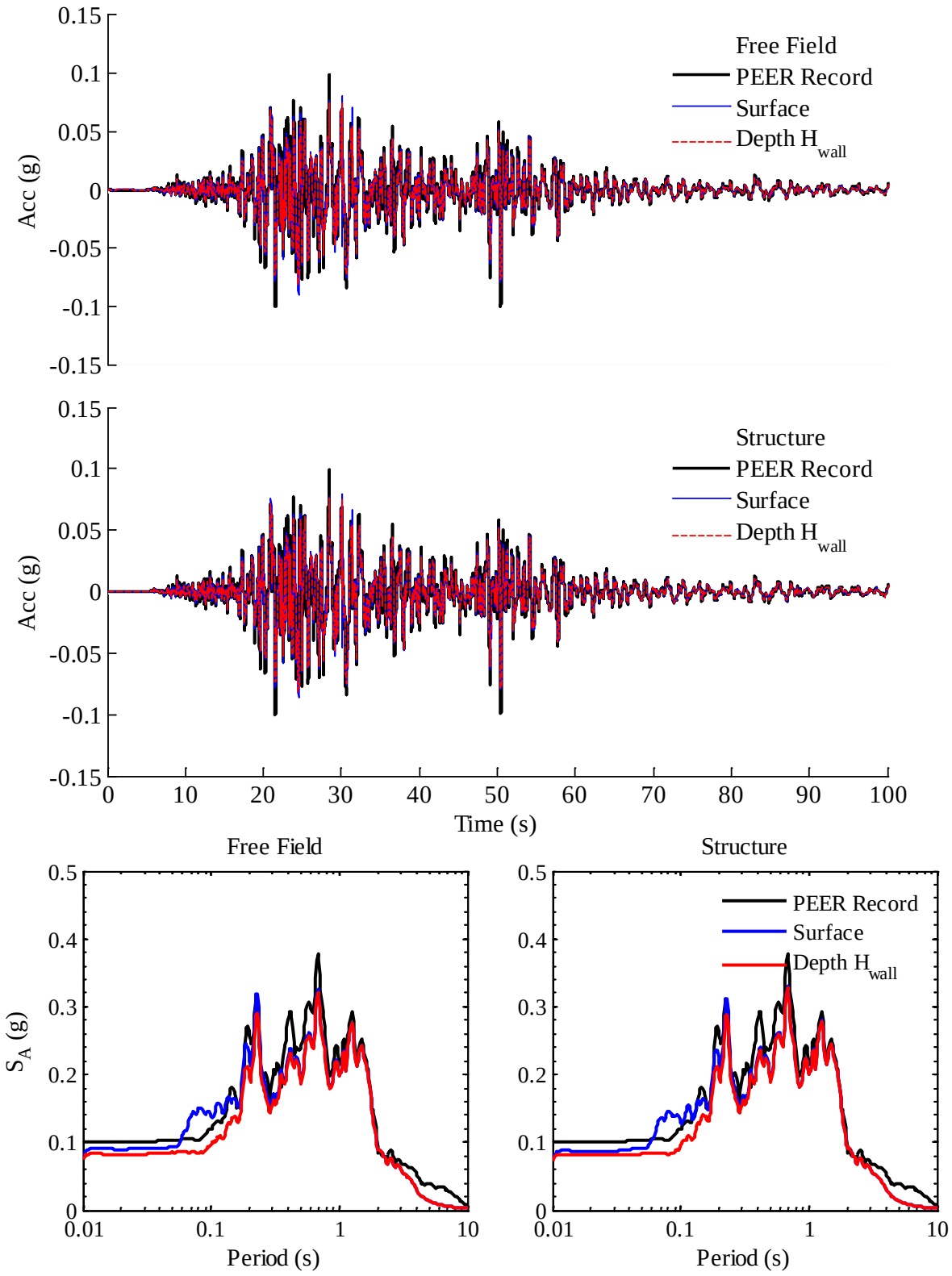

Figure B.67: Computed accelerations and response spectra at 5% damping in free field and structure during Kocaeli BUR 090 for one bay, one level basement; Site Class D

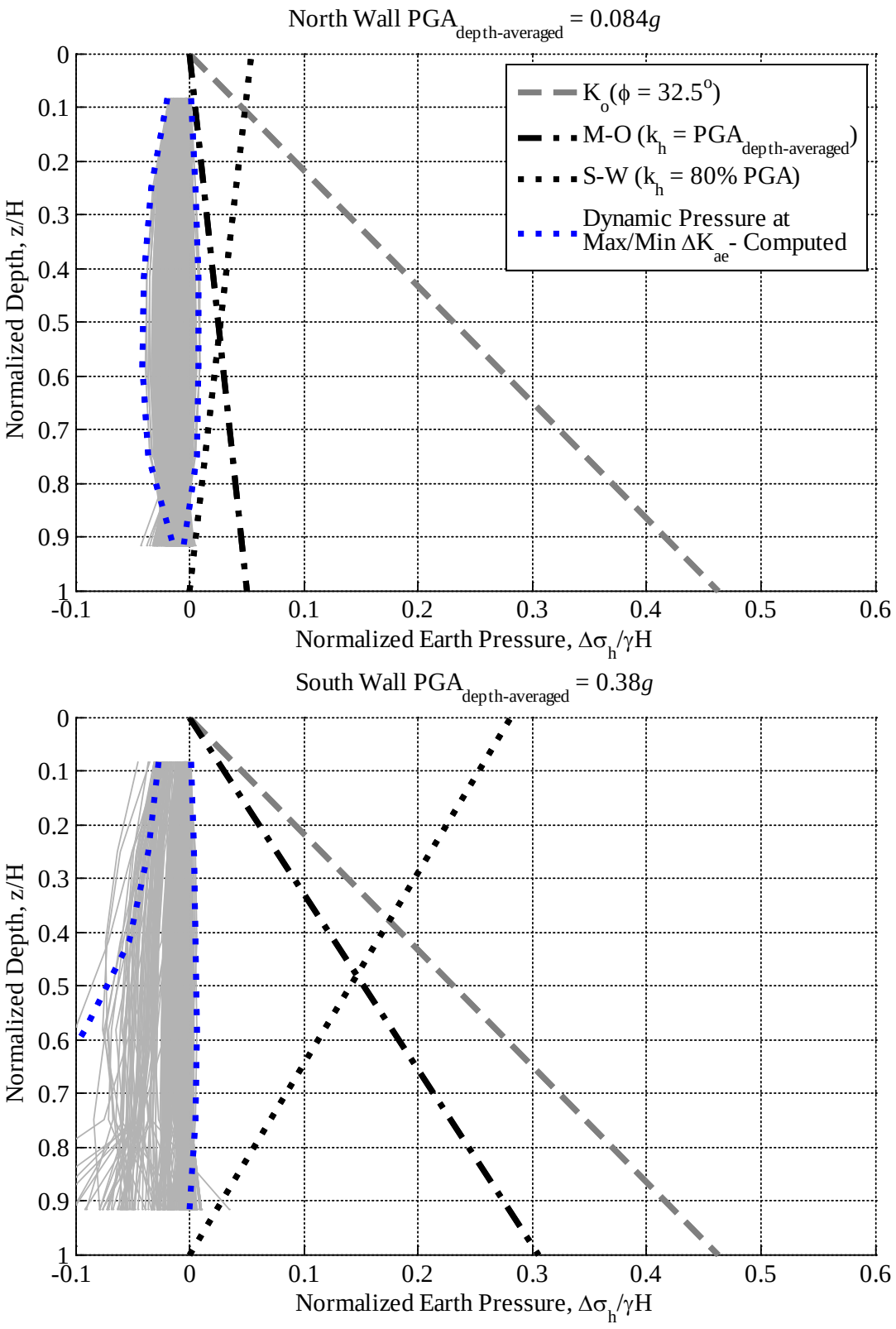

Figure B.68: Computed normalized dynamic earth pressure distributions at maximum and minimum ΔK_{ae} during Kocaeli BUR 090 for one bay, one level basement; Site Class D

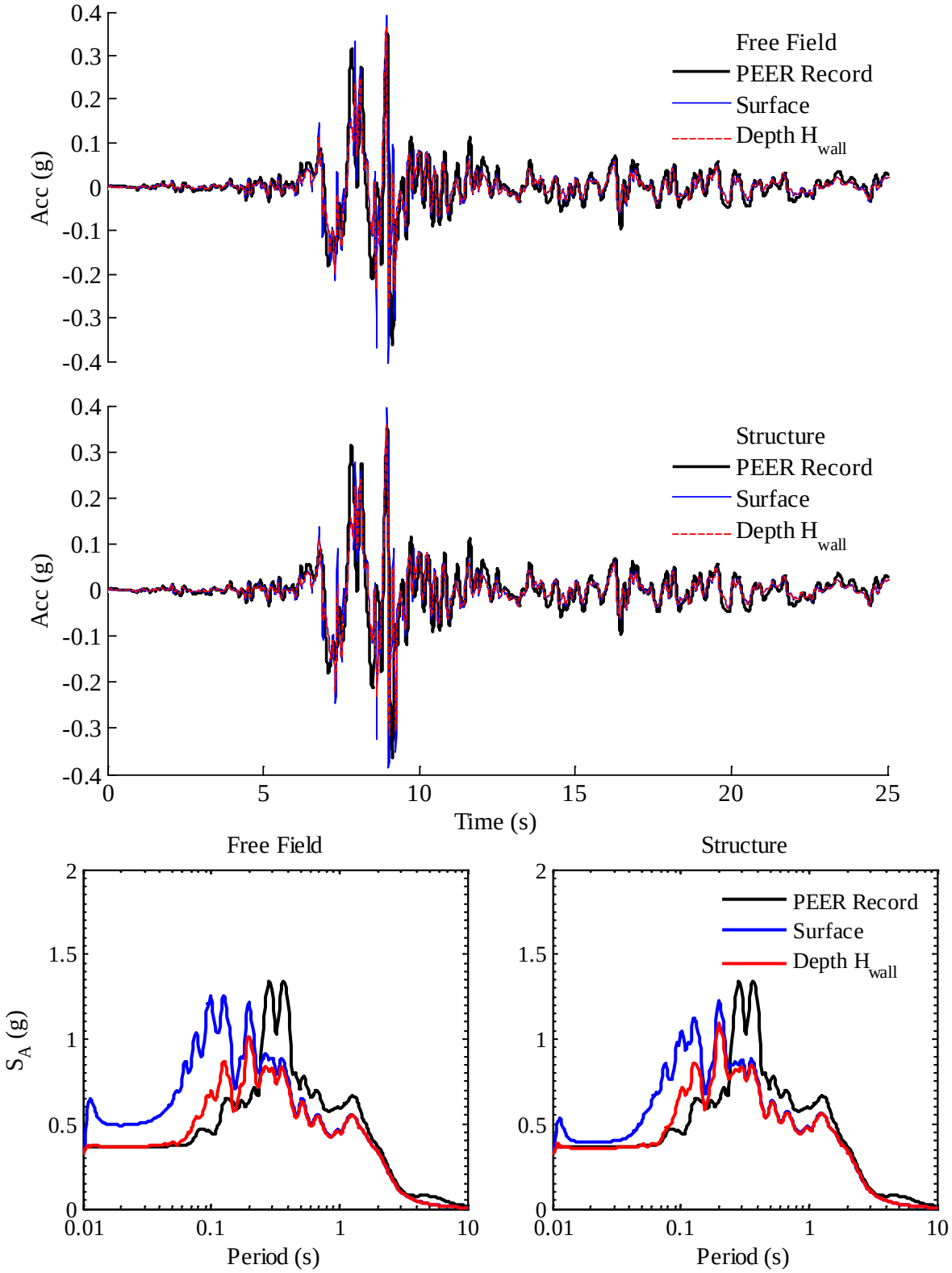

Figure B.69: Computed accelerations and response spectra at 5% damping in free field and structure during Kocaeli DUZ 270 for one bay, one level basement; Site Class D

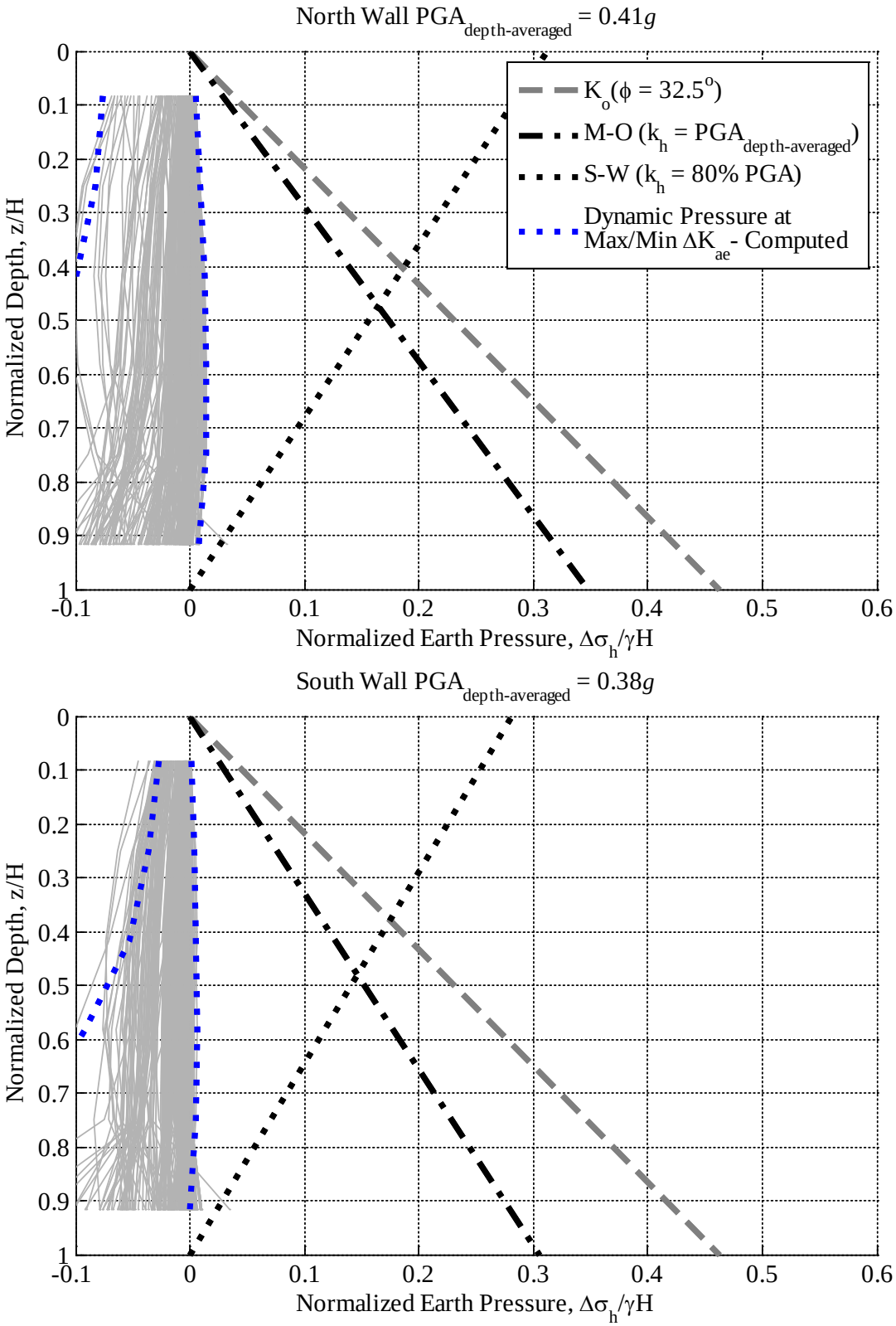

Figure B.70: Computed normalized dynamic earth pressure distributions at maximum and minimum ΔK_{ae} during Kocaeli DUZ 270 for one bay, one level basement; Site Class D

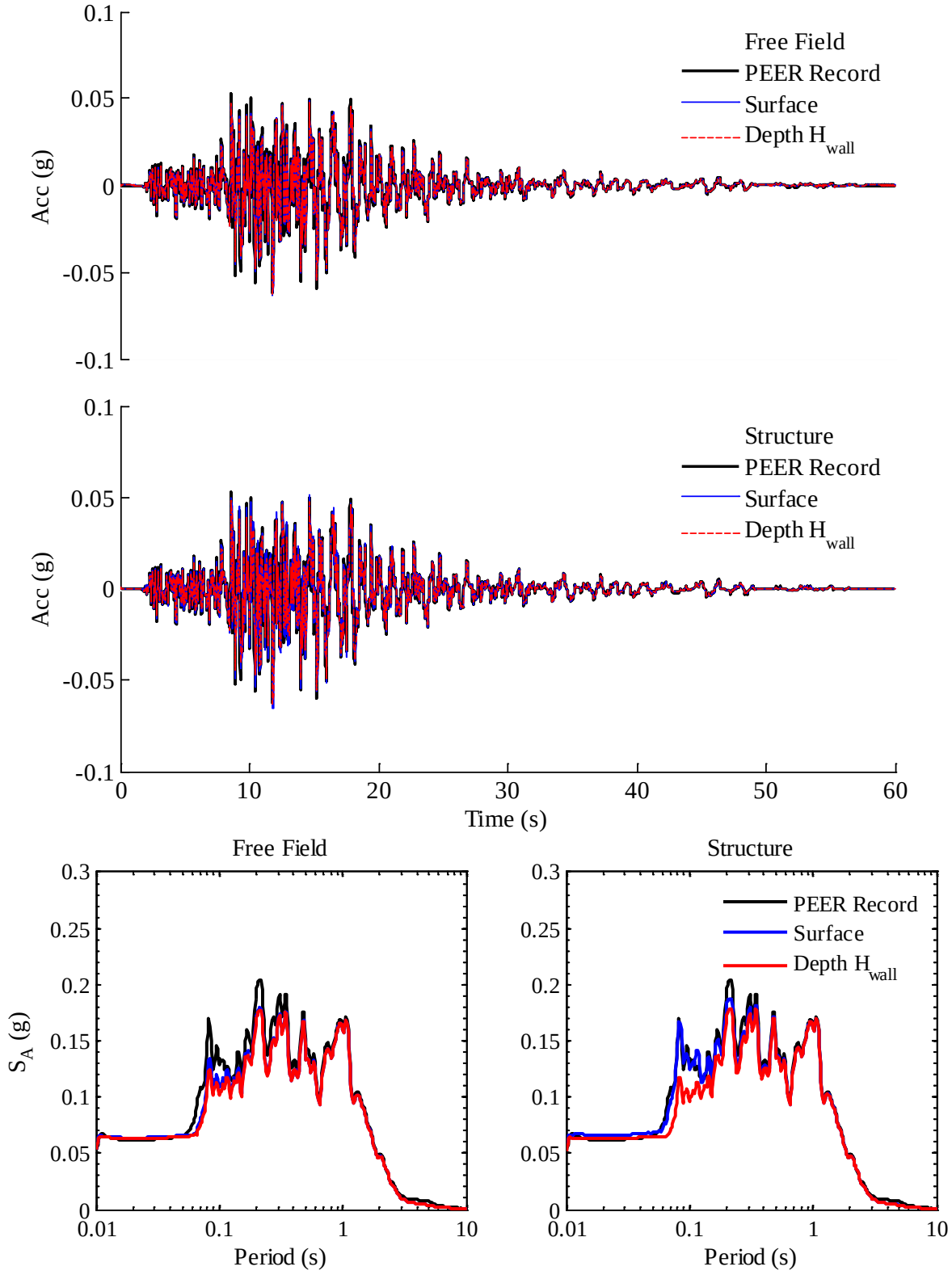

Figure B.71: Computed accelerations and response spectra at 5% damping in free field and structure during Northridge PHP 000 for one level basement; Site Class C

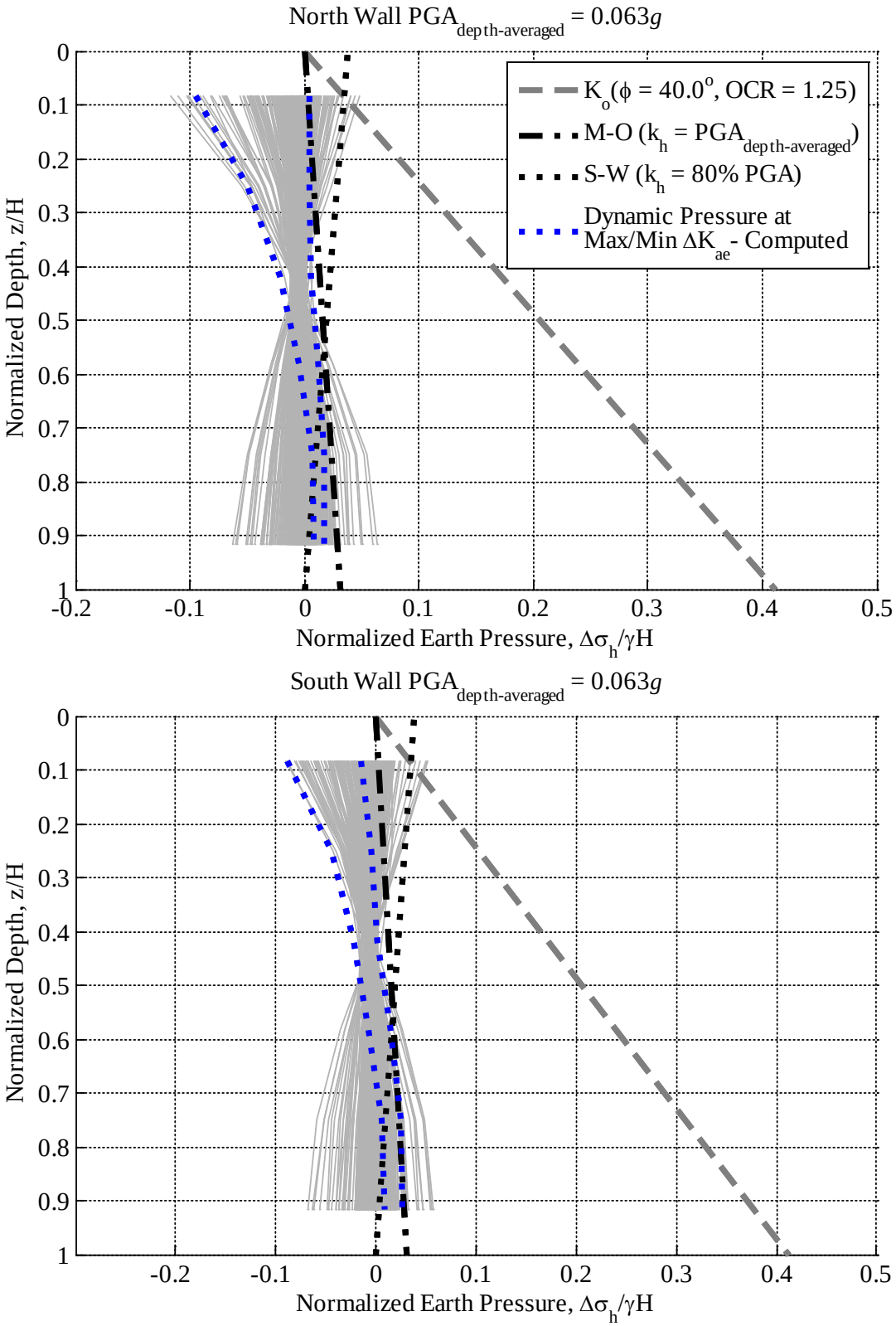

Figure B.72: Computed normalized dynamic earth pressure distributions at maximum and minimum ΔK_{ae} during Northridge PHP 000 for one level basement; Site Class C

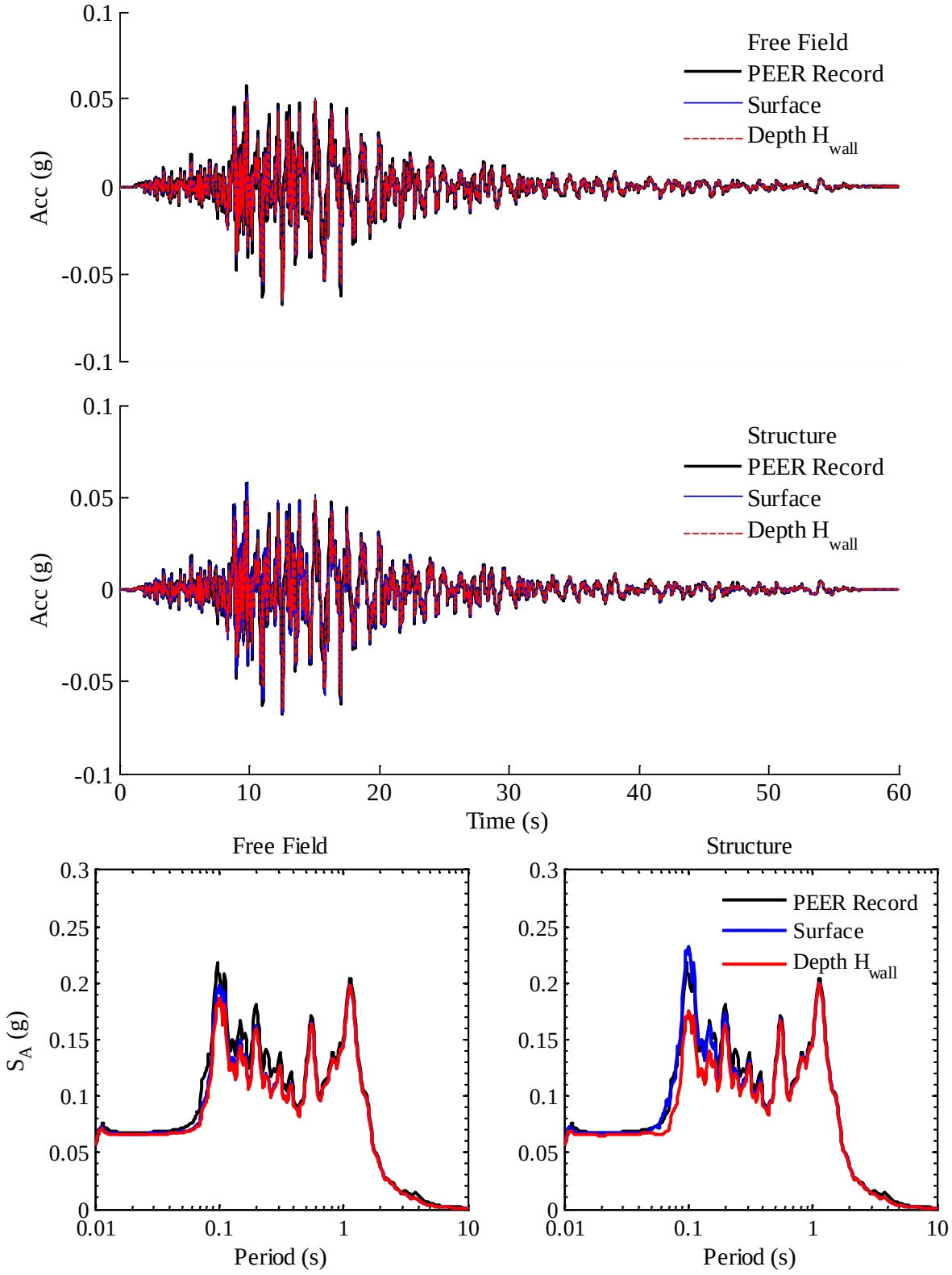

Figure B.73: Computed accelerations and response spectra at 5% damping in free field and structure during Northridge PHP 090 for one level basement; Site Class C

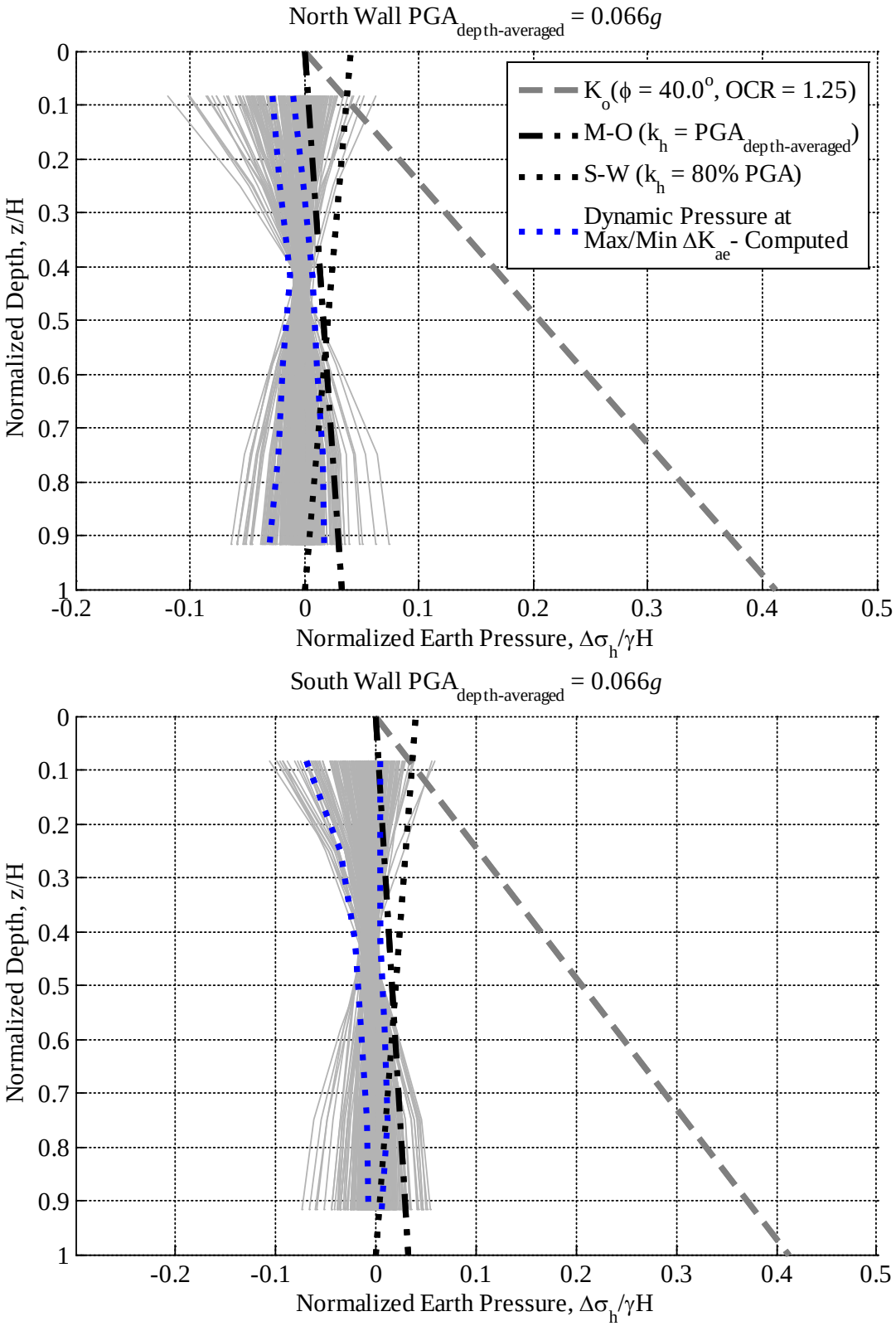

Figure B.74: Computed normalized dynamic earth pressure distributions at maximum and minimum ΔK_{ae} during Northridge PHP 090 for one level basement; Site Class C

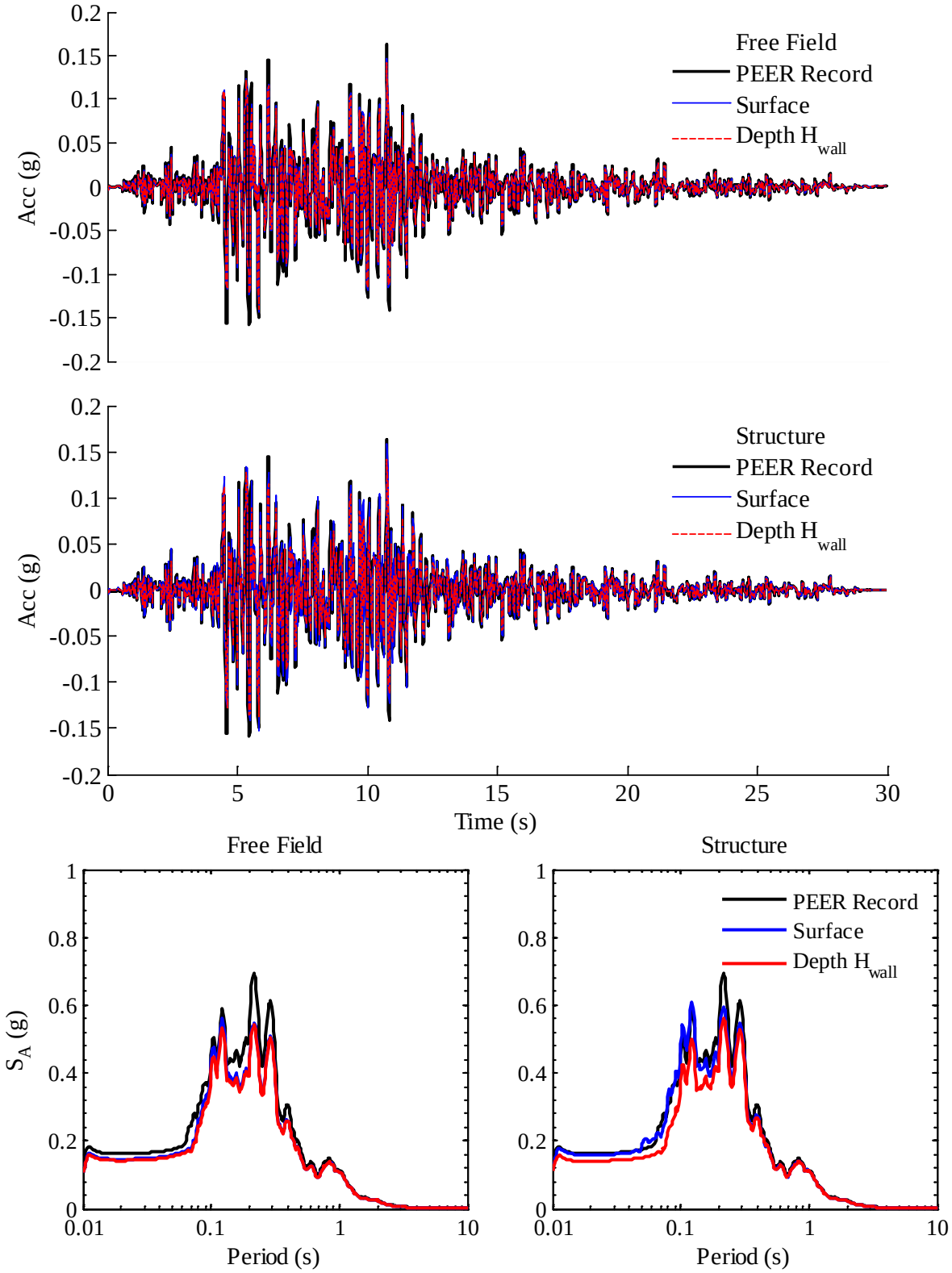

Figure B.75: Computed accelerations and response spectra at 5% damping in free field and structure during Northridge TUJ 262 for one level basement; Site Class C

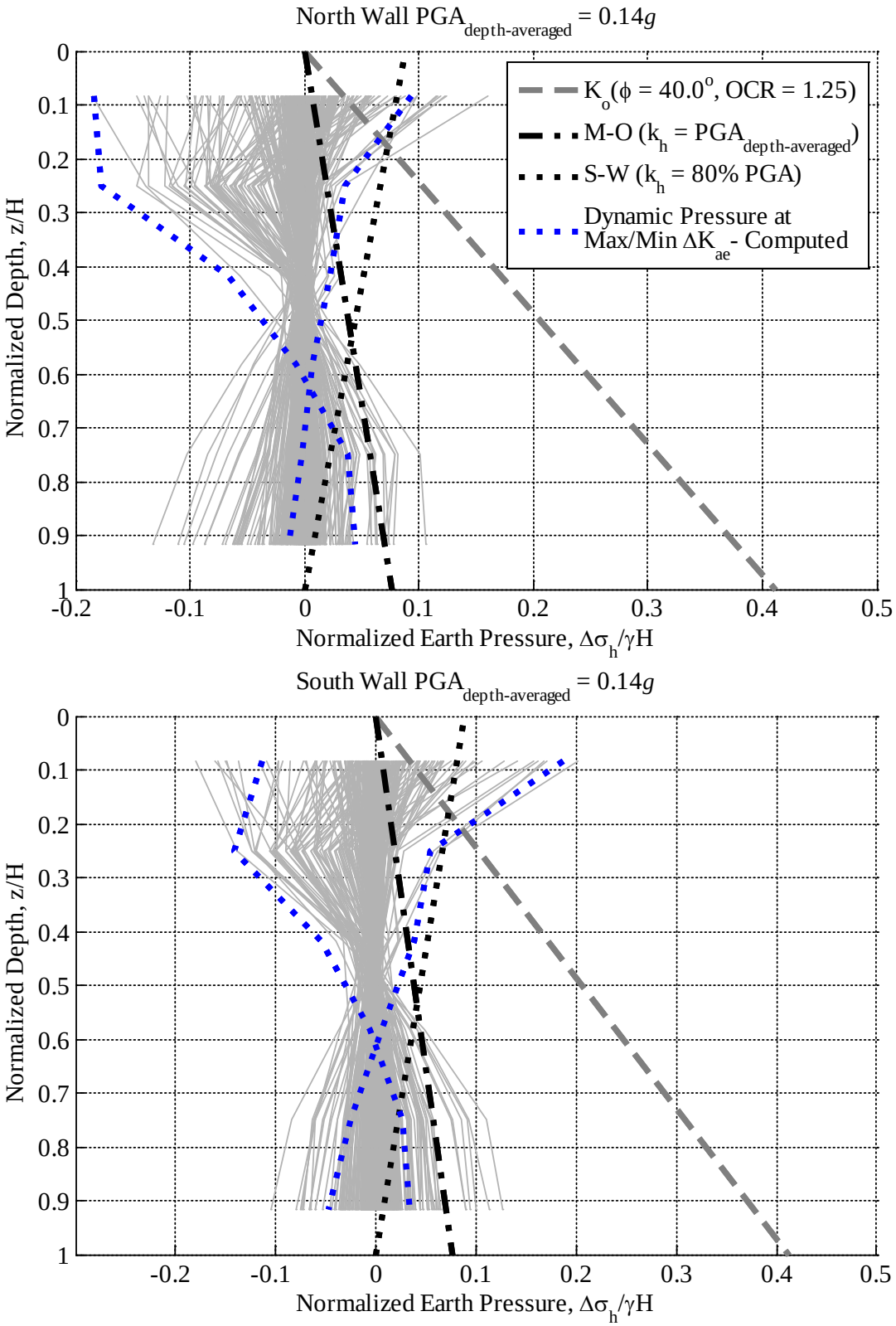

Figure B.76: Computed normalized dynamic earth pressure distributions at maximum and minimum ΔK_{ae} during Northridge TUJ 262 for one level basement; Site Class C

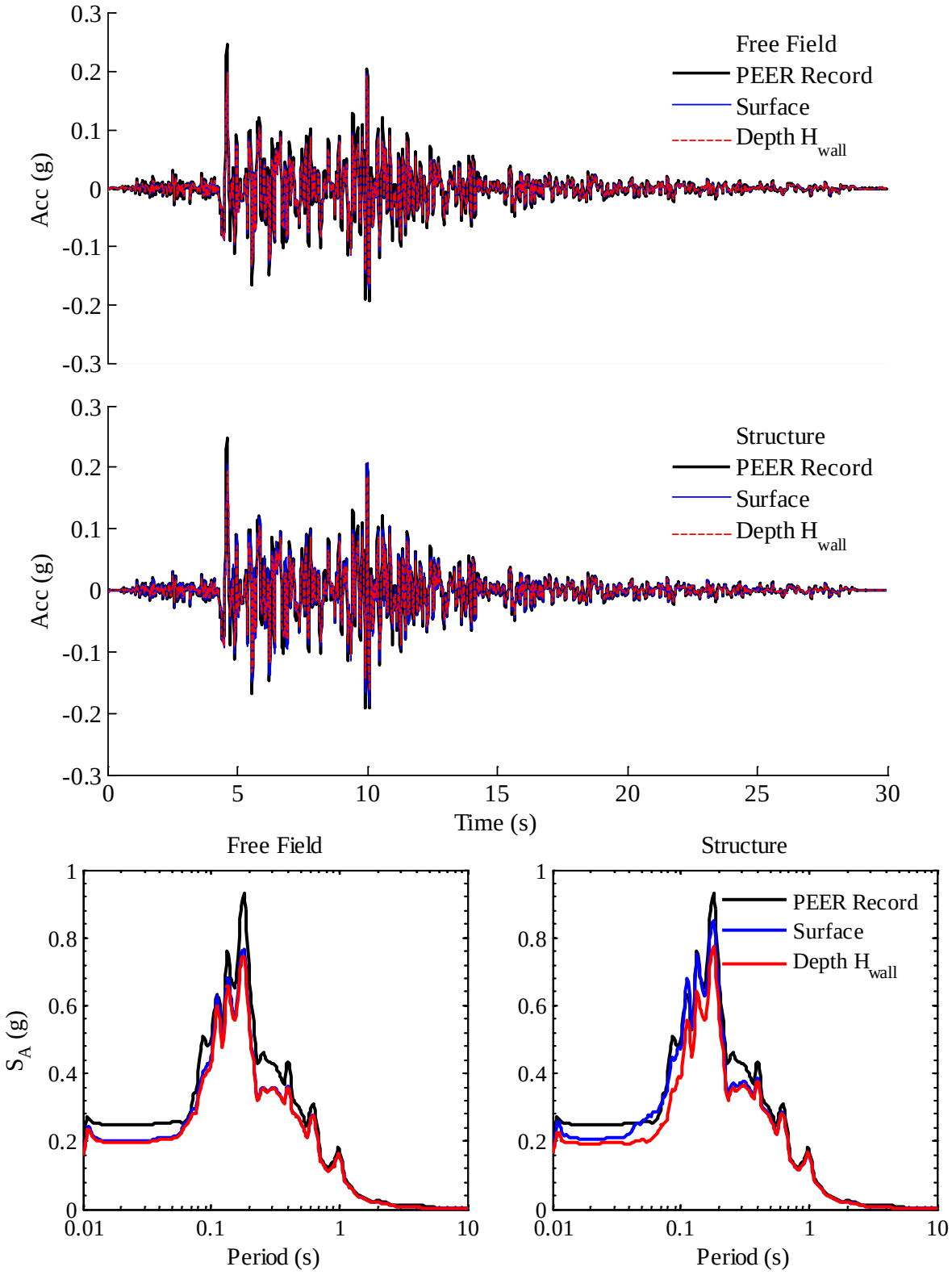

Figure B.77: Computed accelerations and response spectra at 5% damping in free field and structure during Northridge TUJ 352 for one level basement; Site Class C

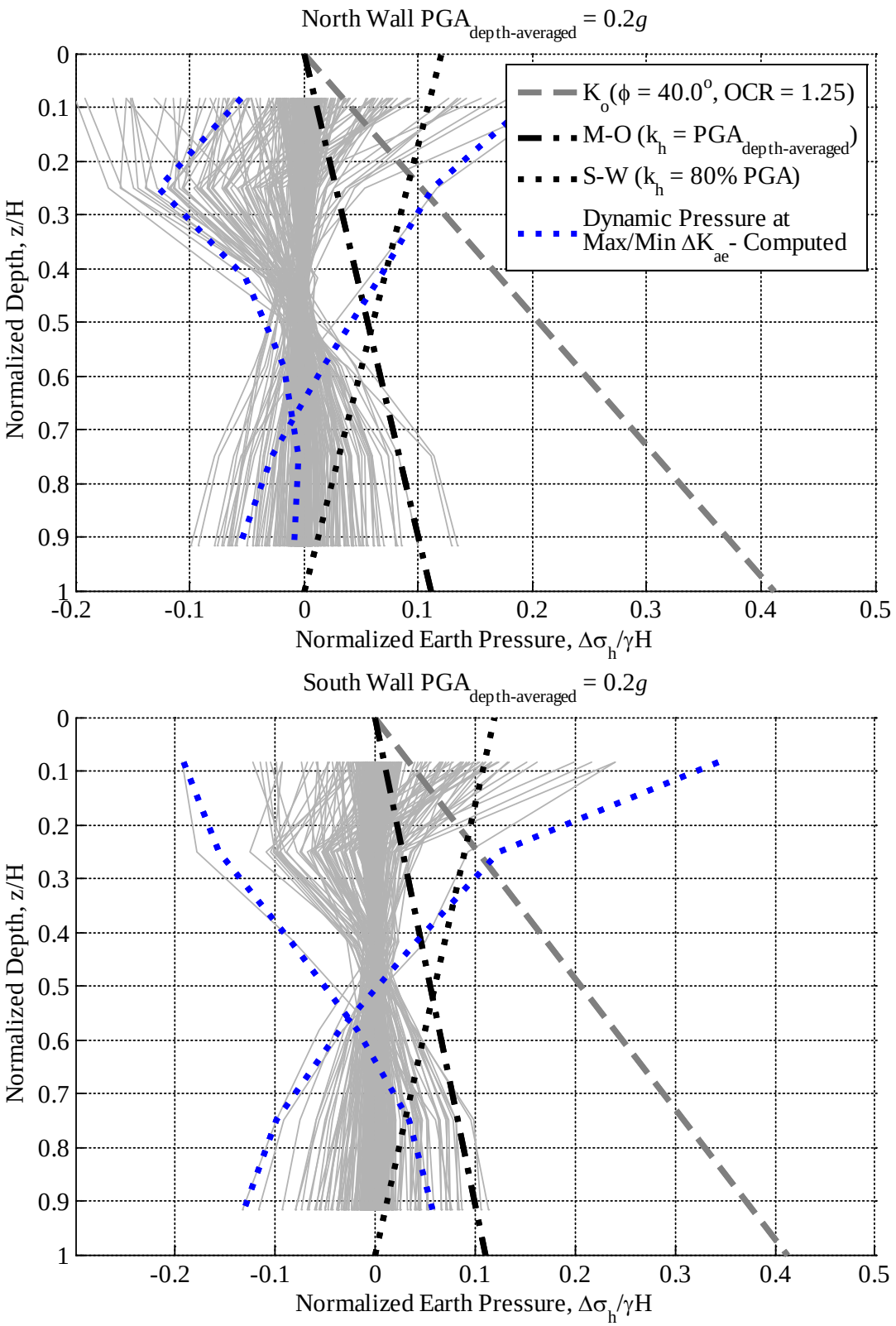

Figure B.78: Computed normalized dynamic earth pressure distributions at maximum and minimum ΔK_{ae} during Northridge TUJ 352 for one level basement; Site Class C

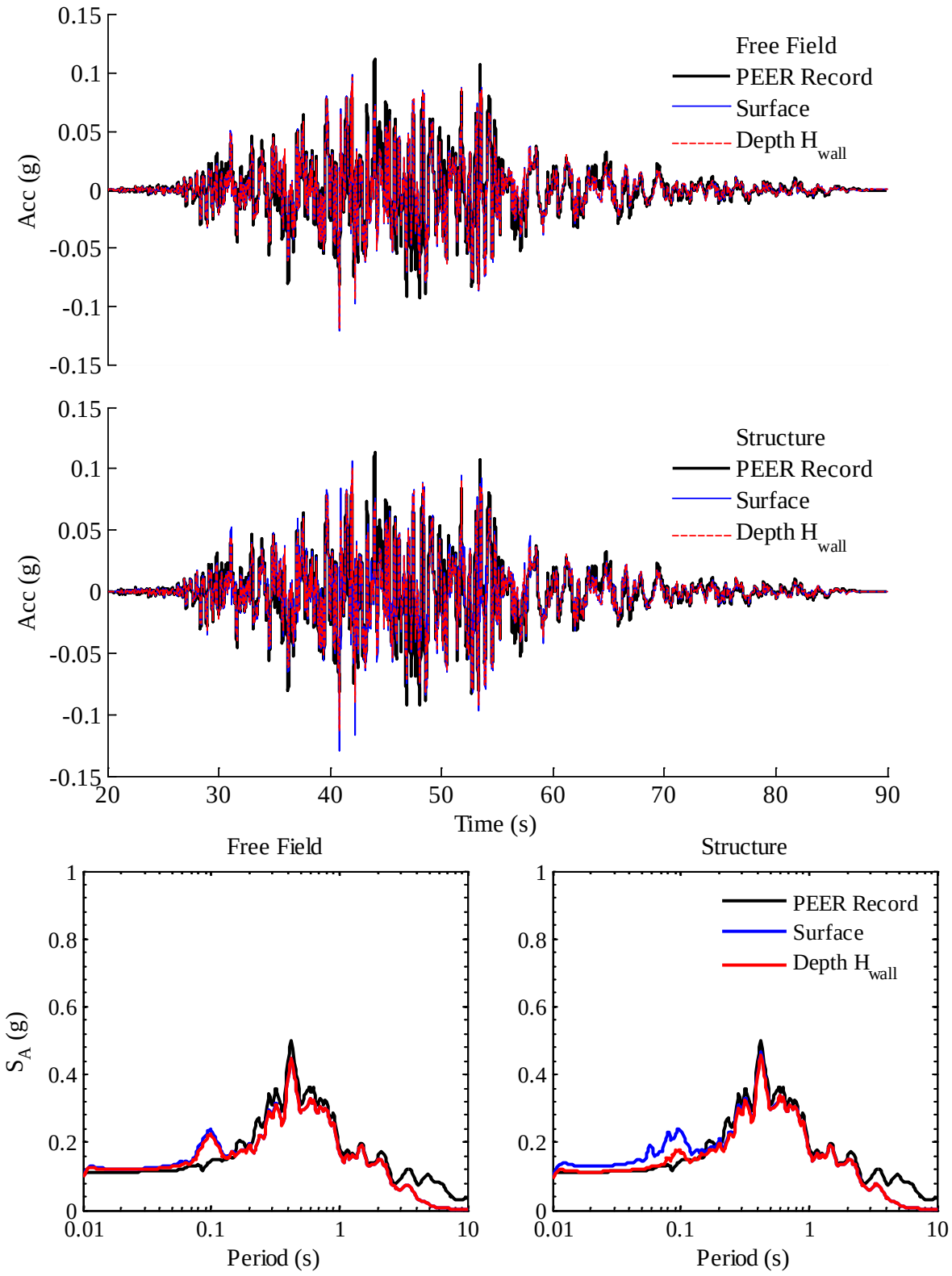

Figure B.79: Computed accelerations and response spectra at 5% damping in free field and structure during Chi Chi TCU 105E for one level basement; Site Class C

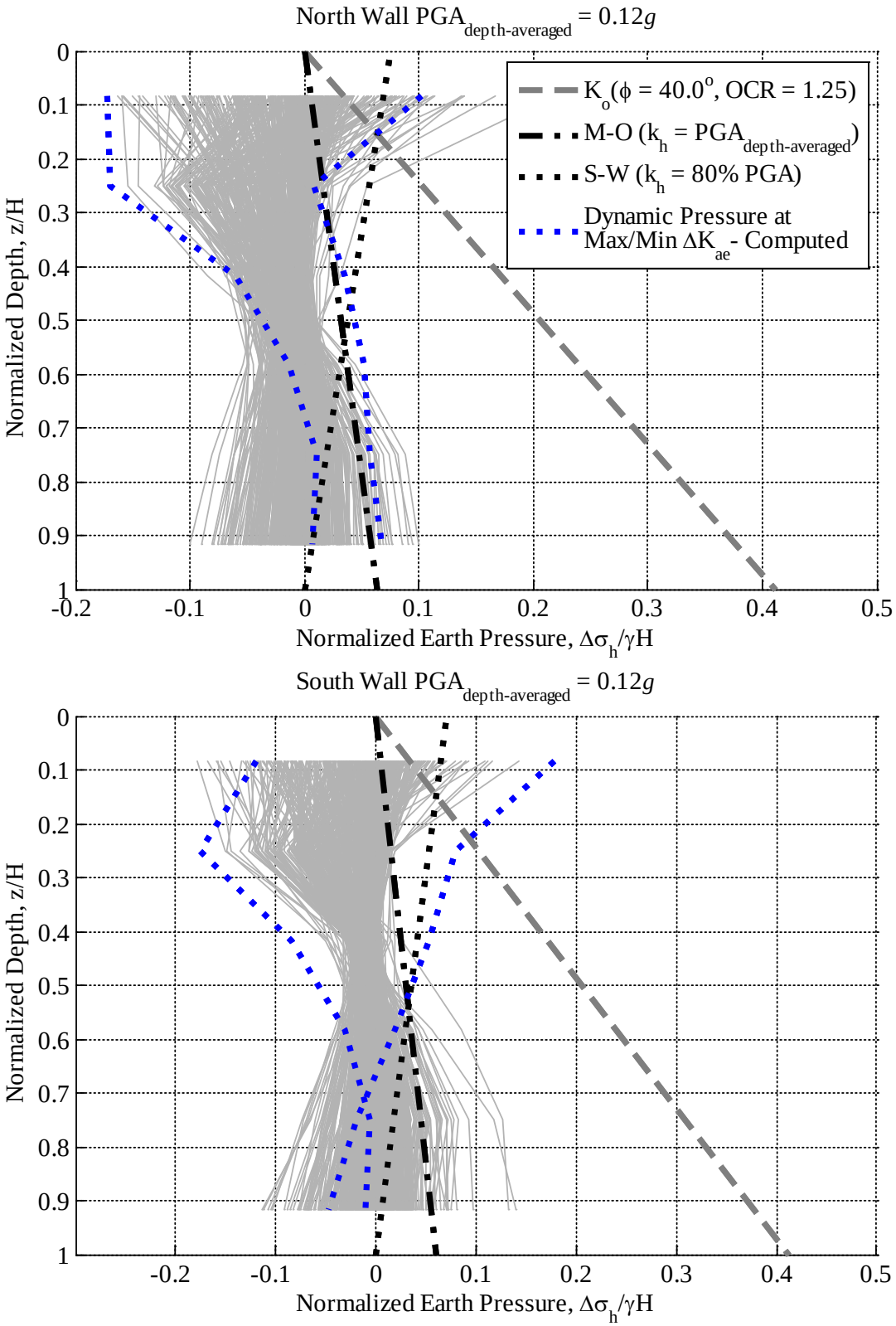

Figure B.80: Computed normalized dynamic earth pressure distributions at maximum and minimum ΔK_{ae} during Chi Chi TCU 105E for one level basement; Site Class C

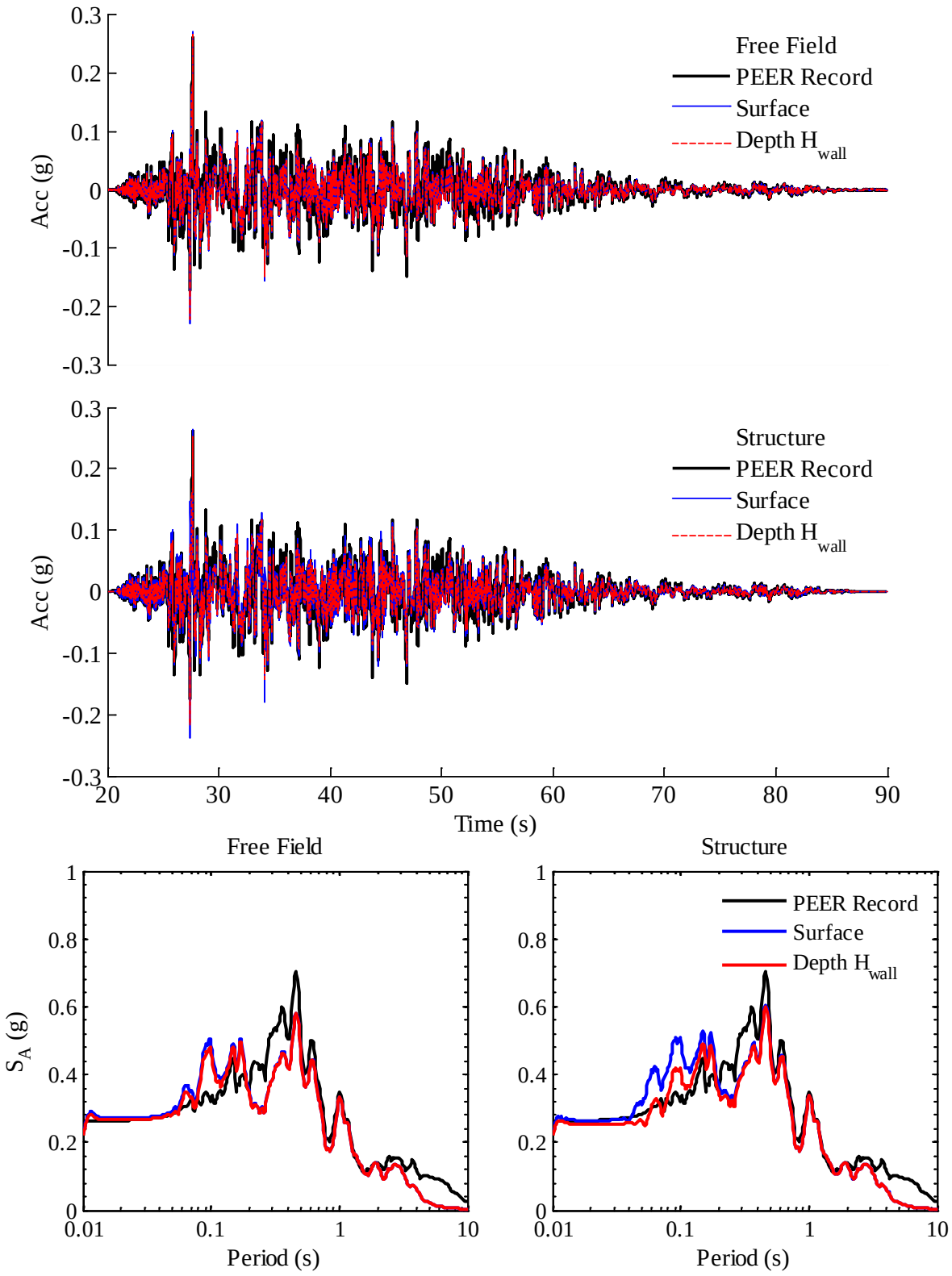

Figure B.81: Computed accelerations and response spectra at 5% damping in free field and structure during Chi Chi TCU 075N for one level basement; Site Class C

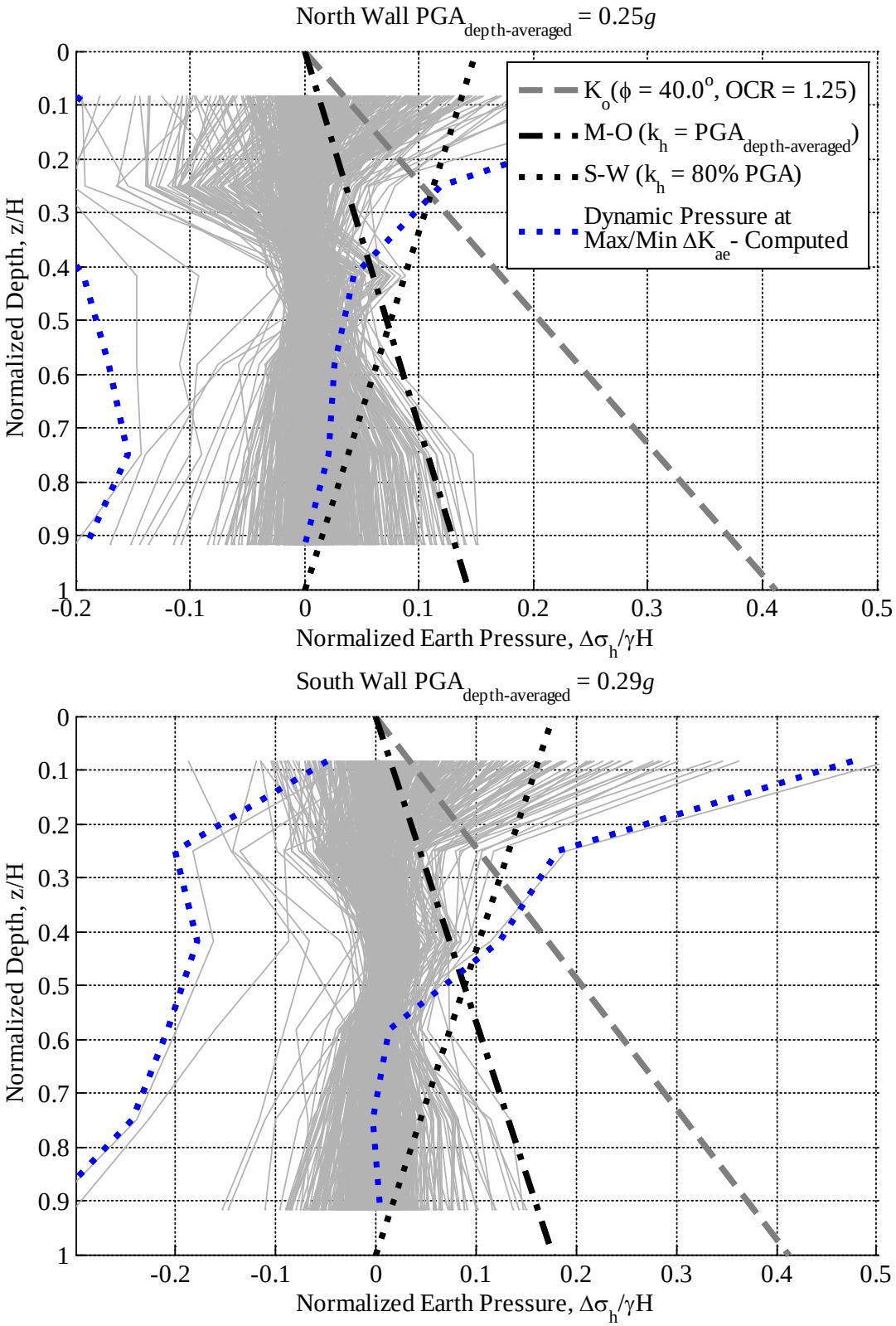

Figure B.82: Computed normalized dynamic earth pressure distributions at maximum and minimum ΔK_{ae} during Chi Chi TCU 075N for one level basement; Site Class C

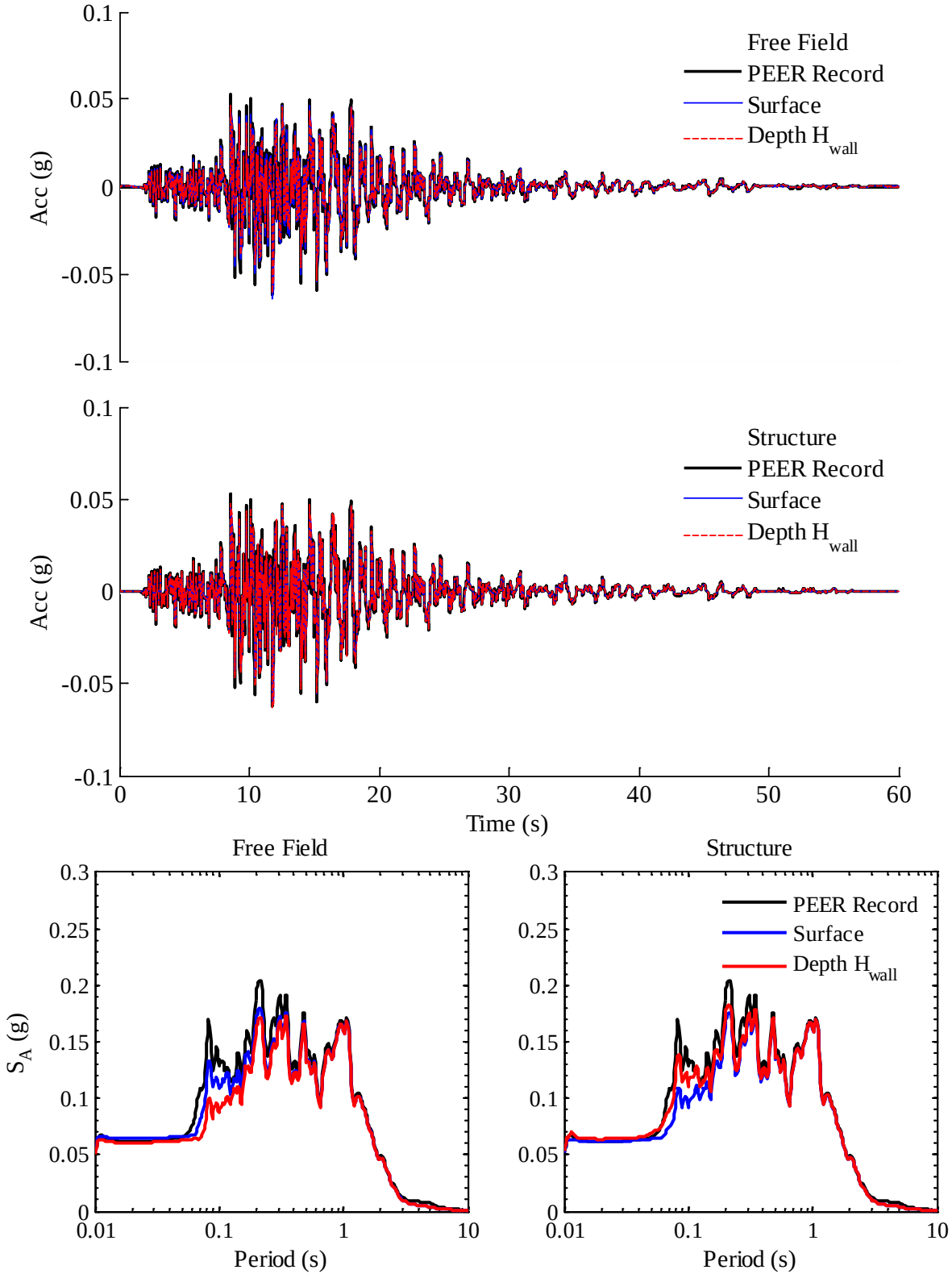

Figure B.83: Computed accelerations and response spectra at 5% damping in free field and structure during Northridge PHP 000 for two level basement; Site Class C

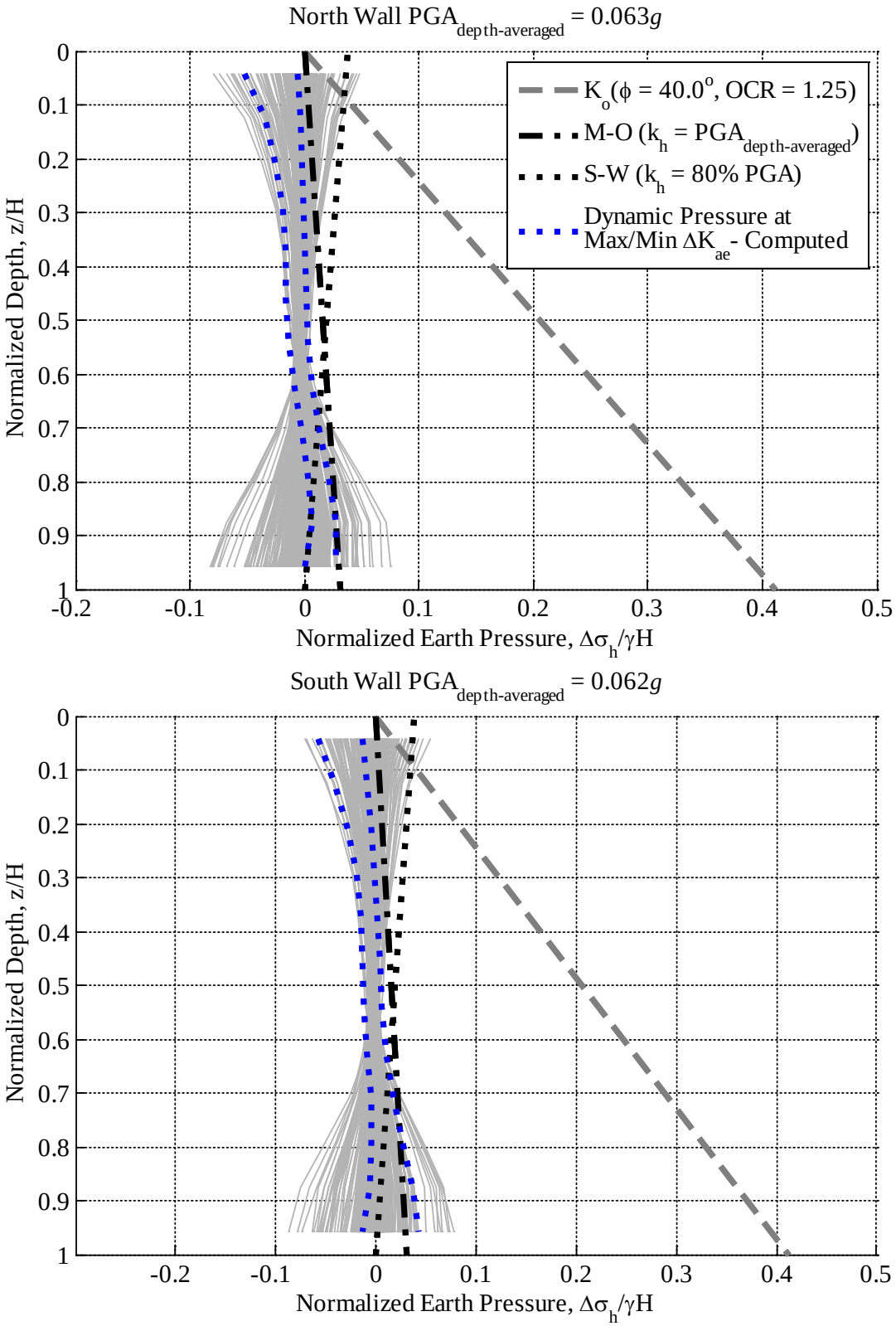

Figure B.84: Computed normalized dynamic earth pressure distributions at maximum and minimum ΔK_{ae} during Northridge PHP 000 for two level basement; Site Class C

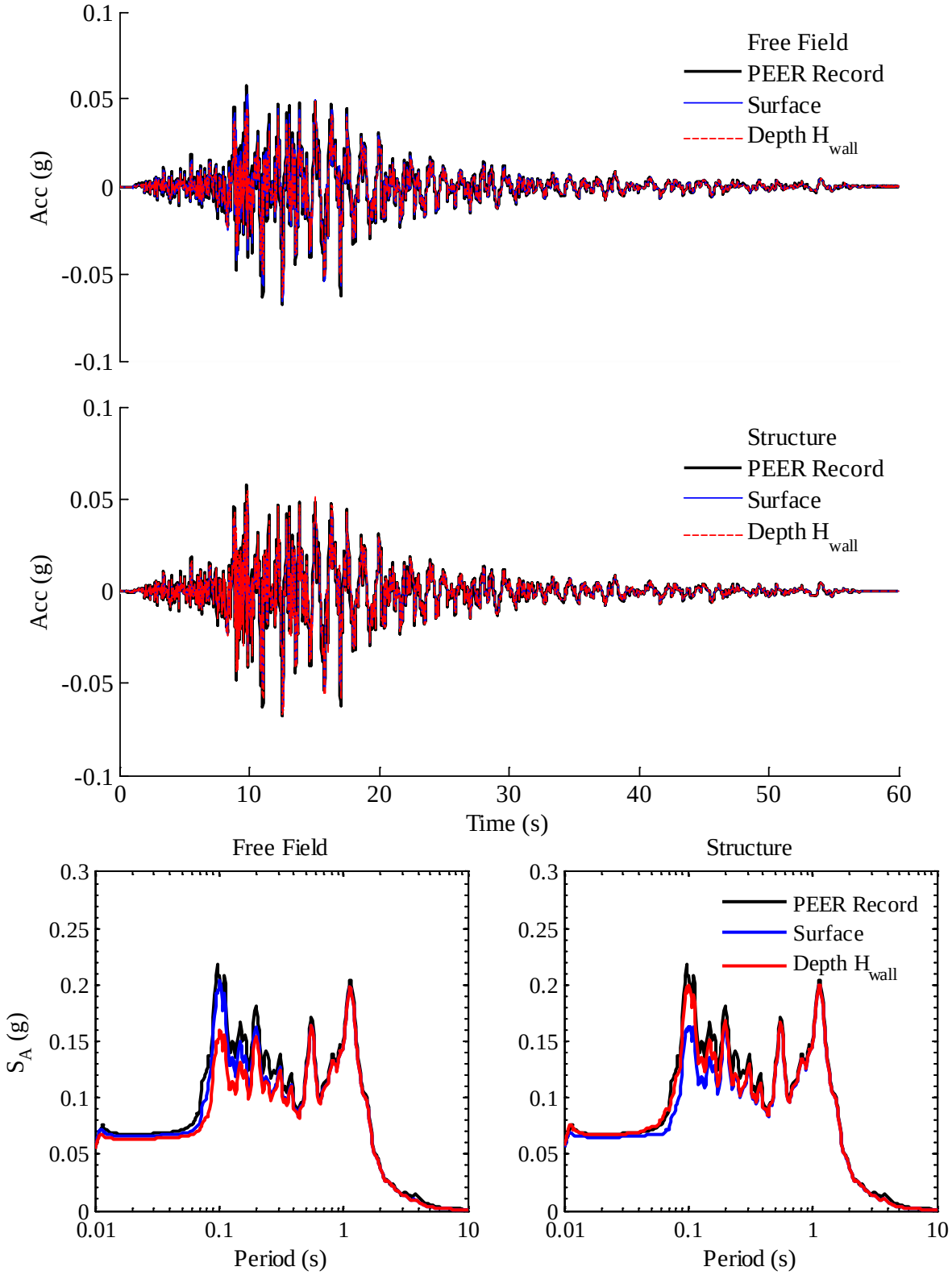

Figure B.85: Computed accelerations and response spectra at 5% damping in free field and structure during Northridge PHP 090 for two level basement; Site Class C

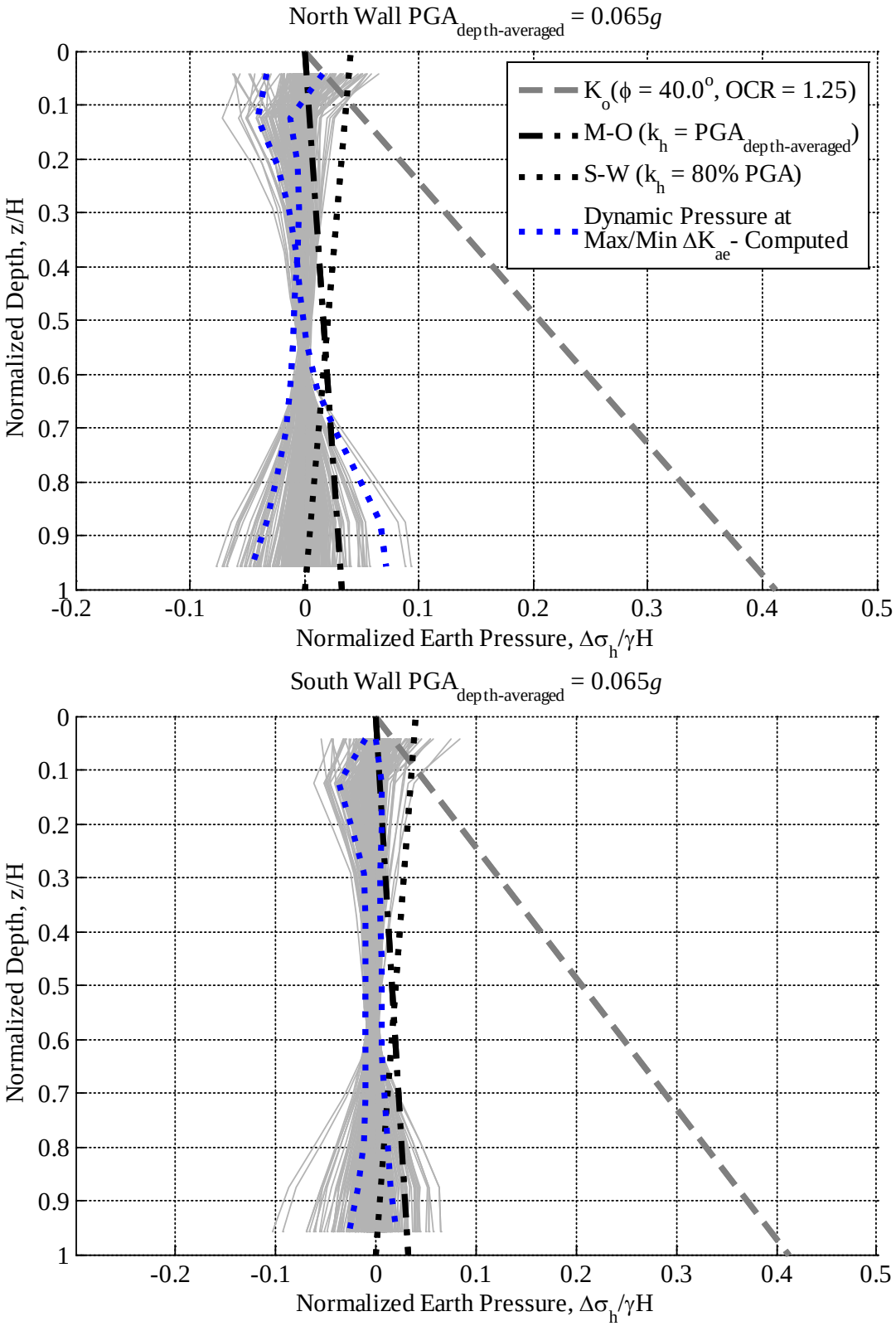

Figure B.86: Computed normalized dynamic earth pressure distributions at maximum and minimum ΔK_{ae} during Northridge PHP 090 for two level basement; Site Class C

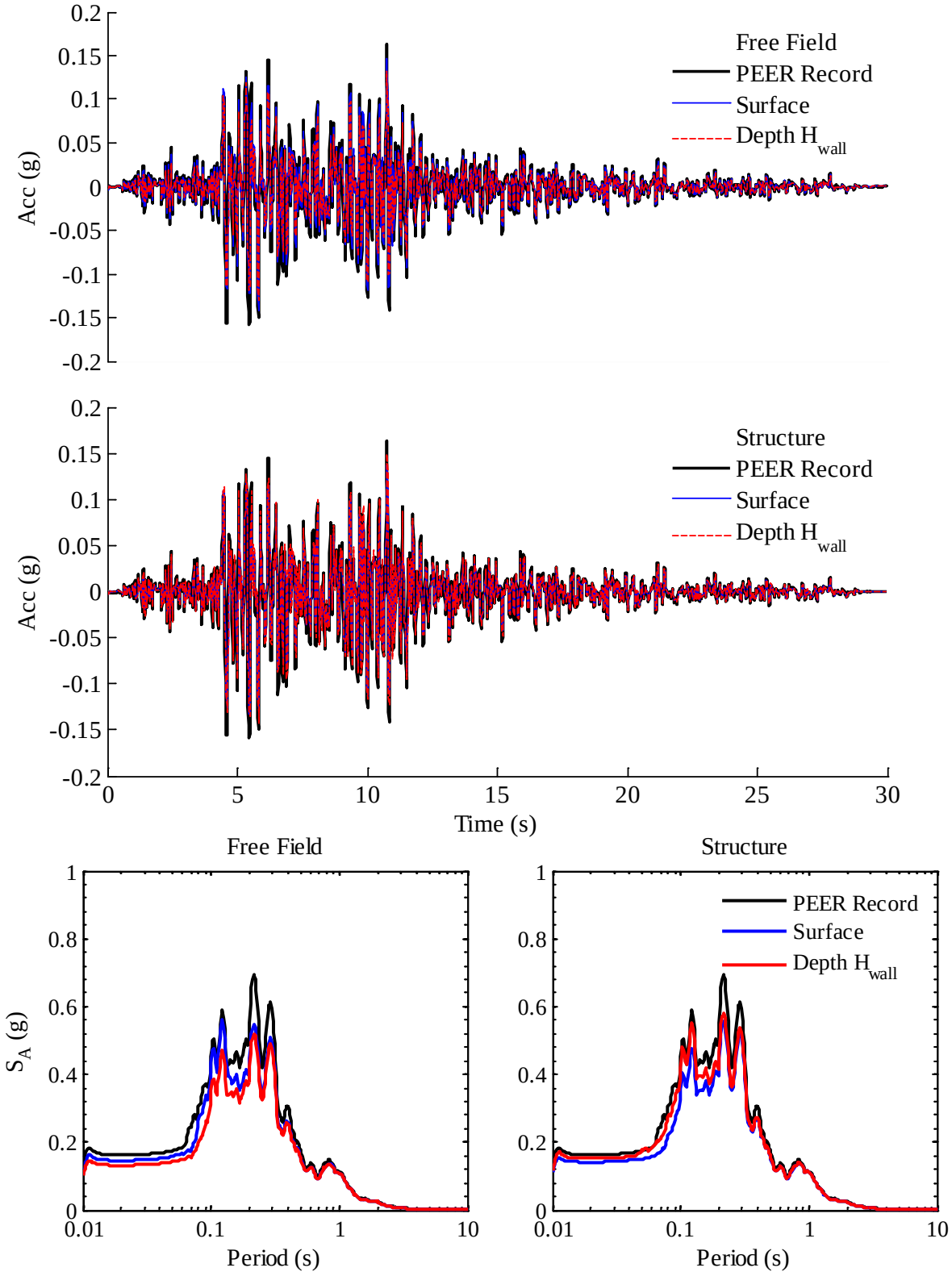

Figure B.87: Computed accelerations and response spectra at 5% damping in free field and structure during Northridge TUJ 262 for two level basement; Site Class C

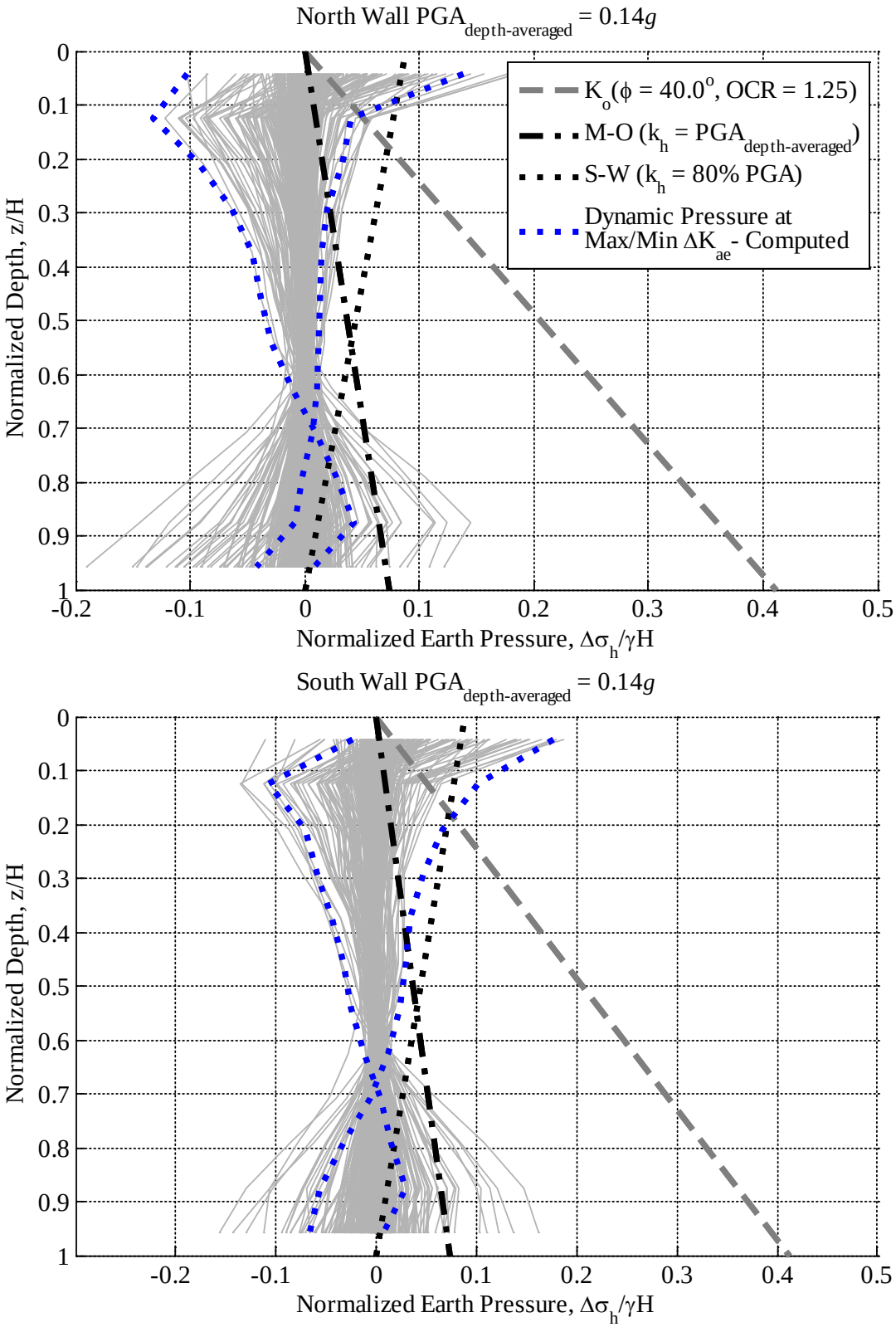

Figure B.88: Computed normalized dynamic earth pressure distributions at maximum and minimum ΔK_{ae} during Northridge TUJ 262 for two level basement; Site Class C

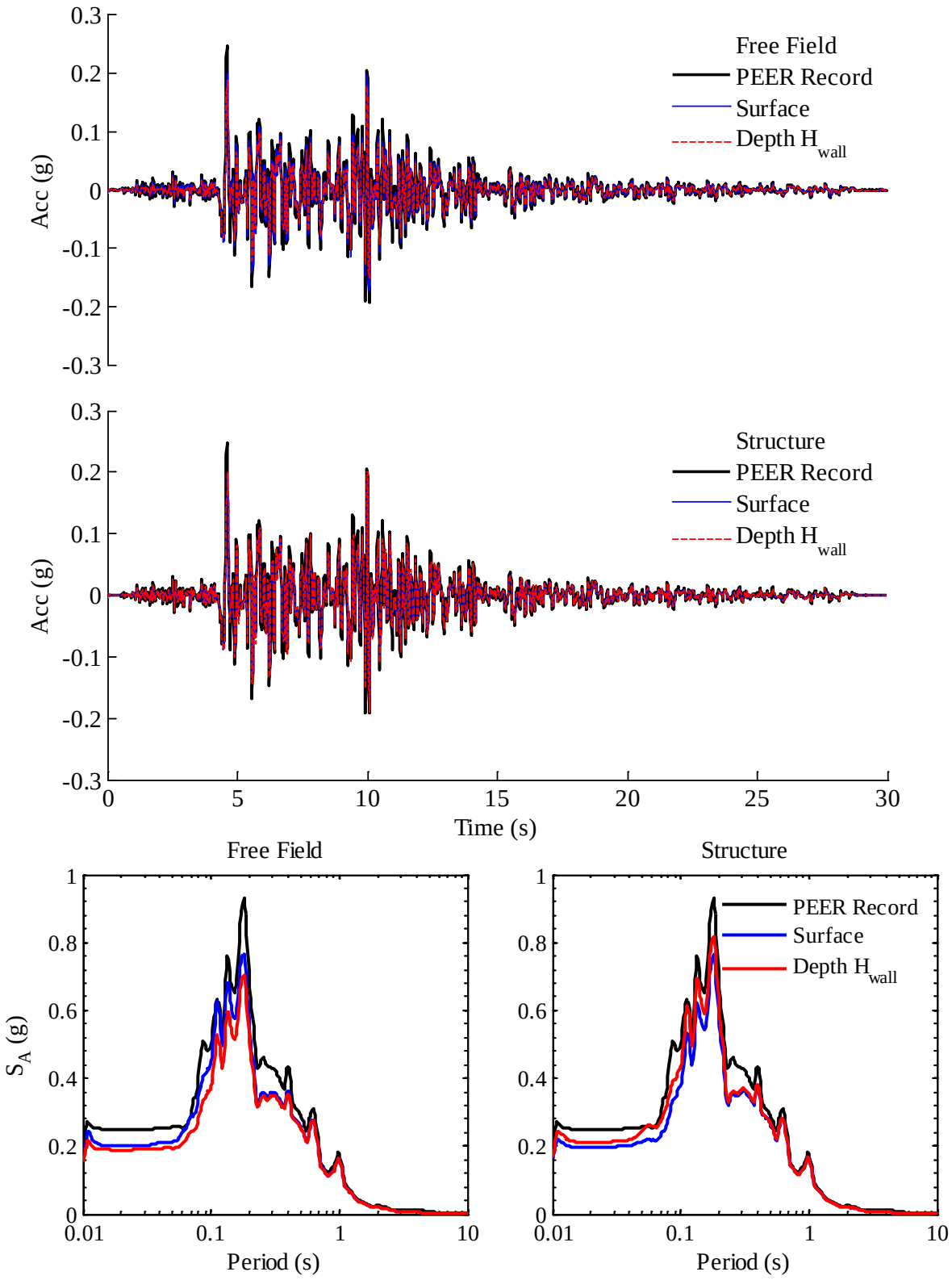

Figure B.89: Computed accelerations and response spectra at 5% damping in free field and structure during Northridge TUJ 352 for two level basement; Site Class C

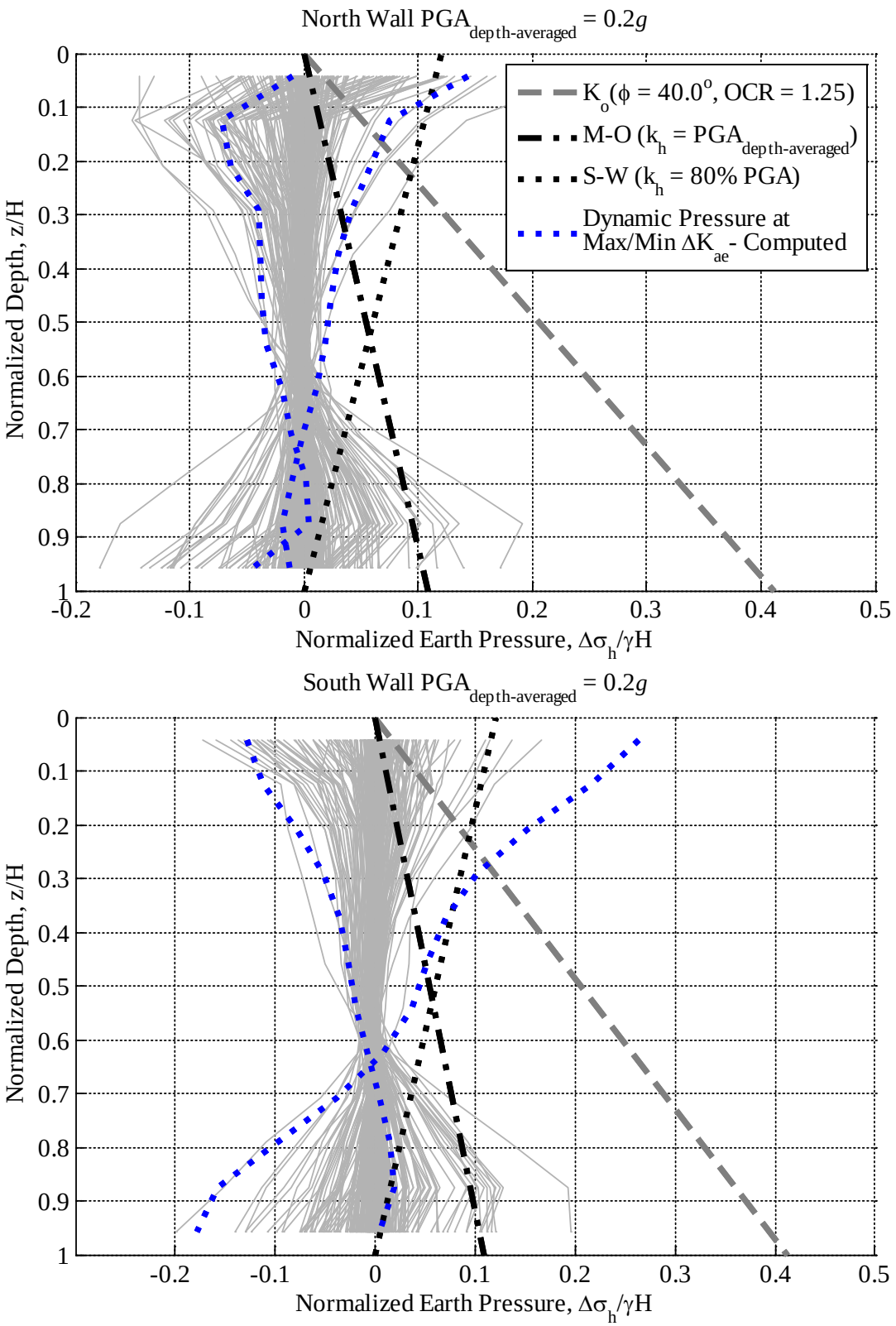

Figure B.90: Computed normalized dynamic earth pressure distributions at maximum and minimum ΔK_{ae} during Northridge TUJ 352 for two level basement; Site Class C

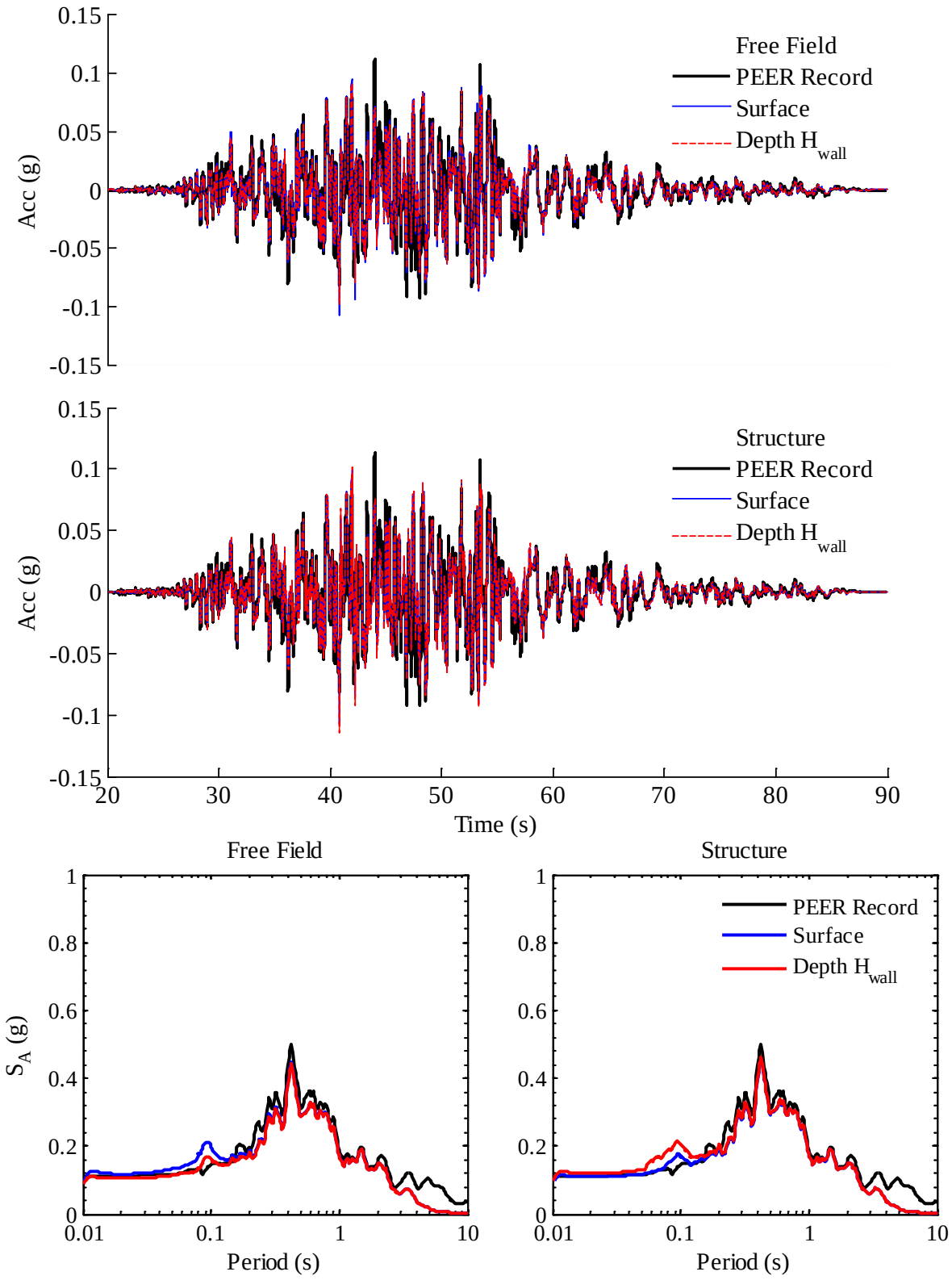

Figure B.91: Computed accelerations and response spectra at 5% damping in free field and structure during Chi Chi TCU 105E for two level basement; Site Class C

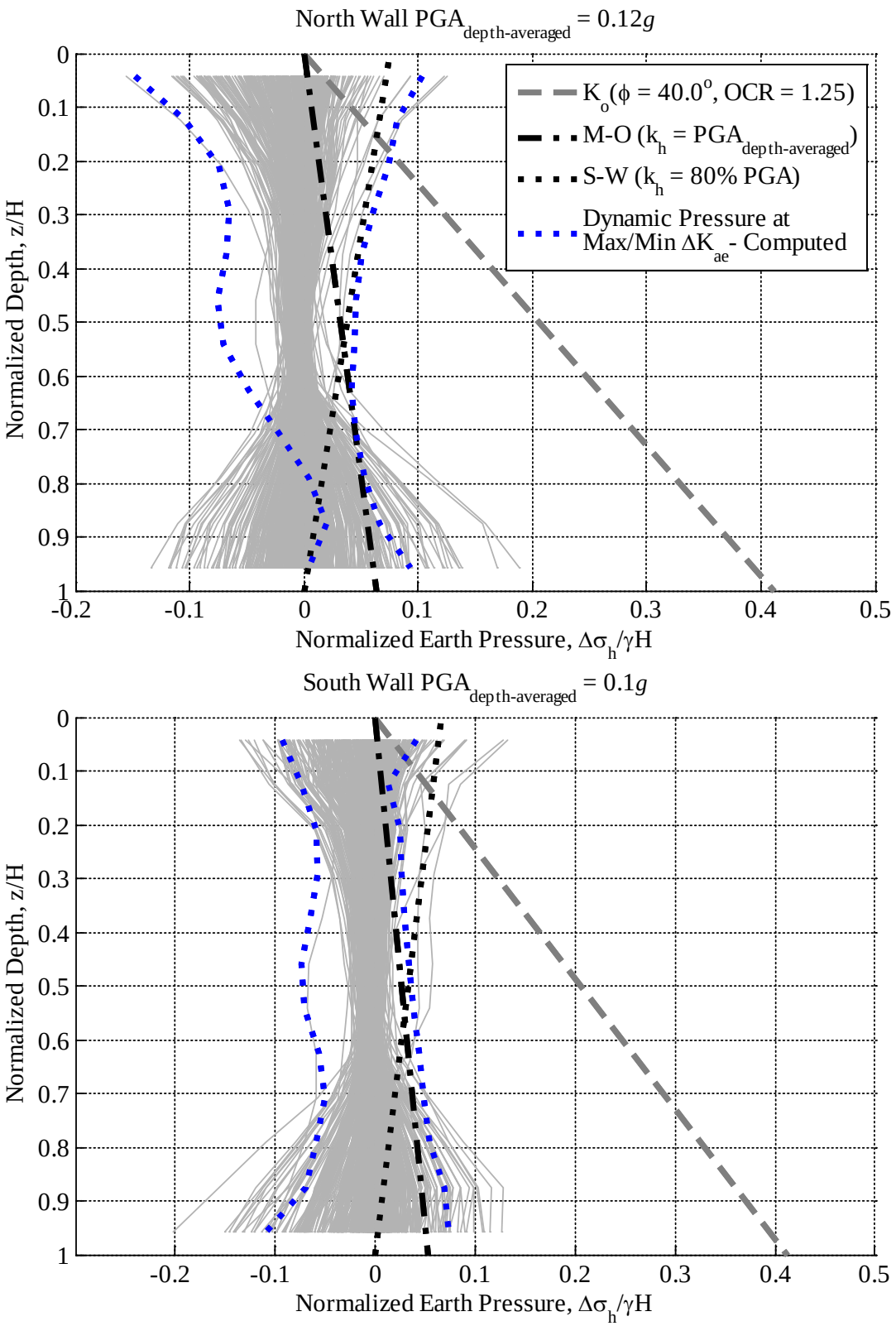

Figure B.92: Computed normalized dynamic earth pressure distributions at maximum and minimum ΔK_{ae} during Chi Chi TCU 105E for two level basement; Site Class C

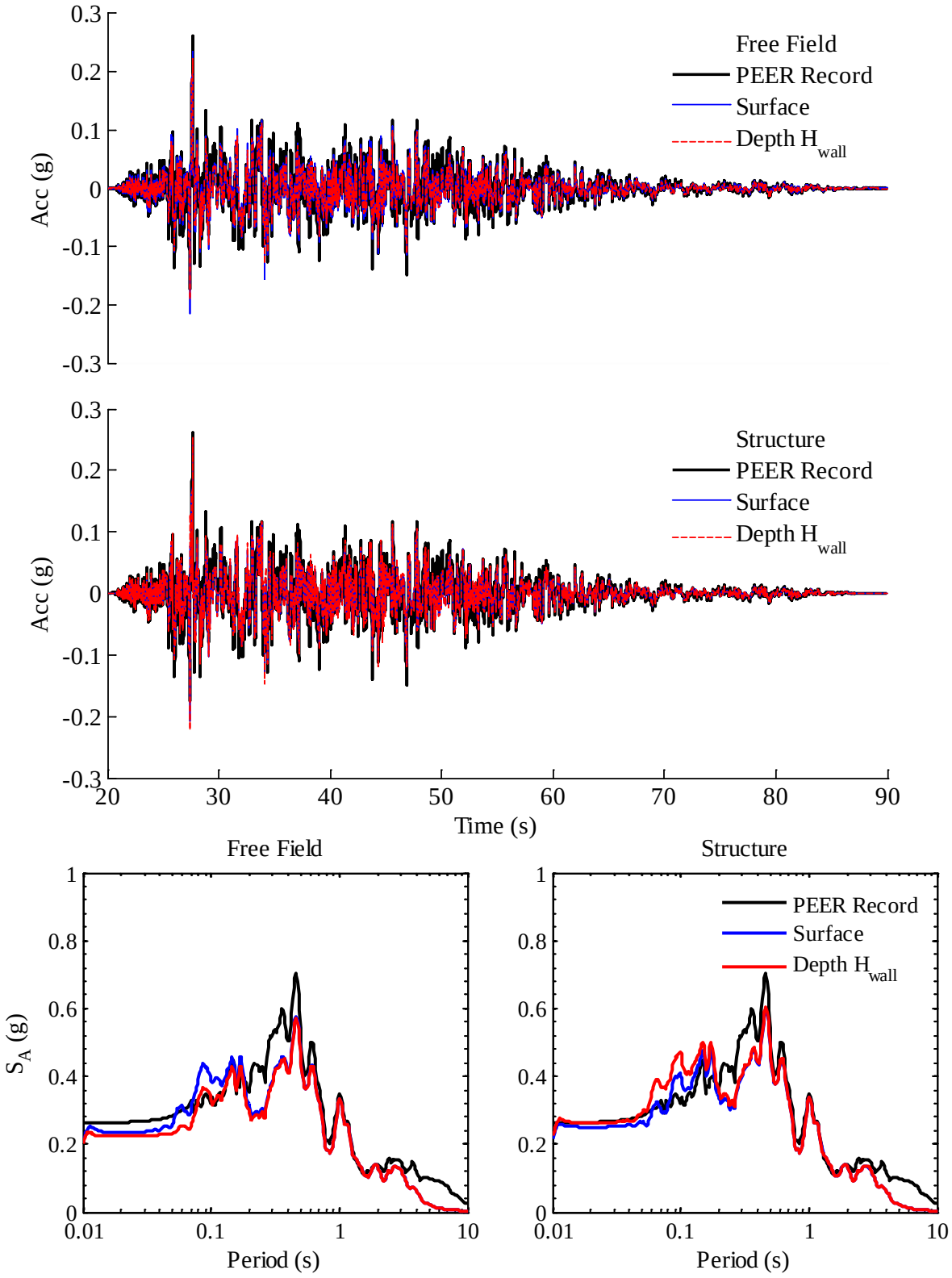

Figure B.93: Computed accelerations and response spectra at 5% damping in free field and structure during Chi Chi TCU 075N for two level basement; Site Class C

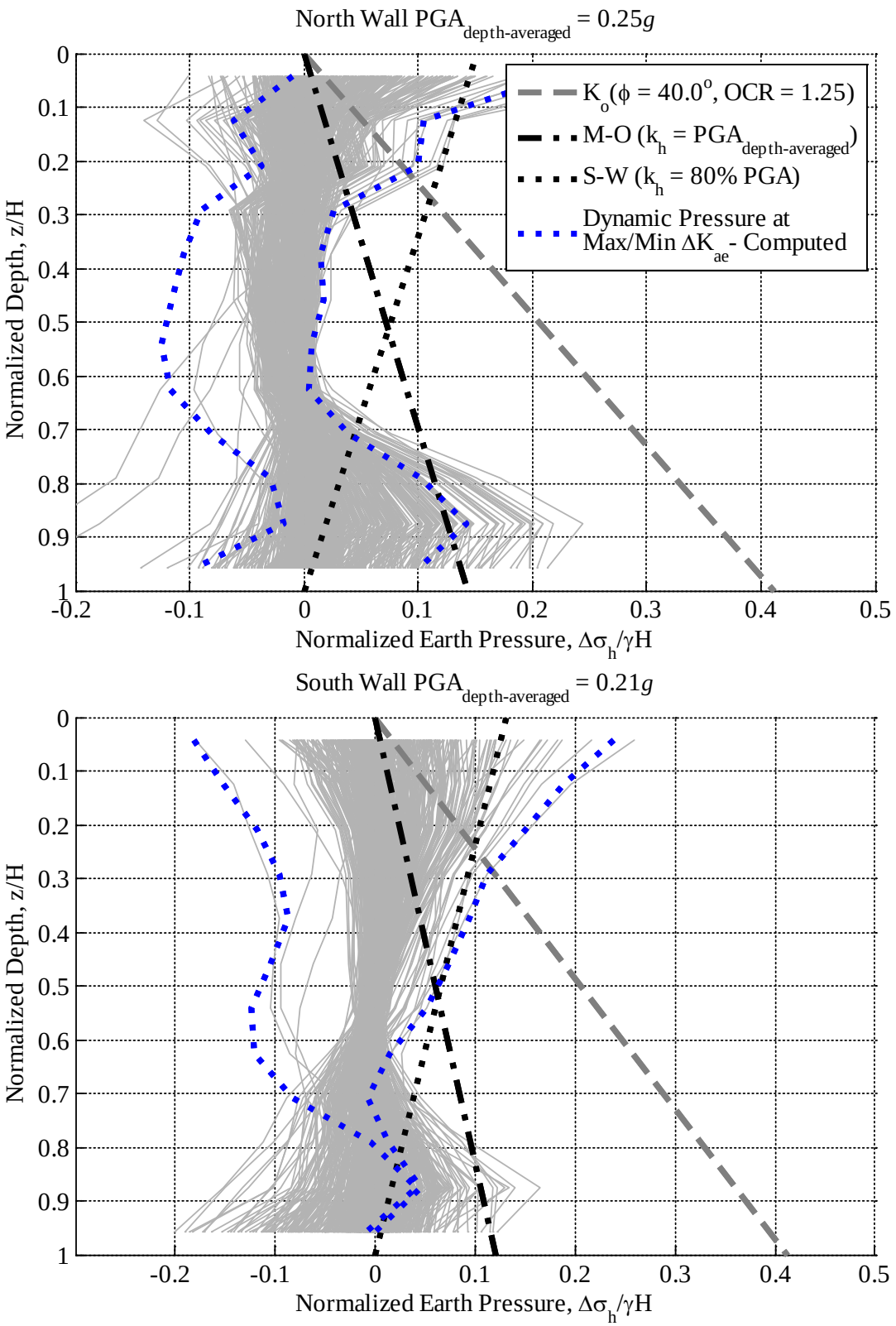

Figure B.94: Computed normalized dynamic earth pressure distributions at maximum and minimum ΔK_{ae} during Chi Chi TCU 075N for two level basement; Site Class C

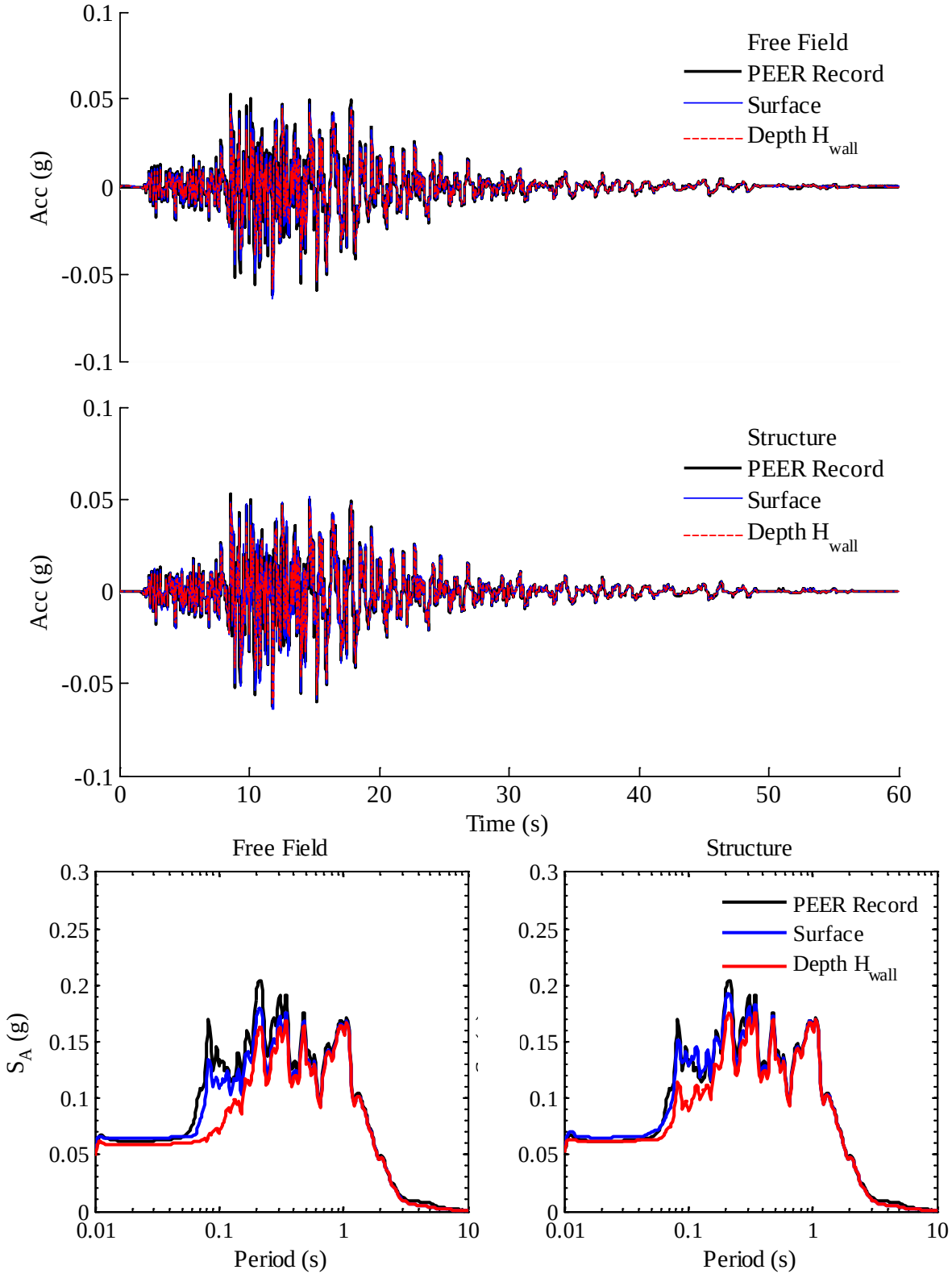

Figure B.95: Computed accelerations and response spectra at 5% damping in free field and structure during Northridge PHP 000 for three level basement; Site Class C

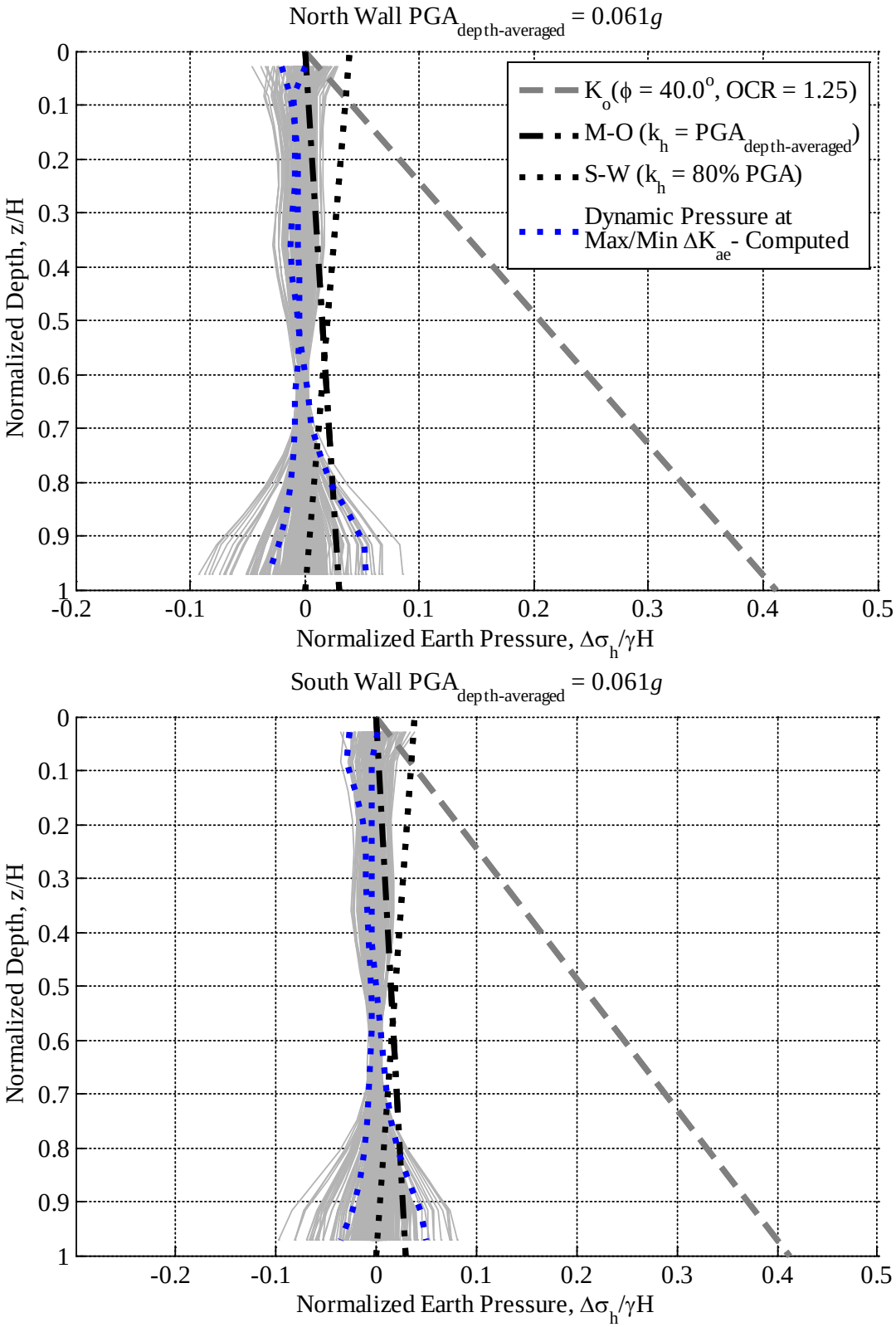

Figure B.96: Computed normalized dynamic earth pressure distributions at maximum and minimum ΔK_{ae} during Northridge PHP 000 for three level basement; Site Class C

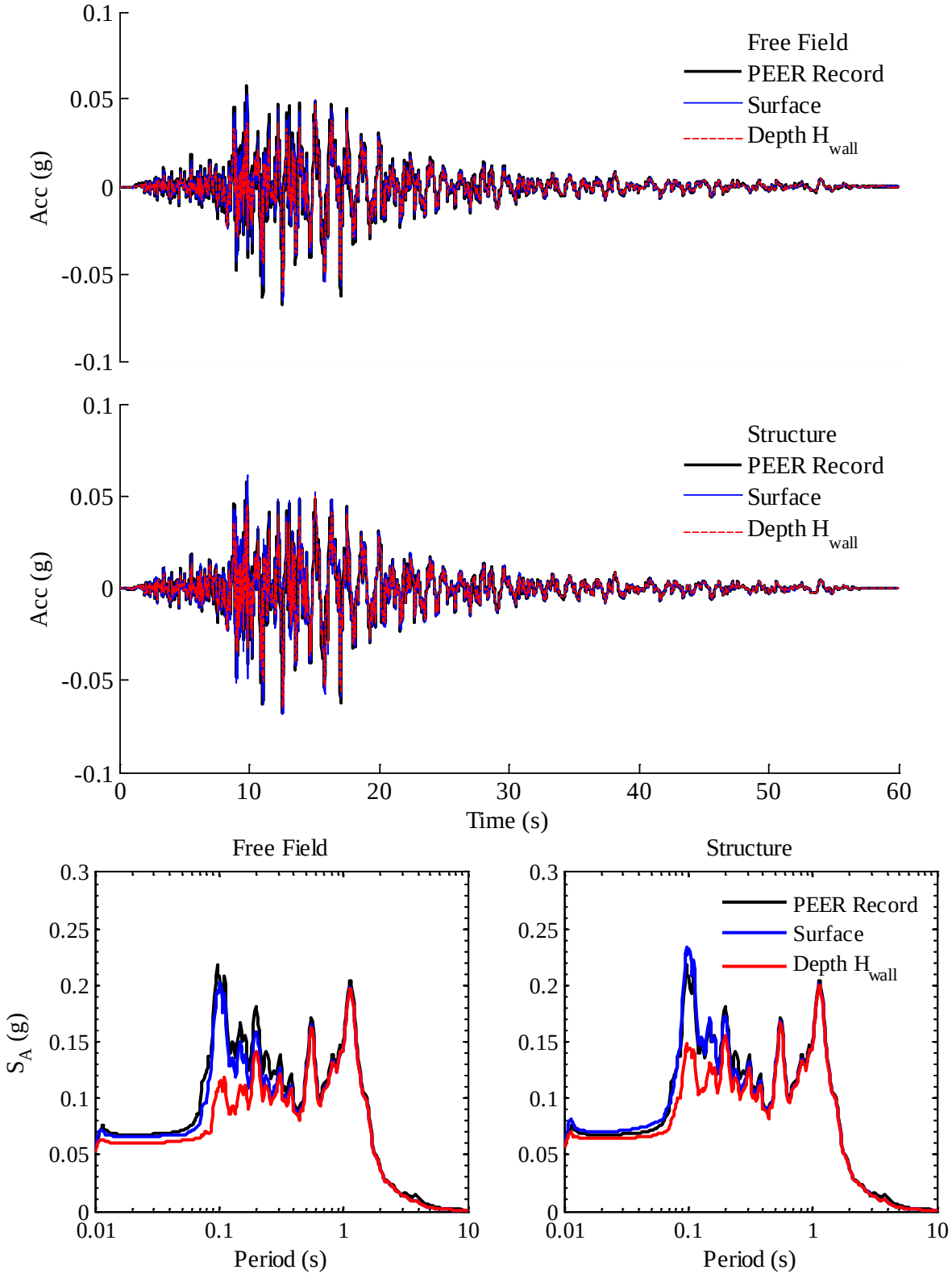

Figure B.97: Computed accelerations and response spectra at 5% damping in free field and structure during Northridge PHP 090 for three level basement; Site Class C

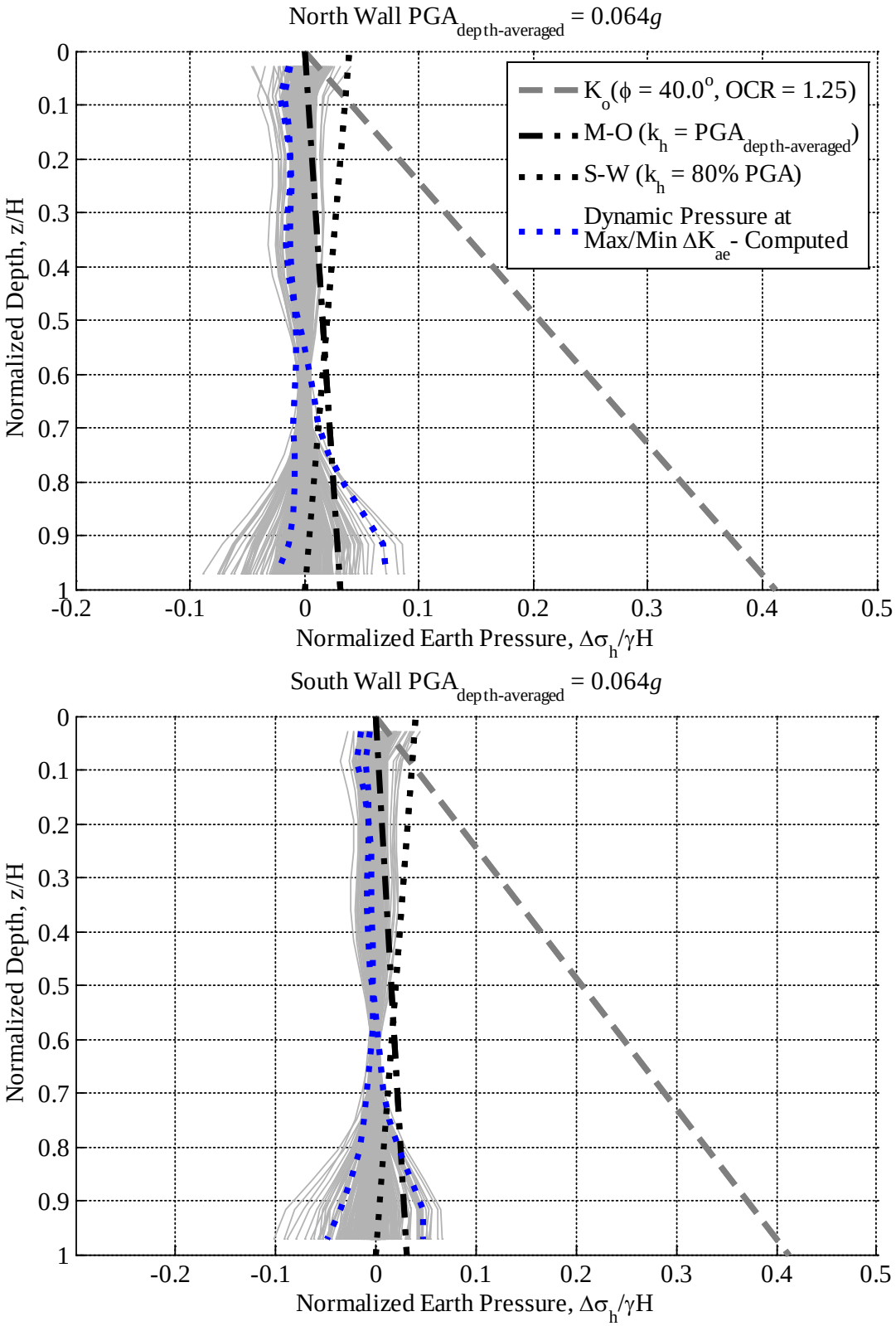

Figure B.98: Computed normalized dynamic earth pressure distributions at maximum and minimum ΔK_{ae} during Northridge PHP 090 for three level basement; Site Class C

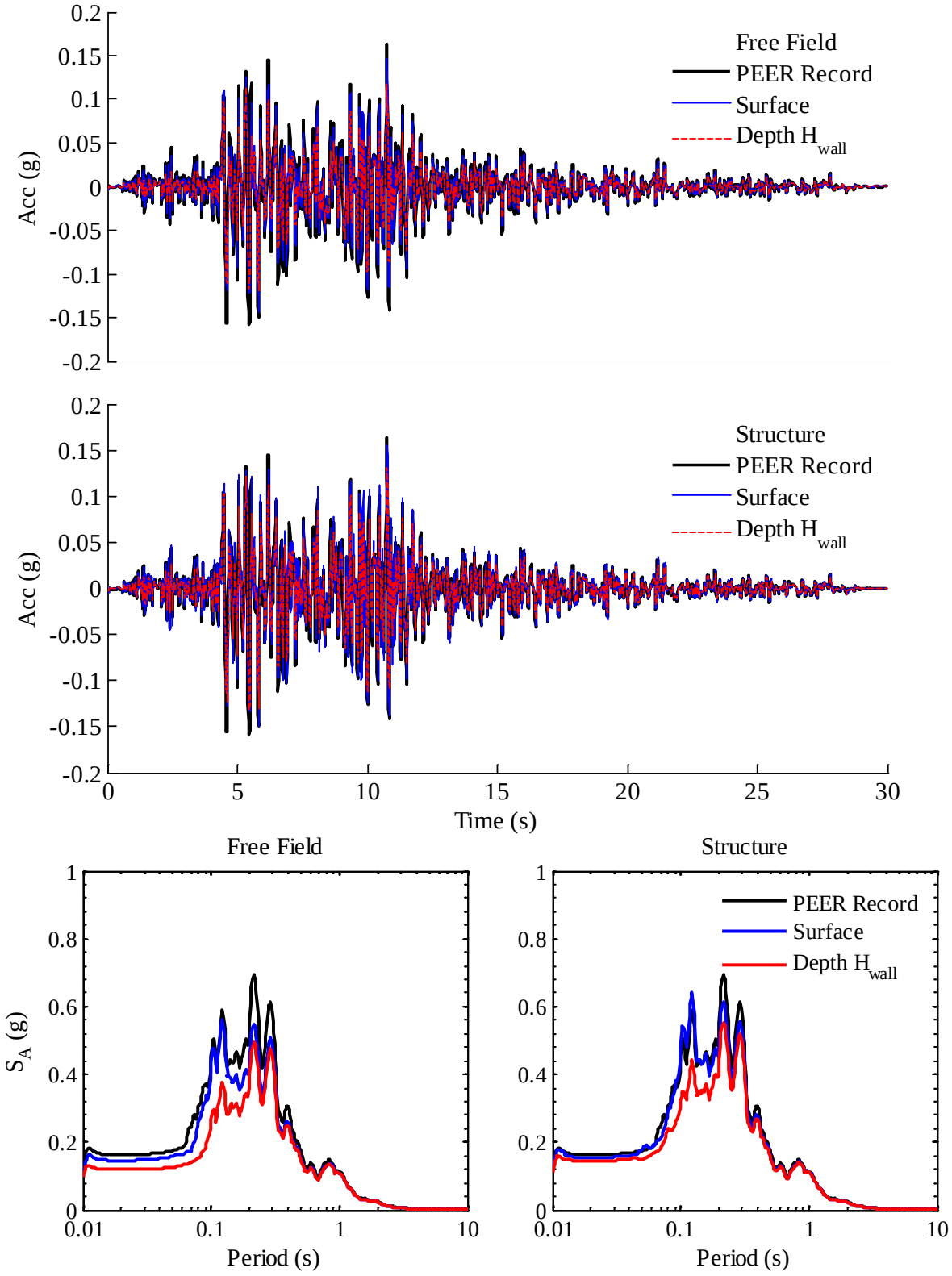

Figure B.99: Computed accelerations and response spectra at 5% damping in free field and structure during Northridge TUJ 262 for three level basement; Site Class C

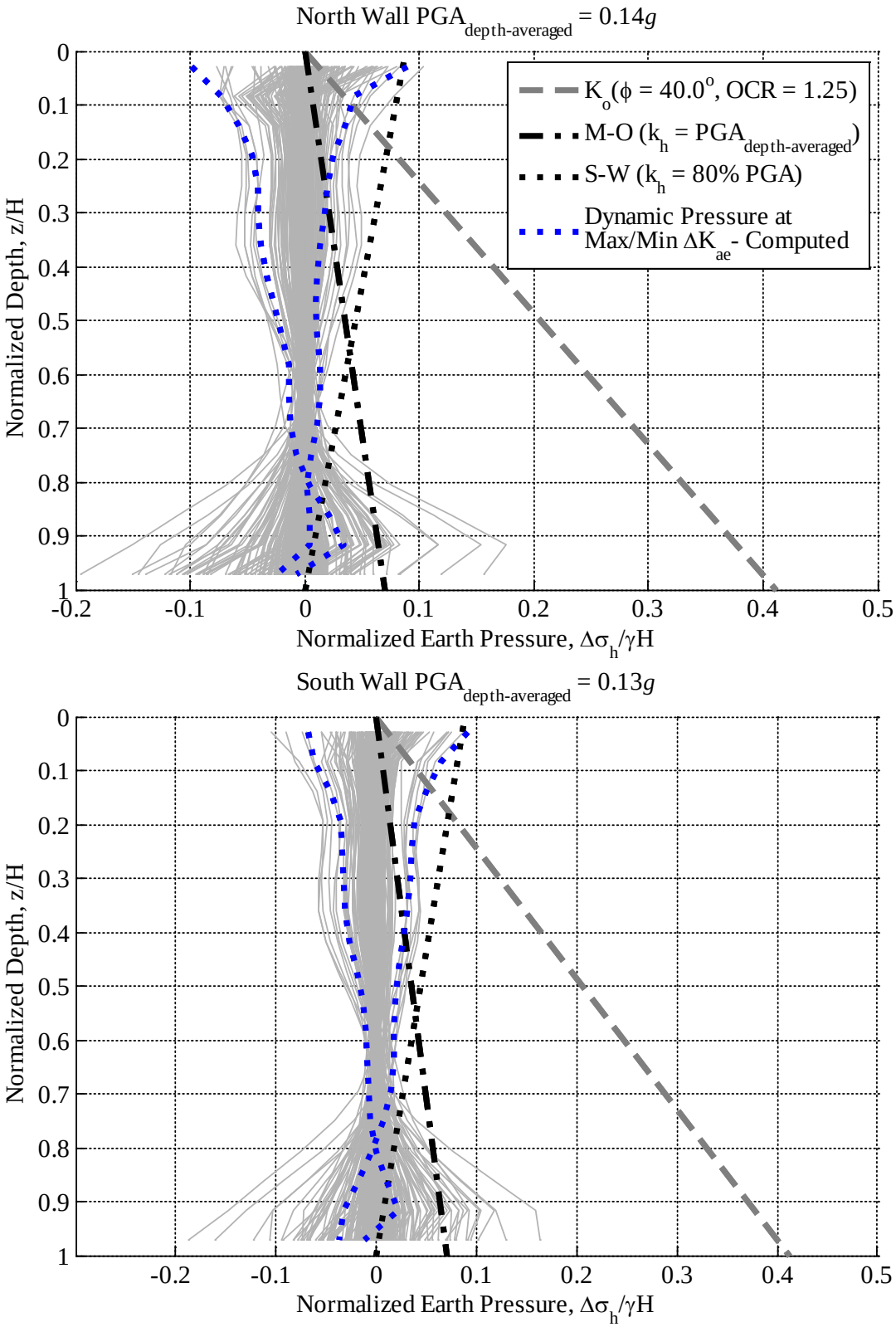

Figure B.100: Computed normalized dynamic earth pressure distributions at maximum and minimum ΔK_{ae} during Northridge TUJ 262 for three level basement; Site Class C

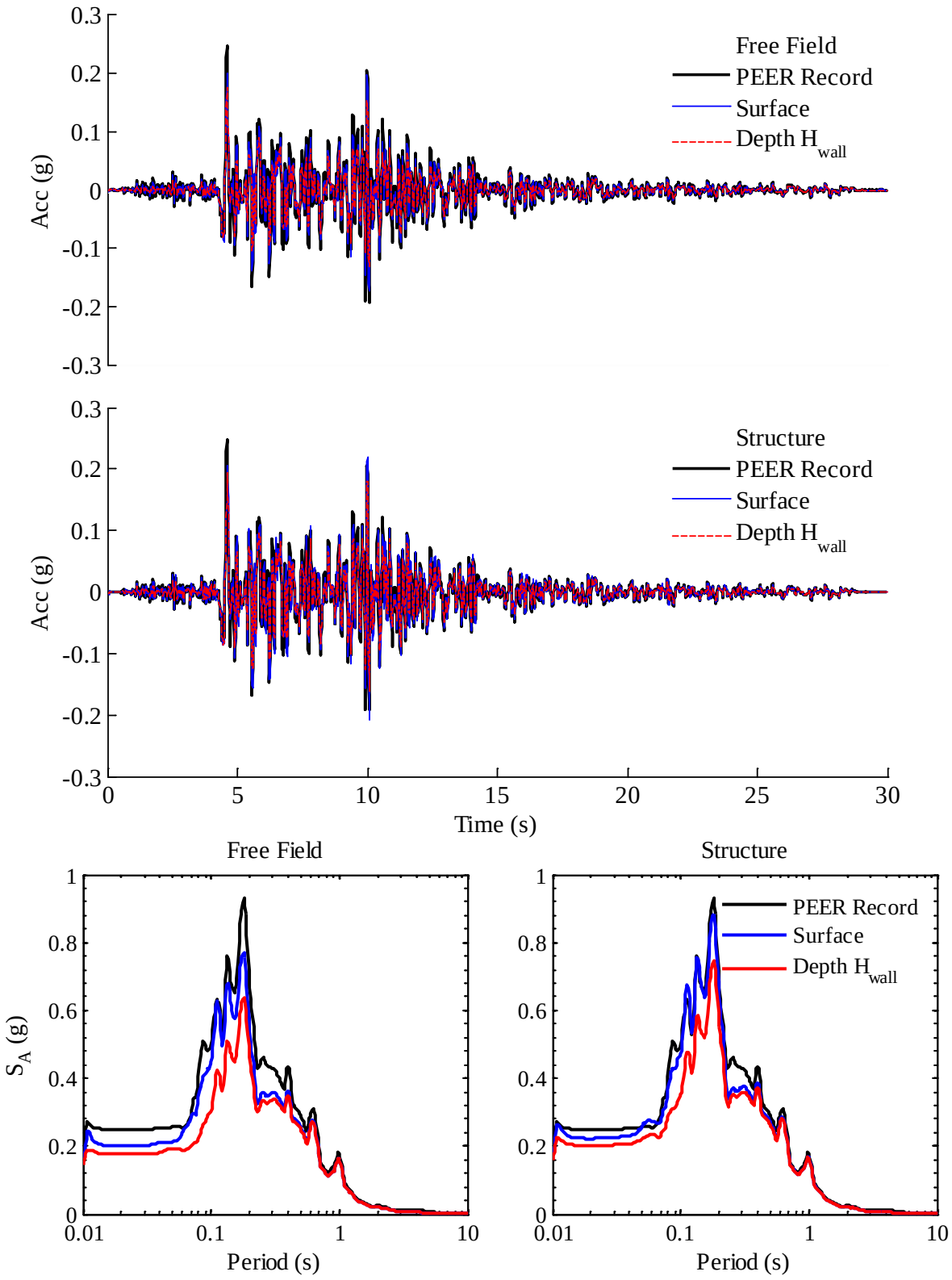

Figure B.101: Computed accelerations and response spectra at 5% damping in free field and structure during Northridge TUJ 352 for three level basement; Site Class C

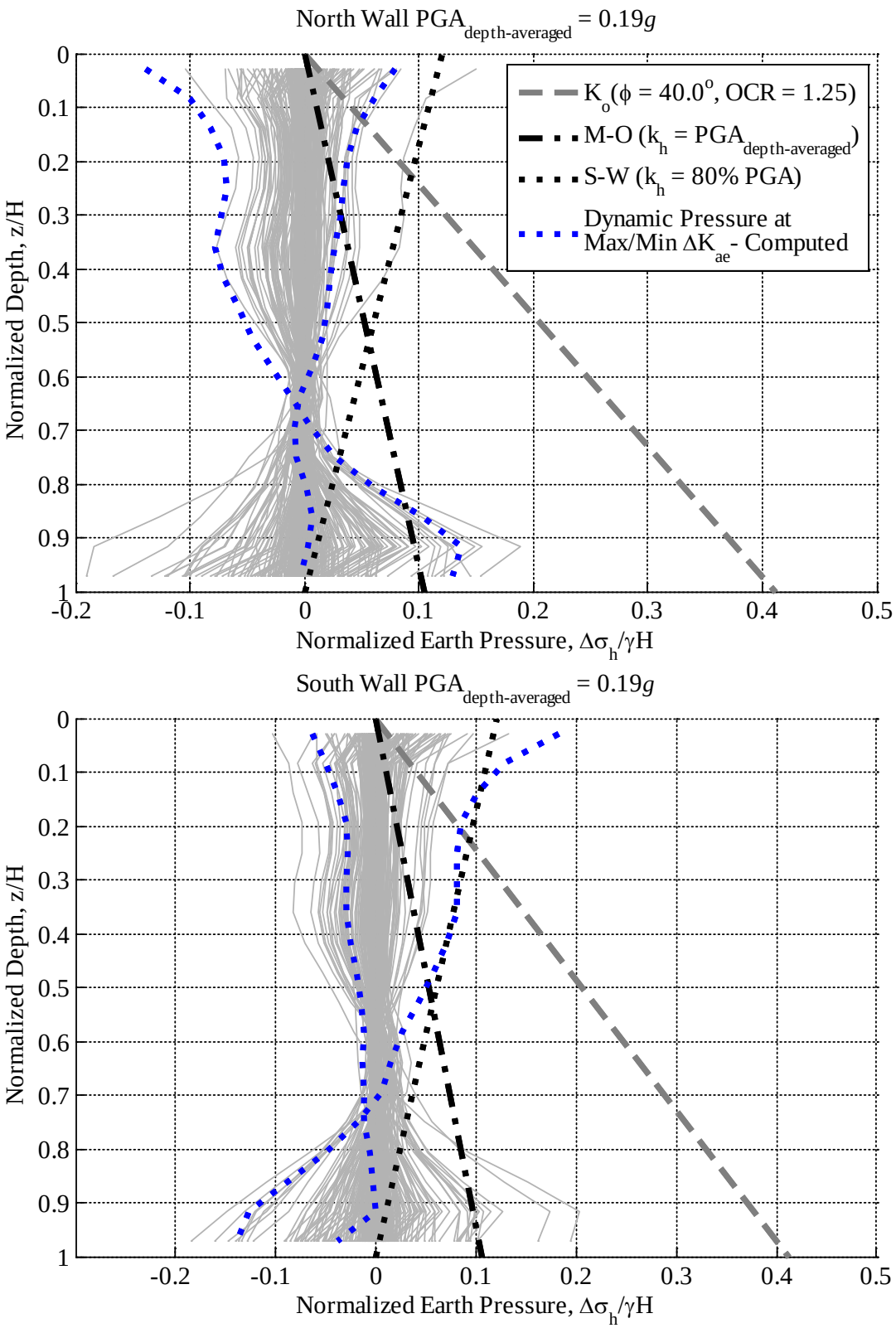

Figure B.102: Computed normalized dynamic earth pressure distributions at maximum and minimum ΔK_{ae} during Northridge TUJ 352 for three level basement; Site Class C

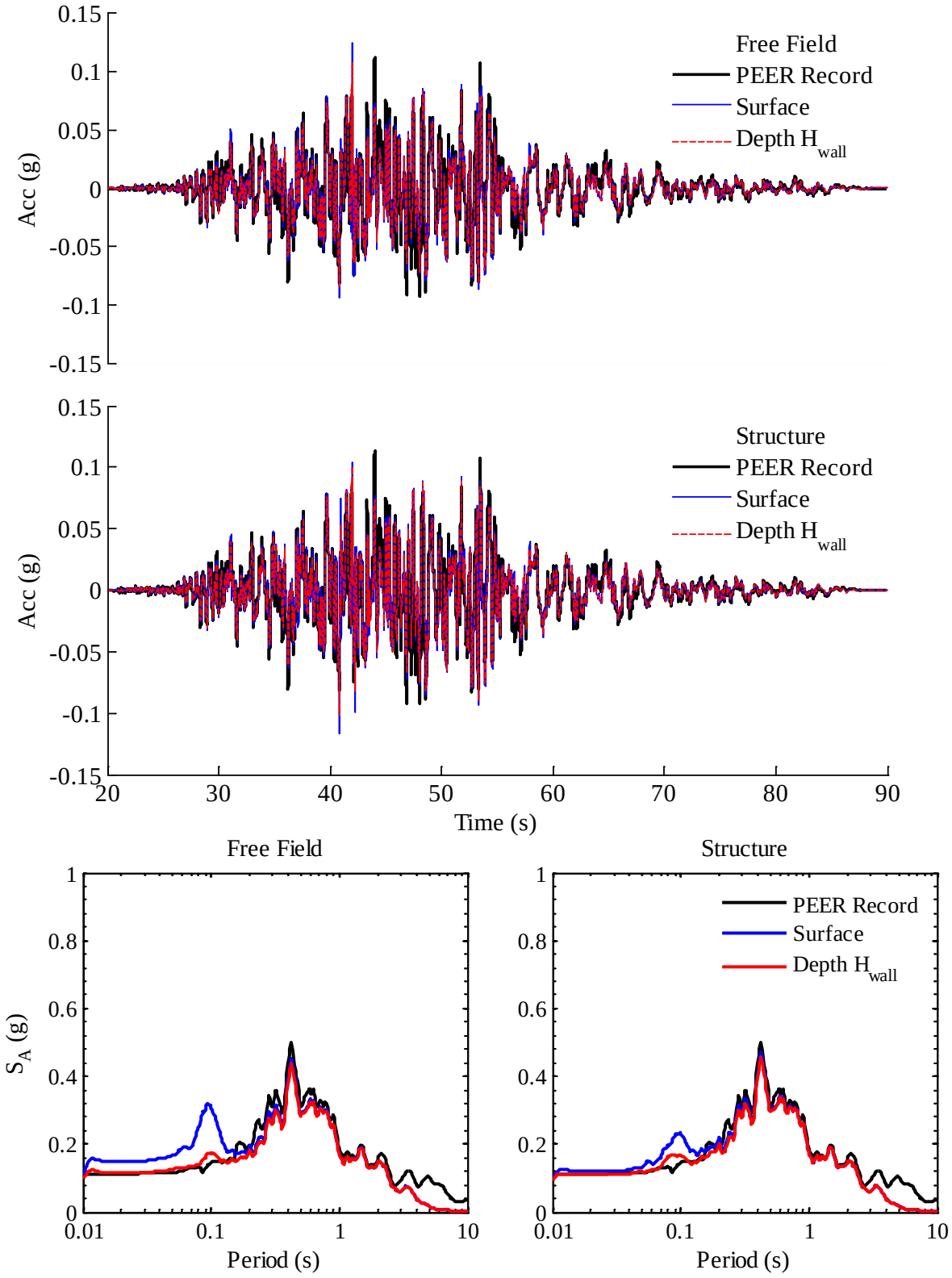

Figure B.103: Computed accelerations and response spectra at 5% damping in free field and structure during Chi Chi TCU 105E for three level basement; Site Class C

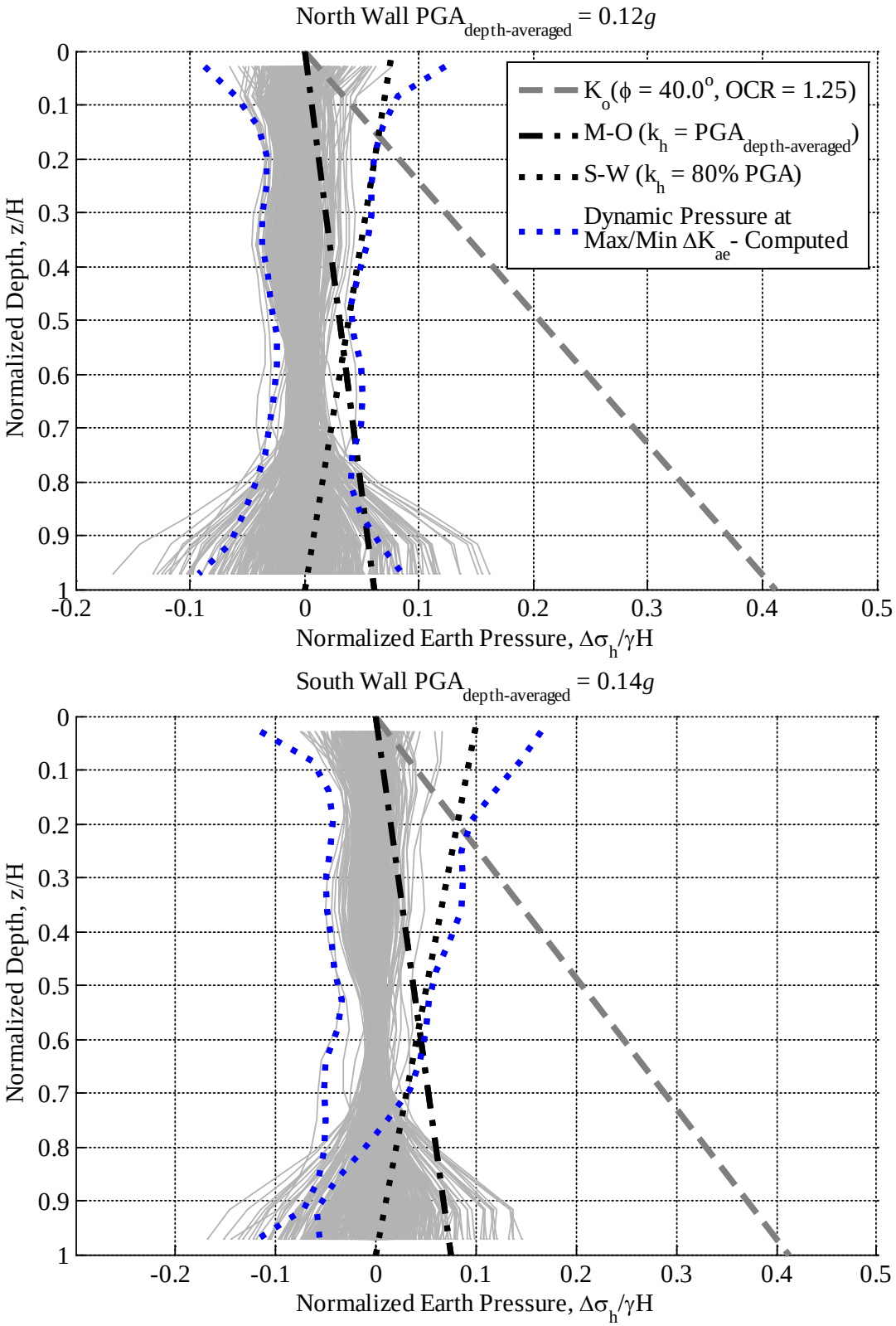

Figure B.104: Computed normalized dynamic earth pressure distributions at maximum and minimum ΔK_{ae} during Chi Chi TCU 105E for three level basement; Site Class C

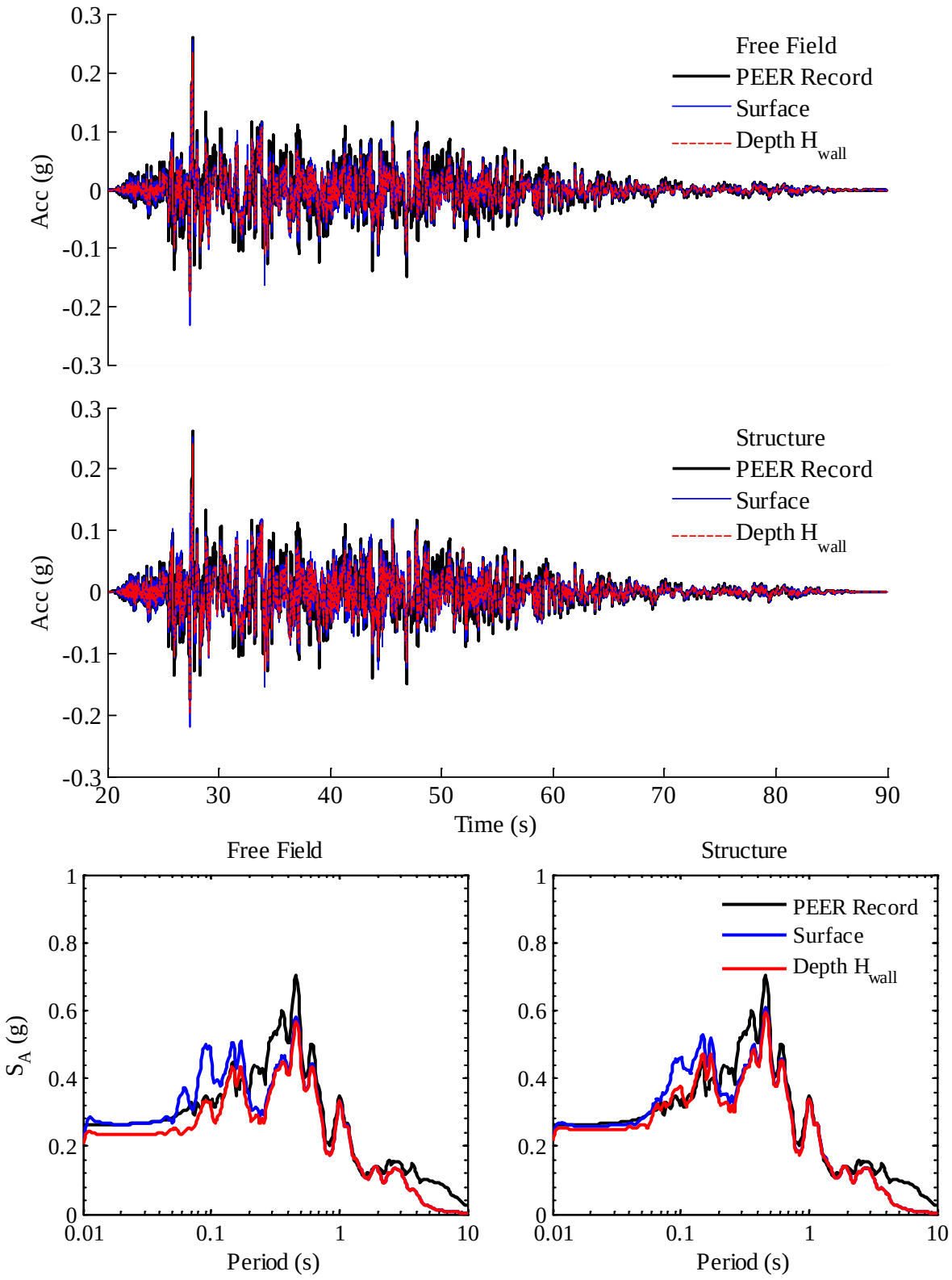

Figure B.105: Computed accelerations and response spectra at 5% damping in free field and structure during Chi Chi TCU 075N for three level basement; Site Class C

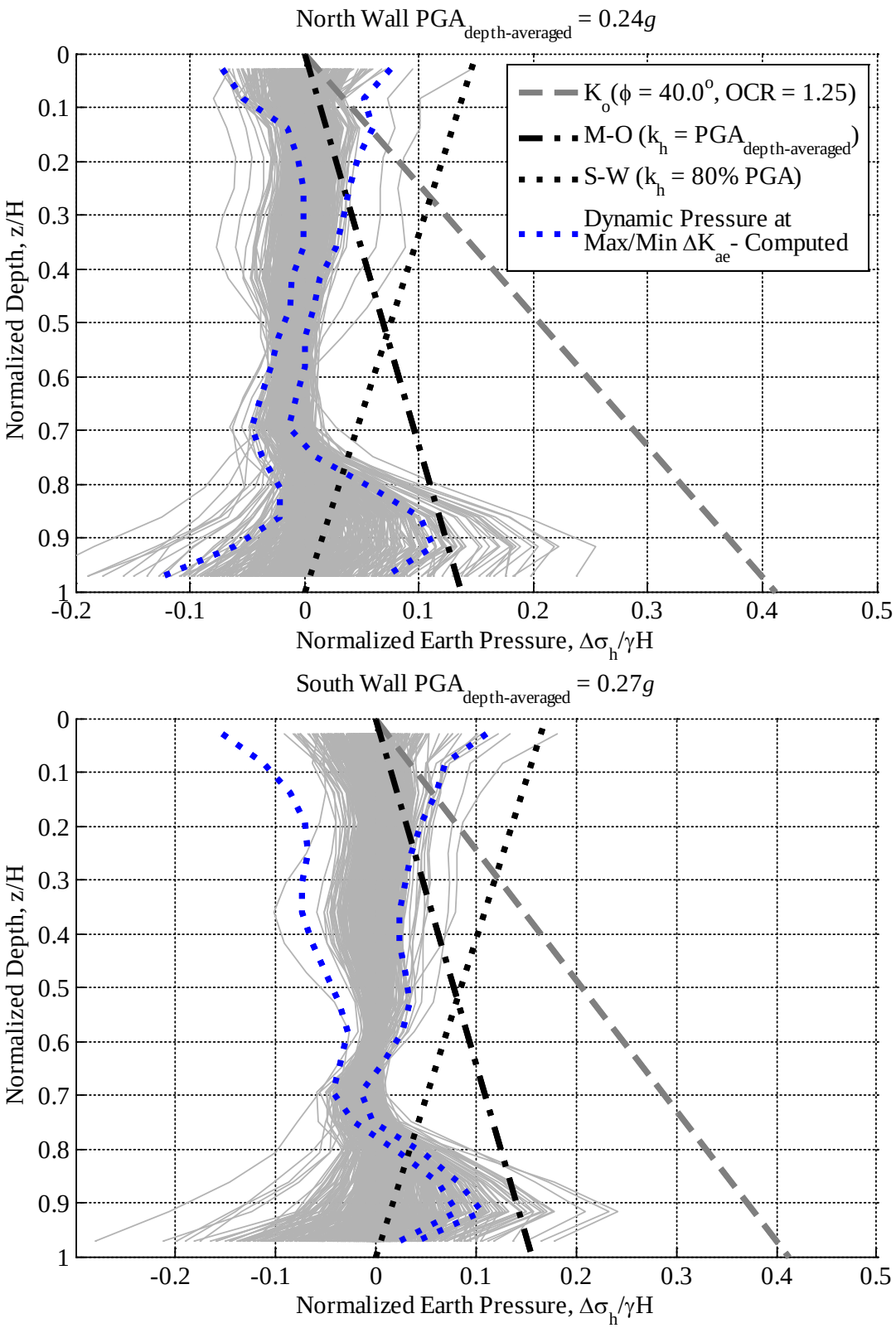

Figure B.106: Computed normalized dynamic earth pressure distributions at maximum and minimum ΔK_{ae} during Chi Chi TCU 075N for three level basement; Site Class C

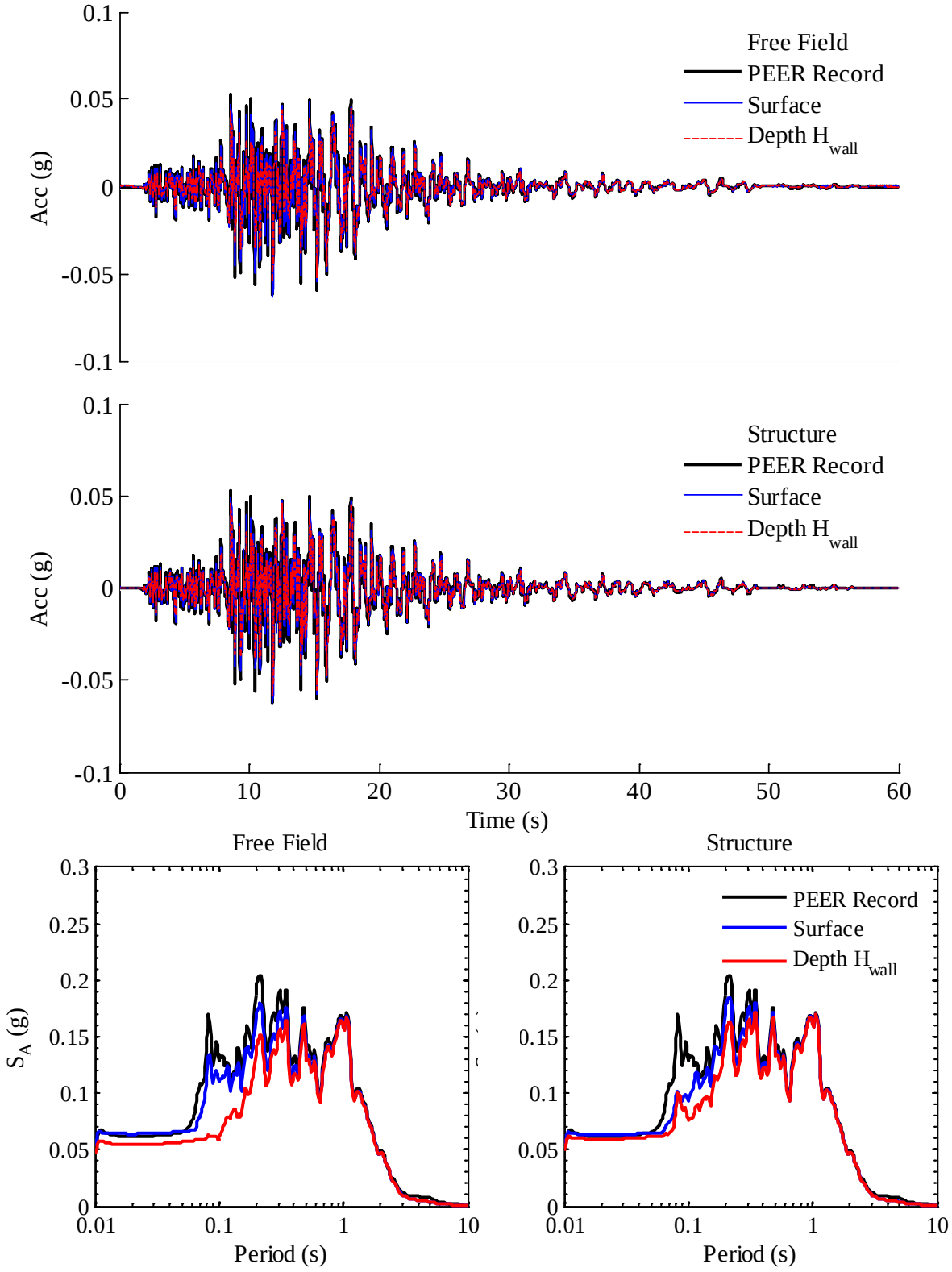

Figure B.107: Computed accelerations and response spectra at 5% damping in free field and structure during Northridge PHP 000 for four level basement; Site Class C

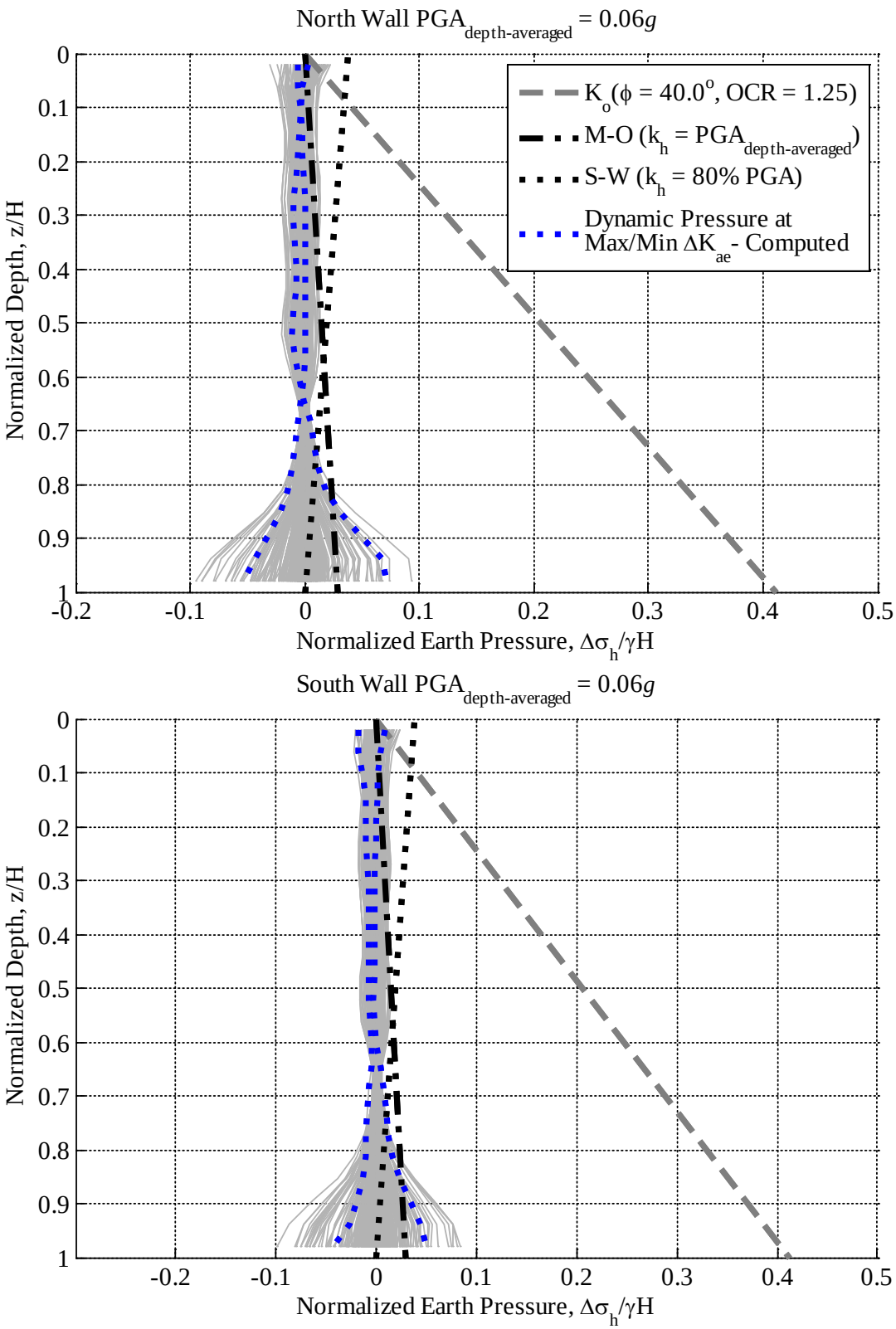

Figure B.108: Computed normalized dynamic earth pressure distributions at maximum and minimum ΔK_{ae} during Northridge PHP 000 for four level basement; Site Class C

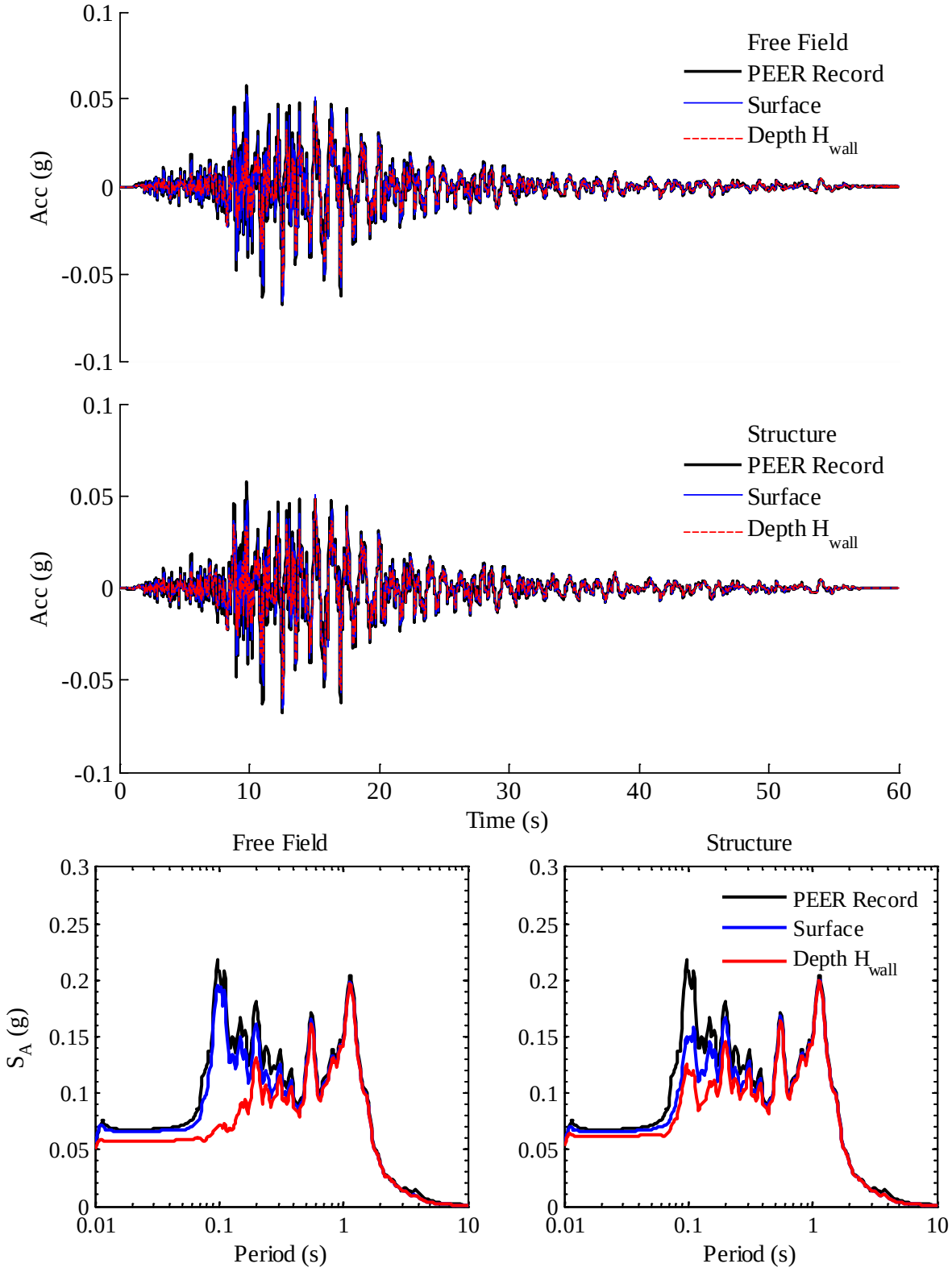

Figure B.109: Computed accelerations and response spectra at 5% damping in free field and structure during Northridge PHP 090 for four level basement; Site Class C

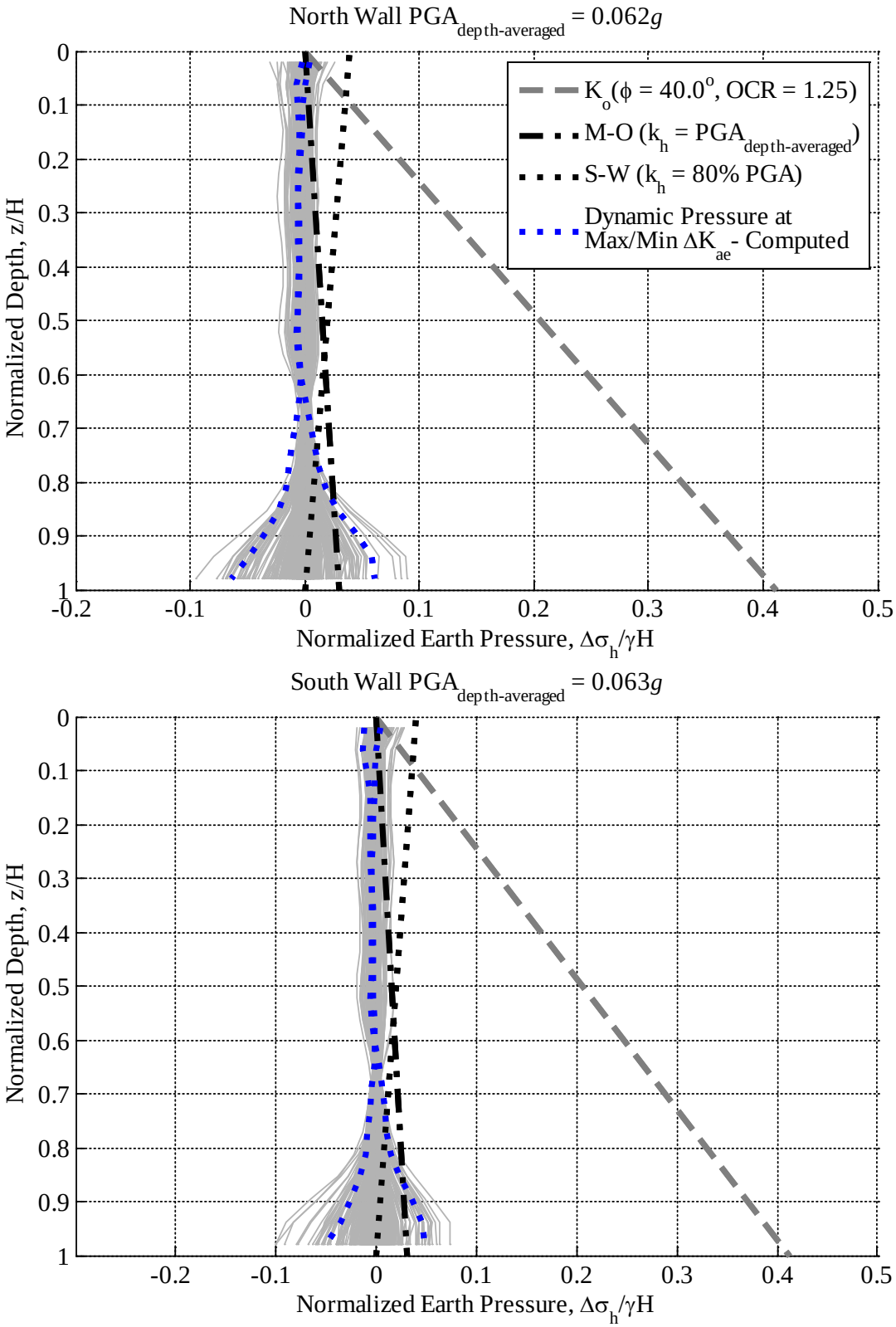

Figure B.110: Computed normalized dynamic earth pressure distributions at maximum and minimum ΔK_{ae} during Northridge PHP 090 for four level basement; Site Class C

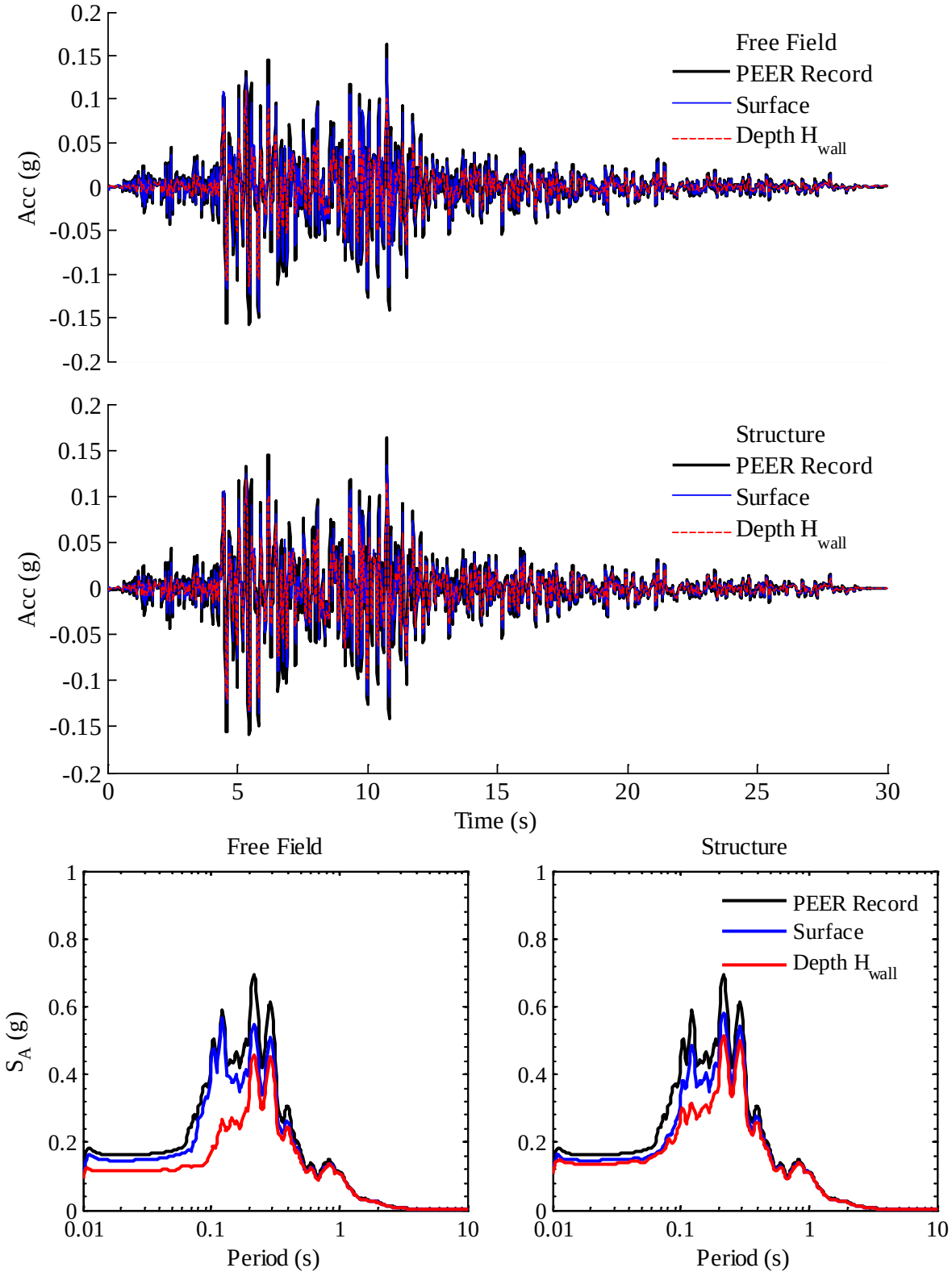

Figure B.111: Computed accelerations and response spectra at 5% damping in free field and structure during Northridge TUJ 262 for four level basement; Site Class C

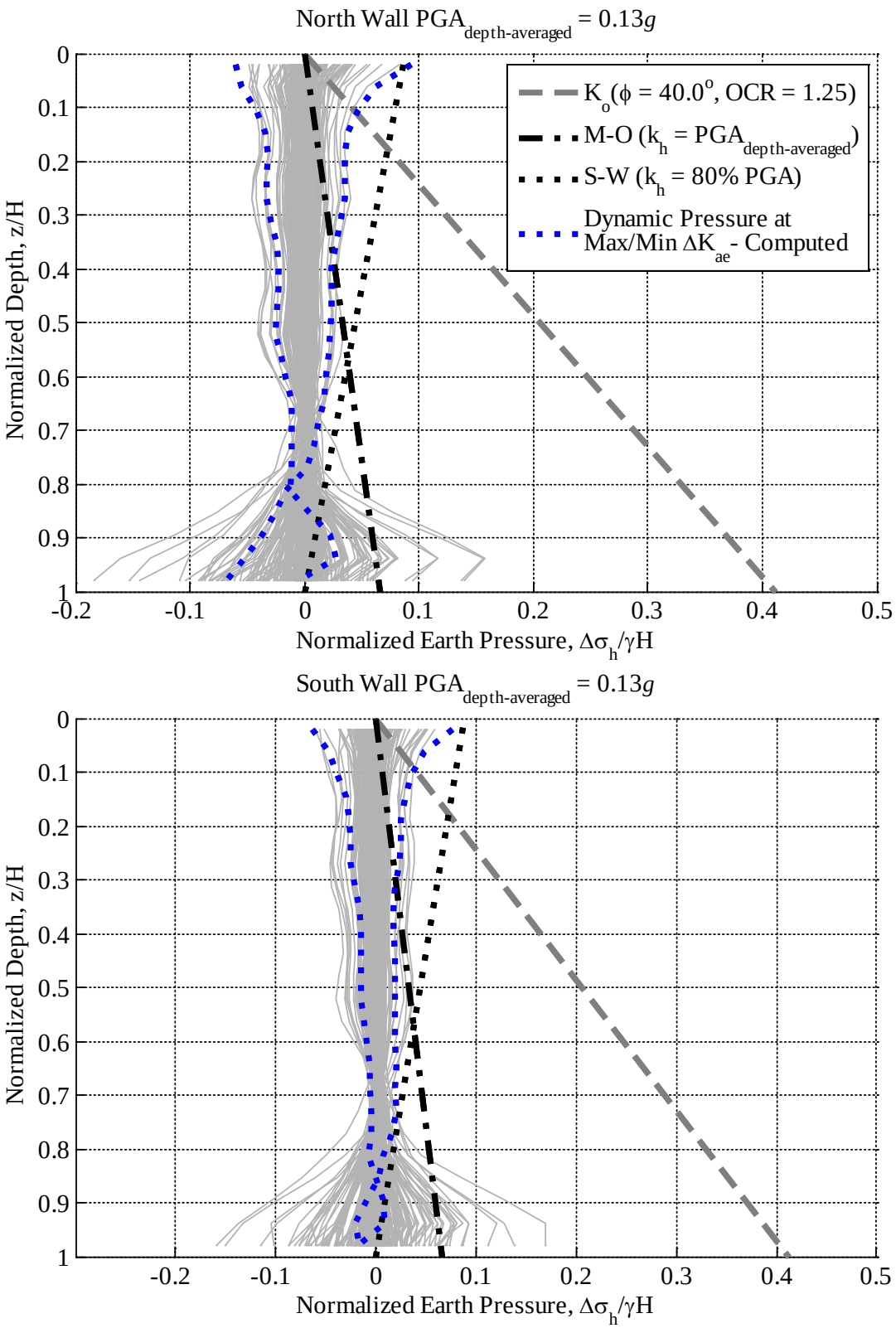

Figure B.112: Computed normalized dynamic earth pressure distributions at maximum and minimum ΔK_{ae} during Northridge TUJ 262 for four level basement; Site Class C

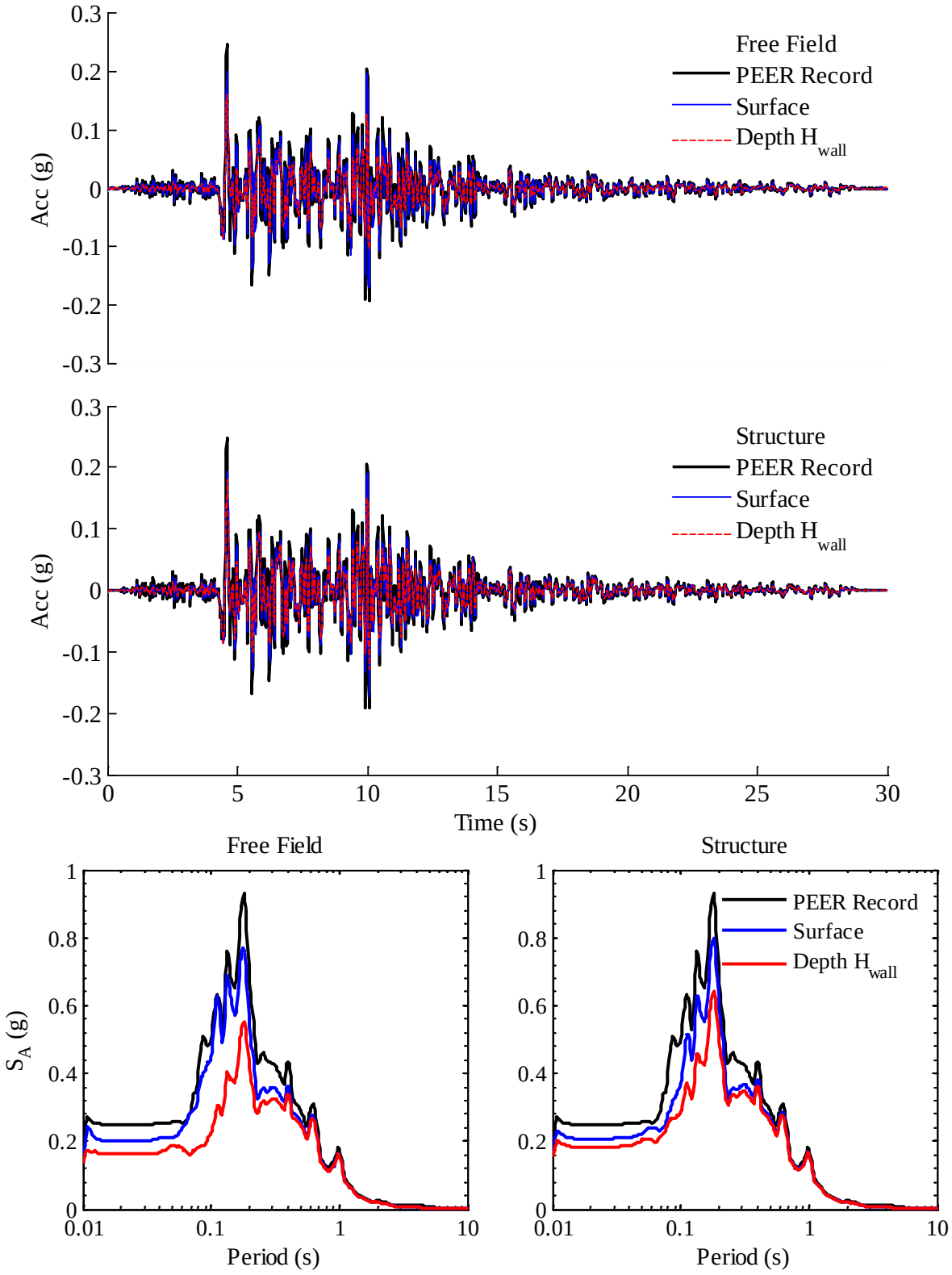

Figure B.113: Computed accelerations and response spectra at 5% damping in free field and structure during Northridge TUJ 352 for four level basement; Site Class C

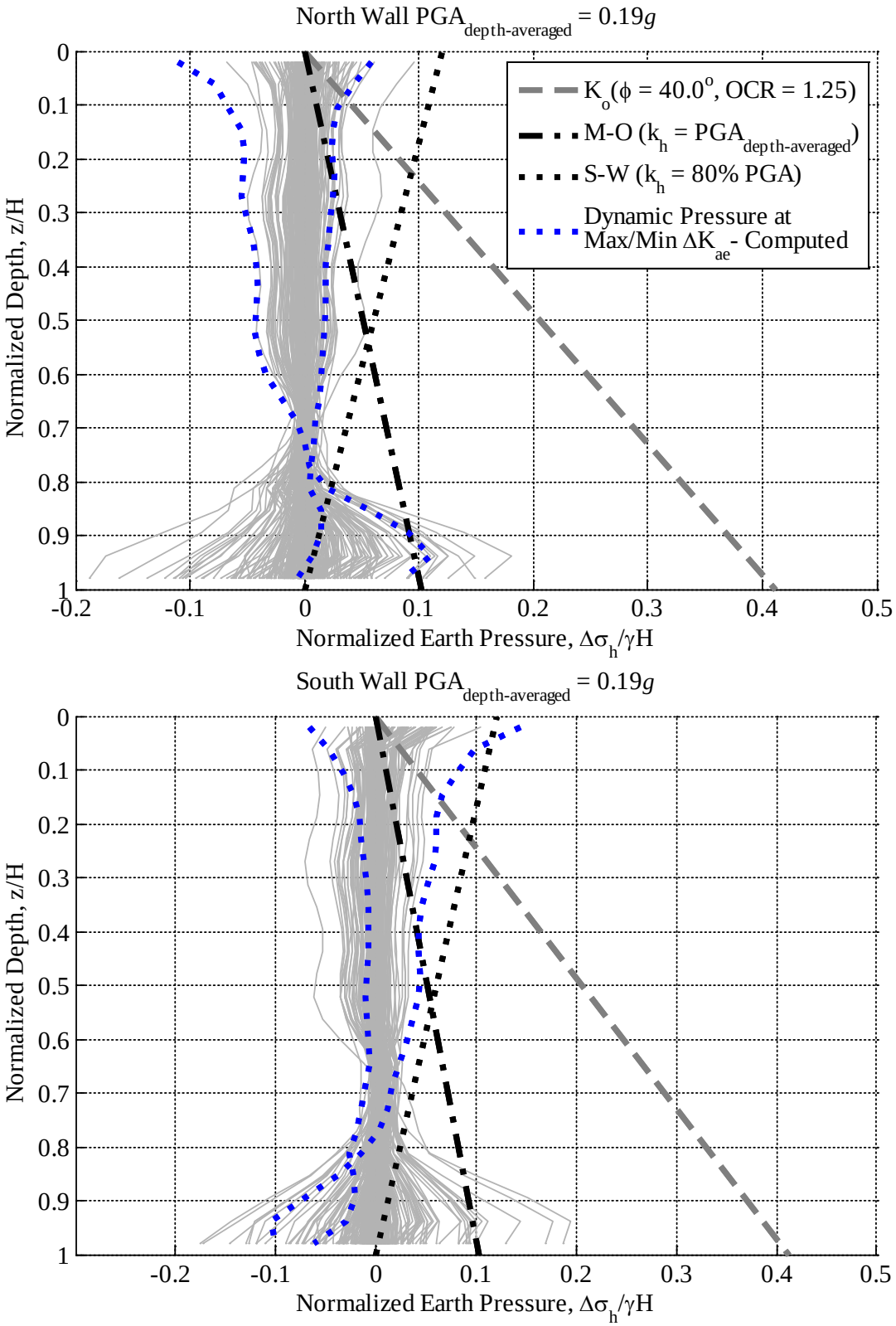

Figure B.114: Computed normalized dynamic earth pressure distributions at maximum and minimum ΔK_{ae} during Northridge TUJ 352 for four level basement; Site Class C

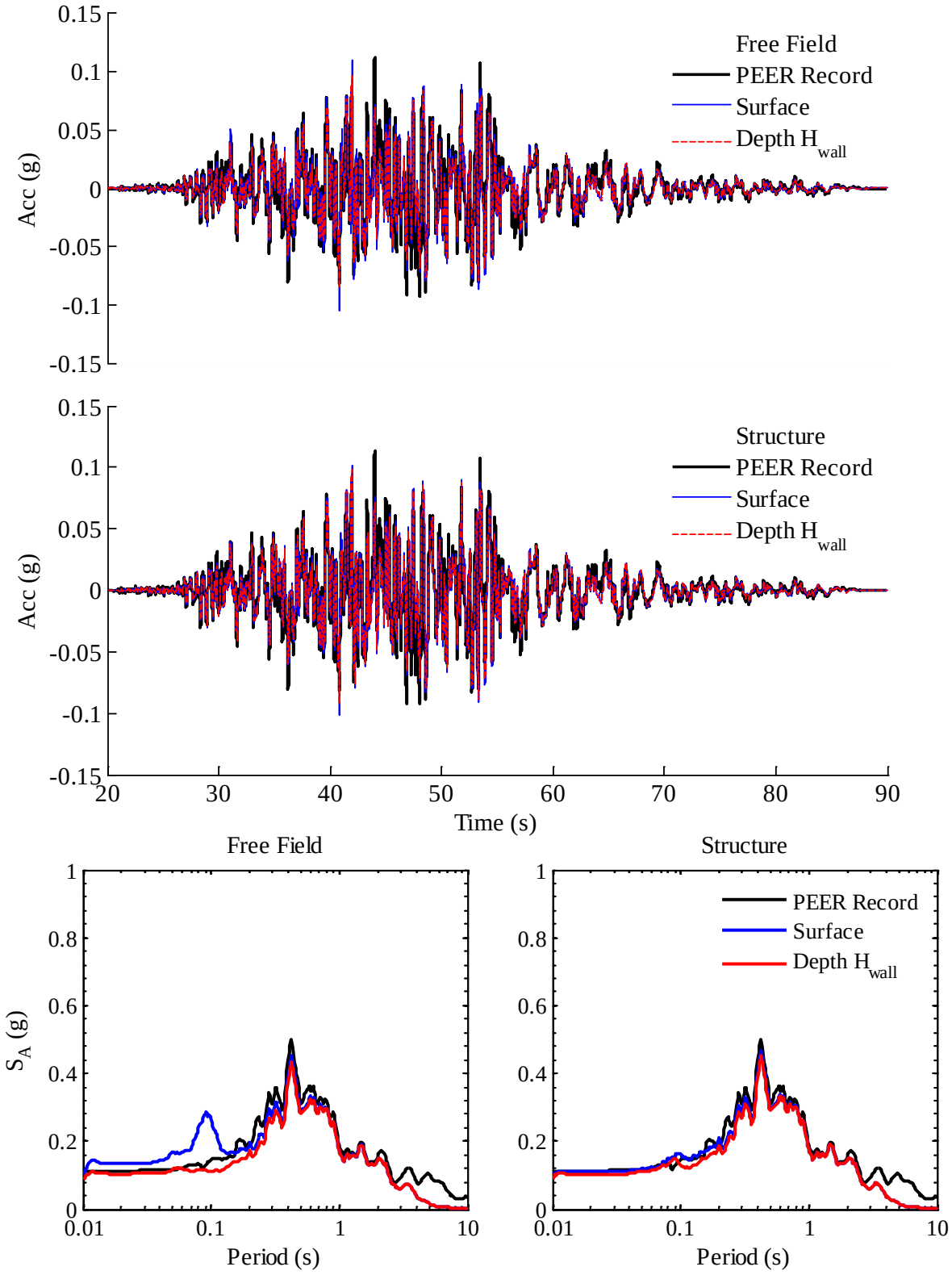

Figure B.115: Computed accelerations and response spectra at 5% damping in free field and structure during Chi Chi TCU 105E for four level basement; Site Class C

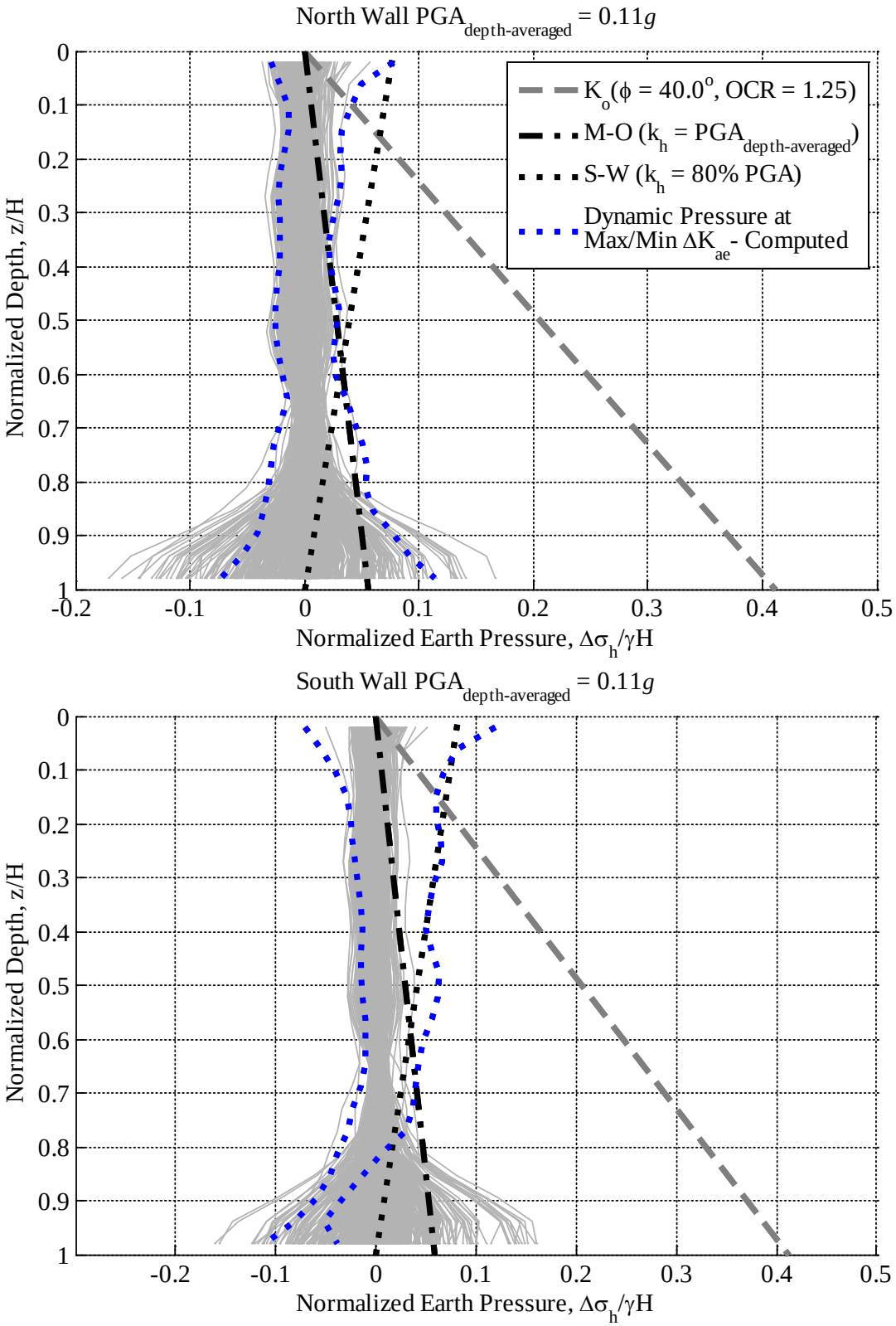

Figure B.116: Computed normalized dynamic earth pressure distributions at maximum and minimum ΔK_{ae} during Chi Chi TCU 105E for four level basement; Site Class C

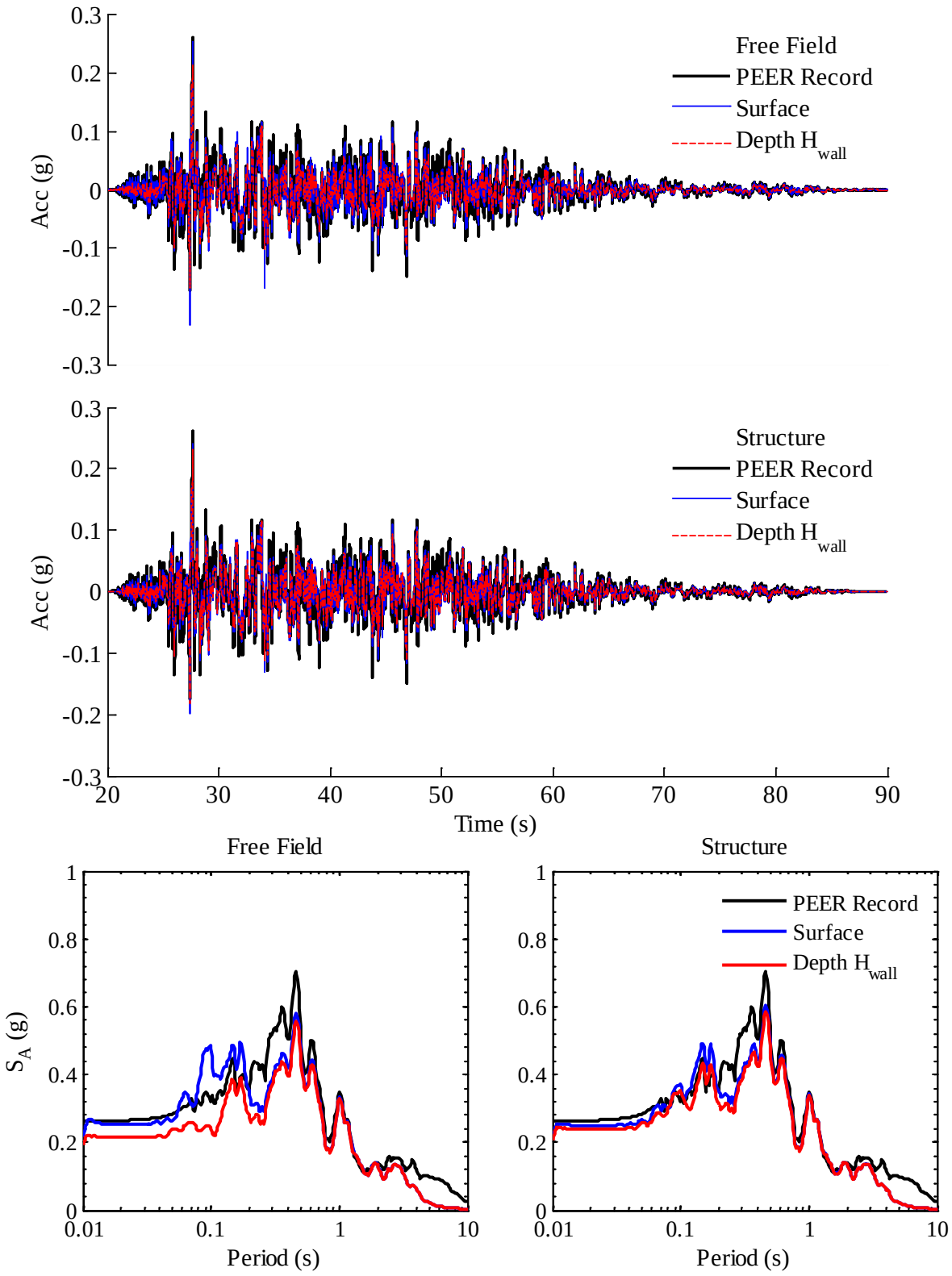

Figure B.117: Computed accelerations and response spectra at 5% damping in free field and structure during Chi Chi TCU 075N for four level basement; Site Class C

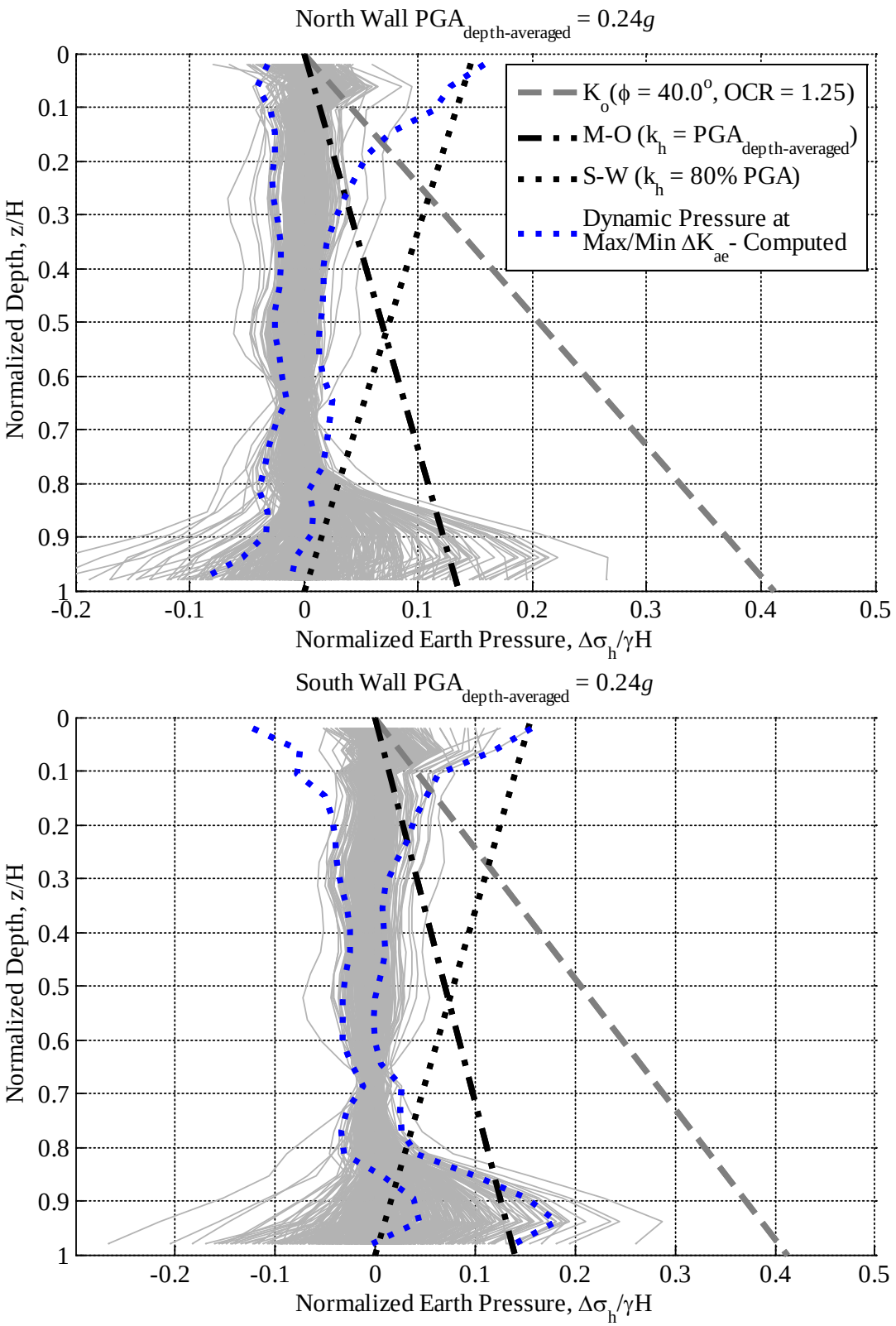

Figure B.118: Computed normalized dynamic earth pressure distributions at maximum and minimum ΔK_{ae} during Chi Chi TCU 075N for four level basement; Site Class C

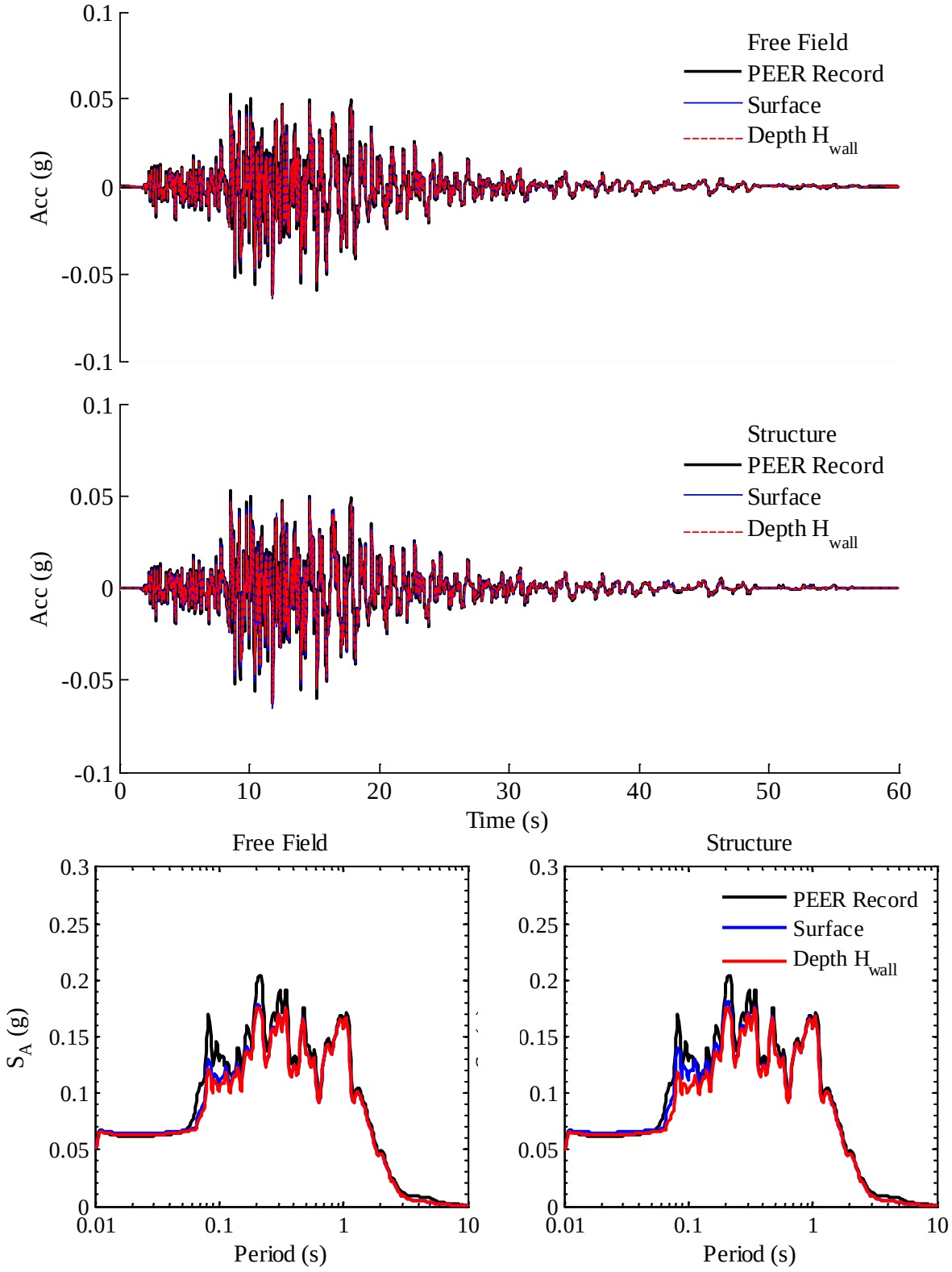

Figure B.119: Computed accelerations and response spectra at 5% damping in free field and structure during Northridge PHP 000 for one bay, one level basement; Site Class C

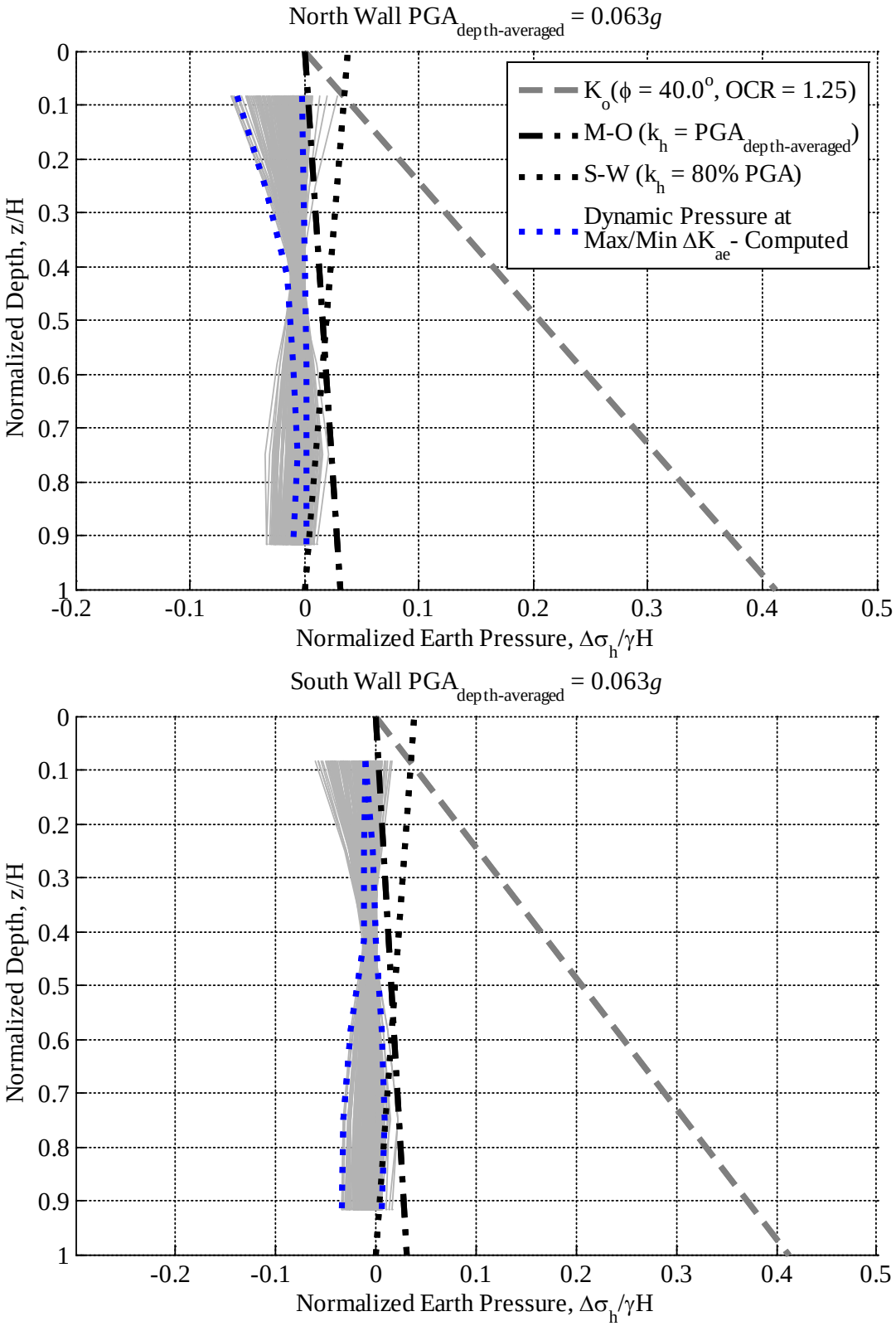

Figure B.120: Computed normalized dynamic earth pressure distributions at maximum and minimum ΔK_{ae} during Northridge PHP 000 for one bay, one level basement; Site Class C

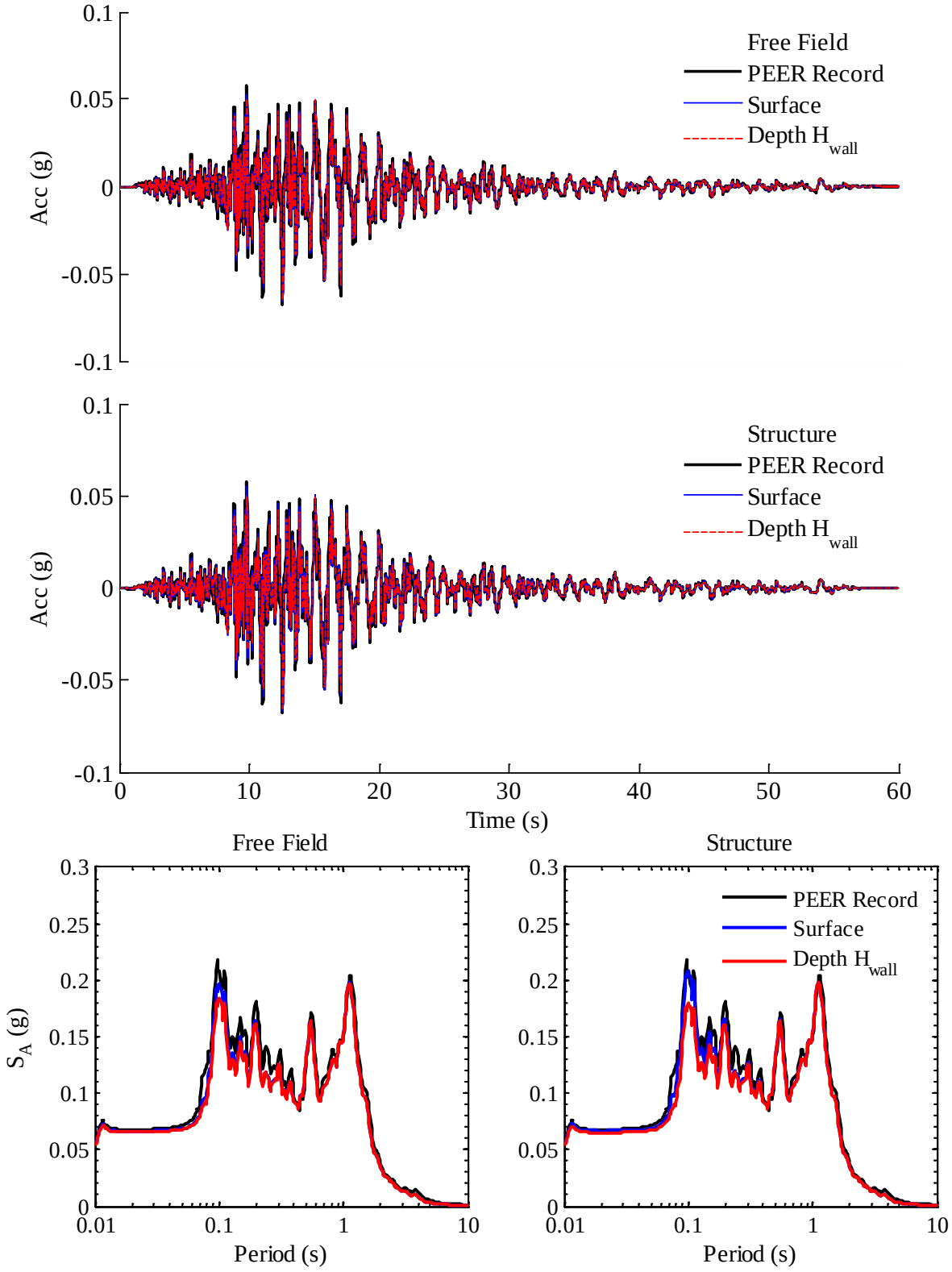

Figure B.121: Computed accelerations and response spectra at 5% damping in free field and structure during Northridge PHP 090 for one bay, one level basement; Site Class C

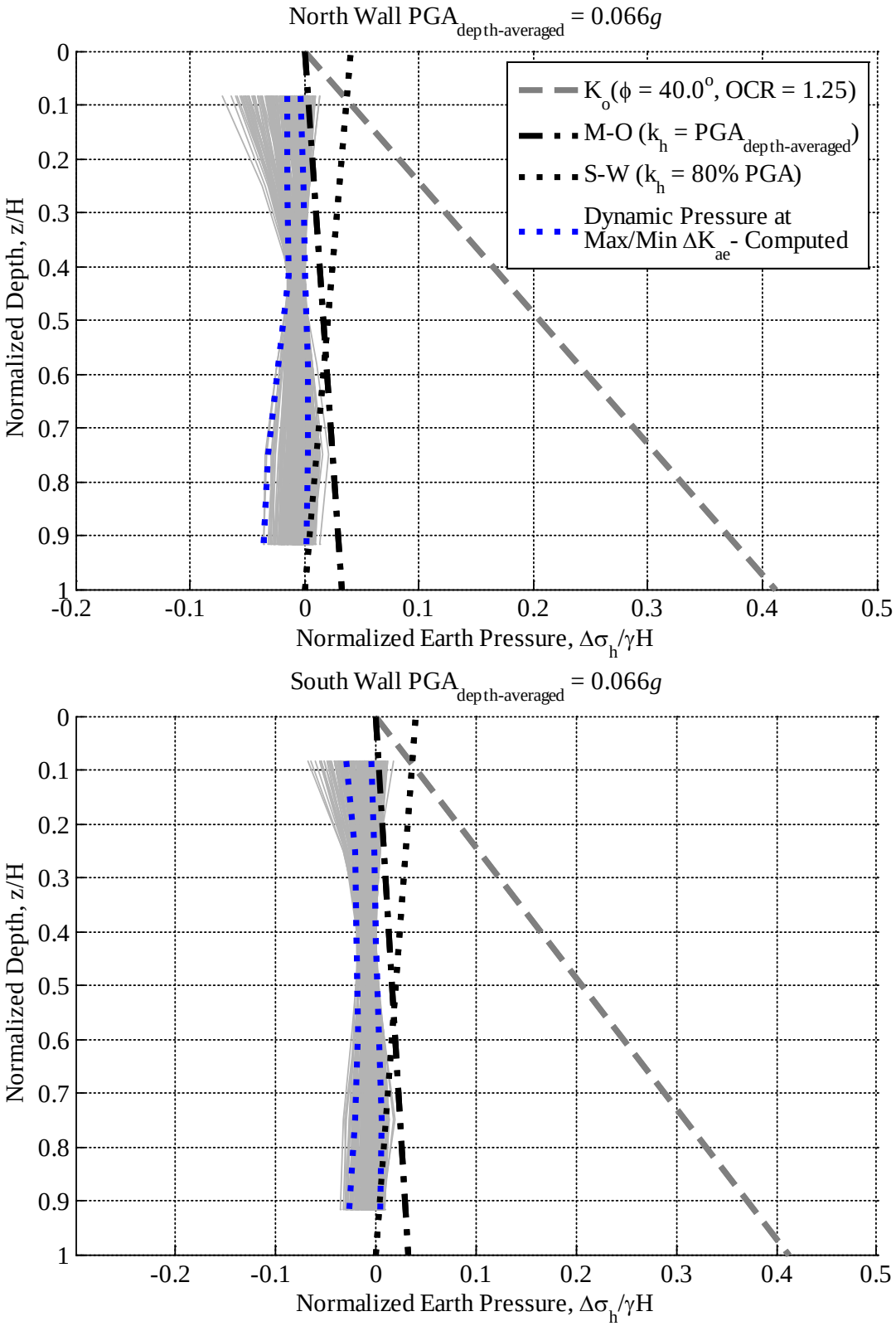

Figure B.122: Computed normalized dynamic earth pressure distributions at maximum and minimum ΔK_{ae} during Northridge PHP 090 for one bay, one level basement; Site Class C

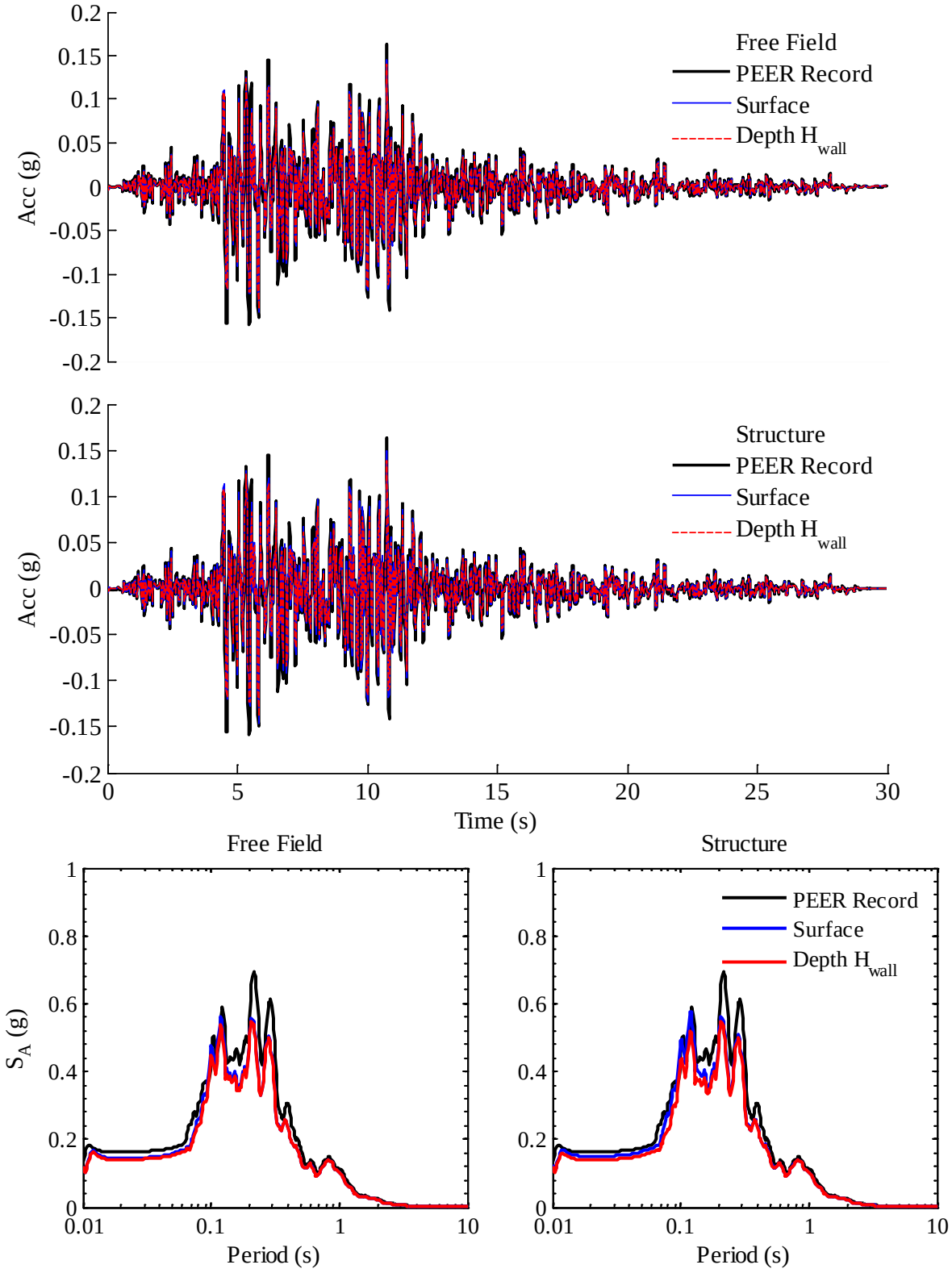

Figure B.123: Computed accelerations and response spectra at 5% damping in free field and structure during Northridge TUJ 262 for one bay, one level basement; Site Class C

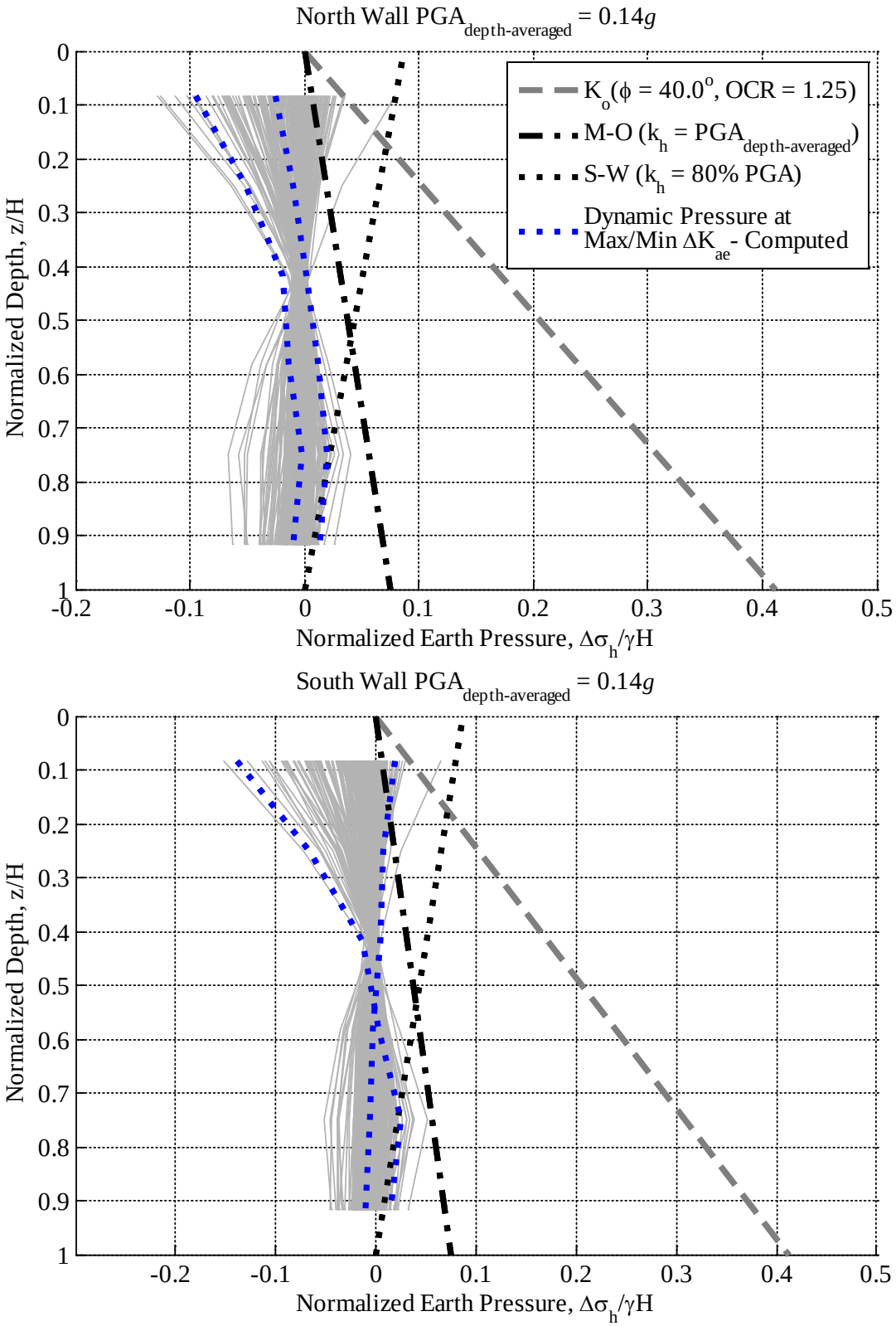

Figure B.124: Computed normalized dynamic earth pressure distributions at maximum and minimum ΔK_{ae} during Northridge TUJ 262 for one bay, one level basement; Site Class C

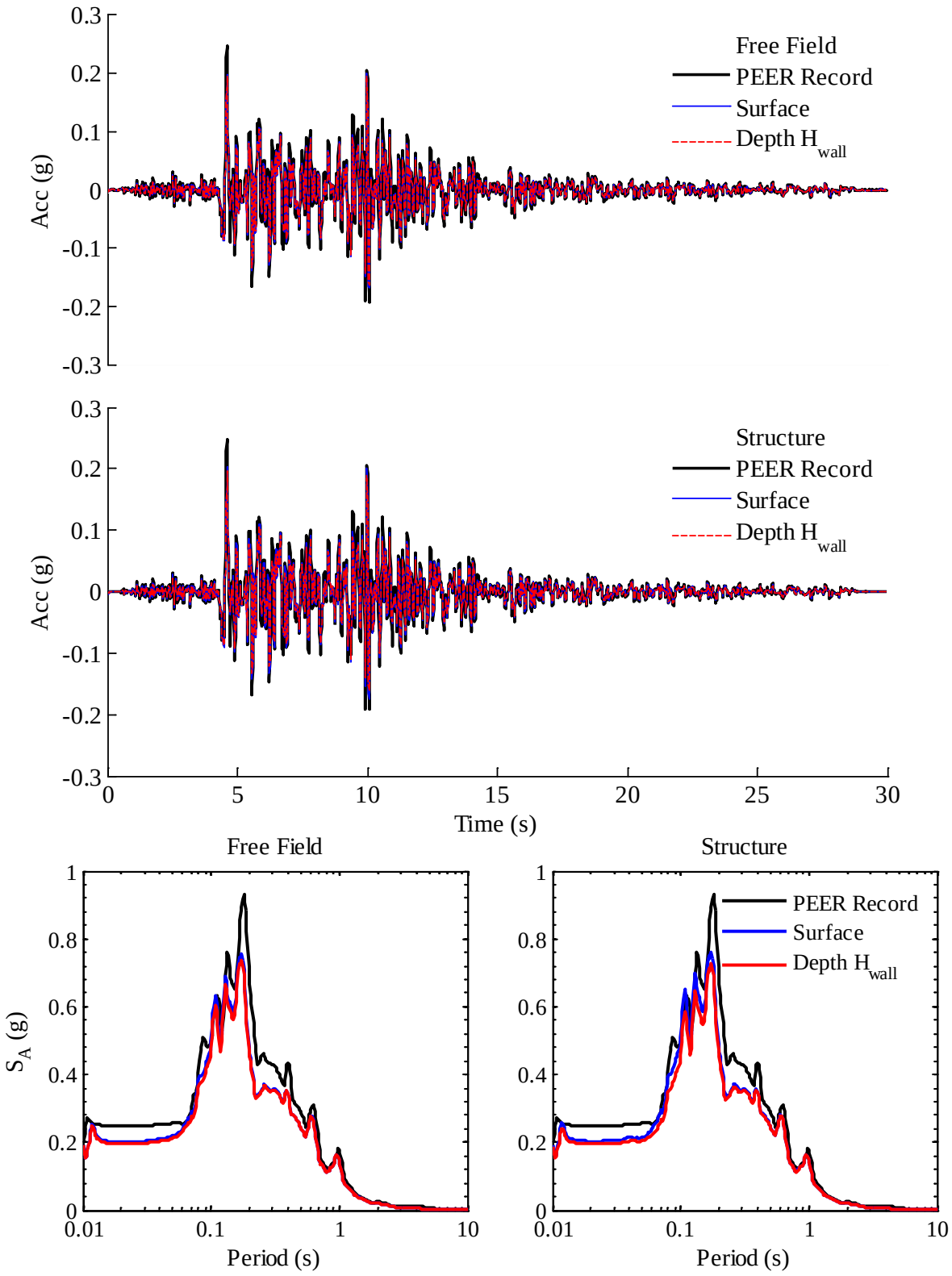

Figure B.125: Computed accelerations and response spectra at 5% damping in free field and structure during Northridge TUJ 352 for one bay, one level basement; Site Class C

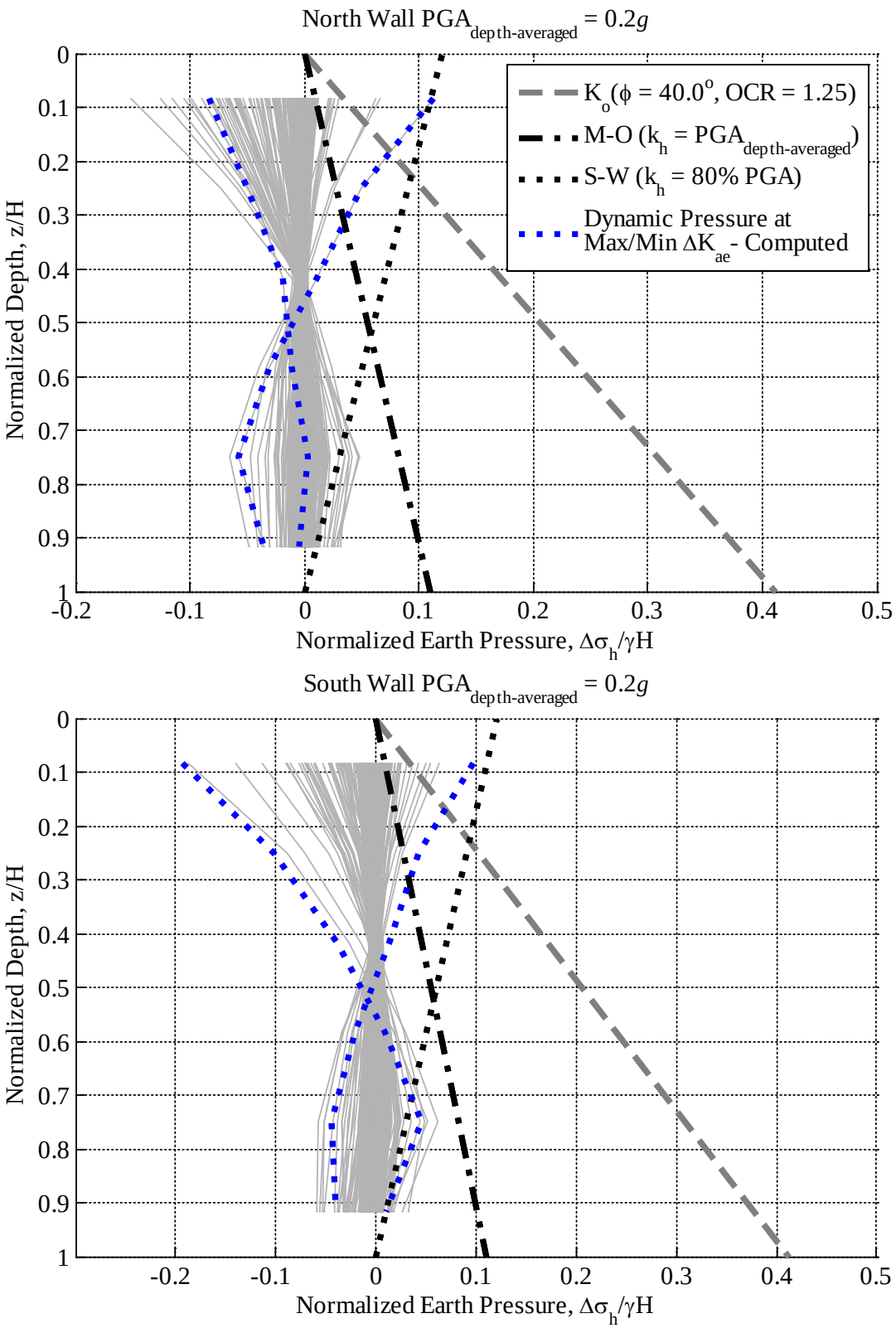

Figure B.126: Computed normalized dynamic earth pressure distributions at maximum and minimum ΔK_{ae} during Northridge TUJ 352 for one bay, one level basement; Site Class C

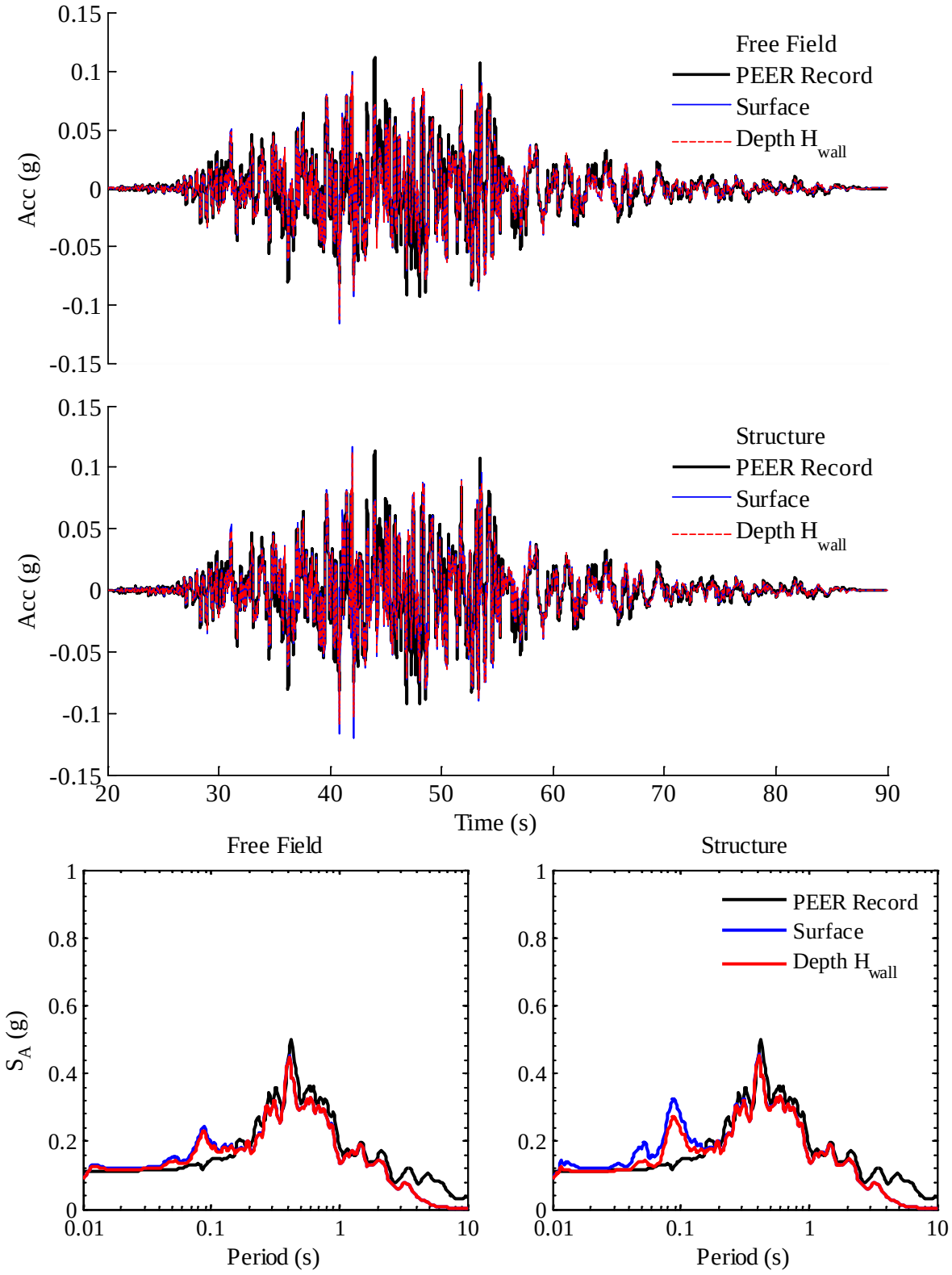

Figure B.127: Computed accelerations and response spectra at 5% damping in free field and structure during Chi Chi TCU 105E for one bay, one level basement; Site Class C

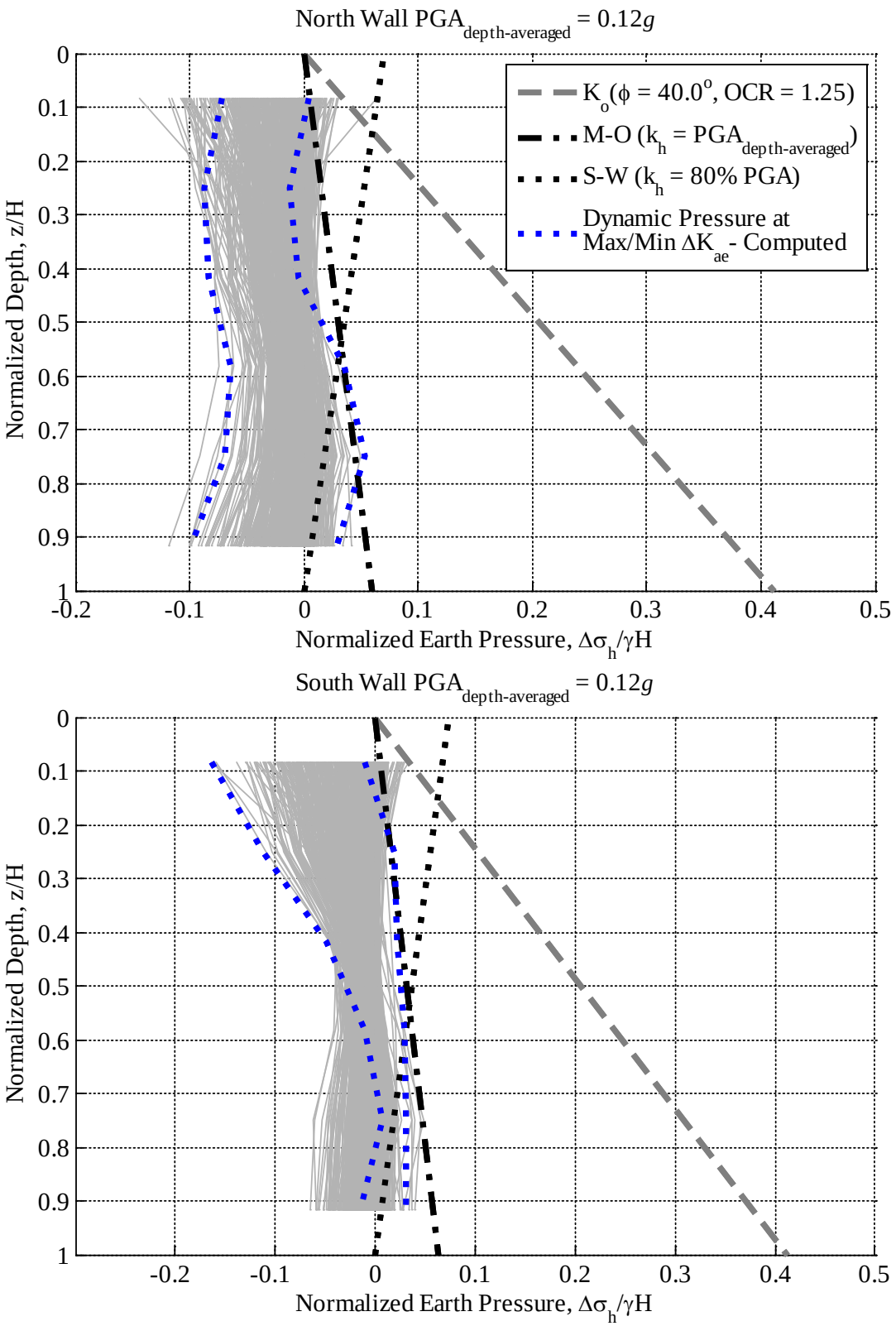

Figure B.128: Computed normalized dynamic earth pressure distributions at maximum and minimum ΔK_{ae} during Chi Chi TCU 105E for one bay, one level basement; Site Class C

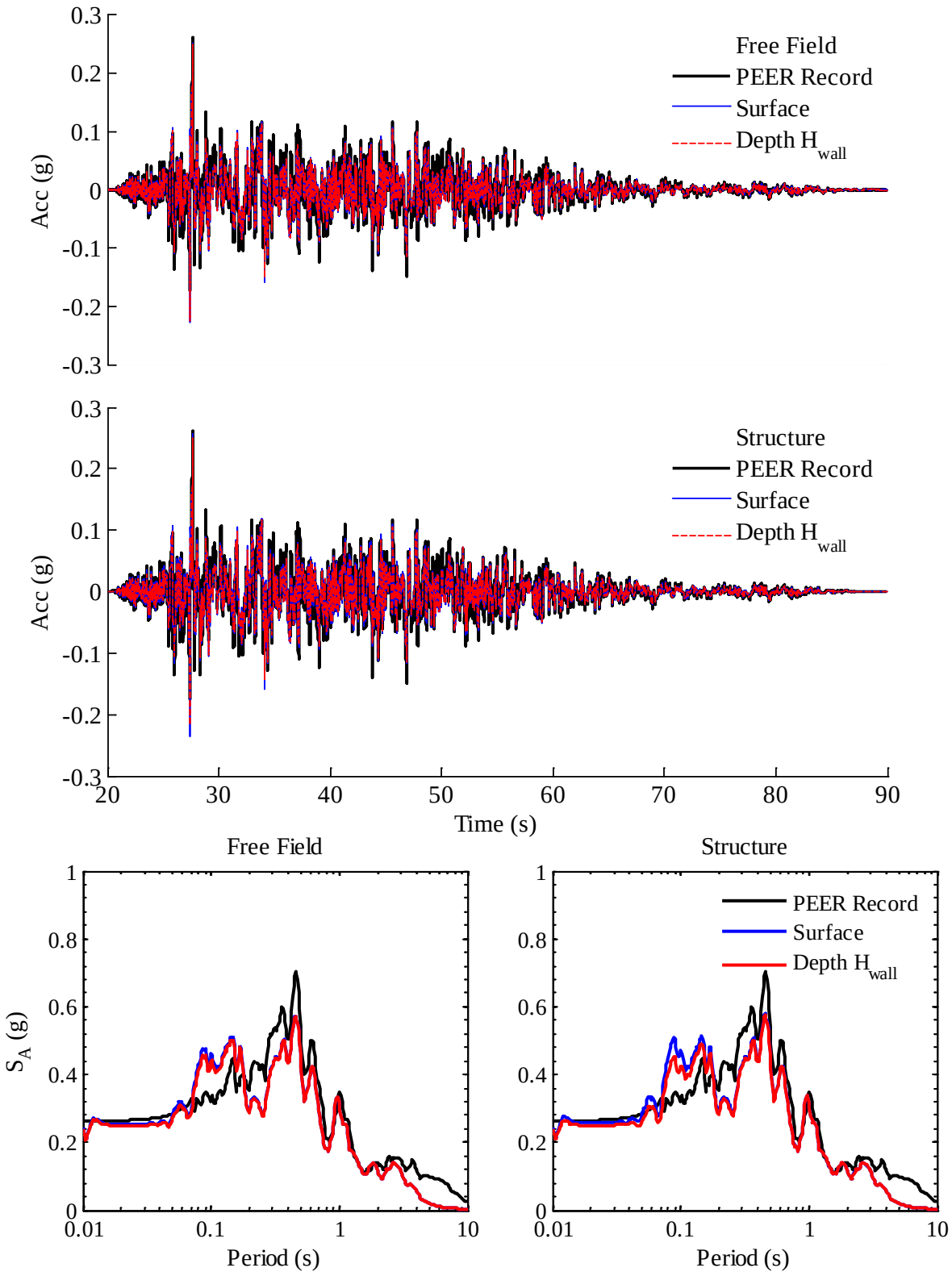

Figure B.129: Computed accelerations and response spectra at 5% damping in free field and structure during Chi Chi TCU 075N for one bay, one level basement; Site Class C

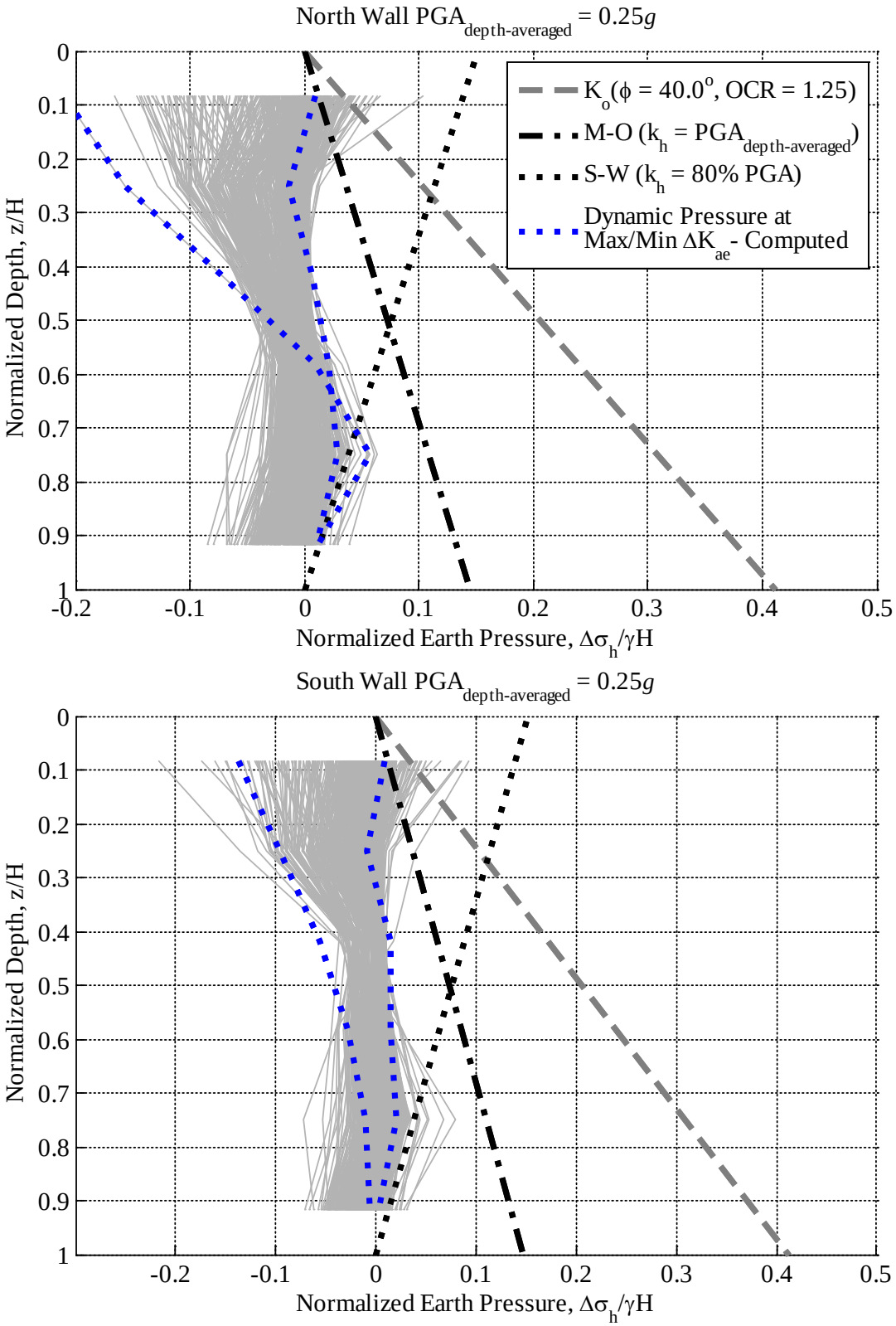

Figure B.130: Computed normalized dynamic earth pressure distributions at maximum and minimum ΔK_{ae} during Chi Chi TCU 075N for one bay, one level basement; Site Class C

Appendix C Design ground motion deconvolution procedure

This section describes the development of the one-dimensional soil column model and deconvolution procedure used to obtain input shear stress wave input for the prototype structure. Two procedures are outlined: one for a sandy soil profile similar to the centrifuge model (Darendeli, 2001) and one for a gravelly soil profile (Menq, 2003).

The basic parameters of the soil layer and the loading conditions are selected: density (ρ), specific gravity (G_s), friction angle (ϕ), cohesion (c), overconsolidation ratio (OCR), plasticity index (PI), vertical stress (σ_v), number of loading cycles (N), and loading frequency (f). For the gravelly soil profile, the following parameters are also required: coefficient of uniformity $(C_U = D_{60}/D_{10})$, and median grain size (D_{50}). The coefficient of at-rest earth pressure is estimated using Equation C.1 (Mayne & Kulhawy, 1982) and the mean confining stress is determined using Equation C.2.

$$K_o = \frac{\sigma_h}{\sigma_v} = (1 - \sin\phi) OCR^{\sin\phi} \quad \textbf{(C.1)}$$

$$\sigma_m = \frac{\sigma_v + 2\sigma_h}{3} = \sigma_v \frac{1 + 2K_o}{3} \quad \textbf{(C.2)}$$

For the sandy soil profile, the void ratio is estimated using basic volume relationships and the reference shear modulus is estimated using the Hardin (1978) relationship, where P_a is the reference pressure. Then, the maximum shear modulus and the maximum shear strength are computed. The relevant computations are shown in Equation C.3a,b,c and d.

$$e = \frac{G_s}{\rho} - 1 \quad \text{(a)} \qquad G_r = \frac{625}{0.3 + 0.7e^2} P_a \quad \text{(b)}$$

$$G_{max} = G_r \left(\frac{\sigma_m}{P_a}\right)^{0.5} \quad \text{(c)} \qquad \tau_{max} = c + \sigma_v \tan\phi \quad \text{(d)} \quad \textbf{(C.3)}$$

For the gravelly soil profile, a shear wave velocity is assumed at each layer and the maximum shear modulus is determined using Equation C.4.

$$G_{max} = \rho (V_s)^2 \quad \textbf{(C.4)}$$

The procedure developed by Darendeli (2001) is used to estimate the shear modulus degradation curve in the small strain range. The hyperbolic backbone curve in the small strain range defined in Equation C.5a is converted to a modulus degradation curve, as defined in Equation C.5b:

$$\tau = \frac{G_{max}\gamma}{1 + \beta\left(\frac{\gamma}{\gamma_r}\right)^{\alpha}} \quad \text{(a)} \quad \Rightarrow \quad \frac{G}{G_{max}} = \frac{1}{1 + \beta\left(\frac{\gamma}{\gamma_r}\right)^{\alpha}} \quad \text{(b)} \quad \textbf{(C.5)}$$

where β and α are fitting coefficients taken as $\beta = 1.0$, $\alpha = 0.9190$ for the sandy soil profile and $\alpha = 0.86 + 0.1\log(\sigma'_m/P_a)$ for the gravelly soil profile. The pseudo-reference strain for the sandy soil profile is estimated using Equation C.6, which has been simplified for use with clean, normally consolidated sand (i.e., $\mathrm{PI} = 0, \mathrm{OCR} = 1$). The pseudo-reference strain for the gravelly soil profile is estimated using Equation C.7.

$$\gamma_r = (0.0352 + 0.0010 \cdot \mathrm{PI} \cdot \mathrm{OCR}^{0.3246})\left(\frac{\sigma_m}{P_a}\right)^{0.3483} = 0.0352\left(\frac{\sigma_m}{P_a}\right)^{0.3483} \quad \textbf{(C.6)}$$

$$\gamma_r = 0.12(C_U)^{-0.6}\left(\frac{\sigma_m}{P_a}\right)^{0.5(C_U)^{-0.15}} \quad \textbf{(C.7)}$$

For the large strain range, the Yee et al. (2013) procedure is used, wherein a second hyperbola is appended to the original small strain hyperbola at a user specified transitional shear strain, γ_1, with an initial modulus $(G_{\gamma 1})$ that is the tangent modulus of the first hyperbola at γ_1. The second hyperbola asymptotically approaches the specified shear strength at large strains. The transitional shear strain is selected based on two limiting criteria: (1) γ_1 up to 0.3-0.5%, which is the upper bound of usable strain of the Darendeli (2001) model, and (2) the shear stress at γ_1 predicted with Equation C.5a (τ_1) provides an upper limit, with a practical limit of $\tau_1 \leq 0.3\tau_{max}$. For this study, $\tau_1 \leq 0.25\tau_{max}$ was selected as the limiting criteria for γ_1. With the transitional shear strain determined, the form of the second hyperbola can be written as Equation C.8:

$$(\tau - \tau_1) = \frac{G_{\gamma 1}\gamma'}{1 + \frac{\gamma'}{\gamma'_{ref}}} \quad \textbf{(C.8)}$$

where $\gamma' = \gamma - \gamma_1$, $\gamma'_{ref} = (\tau_{max} - \tau_1)/G_{\gamma 1}$, and $\tau_1 = G_{max}\gamma_1/[1 + (\gamma_1/\gamma_r)^{\alpha}]$. The equation for the second hyperbola mimics the first hyperbola except that $\beta = \alpha = 1$, the ordinates are expressed relative to a shifted set of axes with origin (γ_1, τ_1), and the pseudo-reference strain has been replaced by γ'_{ref}. The tangent shear modulus $G_{\gamma 1}$ is obtained as the derivative of Equation C.5a evaluated at γ_1 (Equation C.9).

$$G_{\gamma 1} = \left.\frac{\partial \tau}{\partial \gamma}\right|_{\gamma_1} = \frac{1 + (1-\alpha)\beta\left(\frac{\gamma_1}{\gamma_r}\right)^{\alpha}}{\left[1 + \beta\left(\frac{\gamma_1}{\gamma_r}\right)\right]^2} G_{max} \quad \textbf{(C.9)}$$

For $\gamma > \gamma_1$, the secant modulus corresponding to points on Equation C.8 can be computed as the sum of τ_1 (from Equation C.5a) and $\tau - \tau_1$ (from Equation C.8) normalized by the sum of γ_1 and γ', then converted to an equivalent modulus degradation curve as Equation C.10.

$$\frac{G}{G_{max}} = \frac{\frac{\gamma_1}{1+\beta(\gamma_1/\gamma_r)^{\alpha}} + \frac{(G_{\gamma 1}/G_{max})\gamma'}{1+(\gamma'/\gamma'_{ref})}}{\gamma} \quad \textbf{(C.10)}$$

For clarity, the equations for the modulus degradation in both regions are repeated (Equation C.11a and b).

$$\begin{aligned} \frac{G}{G_{max}} &= \frac{1}{1+\beta\left(\frac{\gamma}{\gamma_r}\right)^{\alpha}} && \gamma < \gamma_1 \quad \text{(a)} \\ \frac{G}{G_{max}} &= \frac{\frac{\gamma_1}{1+\beta(\gamma_1/\gamma_r)^{\alpha}} + \frac{(G_{\gamma 1}/G_{max})\gamma'}{1+(\gamma'/\gamma'_{ref})}}{\gamma} && \gamma > \gamma_1 \quad \text{(b)} \end{aligned} \quad \textbf{(C.11)}$$

The procedure developed by Darendeli (2001) is used to estimate the damping curve for both soil profiles; the assumptions of Masing (1926) behavior are utilized with a reduction factor to reduce the overdamped response at high strains. First, the stored strain energy is computed as Equation C.12a and the dissipated energy (the area inside a complete hysteresis loop) is related to the integral of the stress-strain curve as Equation C.12b

$$A_T = \frac{1}{2}\tau\gamma \quad \text{(a)} \qquad A_L = 8\left(\int \tau d\gamma - \frac{1}{2}\tau\gamma\right) \quad \text{(b)} \quad \textbf{(C.12)}$$

Equivalent viscous damping is expressed as Equation C.13, and substituting Equation C.12a and b, Masing-behavior damping is written as a function of strain amplitude as Equation C.14.

$$D_{eq} = \frac{A_L}{4\pi A_T} \quad \textbf{(C.13)}$$

$$D_{Masing} = \frac{4}{\pi}\frac{\left(\int \tau d\gamma - \frac{1}{2}\tau\gamma\right)}{\tau\gamma} \quad \textbf{(C.14)}$$

The integration in Equation C.14 cannot be evaluated algebraically for most $\alpha \neq 1.0$, or when the shear stress is governed by the piecewise hyperbolic function described by Equation C.11a and b. Instead, the integration is performed numerically with a trapezoidal integration rule and a step-size of $\Delta\gamma = 10^{-4}\%$. The Masing damping values calculated for high strains are larger than experimental results, and Masing behavior lacks small strain damping, D_{min}. To alleviate this, Darendeli (2001) proposed a correction for the damping curve as Equation C.15:

$$D = F \cdot D_{Masing} + D_{min} \quad \textbf{(C.15)}$$

where the function F is defined in Equation C.16 and D_{min} is defined in Equation C.17 for the sandy soil profile and Equation C.18 for the gravelly soil profile.

$$F = (0.6329 - 0.0057\ln(N))\left(\frac{G}{G_{max}}\right)^{0.1} \quad \textbf{(C.16)}$$

$$D_{min} = (0.8005 + 0.0129 \cdot \mathrm{PI} \cdot \mathrm{OCR}^{-0.1069})\left(\frac{\sigma_m}{P_a}\right)^{-0.2889}[1 + 0.2919\ln(f)] = 0.8005\left(\frac{\sigma_m}{P_a}\right)^{-0.2889}[1 + 0.2919\ln(f)] \quad \textbf{(C.17)}$$

$$D_{min} = 0.55(C_U)^{0.1}(D_{50})^{-0.3}\left(\frac{\sigma_m}{P_a}\right)^{-0.05} \quad \textbf{(C.18)}$$

The procedure developed by Silva (1988) was followed for the deconvolution of the target surface motions. The approach of Silva (1988) is intended to avoid the situation of unrealistic motions being calculated at depth from assuming that the total surface motion is due to vertically propagating shear waves. The steps suggested by Silva (1988), which were used in this study, are outlined as follows:

1. Process the target recorded surface motion with a 15 Hz low pass filter and scale by 0.87.
2. Input the processed surface motion at top of soil column and perform an equivalent linear deconvolution analysis.
3. Obtain the final iteration values of shear modulus degradation (G/G_{max}) and material damping (D) for each layer during the deconvolution analysis.
4. Apply the values obtained in Step 3 to each of the layers in the soil column, and perform a linear deconvolution analysis using the target recorded surface motion with a 15 Hz low pass filter and scaled by 1.0.
5. Obtain the deconvolved motion at the depths of interest as an outcropping or within motion.

SHAKE2000 (Ordonez, 2011), which incorporates SHAKE (Schnabel, Lysmer & Seed, 1972) and SHAKE91 (Idriss & Sun, 1992), was used to perform the deconvolution analysis. The effective strain ratio proposed by Idriss & Sun (1992) was used (Equation C.19).

$$\left|\gamma_{eff}/\gamma_{max}\right| = (M_w - 1)/10 \quad \textbf{(C.19)}$$

The outcropping motion obtained from the deconvolution analysis at the base of the soil column was converted to the upward propagating motion by multiplying the outcropping acceleration record by 0.5. The upward propagating motion was integrated in the frequency domain with a 5th order Butterworth 0.25 Hz high pass filter and a 5th order Butterworth 15 Hz low pass filter to obtain the upward propagating velocity. The upward propagating velocity was then converted to a shear stress wave using Equation C.20:

$$\sigma_s = 2C_s\rho v_s \quad \textbf{(C.20)}$$

where $C_s = \sqrt{G_{max}/\rho}$ is the shear wave velocity at the base of the numerical model and the factor of 2 accounts for the fact that half of the input energy is absorbed by the quiet boundary.

The acceleration record obtained from SHAKE2000 was processed in a linear deconvolution process; however, the shear modulus at the base of the soil column in the analysis was the degraded modulus G, not G_{max}. Also, continuity of shear stresses are utilized in the formulation of the frequency domain solution, so an additional factor of $\sqrt{G/G_{max}}$ is necessary to obtain the strain compatible shear stress wave. The modified conversion from a velocity wave to a shear stress wave is then Equation C.21.

$$\sigma_s = 2C_s\rho\sqrt{G/G_{max}}\,v_s = 2\sqrt{G\rho}v_s \qquad \textbf{(C.21)}$$